Ex-situ Observation and Characterization of Mild Hydrotreated Liquid Products

by

Daniel Palys

A thesis submitted in partial fulfillment of the requirements for the degree of

Master of Science
in
Chemical Engineering

Department of Chemical and Materials Engineering
University of Alberta

Abstract

On-line analytical tools are needed to optimize the upgrading process. This technology could reduce environmental impacts, reduce costs, and enhance quality control of heavy oil feeds. Ultraviolet and visible spectroscopy, a well established ex-situ technique, is one example that could potentially be developed. The current challenge of this technology is heavy oil chemical complexity and its dynamic compositional transformations in upgrading.

The current study focuses on enhancing knowledge of hydrotreating reactions of an intermediate Heavy Vacuum Gas Oil (HVGO) feed derived from Athabasca Bitumen. A batch microreactor with sulfided Ni-Mo/γ-Al$_2$O$_3$ catalyst pellets and <45μm solids were used. A range of reaction temperatures, 290-390°C, and times, 0.25-2h, were tested. To assess product quality, ex-situ observation and characterization of the hydrotreated liquid products were completed. Carbon, hydrogen, sulfur, nitrogen, density, boiling point distribution, and hydrogen nuclear magnetic resonance were completed to characterize the liquid products. A visible spectroscope was developed to observe and measure the hypsochromic color changes of the liquid products.

Chemometric analysis with four modeling methods were completed to calibrate the visible adsorption spectra to the physicochemical properties obtained from characterization. Multiple linear regression and partial least squares regression were found as optimal modeling methods. Depending on the data set used, sulfur, nitrogen, initial boiling point to 300°C fraction, 400 to 500°C fraction, density, total aromatic hydrogen and its conversion, were found as the best properties calibrated. The 57, 81, and 77wt.% fractions off from the boiling point distribution curve using multiple linear regression were found to be the best models overall.

Acknowledgements

Thank you to the University of Alberta and the Chemical and Materials Engineering Department in the opportunity given to purse research for the public good in a diverse, friendly, and safe environment.

Thank you to several on campus organizations for assistance throughout the course of this research. The nuclear magnetic resonance group in the chemistry department, the ICPMS Facility from Earth and Atmospheric Sciences, Dr. de Klerk's group, the CME machine shop, the Institute for Oil Sands Innovation, the Graduate Students Association, the Chemical and Materials Engineering Graduate Student Association, the Canadian Heavy Oil Association student chapter, Cameron library, and the Van Vliet Complex.

Thank you to lab personnel and friends for assistance, encouragement, and kindness in the journey of this research: Cedric Laborde-Boutet, Shaofeng Yang, Andree Koeing, Xiaoli Tan, Brittany Mackinnon, Cibele Melo Halmenschlager, Miguel Medina, David Dinh, Samuel Cardozo D'Armas, Geraldine Fournier, Allen Reule, Gonzalo Rocha Aguilera, Benjamin Antwi Peprah, and Benjamin Wiltshire.

Thank you to the Chemical and Materials Engineering Department and Staff for the professional support and providing a valuable education. Thank you to Dr. Murray Gray and Dr. Vinay Prasad for the helpful technical discussions. Thank you to Sandra McFadyen, Marion Pritchard, and Lily Laser for providing excellent assistance.

With all the generous time, conversations, technical discussions, assistance, support, opportunities, kindness, mentorship, and patience, thank you to Dr. William McCaffrey for the valuable and rewarding educational experience. It has been a delightful time that I am personally grateful for.

Thank you to my family for supporting me throughout graduate school. Thank you to *Jennifer*, your endless patience and unconditional love has provided me strength, courage, and resiliency in pursuing my passions.

Table of Contents

List of Figures

List of Tables

Nomenclature and Abbreviations

^{1}H NMR	Hydrogen Nuclear Magnetic Resonance	R^{2}_{adj}	Adjusted Coefficient of Determination
AIC	Akaike Information Criterion	RGO	Reference Gas Oil
AIC$_c$	Corrected Akaike Information Criterion	RMSE	Root Mean Squared Error
AIC$_{min}$	Minimum Akaike Information Criterion	RSE	Relative Squared Error
AIC$_u$	Unbiased Akaike Information Criterion	SSE	Sum of Standard Errors
ASTM	American Standard Test Methods	UV-Vis	Ultraviolet-Visible
BIC	Bayesian Information Criterion		
BPD	Boiling Point Distribution		**Variables**
CHNS	Carbon, Hydrogen, Nitrogen, Sulfur	A	Absorbance
SLS	Simple Least Squares	C	Carbon (wt.%)
DBE	Double Bond Equivalence	E_a	Activation energy (kJ/mol)
DCM	Dichloromethane	H	Hydrogen (wt.%)
EMR	Electromagnetic Resonance	k	Number of parameters Rate constant
FBP	Final Boiling Point	l	Path length (mm)
FID	Flame Ionization Detector	N	Nitrogen (wt.%)
H/C	Hydrogen to Carbon Ratio	n	Reaction order
HDA	Hydrodearomatization	S	Sulfur (wt.%)
HDM	Hydrodemetallization	ε	Molar absorptivity, Emissivity, Intercept
HDN	Hydrodenitrogenation	λ	Wavelength (nm)
HDO	Hydrodeoxygenation	ν	Frequency (Hz)
HDS	Hydrodesulfurization		
HVGO	Heavy Vacuum Gas Oil		**Units**
IBP	Initial Boiling Point	°C	Degrees Celsius
ICP-MS	Inductively Coupled Plasma Mass Spectrometry	g/ml	Density, grams per millilitre
LHSV	Liquid Hourly Space Velocity	h	Hour
MSPE	Mean Squared Prediction Error	K	Kelvin
NIR	Near-Infrared	kg	Kilograms
OATs	Online Analytical Tools	kg/m^3	Kilograms per cubic meter
OD	Optical Density	nm	Nanometer
PAHs	Polycyclic Aromatic Hydrocarbons	m^3	Cubic Meters
PAT	Process Analytical Technology	MPa	Megapascal
PC	Principal Component	RPM	Rounds Per Minute
PCA	Principal Component Analysis	Sm^3	Standard cubic meters
PCR	Principal Component Regression	wppm	Parts per million by weight
PLSR	Partial Least Squares Regression	wt.%	Weight percent
R^2	Coefficient of Determination	μm	Micrometers

Chapter 1: Introduction and Objectives

1.1 Introduction

The International Energy Agency (IEA) reported worldwide oil product demand (including biofuels) averaged 95.5 million barrels per day (mb/d) in the year 2016 [1-2]. Global oil product demand is forecasted to span anywhere from 80 to 122mb/d by 2040 contingent on energy frameworks and policies in place [2]. With such a reliance on the fossil fuel, production of unconventional petroleum is one source of global energy demands. From 2015-2016, this production accounted for 8.4 to 8.5mb/d and forecasted to reach anywhere from 11 to 20mb/d by 2040 [2-4]. Sources of unconventional petroleum include extra-heavy oil and crude bitumen, this accounted for 3.3mb/d of production in 2016 [2].

Crude bitumen is an extra-heavy dense petroleum comprised of large carbon based molecular structures. This complex mixture of large molecules results in a highly viscous property ($>10^5$mPa·s), causing bitumen recovery to be challenging. With current extraction and production technologies, Alberta has circa 165 billion barrels of proven crude bitumen reserves [5]. Of these 165 billion barrels, crude bitumen is found blended with sand and clay on the surface, oil sands (32 billion barrels), or in underground reservoirs, in-situ (133 billion barrels).

From 2015-2016, production of crude bitumen in Alberta averaged 2.45-2.5mb/d and forecasted to increase to 4mb/d by 2025, contingent on favorable economics, market access, energy policies, limited production upsets (e.g. environmental disasters, transportation failures, shutdowns etc.), and global energy demands [2][5-6]. However, critical assessment should be used when such production forecasts are reported. For example, in 2008 the Alberta Energy Regulator (AER), formerly the Energy Resources Conservation Board (ERCB), forecasted production to reach 3.23mb/d by 2017 [7].

Extracted crude bitumen can be diluted to reduce viscosity for transportation by pipeline or rail to global markets. Alternate crude bitumen can be upgraded and refined in Alberta to higher valued liquid products. Upgrading, a generic term that describes processing of crude bitumen, heavy oil, and vacuum residue, adds economic value by one or a combination of the following [8]:

- Increasing American Petroleum Institute (API) gravity (or decreasing density)

- Reducing viscosity

- Increasing hydrogen to carbon Ratio (H/C)

- Removing undesirable atoms and contaminants chemically bonded within the carbon based molecular structures

An upgrader processing complex, illustrated in *Figure 1.1*, can include separation, primary, and secondary upgrading technologies. Separation includes desalting, distillation, and deasphalting (solvent refining) [8-9]. Primary upgrading technologies include thermal cracking and thermal catalytic (e.g. visbreaking, coking and hydroconversion) [8][10]. Secondary upgrading technologies include hydrotreating and hydrocracking [8][10]. Technologies with hydrogen addition and catalysts can be classified as hydroprocessing (e.g. hydroconversion, hydrotreating, and hydrocracking); the major differences between these hydroprocessing technologies are feedstocks, operating conditions, and catalysts [8]. Technologies in separation, primary, and secondary upgrading are also found in conventional refineries.
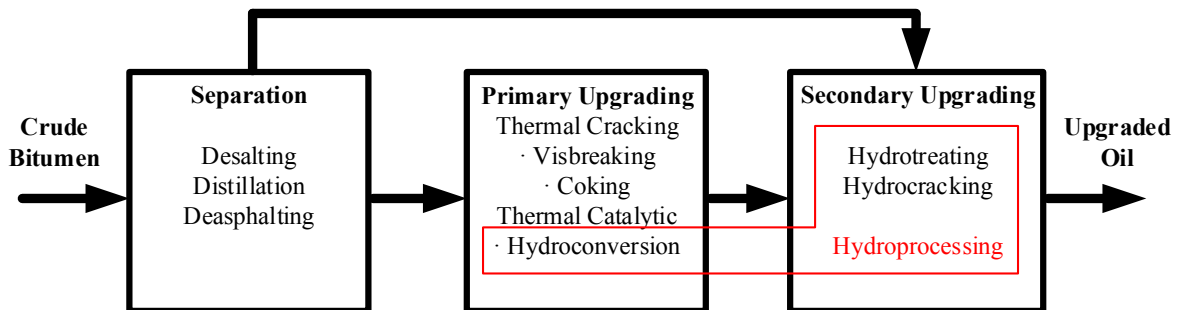
Figure 1.1. Upgrader Processing Complex.

Refining is the processing of intermediate, upgraded or conventional crude oil feeds to lighter (lower boiling) and highly specified liquid products [8]. Upgraded oil can be refined in Alberta or transported to worldwide refineries. Refineries produce higher value transport fuels such as aviation, diesel, gasoline, and feedstocks for petrochemical processes.

The unconventional feeds processed (crude bitumen and extra-heavy oils) in upgrading comprise of higher boiling point molecular structures, higher aromatic, sulfur, nitrogen, oxygen, and metal

contaminant concentrations compared to conventional crude oils. These molecular structures, atoms, and contaminants (e.g. +525°C residue, aromatics, sulfur, nitrogen, oxygen, and metals) are undesirable to refineries for several reasons [11-12]:

- Increased material corrosion in transportation, storage, and refining
- Increased maintenance of processing equipment and catalysts
- Reduced product quality (impacts downstream transportation fuel stability and efficiency)
- Increased environmental regulations and restrictions (e.g. 10ppmw sulfur in gasoline, 15ppmw sulfur in diesel [13-14])

Due to these undesirable qualities, raw unconventional feeds (non-upgraded) are discounted in price compared to conventional crude oil, specifically by American refiners [15]. In secondary upgrading, hydrotreating technology reduces concentrations of sulfur, nitrogen, oxygen, and contaminants (halides and metals) catalytically under hydrogen pressure and un-destructive temperature to improve product quality. Olefins and aromatics are saturated to paraffins and naphthenes, respectively. The reactions to reduce such concentrations and saturate hydrocarbon molecules are defined in literature [8]:

- Hydrodesulfurization (HDS)
- Hydrodenitrogenation (HDN)
- Hydrodearomatization (HDA)
- Hydrodemetallization (HDM)
- Hydrodeoxygenation (HDO)

Catalyst performance is crucial to hydrotreating operation. The importance of an active and stable catalyst throughout the duration of operation is imperative to produce consistent product quality. The size and shape of the catalyst impacts the rates of the five reactions listed. Factors such as reaction temperature and time impact product quality. The effects of catalyst activity, catalyst size, reaction temperature, and reaction time on liquid product quality are known in hydrotreating literature. Questions regarding these effects are complimentary objectives in the current study.

To assess product quality, samples of intermediate feeds and products are analyzed using standard analytical methods (e.g. American Society for Testing and Materials or ASTM [16]) to quantify

their physicochemical properties [17]. Accurate property data is significant for operators to assess performance and optimize process control. Over significant periods of operation, researchers use property data to enhance fundamental knowledge of the process, understand reaction chemistry, hypothesize reaction mechanisms, and develop modeling algorithms. Results from these models lead to operational improvements and enhanced process design, an example is optimal catalyst development for increasing fuel regulations [18].

Standard analytical methods can be complex, time consuming, require skilled lab technicians, and expensive equipment [19-23]. Accuracy and consistency between laboratories as well as lab technicians could yield unreliable results [20][23]. The argument of additional environmental impacts of standard laboratory analysis is debated [21]. Development of effective analysis technology to accurately measure properties online with real time feedback (Process Analytical Technology (PAT) [24]) is desired for extraction, upgrading, and refinery process. Implications in the field could:

- Reduce environmental impacts
- Decrease the time required to quantify product properties and enhance quality control
- Maximize process control and optimize in real time
- Enhance understanding of the physical and chemical phenomena in the process

All these implications could improve understanding for optimization and address sustainability challenges. In addition to addressing questions regarding catalyst performance and reaction condition effects, the current study is the initial background research to develop a potential online analysis tool following heavy oil hydrotreating processes. Examples of spectroscopic Online Analytical Tools (OATs) developed by Oliver Mullins et al., Schlumberger, and others for in-situ oil characterization of crude oil in reservoirs exist [25-29]. Insight Analytical uses online infrared spectroscopy for determination of physicochemical properties of crudes and condensates [30]. Several of the spectroscopic examples depend on data processing and advanced chemometric models. Accurate models are crucial for OAT software. Calibration, validation, and maintenance of these models are imperative for industrial implementation [23].

However, current challenges to OATs exist for oil sands extraction and crude bitumen upgrading processes [23]:

1. Probe or sampling port erosion and corrosion
2. Multiphase flow complexity (solids and liquids)
3. Controlled sampling and measurement
4. Chemical complexity of heavy oil feeds and their dynamic compositional transformations

1.2 Objectives

To address the fourth challenge of OATs, the goal of this thesis is to enhance knowledge of mild hydrotreating reactions for a heavy vacuum gas oil (HVGO) feed derived from Athabasca bitumen. The thesis objective is implemented into four parts:

1) Conduct experimental hydrotreating reactions in a batch microreactor.
2) To assess product quality, characterize hydrotreated liquid products by several analytical methods to understand the chemical complexity:
    a) Carbon and Hydrogen
    b) Sulfur and Nitrogen
    c) Density
    d) Boiling Point Distribution
    e) Hydrogen Proton Nuclear Magnetic Resonance
    f) Visible Absorption Spectrum
3) Evaluate the dynamic compositional transformations tested:
    a) What are the experimental control effects?
    b) What is the effect of using a catalyst on product quality?
    c) What is the effect of mixing on product quality?
    d) What is the effect of using unsulfided versus sulfided catalyst on product quality?
    e) What is the effect of reaction temperature and time on product quality?
    f) What is the effect of catalyst size, trilobed pellets versus <45μm solids, on product quality?

4) Investigate if visible spectra of the liquid products can be calibrated to their analytical characterization results through chemometric analysis. The following three questions are addressed:

    a) Can the visible spectra of the liquid products be calibrated to their physicochemical properties characterized in objective two?

    b) Which data sets and modelling methods provide the best calibration results?

    c) Through selection criterion, which calibration models are optimally favoured?

Chapter 2: Literature Review

2.1 Hydrotreating

Background understanding of hydrotreating and the dynamic compositional transformations of intermediate oil feeds are important prior to the development of spectroscopic Online Analytical Tools (OATs). A review of the history, oil feeds, process, catalyst, chemistry, and reactions are reviewed in section 2.1.

2.1.1 History of Hydrotreating

A commendable summary of hydrotreating history is found in the Handbook of Petroleum Processing (pg. 322) [1]. In 1897, Sabatier and Senderens discovered hydrogenation of hydrocarbons with a nickel catalyst. Ipatieff found increasing hydrogen pressure was feasible for hydrogenation reactions in 1904. In 1910, Bergius used ferric oxide to remove sulfur from heavy oils. Sweeting to reduce sulfur and odor from crude oils was first implemented in 1916 [2]. In 1927, hydrogenation of brown coal started in Germany. In the 1930s, the Standard Oil Company of Louisiana constructed the first hydrorefiner in Baton Rouge (hydrogenation to remove sulfur in 1932 [2]). In 1943, cobalt-molybdenum supported on alumina catalysts were used for sulfur removal [3]. Over the 20th century, significant advances in catalyst science and hydrotreating technology have been developed to process higher sulfur, nitrogen, and metal feeds compared to conventional crude oils. In 1990, approximately 30 hydrotreating technologies were available for licensing [2][4]. By 2001, 1,600 hydrotreaters were operating worldwide [1]. Approximately 20% of the total energy consumption of an upgrader/refinery is for hydrotreating [2].

2.1.2 Hydrotreating Key Factors

A visual diagram highlighting the key factors that affect hydrotreating are shown in *Figure 2.1* [4-5].

- Density
- Boiling Point Distribution
- Sulfur Concentration
- Nitrogen Concentration
- Aromatics Concentration
- Physicochemical Properties

- Reactor Configuration
- Bed Configuration
- Process Conditions
- Pressure Drop

Feed ← **Process**

Hydrotreating

↓

Catalyst

- Preparation
- Supports
- Sulfidation
- Active Metals
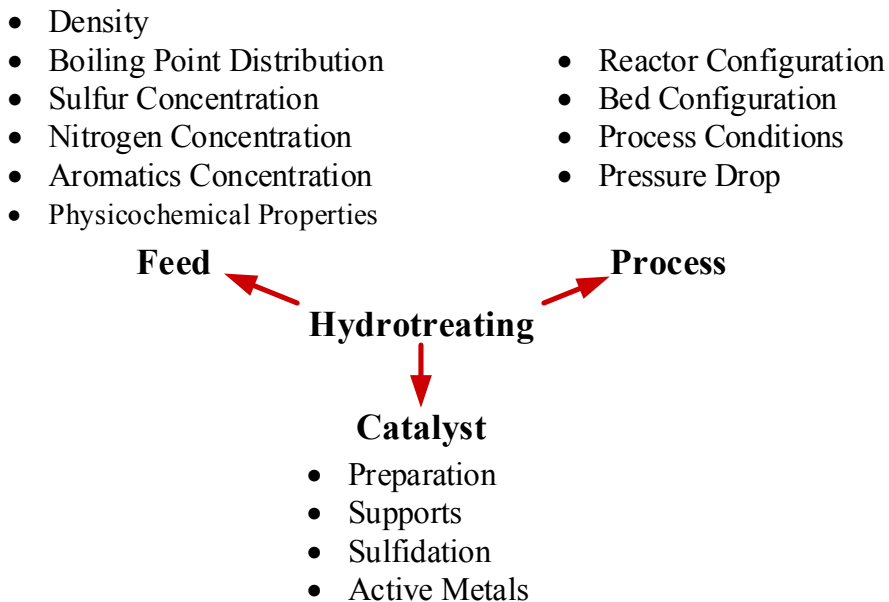
Figure 2.1. Key factors that affect hydrotreating [4-5].

2.1.3 Hydrotreating Feeds

Typical hydrotreating feeds derived from Athabasca Bitumen with properties found in upgrading facilities are presented in *Table 2.1* [5-14]. Products from separation and primary upgrading technologies, or untreated intermediate feedstocks, are hydrotreated prior to storage or further refinement. As each upgrader and refinery is unique, properties reported are not absolute and fall under different naming or property classifications depending on the operator.

Table 2.1. Typical hydrotreating feeds in upgrading facilities derived from Athabasca Bitumen and their respective properties found in upgrading facilities [5-14].

Property	Hydrotreating Feeds				
	Virgin Light Gas Oil	Light Vacuum Gas Oil	Heavy Vacuum Gas Oil	Fluid Coker Naphtha	Fluid Coker Gas Oil
Boiling Point Range (°C)	122 - 447[6] 136 - 358[9]	255 - 436	244 - 623	15.4 - 290[8]	196 - 655
Density (kg/m^3)	880 – 900	935 - 940	967 - 971	782 - 799	980 - 1004
Sulfur (wt.%)	1.34 - 1.76	2.34 - 2.67	2.92 - 3.59	1.44 - 1.68	4.01 - 4.27
Nitrogen (wt.%)	0.02 - 0.03	0.034 - 0.063	0.14 - 0.19	0.18 - 0.24	0.297 - 0.40
H/C	1.72 - 1.77	1.67	1.53 - 1.56	1.76	1.44 - 1.48
Aromatics (wt.%)	32.1 - 36.3	-	59.7 - 65.6	27	70.1
Saturates (wt.%)	-	-	28.7 - 31.2	72-73	20.6

Hydrotreating feeds derived from Athabasca Bitumen have distributions of properties that are dependent on how separation and primary technologies are operated in upgrading facilities. The data in *Table 2.1* highlights the chemical complexity of the oil feeds. The virgin light gas oil is a liquid product from atmospheric separation. The light and heavy vacuum gas oils are liquid products from vacuum separation. The fluid coker gas oil is typically a combined blend of light and heavy coker gas oil products of fluid coking technology (i.e. thermal cracking).

Boiling Range Classification

The properties in *Table 2.1* are in constant flux. The operation of upgrading processes are continuously dynamic (i.e. not steady-state). This causes deviations in the liquid products, resulting in the range of concentrations specified. Boiling range classifications depend on the upgrader distillation technology used in separation. Depending on the measurement, boiling temperatures overlap in the ranges cited. The boiling range presented in *Table 2.1* is the minimum initial boiling point (IBP) to the maximum final boiling point (FBP) reported from the references specified. Oil assay's report specific fraction designations or the 5-10% to 90-99% boiling point temperature range because of distillate tails generated from the analytical method. The boiling

range temperatures are dependent on additional distillation technologies following primary upgrading.

Light and Heavy Classification

A second classification is light and heavy oil feeds. Characteristics of light feeds are defined by low boiling point ranges (<343°C final boiling point), low density (<900kg/m^3), and low viscosity (<100mPa.s). Examples include naphtha, gasoline, diesel, kerosene, jet fuels, and light gas oils [15]. These light feeds are low molecular weight distributions of well-defined chemical structures and have higher concentrations of saturated molecules compared to aromatic molecules. Characteristics of heavy feeds are described by high boiling point ranges (+343°C initial boiling point), high density (>900kg/m^3), and high viscosity (>100mPa.s). Examples include heavy gas oils, vacuum gas oils, and residues (+500°C initial boiling point) [15]. These heavy feeds are chemically complex with higher molecular weight distributions (>300g/gmol), higher concentrations of sulfur, nitrogen, and aromatics compared to light feeds.

Sulfur Concentration Classification

Regarding sulfur concentration, sour crude is defined as greater than 0.5wt.%, sweet crude is defined as less than 0.5wt.%.

Property Relationships

Relationships exist relating physical characteristics to chemical composition of oils. The liquid density is related to molecular composition [15]. The following is an example of a linear correlation developed to predict density for heavy oil and intermediate feeds found in Alberta [16]:

$$\rho = 1033 - 13.69 \cdot H + 13.85 \cdot S + 115.7 \cdot N \qquad (2.1)$$

Where **H** is the hydrogen concentration (wt.%), **S** is the sulfur concentration (wt.%) and **N** is the nitrogen concentration (wt.%). The linear model had a coefficient of determination (R^2) of 0.95 in predicting heavy oil densities [16]. From the correlation, the addition of hydrogen or the removal of sulfur and nitrogen decreases the density, as indicated by the sign of each coefficient. Therefore, as these chemical reactions occur in hydrotreating, the density of the liquid product is expected to

decrease. However, this equation is limited and does not include other carbon and oxygen atoms part of the oil composition.

The hydrogen to carbon ratio (H/C) is the molecular ratio of hydrogen to carbon atoms in found in hydrocarbon molecules. For example, straight paraffins (C_nH_{2n+2}) from C_4 to C_{100} have an average H/C ratio of 2.1. Aromatics as in benzene (C_nH_n), have a H/C ratio of 1. From *Table 2.1*, the H/C range of the hydrotreating feeds provide insight into the complex distribution of chemical structures present. Lower values suggest the oil is comprised of additional aromatic and less paraffinic hydrocarbon molecules. Higher values suggest the oil is comprised of more paraffinic and less aromatic hydrocarbon molecules.

Accurate property data from *Table 2.1* is imperative in upgrading operation to identify the physical or chemical transformations happening. Operators and control systems apply adjustments to the process conditions (e.g. temperature, pressure, flow rate, etc.) to mitigate significant deviations of these properties. With continuous on-stream time, these adjustments are completed because of cumulative fouling, corrosion, condensation of heavier fractions, and solid fine contamination in separation and primary upgrading processes. As stated in the objective, the current study focuses on Heavy Vacuum Gas Oil (HVGO) feedstock as highlighted in the middle column of *Table 2.1*.

2.1.4 Hydrotreating Process

A generic Block Flow Diagram (BFD) of hydrotreating processes in an upgrader complex is illustrated in *Figure 2.2* [10][12][17]. Hydrotreating process conditions for feeds are presented in *Table 2.2* [3][18-19]. Hydrotreaters receive intermediate feedstocks from separation or primary upgrading processing technologies. Distillates and cracked liquid product distillates are the intermediate feedstocks for hydrotreaters from *Table 2.1*.
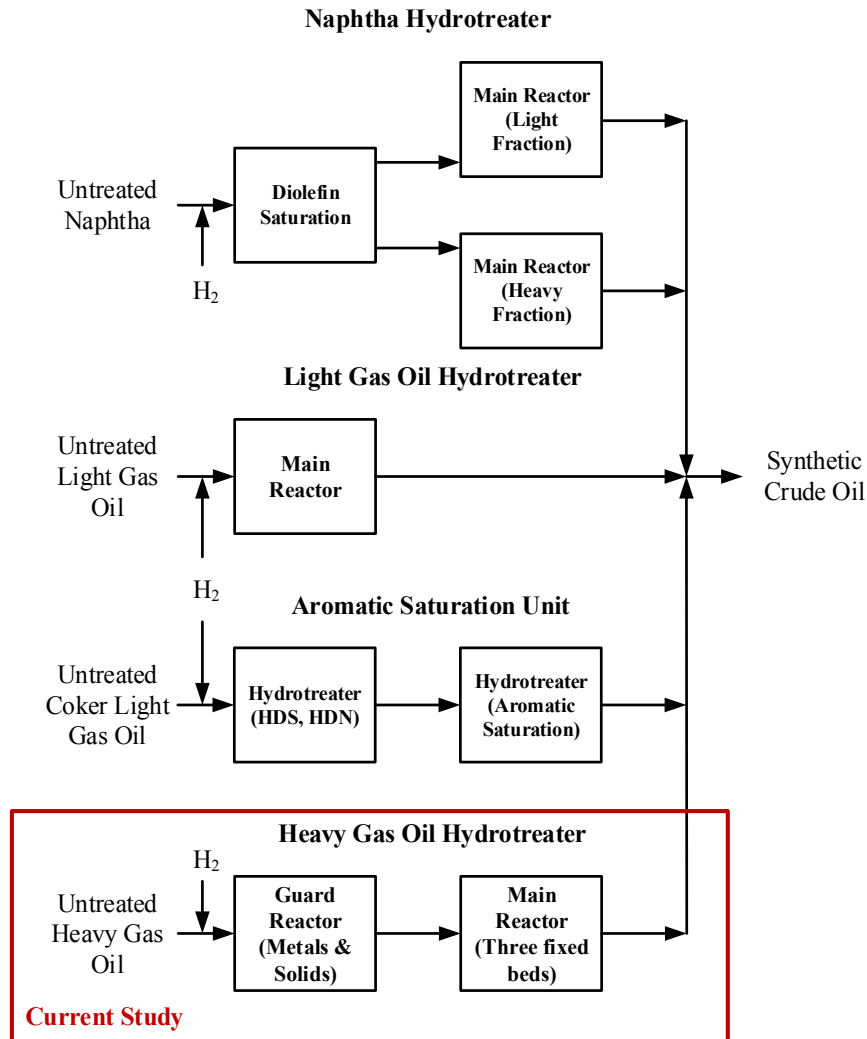
Figure 2.2. Block flow diagram of hydrotreating processes [10][12][17].

Untreated intermediate feedstocks are processed in specific hydrotreating trains; each train consists of multiple reactors for specific catalytic reactions to stabilize and remove unwanted (sulfur, nitrogen, and metals). The feeds are heated and blended with hydrogen prior to each packed bed reactor. The fixed bed configuration is co-current downflow with liquid feed trickling through a packed bed of catalyst pellets. Optimal liquid feed and hydrogen gas dispersion is vital through the catalyst bed for ideal performance. The wetting efficiency of the liquid feed through the catalyst bed is a key factor in the reactor design. Research on catalyst wetting for trickle bed reactors with comparison to other configurations for future reactor designs is found elsewhere [20-22].

Hydrotreating reactions are exothermic and generate heat, therefore temperature control is important in operation. To maintain temperature and hydrogen partial pressure, cold hydrogen is added [15]. Excess hydrogen from a recycle and a make-up stream are used. Multiple beds of catalyst are used in the reactor to allow for targeted hydrotreating reactions. The top bed comprises of catalyst that remove metals and solid fines. The bottom bed typically contains catalyst that remove sulfur and nitrogen atoms. For heavier feeds (heavy gas oils) the addition of a guard reactor to the configuration prior to the main reactor is common for metal removal and other entrained matter [23]. Each train consists of the reactors section followed by a separation section. Hydrogen sulfide and ammonia gases are separated following the reactors section. These gases are treated in alkanolamine absorption units. As noted in *Figure 2.2*, the current study is narrowed to untreated heavy gas oil, specifically heavy vacuum gas oil.

Table 2.2. Hydrotreating process conditions for four feedstocks [3][18-19].

Feed	Operation Temperature (°C)	Hydrogen Partial Pressure (MPa)	Liquid Hourly Space Velocity (h^{-1})	Hydrogen Consumption (Nm^3 / m^3 feed) [3] Hydrogen Rate (Nm^3 / m^3 feed) [18]	Catalyst Life (Months)	Catalyst Use (m^3 feed / kg catalyst)
Naphtha	300 - 370	0.7 - 3.2	3 - 8	2 - 10 40 - 250	36 - 48	175 - 420
Kerosene	330 - 370	1 - 4.2	2 - 6	5 - 15 80 - 250	36 - 48	105 - 210
Gas Oil	340 - 400	1 - 4.9	1.5 - 6	20 - 40 170 - 340	36 - 48	70 - 140
Vacuum Gas Oil	360 - 400	3.2 - 13.9	0.8 - 3	50 - 80 170 - 680	36 - 48	20 - 120

Operation Temperature

The operation temperature increases as the oil feeds become chemically complex because of higher concentrations of sulfur, nitrogen, and aromatics shown in *Table 2.2*. As hydrotreating reactions are exothermic, the temperature increases through the catalyst bed cause the inlet to be less than outlet temperature [24]. Over the course of operation (36-48 months), the catalyst deactivates. To offset this, the operators increases the average temperature of the bed to maintain constant product properties. However, an optimal balance is required to not operate at excessive temperatures to prevent thermal degradation and sintering of the catalyst [25]. The operation temperature is un-destructive and less than 400 to 420°C. Operation greater than these temperatures are undesired to prevent hydrocracking reactions. Additionally, operation below 400°C reduces the rate of coke formation in the bed [15].

Hydrogen Partial Pressure

The hydrogen partial pressure increases for heavier oil feeds, as highlighted in *Table 2.2*. To minimize thermal cracking and coking reactions, hydrogen in the presence of a catalyst, saturates the oil molecules. Increasing the pressure raises the solubility of hydrogen in the liquid phase [26]. A high solubility of hydrogen in the liquid phase enhances the mass transfer through the porous catalyst, thus improving the rate of hydrotreating reactions. Experiments to obtain hydrogen solubility coefficients, for the HVGO used is this study, have been reported to range from 0.014 to 0.072 moles hydrogen/kg of HVGO/MPa at 80°C to 330°C, respectively [26].

Liquid Hourly Space Velocity

As reported in *Table 2.2*, the Liquid Hourly Space Velocity (LHSV) decreases for heavier oil feeds. The LHSV is defined as the volumetric flow rate of the feed over the volume of catalyst in a fixed bed reactor:

$$LHSV\ (h^{-1}) = \frac{Feed\ Flowrate\ (\frac{m^3}{h})}{Volume\ of\ Catalyst\ (m^3)} \tag{2.2}$$

The ratio is the inverse of residence time; the total time liquid remains in the packed bed of catalyst. A lower LHSV is used for heavier feeds because of higher concentrations of sulfur, nitrogen, and aromatics compared to lighter feeds.

Hydrogen Consumption and Hydrogen Rate

The hydrogen consumption and hydrogen rate increase with heavier oil feeds, as shown in *Table 2.2*. In operation, hydrogen consumption is new hydrogen feed added to the process. The hydrogen rate is the addition of recycled hydrogen after product gas-liquid separation and amine scrubbing following the reactor. The Nm^3 is normal conditions at 20°C and 101.3kPa. The rate is used to define the gas to oil ratio. In operation, the gas to oil ratio is at least four times the amount of hydrogen consumption reported [1]. The four times rule is seen from hydrogen consumptions in *Table 2.2*. Operation and maintenance of hydrotreating vessels is important as hydrogen is highly flammable. Safety precautions and leak detections are implemented prior to operation.

Catalyst Life and Catalyst Use

The catalyst life is consistent for the feeds; however, the usage decreases with heavier feeds. These heavier feeds contain metals, solid fines, and high concentrations of heteroatoms that accumulate inside the catalyst pores and cause faster deactivation compared to lighter feeds. Depending on the properties of the feed, a catalyst life of 1 to 3 years is common. In a shutdown, the catalyst is replaced.

Pressure Drop

Pressure drop in the reactor affects hydrotreating performance. The pressure drop is the difference in pressure between the top and bottom of the reactor. The pressure drop divided by the vertical length of the vessel or bed is commonly reported in literature. A significant increase in pressure drop could cause a reactor shutdown. The feed flow pattern becomes restricted and causes damage to the internal parts of the reactor [19]. One cause of pressure drop from heavier oil feeds is the accumulation of fine material deposited in the reactor [27-28]. Coke accumulation is another cause of pressure drop build up [15].

2.1.5 Hydrotreating Catalysts

Effective, active, and stable heterogenous catalysts are important to the operation of hydrotreaters. Development of highly active catalysts are a concern today because of increasing regulations and restrictions for transport fuels [29]. Catalyst science in hydrotreating oil feeds is a subject of its own research field with ample literature on preparation, characterization, and performance.

Publication literature on the topic is found in Catalysis Today, Applied Catalysis, Catalysis Reviews, and Journal of Catalysis. The science of catalysis is multidisciplinary from microscopic, to mesoscopic, and macroscopic scales [30]. Each of these scales play a role in the performance of hydrotreating catalyst activity and future development. Key factors of hydrotreating catalysts from *Figure 2.1* are briefly discussed. The catalyst preparation procedure directly affects the performance. A summary of the important steps in preparation of catalysts include [18]:

- Precipitation
- Filtration or centrifugation with washing and drying
- Forming
- Calcining
- Impregnation
- Size
- Activation

Precipitation, Filtration, and Forming

Precipitation, filtration with washing and drying, are completed to create a pure and dry catalyst support. Gamma alumina oxide (γ-Al_2O_3) is used in this study because of better pore size distribution, surface area, pore volume, and high thermal stability [31]. Other supports such as silica, zeolites, titanium dioxide, and mesoporous supports, SBA-15, MCM-41, and Al-SBA-15, have been tested as potential supports [29, 32-33]. Phosphorous is added to the support to improve pore structure, acidity, and metal dispersion as consistently reported by others [34-36]. When forming catalysts into pellets, the shape and size are important mesoscopically for several reasons [15]:

- Hydrotreating reaction effectiveness
- Pressure drop
- Crush Strength (4 - 20 psi [1])
- Cost

Pellet shapes are cylinders, hollow rings, trilobe, quadrilobe, and pentalobe that are approximately 2mm in diameter [3][15]. The ratio of catalyst volume to external surface area is related to reaction effectiveness and pressure drop. Different shapes and sizes yield different ratios. Visual diagrams

highlighting these effects are shown elsewhere [3][15]. Trilobe is the most common shape and is used in this study. Less than 45μm solids are formed in the current study to assess hydrotreating reaction effectiveness.

Drying and Calcination

Drying and calcination follow the forming step. Calcination decomposes residual support reactants to gamma aluminum oxide (Al_2O_3). The heating rate, hold temperature, and cooling rate are parameters in calcination that affect the porous structure of the support. Higher holding temperatures lead to less desirable alumina (alpha, beta) that are not as effective for hydrotreating heavy gas oil feeds [18]. Important textural properties of hydrotreating catalysts are presented in *Table 2.3*.

Table 2.3. Important textural properties of hydrotreating catalysts [1][18][23].

Property	Distribution Range
Surface Area	100 - 500 m^2/g
Pore Volume	0.2 - 1 cm^3/g
Average Pore Diameter	75 - 250 Å
Bulk Density	0.49 - 1 g/cm^3
Average Pellet Length	3.2 - 9.5 mm

Hydrotreating catalysts exhibit a distribution of textural properties as highlighted *Table 2.3*. These properties are adjusted based on the procedures used in the precipitation to calcination steps. Optimization of these properties is a current research subject in the catalyst field when processing unconventional derived oil feeds. For heavier feeds, small shapes with large pore diameters and surface areas are desired to maximize internal diffusion. If heavy oil is derived from oil sands, the problem of fines (<20μm) lead to plugging of catalyst pores and reduce the overall catalyst effectiveness [27-28].

Impregnation

Metals and promoters with their concentrations in hydrotreating catalysts are shown in *Table 2.4* [3]. The impregnation step adds metals and promoters to the support. High dispersion of the metals

in the γ-alumina porous support is necessary for optimal hydrotreating performance. Additional drying and calcination steps are completed after metal impregnation.

Table 2.4. Metal and promoter concentrations in hydrotreating catalysts [3].

Type	Metal	Concentration (wt.%)
Metal	Molybdenum (Mo)	8 - 16
	Tungsten (W)	12 - 25
Promoter	Cobalt (Co)	1 - 4
	Nickel (Ni)	1 - 4

The metal concentrations in the support are based on the catalyst impregnation procedure. The metals exist in combinations with promoters each dispersed throughout the support. For example, CoMo, NiMo and NiW are common metal combinations on gamma alumina supports for hydrotreating catalysts. The addition of the promoter stabilizes the metals and increases catalytic performance. The choice of metal combinations is based on the application required; catalysts with CoMo metals are reported and used for hydrodesulfurization. Catalysts with NiMo metals are used for hydrodenitrogenation, and catalysts with NiW are used for hydrodearomatization [3]. Once in the active state, the ranking in catalyst activity for the combinations of metals in *Table 2.4* are [5][23]:

$$NiW > NiMo > CoMo > CoW$$

The NiW combination is higher cost compared to CoMo and NiMo, therefore nickel-molybdenum (NiMo) is common in industrial applications and used in the current study.

Size

Following impregnation, catalyst size is adjusted to impact the previously mentioned textural properties in *Table 2.3*. As mentioned, external and internal diffusion of feeds are important to prevent reaction limitations. A wealth of information on catalyst diffusion and reaction effectiveness is found elsewhere for further insight [15][37-38]. The current study examines two different catalyst sizes, pellets and <45μm solids, for this reason. If diffusion limitations exist, different catalyst sizes would impact the liquid product results significantly.

18

Activation

A visual schematic of the sulfiding reaction is presented in *Figure 2.3*. Hydrotreating catalysts are activated through sulfidation of impregnated metals and promotors in the support.
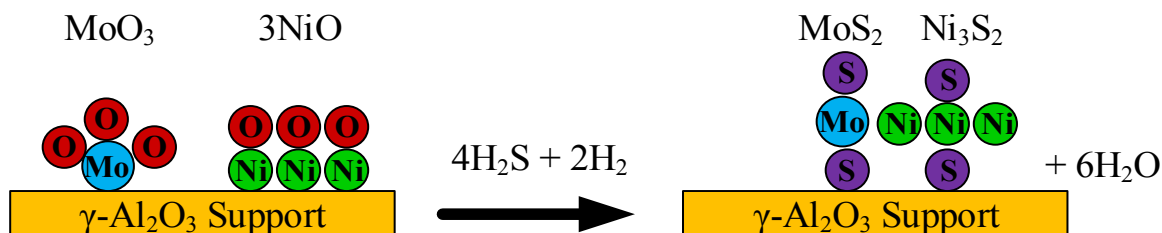
Figure 2.3. Visual schematic of the sulfiding reaction.

Sulfidation reactions reduce the metal and promoter oxides to active sulfides (e.g. MoS_2, Ni_3S_2). The reaction for the sulfidation procedure and its conditions affect the catalyst activity and stability [3]. Crystal structures and phases of molybdenum disulfide with nickel sulfide/cobalt sulfide is subject to debate [39-41]. Structures are highly dependent on preparation procedure and sulfiding reaction conditions. Molybdenum disulfide slabs or stacks (hexagonal, triangular, pyramidal) with nickel sulfide or cobalt sulfide edges are found in scanning tunneling microscope and transmission electron microscope images [39][41].

Activation by Sulfidation

In-situ sulfiding is either completed in the gas phase with hydrogen sulfide (H_2S) or the liquid phase with organosulfide agents or a high sulfur oil feed. Ex-situ sulfided catalysts are also possible for industrial hydrotreaters. The advantage is the time saved from the sulfidation reactions [42-43]. However, with this method, the metal sulfides are pyrophoric, therefore handling and transportation of the catalyst material is done with controls [44]. Liquid sulfiding agents decompose to H_2S and react with metals and promoters in the catalyst support [45]. Dimethyl disulfide (**DMDS**), an example of a liquid organosulfide agent with the second highest sulfur content (68wt.%), a low vapor pressure (3.8kPa at 25°C), is used in the current study.

The catalyst performance of gas phase sulfiding versus liquid phase sulfiding is subject to debate in literature. Liquid phase sulfiding is preferred industrially because of optimal wetting distribution of sulfur molecules throughout a catalyst bed reactor [42]. The liquid phase serves as a heat sink

because the sulfidation reaction is exothermic [42][46]. Texier et al. showed liquid phase sulfidation with DMDS resulted in a limited gain in catalyst performance compared to gas phase sulfidation [47]; however, the activation temperature (>270°C) and the hydrogen/hydrogen sulfide partial pressure ratio (~23) are important in the comparison [48].

Marroquin et al. found that using a straight run gas oil with at least 1wt.% sulfur in the form of DMDS was optimal for sulfiding a NiMo/γ-Al_2O_3 catalyst [42]. Yin and Wang found sulfidation at 330°C with dimethyl sulfide resulted in optimal catalyst performance for a straight run gas oil with a Ni-Mo-W catalyst [49]. The LHSV of 2-3h^{-1} was optimal for H_2S formation and catalyst performance compared to 1h^{-1}. Higher sulfiding temperatures, 350°C compared to 290°C, resulted in higher catalyst performance. The maximum temperature chosen for this study was 350°C.

Decomposition of Dimethyl Disulfide reactants and products as a function of temperature is presented in *Figure 2.4*. Decomposition of Dimethyl Disulfide products and temperature profile as a function of time is shown in *Figure 2.5*. The decomposition mechanism of DMDS has been studied in literature for sulfidation of hydroprocessing catalysts. These reaction steps are reported [47-48][51]:

$$CH_3\text{-}S\text{-}S\text{-}CH_3 + H_2 \rightarrow 2\ CH_3\text{-}S\text{-}H$$

$$CH_3\text{-}S\text{-}S\text{-}CH_3 + 3\ H_2 \rightarrow 2\ CH_4 + 2\ H_2S$$

$$2\ CH_3\text{-}S\text{-}H \rightarrow CH_3\text{-}S\text{-}CH_3 + H_2S$$

$$CH_3\text{-}S\text{-}CH_3 + H_2S \rightarrow 2\ CH_3\text{-}S\text{-}H$$

$$2\ CH_3\text{-}S\text{-}H + 2\ H_2 \rightarrow 2\ CH_4 + 2\ H_2S$$

$$CH_3\text{-}S\text{-}CH_3 + H_2S + 2\ H_2 \rightarrow 2\ CH_4 + 2\ H_2S$$
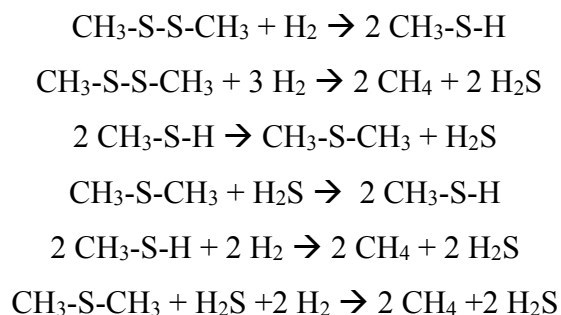
Where $CH_3\text{-}S\text{-}S\text{-}CH_3$ is DMDS, $CH_3\text{-}S\text{-}H$ is methanethiol, $CH_3\text{-}S\text{-}CH_3$ is dimethyl sulfide (DMS), H_2S is hydrogen sulfide and CH_4 is methane.

Figure 2.4. Decomposition of Dimethyl Disulfide reactants and products as a function of temperature [52-53].

M. Echard measured the molar fractions of DMDS and the products formed from decomposition as a function of temperature for sulfidation of a CoMo/Al$_2$O$_3$ catalyst [52-53]. Methanethiol (MeSH) formed at ~80°C rises in concentration to 240°C. DMDS concentration falls gradually in the decomposition reaction. The increase in DMS, hydrogen sulfide, and methane concentrations start at 200°C. Methane precedes hydrogen sulfide detection as the sulfidation reaction happens simultaneously. Methane and hydrogen sulfide concentration profiles increase significantly after 240°C and stabilize beyond 350°C. Detection of hydrogen sulfide after methane suggests the metal and promoters are sulfided first. The formation of hydrogen sulfide and methane are dependent on the heating rate.
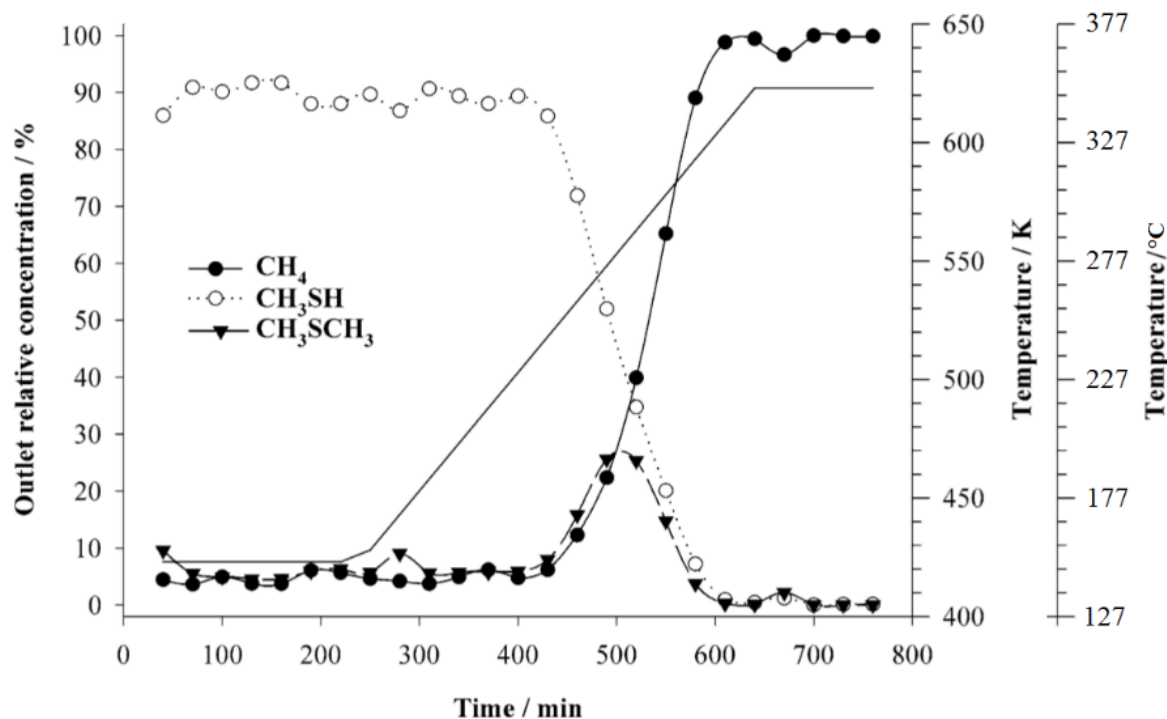
Figure 2.5. Decomposition of Dimethyl Disulfide products and temperature profile as a function of time [47].

Texier et al. measured the heating rate with methane, MeSH, and DMS concentration profiles as a function of time for sulfidation of a NiMo/Al$_2$O$_3$ catalyst in *Figure 2.5* [47]. The online gas chromatograph measured carbon based compounds. The DMDS was 7.6mol% in heptane with 587L/L H$_2$ gas/liquid ratio at 4MPa and a heating rate of 0.5°C/min. MeSH forms below 230°C. As the temperature increases, MeSH decreases and methane increases. Similar to M. Echard [52-53], the DMS concentration peaks around 270-290°C. At 330°C, methane, and the assumed hydrogen sulfide are formed from the decomposition reactions.

Water is a byproduct from the sulfidation reaction, as illustrated in *Figure 2.3*. Laurent and Delmon found the catalytic performance decreased by 2/3 when water was present in a sulfided NiMo/γ-Al$_2$O$_3$ catalyst [54]. Water partially crystallized the γ-alumina support into a boehmite phase. A structural modification of the support deactivated the nickel promoter. The authors did not examine sulfur or nitrogen species. Although important, water effects were mitigated by drying the catalyst prior to use in the current study.

A sulfidation reaction temperature summary is highlighted in *Table 2.5*. Both studies, *Figures 2.4 and 2.5*, provide evidence that hydrogen sulfide formation occurs at 250-300°C from DMDS decomposition. These findings are important for the current study.

Table 2.5. Sulfidation reaction temperature summary [42][45].

Step	Temperature (°C)
Drying	80-120
Soaking or Catalyst Pre-wetting	130-160
Initial Sulfidation	210-260
H_2S Formation	240-270
Second Sulfidation	>270

The steps in the sulfidation reaction occur at increasing temperatures presented in *Table 2.5*. The temperature steps are used in developing a procedure for catalyst sulfidation reactions in the current study. The sulfided catalysts are then used for hydrotreating reactions.
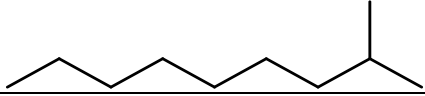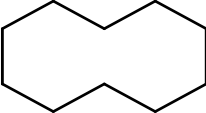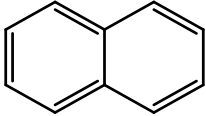
2.2 Chemistry of Hydrotreating Feeds

The characteristics of the hydrotreating feeds highlighted in *Table 2.1* depend on the process configuration. The chemistry of the hydrocarbon structures found in these feeds are classified into compositional groups to understand their complexity. Section 2.2 highlights known structures found specifically in the heavy vacuum gas oil feed used. Further information on heavy oil and bitumen chemistry is found elsewhere [55].

2.2.1 Carbon and Hydrogen

The paraffin, isoparaffin, olefin, naphthene, and aromatic classification of hydrocarbon structures for ten carbon atoms are shown in *Table 2.6*. The information presented is an adaptation of Table 3.12 from Gray's six carbon atom [15].

Table 2.6. Paraffin, isoparaffin, olefin, naphthene, and aromatic classification of hydrocarbon structures for ten carbon atoms.

Class	C$_{10}$ Structure	H/C Ratio	Density (kg/m^3) (At 25°C)	Molecular Weight (g/mol)	Boiling Point (°C)[59]
Paraffin *Decane*		2.2	728 [56]	142.3	174
Isoparaffin *2-Methylnonane*		2.2	723 [57]	142.3	167
Olefin *1-Decene*		2	738 [56]	140.2	171
Naphthene *Cyclodecane*		2	854 [58]	140.2	201
Aromatic *Naphthalene*		0.8	1020[56]	128.2	218

The hydrogen to carbon ratio (H/C) and molecular weight increase as hydrogen is added to the C$_{10}$ structures. The density and boiling point decrease as hydrogen is added. The trends are evident:

<div align="center">

Hydrogen Addition

→

Aromatics → Naphthenes → Olefins → Paraffins → Isoparaffins

→

Decreasing Density and Boiling Point

</div>
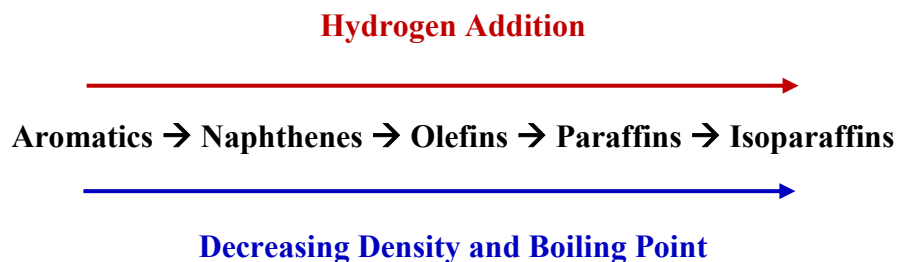
Paraffins

Straight chain alkanes are in the paraffin group. The formula is C$_n$H$_{2n+2}$. Alkanes are formed from side chain alkyl aromatics in upgrading [15]. Bitumen or heavy oils as in HVGO do not contain paraffins. From primary upgrading, paraffins form from cracking reactions.

Isoparaffins

Like paraffins, isoparaffins have similar atom numbers but are in isomeric arrangements. Isoparaffins are formed from side chain alkyl aromatics. These branched molecules are desired in transport fuels to increase octane numbers in downstream refining.

Olefins

Olefins are not found in heavy oil or bitumen feeds, however in upgrading, cracking can cause formation of these molecules. Gas phase cracking forms a higher yield of olefins compared to liquid phase cracking [15].

Naphthenes

Naphthenes are cycloalkanes. Hydrotreating saturates aromatics to form naphthenes.

Aromatics

The core structures of heavy oils and bitumens are aromatic molecules. Aromatics exist in many isomeric arrays and distributions. Monoaromatics, diaromatics, triaromatics and polynuclear Aromatic Hydrocarbons (PAHs) are examples of aromatics structures found in heavy oils.

Asphaltenes

Asphaltenes are large carbon-based structures that are described by their solubility in n-alkane solvents. Asphaltenes are precipitated out from the heavy oils and bitumens by dilution of these solvents. Separation of the insoluble material, through a filter paper, is quantified as asphaltenes. The American Society for Testing and Materials' (ASTM) methods for asphaltene quantification are D3279 and D6560 [60-61]. Asphaltene structures, composition, aggregation, properties, as well as processing ability are widely and highly debated throughout literature [62-65]. Although important in the heavy oil and bitumen characterization, asphaltene concentration of the HVGO feed and the liquid products are not studied.

The PIONA hierarchy classification is used as an example to highlight the property changes with hydrogen addition in *Table 2.6*. These structures are found in large branches, alkyl branches, or other heteroatom molecules in the HVGO and not directly as they appear in this example. Products

are expected to have less aromatics. As hydrogen is added to their structures through hydrotreating, the liquid products are expected to follow these property trends. Higher H/C, lower density, boiling point, and molecular weights are expected in the liquid products compared to HVGO feed.
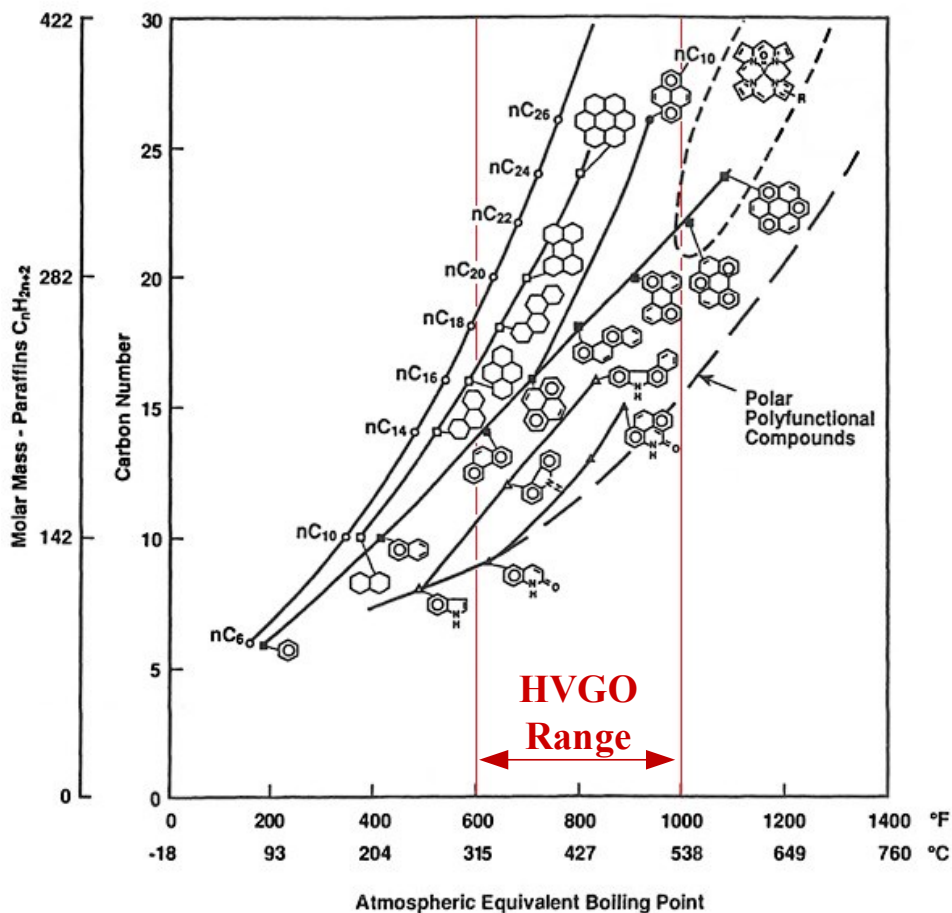
Figure 2.6. Altgelt's and Boduszynski's distribution of molecular structures found in petroleum as a function of boiling point [66].

Reprinted from H. Altgelt and M. M. Boduszynski, *Composition and Analysis of Heavy Petroleum Fractions.* Boca Raton, Fla.: CRC Press, 1993, Chapter 10 Composition of Heavy Petroleum Fractions, pp.398, Figure 10.1, with permission from Taylor and Francis Group LLC Books.

Altgelt's and Boduszynski's distribution of molecular structures found in petroleum as a function of boiling point is presented in *Figure 2.6*. The relationship of carbon number to boiling point is dependent on the class of paraffins, saturated rings, alkyl aromatics, and polar polyfunctional structures. When comparing constant carbon numbers, the trend is similar to that of *Table 2.6* with hydrogen addition. The approximate HVGO temperature range 315-538°C used in this study is

displayed in *Figure 2.6*. Critical assessment is important in the extrapolation of these structures and carbon numbers. It is unknown whether this trend is continuous to higher boiling point fractions.

The properties of HVGO feed and it's eight distillate cut fractions are presented in *Table 2.7* [67]. Researchers from the National High Magnetic Field Laboratory from Florida State University, Smith et al. and McKenna et al., in collaboration with Alberta researchers, conducted characterization and exhaustive compositional analysis of the HVGO used in the current study [67-70]. Negative and positive electrospray ionization, plus field desorption, Fourier transform ion cyclotron resonance mass spectrometry with atmospheric pressure photoionization were used in these characterizations. The HVGO was distilled (ASTM D1160) into eight boiling point fractions. Characterization of the HVGO and its distillate cuts were completed.

Table 2.7. Properties of HVGO and its eight distillate cut fractions [67].

Fraction (°C)	HVGO Feed	IBP-343	343-375	375-400	400-425	425-450	450-475	475-500	500-525
Weight % Distilled		4.32	15.87	17.13	9.87	18.91	17.02	9.13	7.47
Density (kg/m^3 at 15.6°C)	965	922	945	958	966	971	976	979	994
Carbon (wt.%)	85.33	85.58	84.76	84.19	84.2	84.24	83.96	85.2	84.7
Hydrogen (wt.%)	10.44	11.37	10.98	11.4	11.38	10.97	10.8	10.84	10.24
Sulfur (wt.%)	3.48	2.34	-	3.31	3.43	3.48	3.45	3.80	4.27
Nitrogen (wt.%)	0.14	0.03	0.06	0.09	0.12	0.14	0.18	0.19	0.26
Oxygen (wt.%)	0.83	0.85	1.14	1.14	1.28	1.34	1.36	1.5	1.71
H/C	1.47	1.60	1.56	1.63	1.62	1.56	1.54	1.53	1.45
Molecular Weight (g/mol)	345	288	287	304	328	359	402	461	578
Total Acid Number (mg KOH/g oil)	4.32	1.14	2.35	3.50	4.04	4.75	5.32	5.61	5.06

The properties of the HVGO seen in *Table 2.7* appear similar to those reported in *Table 2.1* with the addition of carbon, hydrogen, oxygen, molecular weight and total acid number. These

characterization results provide a deeper insight into the chemical complexity of the HVGO. Critical assessment is important for these quantification results. Summation of carbon, hydrogen, sulfur, nitrogen and oxygen weight percent are greater than 100%. All properties, except the H/C, increase as the boiling fraction temperature range increases. Molecular structures increase in size and complexity at higher boiling fractions as suggested in *Figure 2.6*.

The number average molecular weight, a statistical average from a molecular weight distribution, was measured with the vapor pressure osmometry (VPO) technique (ASTM D2503). The molecular weight for the HVGO averaged 345g/gmol. As shown in *Figure 2.6*, using the molecular formula of paraffins, 345g/gmol corresponds to an average straight chain structure of $C_{24}H_{50}$. Assuming an aromatic formula structure, 345g/gmol corresponds to $C_{26}H_{34}$. These exact structures do not necessarily exist in the HVGO; however, the molecular weight provides a theoretical understanding of different molecular structures possible within the paraffinic to aromatic range. The colour contoured plots of each distillate fraction provides a deeper insight into approximating chemical structures found in the HVGO. Contoured double bond equivalent plots as a function of carbon number for each distillation cut fraction of the HVGO is presented in *Figure 2.7* and a combined contoured is presented in *Figure 2.8* [68].
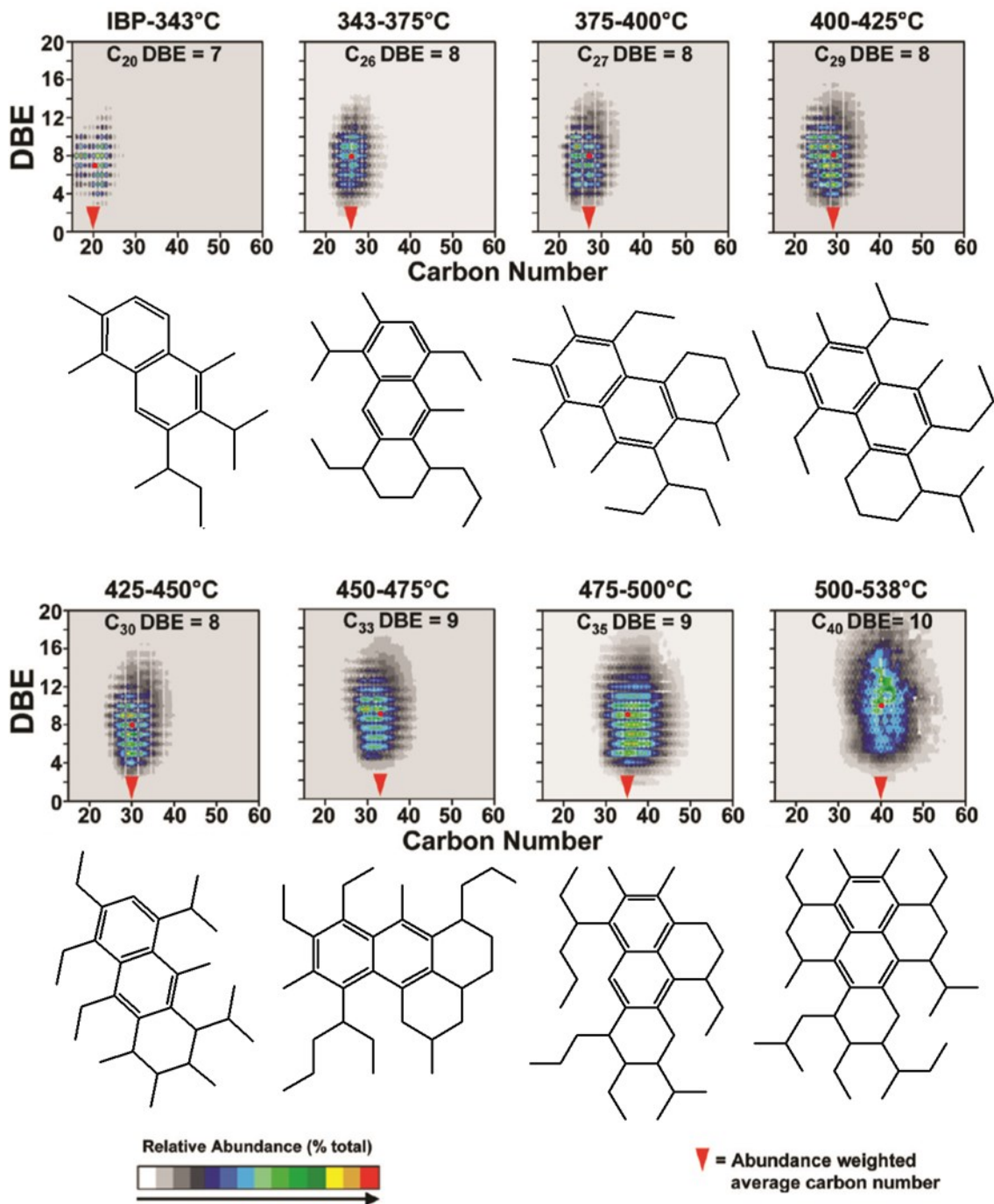
Figure 2.7. Double bond equivalent contoured plots as a function of carbon number for each distillate cut fraction in HVGO [68].

The color contoured plots provide a distribution of the theoretically constructed structures found in each distillate fraction. The double bond equivalence (**DBE**) is the number of double bonds to carbon plus the number of cyclic rings. For example, benzene (C_6H_6) has a DBE of 4 with a carbon number of 6. Hexylnaphthalene ($C_{16}H_{20}$) has a DBE of 7 with a carbon number of 16. Straight chain paraffins have a DBE of zero. The color mapped in the plots is scaled to 100%, where white is zero and red is 100. These structures presented in each distillate fraction are molecular representations for the maximum abundance as marked by the red dots. These structures may not necessarily exist but are used in this context for illustration and understanding. As the distillate cut temperature increases, the abundance weighted average carbon number and DBE increase to larger hydrocarbon structures. The representations in *Figure 2.7* highlight examples of hydrogen and carbon atom distributions.
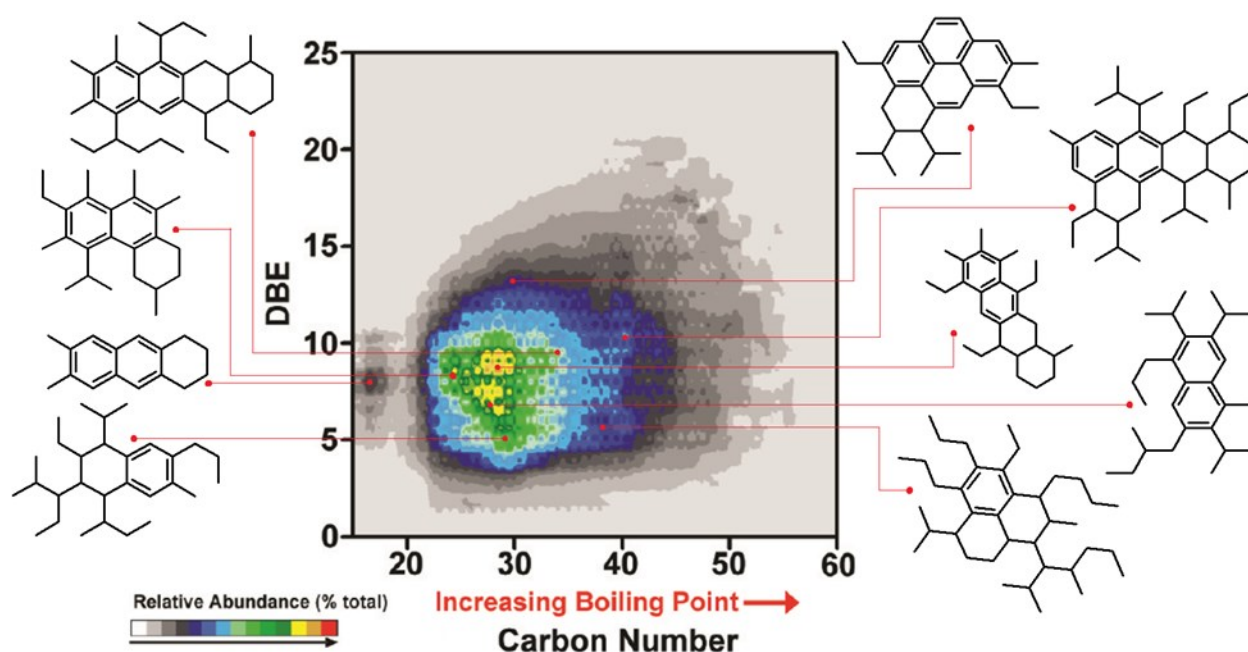
Figure 2.8. Combined double bond equivalent contoured plot as a function of carbon number in HVGO [68].

Reprinted (adapted) with permission from Figure 9, A. M. McKenna *et al*, "Heavy Petroleum Composition. 1. Exhaustive Compositional Analysis of Athabasca Bitumen HVGO Distillates by Fourier Transform Ion Cyclotron Resonance Mass Spectrometry: A Definitive Test of the Boduszynski Model," *Energy Fuels,* vol. 24, *(5),* pp. 2929-2938, 2010. Copyright 2010 American Chemical Society.

The eight distillate cut contoured plots from *Figure 2.7* are combined to represent the whole HVGO. The red to yellow color regions suggest high abundance of carbon atoms (>80%), C_{26} to C_{30} with DBEs of 6 to 9 and dark grey to white colors are low abundant carbon atoms (<30%),

<C22, and >C44 with DBEs < 3 and >13. Similar to *Figure 2.7*, random red dots in the contoured plot are selected to illustrate molecular representative hydrocarbon structures in the HVGO. The combined plot highlights the abundant distribution of carbon and hydrogen structures within the complex HVGO. Additional sulfur, nitrogen, and oxygen atoms are not shown in these representative illustrations but are known to exists in the HVGO matrix.

2.2.2 Sulfur

Distinct sulfur atom structures found in heavy oils and bitumens are presented in *Figure 2.9* [15][55][70][71]. From *Tables 2.1 and 2.7*, the concentration of sulfur is based on the oil type or boiling fraction characterized. The reported HVGO sulfur content used in the current study is sour at 3.48wt.%.
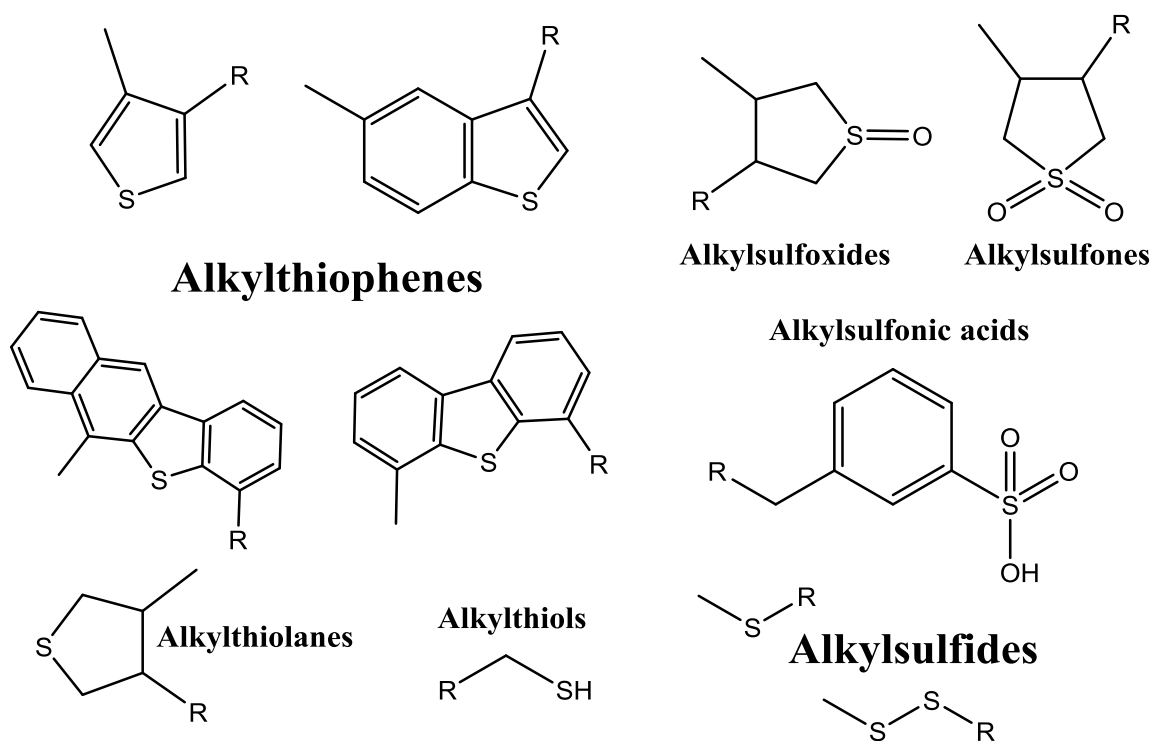
Figure 2.9. Sulfur structures found in heavy oils [15][55][71].

Figure 2.9 shows a distribution of alkylthiophenes, alkylsulfoxides, alkylsulfones, alkylsulfonic acids, alkylthiolanes, alkylthiols (mercaptans), and alkylsulfides structures that are found in oils.

Alkyl or **R** substituent derivatives range from $CH_3\cdot$ (methyl) to $C_{10}H_{21}\cdot$ (decyl), or higher [15]. In addition, **R** may represent aromatics (e.g. phenyl, benzyl) or other cycloalkyl naphthalene ring groups. The alkylsulfides, aliphatic sulfur, and alkylthiophenes (thiophenic sulfur) are sulfur structures reported in literature [15][55][71]. Brons and Yu reported that bitumen contains 62% alkylthiophenic sulfur compared to 38% alkylsulfide or aliphatic sulfur [71-72].

Of the circa 3.5wt.% of sulfur in the HVGO, sulfur is distributed throughout different structures presented in *Figure 2.9*. From the characterization and exhaustive compositional analysis of the HVGO [67-70], sulfur concentration increases as distillate cut temperature increases (see *Table 2.7*). Color contoured plots, seen in *Figure 2.7*, for sulfur atoms, S_1 and S_2 classes, for each distillate cut temperature of HVGO are found in the original work by McKenna *et al.* [68]. A combined double bond equivalent contoured plot as a function of carbon number for single thiophenic sulfur (S_1 class) in HVGO is presented in *Figure 2.10* [68].
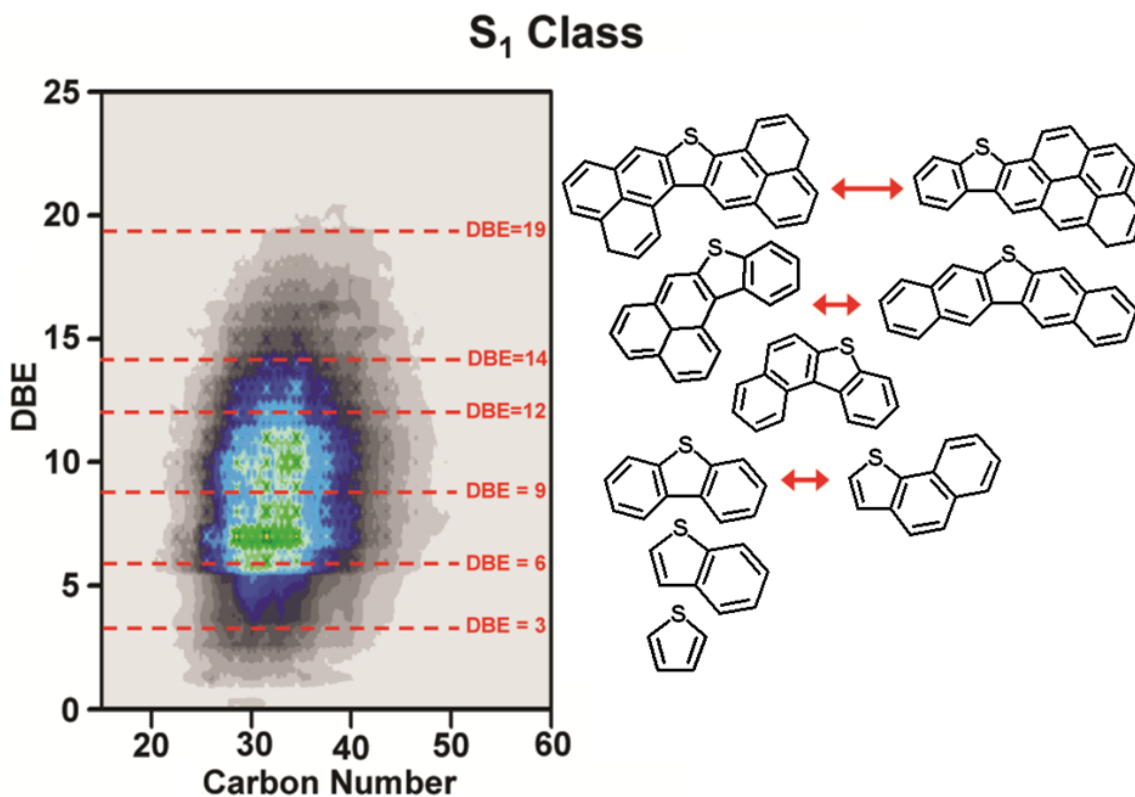
Figure 2.10. Combined double bond equivalent contoured plot as a function of carbon number for single thiophenic sulfur in HVGO [70].

Thiophenic sulfur is distributed throughout the diverse carbon atom arrangements shown in *Figure 2.10*. Benzothiophene (DBE of 6) and dibenzothiophene (DBE of 9) based structures are highly abundant in the S_1 class. McKenna et al. suggested cycloalkane ring addition to these thiophene structures provide DBEs 7-8 and 10-11 in the green color abundance region [68]. As the DBE increases, the sulfur structures become larger in carbon number and supplementary isomers are possible. In addition, alkyl or R groups are attached to sulfur heteroatom structure combinations to reach carbon numbers of 30-40 for higher abundant regions in *Figure 2.10*. Aliphatic sulfur with rings of carbon and hydrogen atoms, arylalkyl-sulfides, and diarylsulfides were not discussed in the contour plots but these are probable structures found in the HVGO matrix [66].

2.2.3 Nitrogen

Diverse nitrogen atom structures found in heavy oils and bitumens are presented in *Figure 2.11* [15][55][66][73]. From *Tables 2.1* and *2.7*, the concentration of nitrogen is based on the oil type or boiling fraction characterized. Total nitrogen content is classified into basic nitrogen and non-basic nitrogen [15]. Total nitrogen is characterized in the current study.

Alkylpyrroles **Alkylindoles** **Alkylcarbazoles**

Alkylpyridines **Alkylquinolines** **Alkylacridines**

Alkylamides **Alkylarylamines**

Alkylmetalloporphyrins **Alkylamines**
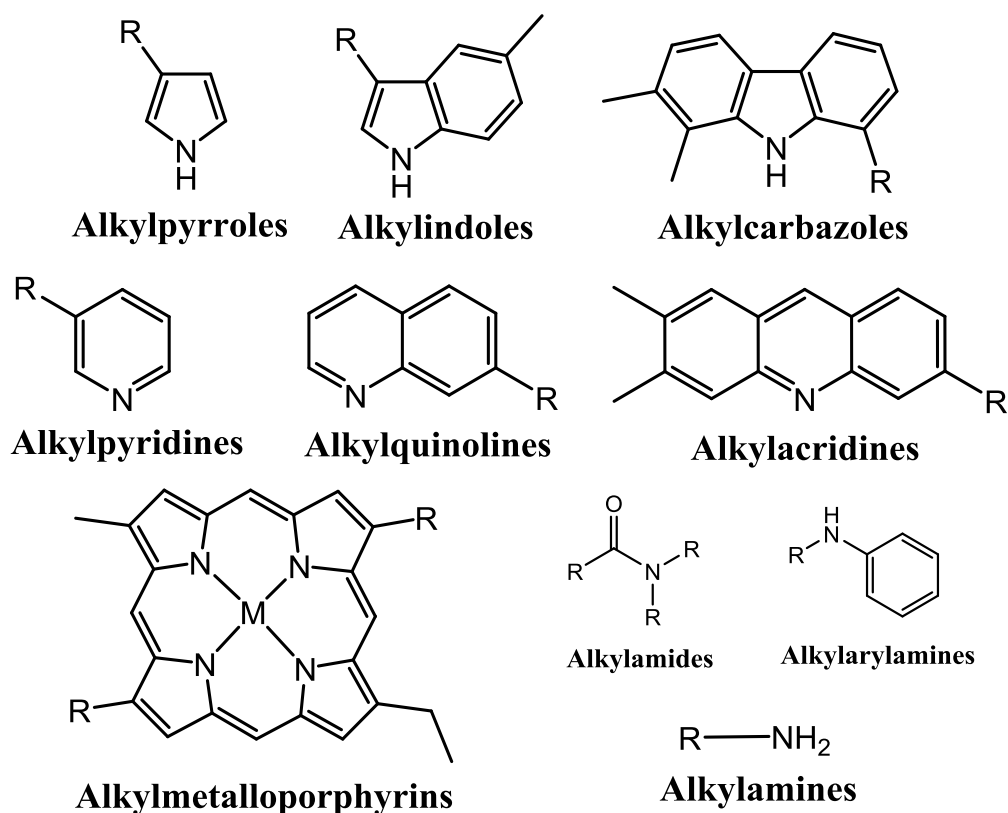
Figure 2.11. Nitrogen atom structures found in heavy oils [15][55][66][73].

A distribution of alkylpyrroles, alkylindoles, alkylcarbazoles, alkylpyridines, alkylquinolines, alkylacridines, alkylmetalloporphyrins, and alkylamines structures are shown in *Figure 2.11*. Alkyl or **R** substituent derivatives range from $CH_3\cdot$ (methyl) to $C_{10}H_{21}\cdot$ (decyl), or higher. In addition, **R** may represent aromatics (e.g. phenyl, benzyl) or other cycloalkyl naphthalene ring groups. The M in the center of the alkylmetalloporphyrins represent metal atoms. The alkylpyrroles, alkylindoles, alkylcarbazoles, alkylmetalloporphyrins, and alkylamines are non-basic. These non-basic structures have electrons delocalized around the ring structures. The alkylpyridines, alkylquinolines, and alkylacridines are basic nitrogen heterocyclic structures because of unshared electrons on the nitrogen atom. Other structures with more than one nitrogen atom have been identified in crude oils; these structures include imidazole, pyrrole carboxylic acid, isobutyraminde, quinolone [73].

The 0.14-0.19wt.% nitrogen in the HVGO is distributed throughout the structures presented in *Figure 2.11*. From the characterization and exhaustive compositional analysis of the HVGO [67-70], nitrogen concentration increases as the distillate cut temperature increases as seen in *Table 2.7*. Positive electrospray ionization of select distillate cut temperatures of HVGO for basic nitrogen heteroatoms are found in Smith *et al.* [67]. As the distillate cut temperature increases, single N_1 class abundance decreases. Multiheteroatom classes increase in abundance at higher distillate cuts [67]. Positive ion double bond equivalent isoabundance contour plots as a function of carbon number for the N_1 class in HVGO is presented in *Figure 2.12* [67]. Negative ion double bond equivalent isoabundance contour plots as a function of carbon number for the N_1 class in HVGO is presented in *Figure 2.13* [69].
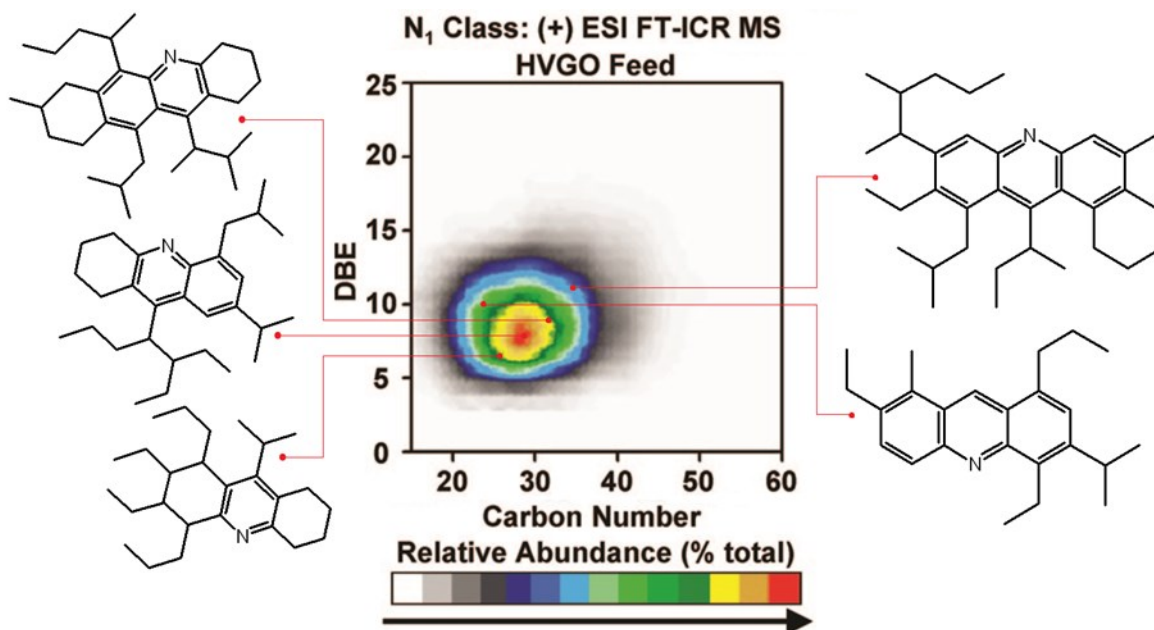
Figure 2.12. Positive ion double bond equivalent isoabundance contour plots as a function of carbon number for the N_1 class in HVGO [67].

High abundance of basic nitrogen atoms are found in red to yellow color regions (>80%), C_{22} to C_{30} with corresponding DBEs of 6 to 10. Low abundance basic nitrogen atoms are found in dark grey to white color regions (<30%), $<C_{16}$, and $>C_{35}$ with corresponding DBEs of <5 and >14. Quinoline-like and acridine-like core structures are illustrated in *Figure 2.12*. Similar to *Figures 2.7* and *2.8*, red dots in the contoured plot are selected to illustrate molecular representative basic nitrogen structures in the HVGO. These structures may not necessarily exist but are used in this context for illustration and hypothetical understanding. The combined contour plot of all distillate cuts for basic nitrogen are presented in Smith et al. [67].
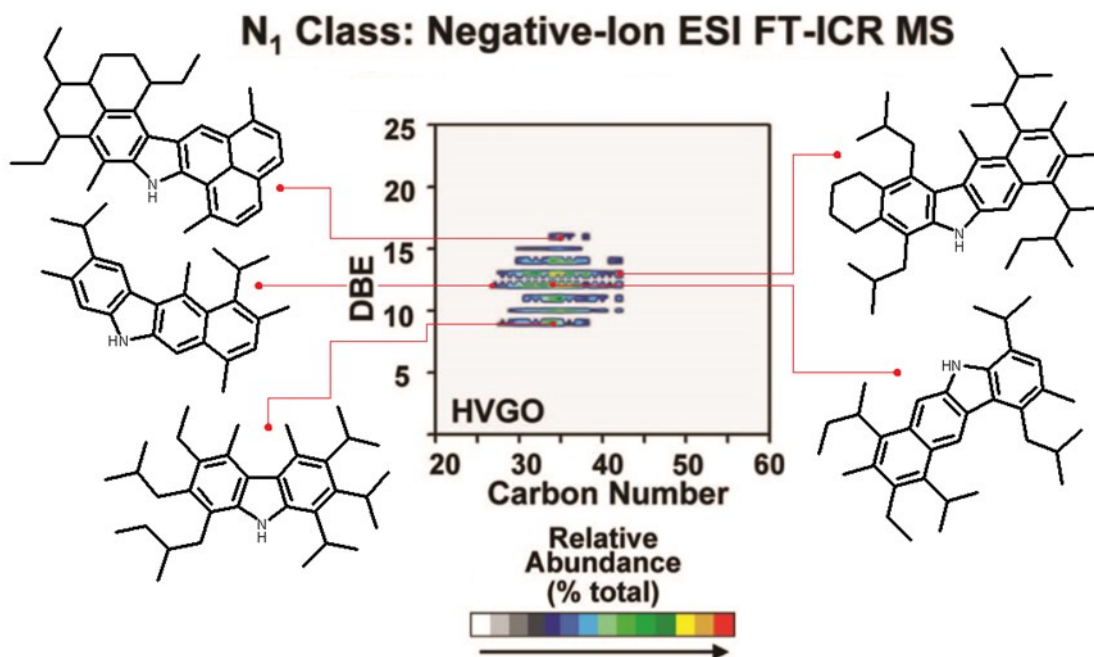
Figure 2.13. Negative ion double bond equivalent isoabundance contour plots as a function of carbon number for the N$_1$ class in HVGO [69].

The negative ion contour plot in *Figure 2.13* presents the distribution of non-basic nitrogen heteroatoms in the HVGO. The red to yellow color regions suggest high abundance of non-basic nitrogen atoms (>80%), C$_{34}$ to C$_{35}$ with DBEs of 12 to 13. Pyrrolic-like core structures are common. Acid and acid-free non-basic nitrogen contour plots are presented in Smith et al. for HVGO [69]. Alkylamines and alkylamides, non-heterocyclic nitrogen, are not discussed in these contour plots, but are found in oils at low concentrations [74].

2.2.4 Oxygen and Metals

From *Table 2.7*, oxygen is found in the HVGO. However, due to difficultly in characterization, oxygen concentrations are not measured in the current study. Additional information of oxygen structures and its distribution in the HVGO are found elsewhere [14-15][55][66][69].

Metal atom structures found in heavy oils and bitumens are presented in *Figure 2.14* [15][55][66]. Metal concentrations of HVGO measured by inductively coupled plasma mass spectrometry are presented in *Table 2.8* [14].

Alkyl nickel porphyrin   **Alkyl vanadyl porphyrin**
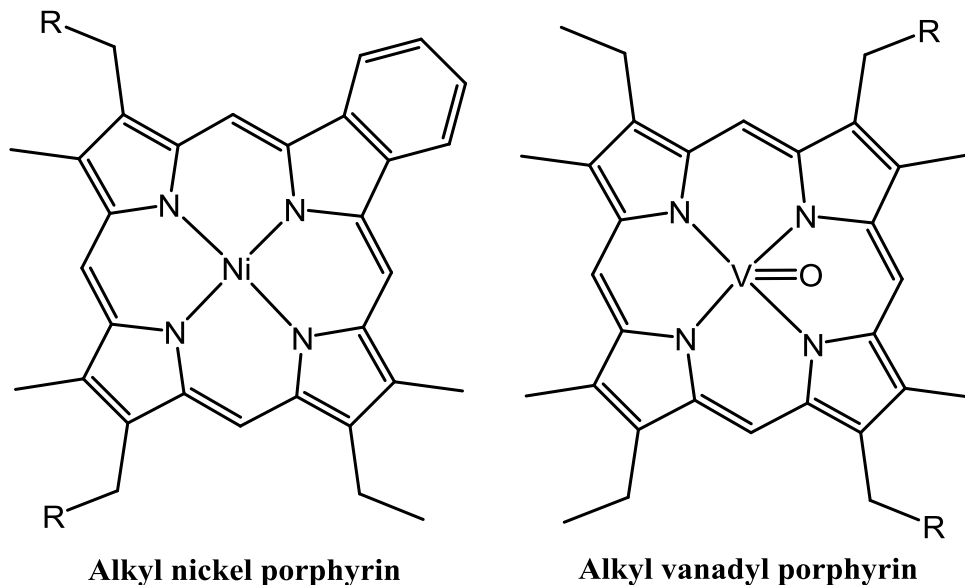
Figure 2.14. Metal structures found in heavy oils [15][55].

Alkyl nickel and vanadium porphyrin are metal structures are found in heavy oils and bitumens. These structures are found in the high distillate cuts, >500°C, and asphaltene fractions. Alkyl or **R** substituent derivatives range from $CH_3\cdot$ (methyl) to $C_{10}H_{21}\cdot$ (decyl), or higher. In addition, **R** also represent aromatics (e.g. phenyl, benzyl) or other cycloalkyl naphthalene ring groups. Additional information on metals in heavy oils and bitumens is found elsewhere [76].

Table 2.8. Metal concentrations of HVGO measured by inductively coupled plasma mass spectrometry [14].

Element	Symbol	Concentration (wppm)	Element	Symbol	Concentration (wppm)
Aluminum	Al	0.6	Arsenic	As	0.1
Barium	Ba	<0.1	Boron	B	1.6
Cadmium	Cd	<0.1	Calcium	Ca	8.5
Chromium	Cr	0.4	Copper	Cu	0.2
Iron	Fe	0.1	Lead	P	<0.1
Magnesium	Mg	1.2	Manganese	Mn	0.6
Molybdenum	Mo	1.4	Nickel	Ni	1
Phosphorus	P	7.6	Potassium	K	0.2
Silicon	Si	325	Sodium	Na	21.2
Tin	Sn	<0.1	Titanium	Ti	<0.1
Vanadium	V	1.2	Zinc	Zn	0.3

Nickel and vanadium metal concentrations suggest parts per billion levels of alkyl metal porphyrins are found in the HVGO from *Table 2.8*. Silicon and sodium had higher concentrations. This suggests clay and salt contamination. The current study does not examine the extent of these metals. However, these metal porphyrin structures in *Figure 2.14* are known to highlight visible absorbance from the conjugated π bonds [77].

Inductively Coupled Plasma Mass Spectrometry

Inductively coupled plasma mass spectrometry (ICP-MS) was used to measure the elemental metal concentrations in the HVGO shown in *Table 2.8*. Argon plasma ionizes the sample into positive ions using inductive energy. The positive ions are extracted through a quadrupole to a calibrated mass spectrometer [78-79]. The calibration is based on the mass to charge ratio. The signal from the detector is proportional to the metal concentration. The ICP-MS analysis is used to verify the elemental metal concentrations in the Ni-Mo/γ-Al$_2$O$_3$ catalyst in the current study.

2.3 Hydrotreating Chemical Reactions

Operating conditions and catalyst performance directly impact the concentration of sulfur, nitrogen, and aromatics in the liquid products. Understanding the chemical reactions of carbon, hydrogen, sulfur, and nitrogen is important in addressing the dynamic compositional transformations objective. Section 2.3 reviews the chemical reactions of hydrotreating.

2.3.1 Hydrodesulfurization

Hydrodesulfurization (HDS) reactions are one of the most studied reactions in heavy oil processing [81-82]. Increasing environmental regulations and restrictions of sulfur in liquid fuels is a reason for HDS research. Prevention of SO$_x$ formation from combustion is desired. The sulfur structures in *Figure 2.9* undergo HDS reactions in hydrotreating. Understanding the sulfur removal reaction mechanism pathway on a catalyst provides insight to the types of liquid products formed. The use of model compounds found in literature aid in understanding how HDS reactions happen in heavy oil feeds. Thermodynamically, HDS reactions are exothermic and irreversible. As previously mentioned in section 2.2.2, alkylsulfides and alkylthiophenes are common structures found in oil feeds. Alkylthiols (mercaptans), alkylsulfides, and alkyldisulfides are favorable for removal with

high relative reaction rates [1][81]. Thiophenic compounds are less reactive and are unfavorable for removal with lower reaction rates in the organosulfur group. Thiophenic based compounds are used in HDS research [81-83]. Sulfur removal and hydrogen addition reactions of select model compounds in hydrotreating are shown in *Figure 2.15* [1].

Alkylthiols

$$R\text{—}CH_2\text{—}SH \;+\; H_2 \;\longrightarrow\; R\text{—} \;+\; H_2S$$

Alkylsulfides

$$R_1\text{—}S\text{—}R_2 \;+\; 2H_2 \;\longrightarrow\; \begin{matrix} R_1\text{—}H \\ R_2\text{—}H \end{matrix} \;+\; H_2S$$

$$R_1\text{—}S\text{—}S\text{—}R_2 \;+\; 3H_2 \;\longrightarrow\; \begin{matrix} R_1\text{—}H \\ R_2\text{—}H \end{matrix} \;+\; 2H_2S$$

Alkylthiophenes

$$+\; 4H_2 \;\longrightarrow\; +\; H_2S$$

$$+\; 3H_2 \;\longrightarrow\; +\; H_2S + R_1\text{—}H$$
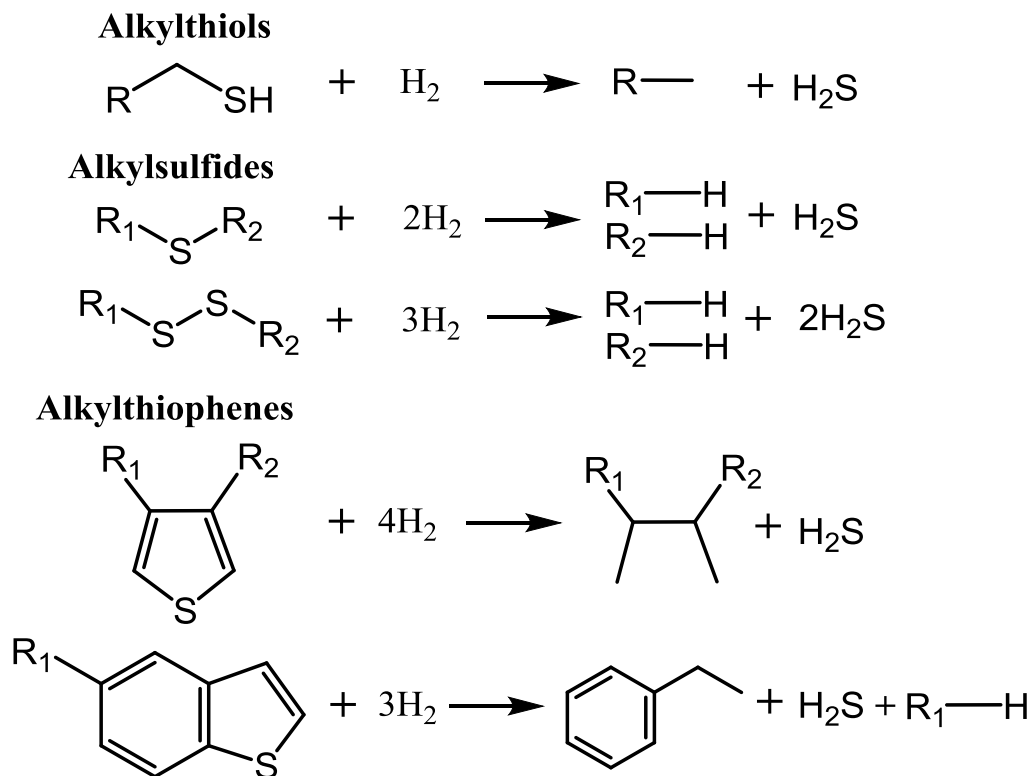
Figure 2.15. Sulfur removal and hydrogen addition reactions in hydrotreating [1].

Reactions illustrated in *Figure 2.15* are with stoichiometric hydrogen requirement. The sulfur is removed in a catalytic hydrogen atmosphere. A sulfur-free structure with hydrogen sulfide is formed. Detailed mechanistic pathways with intermediate steps on catalytic surfaces are explored in literature for these reactions in *Figure 2.15* [83]. An HDS reaction mechanism for dibenzothiophene is presented in *Figure 2.16* [80].
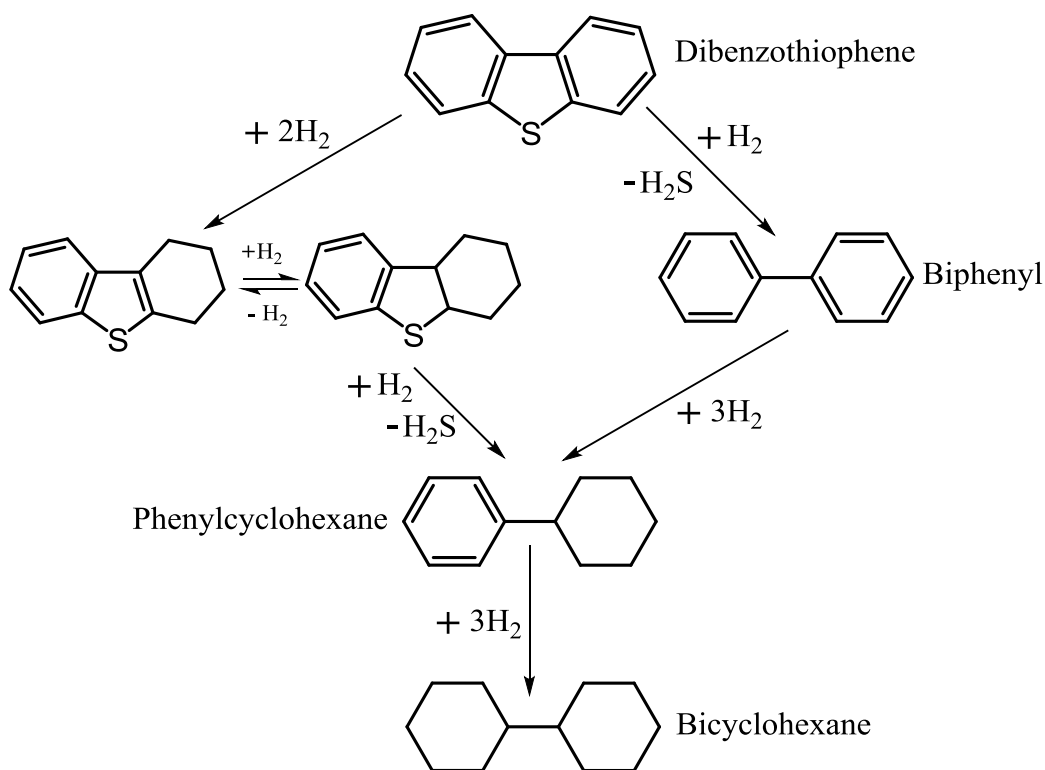
Figure 2.16. Sulfur removal mechanism of dibenzothiophene [80].

Houalla et al. proposed the sulfur removal mechanism for dibenzothiophene [80][83]. Each arrow in *Figure 2.16* represents a reaction step that is modeled with rate equations. Reaction conditions (temperature, pressure, catalyst etc.) concentrations of hydrogen, and hydrogen sulfide affect the rates of reaction in each step. Two pathways are possible with different rates of reaction. The left side of *Figure 2.16*, with hydrogenation of the aromatic rings followed by sulfur removal to phenylcyclohexane (cyclohexylbenzene). The right side of *Figure 2.16*, sulfur removal to form biphenyl (hydrogenolysis pathway) followed by hydrogenation of the rings to phenylcyclohexane. The biphenyl path is favorable when there is a sulfur vacancy on a sulfided metal catalyst [15][84]. However, if alkyl groups are attached on the sulfur side of the dibenzothiophene, the left side pathway is favorable because of adsorption on a catalytic surface followed by sulfur removal. These alkylthiophenes are lower reactivity because of steric hindrance limiting adsorption on the catalytic surfaces. The 4,6-dimethyldibenzothiophene sulfur is an example with steric hinderance [15][85-89]. Properties of dibenzothiophene, biphenyl, phenylcyclohexne, and bicyclohexane are presented in *Table 2.9* [59].

Table 2.9. Properties of dibenzothiophene, biphenyl, phenylcyclohexne, and bicyclohexane [59].

	Dibenzothiophene	Biphenyl	Phenylcyclohexane	Bicyclohexane
T_{boil} (°C)	333	254±2	240	235±10
H/C Ratio	0.67	0.83	1.33	1.83
Density (g/cm³)	1.25	1.04	0.95	0.86-0.89
MW (g/mol)	184.26	154.21	160.26	166.3

Dibenzothiophene with its hydrotreated derivatives illustrated in *Figure 2.16* highlight identical property trends to that of *Table 2.6*. As hydrogen is added and sulfur is removed, the boiling point and density of each structure decreases.

Sulfided NiMo/Al$_2$O$_3$ catalysts favor hydrogenation reactions as illustrated in the left side pathway of *Figure 2.16*. Sulfided CoMo/Al$_2$O$_3$ catalysts favor hydrogenolysis as illustrated in the right side pathway of *Figure 2.16* [3][71]. The HVGO contains higher concentrations of alkylthiophenes (e.g. dibenzothiophenes, 4,6-dimethyldibenzothiophene) from the abundance plot *Figure 2.10*. This is a reason why NiMo/Al$_2$O$_3$ catalyst is used in the current study.

A distribution of the monosulfur class before and after hydrotreating of a coker gas oil is presented in *Figure 2.17* [90]. Fu et al. characterized untreated and hydrotreated samples of a coker gas oil cut (483-504°C) [90]. The feed fraction had 4.9wt.% sulfur and 2.1wt.% nitrogen (untreated). The hydrotreated product had 1.1wt.% sulfur and 1.8wt.% nitrogen. The characterization of the 483-504°C distillate fraction before and after hydrotreatment provides insight to the molecular transformations.
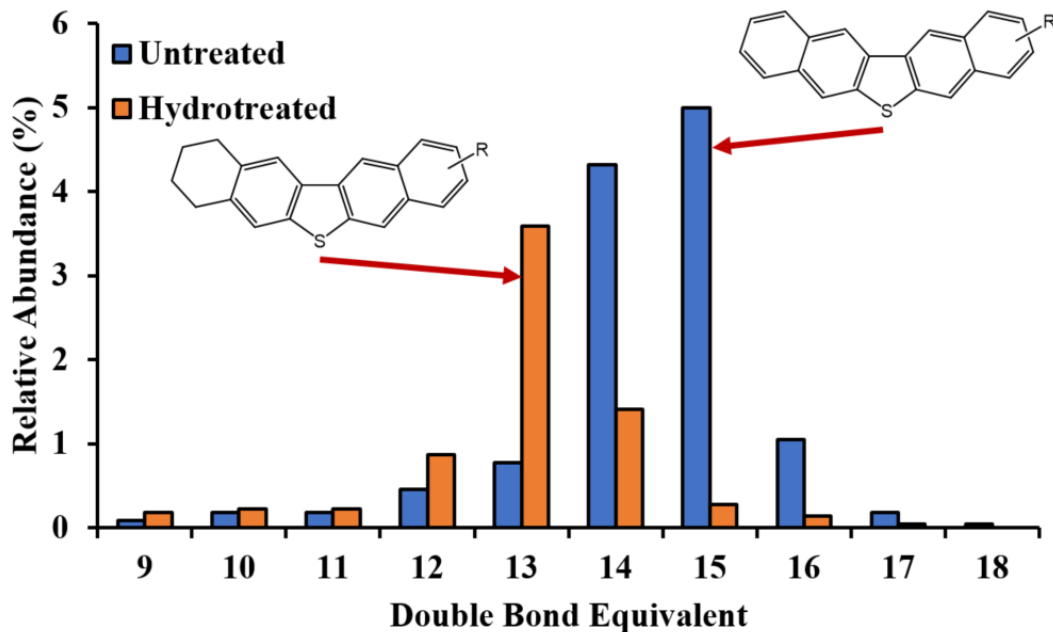
Figure 2.17. Distribution of the monosulfur class before and after hydrotreating of a coker gas oil [92].

A shift occurs in the abundant monosulfur compounds from DBE 15 of the untreated fraction to DBE 13 of the hydrotreated fraction is seen in *Figure 2.17*. Fu et al. suggested hydrogenation of the polyaromatic sulfur compounds [90]. Similar to the hydrogenation pathway of *Figure 2.16*, the higher distillate fraction of monosulfur species is partially hydrogenated. The direct hydrogenolysis pathway is restricted for large alkyl polyaromatic sulfur compounds in higher distillate fractions.

2.3.2 Hydrodenitrogenation

Hydrodenitrogenation (HDN) reactions are studied because of increasing environmental regulations and restrictions of nitrogen in liquid fuels. Prevention of NO_x formation from combustion is desired. Prado et al. published a noteworthy review for nitrogen removal from oil [73]. The nitrogen structures in *Figure 2.11* undergo HDN reactions in hydrotreating. Understanding the nitrogen removal reaction mechanism pathway on a catalyst surface for both basic and non-basic nitrogen provides insight to the types of liquid products formed. Nitrogen

removal and hydrogen addition reactions of select model compounds in hydrotreating are shown in *Figure 2.18* [1][91].

Alkylamines

$$R-NH_2 \ + \ H_2 \ \longrightarrow \ R- \ + \ NH_3$$

Alkylpyrroles

Pyridine
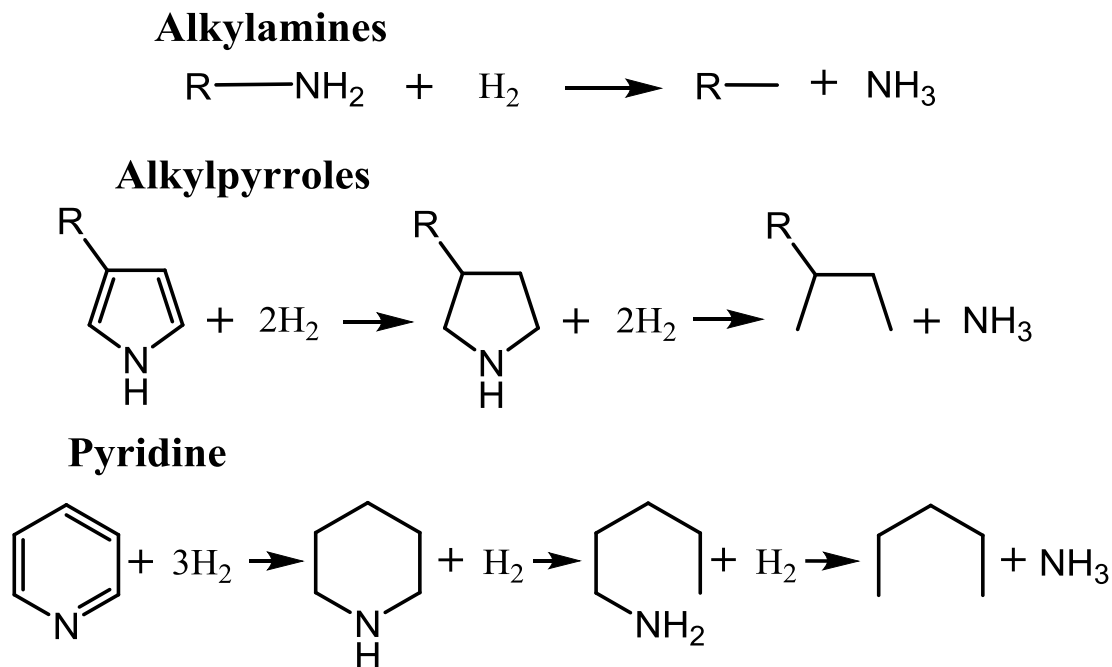
Figure 2.18. Nitrogen removal and hydrogen addition reactions of select model compounds in hydrotreating [1][91].

Nitrogen structures undergo aromatic saturation on a catalytic surface followed by nitrogen removal to form ammonia (NH_3). The carbon-nitrogen bond breakage is unlike the hydrogenolysis pathway. Alkylamine HDN reactions are rapid compared to heterocyclic nitrogen [83]. The reaction steps presented in *Figure 2.18* are with stoichiometric hydrogen requirement. Detailed mechanistic pathways with intermediate steps for other heterocyclic nitrogen structures are found elsewhere [83][91-96].
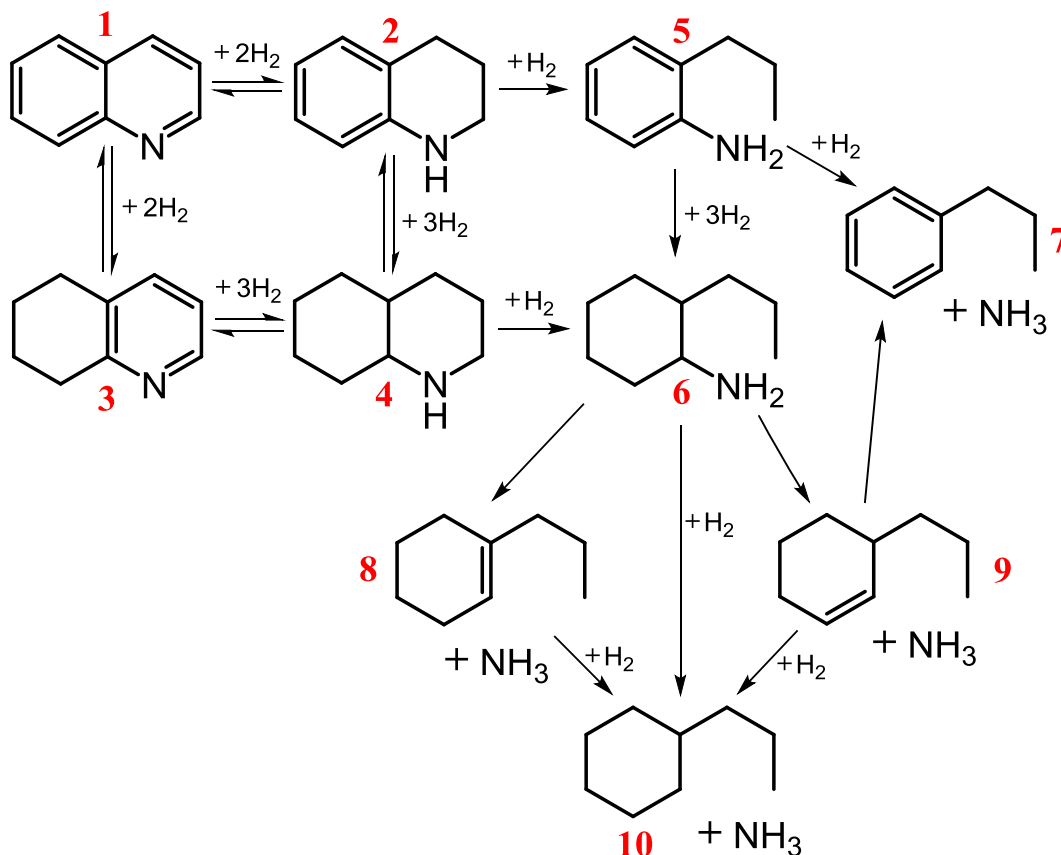
Figure 2.19. Nitrogen removal mechanism of quinoline [92-96].

An example of a reaction mechanism for quinoline HDN is presented in *Figure 2.19* [92-96]. The nitrogen removal mechanism is complex with several reaction steps. Quinoline (**1**) is adsorbed onto a catalytic surface where hydrogen saturates the inner or outer nitrogen ring to tetrahydroquinoline; 1,2,3,4-tetrahydroquinoline (**2**) or 5,6,7,8-tetrahydroquinoline (**3**). Further hydrogen addition ($3H_2$) on the surface leads to decahydroquinoline (**4**). The first four structures are equilibrium reactions. A slower step, the C-N breaks from tetrahydroquinoline (**2**) to form 2-propylaniline (**5**). With hydrogenation, decahydroquinoline (**4**) and 2-propylaniline (**5**) forms 2-propylcyclohexylamine (**6**). As the ring is saturated, the $C-NH_2$ bond breaks from 2-propylcyclohexylamine (**6**) to 1,1-propylcyclohexene (**8**), 1,3-propylcyclohexene (**9**), and/or propylcyclohexane (**10**) with ammonia. Depending on the conditions and catalytic surface, 2-propylaniline (**5**) undergoes $C-NH_2$ bond breakage to form propylbenzene (**7**) with ammonia. Similar to *Figure 2.18*, quinoline undergoes aromatic saturation on a catalytic surface followed by nitrogen removal to form ammonia (NH_3). Larger ring systems in the HVGO, highlighted in

44

Figures 2.12 and *2.13*, are complex nitrogen removal mechanisms with additional intermediate steps and structures. The addition of alkyl or **R** groups to these structures provide steric hinderance in removing nitrogen in hydrotreating [97].

Bej et al. compared the HDN reactions of both basic and non-basic nitrogen structures for a heavy gas oil using a NiMo/Al$_2$O$_3$ catalyst [11]. Similar HDN reactions using model compounds as in basic acridine and non-basic carbazole were compared by the same group [98]. Both studies found the removal rate of basic nitrogen (e.g. alkylpyridines, alkylquinolines, acridine) was much higher compared to non-basic nitrogen (e.g. alkylpyrroles, alkylindoles, carbazole) at similar reaction conditions. Yui and Ng corroborated these results [99]. Stoichiometric hydrogen requirement is higher for HDN compared to HDS because of the aromatic saturation steps. As a result, hydrogen partial pressure in HDN reactions is important.
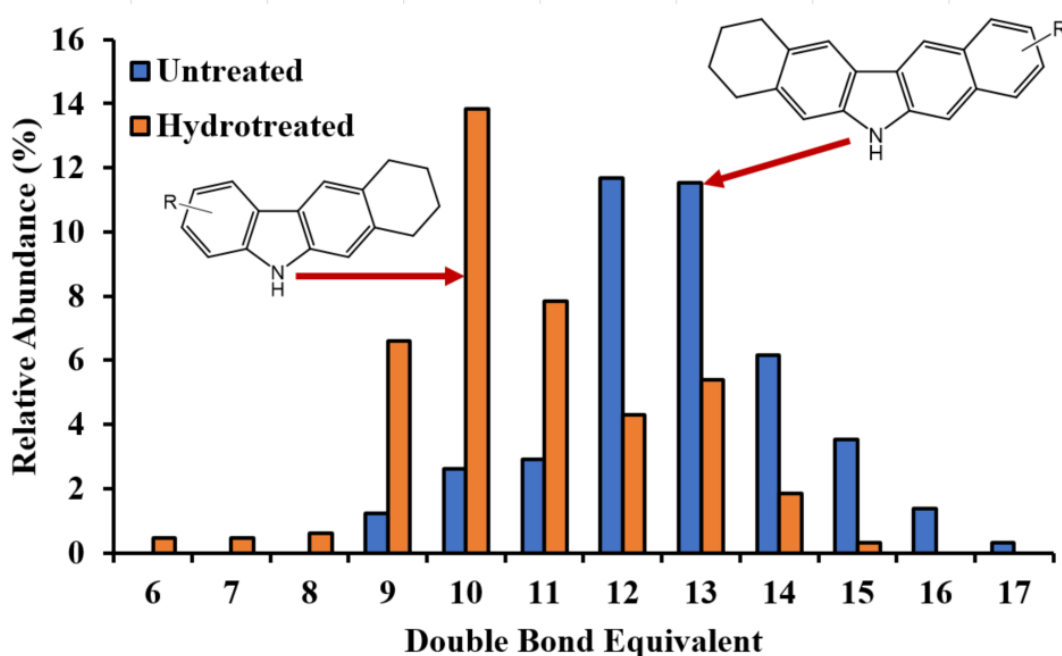
Figure 2.20. Distribution of mononitrogen class before and after hydrotreating of a coker gas oil [90].

Reprinted (adapted) with permission from Figure 11, J. Fu *et al*, "Comprehensive Compositional Analysis of Hydrotreated and Untreated Nitrogen-Concentrated Fractions from Syncrude Oil by Electron Ionization, Field Desorption Ionization, and Electrospray Ionization Ultrahigh-Resolution FT-ICR Mass Spectrometry," *Energy Fuels,* vol. 20, *(3),* pp. 1235-1241, 2006. Copyright 2006 American Chemical Society.

Distribution of the mononitrogen class before and after hydrotreating of a coker gas oil is shown in *Figure 2.20* [90]. The abundant nitrogen class of the untreated coker gas oil cut (483-504°C)

had a DBE of 12-13. The hydrotreated liquid product had a lower DBE of 10. The results provide evidence for the hydrogenation pathway of heterocyclic rings as illustrated in *Figure 2.19*. The results in *Figure 2.20* are for non-basic nitrogen compounds (e.g. alkylcarbazoles). Basic nitrogen results from positive ionization did not show a meaningful change in DBE distribution in Figure 7 of [90]. The appearance of aromatic saturation of nonbasic nitrogen was evident compared to basic nitrogen compounds [90]. Comparable results were obtained by Zhang et al. with a classification of HDN reactivity criteria in Figure 9 of [100]. The formation of amines, 2-propylaniline (**5**), 2-propylcyclohexylamine (**6**), and propylbenzene (**7**) in *Figure 2.19*, are basic in nature. These alkylamines form from higher DBE alkylcarbazole derivatives in hydrotreating. This suggests the conversion of basic nitrogen is difficult to determine [101].

2.3.3 Hydrodearomatization

Hydrodearomatization (HDA) reactions are important in understanding the chemical transformations in hydrotreating. A review on aromatic hydrogenation catalysis by Stanislaus and Cooper provides extensive insights [102]. Depending on the catalytic pathway, HDS and HDN reactions are completed through HDA reactions. Hydrogen saturates the aromatic cores prior to heteroatom removal. The hydrocarbon structures presented in *Figures 2.7* and *2.8* undergo HDA reactions in hydrotreating. Understanding the reaction mechanism pathway on a catalyst provides insight to the types of liquid products formed. One classification of aromatic molecules found in heavy oils is clustered into three types: monoaromatic, diaromatic, and polyaromatics. Higher distillate fractions have increased polyaromatic abundance as highlighted in *Figure 2.7*. Analytical techniques such as supercritical fluid chromatography, high pressure liquid chromatography, and ^{13}C nuclear magnetic resonance are known to determine the concentrations of these clusters [5][102].
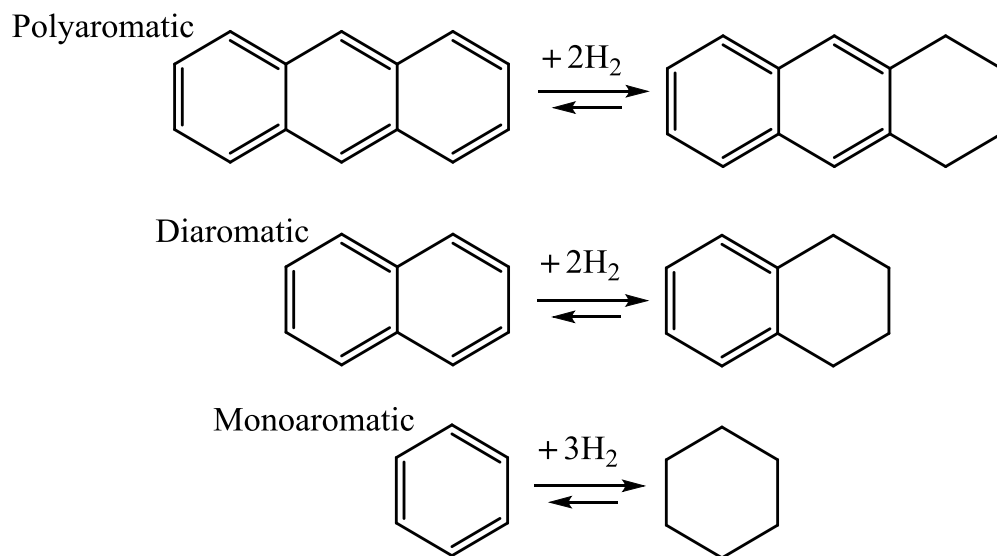
Figure 2.21. Aromatic saturation reactions in hydrotreating [83].

Aromatic saturation reactions in hydrotreating are presented in *Figure 2.21* [83]. These HDA reactions that are exothermic and thermodynamically reversible on catalytic surfaces. Hydrogenation and dehydrogenation of aromatic compounds are contingent on the reaction conditions [6]. Monoaromatics as in benzene, have stronger resonance stabilization energy compared to diaromatics and polyaromatics like naphthalene and anthracene, respectively [15]. The following order of total resonance energies are compared [102]:

Benzene < Naphthalene < Anthracene

Hydrogenation of diaromatics and polyaromatics have lower bond energies distributed throughout the rings. This suggests favorable hydrogenation thermodynamically compared to monoaromatics. As a result, and shown in *Figure 2.21*, the reactivity order for one ring hydrogenation was determined [102]:

Anthracene > Naphthalene > Benzene

Saturation of polyaromatics to monoaromatics are favorable on catalytic surfaces compared to saturation of monoaromatics to naphthenes [5]. Similar to HDN reactions, high or hydrogen pressure with and lower space velocities favor aromatic saturation. Monoaromatics require higher

temperature and pressure to form naphthenes compared to single ring saturation of anthracene and naphthalene. In hydrotreating, complete HDA is not possible. Adsorption and desorption of all types of aromatics, including heteroatomic aromatics with their intermediates compete on the catalyst surface. HDS and HDN reactions of heteroatoms are highly competitive for catalytic sites compared to aromatic hydrocarbons [5][83]. To overcome this challenge, two-stage hydrogenation units are used in industry; the first reactor for HDS and HDN reactions and the second reactor for HDA reactions as seen in *Figure 2.2*. An example of a reaction mechanism for HDA of naphthalene is presented in *Figure 2.22* [83][103].
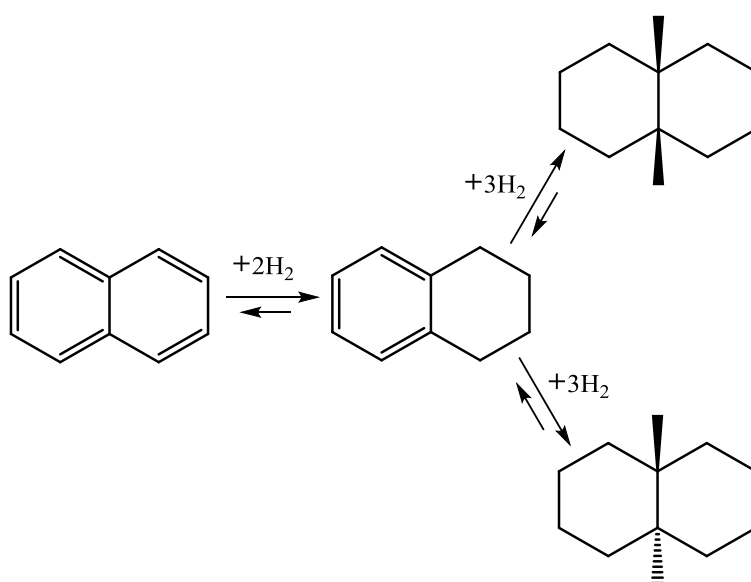
Figure 2.22. Hydrogen saturation mechanism of naphthalene [83].

The hydrogenation saturation mechanism of naphthalene contains limited steps. The reaction rate of naphthalene to tetrahydronaphthalene (tetralin) is higher compared to its saturation to cis and trans decalin isomers [83][103]. Reversible reactions are possible with lower reaction rates. Decreasing the H_2/naphthalene ratio decreased the yield of decalin. The results confirm thermodynamic limitations for complete HDA [83][102-103]. Reactions after initial saturation (e.g. tetralin to decalin), require higher temperature and pressure to favor complete HDA. Larger ring systems, polyaromatics in the HVGO highlighted in *Figures 2.7* and *2.8*, have complex HDA mechanisms with intermediate steps and structures. Additional mechanistic pathways with intermediate steps for HDA reactions are found elsewhere [83].

Table 2.10. Properties of select aromatic structures [59].

	Naphthacene	Anthracene	Naphthalene	Benzene
T_{boil} (°C)	399-450*	340	217±5	80
H/C Ratio	0.67	0.71	0.8	1
Density (g/cm³)	1.35*	1.24-1.28	1.14-1.16	0.88
MW (g/mol)	228.29	178.23	128.17	78.11
		Tetrahydroanthracene	Tetrahydronaphthalene	Cyclohexane
T_{boil} (°C)		318-324*	208±3	81
H/C Ratio		1	1.2	2
Density (g/cm³)		1.1	0.97	0.8
MW (g/mol)		182.26	132.20	84.16

*Predicted properties from ChemDraw Prime 16.0 & Royal Society of Chemistry. *ChemSpider*. Available: http://www.chemspider.com/.

Properties of select aromatic structures are presented in *Table 2.10* [59]. Anthracene, naphthalene, and benzene with their corresponding saturated structures from *Figure 2.21* are identical property trends similar to *Tables 2.6* and *2.9*. As hydrogen is added, the boiling point, H/C, and density of each hydrotreated compound decreases.
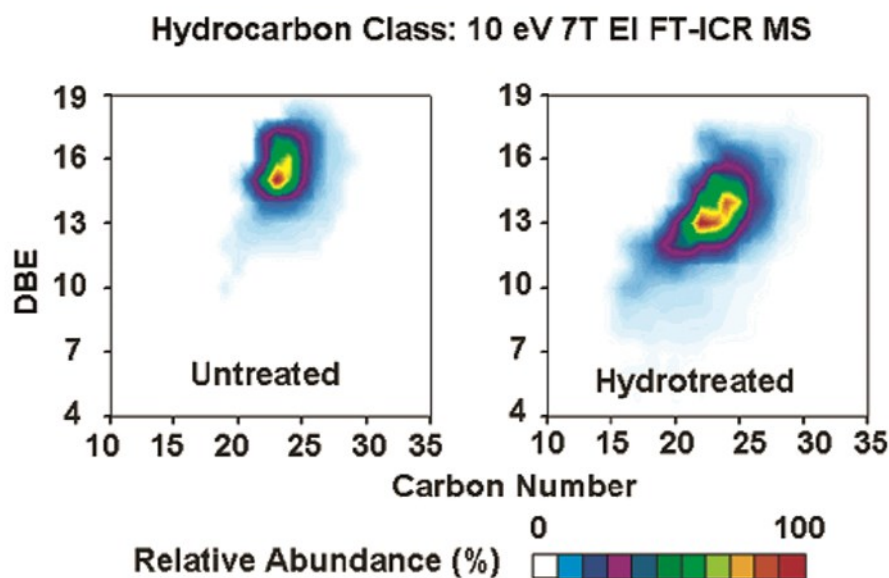
Figure 2.23. Relative double bond equivalent isoabundance contour plot as a function of carbon number for the untreated and hydrotreated coker gas oil cut [90].

Reprinted (adapted) with permission from Figure 11, J. Fu *et al*, "Comprehensive Compositional Analysis of Hydrotreated and Untreated Nitrogen-Concentrated Fractions from Syncrude Oil by Electron Ionization, Field Desorption Ionization, and Electrospray Ionization Ultrahigh-Resolution FT-ICR Mass Spectrometry," *Energy Fuels,* vol. 20, *(3),* pp. 1235-1241, 2006. Copyright 2006 American Chemical Society.

Relative double bond equivalent isoabundance contour plot as a function of carbon number for the untreated and hydrotreated coker gas oil cut is presented in *Figure 2.23* [90]. Fu et al. showed how the carbon atoms are distributed with high DBEs in the coker gas oil; similar to *Figure 2.8* for the HVGO. The hydrotreated product had a reduction in the DBE and a wider distribution of low abundant carbon atoms. These results suggested HDA reactions reduce highly abundant DBE hydrocarbons through 1-2 ring saturations. The carbon number remains in the same range, which is expected because of limited cracking or carbon removal that occurs in hydrotreating. HDS and HDN reactions of heteroatomic polyaromatic compounds increase in relative abundance for the hydrocarbon class and adds to the broad carbon range observed [90]. Similar results are expected for hydrotreatment of the HVGO.

2.3.4 Hydrodeoxygenation and Hydrodemetallization

Hydrodeoxygenation (HDO) and Hydrodemetallization (HDM) reactions, although less reported, occur in hydrotreating. A wealth of information on HDO reactions is found elsewhere [104-106]. From *Figure 2.14* in section 2.2.4, metals exist in the center of large porphyrin structures. Removal is difficult because of the steric hindrance and simultaneous nitrogen removal. Evidence suggests HDM proceeds through partial hydrogenation of the large porphyrins prior to metal removal [3]. The metals, nickel and vanadium, become sulfided from the catalyst surface. As metal concentrations are part per billion levels from *Table 2.8* in the HVGO, the assessment in the liquid products is not examined.

2.3.5 Conversion and Kinetics

Literature contains several conversion and kinetic studies for the reactions of model compounds, heavy feeds, catalysts, operating conditions, and reactor systems. A review of conversion and kinetic studies of hydrotreating industrials feeds is found in *Appendix A*. Conversion is a ratio of how much the reactants changed over the initial amount. Formulas of four conversions used in the calibration models of the fourth objective are presented:

$$Sulfur\ Conversion\ \% = \frac{S_{feed} - S_{product}}{S_{feed}} \times 100 \qquad (2.3)$$

$$Nitrogen\ Conversion\ \% = \frac{N_{feed} - N_{product}}{N_{feed}} \times 100 \qquad (2.4)$$

$$+343°C\ Conversion\ \% = \frac{M(+343°C)_{feed} - M(+343°C)_{product}}{M(+343°C)_{feed}} \times 100 \qquad (2.5)$$

$$Aromatic\ Conversion\ \% = \frac{A_{feed} - A_{product}}{A_{feed}} \times 100 \qquad (2.6)$$

Researchers calculate conversion to determine how operating conditions, catalysts, and other controls affect hydrotreating reactions. The +343°C fraction is chosen as a reference to what previous studies have reported. For the current study, aromatic conversion is on a molecular hydrogen basis obtained from nuclear magnetic resonance analysis.

2.4 Analytical Techniques

To assess product quality, characterization of the hydrotreated liquid products by several analytical methods are completed to understand the chemical complexity and assess product quality. An extensive review of color and chemistry as well as background information to the ex-situ visible spectroscopy analysis is covered in this section. A brief review of the hydrogen nuclear magnetic resonance (^{1}H NMR) analysis used in the current study is reviewed.

2.4.1 Color and Chemistry

The electromagnetic spectrum is shown in *Figure 2.24* [107]. Electromagnetic radiation (EMR) propagates as electrical and magnetic fields of sinusoidal waves that oscillate orthogonally [108]. Under vacuum conditions, EMR travels under 300,000km/s, termed "the speed of light." The speed of light is equivalent to the product of frequency (v) and wavelength (λ). The electromagnetic spectrum is a range of radiation; energy that travels from a source through a medium or a vacuum. Energy reported on frequency basis and is expressed in electronvolts (eV). One eV is equivalent to 1.602×10^{-19}J. Max Plank developed the relationship between the energy of EMR and frequency [108-110]:

$$E = n \times h \times v \qquad (2.7)$$

Where

E is the energy of quanta (eV or J).

n is the quantum number (positive number, 1, 2, 3…).

h is Plank's constant, $6.626×10^{-34}$J·s.

ν is the frequency as determined from the EMR spectrum (Hz or s^{-1}).
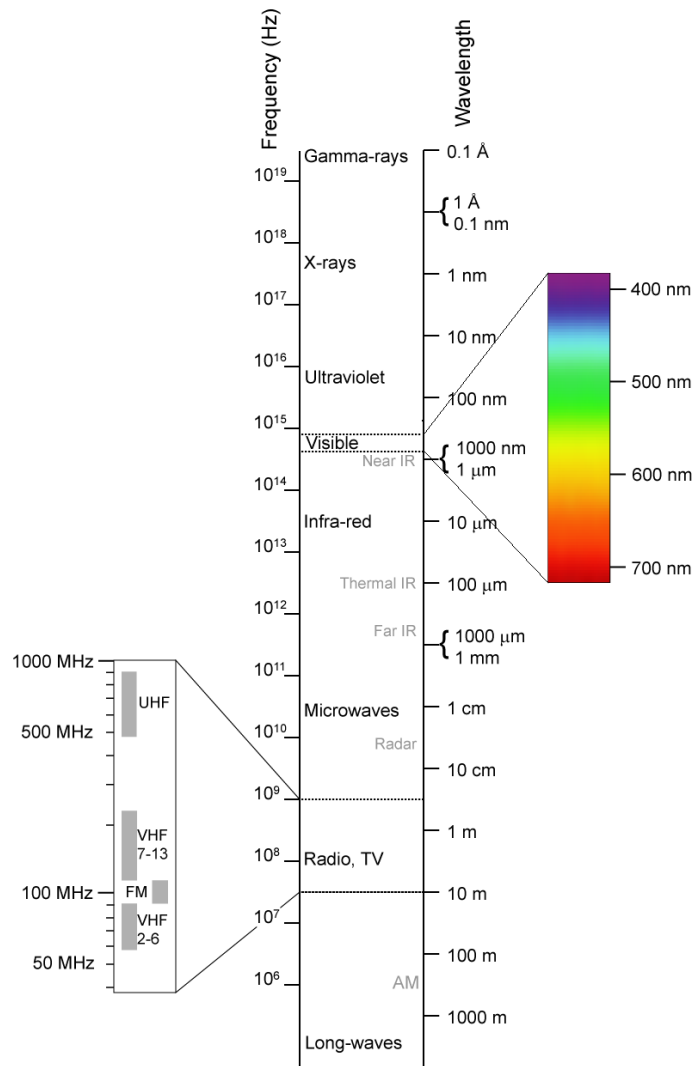
Figure 2.24. Electromagnetic Spectrum [107].

The wavelength of visible light is quantitatively 380 to 750 nanometers (nm) on the electromagnetic spectrum. Other regions, ultraviolet, infrared, microwave, radio, etc. are defined by different wavelengths or frequencies as specified. Electromagnetic radiation wave illustrations are presented in *Figure 2.25*.
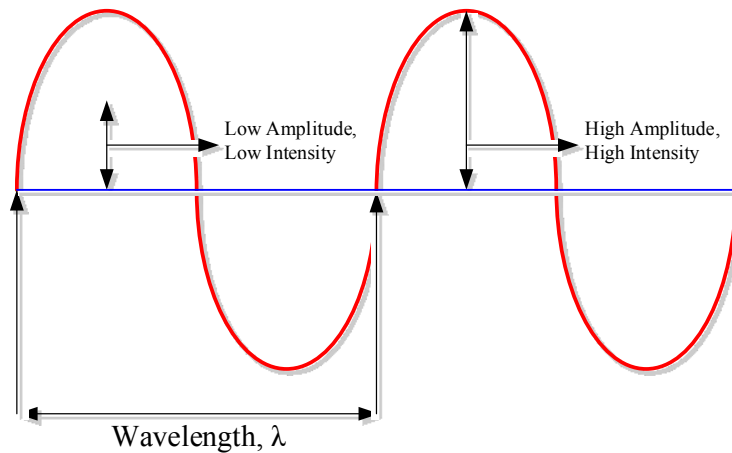
Figure 2.25. Electromagnetic radiation wave illustrations.

EMR travels in singular (mono) or as many (poly) wavelengths. Intensity of EMR is proportional to the amplitude of the wave. Electromagnetic radiation travels as packets of energy termed quanta or photons. Voluminous quantum (smallest unit of energy) is quanta. Through a medium, EMR interacts with matter (atoms or molecules) in several ways as highlighted in *Figure 2.26* [109][111].
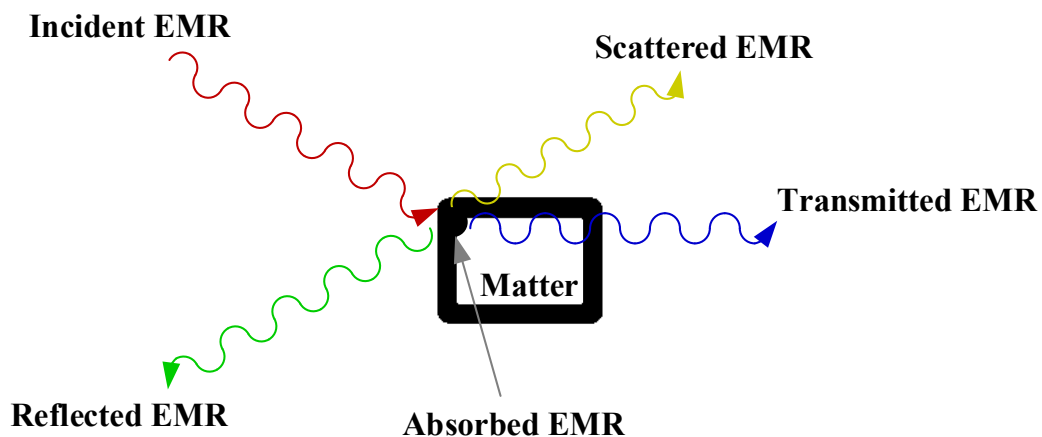
Figure 2.26. Electromagnetic radiation interactions with matter [109][111].

Electromagnetic radiation interacts with matter through absorption, transmission, reflection, and scattering. Absorption is quanta transformed into energy (vibrational motion etc.) taken up by matter. Transmission is quanta passing through the medium unchanged. This happens in transparent materials. Reflection is quanta that mirrors off in a direction equal to the angle of

incidence. Scattering is quanta that reflects off into a different direction because of uneven surfaces. Through transmission, quanta are either refracted, interfered, and/or diffracted. Simultaneous combinations of all the interaction phenomena described are possible.

As EMR undergoes a change in energy, velocity, frequency, etc. from one of the interactions described in *Figure 2.26*, a spectroscopic measurement is possible [110]. Spectroscopy is the study of EMR and the interactions with matter. Measurement of reflected, transmitted and/or scattered EMR provides insight to the atomic and molecular composition of the matter. Absorbed EMR is the difference between the transmitted and incident. Including the reflected and scattered light completes a rigorous EMR balance. Examples of spectroscopic techniques are presented in *Table 2.11*.

Table 2.11. Transitions, energy transfers, spectroscopic techniques, and their electromagnetic radiation regions [110].

Electromagnetic Radiation Region	Atomic or Molecular Transition	Energy Transfer	Spectroscopic Technique
Gamma (γ) rays (<0.01nm)	Nuclear	Absorption	Mossbauer
X-rays (0.01-10nm)	Core electrons	Absorption Photoluminescence	X-ray absorption X-ray fluorescence
Ultraviolet (10-380nm)	Valence electrons	Absorption Emission Photoluminescence Chemiluminescence	Atomic absorption Atomic emission Atomic fluorescence Atomic phosphorescence
Visible (380-750nm)	**Valence electrons**	**Absorption** Emission Photoluminescence Chemiluminescence	Atomic absorption Atomic emission Atomic fluorescence Atomic phosphorescence
Infrared (750nm-1mm)	Molecular vibrations	Absorption	Infrared Raman
Microwaves (1-1000mm)	Electron spin, molecular rotations	Absorption	Microwave
Radio (>1m)	Nuclear spin	Absorption	Electron spin resonance Nuclear magnetic resonance

Atomic or molecular transitions are examined based on the EMR source. Absorption of EMR is the energy transition from a lower state to a higher state. Emission of EMR is the energy transition from a higher state to a lower state. Emission of EMR happens through photoluminescence (following the absorption of EMR) or chemiluminescence (EMR emitted from a chemical reaction). Depending on the strength of the EMR absorbed, from largest to smallest, the transition of energy is either electronic, vibrational or rotational, respectively. Ultraviolet-visible (UV-Vis) regions result in electronic transitions of valence electrons. Infrared to radio waves, less energy intensive EMR, result in vibrational, electron spin and rotational transitions. As highlighted highlight in red of *Table 2.11*, the current study focuses specifically in the visible EMR region and the electronic transition of valence electrons. The use of absorption visible spectroscopy is the analytical method of the second objective. Section 2.4.3 reviews hydrogen nuclear magnetic resonance spectroscopy which examines the spin of hydrogen atoms in the radio EMR region. Color is an attribute of visual perception [108]. Human eyes are sensitive to the band of visible light in the EMR spectrum. Qualitatively, color is described by terms such as Red, Orange, Yellow, Green, Blue and Violet (ROYGBV). Color is quantitatively defined by the wavelength of visible light. What is observed as perceived color is the reflection or transmission of specific wavelengths of visible light. A distinction is made between black and white. The color black is the absorbance of all visible light. The color white is the reflection of all visible light. Visible colors from the EMR spectrum, ROYGBV or 750 to 380nm wavelengths, are either reflections or absorptions of the complementary color to that specific wavelength. An approximate complementary color wheel to demonstrate this idea of absorption to transmission is shown in *Figure 2.27*.
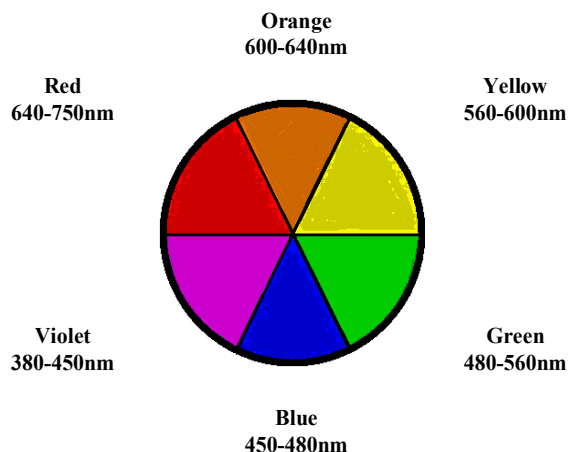
Figure 2.27. Complementary color wheel.

If an object or molecule absorbs all visible wavelengths except that of the 600 to 640nm region, the reflected color is the specified wavelength region or qualitatively orange. If an object or molecule absorbs visible wavelengths in the 450 to 480nm region or blue, the complementary color is the transmitted wavelength, 600 to 640nm or orange. Absorption of specific visible wavelengths cause energy transitions of valence electrons within the molecules and their molecular bonds. From equation 2.7, the energy region of visible light, 380 to 750nm, is calculated. Assuming the speed of light in a vacuum, 299,792,458m/s and a constant quantum number of 1:

$$E_{380nm} = \frac{1 \times 6.626 \times 10^{-34} \text{ J} \bullet \text{s} \times 299792458 \text{ m/s}}{380 \times 10^{-9} m} = {\sim}5.23 \times 10^{-19} \text{ J or } 3.26\text{eV}$$

$$E_{750nm} = \frac{1 \times 6.626 \times 10^{-34} \text{ J} \bullet \text{s} \times 299792458 \text{ m/s}}{750 \times 10^{-9} m} = {\sim}2.65 \times 10^{-19} \text{ J or } 1.65\text{eV}$$

The energy of one quantum of monochromatic visible light ranges from 1.65 to 3.26eV. These energies are enough to excite electrons of the Highest Occupied Molecular Orbital (HOMO), lower energy state, to the Lowest Unoccupied Molecular Orbital (LUMO), higher energy state. In the ultraviolet to visible EMR region the excitation of electrons are sigma-bonds (σ), pi-bonds (π) and non-bonding (n) orbitals to anti-pi (π^*) and anti-sigma (π^*) orbitals (texcited states) [108][110]. *Figure 2.28* illustrates these electronic energy transitions from EMR absorption.
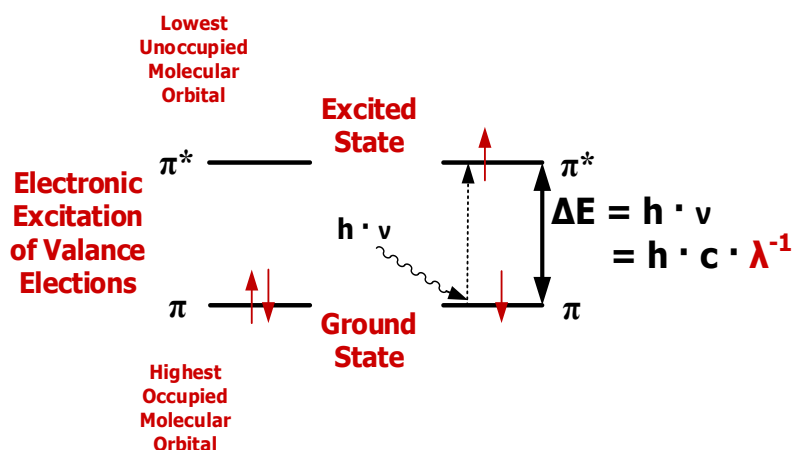
Figure 2.28. Energy changes in electron excitation.

Electrons excited from non-bonding (n) to anti-pi-bonding (π^*) and pi-bonding (π) to anti-pi-bonding (π^*) require EMR energies found in the visible light region (200-600nm). Examples of molecular bonds that have electronic transitions in the visible region include: C=C, C=O, C=N, etc. These molecular bonds that absorb, reflect or transmit visible light are termed chromophores. As chromophores become conjugated with additional double bonds in large molecules, the energy difference between pi-orbitals and anti-pi orbitals decrease. As a result, lower absorption energy is required to excite the electrons (i.e. longer wavelengths of EMR). For example, vitamin A and β-carotene have five and eleven C=C bonds, respectively. Vitamin A appears yellow as it absorbs light in the 380-450nm violet region, while β-carotene appears orange as it absorbs longer wavelength light in the 450-480nm blue region.

To measure the absorbed light (i.e. the probability a photon is absorbed), spectroscopy is used to quantify this energy. This is reported as function of wavelength in the absorption spectra. Determination of how much EMR passes through a sample at a specific wavelength over a controlled reference is used to determine how much EMR is absorbed (transmittance). The absorbance (A) is defined as:

$$A = -\log\left(\frac{I}{I_o}\right) \tag{2.8}$$

Where I is the intensity of light passing through the sample (sample minus dark spectra) and I_o is the intensity of light passing through a reference sample (reference minus dark spectra). The ratio, I/I_o is the transmittance at a specific wavelength. Intensity is the concept of brightness. From *Figure 2.25*, a larger amplitude wave visually appears bright, a lower amplitude wave appears dark. For pure substances dissolved in a solvent or solution, the absorbance (A) is used to find the molar absorptivity (ε):

$$\varepsilon = \frac{A}{c \cdot l} \qquad (2.9)$$

Where

ε is molar absorptivity (L mol^{-1} cm^{-1})

c is the sample concentration (mol/L)

l is the path length (cm)

The relationship in equation 2.9 is famously known as the Beer-Lambert law. If the concentrations of pure substances are low in solution, a linear relationship is expected between absorbance of light and concentration. Assuming a constant path length, the molar absorptivity is the slope at a specific wavelength of light. The molar absorptivity is dependent on the wavelength of light used. Model compounds from *Tables 2.9* and *2.10* ultraviolet-visible absorption spectra are shown in *Figures 2.29* to *2.31* [59][112-113]. The natural logarithm of molar absorptivity, which is constant at any concentration or path length assuming the Beer-Lambert law is valid, is used for comparison of model compounds.
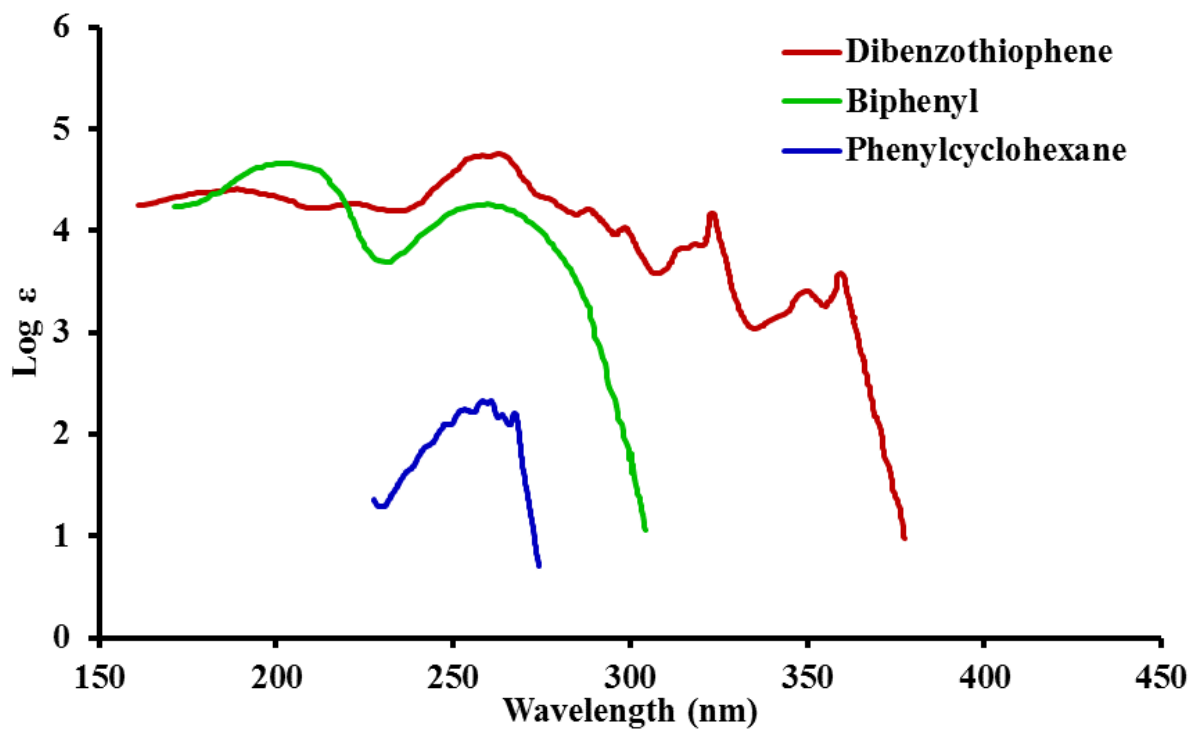
Figure 2.29. Dibenzothiophene, biphenyl, and phenylcyclohexane absorption spectra [59][112-113].
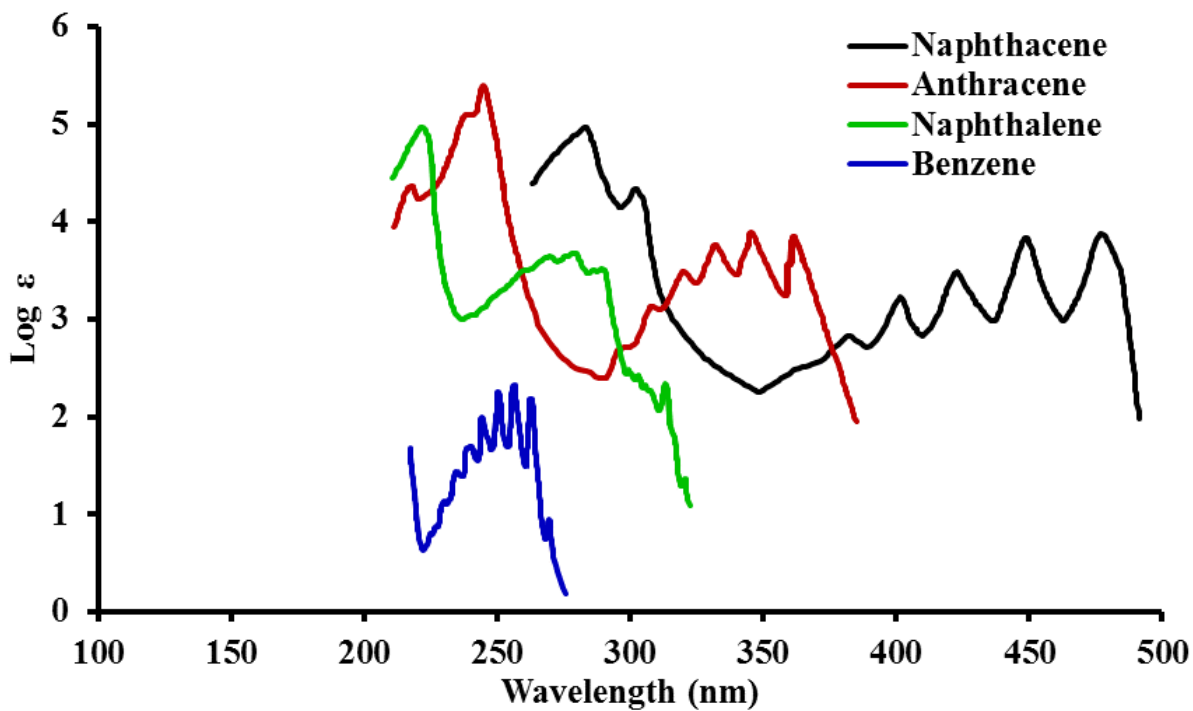
Figure 2.30. Naphthacene, anthracene, naphthalene, and benzene absorption spectra [59][112-113].
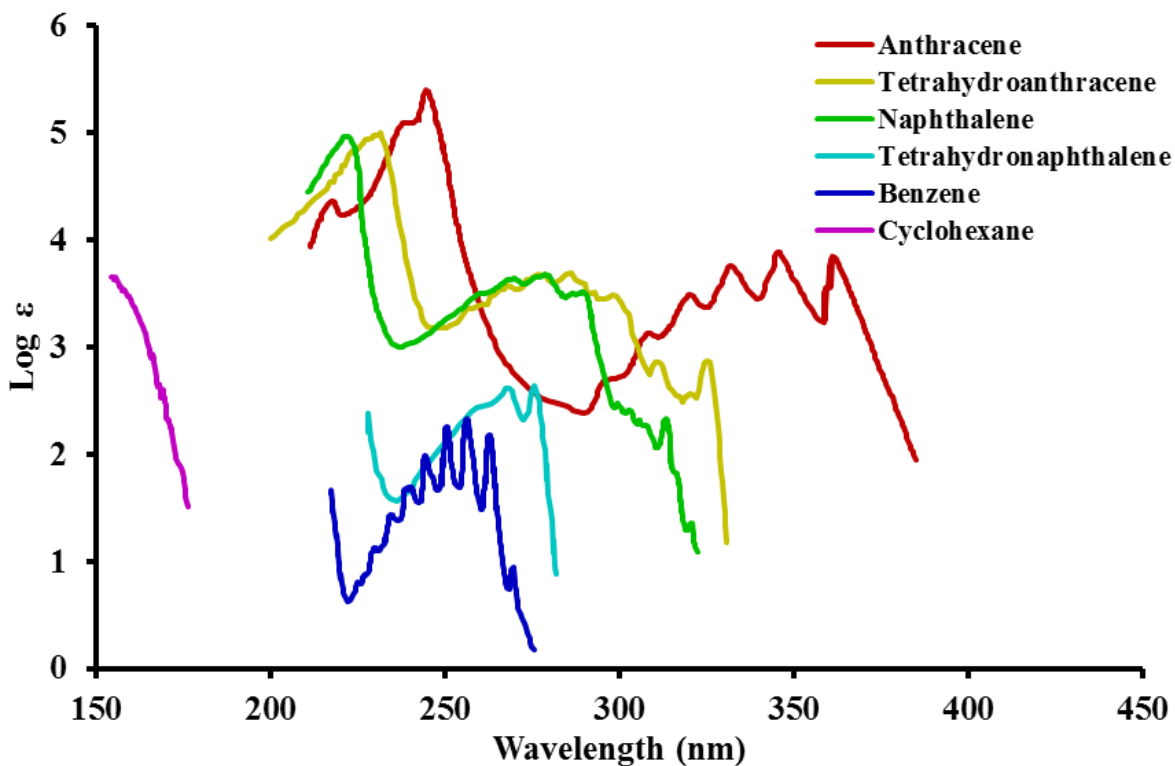
Figure 2.31. Anthracene, naphthalene, benzene, tetrahydroanthracene, tetrahydronaphthalene, and cyclohexane absorption spectra [59][112-113].

As shown in *Figures 2.29* to *2.31*, trends are listed:

- Sulfur removal and hydrogen addition cause hypsochromic and hypochromic shifts in the adsorption spectra.

- Aromatic ring removal (naphthacene to benzene) causes hypsochromic and hypochromic shift in the adsorption spectra. This decreases the number of conjugated C=C bonds and increases the energy transition gap from π to π^* causing shorter wavelengths of absorption.

- Hydrogen addition of aromatics causes hypsochromic shift in the adsorption spectra through deconjugation of the C=C bonds.

These trends are expected for hydrotreatment of the HVGO because of HDS, HDN, and HDA reactions causing deconjugation and reduction of C=C bonds in the multicomponent mixture of molecules highlighted in section 2.2.

For multicomponent mixtures as in the HVGO, deviations from the Beer-Lambert law are expected. As the concentration increases the mixture becomes complex with multi light

60

interactions. The transmitted light is a result of multiple interacting interchromophoric molecules. An example illustration of light transmission for pure and complex substances is shown in *Figure 2.32*.
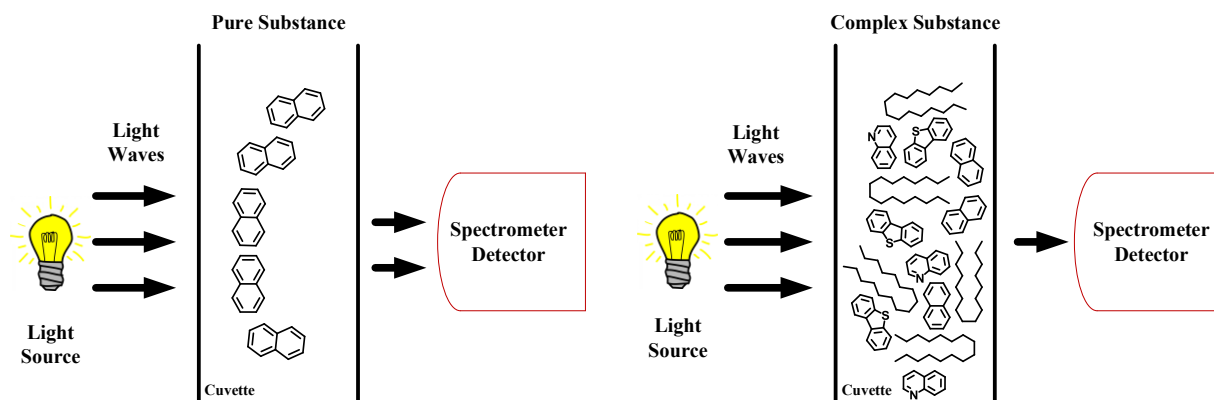
Figure 2.32. Example illustration of light transmission for pure and complex substances [114].

The pure substance (naphthalene) diluted in a solvent absorbs light at specific wavelengths based on its concentration present. Increasing the concertation of the pure substance causes coupling interchromophoric interactions and deviates the Beer-Lambert law from linearity. A complex substance like heavy oil, the right side of *Figure 2.32*, has multiple interchromophoric light interactions with several highly π-conjugated molecules. The molecular absorptivity is no longer constant as an array of molecules at different concentrations produce multiple absorbance values. These absorbances are coupled into a distribution over a broad range of wavelengths. The current study examines these multiple interchromophoric interactions of hydrotreated liquid products. Although not valid, the Beer-Lambert law is tested as a simple least squares calibration model for comparison in the fourth objective.

2.4.2 Color of Oils

Historically, industry used color of oil as an approximate indication of refinement. Black oils tend to represent raw crudes, bitumens, and asphalt material. Condensates, jet fuel, diesels, gasoline, etc. transition from brown to yellow-clear, respectively. These qualifications are based on the

reflected light and visual interpretation. Standard test methods have been developed to characterize color based on scales. Examples include ASTMs D156, D1209, D1500, D1544, D2392, D5386, D6045 [115-121]. These methods are based on standard color scales and recorded as a value that could be included in a crude oil assay. Standard spectroscopic techniques (ultraviolet to visible region) have also been developed to measure naphthalene hydrocarbons in aviation turbine fuels (ASTM D1840) and petroleum products (ASTM D2008) [122-123]. Additional information on these standard techniques, calibration, and performance of ultraviolet-visible spectroscopy is found elsewhere (ASTM E169, E275, and E925) [124-126].

Mullins et al. studied the optical density spectra of crude oils [127]. Optical density (OD) is defined as

$$OD = c \times \varepsilon = \frac{A}{l} \qquad (2.10)$$

This equation is a rearrangement of the beer-lambert law. The absorbance over the optical path length is plotted as a function for 22 crude oils in *Figure 2.33* [128].
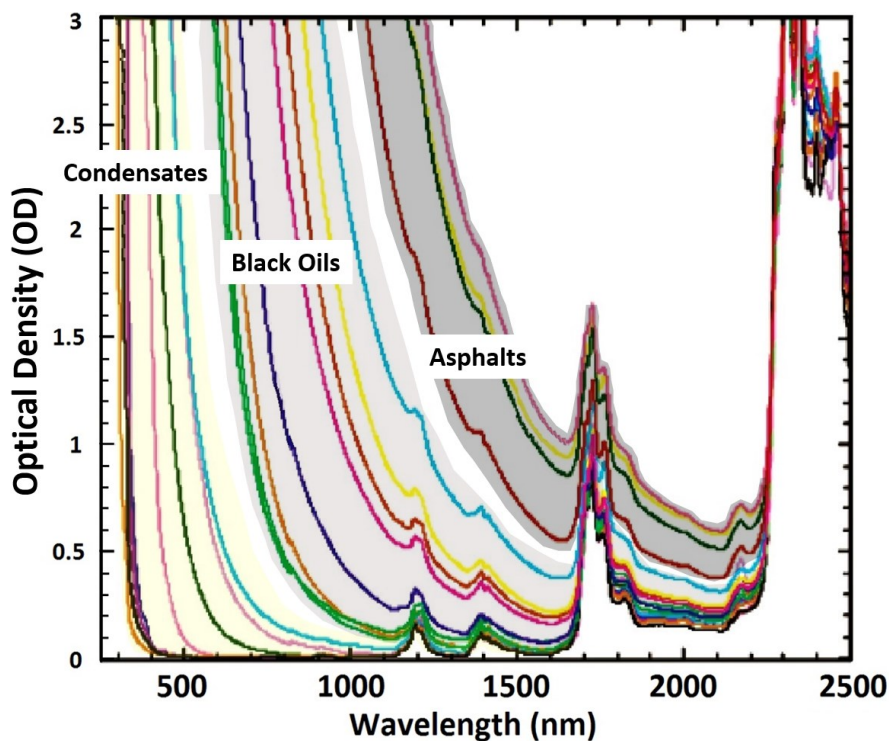
Figure 2.33. Absorption spectra of 22 crude oi samples [128].

Hypsochromic shifts from asphalts to condensates is evident in *Figure 2.33* [128]. The authors sugguest the polycyclic aromatic hydrocarbon (PAH) concentrations are associated with absorbance in the visible region. These structures described as 4-10 fused rings or asphaltenes. The coupling interactions of these chromophoric aromatics cause expontential decay absorbance with increasing wavelength. As the concentration of PAHs decreases, the spectra continuum hypsochromically shifts to lower absorbance wavelengths. The authors suggest the condensates are oils with low concentrations of PAH-asphaltene structures because they do not exhibt absorbances in longer wavelength regions as in black oils and asphalts. However, this attribute is not nessesaryly a reduction of PAH-asphaltene structures, but aromatic saturation and heteratom removal shown in *Figures 2.29* to *2.31*. Other deaggregation or disentanglement phenomea of chromophoric molecules is possible. Noteworthy information on this subject is found elsewhere [129].

Yoon et al. characterized fractions of Athabasca bitumen [130]. Athabasca bitumen was separated into three fractions, saturates with aromatics, resins and asphaltenes. A Shimadzu UV-2100 spectrometer ranging from 240-600 nm was used to measure absorbance of Athabasca bitumen and its separated fractions. Intensity of absorbance spectra from largest to smallest were asphaltenes, resins, saturates with aromatics, respectively. These results are similar to the trends in *Figure 2.33*. A small peak at 410 nm was seen in bitumen, resins, and asphaltene samples. The authors attributed this peak to the VO^{2+} complex, similar to what Evdokimov et al. found [131]. The authors concluded UV-Vis spectroscopy displayed different aromatic constituents of the three fractions measured.

The current study does not examine the extent of asphaltenes, phorphyrins, or vanadium complexes in hydrotreatment. The hydrotreated liquid products are expected to display similar trends to that of the condensates shown in *Figure 2.33*.
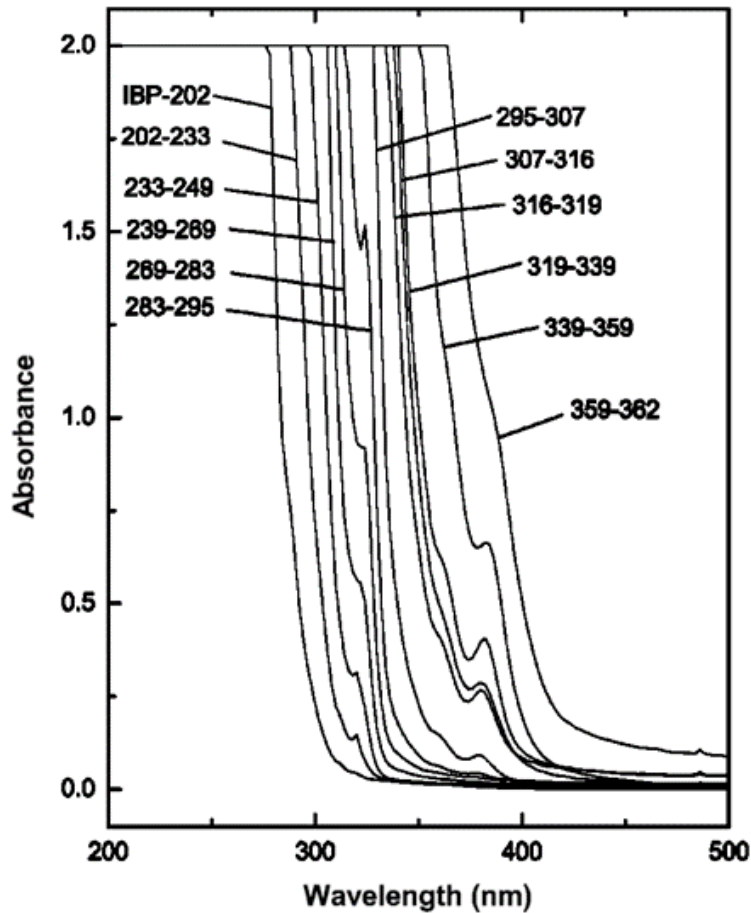
Figure 2.34. Adsorption spectra of oil distillation cuts [132].

Ultraviolet-visible absorption spectra was collected for oil distillation cuts in *Figure 2.34* by Shoute *et al.* [132]. The boiling point correlated with half the maximum absorbance values in the UV region. The authors concluded a positive relationship between UV absorption spectra and the oil distillate boiling point temperatures.
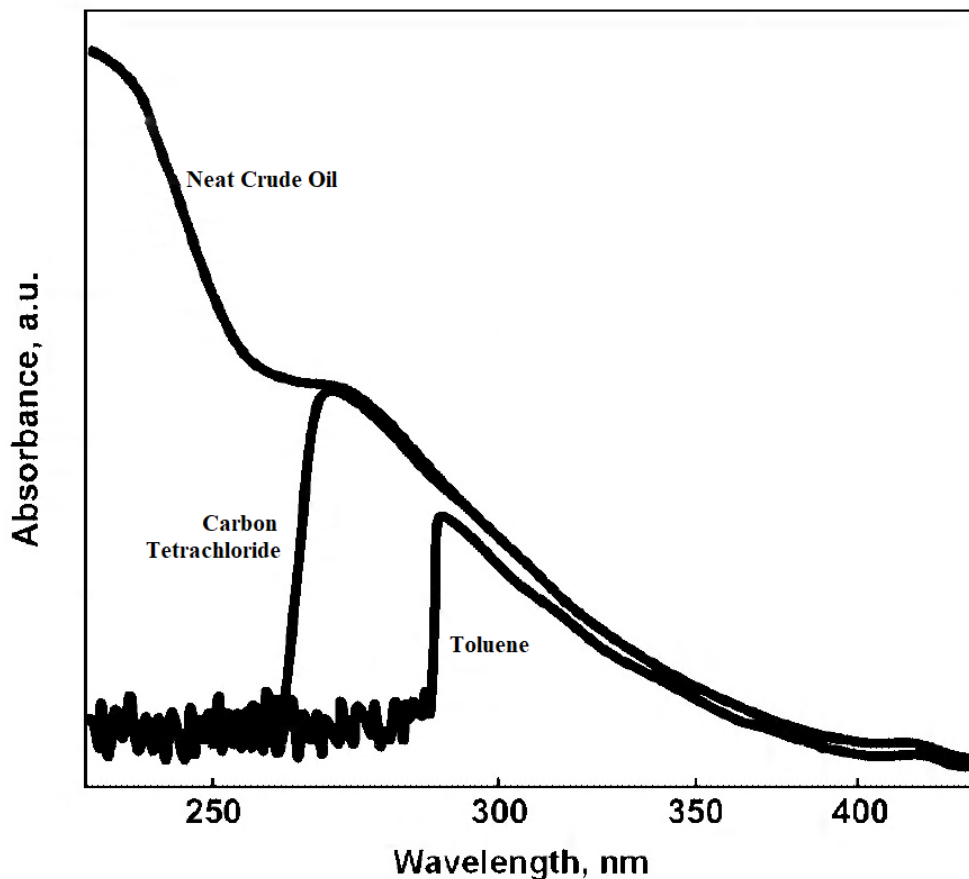
Figure 2.35. Solvent diluted and neat crude oil UV-Vis absorption spectra [133].

Evdokimov and Losev studied the solvent dilution effect of neat crude oil as highlighted in *Figure 2.35* [133]. The neat crude was diluted in toluene and carbon tetrachloride. The absorbance signal significantly drops respective to the solvent used. This is directly impacted by the solvent used in the dilution. Toluene (235-275nm) and carbon tetrachloride (<200nm) have strong absorption in the UV region. The significant drop is termed the absorption edge [133]. The solvent diluted oil follows the spectral trend (significantly overlaps) of the neat crude until the respective absorption edge of the solvent. The authors suggest researchers ignore solvent effects and claim experimental artifacts to the UV-Vis absorption spectrum of crude oils/asphaltenes. The current study does not dilute the hydrotreated liquid products in solvent for visible adsorption measurement. This is advantageous in development of a probe or tool in an online process where a sub-sample and solvent addition is avoided for a visible measurement.

UV-Vis Development

From much of the research [127-128], Mullins developed and patented a probe to measure absorption spectra of crude oils [134]. The OD, equation 2.10, is used with a model to output a value that is correlated to an oil classification (i.e. asphalt, blank oil, condensate). The technology has been useful for classification of in-situ formations to determine whether crude oil or mud filtrate exist. Haberman and Overfield used ultraviolet absorption to determine aromatics concentration in hydrocarbon oil [135-136]. The authors developed correlations to predict one to four aromatic ring core concentrations based on an integrated oscillator strength, the integral of absorbance as function of photon energy. Standard errors were about 1% for all oil samples. Koseoglu et al. patented a crude oil characterization method using a UV-Vis to determine the density and aromaticity of the sample [137]. The mass of sample and spectra are used to determine a UV-Vis index which characterizes the oil from a calibration set.
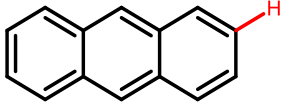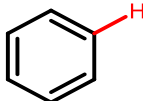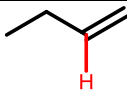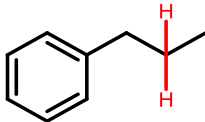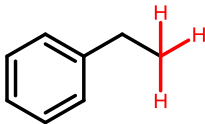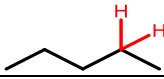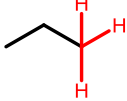
2.4.3 Hydrogen Nuclear Magnetic Resonance

Hydrogen Nuclear Magnetic Resonance (^{1}H NMR) spectroscopy is an analytical technique that examines protons of atomic hydrogen nuclei based on magnetic properties. Hydrogen (^{1}H) is the most abundant proton isotope (>99%) compared to carbon, fluorine, phosphorus, and other atoms. Hydrogen has a ½ spin quantum number (two spin states, +½ or -½) and a magnetic momentum of circa 2.79. Spinning protons in the hydrogen atom have magnetic moments positioned with an axis. When a magnetic field is applied to the hydrogen atoms, the proton spins align from random orientation to a parallel spin state (lower energy, α) or antiparallel spin state (higher energy, β) [108][140]. When a pulsed radio frequency is applied (identical to the Larmor or precessional frequency), the spin axis tips. At the right pulsed radio frequency, the protons become in resonance, absorbing energy that caused the axis to tip [108][140]. The energy is re-emitted seconds later as the spin axis decays back (relaxes) to the parallel or antiparallel state. The re-emitted energy is detected by a radio frequency receiver in a different plane of the magnetic field. This remission energy depends on the electrons adjacent or surrounding each hydrogen proton (i.e. electrons from carbon atoms in this case). For example, aliphatic hydrogen (CH_2, CH_3) has a different frequency compared to aromatic hydrogen (double bonds in rings of carbon). Each compound has a unique ^{1}H NMR spectrum. The spectrum is a plot of intensity (radio frequency applied) as a function of chemical shift (adsorption). The chemical shift is the ratio between the resonance frequency (signal

minus reference) of hydrogen protons in the sample to the external magnetic field applied. This ratio is highly dependent of the adjacent or surrounding electrons of the hydrogen nuclei. Chemical shifts are normalized by the frequency of the spectrometer to compare with other magnetic field strengths. Tetramethylsilane is an example of a standard with a peak at zero chemical shift.

A distribution of hydrogen protons attached to the carbon atoms is expected to generate a broad spectrum for heavy oils as in HVGO and its liquid products. The challenge is to determine how hydrogen atoms are grouped or classified based on chemical shift regions. Previous studies tested known concentrations of model compounds to create standards for hydrogen atoms. The chemical shift regions were determined based on correlating hydrogen concentrations to area under each chemical shift signal. An example of these chemical shift regions based on model compound standards is presented in *Table 2.12* [138-139].

Table 2.12. Chemical shift regions for hydrogen nuclear magnetic resonance [138-139].

Hydrogen Type	Chemical Shift Region (ppm)	Example Structure
Polyaromatic hydrogen	10.7 - 7.4	
Monoaromatic hydrogen	7.4 - 6.2	
Olefinic hydrogen	6.2 - 4.3	
α-Aromatic hydrogen (CH$_2$)	4.3 - 2.4	
α-Aromatic hydrogen (CH$_3$)	2.4 - 2	
Aliphatic hydrogen (CH$_2$)	2 - 1.09	
γ-Aliphatic hydrogen (CH$_3$)	1.09 - -0.5	

The chemical shift regions for hydrogen nuclear magnetic resonance used in the current study is presented in *Table 2.12* [138-139]. Debate on the exact peak assignment regions is found in

literature [141-145]. Speight used several standard organic compounds to build a structural assignment of proton resonance signals to characterize Athabasca bitumen [141]. Other studies reported a table of the chemical shift regions used for their classification [142-145]. All the studies report single aromatic hydrogen within the 6 to 10.7 chemical shift region. Kapur et al. reported similar assignment to *Table 2.12* of polyaromatic hydrogen greater than 7.4 [145]. The total aromatic region was reported as low as 6 by Yang et al. [6]. Mühl and Srića reported an olefinic hydrogen region of 4.5 to 6 [142]. However, olefinic hydrogen is not expected for the HVGO and its liquid products. The distribution of CH_2 and CH_3 groups in aromatic and aliphatic hydrogen is less than 4.5 by all reports. The total α-aromatic hydrogen is reported in agreement between 4.5-4.3 to 1.9-2 chemical shifts, Speight reported as low as 1.7 chemical shift [141]. The total aliphatic hydrogen, including the CH group, is less than 2 and starts at 0.5 chemical shift, Ali et al. reported 2.2 for this chemical shift [144]. *Table 2.12* literature reported -0.5 as the initial chemical shift for γ-Aliphatic hydrogen.

The current study uses *Table 2.12* as the classification region for the ¹H NMR results. Three clusters of molecular hydrogen concentration are examined from the NMR spectra results. These clusters include total aromatic, α-aromatic, and aliphatic hydrogen. The chemical shift ranges are 6.2 to 10.7, 2 to 4.3, and -0.5 to 2, respectively. The chemical shift region assignments agree within what has been reported by others [141-146]. The aliphatic hydrogen is corrected for chloroform-d solvent and the tetramethylsilane reference. Conversion, section 2.3.5, is calculated from aromatic and total aromatic (aromatic + α-aromatic) molecular hydrogen concentration results.

2.5 Chemometric Analysis

To address the fourth objective of the study, chemometric analysis is completed to determine if visible spectra data of hydrotreated liquid products can be calibrated to their analytical characterization results. Chemometrics is the study of chemical data by applying empirical and multivariate modeling [147]. The modeling is data driven and requires background information on the system to extract meaningful information on the physical and chemical phenomena. Further information on the subject is found elsewhere [148-149]. Studies in literature use multivariate models on the EMR interactions as highlighted in *Table 2.11*. The ability to calibrate these spectral measurements to the physicochemical properties of the liquid products is desired.

Unlike single parameter models, were one variable is dependent on another variable, multivariate models utilize a matrix of data. In the current study, that matrix of data is the visible adsorption spectra of the hydrotreated liquid products.

$$y_{unkown} = X \cdot b \tag{2.11}$$

Where $y_{unknown}$ is the physicochemical property variable predicted, X is a $1 \times n$ matrix of the visible adsorption spectrum (1 sample $\times$ n absorbance wavelengths), and b is the regression coefficient (n regressor coefficients $\times$ 1). The key factors in equation 2.11 are the X matrix and the regression coefficient vector b. Absorbance variables included and the regression coefficients are determined based on the calibration modeling method employed. Four methods used in the current study are reviewed further in sections 2.5.1 to 2.5.4.

2.5.1 Simple Least Squares (SLS)

Simple least squares (SLS) is a linear method comparable to the previously discussed Beer-Lambert law [150-151]. The visible spectra data are assumed as a linear correlation of the physicochemical property. The SLS model is useful when the measured adsorption spectrum is related to the pure component in a mixture. As the Beer-Lambert law is successful in calibration of diluted samples to predict their component concentration, oil physicochemical property calibration may be limited due to its multicomponent nature. The assumption that the visible adsorption spectra are linearly correlated to their physicochemical properties is tested in the current study. Duckworth has summarized advantages and disadvantages of the SLS method [150]:

Advantages	Disadvantages
• Mathematical model is simple and easy to calculate rapidly.	• Complete speciation of every component is required. This is a challenge in a multicomponent mixture like oil.
• No specific absorbance wavelength is selected. The current study examines the entire visible spectra collected.	• Multi-interacting molecules do not provide distinct absorbance peaks. Visible spectra are a continuum.
• Comparison of several absorbance channels provide a better understanding of the visible spectra and how it is related to the physicochemical property measured.	• An intercept is required. Complete linearity through an origin, as in the Beer-Lambert law, is unlikely for a multicomponent sample.

2.5.2 Multiple Linear Regression (MLR)

The multiple linear regression (MLR) method is useful when a handful of measured absorbance values are used to predict the physicochemical property of interest. Unlike the SLS model where absorbances at each wavelength are used, the MLR method selects wavelength channels for the calibration model. The model includes selected wavelengths channels equal to or less than the number of samples used in the calibration. Determining the optimum number of wavelength channels is important in building calibration models for each property. A stepwise selection method is used in the current study for MLR. The stepwise method is iterative in comparing the regressors of each wavelength channel. Regressors are added or removed based on a standard test statistic. After each step, a significance test is completed on each variable in the model to determine whether it should be kept or removed. For the stepwise method used in this study, the significance tolerance (p-value) for added and removed variables are 0.05 and 0.1, respectively [152]. Duckworth has summarized advantages and disadvantages of the MLR method [150]:

Advantages	Disadvantages
• Linear relationship to wavelength channels selected.	• Wavelength channel selection is difficult. Stepwise method is used in the current study. This may lead to overfitting. Other selection methods exist [151].
• Mathematical model is simple and easy to calculate rapidly.	• Number of wavelength channels or variables used in the model must be less than the sample size.
• Multicomponent or complex samples with multiple absorbance peaks can be modeled.	• Large sample sets are required.

2.5.3 Principal Component Regression (PCR)

Principal Component Analysis (PCA) is a tool used to reduce the size of a data set [148-149]. The smaller and meaningful data set highlights relevant information. This smaller data set is comprised of principal components that are uncorrelated latent variables. These components are linear combinations of the visible spectra. The first component explains the highest variability in the data set. The second, third, fourth, etc. explain subsequent portions of variability in the data set. Visually, PCA is a unique way to look at the data set and highlight relationships. Principal component regression (PCR) uses these principal components of the visible spectra as variables for multivariate calibration with the physicochemical properties. This calibration is similar to the MLR, however the latent variables are used for the calibration. To prevent overfitting and determine the optimal number of latent variables to use in each model, a cross-validation method is employed [151]. The cross-validation procedure calculates the mean prediction error of the response with each latent variable included in the calibration model [153]. As the total number of latent variables included in the model results in a minimum mean prediction error, the optimum is reached. Additional variables beyond optimum over fit or underpredict the physicochemical property response. Duckworth has summarized advantages and disadvantages of the PCR method [150]:

Advantages	Disadvantages
• No wavelength selection.	• Slow and mathematically complex compared to SLS and MLR.
• Less visible spectral noise effects. Highlights best components or features of the spectral set.	• Large sample set required for an accurate calibration.
• Great for multicomponent mixtures.	• Latent variables included in the models may not be related to physicochemical properties of interest. Cross-validation should help avoid this.

2.5.4 Partial Least Squares Regression (PLSR)

The partial least squares regression (PLSR) is similar to PCR except the latent variables obtained have a maximum covariance between the predictors and response [148-151]. The predictors and response are the visible spectra and the physicochemical properties, respectively. The cross-validation procedure is used to determine the optimum number of latent variables for the calibration model [151][153]. Duckworth has summarized advantages and disadvantages of the PLSR method [150]:

Advantages	**Disadvantages**
• No wavelength selection, all visible spectra is used.	• Slow and mathematically complex compared to SLS and MLR.
• Eigenvectors are related to the physicochemical properties of interest.	• Large sample set required for an accurate calibration.
• Calibration models are robust with fewer components compared to PCR.	• Models are complex.
• Excellent for multicomponent mixtures.	

2.5.5 Chemometric Studies

A review of chemometric studies on industrial feeds with three EMR interactions are reviewed.

[1]H Nuclear Magnetic Resonance

Near infrared and ^{1}H NMR spectroscopy were used in chemometric modeling of FCC feedstocks [154]. A large sample set, >30 for properties measured, from four different FCC units were compared. Properties such as density, sulfur, nitrogen, viscosity, carbon residue, and simulated distillation were modeled with PLSR. Correlation coefficients (R) were >0.88 for all properties measured except for the initial boiling point.

Molina et al. developed a model using PLSR with ^{1}H NMR data to predict physicochemical properties and distillate cut yields of Colombian crudes [155]. Increasing the number of factors in

each model increased the coefficient of determination for each physicochemical property predicted. The studied was limited to six crude samples.

Nielsen et al. used ^{1}H NMR data with multivariate data analysis to predict physicochemical properties of 82 heavy fuel oils [156]. Properties assessed included carbon aromaticity index, density, gross and net calorific values, micro carbon residue, sulfur, and water concentrations. The root mean squared prediction error was less than 1.5 for all models developed.

Souza et al. used PLSR with ^{1}H NMR data to predict the cetane number (ASTM D613) for 50 diesel samples [157]. The coefficient of determination was 0.91 for the calibrated model.

Duarte et al. used PLSR with ^{1}H NMR data to predict distillation temperatures of 74 Brazilian crude oils [158]. The root mean squared prediction error decreased with increasing distillation temperature. Less than 5% error was achieved for the temperatures higher than 55% cumulative mass distilled.

Infrared

Near-Infrared (NIR) spectra of 81 atmospheric residue samples was calibrated to American Petroleum Institute (API) gravity or density, by Chung and Ku [159]. The data was collected in the 1100 to 2500nm spectral region. Partial least squares regression was used to calibrate the API of four spectral intervals. Low standard prediction errors were obtained for the prediction data set. The infrared absorbance spectra in the 1200-2400nm region of 22 crude oil fractions was calibrated to their physiochemical properties by Satya et al. [160]. The saturate, aromatic, resin, asphaltene, carbon residue, carbon, hydrogen, sulfur, nitrogen, density, and molecular weight were calibrated using PLSR. All models resulted in high predictive ability for crude oil samples. As the study was limited to 22 samples, the authors concluded additional samples would improve their calibration curves.

The total acid number (ASTM D664) was calibrated to mid-infrared attenuated total reflection spectroscopy using PLSR by Jingyan, Xiaoli, and Songbai [161]. The sample set consisted of 280 crude oil samples. The spectra ranged from 4000 to 650cm^{-1}. The authors reported at 0.96 coefficient of determination for their calibrated model.

Flash and cloud points of 560 diesel samples were calibrated with an 800-1700nm NIR spectrometer by Chen et al. [162]. Five forms of the PLSR models were compared to determine

which led to optimal predictions. A recursive wavelength-selection method was found as the best PLSR prediction model with the lowest root mean squared prediction error.

Fourier-transform infrared (FTIR) spectroscopy in the 4000-500cm^{-1} region was used by Pinheiro et al. to calibrate density, viscosity, TAN, aromatic, naphtha, and paraffinic concentration data to lubricant oil samples [163]. Several modeling methods including MLR, PCR, and PLS were used in the calibration. The authors found that the optimal predictive models were tailored specifically to the measured property of interest. Density, aromatic, naphthenic, and paraffinic concentration data resulted in the best coefficient of determinations.

Chakravarthy et al. studied the calibration of total carboxylic acid number (TCAN) and sulfur concentrations of 64 vacuum gas oil samples with attenuated total reflectance Fourier transform infrared (ATR-FTIR) spectra [164]. Partial least square regression models were developed. Both PLSR models yielded optimal calibration and prediction results in the infrared regions.

Ultra-Violet and Visible (UV-Vis)

Wentzell et al. completed a multivariate calibration study of UV spectra for 114 light gas oils and diesel fuels [151]. The properties modeled were saturate, monoaromatic, diaromatic, and polyaromatic concentrations obtained from supercritical fluid chromatography (SFC). Four calibration methods, SLS, MLR, PCR, and PLSR, similar to those of the current study, were assessed. The PCR and PLSR models were favored optimally compared to SLS and MLR for predicting saturate, monoaromatic, and diaromatic concentrations. The authors concluded on the excellent use of UV spectroscopy to reliably predict these concentrations with less than 5% relative error. The study was limited to the four properties quantified from SFC.

Ferrer et al. performed chemometric analysis of 42 diesel and vacuum gas oil samples with ultraviolet-visible spectra [165]. A HP8453 spectrophotometer was used to measure the UV-VIS spectra. The samples were diluted in cyclohexane and placed in 1 or 2mm cuvettes. Properties similar to the Wentzell et al. study were measured with a gas chromatograph mass spectrometer (GC-MS). Additional speciation of the samples into paraffins and aromatic sulfur were included in the calibration models. The PLSR method was used to calibrate the spectra to their measured concentrations. All aromatics, including sulfur, and saturates were found to correlate well (>0.9 R^2) with the UV-Vis spectra. Ferrer continued similar research for fluid catalytic cracker feedstocks [166]. In this study, 104 samples were used in the UV-Vis calibration set. Properties

such as sulfur, density, nitrogen, SARA, MCR, nickel, and vanadium concentrations were measured. Supplementary speciation of the aromatics was completed. Nickel, vanadium, saturates, and resins, resulted in lower predictive ability compared to the remaining set of PLSR models.

Corgozinho et al. created a methodology to determine the ASTM color of automotive diesels [167]. The color of diesel is related to quality. In ASTM D1500, the color of petroleum is determined visually and subjective to human error [117]. To improve this method, the ASTM colors (0 to 6.5 scale) and visible spectra of diesels samples were measured [167]. Principal Component Analysis was used to interpret the variability in the samples. From the spectral data, the PLSR method was used to calibrate visible spectra to ASTM colors. The proposed methodology was found to optimally predict diesel color compared to the ASTM D1500 method.

Baldrich et al. compared NIR and UV-VIS spectra of Fluid Catalytic Cracker (FCC) feedstocks [168]. The authors used data from the Ferrer studies [165-166] for this comparison. A ABB FTLA2000-154 NIR spectrophotometer (3600 to 8000 cm^{-1}) was used to collect data in the infrared region. Partial least squares regression was used in the predictive models. The authors concluded, processing UV-VIS spectra resulted in accurate predictions of sulfur, MCR, nickel, and vanadium contents. The NIR spectra accurately predicted nitrogen and density. Enhanced discrimination features between the feeds were seen with PCA in the UV-VIS compared to the NIR spectra.

Kharrat et al. correlated asphaltene concentration of 26 samples to their visible spectra [169]. The optical absorbance difference between 600 and 800nm as a function of asphaltene concentration diluted in toluene resulted in a coefficient of determination of 0.999. The Beer-Lambert law was found evident through this result. Through a one parameter simple least squares model, the asphaltene content of the crude oils were predicted successfully. The authors did not address the solvent dilution effects as pointed out by Evdokimov and Losev [133].

Critical Aspects of Online Spectroscopic Tools

Chen et al. discussed physical and instrumental aspects of online spectroscopic measurements [162]. Fluctuations are inevitable, temperature, pressure, flow, turbulence, air bubbles, impurities cause non-linear spectral variations. As for the instrument, routine maintenance, lamp replacement, and baseline calibration are important. Authors suggested on using adaptive models to provide resiliency in unstable process and environment conditions.

2.5.6 Model Selection Criteria

As there are four calibration methods reviewed, SLS, MLR, PCR, and PLSR, model selection criterions are explored to determine the best overall [170]. The adjusted coefficient of determination (R^2_{adj}) is an example of a model selection criteria. The coefficient incorporates the residual sum of squares, the sample size, and the number of regressors in the model. However, other log-based coefficients are could be better suited for model selection. The Akaike Information Criterion (AIC) and Bayesian Information Criterion (BIC) are log-based methods that are considered in the current study [171]. AIC has two additional corrected and unbiased coefficients of AIC_c and AIC_u, respectively [170]. Similar to the R^2_{adj}, AIC and BIC depend on the residual sum of squares, sample size, and the total number of regressor parameters. From a critical value comparison, Wu et al. found that the AIC_u method had the best tendency to predict a simplified model, while the R^2_{adj} was the worst [170]. Both AIC and BIC were used effectively in comparing as well as ranking probability distribution functions for boiling point curves of petroleum [172].

Chapter 3: Equipment and Procedures

Equipment and procedures for the study are found in chapter three. Liquid feed, solvents, gases, and catalyst used are found in [section 3.1](). Detailed information on the batch microreactors, fluidized baths, and agitators used are found in [section 3.2](). Procedures and operating conditions are found in section 3.3. Characterization techniques are found in [section 3.4](). Detailed information on the visible spectroscope developed is found in [section 3.5](). Calculations for stoichiometric sulfidation reactions, batch microreactor volume, and theoretical air flow rate verification are found in *Appendix A*. Thermodynamic modeling using VMGSim software is found in *Appendix B*. Agitation, temperature, and fluidization profiles for all experimental reactions are found in *Appendix C*. Theoretical evaporation calculations of dichloromethane, mass balance measurements, and recovery calculations are found in *Appendix D*.

3.1 Liquid Feed, Solvents, Gases, and Catalyst

3.1.1 Liquid Feed

Heavy Vacuum Gas Oil (HVGO) was used as the feed for all hydrotreating reactions. Heavy Vacuum Gas Oil was a distilled fraction of Athabasca Bitumen extracted from oil sands. Characterization results of the HVGO are found in chapter 4.

3.1.2 Solvents and Gases

A summary of liquid solvents, standards, gases, and purities used are shown in *Table 3.1*. Nitrogen and hydrogen gases were used for measuring volume, purging, and providing a pressurized atmosphere to the microreactor. Low pressure hydrogen, helium, compressed air and liquid carbon dioxide were used for boiling point distribution analysis. Argon and oxygen were used for sulfur and nitrogen analysis. Helium and Oxygen were used for carbon, hydrogen, nitrogen, and sulfur (CHNS) analysis. Dichloromethane solvent was used to wash liquid oil products and catalyst from the microreactor after each reaction. Toluene and acetone were used as cleaning solvents for the microreactor and glass cuvettes. Carbon disulfide was used as the dilution solvent for the simulated distillation analysis. Toluene was used as the dilution solvent for sulfur and nitrogen analysis. All solvents were used in the fume hood wearing Personal Protective Equipment (PPE).

Table 3.1. Summary of liquid solvents, standards, gases, and purities used.

Solvent or Gas	Supplier	Purity
Nitrogen (Low Pressure 3500psig)	Praxair	99.998%
Hydrogen (Low Pressure)	Praxair	99.999%
Hydrogen (High Pressure)	Praxair	99.999%
Carbon Dioxide (Bone Dry with Liquid Withdrawal)	Praxair	99.9%
Argon	Praxair	99.999%
Oxygen (CHNS)	Praxair	99.993%
Helium (GC & CHNS)	Praxair	99.999%
Compressed Air	Praxair	-
Compressed Air	CME Building	-
Toluene (HPLC Grade, Fisher T290-4)	Fisher Scientific	99.9%
Heptane (HPLC Grade, Fisher H350-4)	Fisher Scientific	99.5%
Dichloromethane (HPLC Grade, Fisher D143-4)	Fisher Scientific	99.9%
Acetone (ACS Grade, Fisher A18P-4)	Fisher Scientific	99.7%
Hydrochloric Acid (ACS Grade, Fisher A144212)	Fisher Scientific	36.5-38%
Carbon Disulfide (ACS Grade, Sigma 676918-4L)	Sigma-Aldrich	>99.9%
Dimethyl Disulfide (Lot U15C053)	Alfa Aesar	99%
Thiophene (extra pure, Lot A0365452)	Acros Organics	99+%
Thiophene (Batch 09221CJ)	Sigma-Aldrich	99+%
Pyridine	Alfa Aesar	>99.5%
Polywax (Supelco 48477 LB82363V)	Sigma-Aldrich	-
C_1-C_{44} (Supelco Lot LC06749V)	Sigma-Aldrich	-
Reference Gas Oil (Supelco Lot LB82363V)	Sigma-Aldrich	-
2,5-Bis(5-tert-butyl-benzoxazol-2-yl)thiophene standard	Sigma-Aldrich	99%
Chloroform-d with 1v/v% TMS (99.8 atom D, Lot A0372661)	Acros Organics	99.75%

3.1.3 Catalyst

Reported values of elemental composition, surface area, pore volume, average pore diameter, and bulk density of S424 catalyst are shown in *Table 3.2* [1-4]. Shell S424 nickel-molybdenum supported on gamma aluminum oxide (Ni-Mo/γ-Al$_2$O$_3$) catalyst was used. The S424 catalyst was used in previous studies conducted at the University of Alberta [5-6]. The diameters of the tri-lobed pellets ranged from circa 1.2 to 1.6mm [1][4]. Pellet sizes were verified using a 150mm Mastercraft® electronic caliper with digital display accurate to two decimal places.

Table 3.2. Reported values of elemental composition, surface area, pore volume, average pore diameter, and bulk density of S424 catalyst.

Elemental Composition		References
Nickel (Ni)	3 - 3.2 wt.%	[1][2][4]
Nickel Oxide (NiO)	3.6 wt.%	[3]
Molybdenum (Mo)	12.9 - 13.2 wt.%	[1][2][4]
Molybdenum Oxide (MoO_3)	18.8 wt.%	[3]
Aluminum (Al)	38 wt.%	[4]
Phosphorous (P)	2.5 wt.%	[4]
Phosphorous Oxide (P_2O_5)	5.7 wt.%	[3]
Surface Area	155 - 160 m^2/g	[1][3][4]
Pore Volume	0.328 - 0.45 cm^3/g	[1][3][4]
Average Pore Diameter	98 – 99 Å	[3][4]
Bulk Density	0.75 - 0.83 g/cm^3	[1][3][4]

A sample of S424 catalyst pellets were crushed using a ceramic pestle and mortar to granular size. W.S. Tyler Company No. 45 355μm, Fisher Scientific No. 80 180μm, Fisher Scientific No. 170 90μm and Fisherbrand™ No. 325 45μm sieves were stacked respectively to separate catalyst solids by size. Solids >45μm were discarded. Catalyst trilobed pellets and <45μm solids were stored at lab temperature in separate Fisherbrand™ 20ml capped glass vials. Precautions such as PPE (face mask, gloves, safety glasses, and a Bulwark™ Excel-FR™ lab coat) and a fume hood use were taken in catalyst handling.

To verify the reported literature elemental composition of the S424 catalyst, two samples of a known mass of <45μm solids were dissolved in hydrochloric acid and sent for Inductively Coupled Plasma Mass Spectrometry (ICP-MS) analysis. The analysis was conducted at the Canadian Centre for Isotopic Microanalysis in the Earth and Atmospheric Sciences department at the University of Alberta (ESB 1-20). The elemental composition with 95% confidence intervals were 3±0.2wt.% nickel, 15.7±1.0wt.% molybdenum, 35.2±1.3wt.% aluminum with balanced 46.1wt.% oxygen, phosphorus, and other trace elements. The ICP-MS results agreed with reported literature nickel contents from *Table 3.2*. The molybdenum and aluminum contents differed by 17% and 8%, respectively.

3.1.4 Drying and Sulfiding Catalyst

Catalyst drying time with measured masses at 2, 6, 24 hours and percent moisture loss are presented in *Table 3.3*. A Salton food dryer (DH1171) was used to dry the catalyst pellets and <45μm solids in Fisherbrand^{TM} aluminum weighing dishes. Two samples of pellets and one sample of <45μm solids were dried. The Salton food dryer provided air at ~80°C to flow over the catalyst pellets and solids to remove physisorption moisture from the pores. The air temperature was recorded using an Omega (HH806AU) Handheld Thermocouple Thermometer with a Type K Thermocouple (KMQXL-062U-18).

Table 3.3. Catalyst drying time, mass, and percent loss.

Catalyst	0 hours	2 hours	6 hours	24 hours	Moisture Loss (%)
Pellets (1)	2.03g	-	1.98g	1.98g	2.5
Pellets (2)	2.01g	1.96g	1.96g	1.95g	2.7
Solids (<45μm)	5.40g	5.26g	5.26g	5.25g	2.8

The moisture loss averaged 2.7±0.2% for pellets and solids in *Table 3.3*. Catalyst pellets and solids were transferred into separate 14.8ml capped glass vials and stored in lab temperature environment. Filled vials of dried catalyst were continuously monitored for mass changes throughout the course of experimental reactions. No significant change (<0.001g) in mass was observed when exposed to lab atmosphere for short periods of sub-sampling into microreactors. Solis et al. found that the long-term exposure (6 months) of a similar Ni-Mo/γ-A$_2$O$_3$ catalyst to ambient conditions did not affect catalyst activity [7].

The NiMo/γ-Al$_2$O$_3$ catalyst required sulfiding to activate nickel and molybdenum metals. The nickel and molybdenum were assumed in oxide form prior to sulfiding. Criterion Catalyst & Technologies guidelines were used to sulfide the dried catalyst pellets and solids [8]. Dimethyl Disulfide (DMDS) was used as the sulfiding agent. To determine the stoichiometric amount of DMDS required, the following reactions were assumed for sulfidation:

$$C_2H_6S_2 + 3H_2 \rightarrow 2CH_4 + 2H_2S$$
$$3NiO + H_2 + 2H_2S \rightarrow Ni_3S_2 + 3H_2O$$
$$MoO_3 + H_2 + 2H_2S \rightarrow MoS_2 + 3H_2O$$
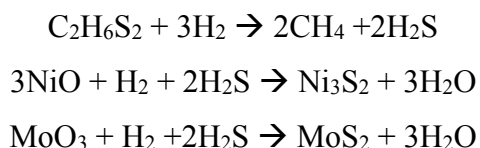
From *Table 3.2* and the ICP-MS results, the nickel and molybdenum contents were assumed to range from 2.8-3.2wt.% and 12.9-16.7wt.%, respectively. The type of nickel sulfide (NiS, millerite, Ni_3S_2, heazlewoodite, Ni_7S_6, Ni_9S_8 etc.) formed from nickel oxide sulfidation is actively debated for catalyst surfaces [9-10]. More evidence supports heazlewoodite formation in Ni-Mo catalysts, however, other forms of nickel sulfide exist [9]. Molybdenum disulfide crystallites are formed on the Al_2O_3 surfaces from molybdenum oxide sulfidation [10-11]. The molecular weights of nickel (58.69g/gmol), nickel oxide (74.69g/gmol), nickel sulfide (240.21g/gmol), molybdenum (95.94g/gmol), molybdenum oxide (143.94g/gmol), molybdenum disulfide (160.08g/gmol), and DMDS (94.21g/gmol) were used to determine the stoichiometric amount of DMDS and hydrogen required for the sulfiding reactions. The range of DMDS and hydrogen required were calculated per gram of catalyst, 0.14-0.18g and 10-20mg, respectively. See *Appendix A* for detailed calculations. To ensure sulfidation of the metals, excess DMDS and hydrogen were loaded with dried catalyst in the microreactor, see section 3.3.2. To ensure complete sulfidation, a second set of reactions with additional DMDS and hydrogen on initial the sulfided catalyst were completed.

3.2 Batch Microreactors, Fluidized Baths, and Agitators

3.2.1 Batch Microreactors

A batch microreactor image and detailed schematic are shown in *Figure 3.1* [12-13]. Modified microreactor designs are shown in *Figure 3.2* [12]. The microreactors, with modified designs, were used for all sulfiding and hydrotreating reactions. One modified design included an internal thermocouple and pressure gauge to verify a hydrotreating reaction. The batch microreactor design was used extensively in previous research studies conducted at the University of Alberta [5][6][14-19].
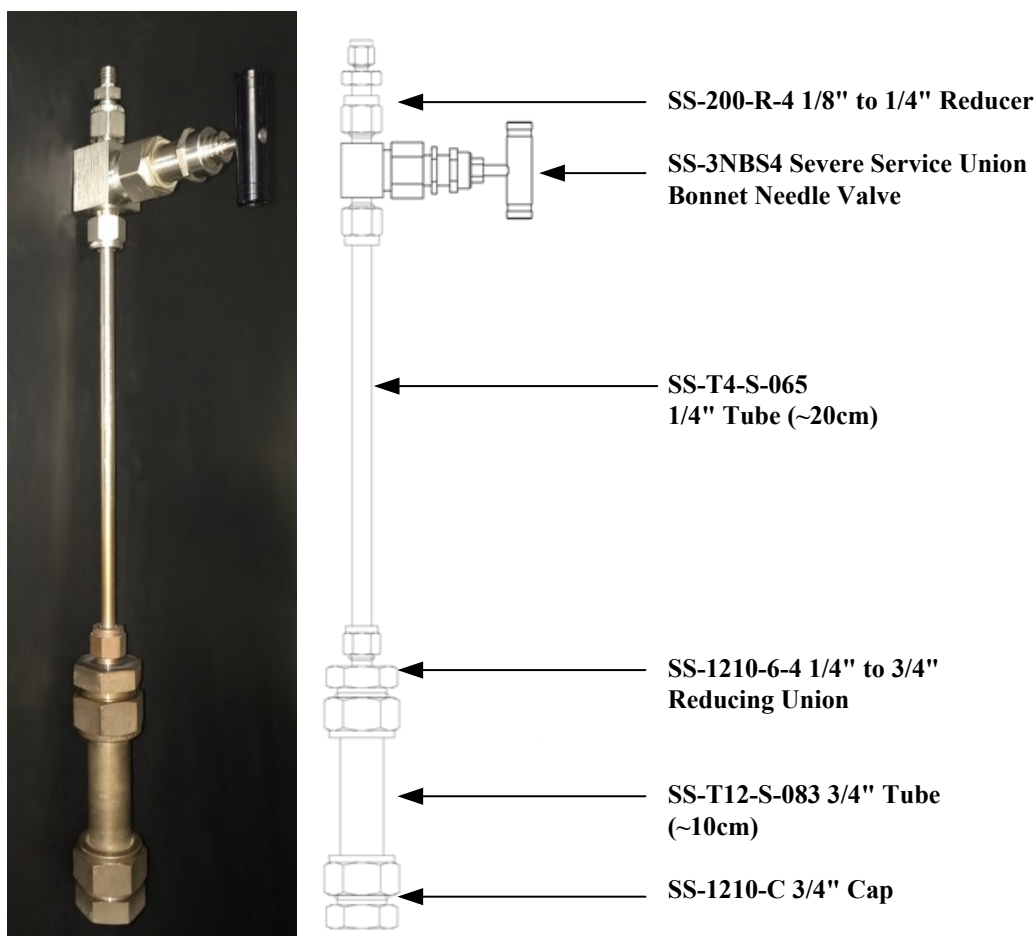
Figure 3.1. Batch microreactor image and detailed schematic [12-13].

The batch microreactor consisted of Swagelok® 316 Stainless-Steel (SS) fittings, tubing, and a needle valve in *Figure 3.1* [12-13]. The top reducer (SS-200-R-4) was used to attach a 1/8" gas line to pressurize the reactor, see section 3.3.3. The severe service union bonnet needle valve was used to open and close the system. The valve used a nonrotating SS ball stem to leak tight the system at elevated temperature and pressure. The 1/4" tube, approximately 20cm and 0.065in. wall thickness, allowed for the microreactor to be submerged into the fluidized bath. The microreactor, of 3/4" tube, approximately 10cm and 0.083in. wall thickness, allowed enough volume for gas, liquid feeds, and catalyst to be loaded inside. Reducing union and cap sealed both ends of the 3/4" tube microreactor.

Design considerations were used to ensure the batch microreactor had suitable temperature and pressure ratings for all experimental reactions. The Ultimate Tensile Strength of 316 SS was 517MPa [20]. With a design factor of 3.75, the allowed stress value of 316 SS was 138MPa [20].

The allowable working pressure of the tubing was factored based on the outer diameter and tube thickness (ANSI B31.3). For the 3/4" tubing and 0.083in. wall thickness, 0.21 or 29MPa working pressure. For the 1/4" tubing and 0.065in. wall thickness, 0.51 or 71.4MPa working pressure. The needle valve had a working pressure of 41.3MPa. The 1/4" fittings, reducing union, and 3/4" cap threads had a working pressure of at least 31.7MPa. All specified working pressures were at 20°C temperature. A second design factor was applied for elevated temperatures. The temperature factor for the needle valve was different; at 426°C the working pressure was 23.8MPa [12]. A reported factor of 0.79 for elevated temperatures at 427°C was applied to the working pressures of the tubing [20]. As the 3/4" tubing was minimum working pressure compared to other tubing and fittings, 29MPa at 20°C temperature rating was used. The **maximum** allowable working pressure for the 3/4" SS tubing was **22.9MPa** at **427°C**. All experimental loading conditions were simulated in VMGSim software to ensure the closed system did not exceed 22.9MPa pressure at 427°C, see section 3.3.3.
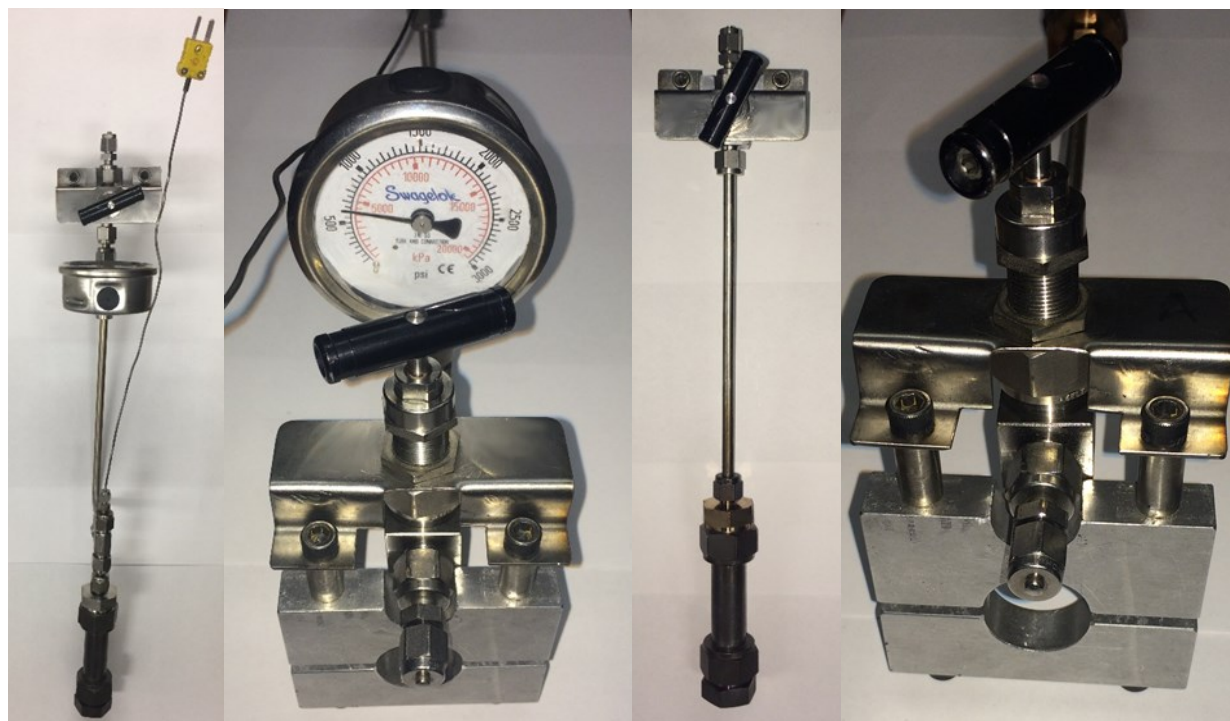
Figure 3.2. Images of modified batch microreactor designs [12].
Left side: Design I, Right side: Design II

Two modified batch microreactor designs in *Figure 3.2* were used. Design **I** included a Swagelok® pressure gauge (PGI-63B-OG3000-LAOX**)** and an Omega Type K thermocouple (KMQXL-

062U-18) to measure internal pressure and temperature, respectively. The needle valve was attached to a 1/4" branched tee (SS-400-3-4TTF) that supported the pressure gauge. The 1/4" tube was circa 23cm with a 90° bend (6cm width, 17cm length). The 1/4" tube was attached to a second tee (SS-400-3). A 1/16" bore through reducer (SS-100-R-4BT) was used to attach the thermocouple. The thermocouple tip was at the bottom cap of the microreactor when closed to ensure temperature measurement of the liquid phase. The second tee was attached to the 1/4" to 3/4" reducer (SS-1210-6-4). Design **II** is the microreactor from *Figure 3.1*, with a custom metal plate attachment piece developed by the University of Alberta machine shop. The attachment piece used adjustable 3/16" hex screws to vary the diameter of the hollow center (2.4cm when closed) for secure placement on a agitation rod for low mixing reactions. Both modified designs included a 1/8" plug (SS-200-P) for the 1/8" to 1/4" reducer on the needle valve.

3.2.2 Batch Microreactor Volume

An image of the batch microreactor measured on the balance scale is shown in *Figure 3.3*. A plot of the measured pressure as a function of nitrogen mass is presented in *Figure 3.4*. The total volume of the microreactor was measured with a 150mm Mastercraft® electronic caliper and the slope of the correlation in *Figure 3.4*. See *Appendix A* for detailed calculations. From the internal diameters and the length of the SS Swagelok® tubing, the volume of the microreactor was 18.7cm^3. There was error in the measured volume as the needle valve and reducing union were not included in this calculation.
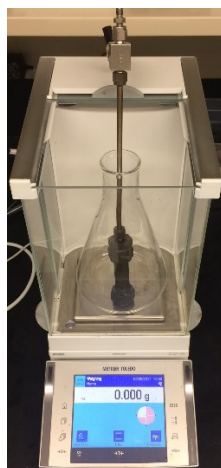
Figure 3.3. Image of batch microreactor measured on balance scale.

The batch microreactor was attached to a 1/8" gas line connected to a low pressure nitrogen cylinder. A ProStar gas regulator was used to adjust the outlet pressure. The microreactor was purged approximately 10 times with nitrogen gas to ensure complete removal of oxygen from the microreactor and lines. The needle valve on the microreactor was closed. As seen in *Figure 3.3*, the microreactor was removed from the 1/8" line and measured on an XP1203S Mettler Toledo analytical balance scale accurate to three decimal places. The microreactor was placed in a 1 liter Erlenmeyer flask to ensure a stable support. The first measurement was at atmospheric pressure of pure nitrogen in the microreactor. The balance scale was tared to zero. The pressure on the regulator was adjusted to 300kPa(g). The reactor was attached to the nitrogen line and purged 10 times. The needle valve was shut and removed from the 1/8" line. The mass of nitrogen was measured on the tared balance scale and recorded. The steps were repeated for 400-700kPa(g). The data is plotted in *Figure 3.4*.
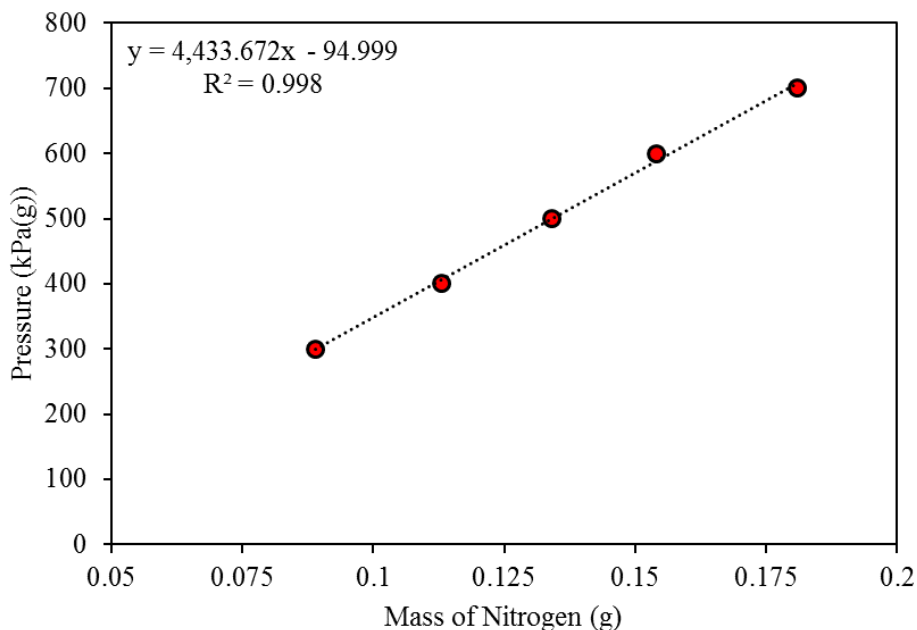
Figure 3.4. Measured pressure as a function of nitrogen mass.

The slope of the measured gauge pressure as a function of nitrogen mass was used to theoretically calculate the microreactor volume in *Figure 3.4*. Assuming nitrogen gas behaves thermodynamically ideal at the reported pressures (Z=0.996 at 700kPa(g) from VMGSim), the ideal gas law equation was used.

$$PV = nRT \qquad (3.1)$$

The fitted linear model had a coefficient of determination (R^2) of 0.998. The intercept represented the atmospheric pressure of pure nitrogen in the microreactor, which was tared at zero on the balance scale. The percent difference compared to nitrogen atmosphere pressure (98.4kPa, assuming 0.79 N_2 0.21 O_2 air at 101.325kPa) was 3.5%. From *Figure 3.4*, the slope was 4434 kPa(g)/g N_2. Using the molecular weight of nitrogen gas (28.02g/mol), the ideal gas constant ($8314cm^3$ kPa mol^{-1} K^{-1}), and assuming a maximum lab temperature (298K), the microreactor volume was $19.94cm^3$. The percent difference to the measured volume using the digital caliper was 6.4%. The nitrogen gas filled the void space the caliper not physically measure in the needle valve and reducing union. Approximately $20cm^3$ was assumed as the volume of the microreactor.

3.2.3 Fluidized Baths and Agitators

Images of the fluidized bath setup and BOSCH agitator used are shown in *Figure 3.5*. Images of the BOSCH agitator RPM controller and custom Swagelok® attachment fitting are shown in *Figure 3.6*. Images of the second fluidized bath setup and attached modified batch microreactors are shown in *Figure 3.7*. The fluidized baths were used extensively in previous research studies conducted at the University of Alberta [5][6][14-19].
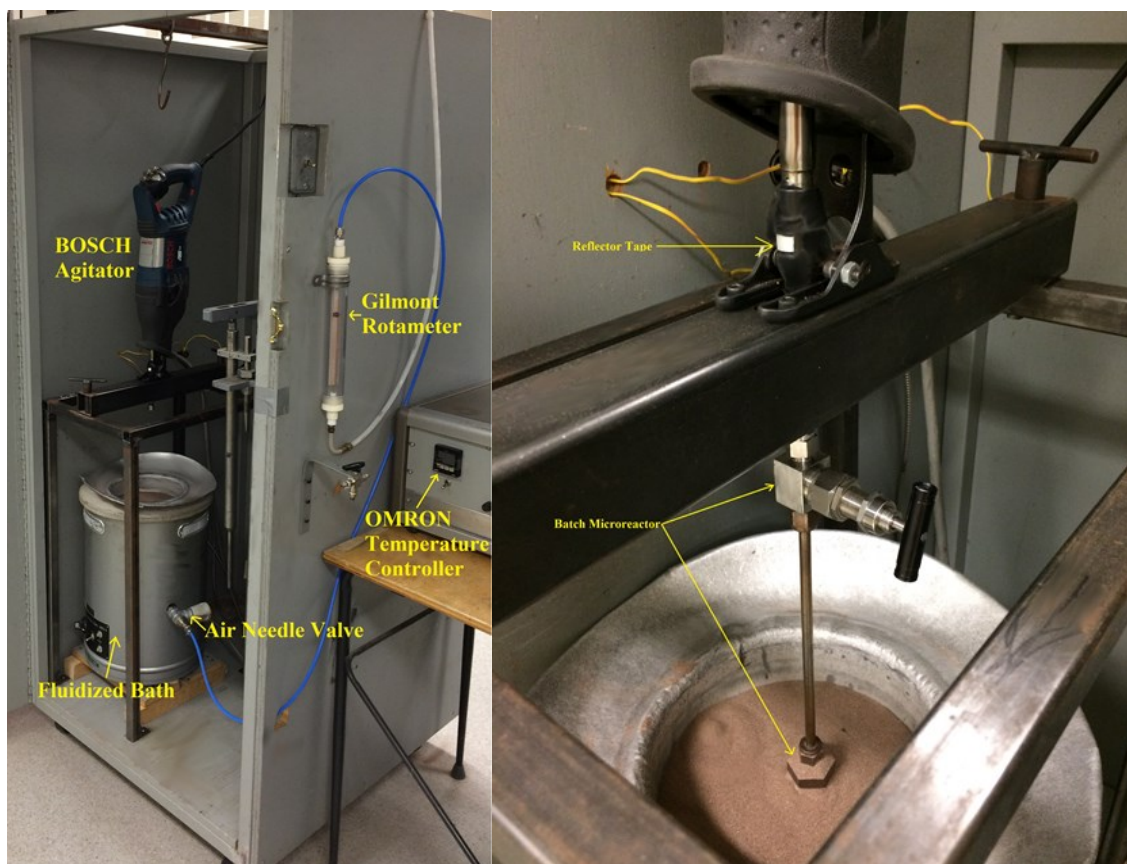
Figure 3.5. Images of the fluidized bath setup and agitator.

Figure 3.6. BOSCH agitator RPM controller and custom Swagelok® attachment fitting.

A Cole Parmer Techne SBS-4 (formerly Tecam®) fluidized bath was used. The bath was filled with approximately 22-25cm of alundum (F0885, 96% Al_2O_3) from the bottom. Air flow was controlled by a needle valve to fluidize the alundum. The air flow rate was measured using a Gilmont (GF-1460) rotameter. At circa 20°C alundum temperature, the air flow rate ranged from 33-36NL/min (normal conditions, 20°C and 1atm). The air flow rate was adjusted as the temperature ramped up. This flow ranged from 15-19NL/min at reaction temperature to prevent excessive fluidization of alundum. The air flow rate (at circa 108kPa(g) air pressure) ranged 47-52L/min at 20°C and 22-27L/min at reaction temperature. The Gilmont manufacture reported a ±5% when reading. See *Appendix A* for theoretical air flow rate verification. The air flow fluidized alundum for a distributed heat transfer between heating elements and solids. The temperature of the alundum was measured using an 8cm thermocouple located above the heating elements. The thermocouple was attached to a OMRON E5CK temperature controller. The controller was optimized to control the power output to the bath heaters. A BOSCH demolition reciprocating saw (RS35) agitator was used for rigorous mixing of the microreactor [21]. The BOSCH agitator was adapted and customized to a welded metal frame constructed by the University of Alberta machine shop. Reflector tape was attached to the agitator tip to measure the RPM. The RPM was measured using a 20713A NIEKO digital tachometer. An additional tachometer from the University of Alberta technical shop was used to verify the RPM measurement of the NIEKO tachometer. The microreactor was attached to the agitator by a custom welded 1/4" SS Swagelok® fitting developed by the University of Alberta machine shop in *Figure 3.6*. The agitator speed was controlled by three stainless steel adjustable hose clamps to ensure RPM stability. The agitator speed varied constantly in operation. The reactor agitated a vertical distance of 2.5cm in operation. The length of the 1/4" tube (20cm) allowed the microreactor to be submerged in the fluidized alundum. To verify the alundum temperature at set point and the outside wall temperature of the microreactor in operation, two additional temperature measurements were recorded. A Mastercraft Digital Temperature Reader (MDTR) and a Type K Thermocouple (KMQXL-062U-18) connected to an Omega (HH806AU) handheld thermocouple thermometer were used to verify alundum temperatures.

Figure 3.7. Images of the second fluidized bath setup and attached modified batch microreactor designs.

Top right: Design I, Bottom: Design II

A second Cole Parmer Techne SBS-4 fluidized bath was used in *Figure 3.7*. A Leeson electric motor (C4C17DC7J) was used to agitate the metal rod a vertical distance of 2cm. The modified microreactor designs, **I** and **II**, were attached to a circa 40cm rod with the metal attachment plate as seen in *Figure 3.7*. The rod diameter was 2.5cm. The metal attachment plate was adjusted with a 3/16" hex wrench to securely place the piece on the rod circa 5-10cm from the bottom. The placement ensured that the microreactor was submerged in the fluidized alundum for both modified microreactor designs. The agitation rate was constant when compared to the BOSCH agitator. The agitation rate was measured using a NIEKO digital tachometer on the attached reflector tape. The agitation ranged from 355-360RPM compared to 800-900RPM for the BOSCH agitator. An OMRON E5CK temperature controller with a Type K thermocouple was used to control the fluidized alundum temperature. The Gilmont rotameter was used to measure the air flow rate. Personal protective equipment (oven gloves, safety glasses, and a Bulwark^{TM} Excel-FR^{TM} lab coat) was worn in microreactor placement, measurements, and operation for both fluidized baths.

3.3 Procedures and Operating Conditions

The procedures plus operating conditions of experimental hydrotreating reactions at reaction temperatures, times, and catalyst size using the batch microreactor are discussed in section 3.3.

3.3.1 Experimental Reactions

All experimental reactions, feed, catalyst size, pressure, temperature, agitation, and reaction times are presented in *Table 3.4*.

Table 3.4. Experimental reactions, feed, catalyst size, pressure, temperature, agitation, and reaction times.

#	Reaction	Feed	Catalyst Size	Pressure (kPa(g))	Temperature (°C)	Agitation (RPM)	Time (h)
1	No Reaction	HVGO	-	-	-	-	-
2	Hydrotreating	HVGO^	-	4500	390	360**	2
3	Hydrotreating	HVGO^	-	4500	390	708	2
4	Hydrotreating	HVGO^	-	4500	390	862	2
5	Hydrotreating	HVGO^	-	4500	390	850	2
6	Hydrotreating	HVGO^	-	4500	390	873	2
7	Hydrotreating	HVGO^	Pellets	4500	390	848	2
8	Hydrotreating	HVGO^	Pellets	4500	390	868	2
9	Hydrotreating	HVGO^	Pellets	4500	390	878	2
10	Hydrotreating	HVGO	Pellets	4500	390	360**	2
11	Hydrotreating	HVGO	Pellets	4500	390	360**	2
12	Hydrotreating	HVGO	Pellets	4500	390	360*	2.25
13	Hydrotreating	HVGO	Pellets	4500	390	884	2
14	Hydrotreating	HVGO	Pellets	4500	390	882	2
15	Hydrotreating	HVGO	Pellets	4500	390	866	2
16	Sulfiding Catalyst	DMDS	Dried Pellets	3000	20 - 360	360**	4.5
17	Sulfiding Catalyst	DMDS	Dried Pellets	3000	20 - 360	360**	4.2
18	Sulfiding Catalyst	DMDS	Dried < 45μm	3300	20 - 360	880	4.2
19	Sulfiding Catalyst	DMDS	Dried < 45μm	3000	20 - 360	863	4.2
20	Hydrotreating	HVGO	Sulfided Pellet	4500	390	878	2
21	Hydrotreating	HVGO	Sulfided Pellet	4500	390	886	2
22	Hydrotreating	HVGO	Sulfided Pellet	4500	390	892	2
23	Hydrotreating	HVGO	Sulfided Pellet	4500	390	896	1.5
24	Hydrotreating	HVGO	Sulfided Pellet	4500	390	889	1
25	Hydrotreating	HVGO	Sulfided Pellet	4500	390	875	1
26	Hydrotreating	HVGO	Sulfided Pellet	4500	370	888	1
27	Hydrotreating	HVGO	Sulfided Pellet	4500	350	900	1
28	Hydrotreating	HVGO	Sulfided Pellet	4500	330	891	1
29	Hydrotreating	HVGO	Sulfided Pellet	4500	310	893	1
30	Hydrotreating	HVGO	Sulfided Pellet	4500	290	898	1
31	Hydrotreating	HVGO	Sulfided Pellet	4500	390	867	0.5
32	Hydrotreating	HVGO	Sulfided Pellet	4500	390	859	0.5
33	Hydrotreating	HVGO	Sulfided Pellet	4500	390	850	0.25
34	Hydrotreating	HVGO	Sulfided < 45μm	4500	390	888	2
35	Hydrotreating	HVGO	Sulfided < 45μm	4500	390	874	2
36	Hydrotreating	HVGO	Sulfided < 45μm	4500	390	879	1
37	Hydrotreating	HVGO	Sulfided < 45μm	4500	390	870	1
38	Hydrotreating	HVGO	Sulfided < 45μm	4500	390	870	0.5
39	Hydrotreating	HVGO	Sulfided < 45μm	4500	390	859	0.5
40	Hydrotreating	HVGO	Sulfided < 45μm	4500	370	894	0.5
41	Hydrotreating	HVGO	Sulfided < 45μm	4500	390	880	0.25
42	Hydrotreating	HVGO	Sulfided < 45μm	4500	390	890	0.25
43	Hydrotreating	HVGO	Sulfided < 45μm	4500	370	900	0.25
44	Hydrotreating	HVGO	Sulfided < 45μm	4500	350	900	0.25

*Modified microreactor design I.
**Modified microreactor design II.
^No liquid product filtration.

The first experiment in *Table 3.4* was liquid HVGO filtration with no reaction to quantify liquid recovery. All liquid products plus catalyst for reactions 2 to 9 were not filtered. Reactions 2, 10 to 11, and 16 to 17, used 360RPM agitation with the modified microreactor design **II**. Reaction 12 used the modified microreactor design **I** for temperature and pressure verification at 360RPM. Four sulfiding reactions, reactions 16 to 19, with dried Ni-Mo/γ-Al$_2$O$_3$ catalyst pellets and solids were completed. Reactions 17 and 19 were the second sulfidation of the initial sulfided catalyst from 16 and 18, respectively. The <45μm solids were sulfided with the microreactor from *Figure 3.1*. Reactions 3 to 9, 13 to 15, and 20 to 44 were hydrotreating reactions that used the microreactor from *Figure 3.1*. Temperature varied from 390°C to 290°C for 1h with sulfided pellets (reactions 24 to 30). Reaction time varied from 2 to 0.25h at 390°C with no catalyst, unsulfided, and sulfided pellets. Temperature varied from 390°C to 350°C for 0.25h with <45μm sulfided solids (reactions 41 to 44). Reaction time varied from 2 to 0.25h at 390°C with <45μm sulfided solids (reactions 34 to 39 and 41 to 42). One reaction at 370°C and 0.5h was completed with <45μm sulfided solids (reaction 40).

3.3.2 Reactor Loading

The batch microreactor of 3/4" tube (10cm) with the bottom cap was measured clean and empty on a XP1203S Mettler Toledo analytical balance scale. The average empty mass for all reactions in *Table 3.4* was circa 217.7±0.1g. The balance scale was tared to zero. For sulfiding reactions, 1.32g of dried Ni-Mo/γ-Al$_2$O$_3$ catalyst pellets and 1.4g of dried <45μm solids were placed in the microreactor. The second set of sulfiding reactions loaded previously sulfided pellets (1.39g) and solids (1.24g). There were minor losses for the <45μm solids when transferring in and out of the microreactor. For hydrotreating reactions, circa 0.1g of unsulfided or sulfided, pellets or <45μm solids were placed in the microreactor. The balance scale was tared to zero. The liquid feeds, Dimethyl Disulfide (DMDS) for sulfiding and Heavy Vacuum Gas Oil (HVGO) for hydrotreating, were pipetted into the microreactor using Fisherbrand® 5.75" pipettes. From *Table 3.4*, no catalyst was loaded for experiment and reactions 1 to 6. From section 3.1.4, excess DMDS, circa 0.34g for pellets and circa 0.5g for solids, was placed in the microreactor with dried catalyst for sulfiding reactions. The second set of sulfiding reactions loaded 0.46g and 0.3g of DMDS for pellets and solids, respectively. The <u>total mass</u> of DMDS was circa 0.8g for both sulfidation reactions (reactions 16 to 19). Circa 0.61g of HVGO was placed in the microreactor for all hydrotreating

reactions and experiment 1. The top portion, needle valve, 20cm 1/4" tube, and reducing union, were attached to the bottom 3/4" tube and cap. The 3/4" threads were screwed onto the reducing union threads. A 1L Erlenmeyer flask was placed on the balance scale and tared. The loaded microreactor was placed in the flask as seen in *Figure 3.3*. The mass was measured and recorded. Reaction 12 used a toploading balance (Denver Instrument Company TR-2102) and 2L Erlenmeyer flask for the mass measurement. The scale was tared to zero. The microreactor was removed, the 3/4" nut threads were loosened and Bostik® Neever·Seez (Anti-Seize & Lubricating Compound, Regular Grade) was applied to the reducing union. The Neever·Seez protected the threads from corrosion, rust, and pitting. From the thermal cycles of heating and cooling at high pressure, Neever·Seez protected the reducing union threads for additional use. The microreactor threads were tightened by hand to ensure no liquid feed leaks. The reducing union was attached to a bench mounted vice grip horizontally and clamped in securely. A 1-1/8" wrench was used to tighten the nut 3/4 rotation as recommend by the Swagelok® manual [12][20]. The mass of Neever-Sieze was recorded and averaged circa 0.01g for all reactions.

3.3.3 Reactor Pressure

A detailed schematic of the Swagelok® tubing, fittings, valves and hydrogen cylinder used to pressurize the batch microreactor and modified designs is shown in *Figure 3.8*.
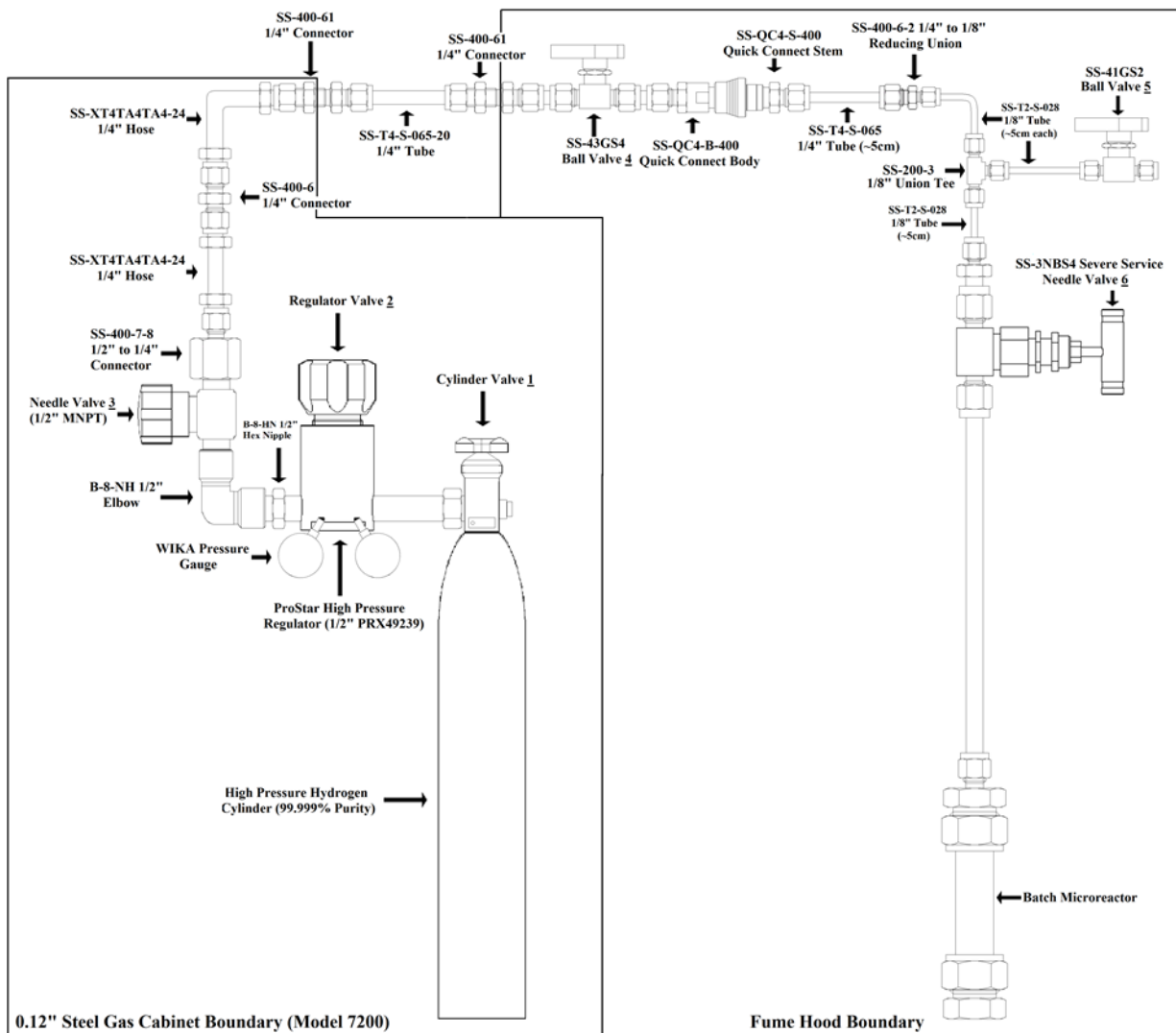
Figure 3.8. Schematic of Swagelok® tubing, fittings, valves and hydrogen cylinder [12-13].

The batch microreactor was attached to the 1/8" nut in the fume hood. A 7/16" wrench was used to tighten the microreactor 1/4" to 1/8" reducer fitting. The hydrogen cylinder valve was opened (valve 1). The pressure was adjusted to 10-14 MPa(g) for a pressure test of microreactor fittings using a ProStar Platinum regulator (valve 2). The SS-41GS2 ball valve was closed (valve 5). The needle valve after the regulator was opened (valve 3). The SS-43GS4 valve was opened (valve 4). The needle valve on the microreactor was opened to allow hydrogen pressure to enter the microreactor (valve 6). Valve 4 was closed. Valve 5 was opened to purge hydrogen out of the line. The microreactor was purged approximately 7-10 times over 10 minutes to ensure a complete hydrogen atmosphere in the lines and microreactor. Valve 6 on the microreactor was closed. Valve

4 was closed. Valve 5 was opened to purge hydrogen out of the line. The microreactor was detached from the 1/8" fitting. The pressurized microreactor was checked for hydrogen leaks using Snoop solution and a Bacharach Leakator® 10 combustible gases detector around all connection fittings. If a leak was detected, the hydrogen gas was released by opening valve 6 in the fume hood. The microreactor was attached to the bench mounted vice grip. The 3/4" tube with the reducing union was readjusted and retightened. The procedure for the pressure test was repeated. After 7 to 10 reactions, the microreactor did not satisfy a pressure test with multiple readjustments and retightening. The microreactor was replaced with a new cap, 3/4" tube, reducing union and 20cm 1/4" tube. After a satisfactory pressure test, the needle valve was opened in the fume hood to release hydrogen gas and closed rapidly. The gas atmosphere in the microreactor was assumed as hydrogen at atmospheric pressure. The microreactor mass was measured on the tared balance scale as a zero baseline. The pressure on the regulator was adjusted to the desired initial reaction pressure, 3000kPa(g) for sulfiding reactions and 4500kPa(g) for hydrotreating reactions as seen in *Table 3.4*. Minor adjustments on the regulator, approximately 3025kPa(g) and 4525kPa(g), were to offset tube line pressure drop. The internal pressure was verified by the pressure gauge in reaction 12. The microreactor reactor was attached to the 1/8" fitting and purged approximately 7 to 10 times of the desired hydrogen pressure. The needle valve was closed and detached. The mass of the pressurized microreactor was measured on the balance scale (mass of hydrogen gas loaded). All experimental loading conditions and operating conditions were simulated in VMGSim to ensure the closed system did not exceed 22.9MPa pressure at 427°C. The initial lab temperature pressures (3000kPa(g) and 4500kPa(g)), mass of liquid feeds, and mass of hydrogen gas were simulated in VMGSim assuming the Advanced Peng-Robinson thermodynamic property package. The microreactor was assumed to behave as a complete closed system, therefore the bulk density was assumed to remain constant at any temperature. The initial pressure was high enough to ensure a fraction of hydrogen was dissolved in the liquid phase for sulfiding and hydrotreating reactions. See *Appendix B* for all reactor loading verification, VMGSim bulk mass density plots, and predicted pressures at reaction temperatures calculations.

3.3.4 Agitation, Temperature, and Fluidization Air Flow Rate

Agitation, temperature, and fluidization air flow rate profiles for the first sulfidation reaction of catalyst pellets are presented in *Figure 3.9*. Agitation, temperature, and fluidization air flow rate profiles for a hydrotreating reaction are presented in *Figure 3.10*. Agitation, internal reactor temperature, external alundum temperature, fluidization air flow rate, and internal gauge pressure profiles for the verification reaction are presented in *Figure 3.11*. All agitation, temperature, and fluidization air flow rate profiles for all reactions in *Table 3.4* are found in *Appendix C*.

From *Figures 3.5 and 3.7*, the fluidized bath temperature was set circa 20°C above the desired hydrotreating reaction temperature as specified in *Table 3.4*, prior to placement of the microreactor. The temperature was adjusted using the E5CK temperature controller. The air flow rate was continuously adjusted with the needle valve to prevent excess fluidization of alundum as the temperature of the bath increased to the set point. The 1/8" to 1/4" reducer on the loaded microreactor was removed to attach the threads of the needle valve to the customized nut on the BOSCH agitator as seen in the right image of *Figure 3.6*. A 1/8" plug was attached to modified microreactor designs **I** and **II** as seen in *Figures 3.2 and 3.7*. An Omega Type K thermocouple measured the starting lab temperature. Once the fluidized bath set point temperature was reached and stable, the loaded microreactor was submerged into the fluidized alundum as seen in *Figure 3.5*. A 9/16" wrench was used to tighten the nut to the needle valve. The needle valve specifically facing out to the side as seen in the right image of *Figure 3.5*. Once secured, the BOSCH agitator was turned on by adjusting the hose camps as seen in the left image of *Figure 3.6*. For the modified microreactor designs, the metal attachment plate was placed circa 4-7cm from the bottom of the agitation rod using a 3/16" hex wrench as shown in *Figure 3.7*.
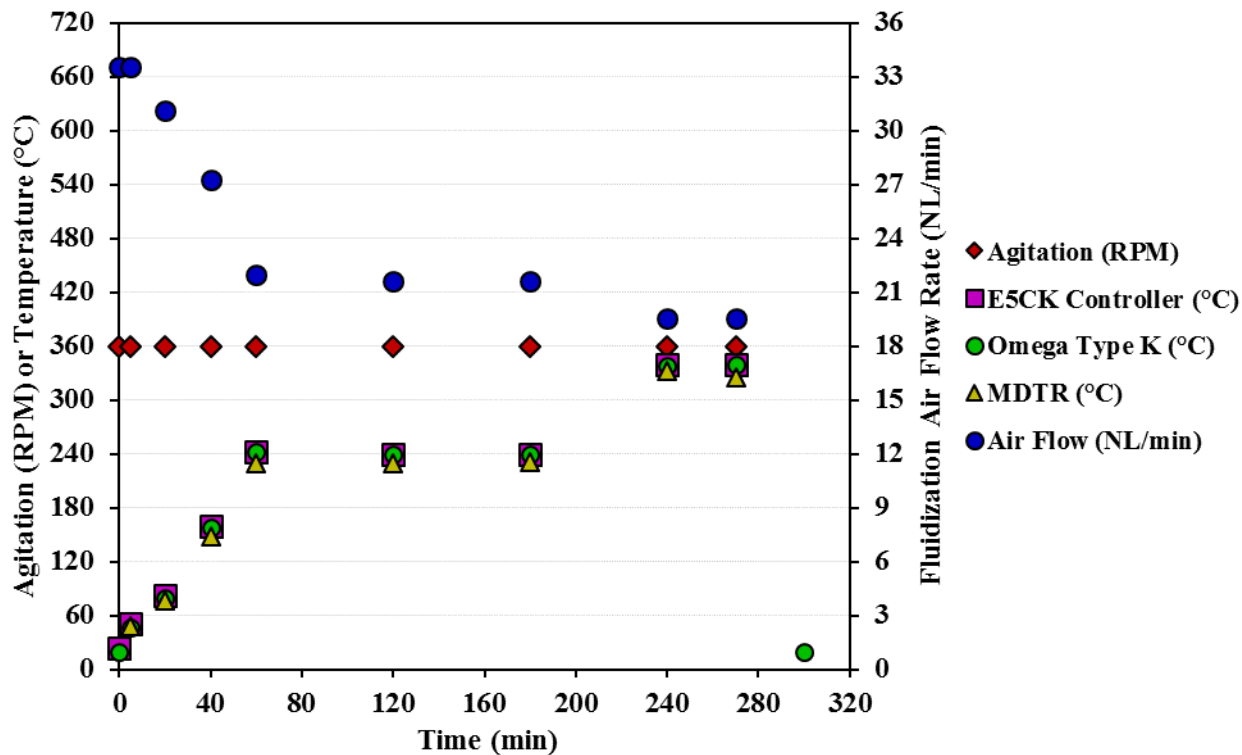
Figure 3.9. Agitation, temperature, and fluidization air flow rate profiles for the first sulfidation reaction of catalyst pellets.

The temperature profile was adapted from Marroquín et al. for liquid phase sulfiding [22]. The microreactor was submerged in the fluidized alundum at lab room temperature. The E5CK temperature controller was turned on. The set point was adjusted to reach 240°C within the first hour of reaction as plotted in *Figure 3.9*. The temperature was held at 240°C for 2 hours to decompose DMDS. At three hours, the temperature was increased to 340°C to allow for H_2S break through. This temperature was held for 1.2 hours. The microreactor was removed and cooled after 4.5 hours for the first sulfidation reaction (16) from *Table 3.4*.
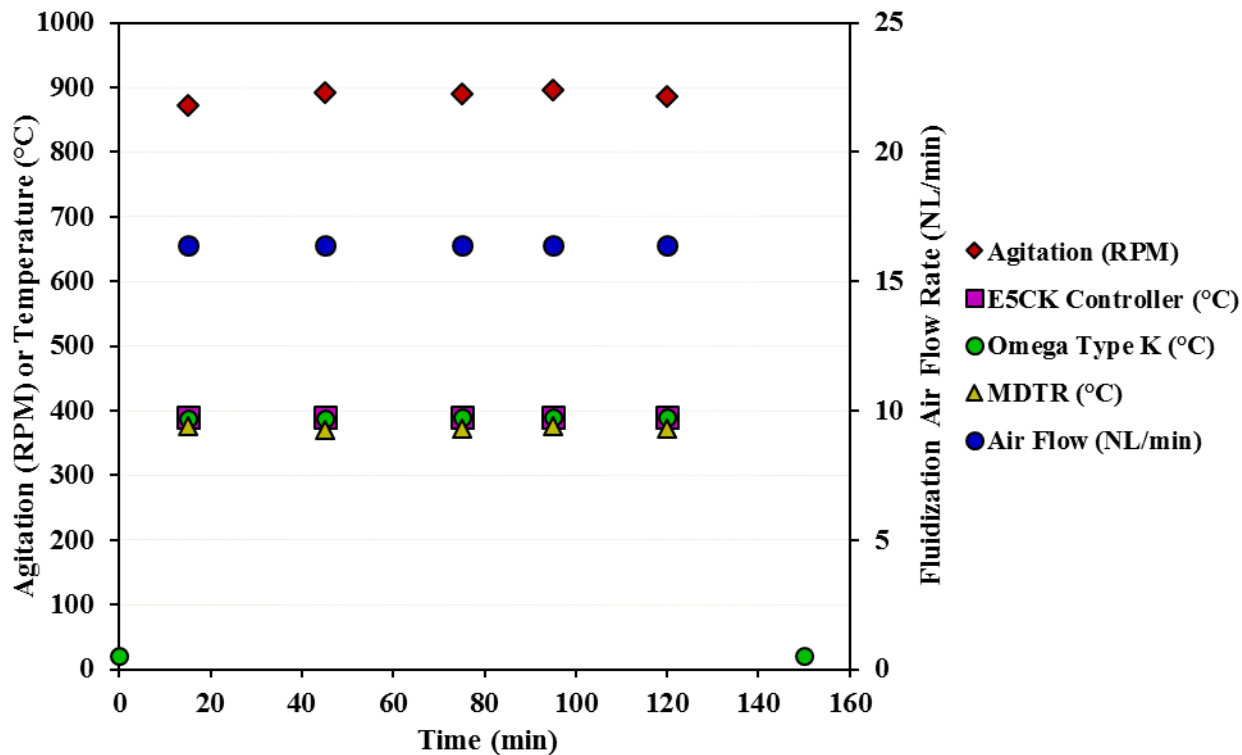
Figure 3.10. Agitation, temperature, and fluidization air flow rate profiles for a hydrotreating reaction.

The temperature profile remained constant for the time specified in *Table 3.4* for reaction 34 (2 hours and 390°C) in *Figure 3.10*. The MDTR was used circa 30-40cm from the fluidized alundum for measurement. The Type K thermocouple was placed inside the fluidized alundum circa 8-15cm as seen in the top right image of *Figure 3.7*. The MDTR resulted in a lower temperature reading because of the default emissivity setting of 0.93. For aluminum oxide, the reported emissivity (ε) ranged from 0.65-0.7 at 600-700K [23]. The metal hose clamps were continuously adjusted throughout reaction after measurement of RPM to ensure stability within an 800-900RPM region. Once the reaction was complete, the agitator was shut off and the microreactor was removed. With PPE, the hot microreactor was removed and placed on a clamp in the fume hood. A stream of high velocity compressed air was turned on to cool the microreactor to lab temperature. Cooling times averaged circa 20-30 minutes for all reactions.
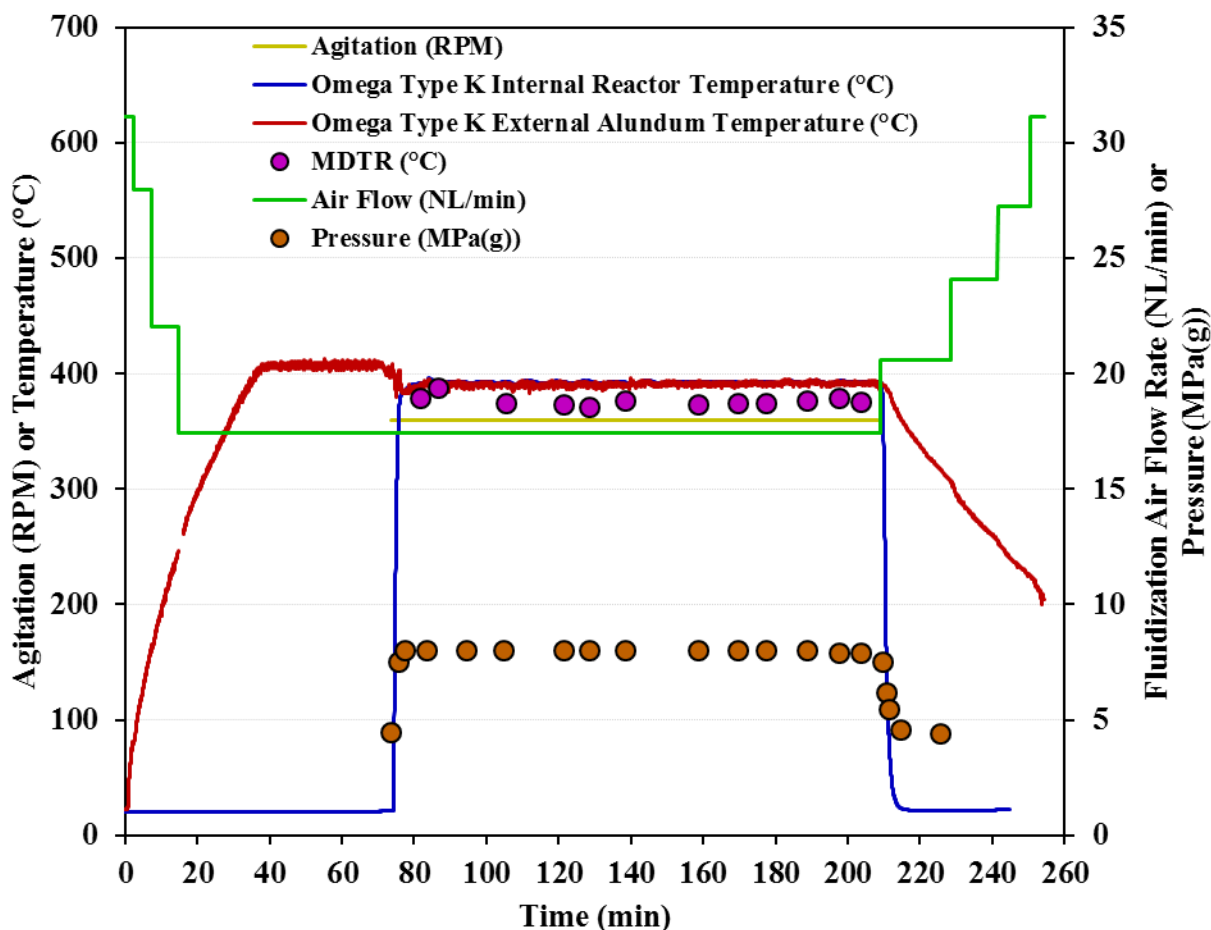
Figure 3.11. Agitation, internal reactor temperature, external alundum temperature, fluidization air flow rate, and internal gauge pressure profiles for the verification reaction.

The verification hydrotreating reaction profile is shown in *Figure 3.11*. To verify temperatures and internal pressure profiles, measurements were recorded for reaction 12 using the modified microreactor design **I** in the top right image of *Figure 3.7*. The Type K thermocouples were connected to the Omega handheld thermocouple thermometer with a software on a laptop to continuously record temperatures every second. The profiles for the fluidized air flow rate and alundum temperature were inversely proportional in ramp up. Once the microreactor was placed into the bath at 75 minutes, the alundum temperature decreased circa 15-20°C. The internal reactor temperature increased to set point within 5-6 minutes. The E5CK controller was adjusted to the reaction temperature 390°C. The internal pressure increased to circa 8000kPa(g). The alundum temperature (MDTR) and gauge pressure were recorded every 15 minutes. Once the reaction time was complete, the agitator and E5CK controller were turned off and the microreactor was removed.

From the profile in *Figure 3.11*, the microreactor was cooled to lab temperature within 5-7 minutes. The alundum temperature and fluidization air flow rate profiles were inversely proportional in cool down. To prevent damage to the heating elements in the bath, fluidization air was kept on overnight after a reaction.

From *Appendix B*, the internal gauge pressure was predicted to reach circa 10396kPa(g) at 390°C. However, 8000kPa(g) was measured as the internal gauge pressure from *Figure 3.11*. The reason for the difference was that the gas phase in the 1/4" tubing at the pressure gauge was not submerged in the fluidized alundum. Therefore, the temperature was not 390°C. Heat transfer up the microreactor to the tubing was reduced significantly from the alundum to surrounding air above the fluidized bath. The MDTR was used on the external 1/4" tubing near the pressure gauge and measured circa 80 to 100°C. The predicted pressure from VMGSim from 80 to 100°C at reaction 12 loading conditions ranged from 5500 to 5800kPa(g). At 8000kPa(g), the vapor inside the tubing was predicted at approximately 235-240°C. The vapor cooled in temperature through the tube section near the pressure gauge.

3.3.5 Product Collection

Images of the filtration equipment and setup used to recover the liquid product are shown in *Figure 3.12*. The evaporation mass profile of dichloromethane solvent in the fume hood for a hydrotreating reaction is shown in *Figure 3.13*. An image of the spent catalyst recovered, solids and pellets, is shown in *Figure 3.14*. Images of the liquid HVGO feed and three hydrotreated liquid products are shown in *Figure 3.15*. A summary of feed and product masses measured with recovery for all reactions in *Table 3.4* is presented in *Table 3.5*. Average valves with standard deviations, and 95% confidence intervals of *Table 3.5* are presented in *Table 3.6*. Theoretical evaporation calculations of dichloromethane from a glass vial in a fume hood are found in *Appendix D*. Complete tables of all measured masses for each reaction specified in *Table 3.4* are found in *Appendix D*.

After the microreactor was cooled, the mass of the microreactor was measured on the balance scale. The total mass difference before and after reaction on averaged -0.009±0.005g for all experimental reactions. Errors were attributed to Neever·Seez burned off or alundum grains wedging into the microreactor fittings from agitation. Effort was placed into ensuring the before and after reaction mass difference was low as possible by cleaning off the alundum grains. If there

was a significant difference in the mass (>0.02g), a gas leak from the microreactor fittings, tubing or valve was evident. The microreactor was placed in the fume hood. The needle valve was opened and closed quickly to release the product gas. The mass of the microreactor was measured to record the mass of product gas. The microreactor was clamped into the bench top vice grip and opened with the 1-1/8" wrench. The top portion and bottom microreactor mass were measured on the balance scale.

For sulfidation reactions and unfiltered hydrotreating reactions (reactions 2 to 9 in *Table 3.4*), the liquid product and/or catalyst masses were measured and poured out into Fisherbrand™ 20ml glass vials and capped. A Mettler Toledo AL204 analytical balance scale was used for mass measurement of 20ml glass vials and filter papers. For all remaining reactions, the liquid product was washed out of the microreactor using dichloromethane (DCM) solvent. Prior to filtration, a 0.22µm membrane filter paper (GVWP02500) was dried in the oven for at least 2 hours in an aluminum weighing dish (~100°C). The mass of the dried filter paper was recorded and placed in the metal filter holder. Filtration separated the liquid product from catalyst pellets and solids for characterization analyses.
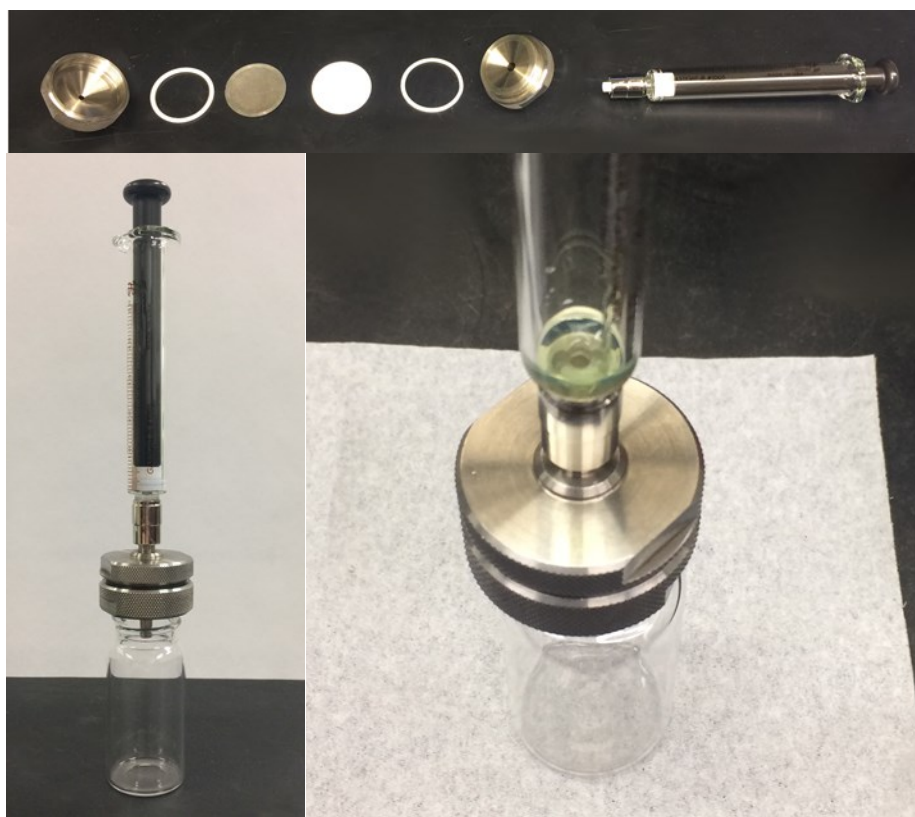
Figure 3.12. Images of the filtration setup used to recover liquid product.

The filtration setup used a EMD Millipore microsyringe filter holder (XX3002514) with a Hamilton™ syringe (luer lock, 5ml, HAM81520) in *Figure 3.12*. The top image shows the order placement of gasket, metal mesh, and filter paper used inside the filter holder. The filter holder was screwed in securely to prevent leaks. The luer lock was attached to the filter holder. The mass of a clean and empty Fisherbrand™ 20ml vial was recorded. The filter holder was placed on top of the vial as seen in the left image of *Figure 3.12*. Cautiously, the microreactor liquid product was poured into the 5ml syringe as seen in the bottom right image of *Figure 3.12*. Dichloromethane was sprayed into the microreactor to solubilize the remaining liquid product off walls and catalyst. The diluted liquid product was poured carefully into the 5ml syringe. The syringe plug was aligned and carefully forced the solution down through the filter holder to remove catalyst impurities. At most, 10-15g of DCM was used to clean the microreactor for each reaction. The washing step was repeated until the solution filtered was clear. The 20ml glass vial with liquid product and DCM solution was left in the fume hood to evaporate overnight.
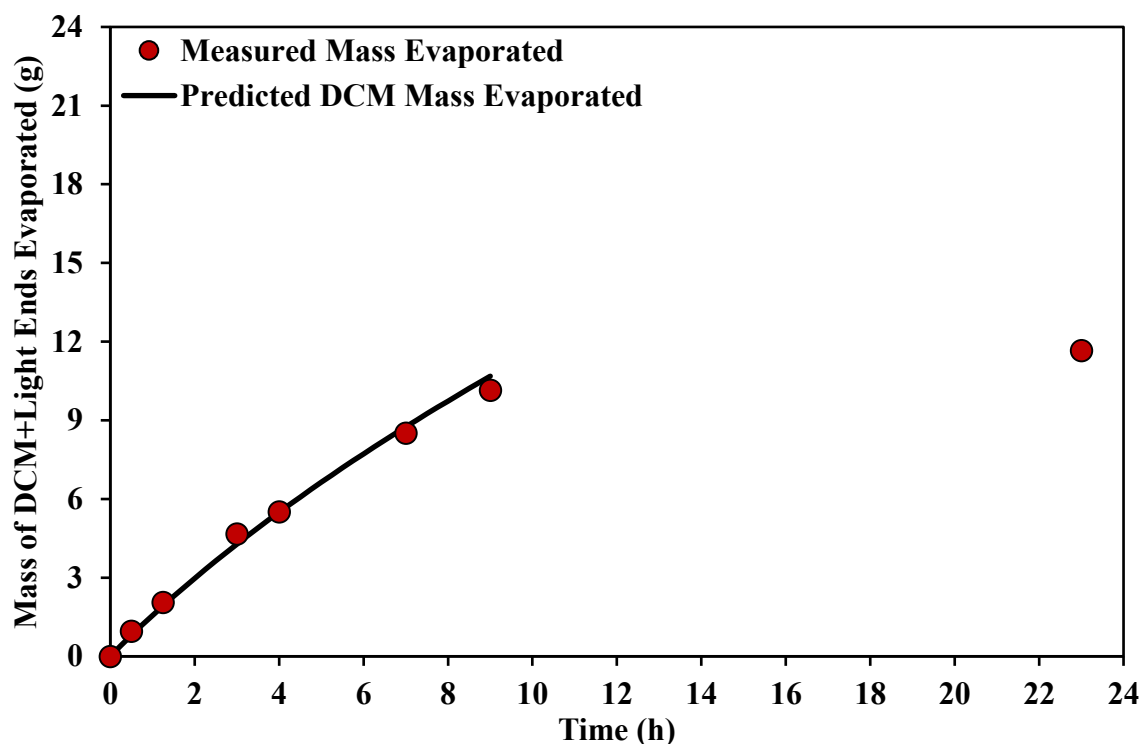
Figure 3.13. Evaporation mass loss profile of dichloromethane (DCM) plus light ends following product filtration.

The evaporation mass loss of dichloromethane plus light ends profile, following product filtration, is shown for the verification reaction in *Figure 3.13*. The calculations for the predicted mass loss of DCM are found in *Appendix D*. The predicted mass loss agreed for the initial 9 hours of DCM evaporation. Beyond 9 hours, the complete evaporation of DCM and light ends of the liquid product occurred. Complete evaporation of DCM occurred between 9 to 11 hours. The liquid product solutions were evaporated for an average of 24-28 hours for all experimental reactions in the fume hood (20°C and 0.41m/s air velocity). The mass of the liquid product remaining in the vial the following day was measured and recorded. The liquid recovery after solvent evaporation is presented in *Table 3.5* for each reaction. The remaining liquid product vial was capped and stored in the fridge (4°C) until each analytical characterization was completed.
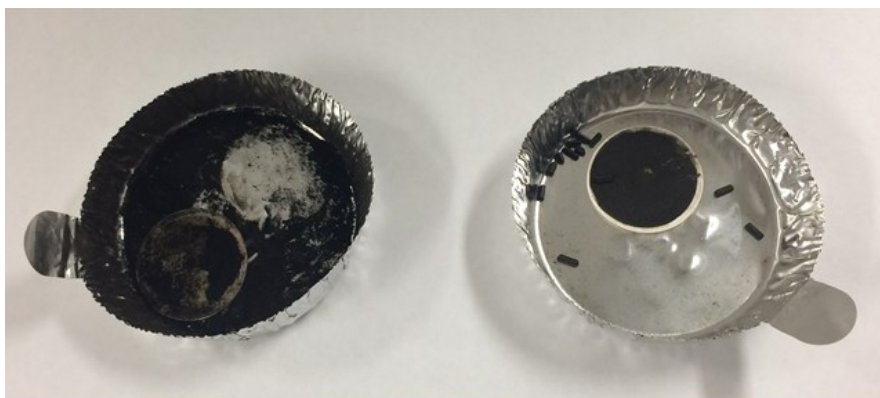
Figure 3.14. Images of spent recovered catalyst.

The spent catalyst recovered for the <45μm solids (left side) and the pellets (right side) are shown in *Figure 3.14*. The filter paper was removed from the filter holder with metal tweezers and placed in the aluminum weighing dish. The pellets were either removed from the syringe or microreactor by metal tweezers and placed in the weighing dish with the filter paper. The collected catalyst plus filter paper was placed in the oven and dried overnight (~100°C). The mass of the dry catalyst plus filter paper was measured and recorded the following day. This was the mass of spent catalyst recovered. The microreactor was cleaned thoroughly with toluene and acetone solvents. Sand paper was used to clean the microreactor walls. The threads of the reducing union and nut threads were cleaned with acetone, Kimwipes™, and a metal tweezer. This step allowed the microreactor to be used multiple times and resulted in satisfactory pressure tests consistently. The top portion of the 20cm SS tube plus needle valve was cleaned with acetone and dried. The clean empty mass of the entire microreactor was measured and recorded.

Table 3.5. Summary of feed and product masses measured with percent recovery.

#	Liquid Feed Loaded (g)	Catalyst Loaded (g)	H$_2$ Gas Loaded (g)	Product Gas Released (g)	Liquid Product + Catalyst Recovered (g)	Total Mass Recovery (%)	Spent Catalyst Recovered (g)	Liquid Product After DCM Evaporation (g)	Liquid Product Recovery After DCM Evaporation (%)
1	0.61	0.1				93	0.11	0.56	91
2	0.6		0.06	0.08	0.57	97		0.47	78
3	0.6		0.08	0.09	0.55	94		0.4	66
4	0.61		0.07	0.08	0.61	100		0.47	76
5	0.6		0.07	0.07	0.64	106		0.47	77
6	0.62		0.08	0.09	0.59	98		0.48	78
7	0.61	0.1	0.07	0.08	0.71	101		0.52***	85
8	0.62	0.11	0.08	0.08	0.71	100		0.57***	92
9	0.61	0.1	0.07	0.08	0.71	101		0.49***	81
10	0.62	0.1	0.07	0.08	0.67	94	0.15	0.42	67
11	0.61	0.11	0.07	0.08	0.7	98	0.13	0.48	79
12	0.62	0.1	0.08	0.09	0.69	97	0.13	0.5	80
13	0.61	0.1	0.08	0.08	0.7	99	0.11	0.45	73
14	0.61	0.11	0.08	0.08	0.71	100	0.14	0.42	70
15	0.6	0.1	0.08	0.08	0.68	97	0.11	0.41	68
16	0.34	1.32	0.05	0.25	1.46	100	1.39	-	-
17	0.46	1.39*	0.04	0.42	1.42	97	1.41	-	-
18	0.5	1.4	0.05	0.4**	1.26	85	1.24	-	-
19	0.3	1.24*	0.05	0.36	1.17	96	1.17	-	-
20	0.61	0.1	0.06	0.08	0.65	95	0.09	0.48	79
21	0.62	0.1	0.07	0.08	0.72	102	0.09	0.54	87
22	0.61	0.1	0.08	0.08	0.71	100	0.09	0.5	81
23	0.62	0.11	0.07	0.08	0.71	99	0.11	0.52	84
24	0.61	0.1	0.07	0.08	0.68	98	0.1	0.53	86
25	0.63	0.1	0.07	0.08	0.71	99	0.11	0.54	86
26	0.63	0.1	0.07	0.08	0.7	98	0.11	0.55	88
27	0.61	0.1	0.07	0.08	0.7	99	0.09	0.52	85
28	0.62	0.1	0.07	0.08	0.7	98	0.11	0.55	89
29	0.64	0.11	0.07	0.08	0.75	101	0.12	0.59	92
30	0.63	0.11	0.07	0.08	0.74	101	0.11	0.57	90
31	0.61	0.1	0.07	0.09	0.68	98	0.11	0.5	81
32	0.61	0.1	0.07	0.08	0.67	96	0.11	0.54	88
33	0.61	0.11	0.07	0.08	0.71	101	0.12	0.51	82
34	0.61	0.1	0.07	0.09	0.69	99	0.09	0.52	85
35	0.61	0.11	0.07	0.09	0.72	103	0.08	0.56	91
36	0.6	0.11	0.07	0.08	0.69	99	0.08	0.54	90
37	0.62	0.1	0.08	0.08	0.73	102	0.09	0.53	85
38	0.62	0.11	0.07	0.08	0.68	96	0.11	0.54	87
39	0.61	0.1	0.06	0.08	0.69	100	0.09	0.53	88
40	0.62	0.1	0.07	0.09	0.71	101	0.09	0.51	82
41	0.62	0.1	0.07	0.08	0.71	101	0.1	0.54	87
42	0.61	0.1	0.07	0.08	0.7	100	0.1	0.48	80
43	0.6	0.1	0.07	0.08	0.64	93	0.09	0.56	93
44	0.61	0.1	0.07	0.08	0.66	95	0.09	0.55	90

*Sulfided catalyst
**<45µm catalyst was lost in the fume hood
***Liquid product poured out into vial, catalyst pellets remained in the microreactor

The mass balance for each reaction is summarized in *Table 3.5*. Experiment 1 was the HVGO feed mixed with catalyst pellets and diluted with DCM for filtration recovery. The recovery of liquid product was 91% suggesting either 9% light ends were lost from evaporation and/or absorbed into the catalyst pellet pores. The mass was higher than 0.11g after catalyst was dried in the oven. For reactions 7 to 9, the liquid product was poured out of the microreactor into glass vials. The catalyst pellets with liquid product remnants remained in the microreactor.

For the sulfidation reaction (16), the mass of spent catalyst pellets recovered was higher compared to the mass loaded. This indicated the catalyst was sulfided. The catalyst was added to the microreactor for the additional sulfidation reaction (17). The mass increased further to 1.41g after recovery. Reaction 18 did not have a complete mass balance as spent catalyst solids were lost in the fume hood from depressurization and transferring to the glass vial. The <45μm solids were difficult to recover after the second sulfidation reaction (19) as solids were lost in the transfer process. The pellets and solids were opaque after the sulfidation reactions. The spent catalyst from reactions 17 and 19 were used for the remaining hydrotreating reactions.

The procedure on dilution with DCM and evaporation overnight was not recommended as evident by the last column of *Table 3.5*, "Liquid Product Recovery After DCM Evaporation (%)." In conducting additional reactions and familiarity, liquid recovery improved by implementation of better DCM washing and mass measurement consistency of the liquid product. The liquid recovery after DCM evaporation averaged 77% for reactions 2 to 15. The liquid recovery after DCM evaporation averaged 86% for reactions 20 to 44.
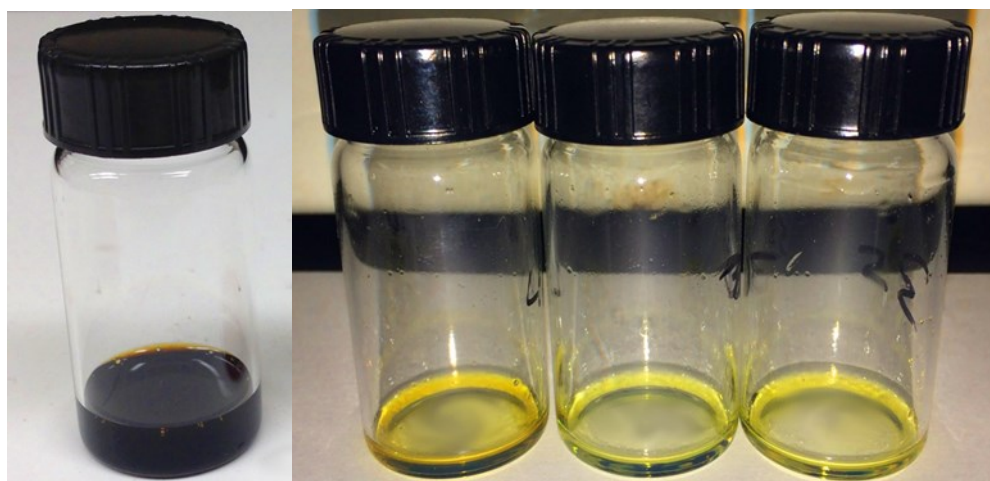
Figure 3.15. Images of the HVGO and three hydrotreated liquid products.

Images of the HVGO feed and three hydrotreated liquid products after DCM evaporation are shown in *Figure 3.15*.

Table 3.6. Average values from *Table 3.5* with standard deviations, and 95% confidence intervals.

	HVGO Loaded (g)	Catalyst Loaded (g)	H₂ Gas Loaded (g)	Product Gas Released (g)	Liquid Product + Catalyst Recovered (g)
Average	0.614	0.103	0.072	0.082	0.684
Standard Deviation	0.009	0.005	0.005	0.004	0.044
95% Confidence Interval	0.003	0.002	0.001	0.001	0.014

	Total Mass Recovery (%)	Spent Catalyst Recovered (g)	Liquid Product After DCM Evaporation (g)	Liquid Product Recovery After DCM Evaporation (%)
Average	99	0.105	0.51	83
Standard Deviation	2.7	0.02	0.05	7
95% Confidence Interval	0.8	0.005	0.01	2

The average valves of all hydrotreating reactions in *Table 3.5* were summarized with standard deviations, and 95% confidence intervals in *Table 3.6*. Experiment and reactions 1 to 15 plus 20 to 44, were averaged. The total mass recovery averaged 99±1%. Errors were attributed to alundum grains wedging into the fittings or Neever·Seez burned off the microreactor nut. The spent catalyst recovered increased because of additional sulfidation, carbon addition through coke deposition or incomplete removal of liquid product remnants from DCM washing and filtration. The liquid product after recovery averaged 83±2%. Light end losses in solvent evaporation from the liquid product was the reason for a reduced recovery. Heavy fractions absorbed on the catalyst surface accounted for a small liquid mass loss. On average, 17% of the total liquid product was not accounted for in subsequent analytical characterizations and calculations. These liquid fractions were either light ends with higher volatiles at room temperature or heavy fractions absorbed inside the catalyst. Minor differences were expected if light ends and extra heavy ends absorbed in the

catalyst were included in subsequent characterizations. However, the liquid product recovery after evaporation ensured minimum DCM was left in the liquid product.

3.4 Characterization Techniques

The liquid products from *Table 3.5* were characterized by the techniques described in section 3.4 to address the second objective of the study. The solid catalysts after sulfidation reactions were analyzed for carbon, sulfur, and nitrogen (CSN).

3.4.1 Carbon and Hydrogen

An image of the flash 2000 organic elemental analyzer used for carbon and hydrogen analysis is shown in *Figure 3.16*. Comparison of the known standard from the organic elemental analyzer is presented in *Table 3.7*. Carbon, hydrogen, nitrogen, and sulfur (CHNS) analysis was conducted on the HVGO feed, hydrotreated liquid products, and the sulfided catalyst. A modified version of ASTM D5291 was used with the addition of sulfur characterization.

Figure 3.16. Flash 2000 organic elemental analyzer used for carbon and hydrogen analysis.

A flash 2000 organic elemental analyzer was used as seen in *Figure 3.16*. Four parts of the analyzer included: the autosampler, reactor, analytical column, and the thermal conductivity detector (katharometer). A small known or unknown sample was placed into a tin foil or aluminum foil capsule. The capsule was folded into a crumpled ball with tweezers. The mass was measured with a Mettler Toledo (MX5) balance scale. The capsule was placed into a known slot of the Thermo-Scientific MAS 200R autosampler. The autosampler injected capsules into a combustion quartz tube reactor (quartz wool, electrolytic copper, and copper oxide filling material). A carrier gas of helium at circa 140ml/min was used. A pyrolysis gas of oxygen at circa 250ml/min for five seconds was used. Once the sample was injected into the reactor (surrounded by a 950°C furnace), an exothermic pyrolysis reaction (as high as 1800°C) with oxygen occurred. The gaseous products generated (CO_2, H_2O, NO_2, SO_2, etc.) entered a 50°C analytical column for separation (steel, 2m length and 5mm ID). Following separation, the product gases entered a thermal conductivity detector. The detector compared the thermal conductivity of the separated product gases (at different temperatures) to the helium gas carrier. The change in resistance (product gases from the reference helium carrier) through the filaments was converted to a voltage signal that was sent to the computer. The Eager Xperience software was used to plot the voltage signals. The software calculated the mass concentrations (wt.%) referenced to a known standard calibration (2,5-Bis(5-tert-butyl-benzoxazol-2-yl) thiophene or BBOT) and the area under each product signal curve. The BBOT standard ($C_{26}H_{26}N_2O_2S$) had a known distribution of carbon, hydrogen, nitrogen, and sulfur atoms as shown in *Table 3.7*. The calibration factor (K) was determined assuming the following equation for each CHNS element:

$$K = \%T_h \cdot \frac{(I-b)}{w} \tag{3.2}$$

Where $\%T_h$ was the theoretical weight percent of each element in the BBOT standard, I was the area under the peak signal (integral) of the standard, b was the blank area with no standard, and w was the mass of the BBOT standard (mg). Once the calibration factor was determined, the CHNS concentrations of unknown (% Unknown, wt.%) samples were determined with the following equation for each element:

$$\% \, Unknown = K \cdot \frac{w}{(I-b)} \tag{3.3}$$

Where K was determined from the standard in equation 3.2, w is the mass of sample (mg), I was the area under the peak signal of the sample, and b was the blank area with no sample.

Table 3.7. Comparison of the known standard from the organic elemental analyzer.

	Carbon (wt.%)	Hydrogen (wt.%)	Nitrogen (wt.%)	Sulfur (wt.%)
Known Standard (BBOT)	72.53	6.09	6.51	7.44
Results (BBOT)	72.53	5.94	6.49	7.48
% Difference from known standard	-	2.49%	0.31%	0.54%

The percent difference was low for the measured results of the BBOT standard in *Table 3.7*. At least three measurements were made for each liquid product. Results for nitrogen and sulfur were non-repeatable. Therefore, results from the sulfur and nitrogen analyzer were used instead. Carbon and hydrogen results from the organic element analyzer are found in section 4.1.

Carbon, Sulfur, and Nitrogen of Sulfided Catalyst

To verify if the catalyst was sulfided, a small sample of sulfided pellets and sulfided <45μm solids were analyzed with the organic elemental analyzer. The sulfided pellets were crushed to small solids and crumpled in the foil capsules. Similar procedures to the liquid analysis were used.

3.4.2 Sulfur and Nitrogen

The MultiTek^{TM} analyzer used for sulfur and nitrogen analysis is shown in *Figure 3.17*. Sulfur and nitrogen standard calibration curves are presented in *Figure 3.18*. A MultiTek^{TM} (Antek by Pac) analyzer was used to determine the sulfur and nitrogen concentrations of the HVGO and its liquid products simultaneously [25]. The analysis was based on slightly adapted versions of ASTM D4294 for sulfur and ASTM D5762 for nitrogen [26-27].

Figure 3.17. MultiTek^{TM} analyzer used for sulfur and nitrogen analysis.

Similar to the organic elemental analyzer, the MultiTek^{TM} in *Figure 3.17* consisted of four components: the sample drive (quartz sample boat in a contained gas box, multi-matrix), pyro-furnace (oxidative furnace), membrane dryer system, and sulfur plus nitrogen detector modules for quantification. The MultiTek^{TM} system and computer were turned on. The MultiTek^{TM} software was loaded on the computer. Preexisting temperature and flow conditions from the software were sent to the MultiTek^{TM}. The gas cylinders, argon and oxygen, were opened. The furnace setpoint was 1050°C. The argon flowrate was set to 130cm^3/min. The pyro oxygen flowrate was set to 450cm^3/min. The ozone (oxygen) flow rate was set to 35cm^3/min. The oxygen carrier flowrate was set to 25cm^3/min. The nitrogen cooling detector was set to 5°C. Both sulfur and nitrogen photomultiplier tubes were set to 600V.

A 25μL syringe (Hamilton 80200) was used for all injections. Fisherbrand™ 20ml glass vials were used for all dilutions of known and unknown samples with 99.9% HPLC grade toluene solvent. Toluene and 99.7% ACS grade acetone were used to clean the syringe multiple times prior to injection of diluted samples. A Mettler Toledo AL204 analytical balance scale was used for all sample mass measurements in 20ml capped glass vials. A known mass of sample was recorded, diluted with a known mass of toluene, and then homogenized in the capped glass vial. A set of injections was set in the software for analysis. Once the setpoint conditions were reached in the MultiTek^{TM}, empty or blank boat injections in triplicates were completed to ensure stable plus consistent sulfur and nitrogen counts. The counts were the integral of measured signals recorded. For the sample, a clean micro syringe was used to withdraw 10μL of solution from the 20ml glass vial. This remained constant for all injections. The 10μL solution was injected into the quartz

sample boat and the sequence was started. The injected sample entered a furnace where combustive oxidation of sulfur and nitrogen species occurred at 1050°C. The reaction is shown:

$$R\text{-}N + R\text{-}S + O_2 \rightarrow CO_2 + H_2O + MO_x + SO_2 + NO*$$
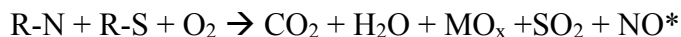
Where MO_x represented other oxides from the sample. Following the reaction, the gaseous products were sent through a membrane dryer to remove water vapor. The SO_2 produced was exposed to ultraviolet (UV) radiation at a specific wavelength (hv'):

$$SO_2 + hv' \rightarrow SO_2* \rightarrow SO_2 + hv''$$

Radiation was released (hv'') through fluorescence and detected by a photomultiplier tube (sensitive EMR detector). The detector converted the fluoresced energy measured. The energy measurement was through dynodes and a collecting anode that caused a current and then converted to a voltage signal. The voltage signal was sent to the computer and the MultiTek^{TM} software. The integral of the signal (or total counts) was proportional to the concentration of sulfur in the sample. An ozone generator (O_3) inside the MultiTek^{TM} was used to create ozone and reacted with NO* to form metastable nitrogen dioxide (NO_2*):

$$NO* + O_3 \rightarrow NO_2* + O_2 \rightarrow NO_2 + hv + O_2$$
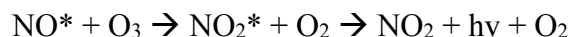
As the excited NO_2* decayed to NO_2, radiation was released through chemiluminescent emission and detected by the photomultiplier tube. The detector converted the measured energy to a signal that was sent to the computer with the MultiTek^{TM} software. The integral of the signal was proportional to the concentration of nitrogen in the sample. The total counts of both sulfur and nitrogen signals were proportional to their concentrations. Prior to injecting unknown hydrocarbon samples, standard calibration curves were developed from thiophene-pyridine liquid mixtures diluted in toluene. Thiophene (84.14g/mol) and pyridine (79.1g/mol), with 38.1wt.% sulfur and 17.1wt.% nitrogen, respectively, were diluted with toluene at other low concentrations in glass vials. The standards were injected into the MultiTek^{TM} and the total counts were obtained. The

average total count of three injections was used for calibration. The standard concentrations were plotted as a function of total counts (integral of signal) as shown in *Figure 3.18*.
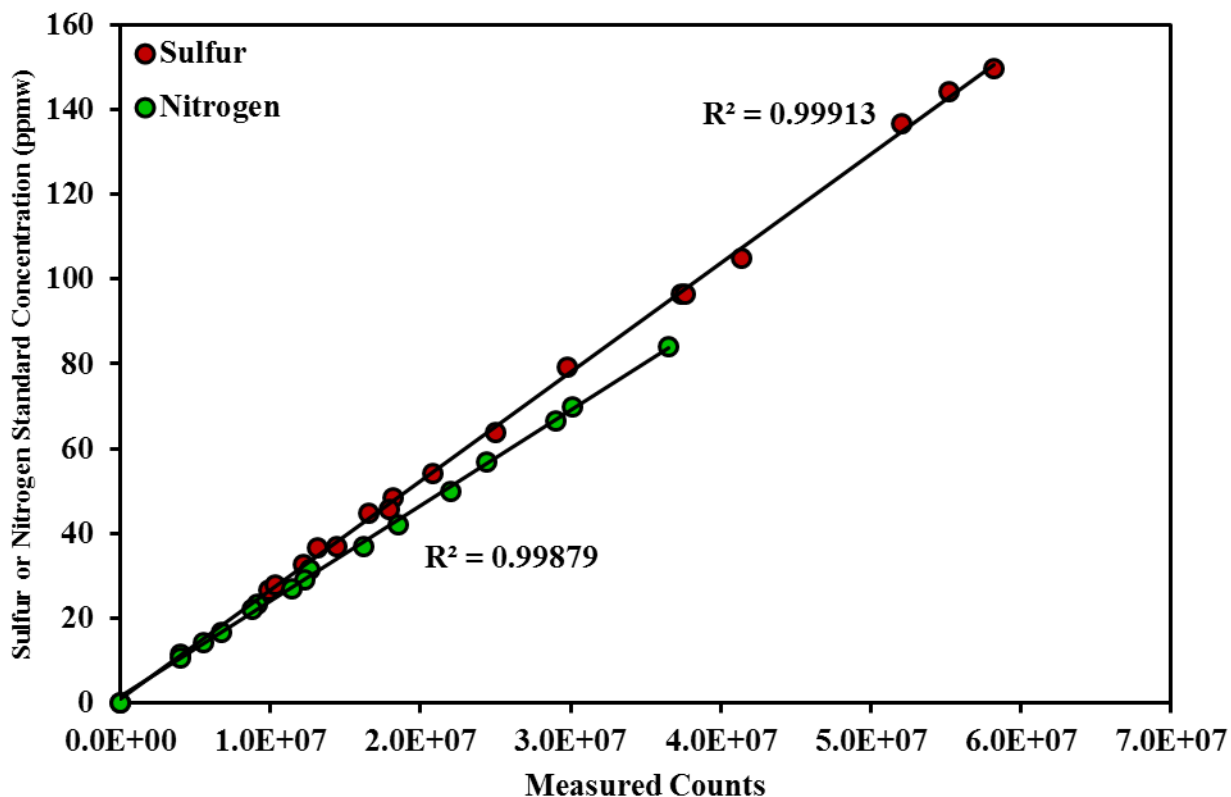
Figure 3.18. Sulfur and nitrogen standard calibration curves.

The standard calibration curves were fitted linearly in *Figure 3.18*. The sulfur and nitrogen standards had linear coefficients of determination of approximately 1. The following calibration equations were generated from the standard curves were used for the unknown HVGO and its liquid products for sulfur and nitrogen characterization, respectively:

$$\textbf{S (ppmw)} = 2.5715 \cdot 10^{-6} \cdot \textbf{S Counts} + 0.8549 \qquad (3.4)$$

$$\textbf{N (ppmw)} = 2.2509 \cdot 10^{-6} \cdot \textbf{N Counts} + 1.5652 \qquad (3.5)$$

Ideally, the intercept should have been zero for both calibration equations. However, signal, mass, and volume measurement errors existed. Circa 0.09g of HVGO was diluted in 14g of toluene. On average, circa 0.01 to 0.02g of a liquid product was diluted in 2 to 6g of toluene. Each sample was

completed with three 10µL injections and repeated once at a different dilution ratio. A total of six injections for each sample was completed. Concentrations were back calculated from the dilution in toluene and the average of the six injections were reported. Results are found in section 4.2.

3.4.3 Density

An image of the syringe on the balance scale is shown *in Figure 3.19*. The density of the HVGO and its liquid products were measured with a Mettler Toledo AL204 analytical balance scale and a 25µL Hamilton syringe (80200). As the liquid products volumes were small after DCM evaporation (<0.7ml), the mass of 20µL for each liquid product was measured. The density was calculated by measured mass of 20µL. The syringe was cleaned multiple times with toluene and acetone prior to each liquid measurement. The syringe was dried with a mild air stream and Kimwipes^{TM}. The empty dry mass of the syringe was tared on the balance scale. The syringe was placed in the liquid product vial and the plunger piston was pulled up slowly to ensure no bubbles inside. The average temperature was assumed as lab conditions, 20 to 25°C. The full syringe at 20µL was placed on the balance scale in the exact position for each measurement and the mass was recorded. The liquid from the syringe was placed back into the vial and the syringe was cleaned with toluene and acetone for the next measurement. The mass measurement of each liquid at 20µL volume was repeated 3 to 5 times. The average density of the 3 to 5 measurements was reported for each liquid in section 4.3.

Figure 3.19. Syringe on balance scale for density measurement.

An image of the Anton Paar 4500M density meter used is shown *in Figure 3.20*. To verify the density measurement from the 20μL syringe method, an Anton Paar 4500M density meter was used. The Anton Paar density meter had an oscillating U-tube to measure the density of a larger volume of liquid. The procedure was based on ASTM D4052 [28].

Figure 3.20. Anton Paar 4500M density meter used for verification.

The theory of this density meter was based on a mass-spring model [29]. The period of resonance was related to the mass of the tube plus the sample inside. After injection of a sample in the U-tube, the density was calculated based on the spring constant, volume injected, the known mass of the U-tube measured, and the period of oscillation. Calibration of the meter was completed with ultra-pure water and dry air (0.99820g/cm^3 and 0.001204g/cm^3 at 20°C, respectively) to obtain calibration constants [30]. Air density was corrected for humidity and atmospheric pressure [30]. Acetone solvent and HVGO were measured separately for verification. A 5ml plastic syringe (S7510-5) was used to inject acetone and HVGO in the clean density meter U-tube. Toluene and acetone solvents were used to clean the U-tube after each HVGO measurement. The air pump was used to dry the inside of the U-tube prior to each measurement. Average density comparisons from the density meter, syringe method, and literature are presented in *Table 3.8*.

Table 3.8. Comparison of density meter, syringe method, and literature for acetone and the HVGO [31-36].

	Acetone Solvent (g/cm^3)	HVGO (g/cm^3)
Density Meter	0.79623 (at 15.6°C)	0.97184 (at 20°C)
Syringe Method	0.789 ± 0.003	0.967 ± 0.006
Literature	0.79603 (at 15.6°C) [31] 0.79125 (at 20°C) [31] 0.790 (ACS, Fisher Scientific)	0.965 (at 15.6°C) [32] 0.967 [33] 0.9683 (at 15°C) [34] 0.969 (at 15°C) [35] 0.9712 (at 15°C) [36]
Average Literature	0.791 (at 20°C)	0.968 (at 15°C)
% Difference Density Meter	0.03%	0.40%
% Difference Syringe Method	0.22%	0.10%

The acetone measurement from the density meter had a low 0.03% difference from the density calculated from literature constants reported in DIPPR Project 801 at 15.6°C [31]. The HVGO had a reported literature average of 0.968g/cm^3 at circa 15°C. The density meter measured the HVGO at 20°C and differed by 0.4% from the literature average. The HVGO density measured by the syringe method differed by 0.1% from the literature average.

3.4.4 Boiling Point Distribution

An image of the Bruker 450-GC used for boiling point distribution measurement is shown in *Figure 3.21*. Screenshot images of measured signals as a function of retention time for the paraffin mixture, HVGO, and a hydrotreated liquid product are shown in *Figure 3.22*. A Bruker 450-GC gas chromatograph with a flame ionization detector (FID) was used to measure the boiling point distribution of the HVGO and its liquid products. The distribution measurement or simulated distillation was based on ASTM D7169 [37].

Figure 3.21. Bruker 450-GC used for boiling point distribution measurement.

The Bruker 450-GC consisted of multiple parts: the autosampler, sampling syringe, injector, the GC column, the FID, and the computer software. Maintenance of all physical parts was important over the course of liquid product characterizations. Prior to injection of unknown samples, calibration was completed with a known paraffin mixture and a reference gas oil. The known paraffin mixture was a Supelco quantitative calibration solution (500658, C_5-C_{44}) with a Supelco polywax 655 (48477, C_{22}-C_{100}). A reference gas oil (5010A) was used to check the calibration and obtain a response standard. Distributions of the standards are found in the ASTM D7169 procedure [37]. A Mettler Toledo AL204 analytical balance scale and a 25μL Hamilton syringe (80200) were used. The 25μL syringe was used to transfer 15 to 20mg of liquid sample into a 1.5ml sample vial. Carbon disulfide (ACS grade, >99.9%) was used to dilute liquid samples to 0.8 to 1wt.% with Fisherbrand® $5^{3/4}$" pipettes. Mass of sample and carbon disulfide (CS_2) were recorded. The masses were entered in the Compass CDS software. The full vial was homogenized rigorously. The polywax standard required heating on a hot plate (80 to 100°C) to dissolve in carbon disulfide prior to injection. Once the sample was homogenized, the 1.5ml glass vial was placed in the autosampler in a known slot. Pure solvent vials were placed in known slots in the autosampler. Prior to a liquid sample, the autosampler syringe underwent multiple 2.5μL CS_2 withdrawals and disposals to ensure no contamination in the syringe. The sequence began with a blank run and was

repeated twice prior to any liquid sample to ensure a clean column, a stable solvent peak, and a stable baseline. Following a stable baseline, the calibration mixture was injected. Following the paraffin mixture, the response factor standard, a reference gas oil, was injected. The Bruker SimDist Reporter software parameters were adjusted with the updated retention time of the calibration (paraffin mixture) and response factor (reference gas oil). The reference gas oil standard was compared to the temperatures reported in ASTM D7169 to ensure the boiling point distribution results measured were within the 95% confidence intervals of the average distribution reported. If an unstable solvent baseline or a large error in the reference gas oil standard was obtained, a maintenance cycle was completed. The automated sample syringe completed two 2.5μL sample withdrawals and disposals prior to the third 2.5μL injection into the GC. The injector consisted of a septum, septum support, glass insert liner, graphite ferrule, and a stainless-steel nut that secured the column to the glass insert liner. The injector was set at 50°C and increased to 425°C (15°C/min) over 35 minutes once the sample was injected. The initial oven temperature was -20°C. The oven temperature increased at 15°C/min to a temperature of 430°C over 45 minutes and held at 430°C for 10 minutes. As the temperature heated up, the sample injected elutes with a helium carrier gas or eluent through a 5 meter column at a flow rate of approximately 20ml/min. As the samples were complex, different fractions of the sample or stationary phase flowed through with the eluent at different rates proportional to boiling temperatures. The GC column length allowed for separation of the complex mixture. These complex fractions exited the column as effluent at different retention times. The exiting effluent entered the FID and mixed with a hydrogen combustion gas plus air (40ml/min and 450ml/min, respectively) at a 435°C. Combustion with hydrogen occurred at the jet inside the electrode. A large potential voltage was applied between the jet and electrode [38]. Ions formed from combustion were impelled by the large potential to the electrode and generated a measurable current proportional to the number of ions at that time. The current was converted to a voltage signal that was sent to the computer software for plotting and processing. The signal (μV) was plotted as a function of retention time in the CompassCDS software as shown in the screenshot images of *Figure 3.22*.
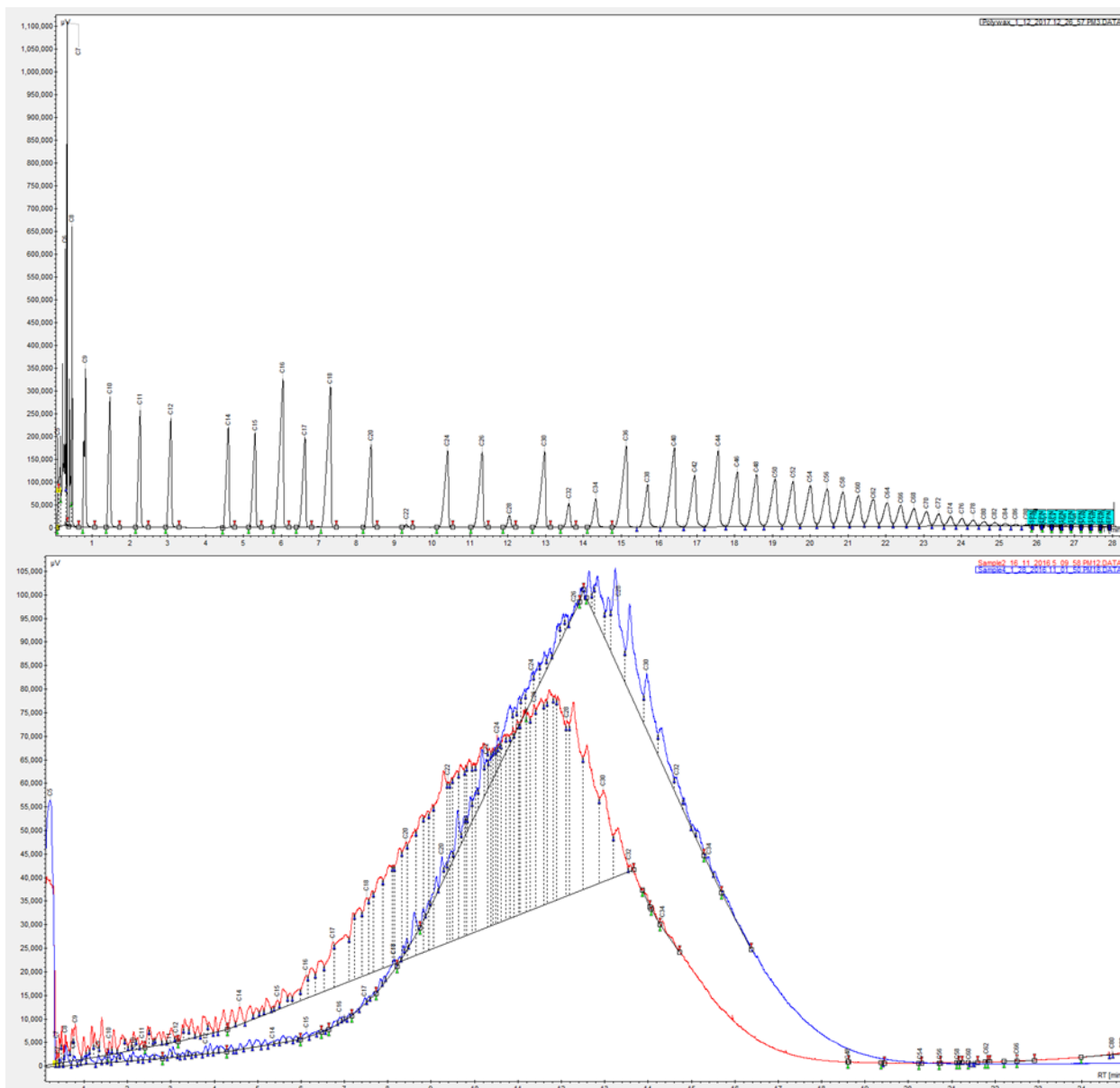
Figure 3.22. Screenshot images of measured signals as a function of retention time for the paraffin mixture (black top), the HVGO (blue bottom), and a hydrotreated liquid product (red bottom).

The data in _Figure 3.22_ was exported to the Bruker SimDist Reporter software to calculate the boiling point distribution for a sample reference to the prior solvent blank injection, calibration mixture, and the reference gas oil response factor. The software measured the area under the signals to determine mass recovered from boiling off the sample.

$$RF = \frac{M_{RGO}}{A_{RGO} \cdot (M_{RGO} + M_{CS2})} \tag{3.6}$$

$$\%RC = \frac{A_{SMP} \cdot RF \cdot (M_{SMP} + M_{CS2})}{M_{SMP}} \cdot 100 \tag{3.7}$$

Where RF was the response factor determined from the reference gas oil (RGO), M_{RGO} was the mass of the reference gas oil in the vial, M_{CS2} was the mass of carbon disulfide solvent in the vial, and A_{RGO} was the area under the signal determined from the SimDist Reporter software. The RF was used for an unknown oil sample to determine the mass recovery percent (%). Where M_{SMP} was the mass of the oil sample, and A_{SMP} was the area under the signal determined from the SimDist Reporter software. The data obtained was mass recovery off (%) and boiling temperature obtained from the calibrated retention time. The HVGO and a couple of the hydrotreated liquid products were repeated to ensure consistent results. Results for the HVGO and all liquid products are found in section 4.4.

3.4.5 Hydrogen Nuclear Magnetic Resonance

An image of the Nanalysis 60MHz benchtop nuclear magnetic spectrometer used is shown in _Figure 3.23_. Proton Hydrogen Nuclear Magnetic Resonance (^{1}H NMR) analysis of the HVGO and its liquid products were completed with 60MHz and 400MHz spectrometers.

The HVGO and six hydrotreated liquid products were submitted to the University of Alberta Chemistry department for ^{1}H NMR analysis that used a 400MHz spectrometer. The advantages of the 400MHz spectrometer compared to the 60MHz spectrometer were better signal-to-noise ratios and resolution. A modified s400 Agilent Inova three-channel 400MHz spectrometer with one dimensional analysis was used. The HVGO and six hydrotreated liquid products were diluted in a deuterated chloroform ($CDCl_3$) solvent. Circa 0.7ml or 55mm height in the NMR tube, of the diluted sample was used. The tube was capped, homogenized, heated to 27°C, and placed in the NMR for analysis. Technical parameters for all analyses: sweep width was 8000Hz, acquisition time was three seconds, relaxation delay was two seconds, 0.12Hz digital resolution, 21 to 24Hz/mm, and 32 scans per sample. As the magnetic field was applied across the sample through sweep coils to align the hydrogen protons, the sample was excited by a radio frequency transmitter to tip the nuclear spin alignments. As the nuclear spins in hydrogen relaxed back to parallel or

antiparallel magnetic alignment, radio energy was released and detected by a radio frequency receiver. This was the free induction decay signal. The radio frequency receiver signal was amplified, and Fourier analysis was completed to decompose the signal. This altered the amplification spectra as a function time to a function of frequency. The plot generated was reported in terms of a dimensionless chemical shift:

$$\delta = \frac{frequency\ of\ signal\ (Hz) - frequency\ of\ reference\ (Hz)}{spectrometer\ frequency\ (Hz)} \cdot 10^6 \qquad (3.8)$$

Where all frequencies were in hertz (Hz). The chemical shift was multiplied by 10^6 and reported as parts per million (ppm). Once the recorded spectrum was completed, the capped tube was removed, and the sample was disposed. A processing software VnmrJ grouped the chemical shift signals into the ranges specified in *Table 2.12*. The software used a spline baseline correction on the chemical shift spectrum prior to integration. Area under each signal was proportional to the molecular concentration of hydrogen atoms in the ranges specified from *Table 2.12*. Seven samples were submitted and completed using the 400MHz spectrometer: the HVGO, reactions 21, 25, 27, 29, 32, and 35 liquid products from *Tables 3.4 and 3.5*.

Figure 3.23. Nanalysis 60MHz benchtop nuclear magnetic spectrometer.

Several samples were analyzed using the 60MHz bench top Nanalysis spectrometer as highlighted in *Figure 3.23*. Similar to the procedure for the 400MHz spectrometer, the HVGO and fourteen

hydrotreated liquid products were analyzed. An average 0.15±0.014g of liquid oil was transferred into 2ml Agilent Technologies glass vials (5190-4030) with Fisherbrand® 5¾" pipettes. The mass was measured using a Mettler Toledo balance scale (XS105). The oil samples were diluted with deuterated chloroform (Acros Organics, $CDCl_3$) with a tetramethylsilane (TMS) reference (1v/v%) to an average of 12.5±1wt.% with a ThermoFisher Scientific finnpipette (F1, with 02-681-168 Fisherbrand® pipet tips) set to 0.75ml. The vials were capped and homogenized rigorously. The diluted samples were transferred to Norell NMR tubes (C-XR-55-7) with 9" Fisherbrand® pipettes to at least the 55mm mark (0.7ml) and capped. The tubes were placed in the Nanalysis (STC-1000) 30°C tube heater prior to analysis. The Nanalysis completed an automatic shim of the magnet for at least 10 minutes to ensure a uniform form field prior to analysis. A standard reference of $CDCl_3$ was used for shimming. Following shimming, the warm sample tube was placed in the tube slot cautiously to start the analysis. The technical parameters set in the Nanalysis interface for all analyses: 12ppm spectral width, acquisition time was six seconds, relaxation delay was 20 seconds, 0.03Hz digital resolution, 128 scans per sample, and 4000 data point collection per sample [39]. Once the NMR analysis was completed, the tube was removed cautiously and disposed. The collected data was saved and transferred to a USB drive. The data files were transferred to a computer with a MestReNova software for signal processing. Similar to the procedure with the VnmrJ software, the chemical shift signals were grouped into the ranges specified in *Table 2.12*. The software used a Bernstein polynomial baseline correction on the chemical shift spectrum prior to integration. The processing identified and corrected the spectrum for the $CDCl_3$ plus TMS reference signals at 7.24 to 7.26 and 0ppm, respectively. Results for the hydrogen groups classified in HVGO and its liquid products are found in section 4.5.

3.5 Visible Spectroscopy

To address the visible characterization of the second objective, development of a spectrophotometer for ex-situ color observation is completed. Details, procedures, and verification with a lab grade spectrometer are discussed in section 3.5.

3.5.1 Visible Spectrophotometer

An image of the visible spectrophotometer developed is shown in *Figure 3.24*. An image of the fixed position placement of the 2mm glass cuvette is shown in *Figure 3.25*. The complete visible spectrophotometer developed included four parts: a fiber optic cable, a glass cuvette, a light source, and a Avantes USB spectrometer. The light source was an Ocean Optics Inc. LS-1 tungsten halogen lamp with a 12V DC power supply. The lamp had a switch to control the light output (5V at 1.3 amps, or 6.5W). The spectral range of the lamp was 360 to 2000nm. The glass cuvette was a 2mm light path length OS absorption cell from Hellma analytics (100-2-20). The cuvette provided >80% transmission of light in the 320 to 2500nm spectral region. The advantage of this cuvette was the detection of light through opaque and viscous oil samples such as the HVGO. Additionally, the 2mm cuvette volume was small which allowed for effective insertion and removal of the liquid products collected. A larger path length did not provide an adequate adsorption measurement of light. This was evident for the HVGO as no light was transmitted through. A 500µm SMA fiber optic cable from Thorlabs was used. The fiber optic cable was attached to the spectrometer. A Avantes AvaSpec-2048 Fiber Optic Spectrometer was used. The spectrometer had a detection region of 200 to 1100nm with a 0.04 to 20nm resolution. The charge-coupled device detector array in the spectrometer was 2048 pixels. The signal to noise ratio was 200:1 with 300 lines/mm grating. As the lamp source had a spectral output of 360 to 2000nm and the spectrometer had a detection of 200 to 1100nm, the region examined in the current study was 360 to 1100nm based on the equipment used. The image of the complete setup is shown in *Figure 3.24*.
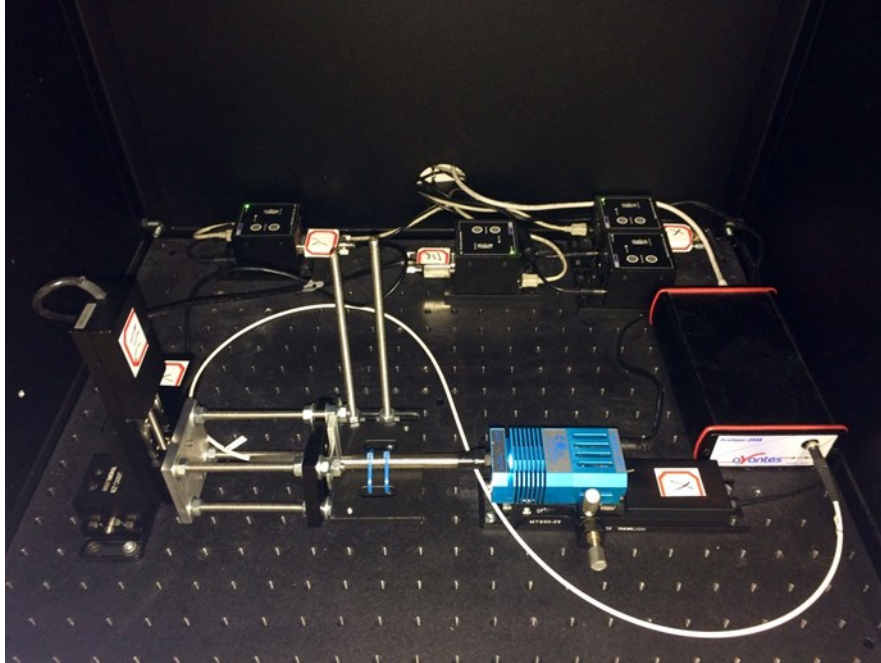
Figure 3.24. Visible spectrophotometer developed.

Several pieces of equipment were used to assemble the visible spectrophotometer in *Figure 3.24*. Several pieces were obtained from Thorlabs [41]. A black box with a black aluminum breadboard (MB12, with 1/4" mounting holes) base was used to house all equipment. Three 50mm low-profile motorized translation stages (MTS50-Z8) were used for XYZ positioning of the light source and fiber optic cable. Two base plates (MTS50A-Z8) secured two stages (X and Y planes) to the breadboard. A right-angle bracket (MTS50C-Z8) secured the Z stage to the Y stage for the fiber optic cable. The stages were connected to T-Cube DC servo motor driver controllers (TDC001) each with a power supply, a 15 pin D-type connector, and a USB connector cable. The motor drivers were secured to baseplates on the breadboard. The USB cables were connected to a PC with a Kinesis control software. Operation of the controllers were used to adjust the initial position of the light source and fiber optic cable to a fixed position prior to measurement. This remained fixed for all measurements. A Pitch and Yaw Tilt Platform with Thumbscrew Drives (APY001) was mounted on the X stage to secured the light source. A steel plate (2.375" by 2.375"), constructed by the University of Alberta machine shop, was mounted on the Z stage with four holes to secure four threaded rods (1/4") with bolts. The end of the four threaded rods secured a black mounting base (BA2, 2" by 3") slightly angled (with 3/8" bolts and washers) that positioned the fiber optic cable end tip. The fiber optic tip was lined through the center of the black mounting

124

base and was secured to an external SM1-threaded fiber adapter (SM1SMA). The adapter was fixed to the mounting base. Two threaded rods (1/4"), attached to the breadboard, secured a black mounting plate that provided a base for the light source tube and the 2mm glass cuvette. The black mounting plate was an extra T-Cube DC servo motor driver controller baseplate. Small steel plates (26 to 28mm by 16mm), attached to the top two threaded rods of the Z stage, were secured with bolts (3/8") to fix the position of the 2mm glass cuvette. A 3/8" stainless steel tube (SS-T6-S-049-20, cut to circa 3.625") was attached to the light source with electrical tape and secured to the black mounting plate (93mm by 2.375") with two zip ties. The hollow 3/8" tube end provided a fixed enclosure position that could be adjusted for any cuvette size. The hollow tube concentrated the emitted light to small area (0.06in.^{2} or 38.9mm^2) directly in line and centered with the 500μm fiber optic cable. The position was adjusted for the 2mm glass cuvette. The cuvette was fixed within the side steel plates and backed against the threaded fiber adapter. The position allowed the glass cuvette to be placed and removed freely without scratching or damaging the glass itself. See *Figure 3.25*.
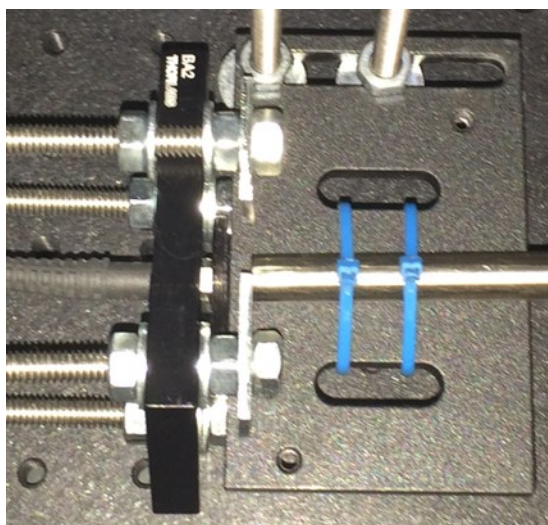
Figure 3.25. Image of fixed position placement of 2mm glass cuvette.

3.5.2 Procedure

The spectral output of the tungsten halogen lamp source is shown in *Figure 3.26*. An image of the HVGO in the 2mm glass cuvette is shown in *Figure 3.27*. Standard methods for absorptivity of petroleum, techniques, and measurement performance (ASTM D2008, ASTM E169, and ASTM

E275, respectively) are recommended for additional information [42-44]. The spectrometer was connected to a computer via USB to provide power. The AvaSoft 8 (8.6 version) software was opened and detected the spectrometer automatically. Directory folders were created to save recorded data. The software plotted spectral intensity (scope, analog to digital counts) as a function of wavelength. Settings of exposure (integration time) was 2 milliseconds that averaged 100 measurements for all samples. Depending on the light source and cuvette, settings were optimized for the 2mm cuvette. The dark spectrum with no light source was captured and saved. A clean and empty 2mm cuvette was placed in the fixed position. The tungsten halogen lamp was turned on for 20 to 30 minutes prior to measurement to stabilize the light output from the filament. The black box housing was closed, and the spectral output of the tungsten halogen lamp was recorded as seen in *Figure 3.26*.
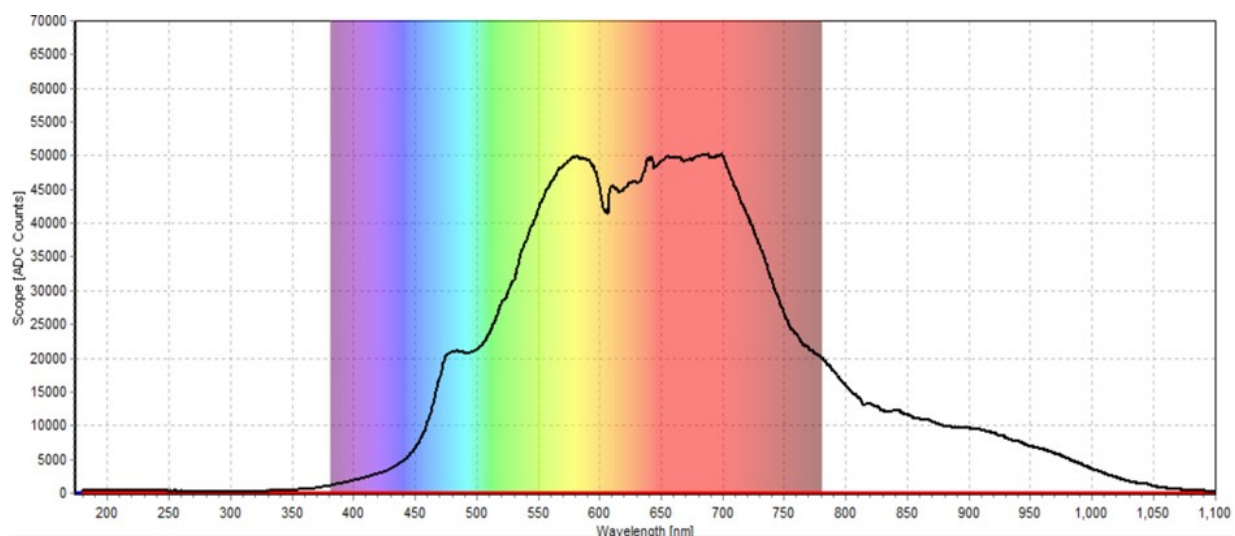
Figure 3.26. Spectral output of the tungsten halogen lamp source.

The tungsten halogen lamp had a 350 to 1100nm visible range of light passing through the empty cuvette in *Figure 3.26*. The red signal measured at the bottom of *Figure 3.26* was the dark spectrum. The black signal spectrum of an empty cuvette in *Figure 3.26* was saved as the reference spectrum in the software. The cuvette was removed. Prior to each placement of samples, acetone with Kimwipes™ were used to ensure a clean glass cuvette. The HVGO and its liquid products were transferred from vials using 9" Fisherbrand® pipettes to the clean glass cuvette (0.1 to 0.2g). A glass cap was placed on top of the cuvette to ensure a closed system. See *Figure 3.27*.

Figure 3.27. Image of HVGO in the 2mm glass cuvette.

The filled cuvette in *Figure 3.27* was placed cautiously in the fixed position slot of *Figure 3.25* and the housing cover was closed. The spectrum of the transmitted light detected from the sample was recorded and saved. The cuvette was removed from the slot and the sample was pipetted out. The cuvette was washed with toluene plus acetone solvents and dried with Kimwipes^{TM} prior to the next measurement. Each sample measurement was repeated at least once. The average recorded spectrum of each sample was calculated. The light source was turned off and the USB cable was removed from the computer to power off the spectrometer. The absorbance (A) at each wavelength was calculated with the following formula:

$$A = log \left[\frac{reference - dark}{sample - dark} \right]$$
(3.9)

Where *reference* was the spectra of the tungsten halogen lamp, *dark* was the spectra with no light source, and *sample* was the average spectra of each oil sample. Results for the HVGO and its liquid products are found in section 4.6.

3.5.3 Ultraviolet-Visible Spectrophotometer Verification

To verify the measurement results of the visible spectrophotometer developed, a lab grade PerkinElmer UV/VIS/NIR Spectrometer Lambda 1050 was used. The source and detection ranged from 175 to 3300nm. The light source was a combination of tungsten-halogen and deuterium. The identical 2mm glass cuvette was used. A UV WinLab software was used to record, plot, and save the data. The HVGO and one hydrotreated liquid product, reaction 22, spectra were measured for direct comparison to the results obtained from the visible spectrophotometer developed.

Chapter 4: Results

To assess product quality, average results for all analytical characterizations are presented and summarized in *Chapter 4*. Each section presents results from the compositional transformations tested. Numerical results for all characterization techniques are found in *Appendix E*. Conversion trends for sulfur and nitrogen concentrations of the hydrotreated liquid products are found in *Appendix F*. Kinetic results for sulfur and nitrogen concentrations are found in *Appendix F*. Chemometric modeling results for six data sets are summarized in section 4.7. Matlab code for all modeling techniques are found in *Appendix G*. Additional chemometric modeling results are found in *Appendix H*.

4.1 Carbon and Hydrogen

All numerical carbon and hydrogen concentration results are found in *Table E1* of *Appendix E*. Carbon content of sulfided catalyst pellets and <45μm solids are found in *Table E2*.

HVGO

The carbon and hydrogen results of the HVGO averaged 86.4±0.3wt.% and 11.3±0.1wt.%, respectively. Assuming 12.01g/gmol for carbon and 1.00g/gmol for hydrogen, the H/C is 1.57.

Solvent Filtration of HVGO

To determine the effect of solvent filtration on the HVGO, filtered liquid feed is compared to the HVGO. The measured results of the collected HVGO following dichloromethane solvent evaporation overnight are 86.1±0.2wt.% and 11.3±0.2wt.%, for carbon and hydrogen, respectively. A 0.3% difference in carbon, and no change in hydrogen compared to the HVGO. The H/C is different by 0.6% at 1.58. The results are not significantly different.

Non-Catalytic Reactor Mixing Effect

To determine the effect of mixing on the liquid product with no catalyst present, the reaction at 360RPM is compared to three reactions with agitation >700RPM. The average mixing for the three reactions ranged from 708 to 862RPM. The carbon and hydrogen results for the 360RPM reaction liquid product are 85.5±0.4wt.% and 11±0.05wt.%, respectively. The H/C is 1.55. Reactions with

>700RPM agitation ranged from 85.4±0.2 to 85.7±0.2wt.% for carbon and 10.8±0.6 to 10.9±0.4wt.% for hydrogen. The H/C for these liquid products ranged from 1.52 to 1.53. There are no significant differences in carbon and hydrogen concentrations.

Reactor Wall Effect

A microreactor with sulfided (contaminated) inner walls with no catalyst is used to determine the reactor wall effect. The collected liquid product carbon and hydrogen results are 87.8±0.7wt.% and 12.1±0.2wt.%, respectively. The H/C of the liquid product is 1.66. The result is significantly higher compared to the HVGO.

Catalytic Reactor Effect with Unfiltered Liquid Products

The effect of using unsulfided catalyst versus no catalyst on unfiltered liquid products is compared. Three liquid product concentrations ranged from 86.3±0.8 to 87.2±1.4wt.% for carbon and 11.6±0.3 to 11.8±0.3wt.% for hydrogen using unsulfided catalyst pellets. The H/C of these liquid products ranged from 1.61 to 1.64. Carbon, hydrogen, and the H/C results differed significantly compared to non-catalytic reactions at 0.05 significance.

Catalytic Reactor with Liquid Product Filtration Effect

The effect of solvent filtration on the liquid products are compared, three unfiltered reactions, 848 to 878RPM agitation, with three filtered reactions, 866 to 884RPM agitation. The carbon and hydrogen concentration results for the three filtered liquid products ranged from 87.7±0.4 to 88.3±1.2wt.% and 12.2±0.1 to 12.3±0.1wt.%, respectively. The H/C of these liquid products ranged from 1.67 to 1.68. Carbon, hydrogen, and the H/C results differed significantly compared to the three unfiltered reactions at 0.05 significance.

Catalytic Reactor Mixing Effect

To determine the effect of mixing using unsulfided catalyst pellets on the liquid products, three reactions, 866 to 884RPM, are compared with two reactions at 360RPM agitation. Carbon ranged from 86.9±0.3 to 87.4±0.6wt.%, while hydrogen is 12.1±0.2wt.%, for reactions at 360RPM. The H/C ranged from 1.66 to 1.67 for 360RPM compared to 1.67 to 1.68 at 848 to 878RPM. Carbon

and hydrogen results of these liquid products are significantly different compared to the higher agitation reactions.

Verification Reaction

For the temperature and pressure verification reaction at 2.25h, the carbon and hydrogen concentrations are 88.1±0.5wt.% and 12.1±0.2wt.%, respectively. The reaction temperature and mixing are identical to the two reactions at 390°C and 360RPM for 2h. The H/C of the liquid product is 1.65, a 0.6 to 1.2% difference compared to the reactions at 2h.

Sulfided Catalyst Pellets and <45μm Solids

Sulfided catalyst pellets and <45μm solids are compared in *Table E2* of *Appendix E*. The carbon concentration results for the sulfided pellets and <45μm solids are 2.11±0.34wt.% and 0.4±0.01wt.%, respectively. In comparison, the carbon results are significantly different.

Catalytic Sulfidation Effect with Pellets

The effect of unsulfided versus sulfided catalyst pellets on the hydrotreated liquid products is assessed. For three reactions using sulfided catalyst, the carbon and hydrogen concentration results ranged from 87.5±1.8 to 87.9±0.8wt.% and 12.1±0.4 to 12.3±0.2wt.%, respectively. The H/C of these liquid products ranged from 1.66 to 1.68. Carbon, hydrogen, and the H/C results are not significantly different when compared to unsulfided catalyst pellet reactions.

Reaction Time and Temperature Effects with Sulfided Pellets

The effect of reaction time at 390°C using sulfided catalyst pellets on filtered liquid product carbon and hydrogen concentrations is presented in *Figure 4.1*. The effect of reaction temperature at 1h reaction time using sulfided catalyst pellets on filtered liquid product carbon and hydrogen concentrations is presented in *Figure 4.2*.
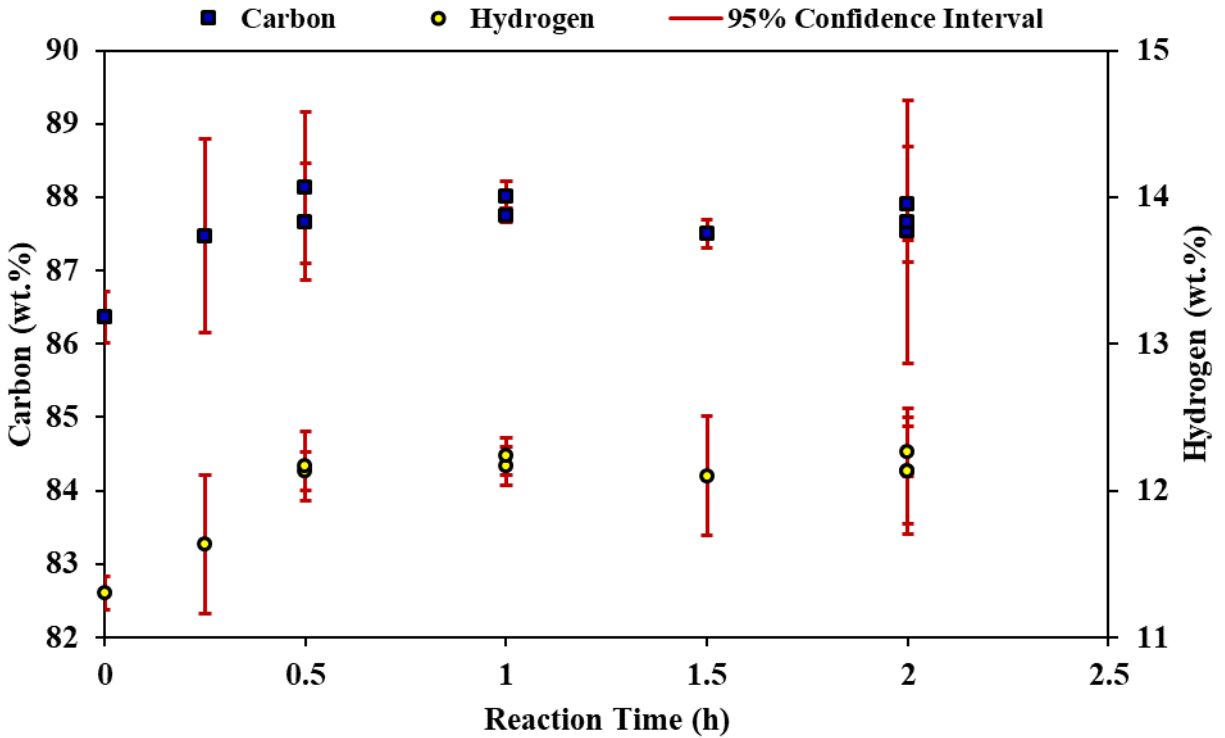
Figure 4.1. The effect of reaction time at 390°C using sulfided catalyst pellets on filtered liquid product carbon and hydrogen concentrations.

The effect of reaction time at 390°C increases carbon and hydrogen concentrations compared to the HVGO at 0h reaction time in *Figure 4.1*. As the reaction time increased to 0.5h, carbon and hydrogen concentrations of the liquid products increased compared to the HVGO. Carbon and hydrogen concentration results of the 0.25h liquid product is not statistically different compared to the HVGO and the 0.5h liquid product. At 0.5 to 2h, the carbon and hydrogen concentrations of the filtered liquid products are not significantly different from each other.
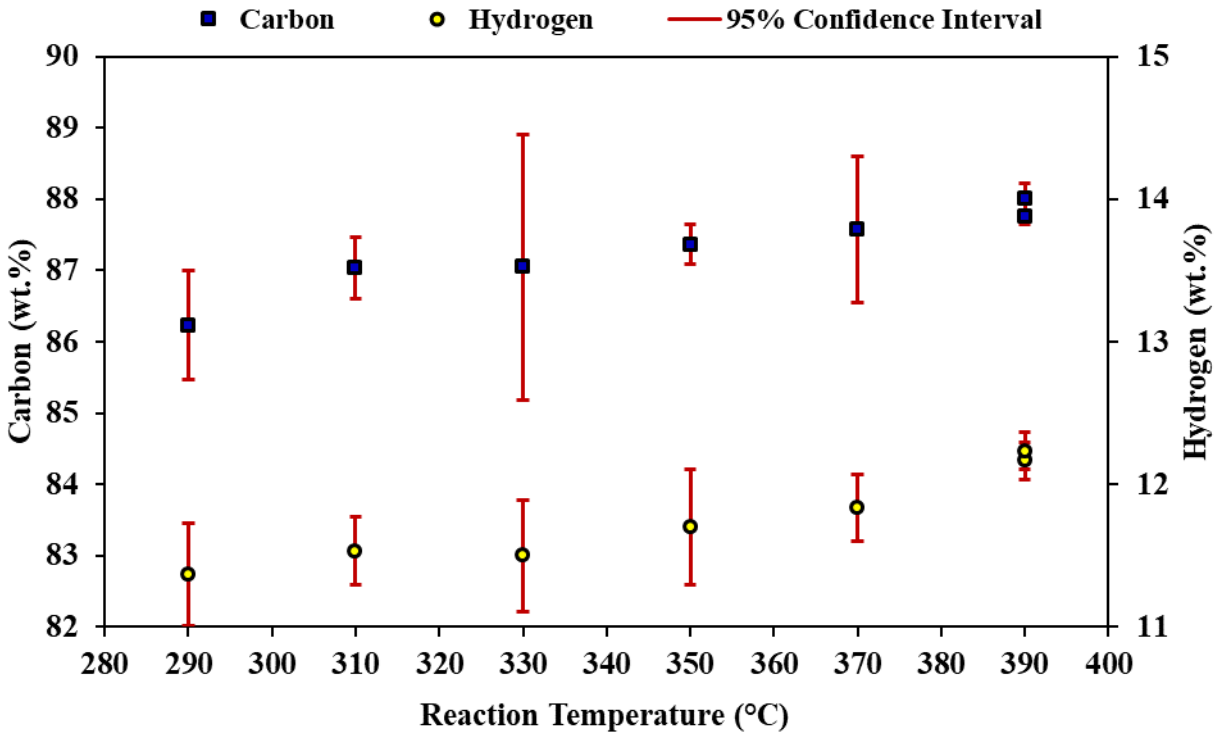
Figure 4.2. The effect of reaction temperature at 1h using sulfided catalyst pellets on filtered liquid product carbon and hydrogen concentrations.

Compared to the HVGO, the effect of reaction temperature at 1h is significantly different for the liquid products higher than 350°C and 370°C for carbon and hydrogen concentrations, respectively. As reaction temperature increased, carbon and hydrogen concentrations of the liquid products increased compared to the HVGO. Liquid products at 290 to 330°C reaction temperatures are not significantly different compared to the HVGO for carbon and hydrogen concentrations.

Reaction Time and Temperature Effects with <45μm Sulfided Solids

The effect of reaction time at 390°C using <45μm sulfided catalyst solids on filtered liquid product carbon and hydrogen concentrations is presented in *Figure 4.3*. The effect of reaction temperature at 0.25 and 0.5h reaction times using <45μm sulfided catalyst solids on filtered liquid product carbon and hydrogen concentrations is presented in *Figure 4.4*.
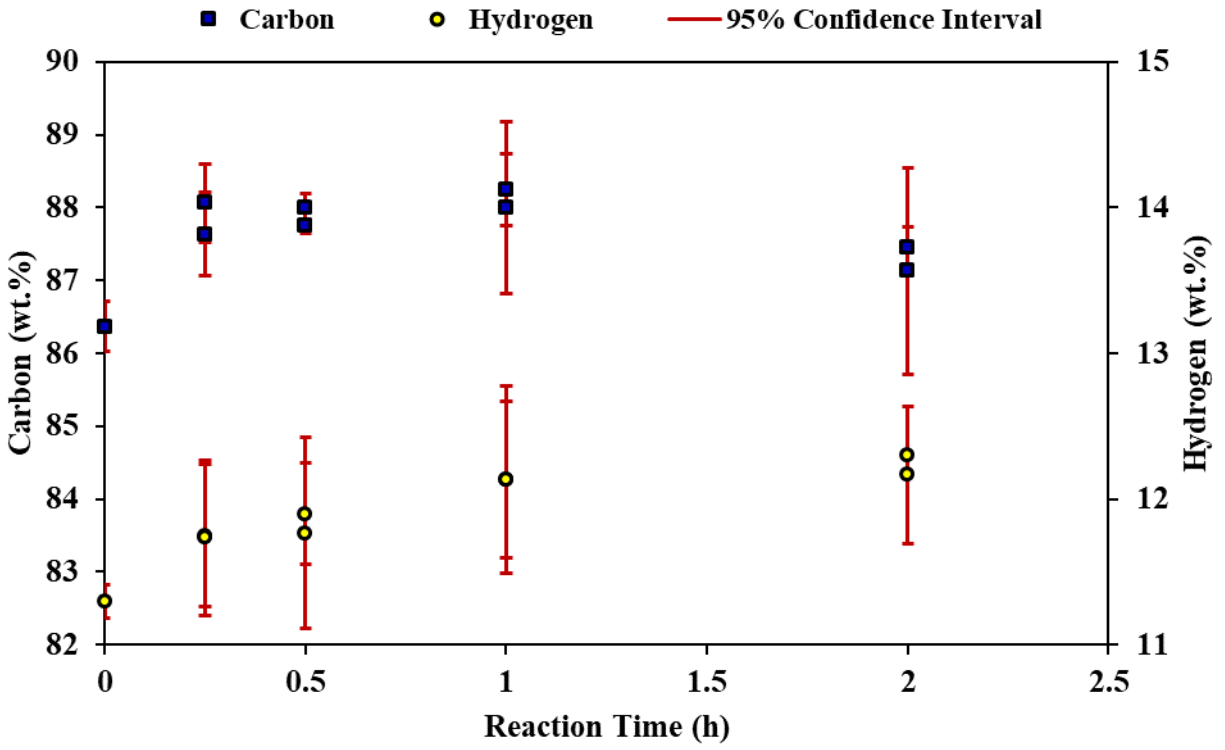
Figure 4.3. The effect of reaction time at 390°C using <45µm sulfided catalyst solids on filtered liquid product carbon and hydrogen concentrations.

The effect of reaction time at 390°C increases carbon and hydrogen concentrations compared to the HVGO at 0h reaction time in *Figure 4.3*. The carbon and hydrogen concentration results of the liquid products are not significantly different from each other after the 0.25h reaction time. The average carbon concentration of the liquid products decreased at the 2h reaction time. The large 95% confidence intervals at 2h provided no significant difference compared to lower reaction times for carbon and hydrogen concentrations.
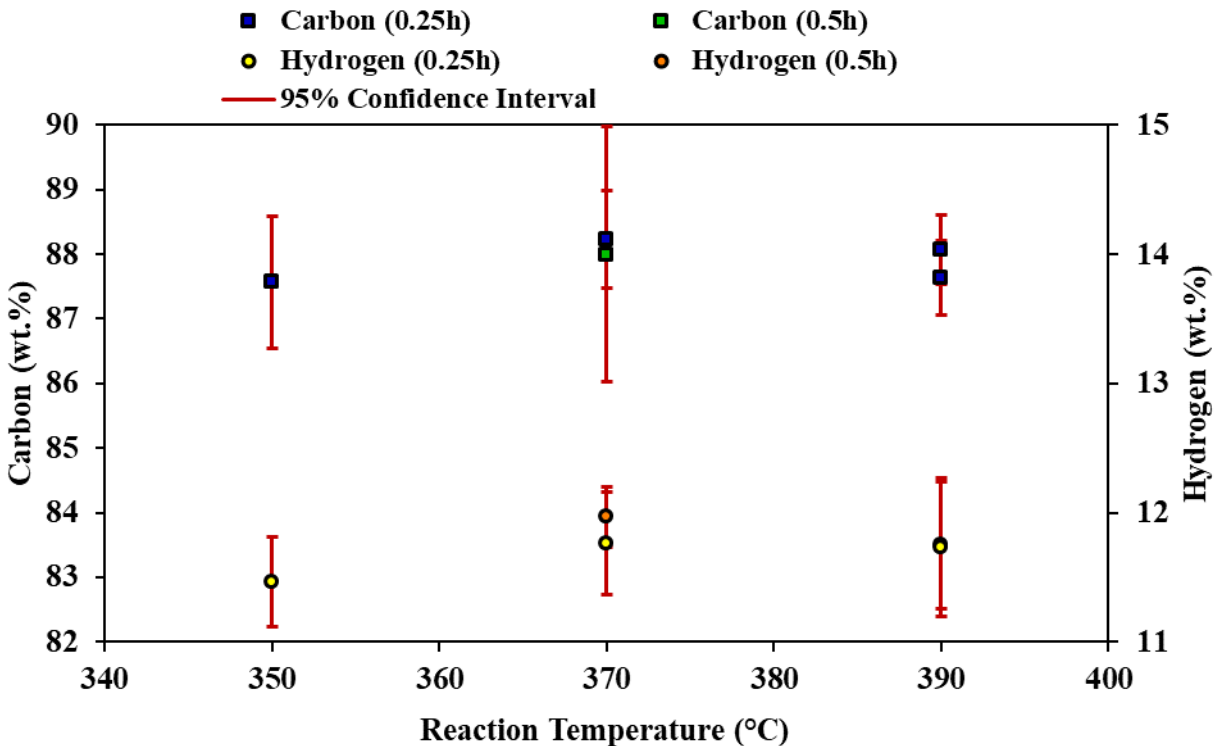
Figure 4.4. The effect of reaction temperature at 0.25 and 0.5h using <45μm sulfided catalyst solids on filtered liquid product carbon and hydrogen concentrations.

Carbon concentrations of the liquid products from 370 to 390°C and 0.25h reaction times are significantly different compared to the HVGO. Hydrogen concentrations of the filtered liquid products are not significantly different for all reaction temperatures at 0.25h compared to the HVGO. The 370°C and 0.5h liquid product carbon concentration is not significantly different compared to the HVGO. The hydrogen concentration for this liquid product is significantly different compared to the HVGO.

Catalyst Size Effects with Sulfided Pellets and <45μm Solids

The hydrogen to carbon ratio (H/C) is calculated for catalyst size comparison of the hydrotreated liquid products. The effect of reaction time at 390°C using sulfided catalyst pellets and <45μm solids on filtered liquid product H/C results is shown in *Figure 4.5*. The effect of reaction temperature at 0.25, 0.5, and 1h reaction times using sulfided catalyst pellets and <45μm solids on filtered liquid product H/C results is presented in *Figure 4.6*.
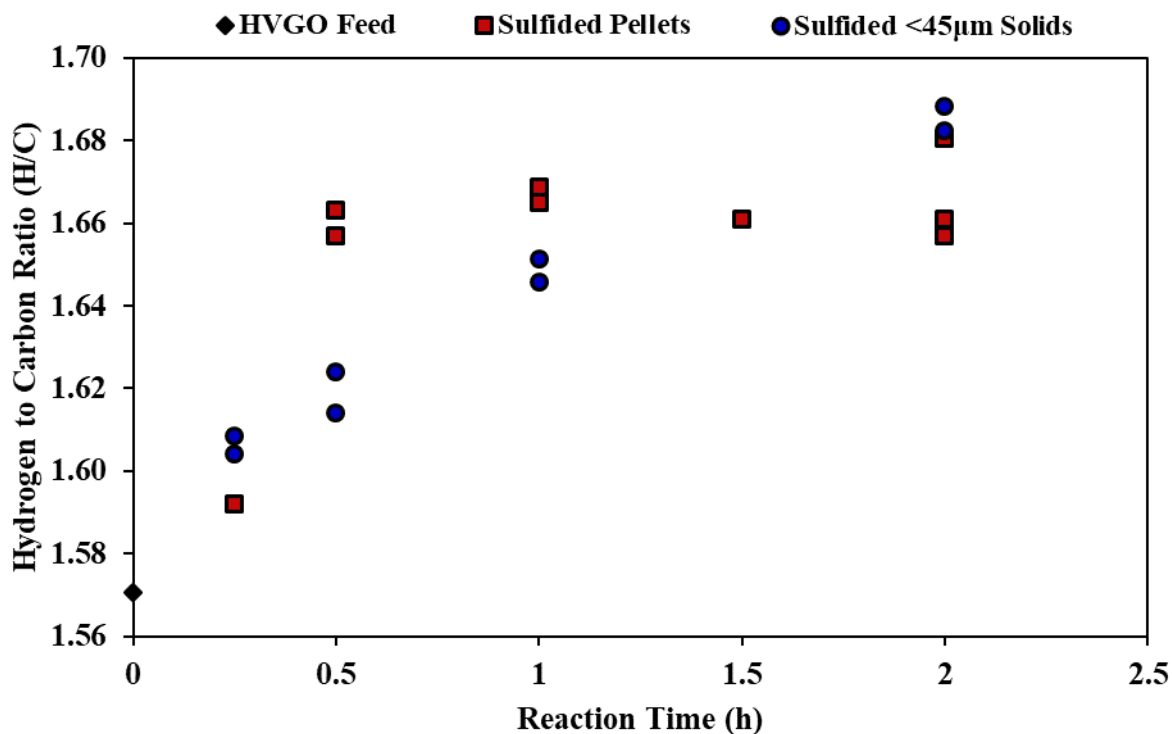
Figure 4.5. The effect of reaction time at 390°C using sulfided catalyst pellets and <45µm solids on filtered liquid product H/C results.

The average H/C results of the liquid products when using sulfided catalyst pellets are not significantly different after 0.5h as highlighted in *Figure 4.5*. The H/C results increase when using the <45µm sulfided catalyst solids from 0.25 to 2h reaction times.
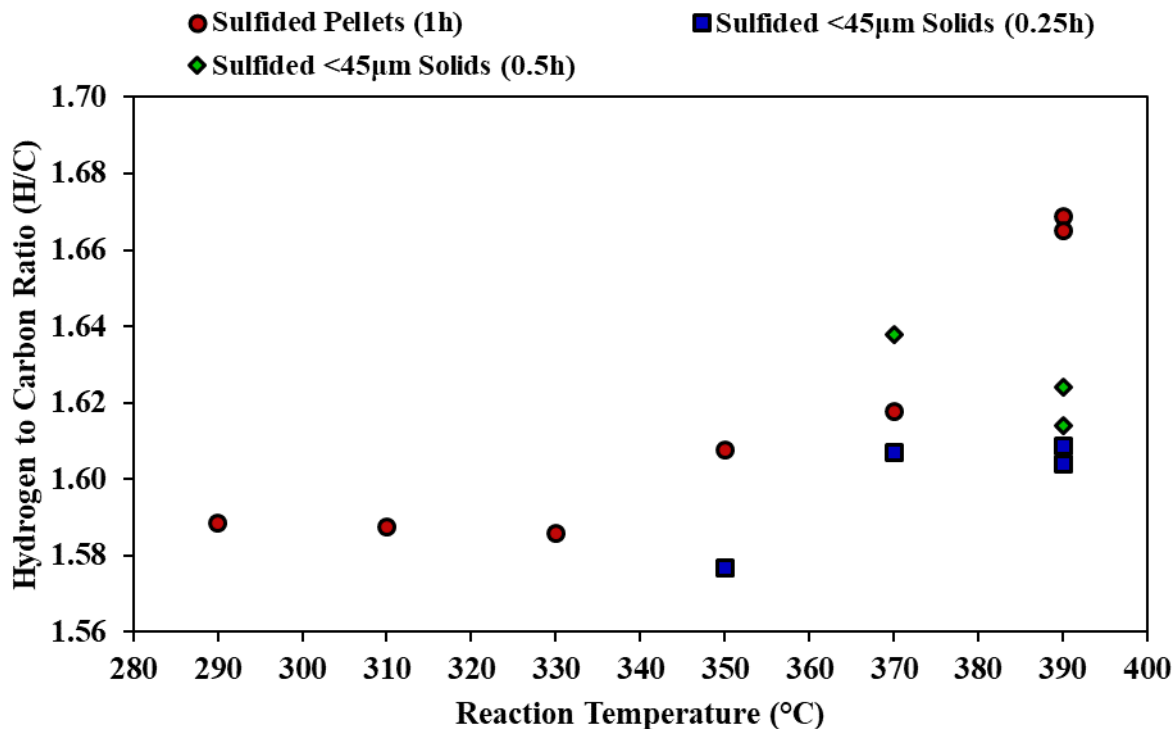
Figure 4.6. The effect of reaction temperature at 0.25, 0.5, and 1h using sulfided catalyst pellets and <45μm solids on filtered liquid product H/C results.

The effect of reaction temperature on the H/C results of the liquid products is not significant until 350°C for pellets at 1h and 370°C for <45μm solids at 0.25 and 0.5h. The liquid product H/C results from 370 to 390°C using sulfided <45μm solids are not significantly different from each other.

4.2 Sulfur and Nitrogen

All numerical sulfur and nitrogen concentration results are found in *Table E3* of *Appendix E*. Sulfur and nitrogen content of sulfided catalyst pellets and <45µm solids are found in *Table E2*.

HVGO

The sulfur and nitrogen results of the HVGO averaged 3.3±0.01wt.% and 0.1762±0.0016wt.%, respectively.

Solvent Filtration of HVGO

To determine the effect of solvent filtration on the HVGO, filtered liquid feed is compared to the HVGO in experiment one. The measured results of the collected HVGO following dichloromethane solvent evaporation overnight are 3.21±0.14wt.% and 0.1689±0.0107wt.%, for sulfur and nitrogen, respectively. The sulfur and nitrogen differ by 2.8% and 4.2%, respectively. The results are not significantly different compared to the HVGO.

Non-Catalytic Reactor Mixing Effect

To determine the effect of mixing on the liquid product with no catalyst present, the reaction at 360RPM is compared to three reactions with agitation >700RPM. The average mixing for the three reactions ranged from 708 to 862RPM. The sulfur and nitrogen results for the 360RPM reaction liquid product are 2.85±0.03wt.% and 0.2203±0.0071wt.%, respectively. Reactions with >700RPM agitation ranged from 2.59±0.09 to 2.89±0.16wt.% for sulfur and 0.1957±0.0045 to 0.2105±0.0054wt.% for nitrogen. Sulfur is not significantly different at higher agitation speeds. The nitrogen concentration differed significantly. All sulfur and nitrogen concentration results from these reactions differed significantly compared to the HVGO.

Reactor Wall Effect

A microreactor with sulfided (contaminated) inner walls with no catalyst is used to determine the reactor wall effect. The sulfur and nitrogen results of the liquid product are 0.53±0.03wt.% and 0.088±0.0.0109wt.%, respectively. These results are significantly different compared to the HVGO.

Catalytic Reactor Effect with Unfiltered Liquid Products

The effect of using unsulfided catalyst versus no catalyst on unfiltered liquid products is compared. Three liquid product concentrations ranged from 0.12 ± 0.01 to 0.18 ± 0.01wt.% for sulfur and 0.0295 ± 0.0075 to 0.0354 ± 0.0049wt.% for nitrogen using unsulfided catalyst pellets. Compared to the HVGO, and the non-catalytic reactions, these sulfur and nitrogen concentration results differed significantly at 0.05 significance.

Catalytic Reactor with Liquid Product Filtration Effect

The effect of solvent filtration on the liquid products are compared, three unfiltered reactions, 848 to 878RPM agitation, with three filtered reactions, 866 to 884RPM agitation. The sulfur and nitrogen concentration results for the three filtered liquid products ranged from 0.22 ± 0.04 to 0.37 ± 0.01wt.% and 0.072 ± 0.0055 to 0.0859 ± 0.005wt.%, respectively. All sulfur and nitrogen liquid product concentration results differed significantly compared to three unfiltered reactions at 0.05 significance.

Catalytic Reactor Mixing Effect

To determine the effect of mixing using unsulfided catalyst pellets on the liquid products, three reactions, 866 to 884RPM, are compared with two reactions at 360RPM agitation. Sulfur ranged from 0.18 ± 0.01 to 0.23 ± 0.03wt.%, while nitrogen ranged from 0.0619 ± 0.0077 to 0.0755 ± 0.0216wt.%, for reactions at 360RPM. Sulfur and nitrogen concentration results of these liquid products are significantly different compared to the higher agitations reactions.

Verification Reaction

For the temperature and pressure verification reaction at 2.25h, the sulfur and nitrogen concentration results are 0.2 ± 0.05wt.% and 0.066 ± 0.0109wt.%, respectively. The concentration results are not significantly different compared to the two reactions at 390°C and 360RPM for 2h.

Sulfided Catalyst Pellets and <45μm Solids

Sulfided catalyst pellets and <45μm solids are compared in *Table E2* of *Appendix E*. The sulfur and nitrogen concentration results for the sulfided pellets are 6.97 ± 1.24wt.% and 0.015 ± 0.01wt.%, respectively. The sulfur and nitrogen concentration results for the <45μm sulfided solids are

9.71±0.01wt.% and 0.01wt.%, respectively. In comparison, the sulfur contents of the catalysts are significantly different. Nitrogen is not significantly different.

Catalytic Sulfidation Effect with Pellets

The effect of unsulfided versus sulfided catalyst pellets on the hydrotreated liquid products is assessed. For three reactions using sulfided catalyst, the sulfur and nitrogen concentration results ranged from 0.17±0.08 to 0.21wt.% and 0.0433±0.0256 to 0.0511±0.0146wt.%, respectively. Both sulfur and nitrogen concentration results differed significantly at 0.05 significance compared to reactions using the unsulfided catalyst.

Reaction Time and Temperature Effects with Sulfided Pellets

The effect of reaction time at 390°C using sulfided catalyst pellets on filtered liquid product sulfur and nitrogen concentrations is presented in *Figure 4.7*. The effect of reaction temperature at 1h reaction time using sulfided catalyst pellets on filtered liquid product sulfur and nitrogen concentrations is presented in *Figure 4.8*.
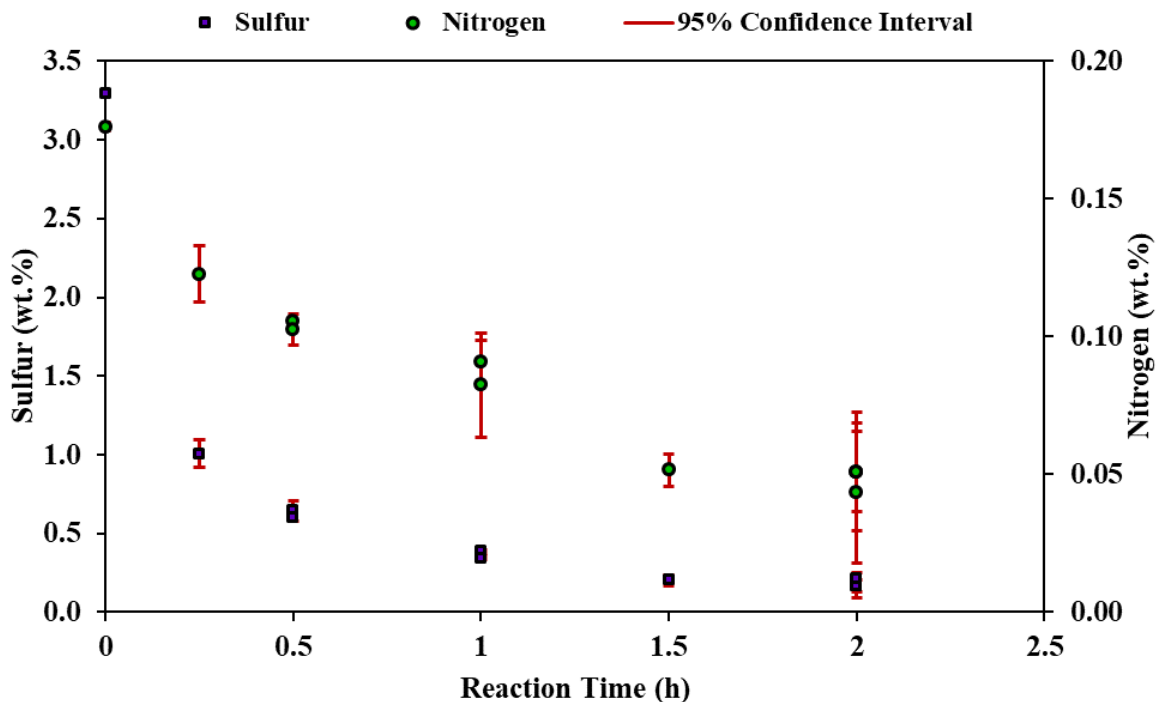
Figure 4.7. The effect of reaction time at 390°C using sulfided catalyst pellets on filtered liquid product sulfur and nitrogen concentrations.

The effect of reaction time at 390°C for all liquid product results compared to the HVGO at 0h reaction time in for both sulfur and nitrogen concentration results are significantly different *Figure 4.7*. As the reaction time increased, sulfur and nitrogen liquid product concentrations decreased exponentially. The 1.5 to 2h reaction time results, for both sulfur and nitrogen concentrations, are not significantly different from one another.
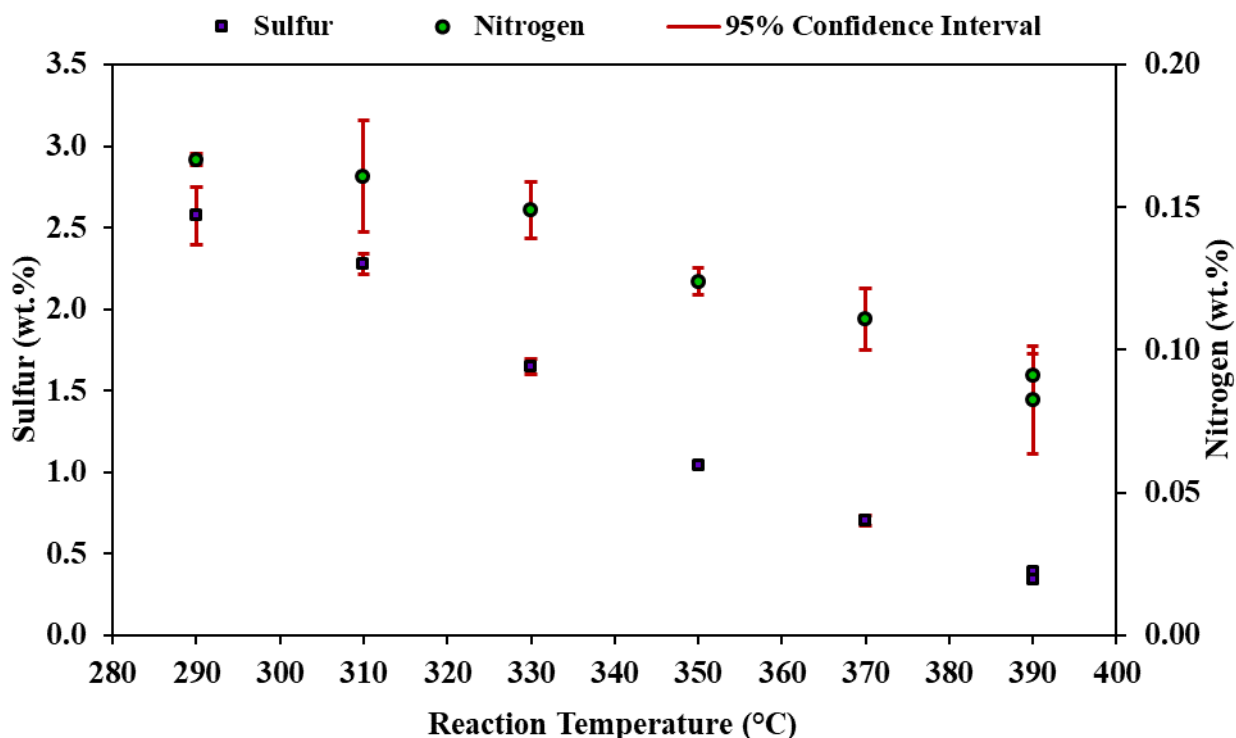
Figure 4.8. The effect of reaction temperature at 1h using sulfided catalyst pellets on filtered liquid product sulfur and nitrogen concentrations.

As the reaction temperature increased, concentrations of sulfur and nitrogen decreased as seen in *Figure 4.8*. All sulfur concentration results at each reaction temperature are significantly different from one another and the HVGO. Nitrogen concentration results at each reaction temperature are significantly different from one another and the HVGO. The nitrogen concentration of the liquid product at 310°C is not significantly different compared to the HVGO.

Reaction Time and Temperature Effects with <45μm Sulfided Solids

The effect of reaction time at 390°C using <45μm sulfided catalyst solids on filtered liquid product sulfur and nitrogen concentrations is highlighted in *Figure 4.9*. The effect of reaction temperature at 0.25 and 0.5h reaction times using <45μm sulfided catalyst solids on filtered liquid product sulfur and nitrogen concentrations is presented in *Figure 4.10*.
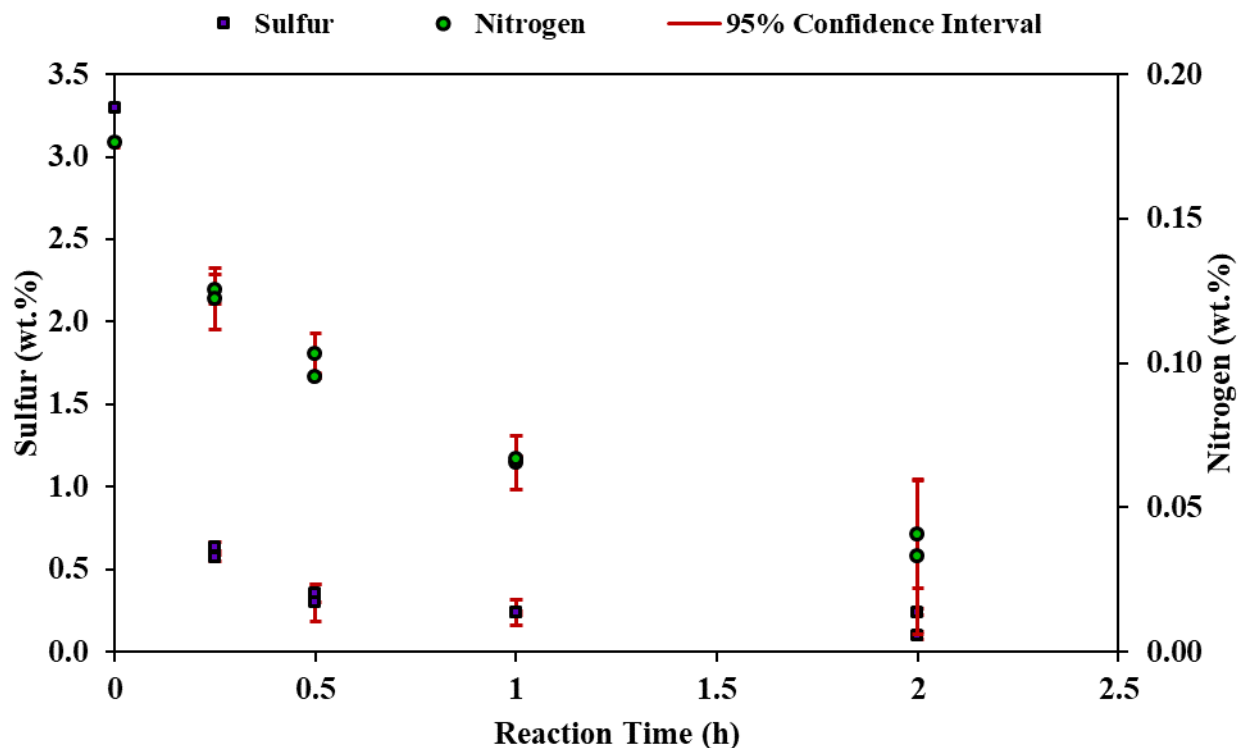
Figure 4.9. The effect of reaction time at 390°C using <45μm sulfided catalyst solids on filtered liquid product sulfur and nitrogen concentrations.

The effect of reaction time at 390°C reaction temperature with <45μm catalyst solids for all liquid products compared to the HVGO at 0h reaction time for both sulfur and nitrogen concentration results are significantly different in *Figure 4.9*. As the reaction time increased, sulfur and nitrogen liquid product concentrations decreased exponentially. The sulfur concentration at 1 and 2h reaction times are not significantly different from one another.
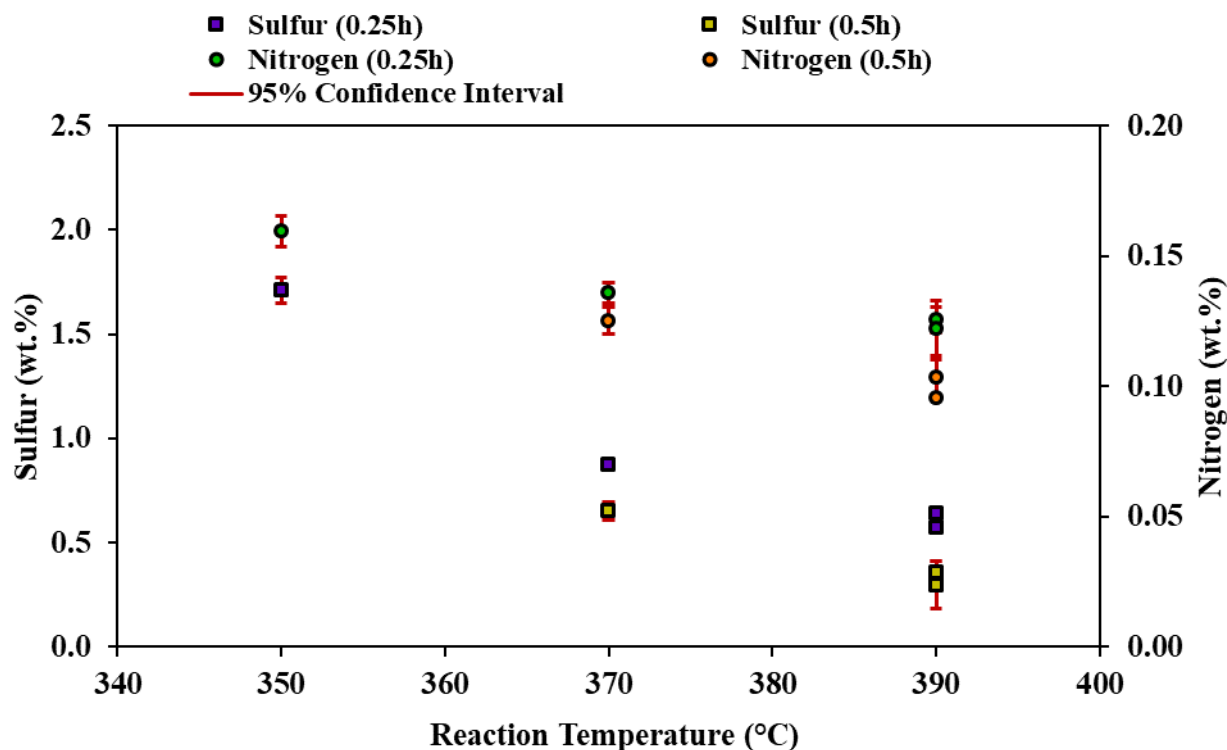
Figure 4.10. The effect of reaction temperature at 0.25 and 0.5h using <45μm sulfided catalyst solids on filtered liquid product sulfur and nitrogen concentrations.

As the reaction temperature increased, concentrations of sulfur and nitrogen decreased as highlighted in *Figure 4.10*. All sulfur and nitrogen concentration results are significantly different from the HVGO. Sulfur and nitrogen concentration results at each temperature are significantly different from one another at their respective reaction time.

Catalyst Size Effects with Sulfided Pellets and <45μm Solids

The effect of reaction time at 390°C using sulfided catalyst pellets and <45μm solids on filtered liquid product sulfur and nitrogen concentrations is displayed in *Figure 4.11*. The effect of reaction temperature at 0.25, 0.5, and 1h reaction times using sulfided catalyst pellets and <45μm solids on filtered liquid product sulfur and nitrogen concentrations is presented in *Figure 4.12*.
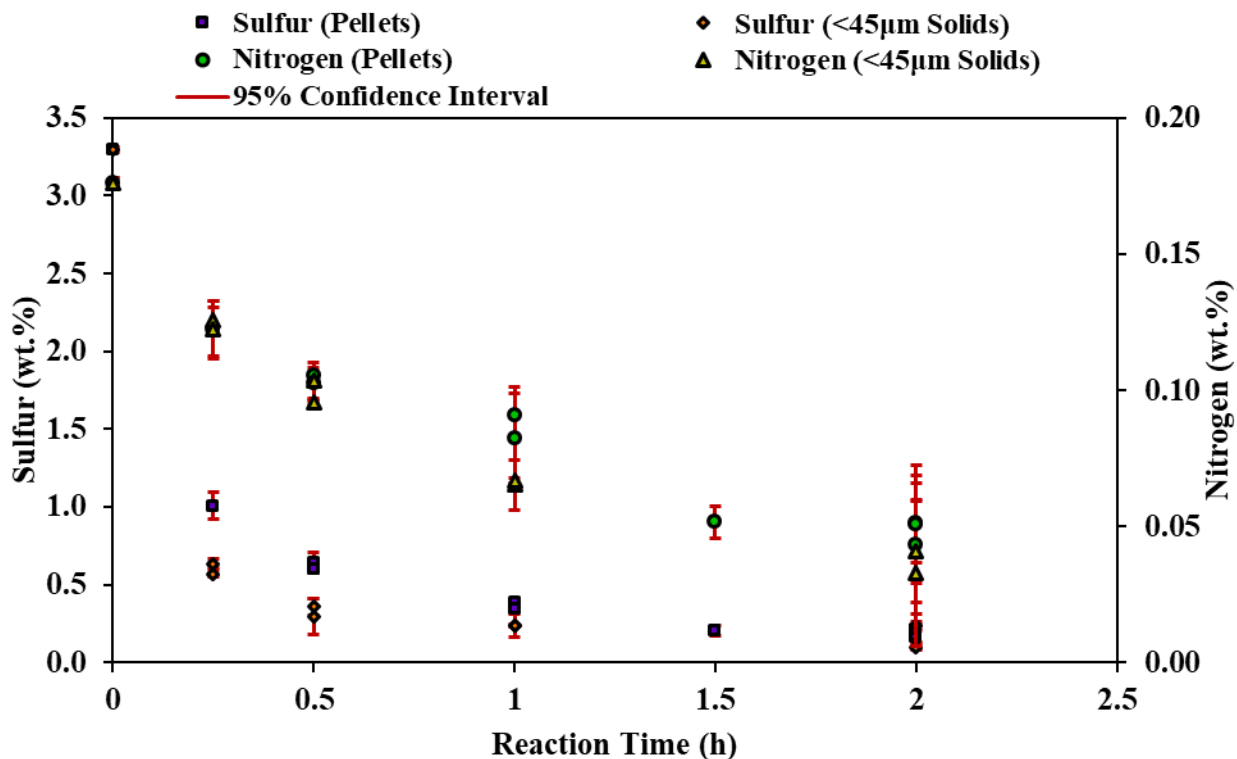
Figure 4.11. The effect of reaction time at 390°C using sulfided catalyst pellets and <45μm solids on filtered liquid product sulfur and nitrogen concentrations.

The sulfided <45μm catalyst solids enhance the sulfur concentration reduction from 0.25 to 1h reaction times compared to sulfided pellets in *Figure 4.11*. These sulfur results are significantly different at 0.05 significance when compared. At 2h, the sulfur and nitrogen concentration results are not significantly different for sulfided catalyst pellets and <45μm solids. Except for the 1h reaction time, the nitrogen concentration results are not significantly different when sulfided catalyst pellets are compared with <45μm solids.
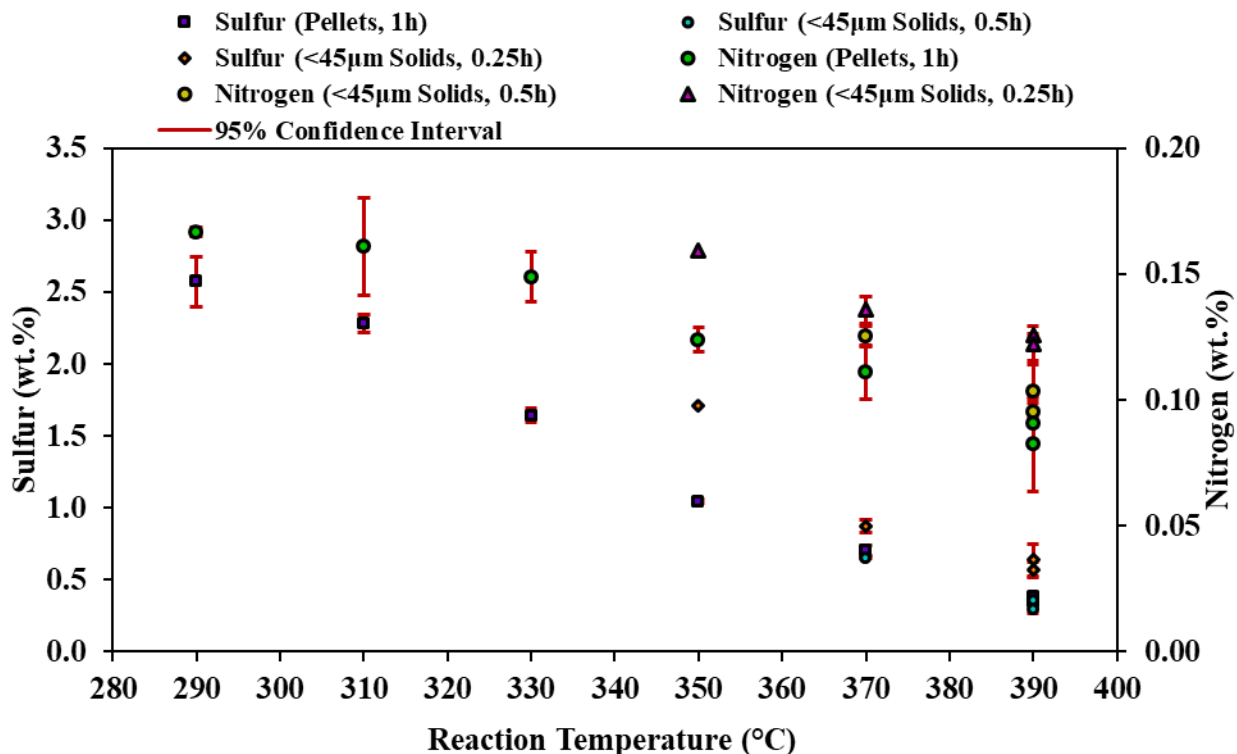
Figure 4.12. The effect of reaction temperature at 0.25, 0.5, and 1h using sulfided catalyst pellets and <45μm solids on filtered liquid product sulfur and nitrogen concentrations.

The reactions of sulfided catalyst pellets and <45μm solids cannot be accurately compared on a temperature basis as the reaction times are different, 1h for pellets versus 0.25 and 0.5h for solids in *Figure 4.12*. All sulfur and nitrogen concentration results at 0.25h are significantly different compared to reactions at 0.5h using <45μm solids and at 1h using pellets. Sulfur and nitrogen concentrations at 0.5h using <45μm solids (cyan and yellow dots) are not significantly different compared to results at 1h using pellets (purple squares and green dots).

145

4.2.1 Sulfur and Nitrogen Conversion

Comparative conversion plots for sulfur and nitrogen are found in *Appendix F*. The concentration results for sulfur and nitrogen reported in section 4.2 are used to calculate their respective conversion from the HVGO. Conversion is calculated using formulas previously mentioned in section 2.3.5. Sulfur and nitrogen conversion results are used for chemometric models in the fourth objective. The effects of reaction time and temperature with sulfided catalyst on liquid product conversion results are highlighted in *Figures F1 to F5* in *Appendix F*.

4.2.2 Sulfur and Nitrogen Kinetics

Sulfur and nitrogen kinetic analysis is completed for the mild hydrotreating reactions. A review table on industrial feed kinetic studies is found in *Appendix A*. Kinetic plots for sulfur and nitrogen models are found in *Appendix F*. Fitted reaction orders, rate constants, activation energies, and preexponential factors results are presented as well as compared for both sulfided catalyst sizes in *Appendix F*.

4.3 Density

All numerical density results are found in *Table E4* of *Appendix E*.

HVGO

The density result of the HVGO is 0.967±0.006g/ml. Compared to literature, in *Table 2.7*, the density is 0.965g/ml. The result from *Table 2.7*, differs by 0.21%. However, from the ranges specified in *Table 2.1*, 0.967 to 0.971g/ml, the measured result obtained fall within the HVGO range from literature sources.

Solvent Filtration of HVGO

The measured density result of the HVGO following dichloromethane solvent evaporation overnight is 0.953±0.017g/ml. The result differs by 1.46% compared to the HVGO. The results are not significantly different.

Non-Catalytic Reactor Mixing Effect

The density result for the 360RPM reaction liquid product is 0.958±0.003g/ml. Reactions with >700RPM agitation ranged from 0.951±0.004 to 0.955±0.008g/ml. All liquid product densities measured at these agitation mixing speeds are not significantly different from each other. The density results of all these liquid products are significantly different compared to the HVGO.

Reactor Wall Effect

The collected liquid product density result is 0.91±0.007g/ml. The result is significantly different compared to the HVGO.

Catalytic Reactor Effect with Unfiltered Liquid Products

Three catalytic unfiltered liquid product density results ranged from 0.897±0.003 to 0.907±0.005g/ml. Compared to the HVGO, and the non-catalytic reactions, all density results are significantly different.

Catalytic Reactor with Liquid Product Filtration Effect

The three catalytic filtered liquid product density results ranged from 0.907±0.005 to 0.908±0.003g/ml. The density results are not significantly compared to the catalytic unfiltered liquid products at 0.05 significance.

Catalytic Reactor Mixing Effect

The filtered liquid product density results ranged from 0.9±0.008 to 0.905±0.008g/ml for reactions at 360RPM. Compared to the reactions at 866 to 884RPM agitation, the liquid product densities are not significantly different.

Verification Reaction

The liquid product density result is 0.905g/ml. The result is not significantly different compared to the two reactions at 390°C and 360RPM for 2h.

Catalytic Sulfidation Effect with Pellets

The filtered liquid product density results for the sulfided pellet reactions ranged from 0.902±0.005 to 0.905±0.005g/ml. The density results are not significantly different compared to the unsulfided pellet reaction results at 0.05 significance.

Reaction Time and Temperature Effects with Sulfided Pellets

The effect of reaction time at 390°C using sulfided catalyst pellets on filtered liquid product density is highlighted in *Figure 4.13*. The effect of reaction temperature at 1h reaction time using sulfided catalyst pellets on filtered liquid product density is displayed in *Figure 4.14*.
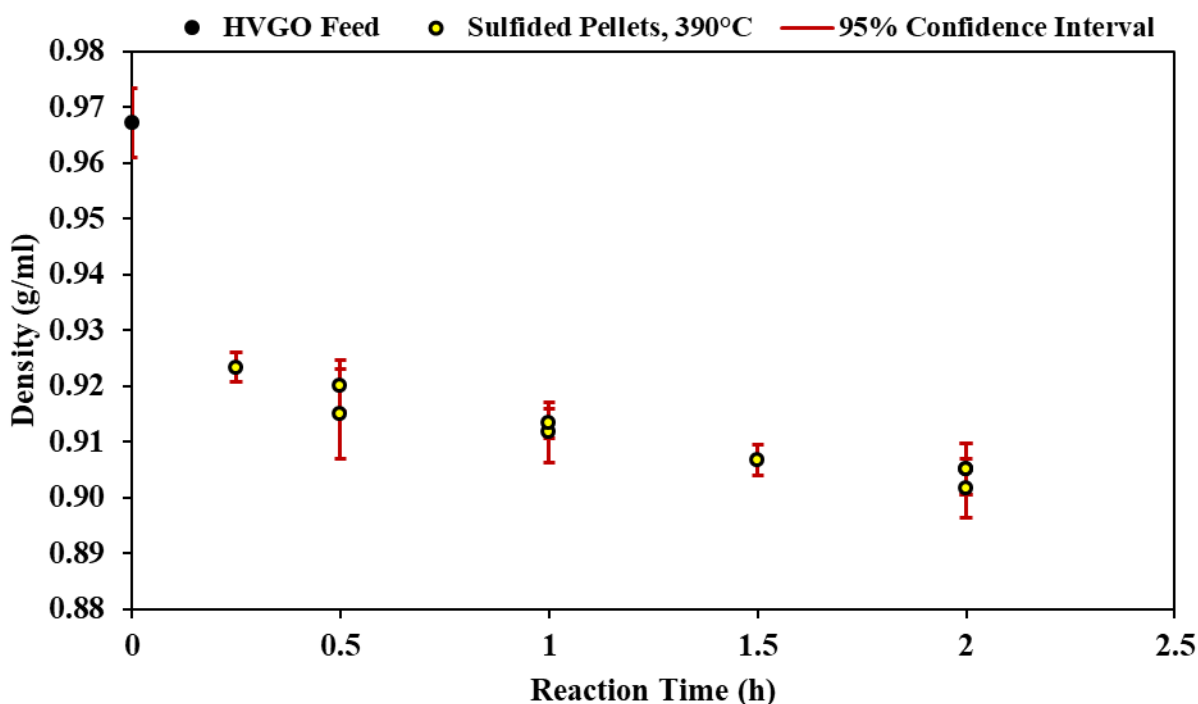
Figure 4.13. The effect of reaction time at 390°C using sulfided catalyst pellets on filtered liquid product density.

The effect of reaction time at 390°C decreases all filtered liquid product density results significantly compared to the HVGO at 0h reaction time in *Figure 4.13*. The 1.5 and 2h reaction time density results are not significantly different. Reaction time differences longer than 0.75h result in significant differences in liquid product densities.
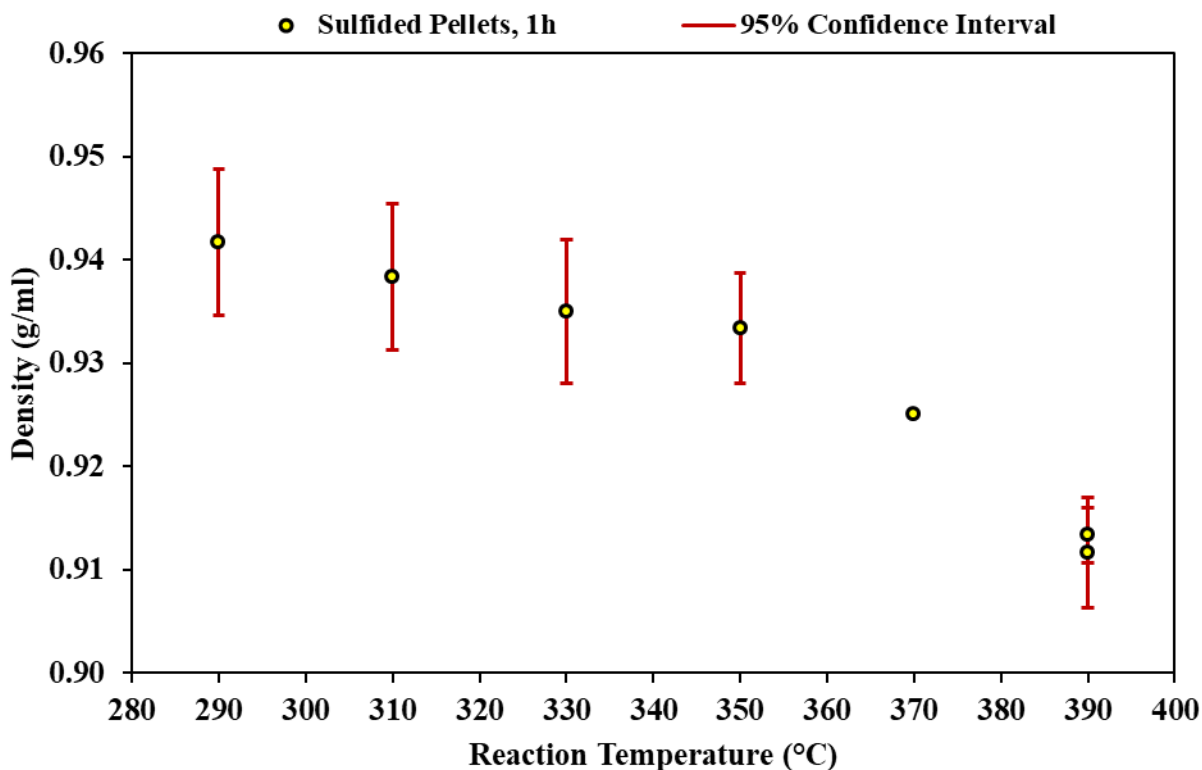
Figure 4.14. The effect of reaction temperature at 1h using sulfided catalyst pellets on filtered liquid product density.

The effect of higher reaction temperature at 1h decreases the filtered liquid product density as highlighted in *Figure 4.14*. There are no significant differences in the density results from 290 to 350°C reaction temperatures. At 370 and 390°C reaction temperatures, density results are significantly different. The large 95% confidence intervals for 290 to 350°C reaction temperatures do not provide enough evidence of significant difference in these liquid product densities.

Reaction Time and Temperature Effects with <45μm Sulfided Solids

The effect of reaction time at 390°C using <45μm sulfided catalyst solids on filtered liquid product density is presented in *Figure 4.15*. The effect of reaction temperature at 0.25 and 0.5h reaction times using <45μm sulfided catalyst solids on filtered liquid product density is highlighted in *Figure 4.16*.
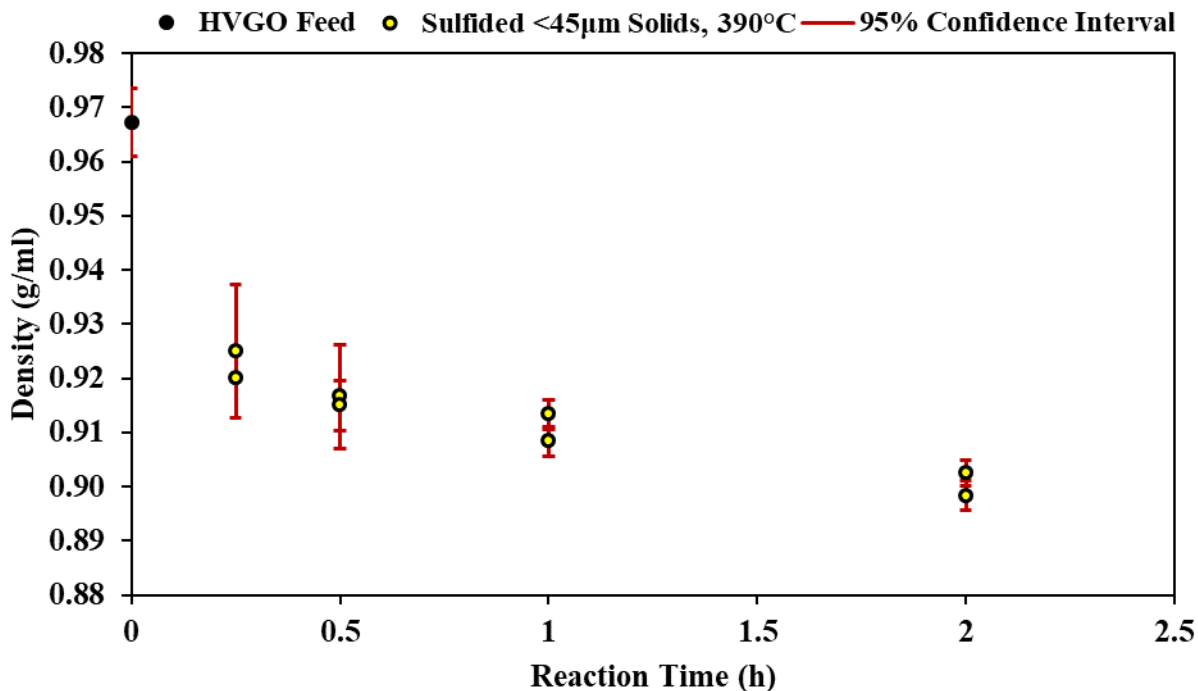
Figure 4.15. The effect of reaction time at 390°C using <45μm sulfided catalyst solids on filtered liquid product density.

The effect of reaction time at 390°C decreases all filtered liquid product density results significantly compared to the HVGO at 0h reaction time as shown in *Figure 4.15*. The density results at 2h differed significantly compared to 1h reaction time. The large 95% confidence intervals for 0.25 to 1h reaction times do not provide enough evidence to differentiate differences significantly.
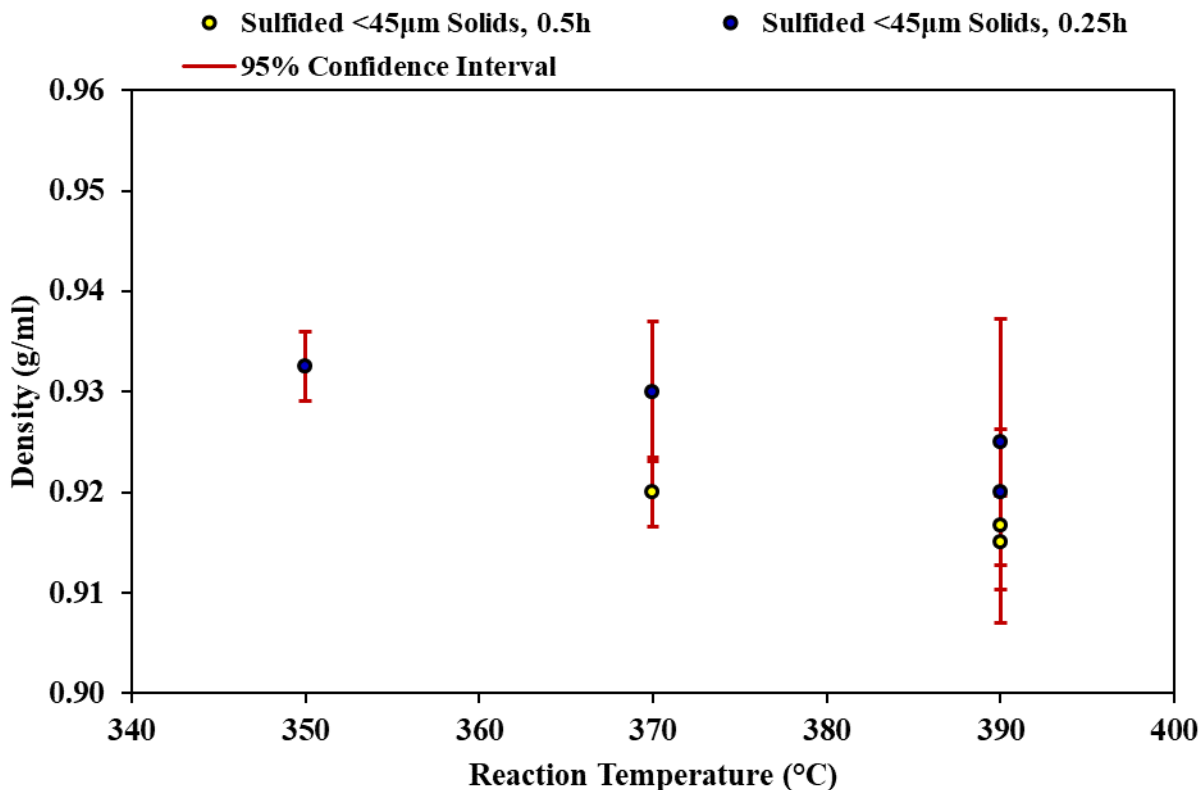
Figure 4.16. The effect of reaction temperature at 0.25 and 0.5h using <45μm sulfided catalyst solids of filtered liquid product density.

The effect of higher reaction temperature at 0.25 and 0.5h decreases the filtered liquid product density as displayed in *Figure 4.16*. All density results shown are significantly different compared to the HVGO. The large 95% confidence intervals did not provide enough evidence to differentiate density differences at the reaction conditions presented.

Catalyst Size Effects with Sulfided Pellets and <45μm Solids

The effect of reaction time at 390°C using sulfided catalyst pellets and <45μm solids on filtered liquid product density is displayed in *Figure 4.17*. The effect of reaction temperature at 0.25, 0.5, and 1h reaction times using sulfided catalyst pellets and <45μm solids on filtered liquid product density results is presented in *Figure 4.18*.
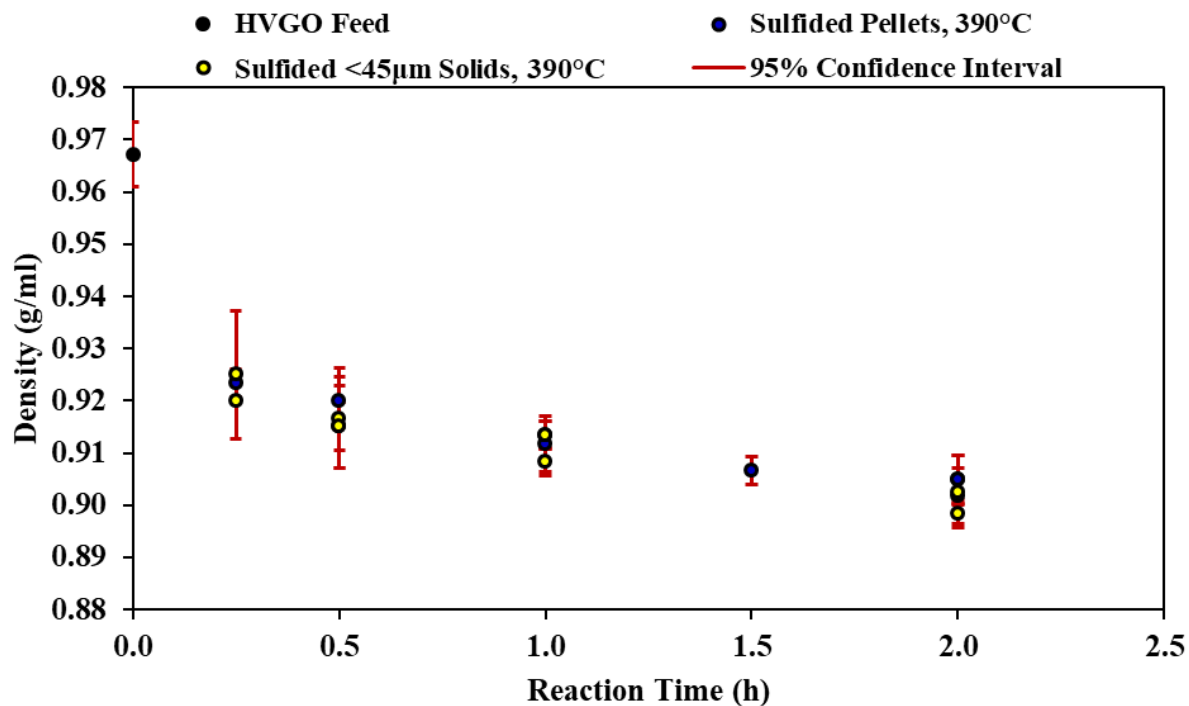
Figure 4.17. The effect of reaction time at 390°C using sulfided catalyst pellets and <45µm solids on filtered liquid product density.

As compared together, the filtered liquid product densities of sulfided catalyst pellets and <45µm solids are not significantly different at similar reaction times as observed in *Figure 4.17*.
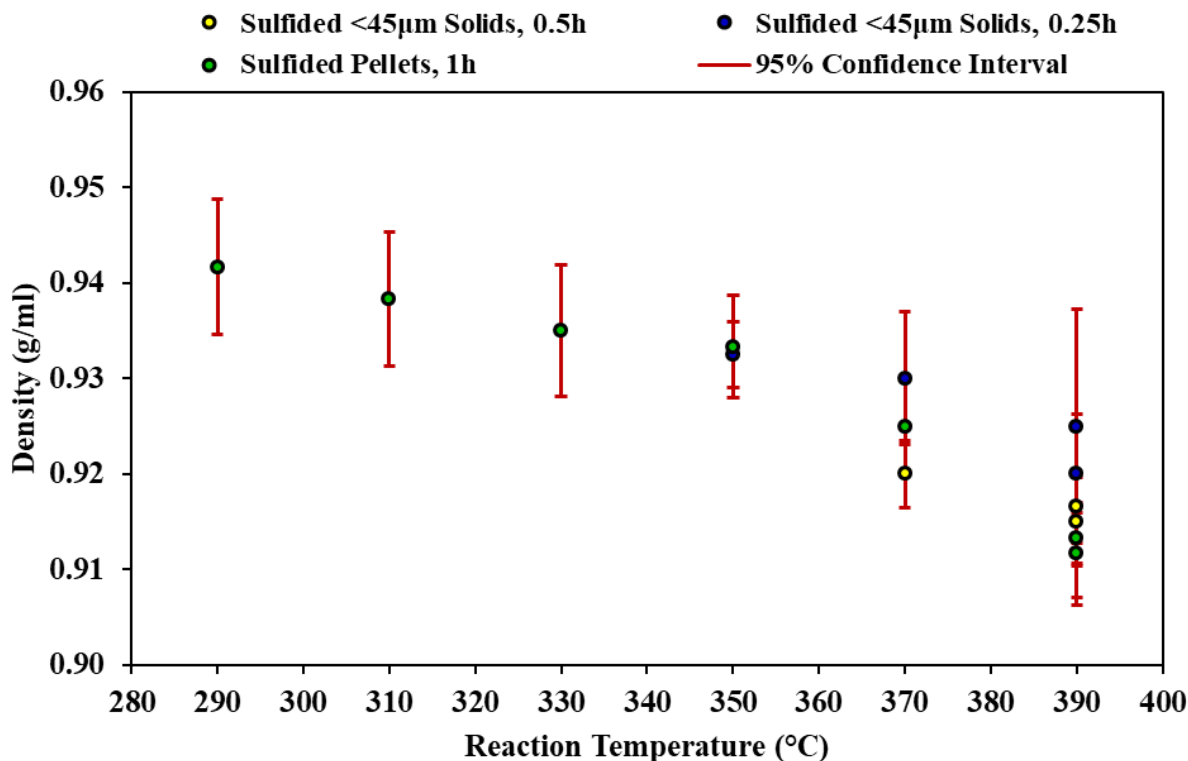
Figure 4.18. The effect of reaction temperature at 0.25, 0.5, and 1h using sulfided catalyst pellets and <45μm solids on filtered liquid product density results.

In *Figure 4.18*, the reactions of sulfided catalyst pellets and <45μm solids cannot be compared as the reaction times are different, 1h for pellets and 0.25 to 0.5h for solids. Large 95% confidence intervals did not provide enough evidence to differentiate liquid product density differences until reaction temperatures reached 370 to 390°C.

4.3.1 Density Prediction

Density prediction results are found in *Appendix F*. As discussed in section 2.1.3, the density is predicted from approximate hydrogen, sulfur, and nitrogen compositions. The Gray regression [1] is compared to an optimal linear regression equation fitted to the hydrogen, sulfur, and nitrogen concentrations highlighted in sections 4.1 *and* 4.2. Both regressions are compared in the predicted versus measured density plot in in *Figure F22* of *Appendix F*.

4.4 Boiling Point Distribution

All numerical boiling point distribution (BPD) results are found in *Table E5* of *Appendix E*. The boiling point distribution results for both the HVGO feed and all hydrotreated liquid products are presented in *Figure 4.19*.
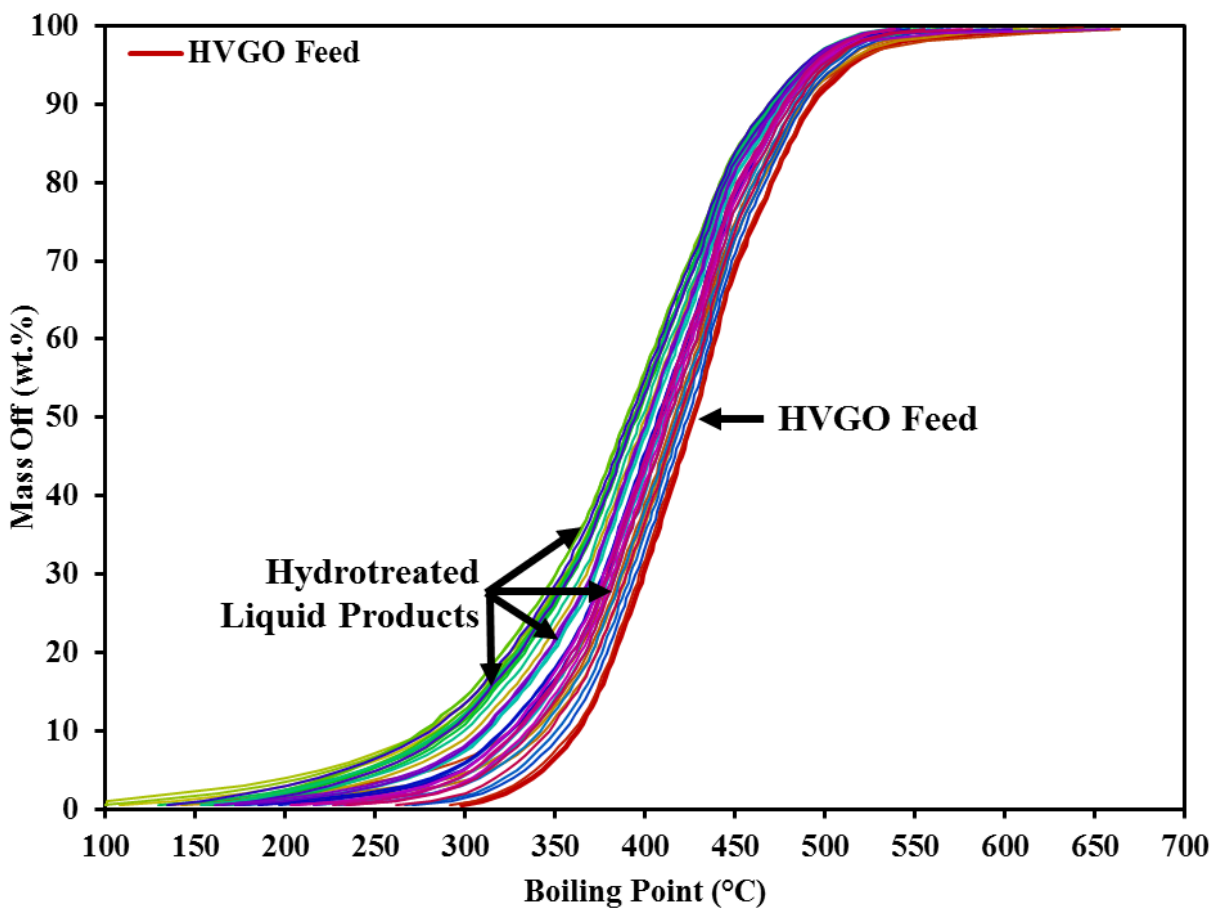
Figure 4.19. The boiling point distribution results of the HVGO and all liquid products.

As shown in *Figure 4.19*, the BPD of the liquid products are shifted to lower boiling temperatures. The boiling point distribution curves are divided into five boiling fractions to highlight the fractional concentration trends for comparisons between reactions. The concentration fractions are specified:

- Initial Boiling Point (IBP) to 300°C

- 300°C to 400°C

- 400°C to 500°C

- 500°C to Final Boiling Point (FBP)

- +343°C Fraction

HVGO

The HVGO BPD ranged from 299 to 643°C that represented nearly 100wt.% of the composition. Concentration results obtained for the HVGO are 0.5wt.%, 30wt.%, 61.5wt.%, 8wt.%, and 95wt.% for the IBP-300°C, 300-400°C, 400-500°C, 500°C-FBP, and +343°C boiling point fractions, respectively.

Solvent Filtration of HVGO

The concentration results of the collected HVGO following solvent filtration the following day are 1wt.%, 31wt.%, 60.5wt.%, 7.5wt.%, and 94wt.% for the IBP-300°C, 300-400°C, 400-500°C, 500°C-FBP, and +343°C boiling point fractions, respectively. The results differ by 66.7%, 3.3%, 1.6%, 6.5%, and 1.1%, compared to the HVGO, respectively,

Non-Catalytic Reactor Mixing Effect

The concentration results for the 360RPM reaction liquid product are 6.5wt.%, 34.5wt.%, 52wt.%, 7wt.%, and 86wt.% for the IBP-300°C, 300-400°C, 400-500°C, 500°C-FBP, and +343°C boiling point fractions, respectively. The >700RPM liquid product concentration results ranged from 3.5-4.5wt.%, 32.5-34.5wt.%, 55.5-57.5wt.%, 5.5-6.5wt.%, and 88-90wt.% in respective order. Compared to >700RPM mixing, the liquid product at 360RPM is shifted to a lower BPD.

Reactor Wall Effect

The concentration results for this liquid product are 9wt.%, 41wt.%, 46.5wt.%, 3.5wt.%, and 79wt.% for the IBP-300°C, 300-400°C, 400-500°C, 500°C-FBP, and +343°C boiling point fractions, respectively. Compared to the HVGO, this liquid product is shifted to a lower BPD.

Catalytic Reactor Effect with Unfiltered Liquid Products

The concentrations for three unfiltered liquid products obtained from a catalytic reaction ranged from 13-14wt.%, 39.5-41wt.%, 42.5-43.5wt.%, 3-4wt.%, and 74-75wt.% for the IBP-300°C, 300-400°C, 400-500°C, 500°C-FBP, and +343°C boiling point fractions, respectively. Compared to the three non-catalytic reactions, all concentrations are significantly different.

Catalytic Reactor with Liquid Product Filtration Effect

The concentrations for three filtered liquid products obtained from a catalytic reaction ranged from 11.5-12wt.%, 41.5-42wt.%, 42.5-43.5wt.%, 3.5wt.%, and 75-76wt.% for the IBP-300°C, 300-400°C, 400-500°C, 500°C-FBP, and +343°C boiling point fractions, respectively. Compared to the three unfiltered catalytic reactions, the IBP-300°C fractional concentration is significantly different.

Catalytic Reactor Mixing Effect

The concentrations for two catalytic reactions at 360RPM ranged from 14-14.5wt.%, 41.5-42wt.%, 40.5wt.%, 3.5wt.%, and 72.5wt.% for the IBP-300°C, 300-400°C, 400-500°C, 500°C-FBP, and +343°C boiling point fractions, respectively. Compared to catalytic reactions at 866-884RPM agitation, IBP-300°C, 400-500°C, and +343°C fractional concentrations are significantly different. The 300-400°C and 500°C-FBP fractional concentrations are not significantly different.

Verification Reaction

The concentration results of this liquid product are 12.5wt.%, 41.5wt.%, 42.5wt.%, 3.5wt.%, and 75wt.% for the IBP-300°C, 300-400°C, 400-500°C, 500°C-FBP, and +343°C boiling point fractions, respectively. Compared to the two reactions at 390°C, 360RPM, and 2h, the IBP-300°C, 400-500°C, and the +343°C fractional concentrations are significantly different.

Catalytic Sulfidation Effect with Pellets

The concentrations for three filtered liquid products using sulfided catalyst pellets ranged from 11-12wt.%, 41-42wt.%, 43.5-44wt.%, 3wt.%, and 75-76wt.% for the IBP-300°C, 300-400°C, 400-500°C, 500°C-FBP, and +343°C boiling point fractions, respectively. Apart from the 500°C-FBP

fractional concentration, these results are not significantly different compared to the results obtained from the unsulfided catalyst reactions.

Reaction Time and Temperature Effects with Sulfided Pellets

The effect of reaction time at 390°C using sulfided catalyst pellets on filtered liquid product boiling point fractional concentrations is presented in *Figure 4.20*. The effect of reaction temperature at 1h using sulfided catalyst pellets on filtered liquid product boiling point fractional concentrations is highlighted in *Figure 4.21*.
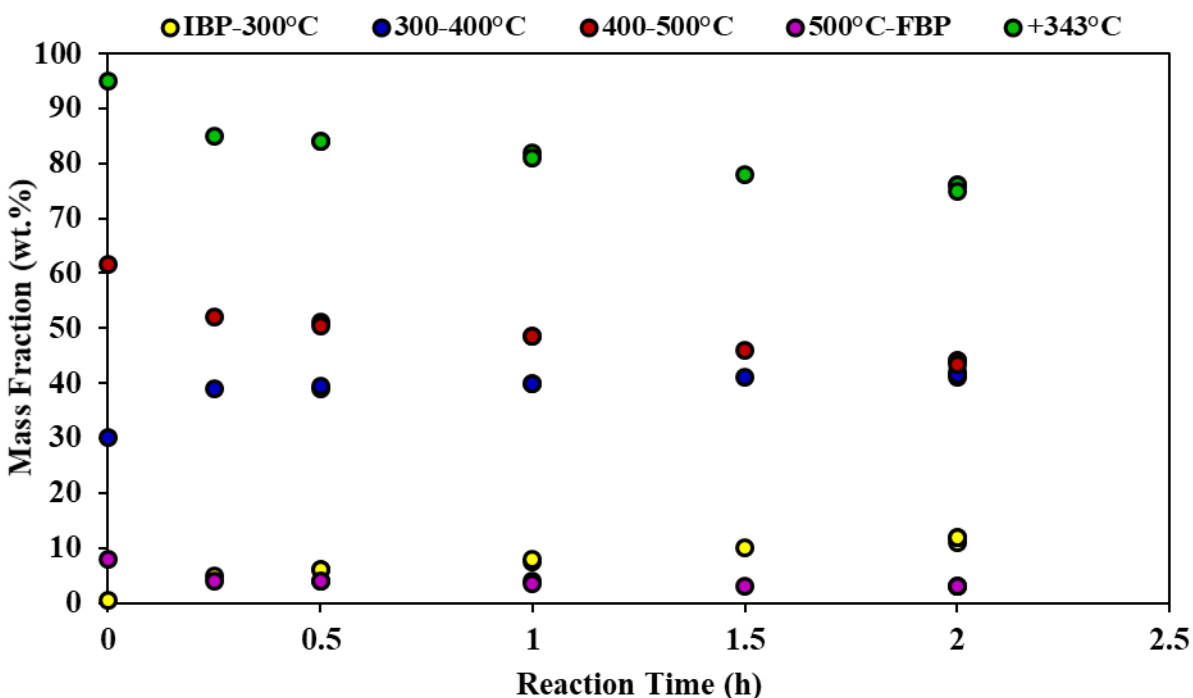
Figure 4.20. The effect of reaction time at 390°C using sulfided catalyst pellets on filtered liquid product boiling point fractional concentrations.

The effect of reaction time at 390°C on the fractional boiling point concentrations is shown in *Figure 4.20*. The lighter IBP-300°C and 300-400°C fractional concentrations increase with reaction time compared to the HVGO at 0h reaction time. The heavier 400-500°C, 500°C-FBP, and +343°C boiling point fractional concentrations decrease with reaction time. Reaction time differences longer than 1h cause significant differences between fractional concentrations.

157
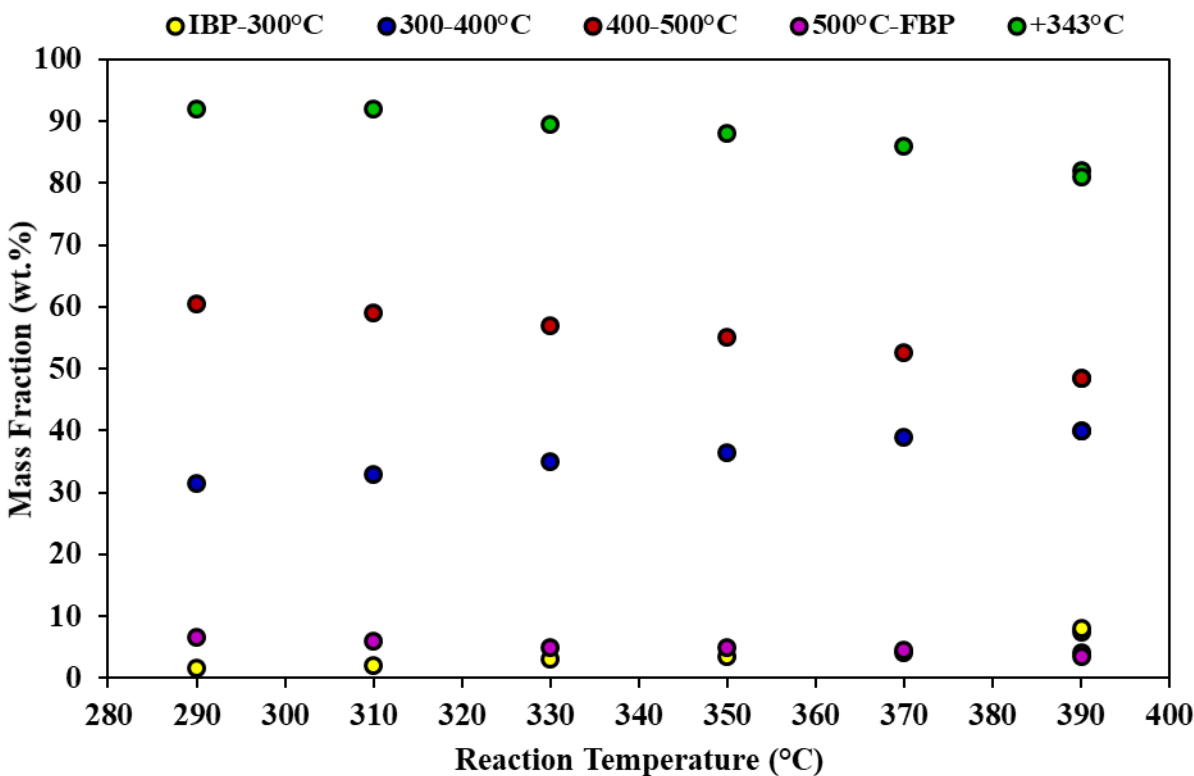
Figure 4.21. The effect of reaction temperature at 1h using sulfided catalyst pellets on filtered liquid product boiling point fractional concentrations.

The effect of reaction temperature at 1h on the fractional boiling point concentrations is shown in *Figure 4.21*. The lighter IBP-300°C and 300-400°C fractional concentrations increase with reaction temperature. The heavier 400-500°C, 500°C-FBP, and +343°C boiling point fractional concentrations decrease with reaction temperature. Apart from the IBP-300°C results, all fractional concentration results have a high linear relationship to reaction temperature (>0.90 R^2).

Reaction Time and Temperature Effects with <45μm Sulfided Solids

The effect of reaction time at 390°C using <45μm sulfided catalyst solids on filtered liquid product boiling point fractional concentrations is displayed in *Figure 4.22*. The effect of reaction temperature at 0.25 and 0.5h using <45μm sulfided catalyst solids on filtered liquid product boiling point fractional concentrations is presented in *Figure 4.23*.
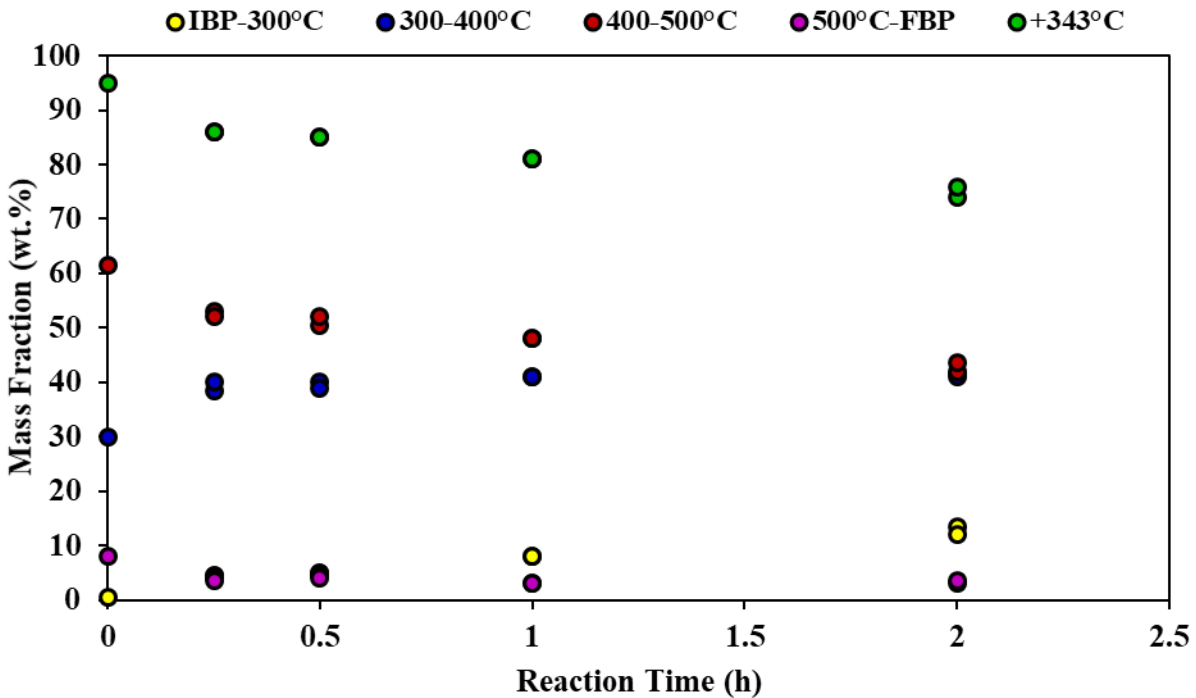
Figure 4.22. The effect of reaction time at 390°C using <45μm sulfided catalyst solids on filtered liquid product boiling point fractional concentrations.

The effect of reaction time at 390°C on the fractional boiling point concentrations is shown in *Figure 4.22*. The lighter IBP-300°C and 300-400°C fractional concentrations increase with reaction time compared to the HVGO at 0h reaction time. The heavier 400-500°C, 500°C-FBP, and +343°C boiling point fractional concentrations decrease with reaction time. Reaction times longer than 1h cause significant differences between fractional concentrations.
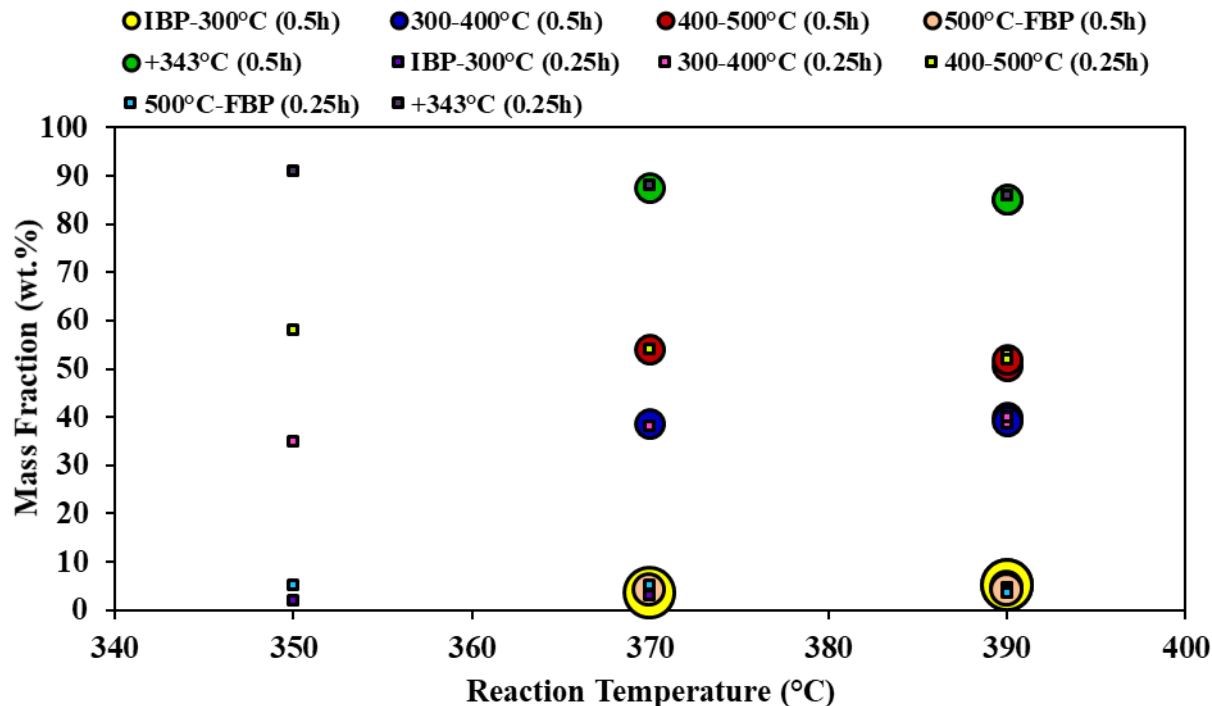
Figure 4.23. The effect of reaction temperature at 0.25 and 0.5h using <45μm sulfided catalyst solids on filtered liquid product boiling point fractional concentrations.

The effect of reaction temperature at 0.25 and 0.5h on the fractional boiling point concentrations is shown in *Figure 4.23*. The lighter IBP-300°C and 300-400°C fractional concentrations increase with reaction temperature. The heavier 400-500°C, 500°C-FBP, and +343°C boiling point fractional concentrations decrease with reaction temperature. There are no significant differences in fractional concentrations between 0.25 and 0.5h using sulfided <45μm solids as seen by data overlaps in *Figure 4.23*.

4.4.1 +343°C Conversion

Catalyst Size Effects with Sulfided Pellets and <45μm Solids

The +343°C fractional concentration results reported in section 4.4 are used to calculate conversion. The effect of reaction time at 390°C using sulfided catalyst pellets and <45μm solids on +343°C conversion of filtered liquid products is shown in *Figure 4.24*. The effect of reaction temperature using sulfided catalyst pellets and <45μm solids on +343°C conversion results of filtered liquid products is presented in *Figure 4.25*.
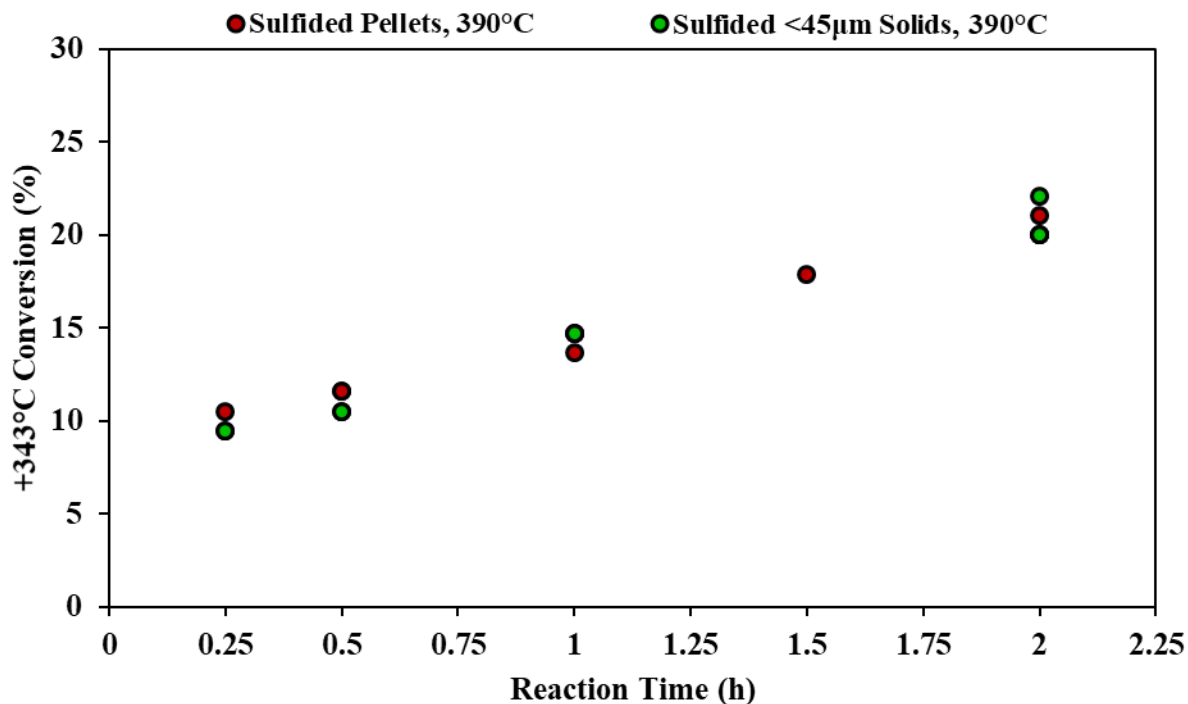
Figure 4.24. The effect of reaction time at 390°C using sulfided catalyst pellets and <45µm solids on +343°C conversion of filtered liquid products.

As the reaction time increases at 390°C, the +343°C conversion increases for both sulfided pellets and <45µm solids in *Figure 4.24*. The relationship between +343°C conversion and reaction time is linear for both catalyst sizes (>0.98 R^2).
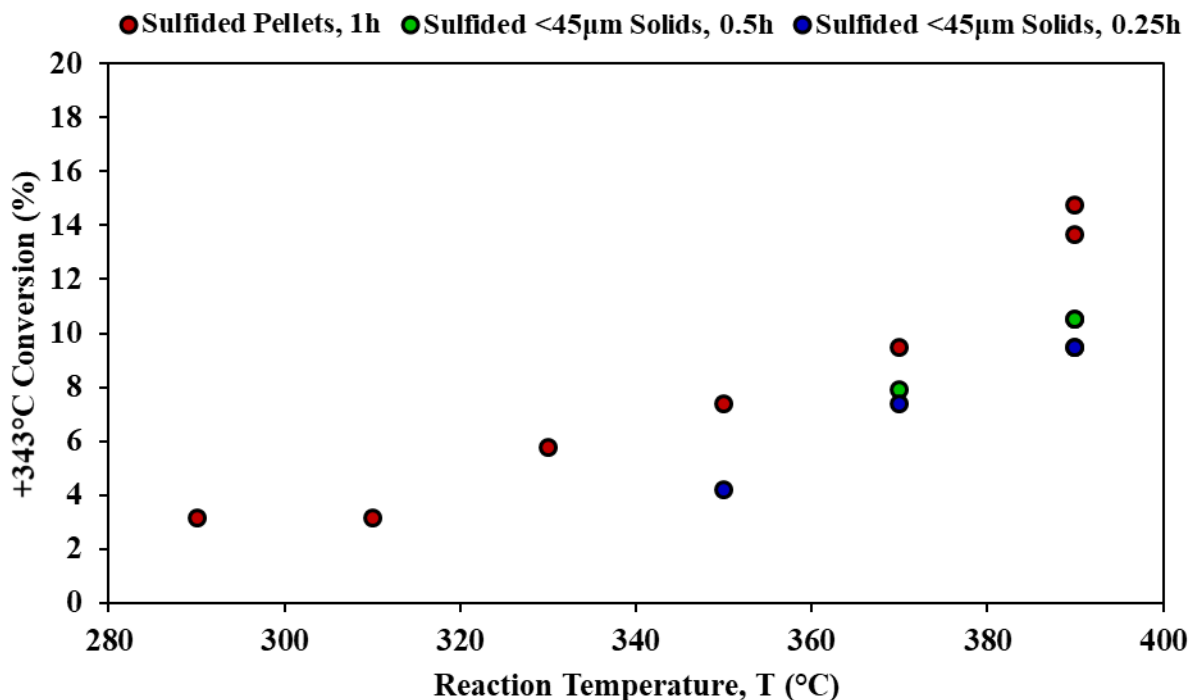
Figure 4.25. The effect of reaction temperature using sulfided catalyst pellets and <45μm solids on +343°C conversion of filtered liquid products.

As the reaction temperature increases higher than 310°C, the +343°C conversion increases for both sulfided pellets and <45μm solids in *Figure 4.25*. Longer reaction times improve +343°C conversion trends. The relationship between +343°C conversion and reaction temperature are linear for both catalysts greater than 310°C (>0.95 R^2).

4.5 Hydrogen Nuclear Magnetic Resonance

All hydrogen nuclear magnetic resonance (^{1}H NMR) chemical shift results are found in *Figures E1 to E22* of *Appendix E*. The chemical shift results from the 400MHz spectrometer are found in *Figures E1 to E7*. The chemical shift results from the 60MHz spectrometer are found in *Figures E8 to E22*. A summary of the chemical shift fractional concentrations for the HVGO and filtered liquid products are presented in *Table E7*. The molecular data from *Table E7* is combined to three hydrogen concentration regions: Aromatic (10.7 to 6.2ppm), α-Aromatic (4.3 to 2ppm), and Aliphatic (2 to -0.5ppm). The three molecular hydrogen concentrations are plotted as a function of reaction time and temperature in section 4.5.

Reaction Time and Temperature Effects with Sulfided Pellets

The effect of reaction time at 390°C using sulfided catalyst pellets on filtered liquid product molecular hydrogen concentrations is displayed *Figure 4.26*. The effect of reaction temperature at 1h using sulfided catalyst pellets on filtered liquid product molecular hydrogen concentrations is presented in *Figure 4.27*. Results in these figures are obtained using the 400MHz spectrometer.
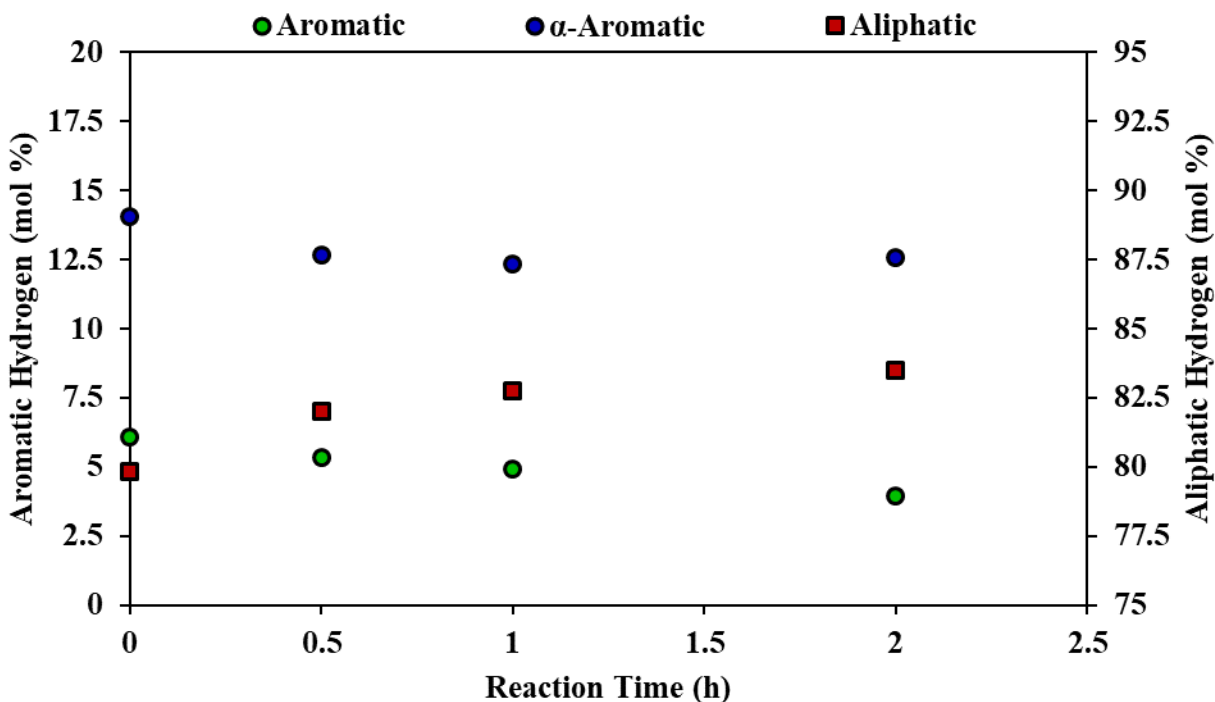
Figure 4.26. The effect of reaction time at 390°C using sulfided catalyst pellets on filtered liquid product molecular hydrogen concentrations (400MHz spectrometer).

As reaction time increases, aliphatic hydrogen concentration increases in the filtered liquid product compared to the HVGO at 0h reaction time as shown in *Figure 4.26*. Aromatic hydrogen concentrations decrease compared to the HVGO. Insignificant changes are seen for α-aromatic hydrogen concentrations longer than 0.5h reaction time.
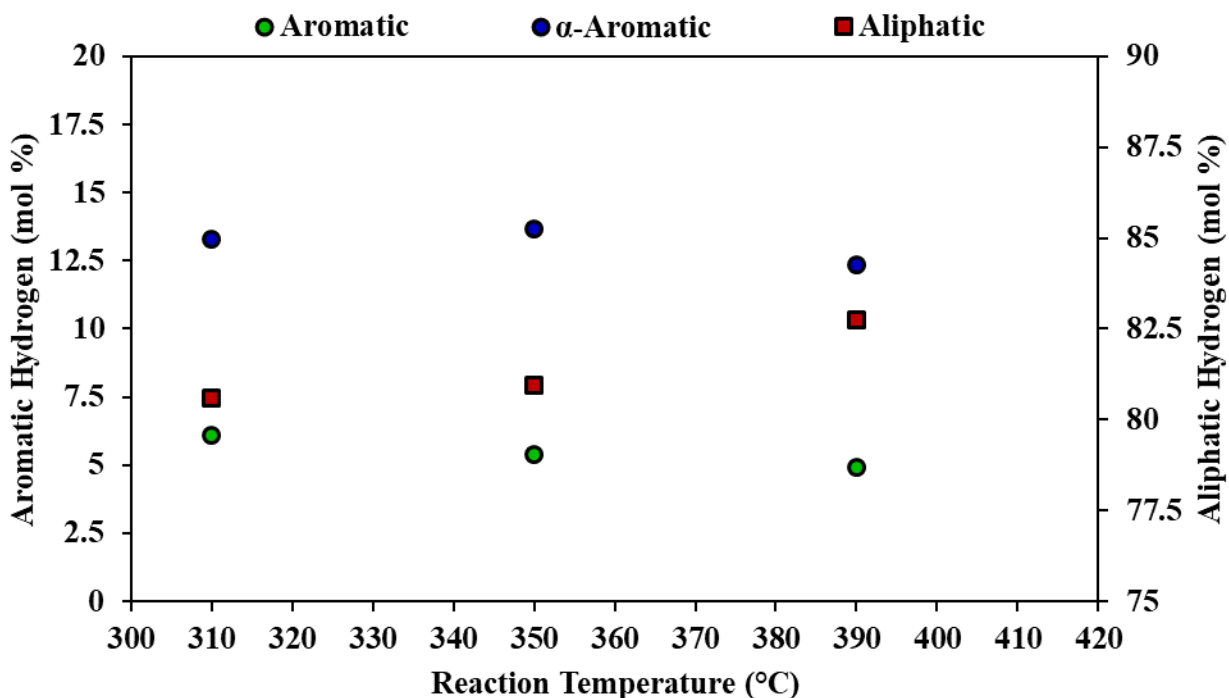
Figure 4.27. The effect of reaction temperature at 1h using sulfided catalyst pellets on filtered liquid product molecular hydrogen concentrations (400MHz spectrometer).

As reaction temperature increases, aliphatic hydrogen concentration increases in the filtered liquid product compared to the HVGO as presented in *Figure 4.27*. Aromatic hydrogen concentrations decrease compared to the HVGO higher than 350°C. Insignificant changes are seen until 390°C for α-aromatic hydrogen concentrations compared to the HVGO.

The effect of reaction time at 390°C using sulfided catalyst pellets on filtered liquid product molecular hydrogen concentrations is displayed *Figure 4.28*. The effect of reaction temperature at 1h using sulfided catalyst pellets on filtered liquid product molecular hydrogen concentrations is presented in *Figure 4.29*.
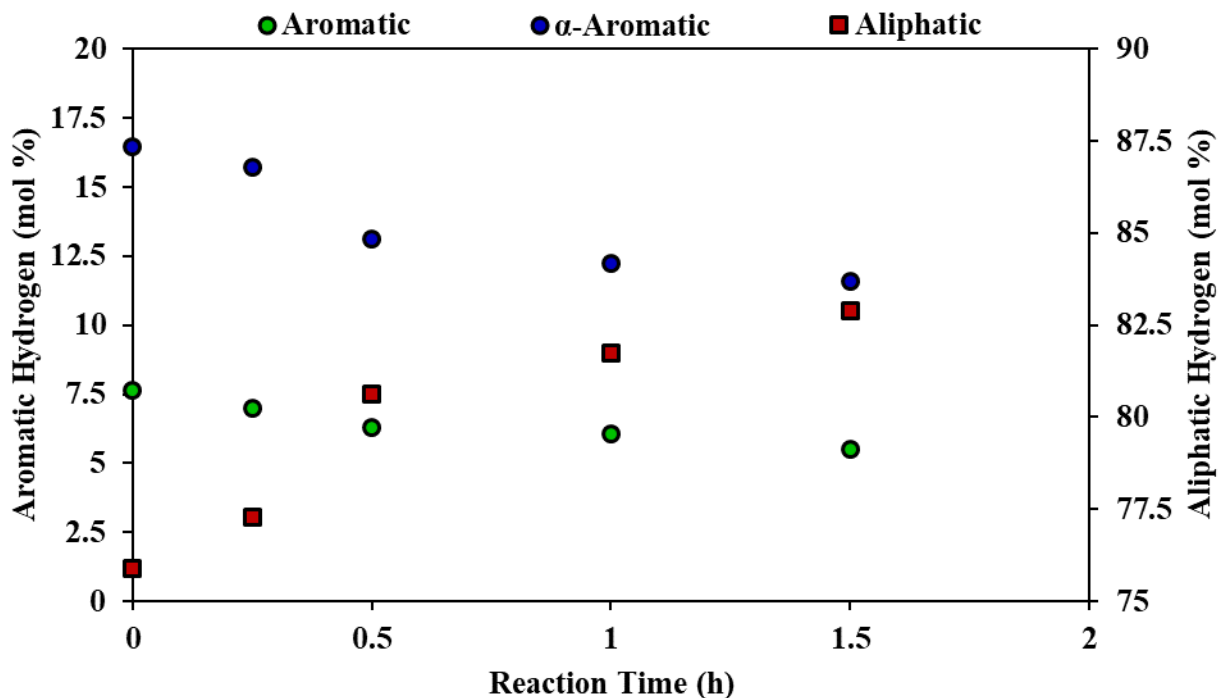
Figure 4.28. The effect of reaction time at 390°C using sulfided catalyst pellets on filtered liquid product molecular hydrogen concentrations (60MHz spectrometer).

Similar to *Figure 4.26*, the 60MHz spectrometer results in *Figure 4.28* are identical in trends for the three molecular hydrogen concentrations. At similar reaction times, results from the 400MHz are up to 20% different from the 60MHz spectrometer for aromatic hydrogen. Except for the HVGO, aliphatic and α-aromatic hydrogen are less than <4% different at similar reaction times.
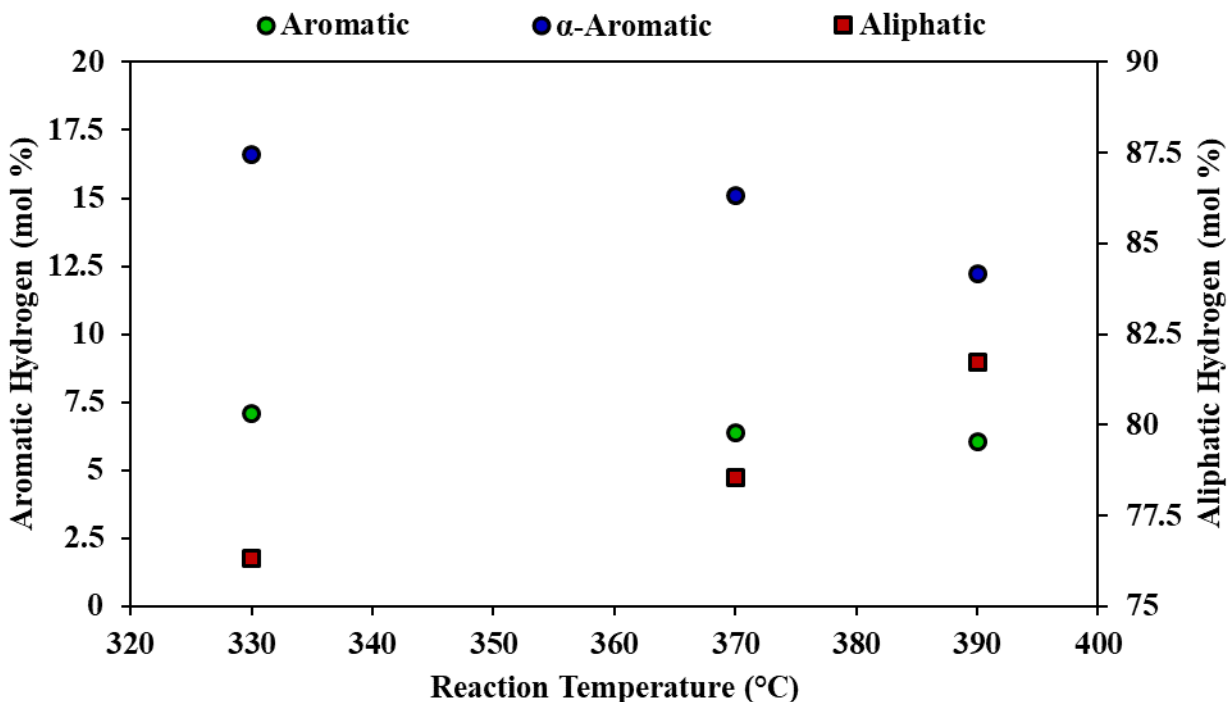
Figure 4.29. The effect of reaction temperature at 1h using sulfided catalyst pellets on filtered liquid product molecular hydrogen concentrations (60MHz spectrometer).

Similar to *Figure 4.27*, the 60MHz spectrometer results in *Figure 4.29* are identical in trends for the three molecular hydrogen concentrations. Insignificant differences are not seen until 370°C for α-aromatic hydrogen concentrations compared to the HVGO. At 390°C, the aromatic hydrogen result from the 400MHz is 20% different from the 60MHz spectrometer. The aliphatic and α-aromatic hydrogen concentrations are different by 1% for the same comparison.

Reaction Time and Temperature Effects with <45μm Sulfided Solids

The effect of reaction time at 390°C using <45μm sulfided catalyst solids on filtered liquid product molecular hydrogen concentrations is highlighted *Figure 4.30*. The effect of reaction temperature at 0.25h using <45μm sulfided catalyst solids on filtered liquid product molecular hydrogen concentrations is shown in *Figure 4.31*. Results in these figures are obtained using the 60MHz spectrometer.
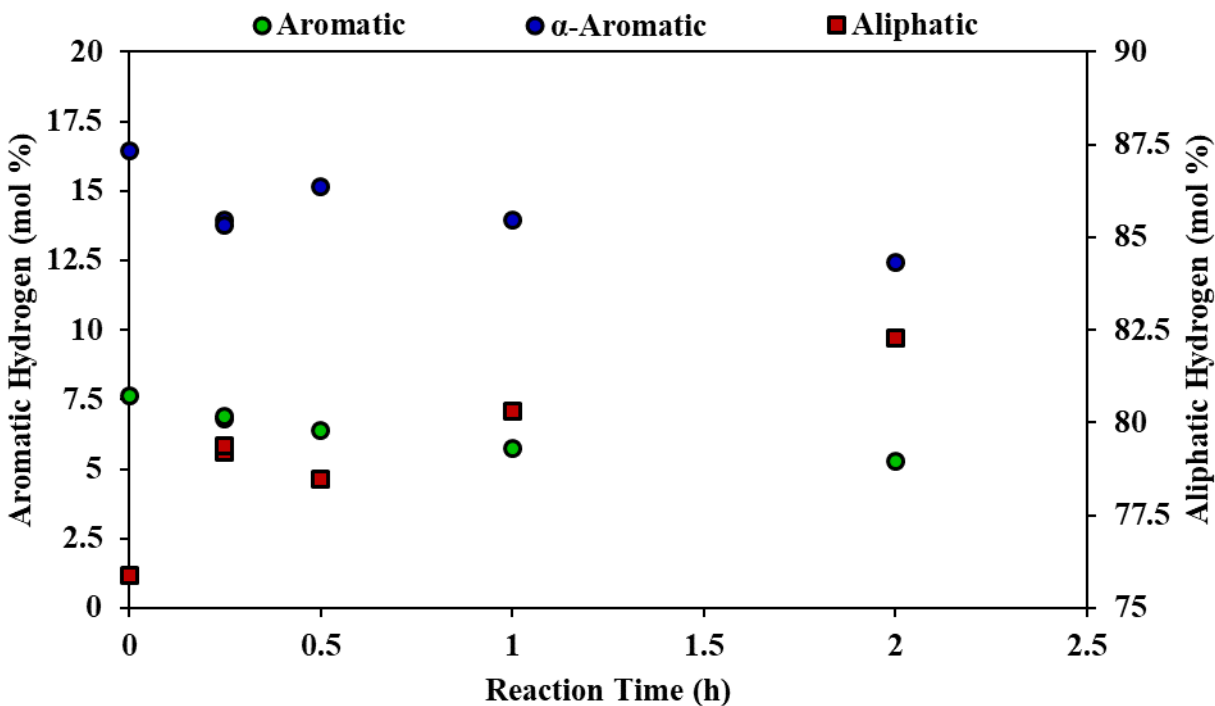
Figure 4.30. The effect of reaction time at 390°C using <45µm sulfided catalyst solids on filtered liquid product molecular hydrogen concentrations (60MHz spectrometer).

Similar to the reactions with catalyst pellets, as reaction time increases, aliphatic hydrogen concentration increases in the filtered liquid product compared to the HVGO at 0h reaction time as shown in *Figure 4.30*. Aromatic and α-aromatic hydrogen concentrations decrease compared to the HVGO with increasing reaction time.
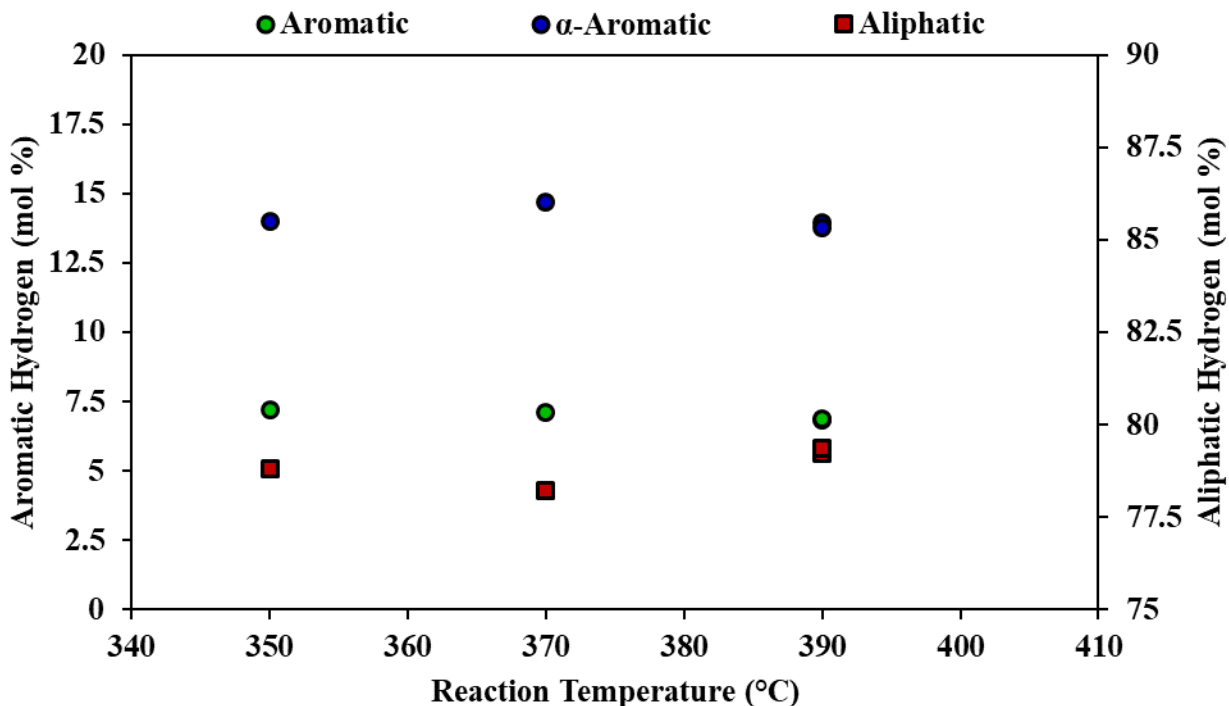
Figure 4.31. The effect of reaction temperature at 0.25h using <45µm sulfided catalyst solids on filtered liquid product molecular hydrogen concentrations (60MHz spectrometer).

Insignificant changes are seen in all molecular hydrogen concentration results for increasing reaction temperature in *Figure 4.31*. Concentration results are significantly different compared to the HVGO.

4.5.1 Aromatic Hydrogen Conversion

Catalyst Size Effects with Sulfided Pellets and <45µm Solids

The aromatic hydrogen concentration results reported in section 4.5 are used to calculate conversion. The formula used to calculate aromatic conversion is presented in section 2.3.5. The effect of reaction time at 390°C using sulfided catalyst pellets and <45µm solids on filtered liquid product aromatic hydrogen conversion results is compared in *Figure 4.32*. The effect of reaction temperature with sulfided catalyst pellets and <45µm solids on filtered liquid product aromatic hydrogen conversion results is compared in *Figure 4.33*.
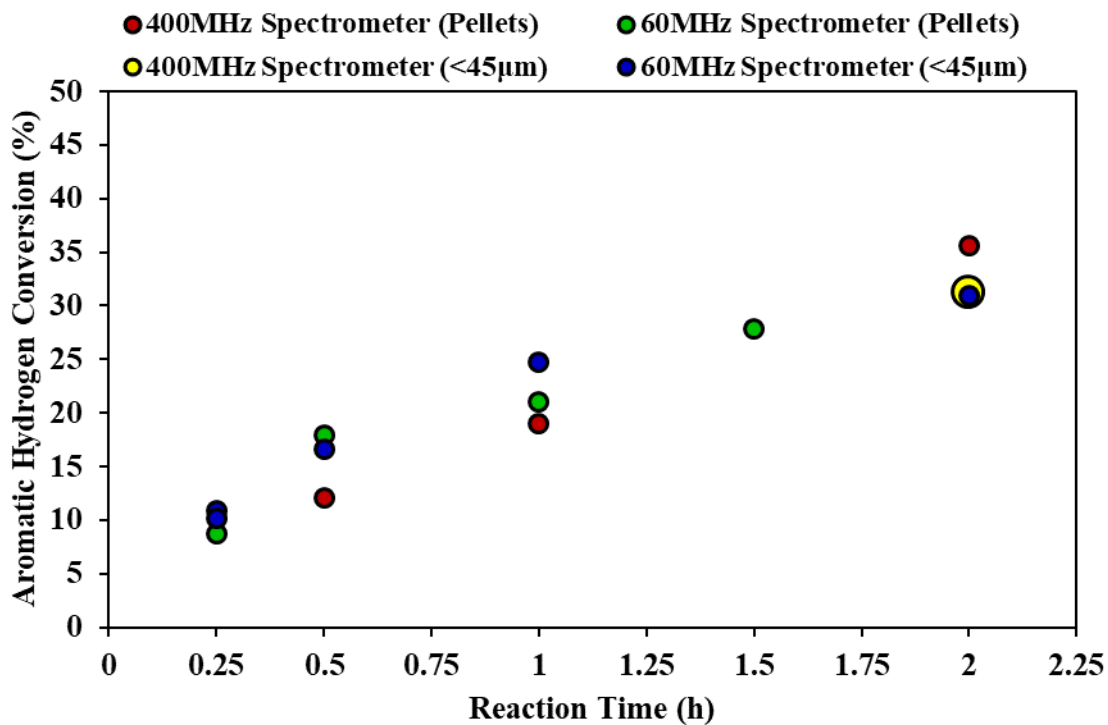
Figure 4.32. The effect of reaction time at 390°C using sulfided catalyst pellets and <45μm solids on filtered liquid product aromatic hydrogen conversion.

As the reaction time increases, aromatic molecular hydrogen conversion increases as shown in *Figure 4.32*. Results from the two spectrometers provide agreement in the linear trend. Insignificant differences are seen when comparing the sulfided catalyst pellet and <45μm solid trends. The data point at 2h for <45μm solids using the 400MHz spectrometer is comparable to the 60MHz result.
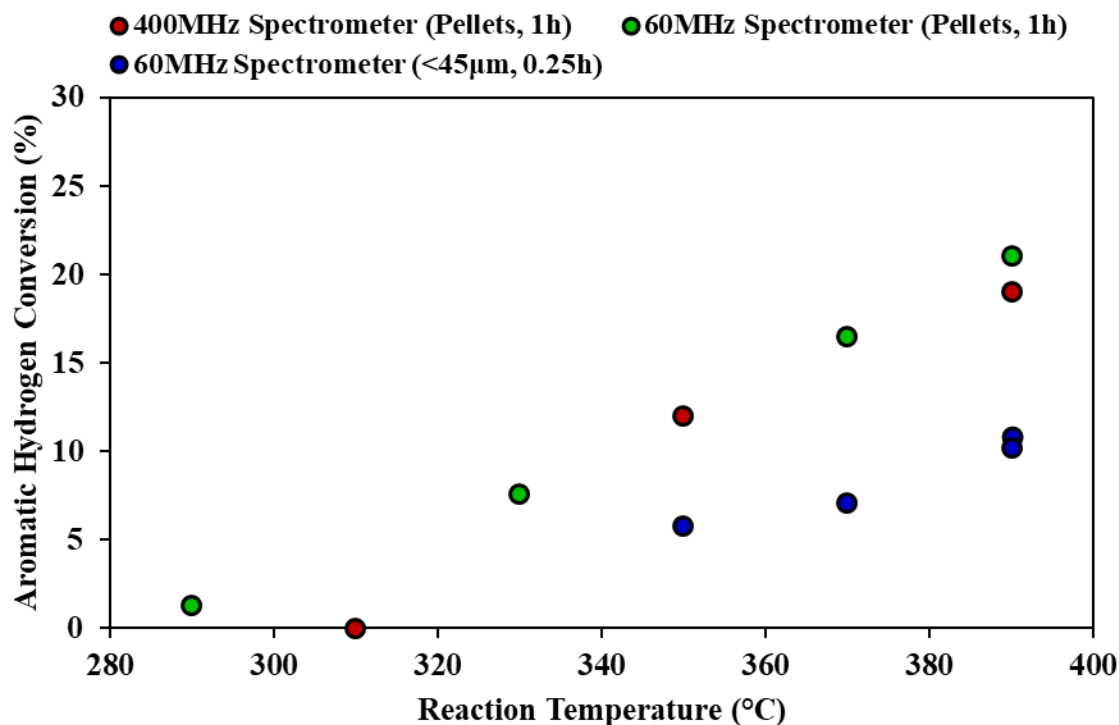
Figure 4.33. The effect of reaction temperature using sulfided catalyst pellets and <45µm solids on filtered liquid product aromatic hydrogen conversion.

The aromatic molecular hydrogen conversion increases with reaction temperature beyond 330°C as presented in *Figure 4.33*. At 1h, results from the two spectrometers provide agreement in the trend. The conversion results for the <45µm solids at 0.25h is lower compared to the 1h reactions with catalyst pellets.

4.6 Visible Spectroscopy

Visible spectroscopy measurement results, absorbance as a function of wavelength, with 95% confidence intervals for the HVGO and its liquid products are found in section 4.6. The first derivative of the absorbance is used to determine the maximum cutoff point in the visible region.

HVGO, Solvent Filtration, and Non-Catalytic Reactor Mixing Effect
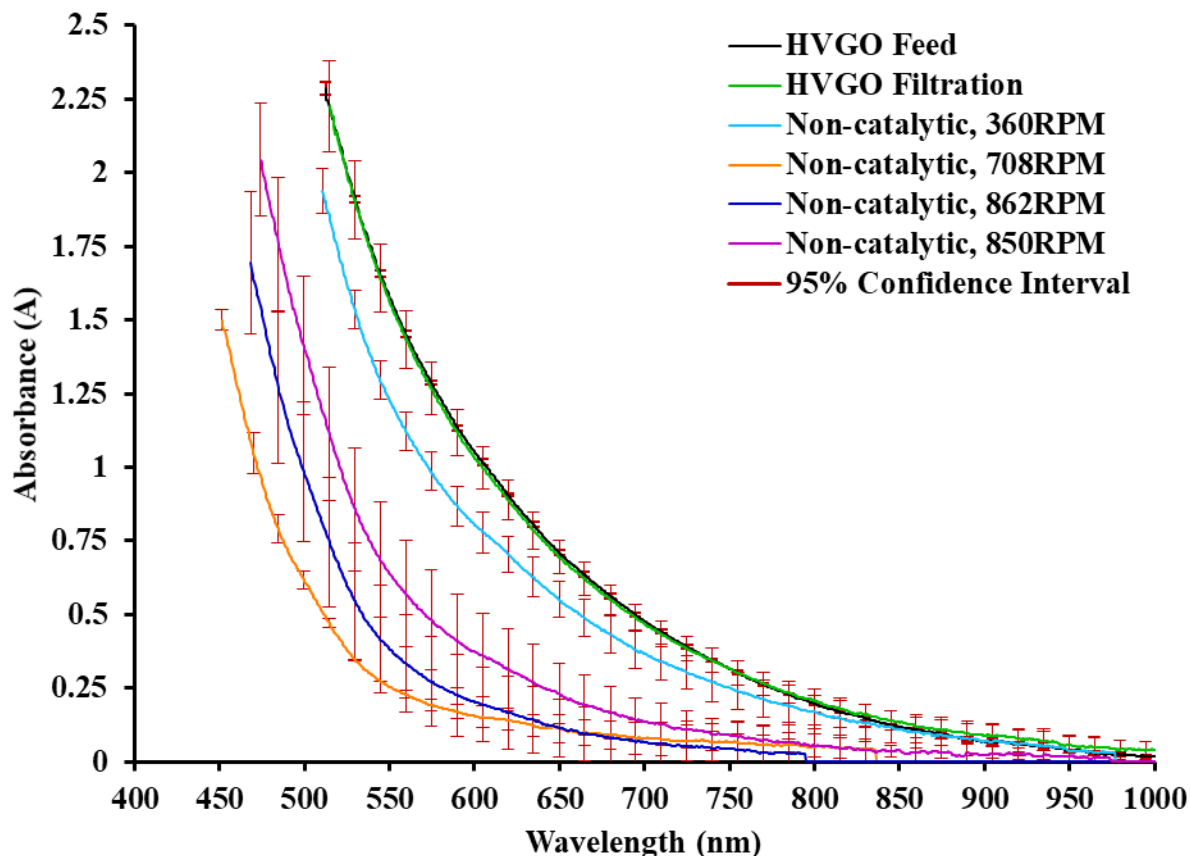
Figure 4.34. Absorption spectra of HVGO, solvent filtrated HVGO, and non-catalytic reactor liquid products.

To determine the effect of solvent filtration on the HVGO, filtered liquid feed is compared to the HVGO. The solvent filtrated HVGO (green result) overlaps the HVGO (black result) in *Figure 4.34*. The results are not significantly different as the 95% confidence intervals overlap. To determine the effect of mixing on the unfiltered liquid product with no catalyst present, the reaction at 360RPM is compared to three reactions with agitation >700RPM. The non-catalytic liquid product adsorption spectra results are hypsochromically shifted significantly compared to the HVGO in *Figure 4.34*. Increasing the mixing to >700RPM, the adsorption spectra of the liquid products are hypsochromically shifted compared to mixing at 360RPM. High variability in the absorption spectra results for >700RPM reactions are seen in *Figure 4.34*.

Catalytic Reactor and Wall Effects with Unfiltered Liquid Products
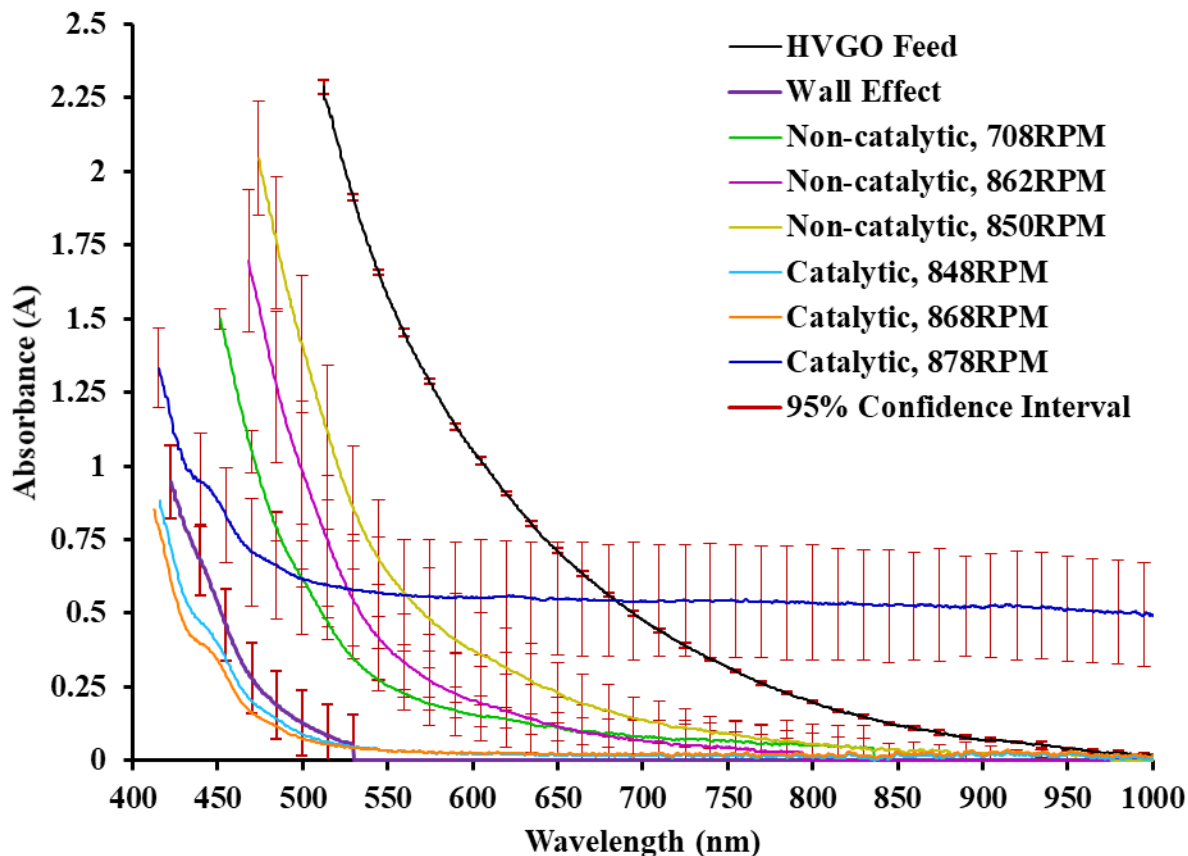
Figure 4.35. Absorption spectra results of HVGO, catalytic, and non-catalytic reactor liquid products.

The effect of using unsulfided catalyst versus no catalyst on unfiltered liquid product visible absorption results is compared in *Figure 4.35*. All unfiltered liquid product results are hypsochromically shifted significantly compared to the HVGO. Apart from the one catalytic reaction (dark blue result), adding a catalyst shifts the adsorption spectra hypsochromically compared to the non-catalytic reactions at similar agitation speeds. The dark blue result is caused by inference from catalyst pellets that remained in the unfiltered liquid product.

Catalytic Reactor with Liquid Product Filtration Effect
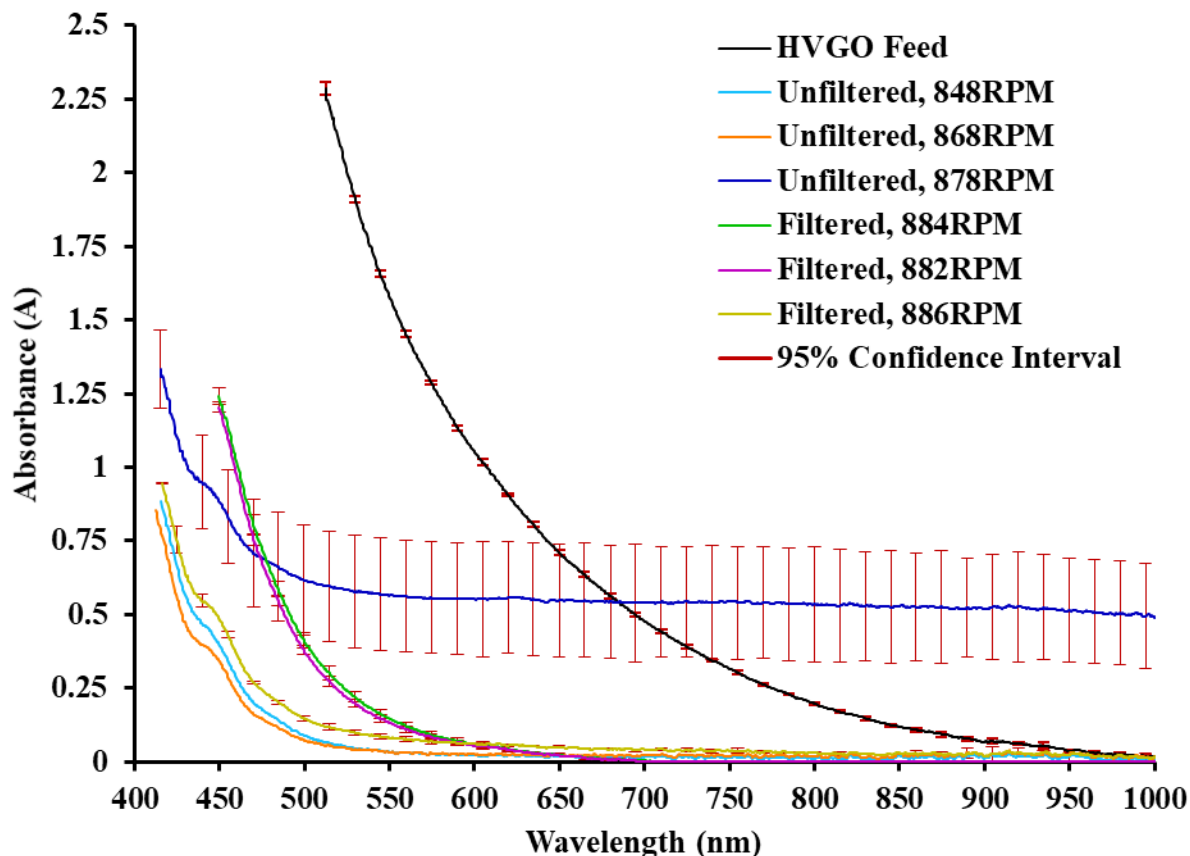
Figure 4.36. Absorption spectra of HVGO, unfiltered, and filtered liquid products.

The effect of adding a solvent and filtering the liquid products on the visible adsorption results is compared to unfiltered liquid products in *Figure 4.36*. The agitation remained in the 800-900RPM region for all reactions. Compared to the HVGO, all results are hypsochromically shifted. The filtered liquid product spectra are bathochromically shifted compared to the unfiltered liquid products. As mentioned from *Figure 4.35*, the one unfiltered result (dark blue) is caused by unfiltered catalytic inference.

Catalytic Reactor Mixing Effect and Verification Reaction
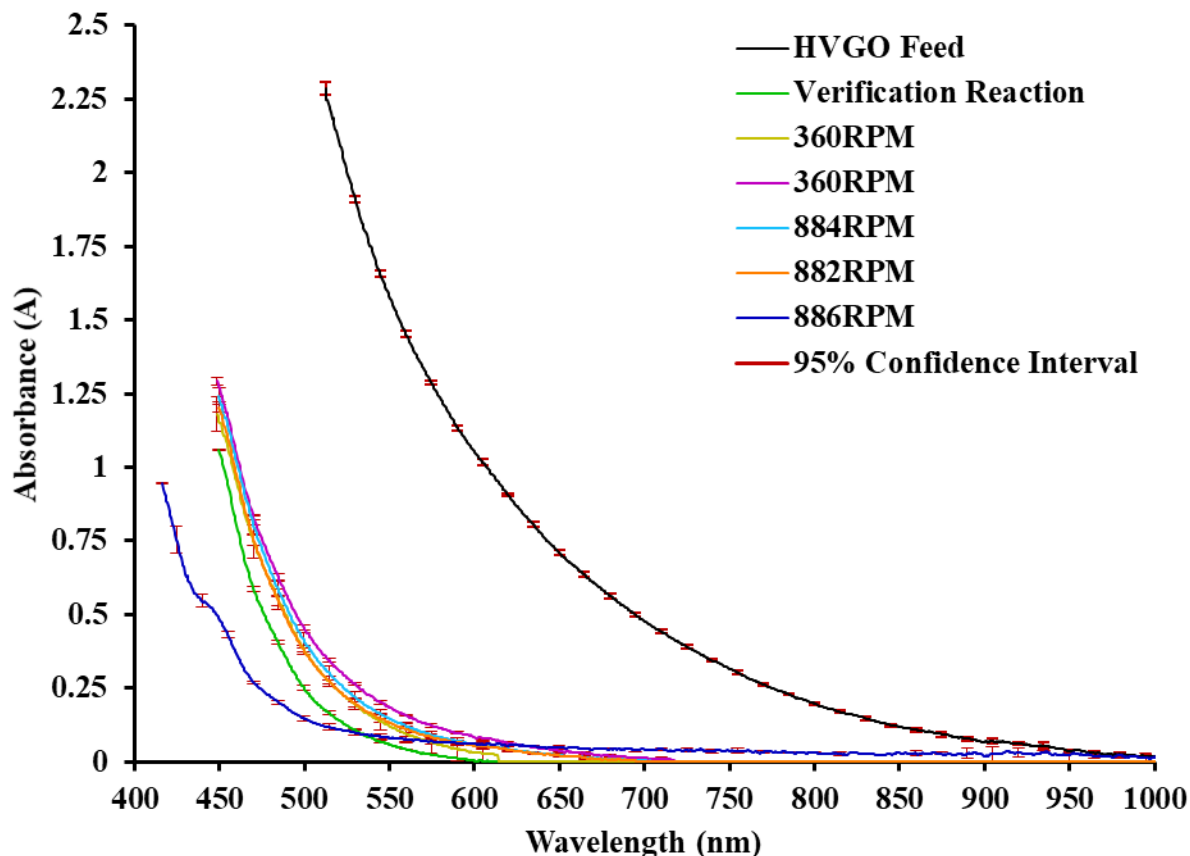
Figure 4.37. Absorption spectra of HVGO, verification reaction, and agitated filtered liquid products.

The effect of mixing using catalyst pellets on the filtered liquid product visible absorption spectra is highlighted in *Figure 4.37*. Compared the HVGO, all visible absorption spectra are hypsochromically shifted. The effect of mixing does not impact the absorption spectra for four of the liquid products as seen by the overlapping spectra (360 and 882-884RPM). The 886RPM results is hypsochromically shifted compared to these four liquid products. This liquid product had minor inference as seen by the absorbance not approaching zero with increasing wavelength. The verification reaction (green result), 2.25h reaction time at 360RPM, is hypsochromically shifted compared to the two results at 360RPM and 2h.

Catalytic Sulfidation Effect with Pellets
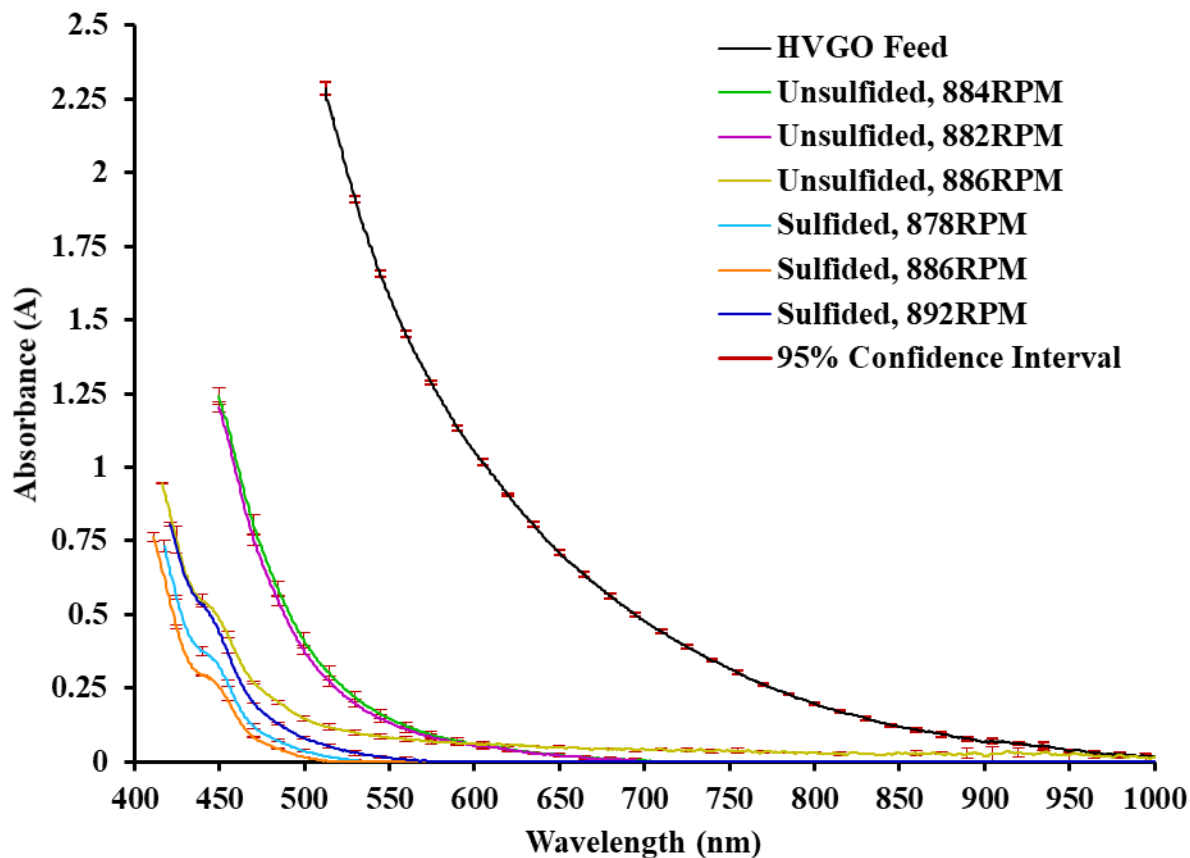
Figure 4.38. Absorption spectra of HVGO, catalytically unsulfided, and sulfided filtered liquid products.

The effect of using unsulfided and sulfided catalyst pellets on the visible adsorption spectra is shown in *Figure 4.38*. All visible absorption spectra are hypsochromically shifted compared to the HVGO. The agitation speed for the reactions in *Figure 4.38* ranged from 878 to 892RPM. The sulfided liquid product spectra are hypsochromically shifted compared to the unsulfided catalyst results.

Reaction Time and Temperature Effects with Sulfided Pellets
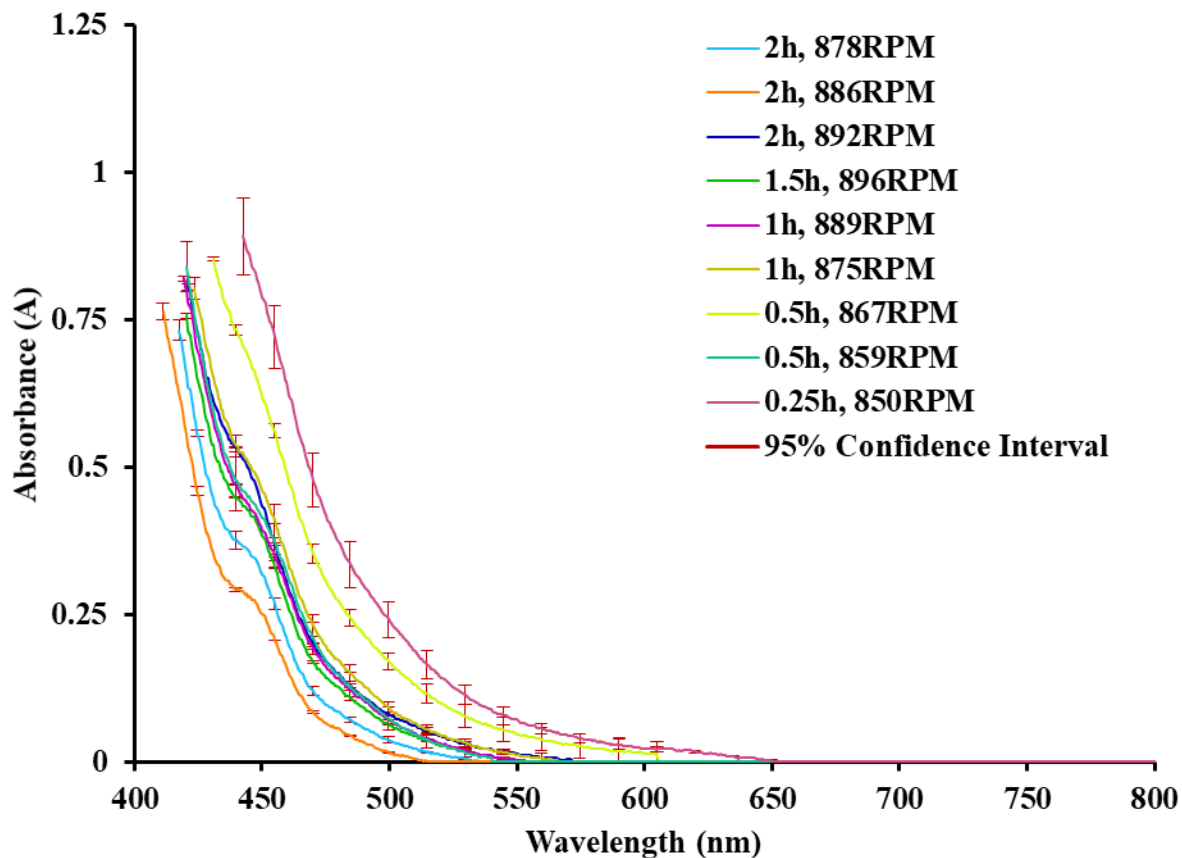
Figure 4.39. The effect of reaction time at 390°C using sulfided catalyst pellets on filtered liquid product visible adsorption spectra.

The effect of reaction time at 390°C using sulfided catalyst pellets on filtered liquid product visible adsorption spectra is shown in *Figure 4.39*. All spectra results are significantly different compared to the HVGO. The agitation ranged from 850 to 896RPM. As the reaction time increases, the visible spectra are hypsochromically shifted to lower wavelength absorbances. Spectra overlap within the 0.5 to 1.5h reaction time region.
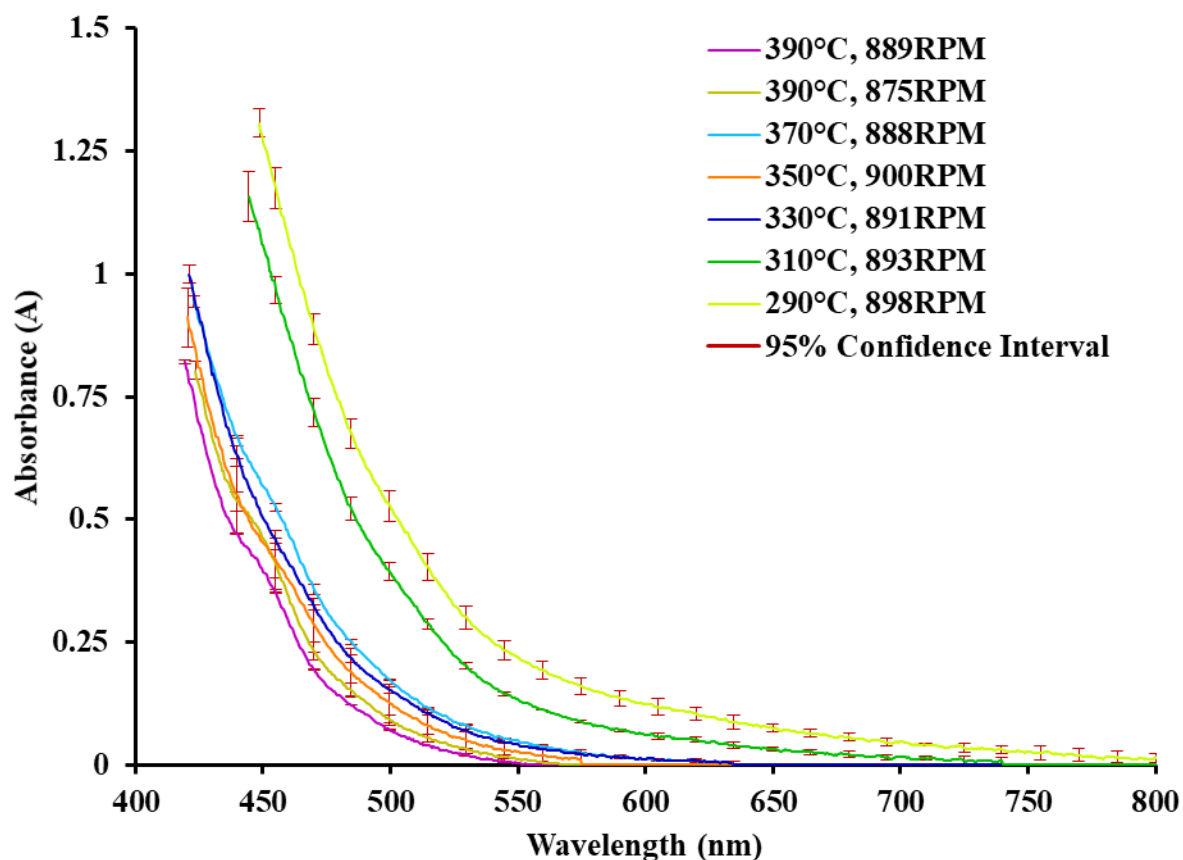
Figure 4.40. The effect of reaction temperature at 1h using sulfided catalyst pellets on filtered liquid product visible adsorption spectra.

The effect of reaction temperature at 1h using sulfided catalyst pellets on filtered liquid product visible adsorption spectra is presented in *Figure 4.40*. All results in *Figure 4.40* are significantly different compared to the HVGO. As the reaction temperature increases, the visible spectra of the filtered liquid products are hypsochromically shifted to lower wavelengths.

Reaction Time and Temperature Effects with <45μm Sulfided Solids
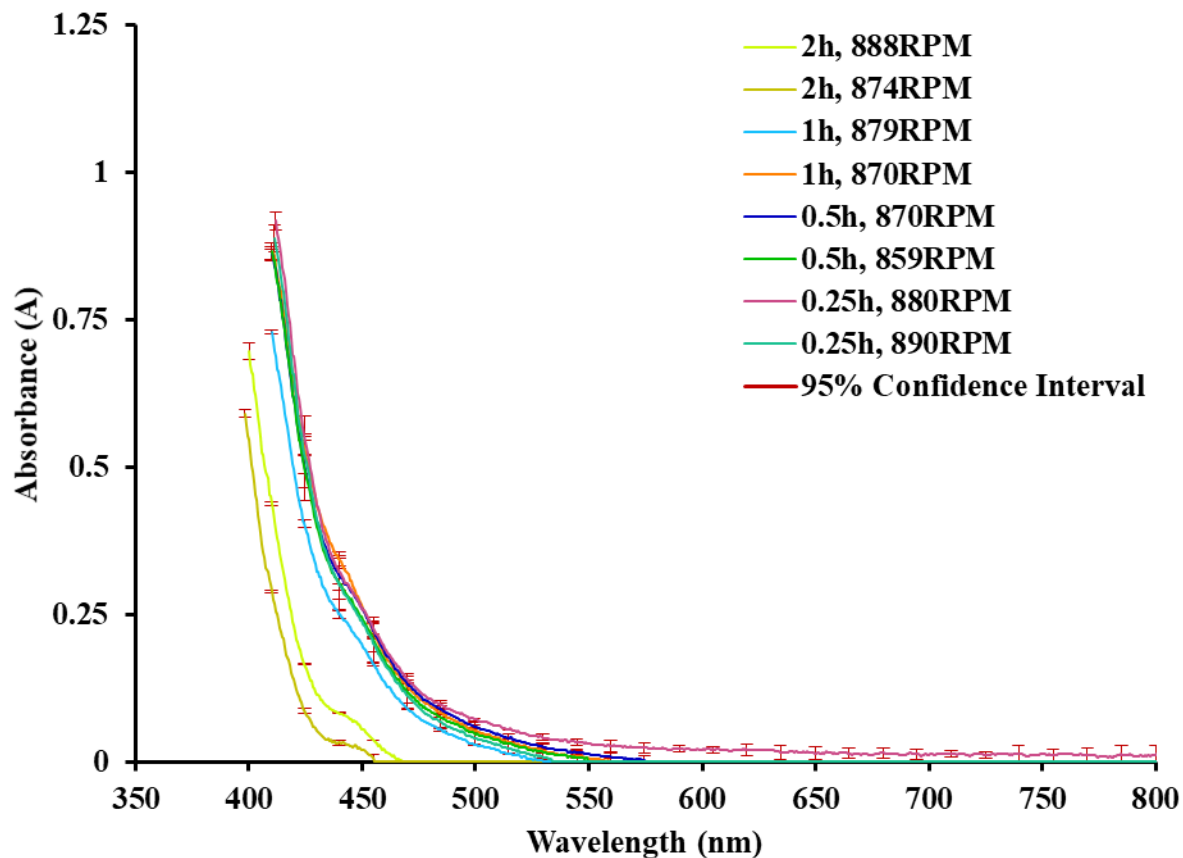
Figure 4.41. The effect of reaction time at 390°C using <45μm sulfided catalyst solids on filtered liquid product visible absorption spectra.

The effect of reaction time at 390°C using <45μm sulfided catalyst solids on filtered liquid product visible absorption spectra is highlighted in *Figure 4.41*. All spectra in *Figure 4.41* are hypsochromically shifted to lower wavelengths compared to the HVGO. Increasing the reaction time causes hypsochromic shifts in the visible absorption spectra. Insignificant differences are seen in the 0.25 to 1h liquid product spectra.
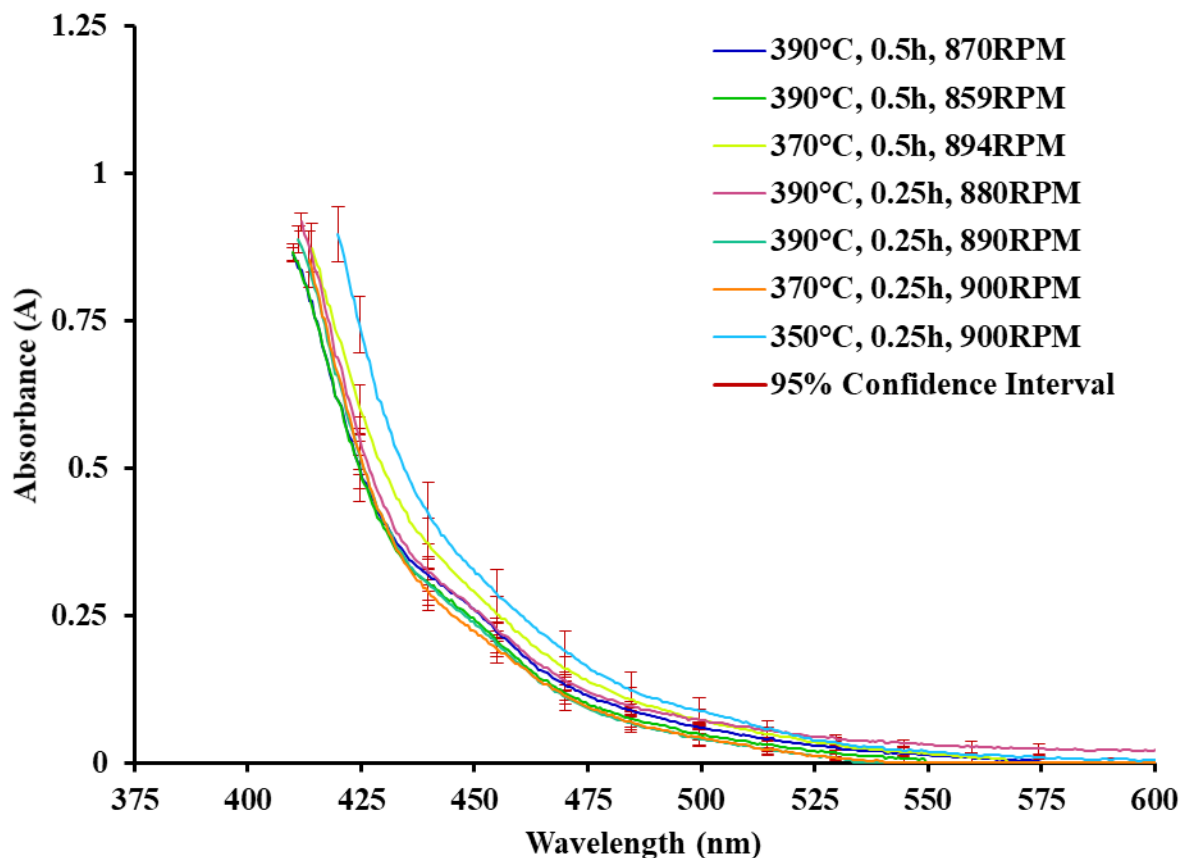
Figure 4.42. The effect of reaction temperature at 0.25 and 0.5h reaction times using <45μm sulfided catalyst solids on filtered liquid product visible adsorption spectra.

The effect of reaction temperature at 0.25 and 0.5h using <45μm sulfided catalyst solids on filtered liquid product visible absorption spectra is highlighted in *Figure 4.42*. All results are hypsochromically shifted significantly compared to the HVGO. Differences in spectra results are seen for increasing reaction time to 0.5h. Increasing reaction temperature causes hypsochromic shifts in the spectra.

Visible Spectrometer Verification

The visible adsorption spectra for the HVGO and a filtered liquid product is verified in *Figure 4.43*. A PerkinElmer UV/VIS/NIR spectrometer is compared to the visible spectrometer developed. The PerkinElmer UV/VIS/NIR Spectrometer Lambda 1050 ranged from 175 to 3300nm. The light source is a combination of tungsten-halogen and deuterium. A 2mm glass cuvette is used for both measurements.
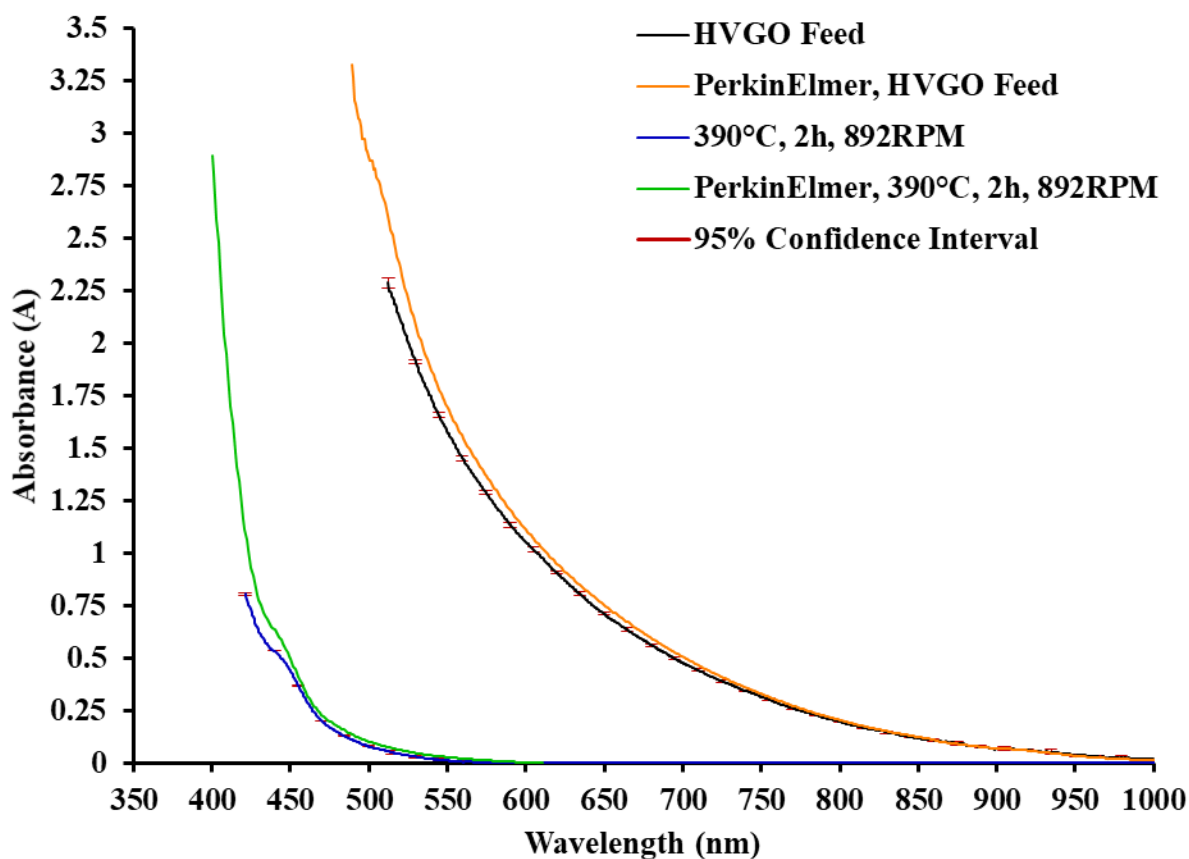
Figure 4.43. Visible adsorption spectra of HVGO and a filtered liquid product using the visible spectrometer developed as well as the PerkinElmer UV/VIS/NIR.

The visible adsorption trends of the spectrometer developed agree with the lab grade PerkinElmer spectrometer results shown in *Figure 4.43*. The percent difference for the HVGO is less than 13% for all absorbance values. The percent difference for the filtered liquid product ranged from 11 to 78% (from 421 to 550nm).

4.7 Chemometric Modeling

Section *4.7.1* highlights data selection and preprocessing. Chemometric modeling results of the visible absorption spectra for each method are presented in sections *4.7.2 to 4.7.5*. Matlab code for all modeling techniques are found in *Appendix G*. Numerical regression coefficients, adjusted coefficient of determinations, principal component analysis and regression, and partial least squares regression results are found in *Appendix H*. Summary of optimal models for each measured

property calibrated are highlighted in section *4.7*. Model section criteria equations and results are found in .

4.7.1 Data Selection and Preprocessing

Six experimental reaction data sets are compared for each calibration model. Four data sets modeled the following 115 liquid product properties measured: carbon, hydrogen, hydrogen to carbon ratio, sulfur, nitrogen, liquid density, IBP to 300°C, 300 to 400°C, 400 to 500°C, +500°C to FBP, +343°C fraction, sulfur conversion, nitrogen conversion, +343°C conversion, and the boiling point distribution curve (101 temperatures). Two data sets used the ^{1}H NMR results from each spectrometer. Liquid products of these two data sets modeled molecular hydrogen properties: aromatic, α-aromatic, aliphatic, aromatic conversion, and total aromatic conversion.

From the visible absorption spectra results shown in , the HVGO and six experimental reactions are not included in the calibration models, five non-catalytic (reactions 1 to 5), and one unfiltered catalytic liquid product (reaction 9). Visible absorption spectrum results of these reactions are significantly different compared to the remaining sets measured. To ensure a valid comparison of each data set with each other, visible absorption spectra are trimmed to measured values greater than **450nm** for all liquid products. The spectral range modeled absorbance values from 450 to 1075nm. A total of 1122 wavelength channels from the spectrometer are measured within this range and used for each calibration model.

First Data Set

The first data set calibrated the visible spectra of 34 liquid product samples. All catalytic (reactions 7, 8, 10 to 15, and 20 to 44) and one non-catalytic (reaction 6, contaminated reactor walls) are used in this calibration set.

Second Data Set

The second data calibrated the visible spectra of 25 liquid product samples. The calibration data set is limited to catalytic reactions with sulfided pellets and <45μm solids (reactions 20 to 44).

Third Data Set

The third data set calibrated the visible spectra of 14 sulfided catalyst pellet liquid product spectra (reactions 20 to 33).

Forth Data Set

The fourth data set calibrated the visible spectra of 11 <45μm sulfided catalyst solid liquid product spectra (reactions 34 to 44).

Fifth Data Set

The fifth data set calibrated the visible spectra of six liquid product samples measured with the 400MHz ^{1}H NMR spectrometer. Five sulfided pellet and one <45μm solid liquid products are modeled (catalytic reactions 21, 25, 27, 29, 32, and 35).

Sixth Data Set

The sixth data set calibrated the visible spectra of 13 liquid product samples measured with the 60MHz ^{1}H NMR spectrometer. Six sulfided pellet (catalytic reactions 23, 24, 26, 28, 31, and 33) and seven <45μm solid (catalytic reactions 34, 37, 38, 41, 42, 43, and 44) liquid products are modeled.

The sample size (m) for each data set is summarized:

Data Set	First	Second	Third	Fourth	Fifth	Sixth
m	34	25	14	11	6	13

Mean Centering

For each data set investigated, the adsorption spectra and property data are mean centered prior to calibration.

$$X_{ij}^{cen} = X_{ij} - \bar{X}_j \tag{4.1}$$

$$Y_{ij}^{cen} = Y_{ij} - \bar{Y}_j \tag{4.2}$$

Where X is the visible absorbance measured at each wavelength and Y is the physicochemical property measured for the liquid product. Mean centering ensured no intercepts are required in the

182

models calibrated. Mean centering reduces multicollinearity issues between variables and their main effects. Without an intercept, the interpretation is the regression coefficients of variables included in the calibration models.

Sum of Squared Errors

The sum of squared errors or sum of squared residuals measures the difference between a model prediction and the measurement:

$$SSE = \sum_{i=1}^{m} \left(Y_i - Y_{p_i}\right)^2 \tag{4.3}$$

Where Y_i is the measured property and Y_{p_i} is the predicted property from the calibration model.

Root Mean Squared Error

The sum of squared errors is used to find the regression error. The root mean squared error (RMSE), or the root mean squared prediction error, is used to determine the error of the regression model:

$$RMSE = \sqrt{\frac{\sum_{i=1}^{m}\left(Y_i - Y_{p_i}\right)^2}{m}} \tag{4.4}$$

Where **m** is the number of samples in the calibrated model. In an alternative comparison of two models with a different number of regressor coefficients, **m** represents the degrees of freedom (number of samples minus number of coefficients, k). The root mean squared error is preferred when comparing models with similar property units. The relative square error (RSE) is used to compare models with different property units:

$$RSE = \frac{\sum_{i=1}^{m}(Y_i - Y_{p_i})^2}{\sum_{i=1}^{m}(Y_i - \bar{Y}_i)^2} \tag{4.5}$$

Coefficient of Determination

The coefficient of determination (R^2) is calculated for each calibration to summarize the fraction of variance explained by the regression model. The highest value of one yields a regression model explaining all forms of variance, a relative squared error of zero.

$$R^2 = 1 - RSE \tag{4.6}$$

$$R^2 = 1 - \frac{\sum_{i=1}^{m}(Y_i - Y_{p_i})^2}{\sum_{i=1}^{m}(Y_i - \bar{Y}_i)^2} \tag{4.7}$$

Where Y_i is the measured property, Y_{p_i} is the predicted property from the calibration model, and $\bar{Y}_i$ is the average measured property in one the six data sets used.

Adjusted Coefficient of Determination

As a model selection criterion, the adjusted coefficient of determination (R^2_{adj}) is calculated to include variable significance for each calibration model. The R^2_{adj} is useful in multivariate regression analysis as extra insignificant variables in the model decrease its value (unlike the coefficient of determination). Supplementary significant variables increase the R^2_{adj}. In addition to the R^2 value, the adjusted coefficient of determination depends on the sample size and the number of regressor parameters.

$$R^2_{adj} = 1 - \left[\frac{(1 - R^2) \cdot (m - 1)}{m - k - 1} \right] \tag{4.8}$$

Where **k** is the number of independent variables or regressor coefficients in the regression model. The adjusted coefficient of determination is calculated and compared for mean centered data in the four modeling methods. The addition of an intercept term to each model is required for prediction of measured properties. This is for correction of the mean centered absorbance and physicochemical property subtraction prior to regression.

4.7.2 Simple Least Squares (SLS)

Appendix H presents the results of the linear regressor parameter (K) calibrated on mean centered property data as a function of wavelength for the six data sets. The adjusted coefficient of determination results as a function of wavelength for each model is plotted and found in *Appendix H.* Visible absorbance at each wavelength channel (1122 points) are assumed to be linearly related to the property measured:

$$Y = K \cdot X \qquad (4.9)$$

Where Y is a m×p matrix of properties measured of the liquid products (m samples × p properties), X is a m×n matrix of the visible absorbance data (m samples × n wavelengths), and K is a p×n matrix of the linear regression parameters (i.e. inverse of molar absorptivity (ε)×path length (l) in the Beer-Lambert law). In this case, n and p equate to 1. K is a scalar number in the matrix multiplication for each wavelength channel. The regressor parameter K is determined by solving the linear equation:

$$K = (X' \cdot X)^{-1} \cdot X' \cdot Y \qquad (4.10)$$

To determine how well the SLS calibration models are fitted, the predicted property, based on the regressor parameter and the mean centered absorbance data, is determined:

$$Y_p = K \cdot X \qquad (4.11)$$

To correct for the mean centered data, an ε factor is added to the predicted property equation:

$$Y_p = K \cdot X_\lambda + \varepsilon \qquad (4.12)$$

Where ε is the intercept to correct for mean centered data:

$$\varepsilon = \bar{Y} - K \cdot \bar{X}_\lambda \qquad (4.13)$$

The highest adjusted coefficient of determination result, out of 1122 (i.e. wavelength channels) SLS models in the data set, and the corresponding wavelength used for each property are shown in *Table 4.1*.

Table 4.1. Absorbance wavelength channel at the highest adjusted coefficient of determination for each property in their respective SLS calibration model.

Measured Property	First Data Set (34)		Second Data Set (25)		Third Data Set (14)		Fourth Data Set (11)	
	λ (nm)	R^2_{adj}	λ (nm)	R^2_{adj}	λ (nm)	R^2_{adj}	λ (nm)	R^2_{adj}
Carbon	1073	0.30	568	0.56	567	0.77	456	0.29
Hydrogen	723	0.06	510	0.42	473	0.64	467	0.55
H/C	1047	0.02	510	0.27	469	0.56	463	0.66
Sulfur	619	0.20	507	0.72	472	0.84	502	0.40
Nitrogen	1056	0.12	472	0.39	469	0.68	467	0.71
Density	1056	0.08	472	0.48	469	0.66	468	0.70
IBP-300°C	1017	0.12	472	0.30	469	0.59	465	0.84
300-400°C	668	0.12	516	0.64	472	0.76	502	0.54
400-500°C	1043	0.07	500	0.44	469	0.70	467	0.83
+500°C	619	0.17	516	0.58	472	0.76	502	0.30
+343°C	1015	0.08	472	0.35	469	0.63	467	0.83
Sulfur Conversion	619	0.20	507	0.72	473	0.84	502	0.40
Nitrogen Conversion	1056	0.12	472	0.39	469	0.68	467	0.71
+343°C Conversion	1057	0.08	472	0.35	469	0.63	467	0.84

Measured Property	Fifth Data Set (6)		Sixth Data Set (13)	
	λ (nm)	R^2_{adj}	λ (nm)	R^2_{adj}
Aromatic Hydrogen	463	0.75	618	0.18
α-Aromatic Hydrogen	456	0.37	555	0.29
Aliphatic Hydrogen	457	0.68	555	0.27
Aromatic Hydrogen Conversion	463	0.75	618	0.18
Total Aromatic Hydrogen Conversion	457	0.68	555	0.27

The third data set, catalytic reactions with sulfided pellets, resulted in the highest average for the adjusted coefficient of determination in *Table 4.1*. The sulfur property, and corresponding sulfur conversion, resulted in best fits for the second and third data sets. Aromatic hydrogen correlated well from the 400Mhz ^{1}H NMR spectrometer data in the fifth set.
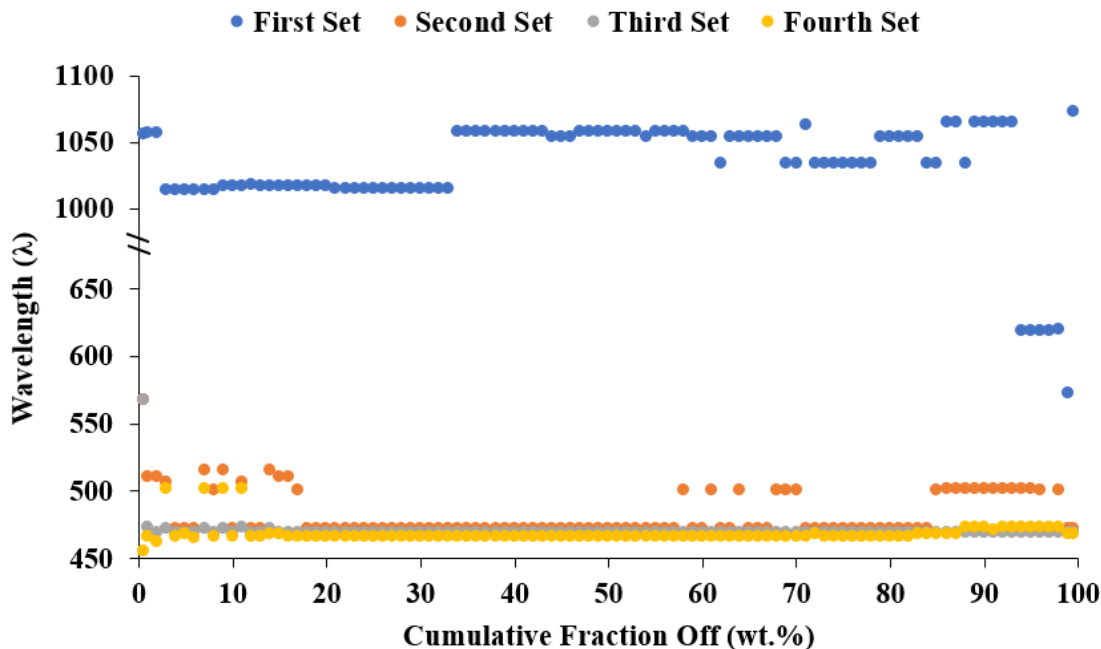
Figure 4.44. Absorbance wavelength of the highest adjusted coefficient of determination obtained from SLS calibration models for the boiling point distribution fractions.
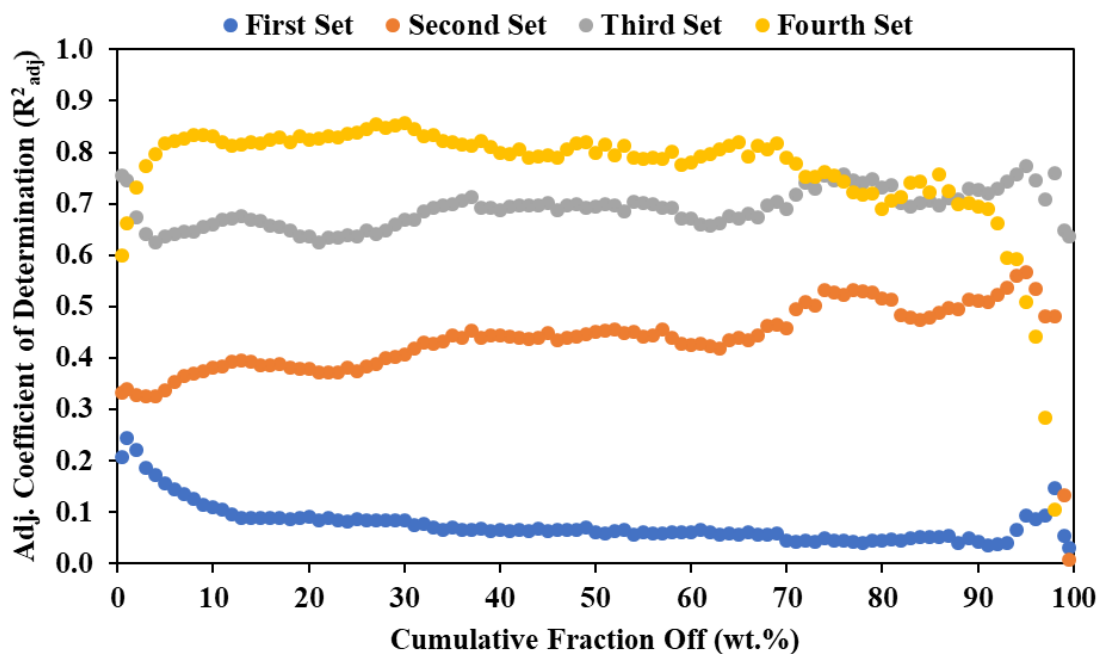
Figure 4.45. Highest adjusted coefficient of determination obtained from SLS calibration models for the boiling point distribution fractions.

The absorbance wavelength of the highest adjusted coefficient of determination obtained from the SLS calibration for the boiling point distribution fractions are presented in *Figure 4.44*. The fourth data set, reactions with <45μm catalyst solids, resulted in the highest adjusted coefficient of determinations for the cumulative boiling point distribution fractions in *Figure 4.45*.

Table 4.2. Linear regressor parameter and intercept of the best SLS calibration model at its corresponding absorbance wavelength channel.

Measured Property	First Data Set (34)			Second Data Set (25)			Third Data Set (14)			Fourth Data Set (11)		
	λ (nm)	K	ε	λ (nm)	K	ε	λ (nm)	K	ε	λ (nm)	K	ε
Carbon	1073	-101	87.7	568	-8.88	87.8	567	-8.56	87.8	456	2.46	87.4
Hydrogen	723	-7.61	12	510	-1.83	12.1	473	-1.18	12.3	467	-2.81	12.3
H/C	1047	2.41	1.64	510	-0.19	1.65	469	-0.12	1.68	463	-0.39	1.69
Sulfur	619	11.8	0.43	507	5.27	0.23	472	3.26	-0.17	502	11.4	0.04
Nitrogen	1056	-2.20	0.09	472	0.13	0.07	469	0.15	0.05	467	0.54	0.03
Density	1056	-0.58	0.92	472	0.04	0.91	469	0.05	0.90	468	0.15	0.90
IBP-300°C	1017	278	7.55	472	-10.3	8.70	469	-12.3	10.7	465	-49.9	12.7
300-400°C	668	-69.6	40	516	-24.3	40.6	472	-12.8	42.4	502	-53.8	41.8
400-500°C	1043	-286	49.1	500	29	47.6	469	20.3	44	467	66.9	42.3
+500°C	619	15.5	3.68	516	8.27	3.45	472	4.44	2.79	502	16.7	3.13
+343°C	1015	-333	81.9	472	16.8	79.9	469	20.1	76.6	467	73.1	74.8
Sulfur Conversion	619	-358	86.9	507	-160	93	473	-101	105	502	-346	98.8
Nitrogen Conversion	1056	1249	46.1	472	-74.5	60	469	-85	71.7	467	-306	81.8
+343°C Conversion	1057	367	13.8	472	-17.6	15.9	469	-21.2	19.4	467	-76.9	21.2

Measured Property	Fifth Data Set (6)			Sixth Data Set (13)		
	λ (nm)	K	ε	λ (nm)	K	ε
Aromatic Hydrogen	463	2.53	4.2	618	41.1	6.2
α-Aromatic Hydrogen	456	2.13	11.7	555	39.7	13.3
Aliphatic Hydrogen	457	-4.52	84.1	555	-52.1	80.5
Aromatic Hydrogen Conversion	463	-41.5	31.5	618	-537	18.6
Total Aromatic Hydrogen Conversion	457	-22.4	21.3	555	-216	19.2

The linear regressor parameters and intercepts from the highest adjusted coefficient results in *Table 4.1* are shown in *Table 4.2*. The results are used in equation *4.12* to predict the calibrated property for each data set. The linear regressor parameters and corresponding intercepts for the cumulative boiling point distribution fractions in *Figures 4.44 and 4.45* are found in *Figures 4.46 and 4.47*, respectively.
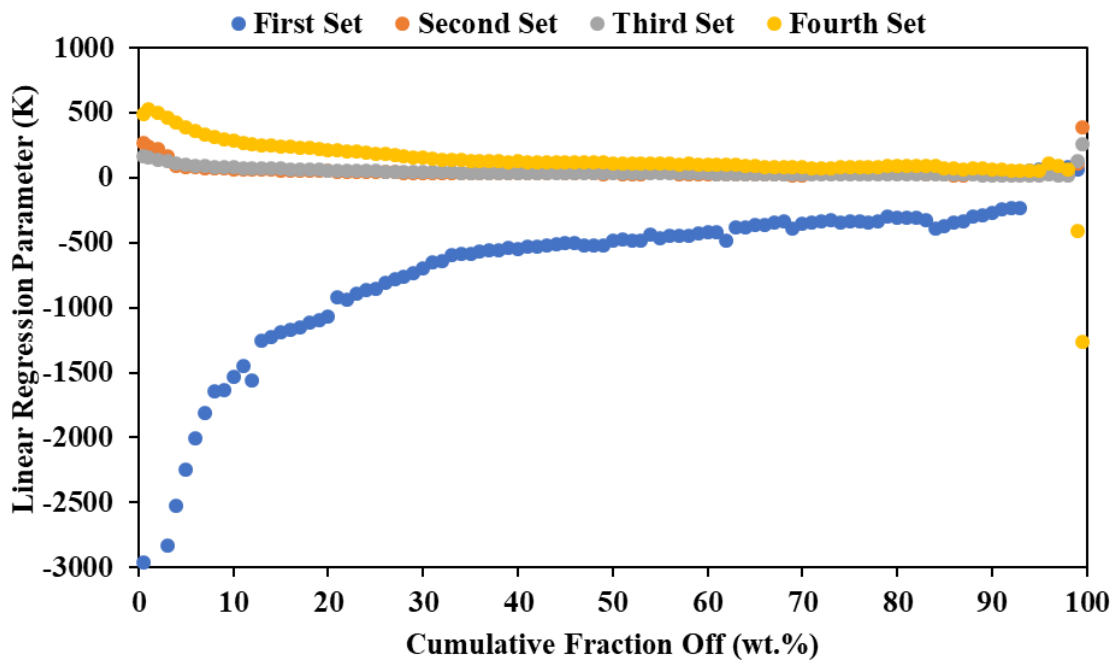
Figure 4.46. Linear regression parameters as a function boiling point distribution fraction of the best SLS calibration model.
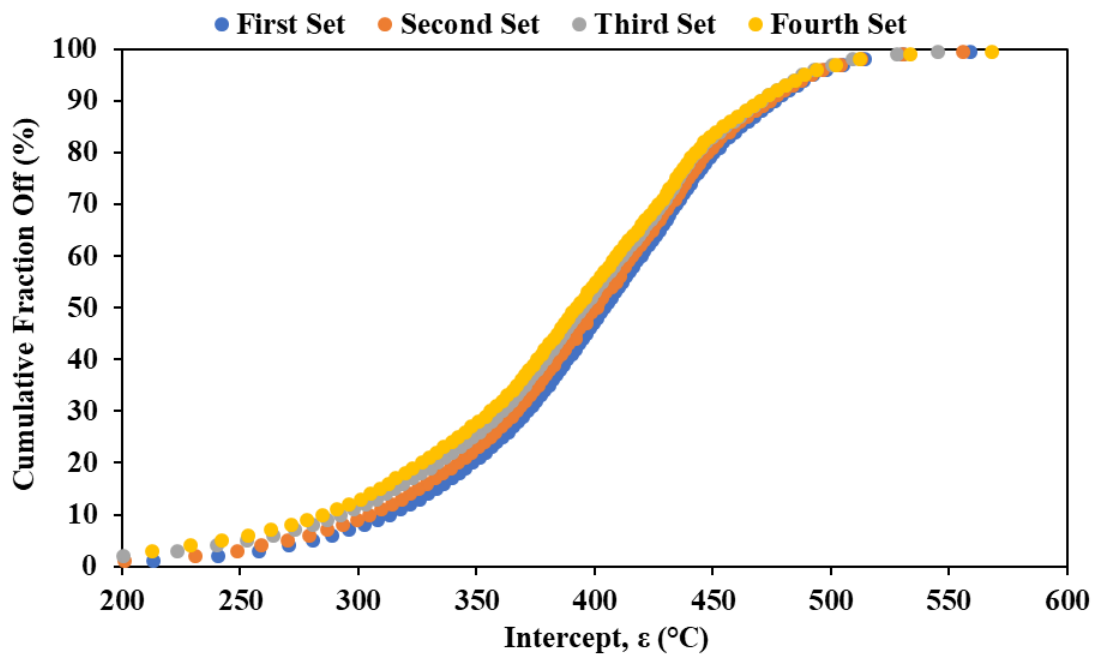
Figure 4.47. Corresponding intercept temperatures of the best SLS boiling point distribution calibration models.

4.7.3 Multiple Linear Regression (MLR)

Visible absorbance at multiple wavelength channels (1122 points) are assumed as linear combinations of the property measured:

$$Y = X_{\lambda_n} \cdot \beta_n + \cdots + X_{\lambda_1} \cdot \beta_1 + \varepsilon \qquad (4.14)$$

Where Y is a m×p matrix of properties measured of the liquid products (m samples × p properties), X is a m×n matrix of the visible absorbance data (m samples × n wavelengths), and β is a n×p matrix of the linear regression coefficients corresponding to each wavelength. In this case, p=1 and n<m. The intercept, ε, is added to correct for the mean centered data.

Stepwise Regression

The stepwise regression tool in Matlab is used for computing regressor coefficients. The regression method adds or removes coefficients based on a F statistic for each wavelength channel. Iterative steps are performed by adding or removing coefficients based on their calculated p-values. The tolerances are 0.05 and 0.1 for adding or removing coefficients, respectively. The iteration ends when no added or removed regressor coefficients improves the model generated based on significance.

$$\beta_n = stepwisefit(X, Y) \qquad (4.15)$$

Where n is the total number of coefficients corresponding to a specific wavelength included in the calibration model. In certain cases, no regressor coefficients are significant for inclusion in the model. For this case, no model is calibrated for the measured property.

Predicted Property

The predicted property is calculated from wavelength channels and the regressor coefficients included in the MLR calibration model.

$$Y_p = X_{\lambda_n} \cdot \beta_n + \varepsilon \qquad (4.16)$$

The absorbance wavelengths, respective regressor coefficients, and intercepts for the calibrated MLR models for all data sets are presented in *Tables 4.3* *to* *4.5*. Hydrogen, H/C, Density, 400-500°C, +343°C, and +343°C conversion did not have MLR models from the stepwise method in the first data set in *Table 4.3*. Carbon did not have a MLR model in the fourth data set of *Table 4.4*. The α-aromatic hydrogen, aromatic hydrogen, and aromatic hydrogen conversion did not have MLR models for the fifth and sixth data sets in *Table 4.5*. The β coefficients are listed in respective order to the absorbance wavelength channels listed in *Tables 4.3* *to* *4.5*. The intercept, ε, is included for all MLR models calibrated. Absorbance wavelength channels and corresponding regressor coefficients for MLR models of boiling point distribution fractions of the first four data sets are found in *Tables H1 to H4* in *Appendix H*.

Table 4.3. Absorbance wavelengths, respective regressor coefficients, and intercepts of the calibrated MLR models for the first two data sets.

Measured Property	First Data Set (34)		Second Data Set (25)	
	Absorbance λ (nm)	β Coefficients	Absorbance λ (nm)	Coefficients
Carbon	602, 604, 901, 1073	-189, 183, 27.3, -124 ε = 87.8	568	-8.88 ε = 87.8
Hydrogen	-	-	490, 493, 500, 504, 510, 512, 512, 529, 535, 554, 816	125, -139, 40.7, -99.8, -48.3, 67.9, 51.8, 17.9, -22.1, 12.2, -32.2 ε = 12.2
H/C	-	-	465, 466, 489, 493, 494, 509, 512, 517, 816	-5.76, 4.79, 6.04, 12.3, -14.5, -18.1, -1.50, 10.3, 7.06 ε = 1.69
Sulfur	614, 615, 619, 630, 902	-513, 324, 284, -71.2, -31.4 ε = 0.398	507	5.27 ε = 0.23
Nitrogen	723, 1056	2.04, -4.13 ε = 0.09	450, 464, 465, 467, 469, 472, 472, 474, 477, 507, 510, 513, 515, 518, 518, 520, 523, 527, 529, 536, 648, 655, 815	-0.439, 2.09, 1.43, 0.476, -0.886, 9.98, -1.93, -12.7, -2.26, 15, 5.33, -7.73, -1.47, -5.92, -0.212, 4.32, -6.69, -11.7, 13.1, 0.015, 0.009, 0.006, 1.62 ε = 0.042
Density	-	-	451, 472, 475, 751	-0.176, 3.03, -2.95, 0.652 ε = 0.91
IBP-300°C	688, 723, 1017	374, -618, 620 ε = 7.54	450, 471, 472, 472, 474, 475, 476, 477, 480, 498, 504, 506, 512, 513, 515, 516, 816	40.5, -1384, -1097, 416, 4069, -1680, -544, 579, -134, 324, -729, -706, -150, 819, 44.2, 181, -584 ε = 11.2
300-400°C	624, 627, 659, 668	1138, -1331, 958, -870 ε = 40.3	516, 517, 518, 574, 575	-1081, -694, 1843, -3515, 3445 ε = 41.6
400-500°C	-	-	500, 500	-1913, 1962 ε = 48.2
+500°C	614, 619	-362, 404 ε = 3.67	515, 516, 518, 518, 528	357, 343, -636, -233, 174 ε = 2.99
+343°C	-	-	450, 450, 472, 474	467, -566, 1895, -1827 ε = 80.2
Sulfur Conversion	614, 615, 619, 630, 902	15579, -9816, -8619, 2162, 955 ε = 87.96	484, 489, 490, 495, 497, 505, 506, 507, 525, 530, 558, 627	-2337, 3005, 3509, -517, -5482, 4862, -5396, 756, 5439, -3996, 536, -564, ε = 94.96
Nitrogen Conversion	723, 1056	-1156, 2346 ε = 48.7	450, 452, 465, 469, 469, 471, 472, 472, 474, 476, 479, 484, 507, 507, 510, 511, 516, 518, 608, 620, 816	3289, -3238, -2130, -875, -182, 137, -3360, -1484, 13576, -5768, 2288, 496, -649, -5500, -1434, -4352, -267, 9715, 1260, -1100, -1841 ε = 63.2
+343°C Conversion	-	-	450, 450, 472, 474	-495, 599, -1995, 1924, ε = 15.5

Table 4.4. Absorbance wavelengths, respective regressor coefficients, and intercepts of the calibrated MLR models for the third and fourth data sets.

Measured Property	Third Data Set (14) λ (nm)	Third Data Set (14) Coefficients	Fourth Data Set (11) λ (nm)	Fourth Data Set (11) Coefficients
Carbon	567	-8.56 $\varepsilon = 87.8$	-	-
Hydrogen	453, 472, 473, 722	2.74, 66.6, -152, 82.6 $\varepsilon = 11.4$	467	-2.81 $\varepsilon = 12.3$
H/C	450, 469	0.491, -0.728 $\varepsilon = 1.604$	463	-0.391 $\varepsilon = 1.69$
Sulfur	454, 457, 470, 472, 472, 474	15.1, -44, 166, -201, 155, -88.8 $\varepsilon = 1.08$	500, 502	-535, 565 $\varepsilon = 0.204$
Nitrogen	451, 469, 472, 476, 507, 510, 520	-0.655, 2.06, 2.54, -4.92, 5.55, -1.59 -3.15 $\varepsilon = 0.123$	467	0.54 $\varepsilon = 0.032$
Density	451, 469, 480	-0.218, 0.562, -0.303, $\varepsilon = 0.927$	450, 463, 467, 468, 472	-0.668, 2.36, 0.679, -7.57, 5.48 $\varepsilon = 0.92$
IBP-300°C	450, 469, 473	59.7, -417, 353 $\varepsilon = 7.13$	465	-49.9 $\varepsilon = 12.7$
300-400°C	454, 472	51.3, -76.4 $\varepsilon = 35.5$	502	-53.8 $\varepsilon = 41.8$
400-500°C	451, 468, 469, 478, 481, 501, 514, 520, 579, 624, 632, 740	-71.5, -638, 840, -110, 1.29, 132, -7.94, -166, -8, -582 627, 12.6 $\varepsilon = 51.1$	465, 467	-1517, 1635 $\varepsilon = 43.2$
+500°C	451, 472	-16, 24.8 $\varepsilon = 5.34$	502	16.7 $\varepsilon = 3.14$
+343°C	451, 469, 476	-89.9, 391, -294 $\varepsilon = 83.4$	467	73.1 $\varepsilon = 74.8$
Sulfur Conversion	454, 473	283, -459 $\varepsilon = 65.1$	500, 502	16259, -17196 $\varepsilon = 93.9$
Nitrogen Conversion	451, 469, 472, 476, 507, 510, 520	372.2, -1184, -1417, 2782, -3144, 884, 1797 $\varepsilon = 30.3$	467	-306 $\varepsilon = 81.8$
+343°C Conversion	451, 469, 476	94.4, -412, 311 $\varepsilon = 12.3$	467	-76.9 $\varepsilon = 21.3$

Table 4.5. Absorbance wavelengths, respective regressor coefficients, and intercepts of the calibrated MLR models for the fifth and sixth data sets.

Measured Property	Fifth Data Set (6)		Sixth Data Set (13)	
	λ (nm)	Coefficients	λ (nm)	Coefficients
Aromatic Hydrogen	463	2.53 ε = 4.18	-	-
α-Aromatic Hydrogen	-	-	529, 553, 555	102.8, -926, 815 ε = 12.9
Aliphatic Hydrogen	457	-4.52 ε = 84.1	510, 553, 555	-55.2, 1152, -1092 ε = 81.1
Aromatic Hydrogen Conversion	463	-41.5 ε = 31.5	-	-
Total Aromatic Hydrogen Conversion	457	-22.4 ε = 21.3	516, 531, 553, 555	-1240, 2069, 3061, -3889 ε = 24.6

A limited number of the properties in the second data set in *Table 4.3* calibrated with a high (n>10) number of variables compared to the remaining properties in other data sets. Wavelength channel variables in the 450 to 600nm region are included in most of the MLR models calibrated. A summary of the number of parameters and the adjusted coefficient of determination for each MLR model calibrated for all data sets is shown in *Table 4.6*.

Table 4.6. Number of parameters and the adjusted coefficient of determination for each MLR model calibrated.

Measured Property	First Data Set (34)		Second Data Set (25)		Third Data Set (14)		Fourth Data Set (11)	
	#	R^2_{adj}	#	R^2_{adj}	#	R^2_{adj}	#	R^2_{adj}
Carbon	4	0.69	1	0.56	1	0.77	-	-
Hydrogen	-	-	11	0.99	4	0.96	1	0.55
H/C	-	-	9	0.98	2	0.74	1	0.66
Sulfur	5	0.85	1	0.72	6	1	2	0.61
Nitrogen	2	0.28	23	1	7	1	1	0.71
Density	-	-	4	0.89	3	0.98	5	1
IBP-300°C	3	0.31	17	1	3	0.98	1	0.84
300-400°C	4	0.71	5	0.94	2	0.93	1	0.54
400-500°C	-	-	2	0.56	12	1	2	0.90
+500°C	2	0.51	5	0.87	2	0.95	1	0.30
+343°C	-	-	4	0.87	3	0.97	1	0.83
Sulfur Conversion	5	0.84	12	1	2	0.94	2	0.60
Nitrogen Conversion	2	0.28	21	1	7	1	1	0.71
+343°C Conversion	-	-	4	0.87	3	0.97	1	0.84

Measured Property	Fifth Data Set (6)		Sixth Data Set (13)	
	#	R^2_{adj}	#	R^2_{adj}
Aromatic Hydrogen	1	0.75	-	-
α-Aromatic Hydrogen	-	-	3	0.79
Aliphatic Hydrogen	1	0.68	3	0.78
Aromatic Hydrogen Conversion	1	0.75	-	-
Total Aromatic Hydrogen Conversion	1	0.68	4	0.86

The third data set, sulfided pellet reactions, resulted in the highest average of adjusted coefficient of determinations for the MLR models calibrated. Aromatic and total aromatic hydrogen conversion resulted in the best coefficients for the fifth and sixth data sets, respectively.
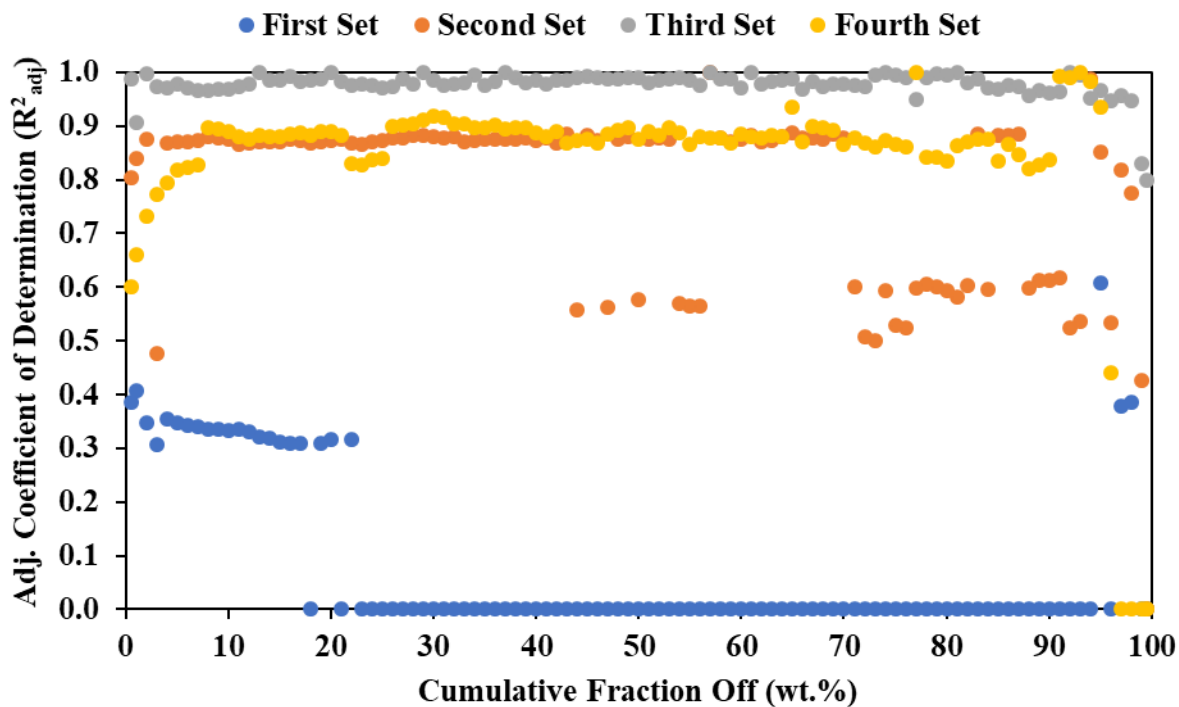
Figure 4.48. Adjusted coefficient of determination obtained from MLR calibration models for the boiling point distribution fractions.

Similar to results in *Table 4.6,* the third data set, reactions with sulfided catalyst pellets, resulted in the highest adjusted coefficient of determination for the cumulative boiling point distribution fractions in *Figure 4.48*. The first data set did not result in calibration models from the stepwise method in the 25 to 95wt.% fractional range.

4.7.4 Principal Component Regression (PCR)

Principal Component Analysis (PCA)

Principal component analysis is performed on all six data sets to reduce the dimensionally of the visible spectra to a limited number of latent variables. These latent variables, or principal components, are uncorrelated with each other and exhibit a high degree of correlation to the visible spectra data set through an orthogonal linear transformation. Each principal component explains a fraction of the variation in the spectral data set. The first principal component explains the maximum variance in the data set. Subsequent components explain the remaining variance. Matlab is used to complete PCA on the six data sets [2].

196

$$[coeff,\ score,\ latent,\ tsquared,\ explained,\ mu] = pca(X); \qquad (4.17)$$

Where X is a m×n matrix of the visible absorbance data (m samples × n wavelengths). Score (S) is a m×(m-1) matrix, coeff (L) is a n×(m-1) loadings matrix, and mu ($\bar{X}$) is the mean (1×n) of the visible absorbance data set. Latent is (m-1)×1 matrix of variances for each principal component and tsquared is Hotelling's statistic of the standardized scores (sum of squares in a m×1 matrix). The data is mean centered in the PCA code. A deeper review of the exact calculation methodology is found elsewhere [3-5]. The decomposition of spectra into scores and loadings is shown:

$$X = S \times L^T + \bar{X} \qquad (4.18)$$

The variance explained (*explained,* (m-1)×1 matrix) for each principal component in the latent matrix is highlighted for each visible absorption data set in *Table 4.7*. The first component explains nearly all, >93%, variation, in the six data sets. The third and subsequent components explain <2% of variation in the six data sets. Variance explained by the remaining principal components are plotted in *Figures H29 to H34* of *Appendix H*.

Table 4.7. Variance explained by principal components for each visible absorption data set.

Principal Component (PC)	First Data Set (34)	Second Data Set (25)	Third Data Set (14)	Fourth Data Set (11)	Fifth Data Set (6)	Sixth Data Set (13)
PC 1	97.7	98.1	99.1	93.7	98.5	98.2
PC 2	1.7	1.5	0.7	5.2	1.3	1.3
PC's 3 to (m-1)	0.6	0.4	0.2	1.1	0.2	0.5

Analysis plots for the second component as function of the first is found in *Figures H35 to H40* in *Appendix H* for all six data sets.

Principal Component Regression

To avoid multicollearity issues, Principal Component Regression (PCR) is used as a modeling approach for the spectral data. The principal components, as calculated with *equation 4.17*, are

used as regressors with the measured property data in each set. Coefficients are solved (as in equation 4.10) to obtain models that calibrate the physicochemical properties in each data set. To determine the optimal number of variables for model inclusion, a cross validation approach similar to Wentzell et al. is used [6]. To avoid overfitting the model, Matlab is used to calculate a mean squared prediction error (MSPE), similar to equation 4.3, for each principal component added to the model. The corresponding PC at the minimum MSPE indicates additional variables overfit the model.

$$PCRmsep = sum(crossval(@pcrsse,X,Y,'KFold',10),1) / m \qquad (4.19)$$

Where PCRmsep is the MSPE, X is the spectral data set, Y is the measured property calibrated, m is the sample size, and 10 is chosen as the maximum number of principal components added to the model. The code in equation 4.19 mean centers the X and Y data sets. From the minimum MSPE, the number of principal component regressors included in the calibrated model for each property is presented in *Table 4.8*.

The minimum number of PC's included the model (n_{min}), columns from the score matrix (S_{min} in equation 4.18), are used to determine the regressor coefficients:

$$\beta_{PCR} = (S_{min}' \cdot S_{min})^{-1} \cdot S_{min}' \cdot Y^{cen} \qquad (4.20)$$

Where β_{PCR} is a ($n_{min} \times 1$) matrix. The regressor coefficients are transformed back to original and uncentered coefficients using the minimum loadings L_{min}^T ($n \times n_{min}$):

$$\beta_{PCR.Cor} = L_{min}^T \cdot \beta_{PCR} \qquad (4.21)$$

The intercept, ε, is calculated from the corrected uncentered regressor coefficients:

$$\varepsilon = \bar{Y} - \bar{X} \cdot \beta_{PCR.Cor} \qquad (4.22)$$

The predicted property is determined:

$$Y_p = X \cdot \beta_{PCR.Cor} + \varepsilon \qquad (4.23)$$

The coefficient of determination and the subsequent adjusted coefficient is calculated with n_{min} for each property in all six data sets. All adjusted coefficient of determination results are shown in *Table 4.8*.

Table 4.8. Minimum number of parameters and the adjusted coefficient of determination for each PCR model calibrated.

Measured Property	First Data Set (34)		Second Data Set (25)		Third Data Set (14)		Fourth Data Set (11)	
	n_{min}	R^2_{adj}	n_{min}	R^2_{adj}	n_{min}	R^2_{adj}	n_{min}	R^2_{adj}
Carbon	2	0.28	1	0.44	6	0.86	1	0.23
Hydrogen	6	0.30	4	0.56	3	0.83	1	0.53
H/C	6	0.27	4	0.44	3	0.78	1	0.63
Sulfur	10	0.82	10	0.88	7	0.91	1	0.34
Nitrogen	10	0.72	5	0.63	3	0.82	9	1
Density	7	0.65	5	0.77	6	0.95	4	0.77
IBP-300°C	10	0.79	5	0.64	6	0.97	1	0.80
300-400°C	6	0.58	5	0.80	4	0.92	1	0.46
400-500°C	7	0.64	5	0.73	6	0.94	9	0.97
+500°C	10	0.72	5	0.78	8	0.97	1	0.24
+343°C	7	0.63	6	0.68	7	0.96	4	0.85
Sulfur Conversion	6	0.65	10	0.88	9	0.97	1	0.34
Nitrogen Conversion	8	0.63	5	0.63	6	0.92	1	0.68
+343°C Conversion	10	0.82	5	0.70	5	0.91	4	0.85

Measured Property	Fifth Data Set (6)		Sixth Data Set (13)	
	n_{min}	R^2_{adj}	n_{min}	R^2_{adj}
Aromatic Hydrogen	3	0.80	4	0.40
α-Aromatic Hydrogen	1	0.29	4	0.68
Aliphatic Hydrogen	1	0.61	4	0.69
Aromatic Hydrogen Conversion	1	0.71	4	0.40
Total Aromatic Hydrogen Conversion	3	0.84	4	0.69

The third data set, reactions with sulfided pellets, resulted in the highest average of adjusted coefficient results compared to the other five in *Table 4.8*. The fourth and fifth data sets had the lowest average of regressor parameters included in their PCR calibration models. Nitrogen in the fourth data set, IBP-300°C, +500°C, and sulfur conversion had high coefficient of determinations in their calibration models.
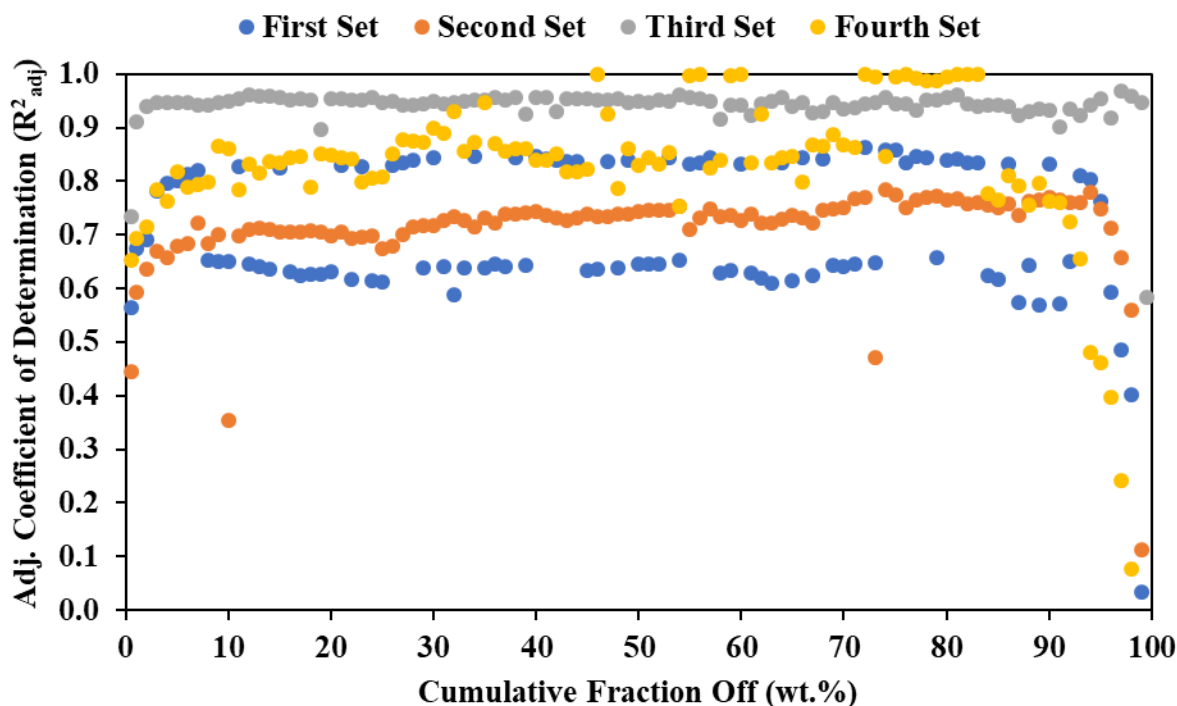
Figure 4.49. Adjusted coefficient of determination results from PCR calibration models for the boiling point distribution fractions.

The third data set, reactions with catalyst pellets, resulted in the highest adjusted coefficient of determination for most of the boiling point distribution fractions models calibrated in *Figure 4.49*.

4.7.5 Partial Least Squares Regression (PLSR)

Partial least square regression (PLSR) is similar to PCR by calculating component variables that are linear combinations of the spectral data set. However, PLSR considers the measured properties in the calibration models. Rather than maximizing the variance of the spectral data set as in PCA, the covariance between the spectral data and measured properties is maximized in each PLS

component. This consideration leads to calibration models with fewer component variables in the overall PLS model. Similar to the PCR, a cross validation approach is used to include the minimum number of relevant variables in each calibration model. A deeper review of the exact calculation methodology is found elsewhere [3-5]. Matlab is used to calculate a mean squared prediction error (MSPE) for each component added to the model [2]. The corresponding component at the minimum MSPE indicates additional variables overfit the model.

$$[Xl,Yl,Xs,Ys,beta,pctVar,PLSmsep] = plsregress(X,Y,k,'CV',k) \qquad (4.24)$$

Where Xl (n×k) and Yl (1×k) are the loading matrices, Xs (m×k) and Ys (m×k) are the score matrices, beta (n×1) is the corrected uncentered linear regressed parameters (similar to equation 4.17), pctVar is the variance explained by each component, and PLSmsep are the calculated MSPE from the cross validation up to k components including zero as coded in equation 4.24. Depending on which component yields the minimum MSPE from PLSmsep up to k, the regression is recalculated with the minimum number of components (n_{min}). For this case, k=10 for the initial cross-validation test. The minimum number of component regressors included for each property calibrated is presented in *Table 4.9* for all six data sets.

$$[Xloadings,Yloadings,Xscores,Yscores,betaPLS] = plsregress(X,Y,n_{min}) \qquad (4.25)$$

The betaPLS is the corrected uncentered linear regressed parameter at n_{min}. The intercept, ε, is calculated from the corrected uncentered regressor coefficients:

$$\varepsilon = \bar{Y} - \bar{X} \cdot betaPLS \qquad (4.26)$$

The predicted property is determined:

$$Y_p = X \cdot betaPLS + \varepsilon \qquad (4.27)$$

The coefficient of determination and the subsequent adjusted coefficient is calculated with n_{min} for each property in all six data sets. All adjusted coefficient of determination results for each calibrated PLSR model is highlighted in *Table 4.9*.

Table 4.9. Minimum number of parameters and the adjusted coefficient of determination for each PLSR model calibrated.

Measured Property	First Data Set (34)		Second Data Set (25)		Third Data Set (14)		Fourth Data Set (11)	
	n_{min}	R^2_{adj}	n_{min}	R^2_{adj}	n_{min}	R^2_{adj}	n_{min}	R^2_{adj}
Carbon	7	0.72	2	0.54	4	0.90	1	0.24
Hydrogen	2	0.08	4	0.62	3	0.85	4	0.65
H/C	8	0.75	9	0.83	3	0.80	4	0.71
Sulfur	8	0.92	4	0.83	5	0.95	1	0.35
Nitrogen	6	0.74	5	0.69	3	0.86	1	0.68
Density	9	0.90	5	0.80	4	0.95	1	0.67
IBP-300°C	8	0.85	4	0.68	5	0.98	1	0.80
300-400°C	9	0.92	10	0.98	3	0.91	1	0.46
400-500°C	8	0.90	4	0.76	4	0.95	7	1
+500°C	8	0.83	4	0.79	4	0.97	1	0.24
+343°C	8	0.87	4	0.72	5	0.97	1	0.80
Sulfur Conversion	8	0.92	8	0.95	5	0.95	1	0.34
Nitrogen Conversion	7	0.78	4	0.67	3	0.86	1	0.68
+343°C Conversion	9	0.88	4	0.72	5	0.97	1	0.80

Measured Property	Fifth Data Set (6)		Sixth Data Set (13)	
	n_{min}	R^2_{adj}	n_{min}	R^2_{adj}
Aromatic Hydrogen	1	0.71	4	0.50
α-Aromatic Hydrogen	1	0.30	4	0.73
Aliphatic Hydrogen	2	0.76	4	0.73
Aromatic Hydrogen Conversion	3	0.83	4	0.50
Total Aromatic Hydrogen Conversion	3	0.86	4	0.73

The third data set, reactions with sulfided pellets, resulted in the highest average of adjusted coefficient results compared to the other five in *Table 4.9*. The fourth and fifth data sets had the lowest average of regressor parameters included in their PLSR calibration models. Boiling point distribution fractions had high adjusted coefficient of determinations in their calibration models with few exceptions.
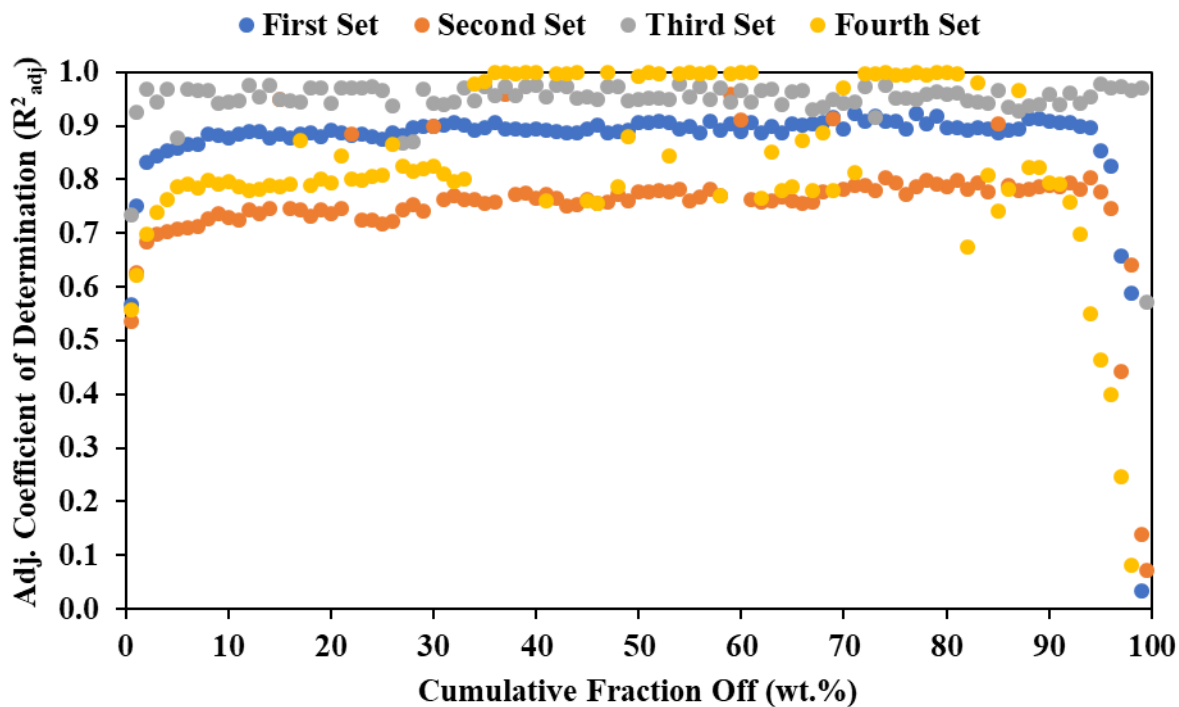
Figure 4.50. Adjusted coefficient of determination obtained from PLSR calibration models for the boiling point distribution fractions.

The third data set, reactions with catalyst pellets, resulted in the highest adjusted coefficient of determination for most of the boiling point distribution fraction models calibrated in *Figure 4.50*.

4.7.6 Model Selection Criteria

Four additional model selection criterions are used to assess which physicochemical calibration models are favorable [7]. All Akaike and Bayesian information criterions are log based functions compared to the adjusted coefficient of determination. A couple of the references report the formula's in terms of sum of square errors to compare models of the same units [7-9]. The current study uses the relative squared error, RSE in equation 4.5, to compare models with different units. This is similar to what is calculated for the adjusted coefficient of determination. The formula for each criterion is presented in section 4.7.6.

Akaike Information Criterion (AIC)

The AIC method explains data based on the minimum number of free parameters in the model [8]:

$$AIC = 2 \cdot k + m \cdot \ln\left(\frac{RSE}{m}\right) \qquad (4.28)$$

Where k is the number of parameters, m is the sample size, and RSE is the relative squared error from equation 4.5. The lower the AIC value, the more likely the model is favored.

Corrected Akaike Information Criterion (AIC$_c$)

For smaller sample sizes, when m/k is less than 40, the corrected Akaike Information Criterion (AIC$_c$) is preferred [9]:

$$AIC_c = AIC + \frac{2 \cdot k \cdot (k+1)}{m - k - 1} \qquad (4.29)$$

Unbiased Akaike Information Criterion (AIC$_u$)

The unbiased Akaike Information Criterion AIC$_u$ is similar to the AIC$_c$, however the sum of squared errors is relative to the degrees of freedom (m-k) rather than then the sample size itself:

$$AIC_u = m \cdot \ln\left(\frac{RSE}{m - k}\right) + 2 \cdot k + \frac{2 \cdot k \cdot (k+1)}{m - k - 1} \qquad (4.30)$$

Relative AIC and Weights

To assess the strength of a physicochemical calibration model, the delta AIC is calculated [8-9]:

$$\Delta_i = AIC_i - AIC_{min} \qquad (4.31)$$

The minimum AIC (AIC$_{min}$) is determined from the data set. Comparison is limited to similar sample sizes (m). Model selection guides suggest $\Delta_i < 2$ is substantial evidence to support the model while $\Delta_i > 10$ is no support at all [9]. Normalization of the relative AIC's to weights help

deduce the relative likelihood or probability the calibration models are favorable compared to the rest [8-9]:

$$\omega_i = \frac{exp(-0.5 \cdot \Delta_i)}{\sum_{p=1}^{p} exp(-0.5 \cdot \Delta_p)} \times 100 \qquad (4.32)$$

Bayesian Information Criterion (BIC)

Compared to AIC, BIC penalizes the number of parameters based on the natural logarithm of the sample size, rather than 2·k. If the sample size is >8, the BIC has a stronger penalization compared to the AIC. The lower the BIC value, the more likely the model is favored.

$$BIC = k \cdot \ln m + m \cdot \ln \left(\frac{RSE}{m} \right) \qquad (4.33)$$

4.7.7 Model Selection Criteria Results

Model selection criteria results are presented in section 4.7.7.

Table 4.10. Selection criteria results for SLS calibration models.

Measured Property	First Data Set (34)				Second Data Set (25)			
	AIC	AIC$_c$	AIC$_u$	BIC	AIC	AIC$_c$	AIC$_u$	BIC
Carbon	-11.4	-11.2	-10.2	-9.8	-19.4	-19.3	-18.2	-18.2
Hydrogen	-1	-0.9	0.1	0.5	-12.6	-12.5	-11.5	-11.4
H/C	0.4	0.5	1.5	1.9	-6.9	-6.7	-5.7	-5.7
Sulfur	-6.8	-6.7	-5.7	-5.3	-30.9	-30.7	-29.7	-29.6
Nitrogen	-3.3	-3.2	-2.2	-1.8	-11.4	-11.3	-10.2	-10.2
Density	-1.8	-1.7	-0.6	-0.3	-15.6	-15.4	-14.4	-14.3
IBP-300°C	-3.3	-3.2	-2.2	-1.8	-8	-7.8	-6.8	-6.8
300-400°C	-3.3	-3.2	-2.2	-1.8	-24.9	-24.7	-23.7	-23.7
400-500°C	-1.5	-1.3	-0.3	0.1	-13.6	-13.4	-12.4	-12.4
+500°C	-5.3	-5.2	-4.2	-3.8	-20.9	-20.8	-19.7	-19.7
+343°C	-2	-1.9	-0.9	-0.5	-10	-9.8	-8.8	-8.8
Sulfur Conversion	-6.8	-6.7	-5.7	-5.3	-30.9	-30.7	-29.7	-29.6
Nitrogen Conversion	-3.3	-3.2	-2.2	-1.8	-11.4	-11.2	-10.2	-10.2
+343°C Conversion	-2.1	-1.9	-0.9	-0.5	-9.9	-9.8	-8.7	-8.7

Measured Property	Third Data Set (14)				Fourth Data Set (11)			
	AIC	AIC$_c$	AIC$_u$	BIC	AIC	AIC$_c$	AIC$_u$	BIC
Carbon	-19.6	-19.2	-18.2	-18.9	-2.9	-2.4	-1.4	-2.5
Hydrogen	-13.2	-12.9	-11.9	-12.6	-8.1	-7.6	-6.6	-7.7
H/C	-10.7	-10.4	-9.4	-10.1	-10.9	-10.5	-9.4	-10.5
Sulfur	-24.9	-24.5	-23.5	-24.2	-4.8	-4.4	-3.3	-4.4
Nitrogen	-15	-14.7	-13.6	-14.3	-12.7	-12.3	-11.2	-12.3
Density	-14.3	-14	-12.9	-13.6	-12.3	-11.8	-10.8	-11.9
IBP-300°C	-11.6	-11.3	-10.2	-11	-19	-18.6	-17.5	-18.6
300-400°C	-19	-18.7	-17.7	-18.4	-7.8	-7.4	-6.3	-7.4
400-500°C	-15.9	-15.6	-14.5	-15.3	-18.8	-18.4	-17.3	-18.4
+500°C	-19.1	-18.7	-17.7	-18.4	-3.1	-2.6	-1.6	-2.7
+343°C	-13.1	-12.8	-11.8	-12.5	-18.9	-18.5	-17.4	-18.5
Sulfur Conversion	-24.8	-24.5	-23.4	-24.2	-4.8	-4.3	-3.3	-4.4
Nitrogen Conversion	-15	-14.7	-13.6	-14.4	-12.7	-12.3	-11.2	-12.3
+343°C Conversion	-13.1	-12.8	-11.7	-12.5	-19.1	-18.6	-17.6	-18.7

Measured Property	Fifth Data Set (6)				Sixth Data Set (13)			
	AIC	AIC$_c$	AIC$_u$	BIC	AIC	AIC$_c$	AIC$_u$	BIC
Aromatic Hydrogen	-7.6	-6.6	-5.5	-7.8	-1.7	-1.3	-0.3	-1.1
α-Aromatic Hydrogen	-2.1	-1.1	-0.1	-2.4	-3.6	-3.2	-2.2	-3
Aliphatic Hydrogen	-6.2	-5.2	-4.1	-6.4	-3.3	-2.9	-1.9	-2.7
Aromatic Hydrogen Conversion	-7.6	-6.6	-5.5	-7.8	-1.7	-1.3	-0.3	-1.1
Total Aromatic Hydrogen Conversion	-6.2	-5.2	-4.1	-6.4	-3.3	-2.9	-1.9	-2.7

Table 4.11. AIC weighted results for SLS calibration models.

Measured Property	First Data Set (34)			Second Data Set (25)		
	AIC	AICc	AICu	AIC	AICc	AICu
Carbon	73.5	72.6	72.6	0.2	0.2	0.2
Hydrogen	0.4	0.4	0.4	0	0	0
H/C	0.2	0.2	0.2	0	0	0
Sulfur	7.4	7.7	7.7	48.5	48.5	48.5
Nitrogen	1.3	1.3	1.3	0	0	0
Density	0.6	0.6	0.6	0	0	0
IBP-300°C	1.3	1.3	1.3	0	0	0
300-400°C	1.3	1.3	1.3	2.4	2.4	2.4
400-500°C	0.5	0.5	0.5	0	0	0
+500°C	3.5	3.6	3.6	0.3	0.3	0.3
+343°C	0.7	0.7	0.7	0	0	0
Sulfur Conversion	7.4	7.7	7.7	48.5	48.5	48.5
Nitrogen Conversion	1.3	1.3	1.3	0	0	0
+343°C Conversion	0.7	0.7	0.7	0	0	0

Measured Property	Third Data Set (14)			Fourth Data Set (11)		
	AIC	AICc	AICu	AIC	AICc	AICu
Carbon	3.3	3.2	3.3	0	0	0
Hydrogen	0.1	0.1	0.1	0.1	0.1	0.1
H/C	0	0	0	0.4	0.4	0.4
Sulfur	46.1	45	46	0	0	0
Nitrogen	0.3	0.3	0.3	1.1	1.1	1.1
Density	0.2	0.2	0.2	0.9	0.8	0.9
IBP-300°C	0.1	0.1	0.1	24.7	25	24.7
300-400°C	2.4	2.5	2.5	0.1	0.1	0.1
400-500°C	0.5	0.5	0.5	22.3	22.6	22.3
+500°C	2.5	2.5	2.5	0	0	0
+343°C	0.1	0.1	0.1	23.5	23.8	23.5
Sulfur Conversion	43.8	45	43.8	0	0	0
Nitrogen Conversion	0.3	0.3	0.3	1.1	1.1	1.1
+343°C Conversion	0.1	0.1	0.1	25.9	25	25.9

Measured Property	Fifth Data Set (6)			Sixth Data Set (13)		
	AIC	AICc	AICu	AIC	AICc	AICu
Aromatic Hydrogen	32.7	32.7	32.7	11.1	11.1	11.1
α-Aromatic Hydrogen	2.1	2.1	2.2	28.6	28.6	28.6
Aliphatic Hydrogen	16.2	16.2	16.2	24.6	24.6	24.6
Aromatic Hydrogen Conversion	32.7	32.7	32.7	11.1	11.1	11.1
Total Aromatic Hydrogen Conversion	16.2	16.2	16.2	24.6	24.6	24.6

Table 4.12. Selection criteria results for MLR calibration models.

Measured Property	First Data Set (34)				Second Data Set (25)			
	AIC	AIC$_c$	AIC$_u$	BIC	AIC	AIC$_c$	AIC$_u$	BIC
Carbon	-36.4	-35	-30.8	-30.3	-19.4	-19.3	-18.2	-18.2
Hydrogen	-	-	-	-	-108.4	-88	-73.6	-94.9
H/C	-	-	-	-	-88.2	-76.2	-65.1	-77.3
Sulfur	-59.1	-57	-51.6	-51.5	-30.9	-30.7	-29.7	-29.6
Nitrogen	-9.3	-8.9	-6.9	-6.2	-796.8	307.2	370.4	-768.7
Density	-	-	-	-	-52.2	-50.2	-45.8	-47.3
IBP-300°C	-9.7	-8.9	-5.8	-5.2	-214.1	-126.6	-98.2	-193.3
300-400°C	-38.4	-37	-32.8	-32.3	-65.4	-62.3	-56.7	-59.3
400-500°C	-	-	-	-	-18.9	-18.3	-16.3	-16.5
+500°C	-22.4	-22	-20	-19.4	-47.1	-43.9	-38.3	-41
+343°C	-	-	-	-	-47.5	-45.5	-41.1	-42.6
Sulfur Conversion	-59	-56.8	-51.4	-51.3	-138.4	-112.4	-96.1	-123.8
Nitrogen Conversion	-9.3	-8.9	-6.9	-6.2	-379.5	-71.5	-25.7	-353.9
+343°C Conversion	-	-	-	-	-47.5	-45.5	-41.2	-42.7

Measured Property	Third Data Set (14)				Fourth Data Set (11)			
	AIC	AIC$_c$	AIC$_u$	BIC	AIC	AIC$_c$	AIC$_u$	BIC
Carbon	-19.6	-19.2	-18.2	-18.9	-	-	-	-
Hydrogen	-43.2	-38.7	-34	-40.6	-8.1	-7.6	-6.6	-7.7
H/C	-17	-15.9	-13.8	-15.8	-10.9	-10.5	-9.4	-10.5
Sulfur	-85.6	-73.6	-65.8	-81.8	-8.7	-7.2	-5	-7.9
Nitrogen	-95.3	-76.6	-66.9	-90.8	-12.7	-12.3	-11.2	-12.3
Density	-50	-47.6	-44.2	-48.1	-78.5	-66.5	-59.8	-76.5
IBP-300°C	-50.9	-48.5	-45.1	-49	-19	-18.6	-17.5	-18.6
300-400°C	-36.6	-35.5	-33.3	-35.3	-7.8	-7.4	-6.3	-7.4
400-500°C	-380	-68	-40.8	-372.3	-23.9	-22.4	-20.2	-23.1
+500°C	-41.7	-40.6	-38.5	-40.4	-3.1	-2.6	-1.6	-2.7
+343°C	-47.6	-45.2	-41.8	-45.6	-18.9	-18.5	-17.4	-18.5
Sulfur Conversion	-36.9	-35.8	-33.6	-35.6	-8.7	-7.2	-5	-7.9
Nitrogen Conversion	-96.2	-77.6	-67.9	-91.8	-12.7	-12.3	-11.2	-12.3
+343°C Conversion	-47.4	-45	-41.7	-45.5	-19.1	-18.6	-17.6	-18.7

Measured Property	Fifth Data Set (6)				Sixth Data Set (13)			
	AIC	AIC$_c$	AIC$_u$	BIC	AIC	AIC$_c$	AIC$_u$	BIC
Aromatic Hydrogen	-7.6	-6.6	-5.5	-7.8	-	-	-	-
α-Aromatic Hydrogen	-	-	-	-	-18.2	-15.6	-12.2	-16.5
Aliphatic Hydrogen	-6.2	-5.2	-4.1	-6.4	-17.2	-14.5	-11.1	-15.5
Aromatic Hydrogen Conversion	-7.6	-6.6	-5.5	-7.8	-	-	-	-
Total Aromatic Hydrogen Conversion	-6.2	-5.2	-4.1	-6.4	-22.8	-17.8	-13	-20.5

Table 4.13. AIC weighted results for MLR calibration models.

Measured Property	First Data Set (34)			Second Data Set (25)		
	AIC	AIC$_c$	AIC$_u$	AIC	AIC$_c$	AIC$_u$
Carbon	0	0	0	0	0	0
Hydrogen	0	0	0	0	0	0
H/C	0	0	0	0	0	0
Sulfur	51.2	52.5	52.5	0	0	0
Nitrogen	0	0	0	100	100	0
Density	0	0	0	0	0	0
IBP-300°C	0	0	0	0	0	74.1
300-400°C	0	0	0	0	0	0
400-500°C	0	0	0	0	0	0
+500°C	0	0	0	0	0	0
+343°C	0	0	0	0	0	0
Sulfur Conversion	48.7	47.5	47.5	0	0	25.9
Nitrogen Conversion	0	0	0	0	0	0
+343°C Conversion	0	0	0	0	0	0

Measured Property	Third Data Set (14)			Fourth Data Set (11)		
	AIC	AIC$_c$	AIC$_u$	AIC	AIC$_c$	AIC$_u$
Carbon	0	0	0	0	0	0
Hydrogen	0	0	0	0	0	0
H/C	0	0	0	0	0	0
Sulfur	0	7.7	17.9	0	0	0
Nitrogen	0	34.7	31	0	0	0
Density	0	0	0	100	100	100
IBP-300°C	0	0	0	0	0	0
300-400°C	0	0	0	0	0	0
400-500°C	100	0.5	0	0	0	0
+500°C	0	0	0	0	0	0
+343°C	0	0	0	0	0	0
Sulfur Conversion	0	0	0	0	0	0
Nitrogen Conversion	0	57.1	51.1	0	0	0
+343°C Conversion	0	0	0	0	0	0

Measured Property	Fifth Data Set (6)			Sixth Data Set (13)		
	AIC	AIC$_c$	AIC$_u$	AIC	AIC$_c$	AIC$_u$
Aromatic Hydrogen	33.4	33.4	33.4			
α-Aromatic Hydrogen	0	0	0	8.6	21.8	32.6
Aliphatic Hydrogen	16.6	16.6	16.6	5.2	12.6	18.8
Aromatic Hydrogen Conversion	33.4	33.4	33.4			
Total Aromatic Hydrogen Conversion	16.6	16.6	16.6	86.1	65.6	48.6

Table 4.14. Selection criteria results for PCR calibration models.

Measured Property	First Data Set (34)				Second Data Set (25)			
	AIC	AIC$_c$	AIC$_u$	BIC	AIC	AIC$_c$	AIC$_u$	BIC
Carbon	-9.1	-8.7	-6.7	-6.1	-13.5	-13.3	-12.3	-12.3
Hydrogen	-6.8	-3.7	2.9	2.3	-17	-15	-10.7	-12.1
H/C	-5.3	-2.2	4.4	3.8	-11	-9	-4.7	-6.2
Sulfur	-51.1	-41.6	-29.7	-35.9	-46.3	-30.5	-17.8	-34.1
Nitrogen	-36.1	-26.5	-14.6	-20.8	-21	-17.8	-12.2	-14.9
Density	-29.6	-25.3	-17.4	-18.9	-32.5	-29.3	-23.7	-26.4
IBP-300°C	-45.7	-36.1	-24.3	-30.4	-21.7	-18.6	-13	-15.6
300-400°C	-24.1	-21	-14.4	-15	-35.6	-32.4	-26.8	-29.5
400-500°C	-28.6	-24.3	-16.5	-17.9	-28.9	-25.7	-20.2	-22.8
+500°C	-36.1	-26.5	-14.7	-20.8	-33.2	-30.1	-24.5	-27.1
+343°C	-28.2	-23.9	-16	-17.5	-24	-19.3	-12.5	-16.7
Sulfur Conversion	-30.6	-27.5	-20.9	-21.5	-46.2	-30.5	-17.7	-34
Nitrogen Conversion	-27.5	-21.7	-12.6	-15.3	-21	-17.8	-12.2	-14.9
+343°C Conversion	-50.1	-40.6	-28.7	-34.9	-25.8	-22.7	-17.1	-19.7

Measured Property	Third Data Set (14)				Fourth Data Set (11)			
	AIC	AIC$_c$	AIC$_u$	BIC	AIC	AIC$_c$	AIC$_u$	BIC
Carbon	-24.1	-12.1	-4.3	-20.3	-2	-1.6	-0.5	-1.6
Hydrogen	-22.7	-20.3	-16.9	-20.8	-7.4	-6.9	-5.9	-7
H/C	-19	-16.6	-13.2	-17.1	-10.2	-9.7	-8.7	-9.8
Sulfur	-30.8	-12.1	-2.4	-26.3	-3.8	-3.4	-2.3	-3.4
Nitrogen	-21.8	-19.4	-16	-19.8	-72.6	107.4	126.1	-69
Density	-37.8	-25.8	-17.9	-33.9	-13.9	-7.2	-2.3	-12.3
IBP-300°C	-45	-33	-25.2	-41.2	-17.1	-16.6	-15.6	-16.7
300-400°C	-32.1	-27.7	-23	-29.6	-5.9	-5.5	-4.4	-5.5
400-500°C	-36	-24	-16.2	-32.2	-45.7	134.3	153.1	-42.1
+500°C	-47	-18.2	-6.3	-41.8	-2.2	-1.7	-0.7	-1.8
+343°C	-40.4	-21.8	-12.1	-36	-18.6	-11.9	-7	-17
Sulfur Conversion	-48.2	-3.2	11.2	-42.4	-3.8	-3.3	-2.3	-3.4
Nitrogen Conversion	-31.4	-19.4	-11.5	-27.5	-11.8	-11.3	-10.3	-11.4
+343°C Conversion	-31.2	-23.7	-17.5	-28	-18.8	-12.1	-7.2	-17.2

Measured Property	Fifth Data Set (6)				Sixth Data Set (13)			
	AIC	AIC$_c$	AIC$_u$	BIC	AIC	AIC$_c$	AIC$_u$	BIC
Aromatic Hydrogen	-9.1	2.9	7	-9.8	-4	1	5.8	-1.7
α-Aromatic Hydrogen	-1.4	-0.4	0.7	-1.6	-12.2	-7.2	-2.4	-10
Aliphatic Hydrogen	-4.9	-3.9	-2.8	-5.1	-12.4	-7.4	-2.6	-10.1
Aromatic Hydrogen Conversion	-6.7	-5.7	-4.6	-6.9	-4	1	5.8	-1.7
Total Aromatic Hydrogen Conversion	-10.4	1.6	5.8	-11	-12.4	-7.4	-2.7	-10.2

Table 4.15. AIC weighted results for PCR calibration models.

Measured Property	First Data Set (34)			Second Data Set (25)		
	AIC	AIC$_c$	AIC$_u$	AIC	AIC$_c$	AIC$_u$
Carbon	0	0	0	0	0	0
Hydrogen	0	0	0	0	0	0
H/C	0	0	0	0	0	0
Sulfur	59.7	59.8	59.1	51	16	1
Nitrogen	0	0	0	0	0	0
Density	0	0	0	0	9	13
IBP-300°C	4	4	4	0	0	0.1
300-400°C	0	0	0	0	43	63
400-500°C	0	0	0	0	1	2
+500°C	0	0	0	0	13	20
+343°C	0	0	0	0	0	0
Sulfur Conversion	0	0.1	0.7	49	16	0.7
Nitrogen Conversion	0	0	0	0	0	0
+343°C Conversion	36.2	36.3	35.8	0	0	0

Measured Property	Third Data Set (14)			Fourth Data Set (11)		
	AIC	AIC$_c$	AIC$_u$	AIC	AIC$_c$	AIC$_u$
Carbon	0	0	0	0	0	0
Hydrogen	0	0	1	0	1	1
H/C	0	0	0	0	2	3
Sulfur	0	0	0	0	0	0
Nitrogen	0	0.1	0.7	100	0	0
Density	0	2	2	0	1	0
IBP-300°C	11	89	70	0	75	87
300-400°C	0	6	23	0	0	0
400-500°C	0.1	1	1	0	0	0
+500°C	31	0	0	0	0	0
+343°C	1	0	0	0	7	1
Sulfur Conversion	56	0	0	0	0	0
Nitrogen Conversion	0	0.1	0.1	0	5	6
+343°C Conversion	0	1	1	0	8	1

Measured Property	Fifth Data Set (6)			Sixth Data Set (13)		
	AIC	AIC$_c$	AIC$_u$	AIC	AIC$_c$	AIC$_u$
Aromatic Hydrogen	29.8	0.9	0.2	0.5	0.5	0.5
α-Aromatic Hydrogen	0.6	4.7	4.8	30.8	30.8	30.3
Aliphatic Hydrogen	3.6	26.8	27.4	34.1	34.1	33.5
Aromatic Hydrogen Conversion	9	65.9	67.3	0.5	0.5	0.5
Total Aromatic Hydrogen Conversion	57	1.7	0.4	34.1	34.1	35.2

Table 4.16. Selection criteria results for PLSR calibration models.

Measured Property	First Data Set (34)				Second Data Set (25)			
	AIC	AIC$_c$	AIC$_u$	BIC	AIC	AIC$_c$	AIC$_u$	BIC
Carbon	-37.2	-32.9	-25	-26.5	-17.6	-17.1	-15	-15.2
Hydrogen	-0.8	-0.4	1.6	2.2	-20.5	-18.5	-14.1	-15.6
H/C	-40.3	-34.5	-25.4	-28.1	-37.5	-25.5	-14.3	-26.5
Sulfur	-80.8	-75	-65.9	-68.6	-40.2	-38.2	-33.8	-35.3
Nitrogen	-41.2	-38.1	-31.5	-32	-25.5	-22.3	-16.7	-19.4
Density	-69.6	-62.1	-51.7	-55.9	-36.6	-33.5	-27.9	-30.5
IBP-300°C	-58.2	-52.4	-43.3	-46	-24.8	-22.8	-18.4	-19.9
300-400°C	-78	-70.5	-60	-64.2	-85.8	-70	-57.3	-73.6
400-500°C	-70.6	-64.8	-55.7	-58.4	-31.9	-29.9	-25.5	-27
+500°C	-54	-48.2	-39.1	-41.8	-35.9	-33.9	-29.5	-31
+343°C	-63.8	-58	-48.9	-51.6	-28.8	-26.8	-22.4	-23.9
Sulfur Conversion	-80.7	-74.9	-65.8	-68.4	-70	-61	-51.4	-60.3
Nitrogen Conversion	-46.1	-41.8	-34	-35.4	-24.3	-22.3	-18	-19.5
+343°C Conversion	-66.3	-58.8	-48.3	-52.5	-28.7	-26.7	-22.3	-23.8

Measured Property	Third Data Set (14)				Fourth Data Set (11)			
	AIC	AIC$_c$	AIC$_u$	BIC	AIC	AIC$_c$	AIC$_u$	BIC
Carbon	-28.8	-24.3	-19.6	-26.2	-2.1	-1.7	-0.6	-1.7
Hydrogen	-23.8	-21.4	-18	-21.9	-9.1	-2.4	2.6	-7.5
H/C	-20.1	-17.7	-14.3	-18.1	-11.2	-4.5	0.4	-9.6
Sulfur	-40.2	-32.7	-26.5	-37	-3.8	-3.4	-2.3	-3.4
Nitrogen	-25.7	-23.3	-19.9	-23.7	-11.8	-11.4	-10.3	-11.4
Density	-39.9	-35.4	-30.7	-37.3	-11.3	-10.8	-9.8	-10.9
IBP-300°C	-51.9	-44.4	-38.2	-48.7	-17.1	-16.7	-15.6	-16.7
300-400°C	-30.7	-28.3	-24.9	-28.8	-6	-5.5	-4.5	-5.6
400-500°C	-38	-33.6	-28.9	-35.5	-61.1	-23.7	-12.6	-58.3
+500°C	-47.1	-42.7	-38	-44.6	-2.2	-1.8	-0.7	-1.8
+343°C	-47	-39.5	-33.3	-43.8	-16.9	-16.5	-15.4	-16.5
Sulfur Conversion	-40.1	-32.6	-26.4	-36.9	-3.8	-3.4	-2.3	-3.4
Nitrogen Conversion	-25.7	-23.3	-19.9	-23.8	-11.8	-11.4	-10.3	-11.4
+343°C Conversion	-46.7	-39.2	-33	-43.5	-17.1	-16.6	-15.6	-16.7

Measured Property	Fifth Data Set (6)				Sixth Data Set (13)			
	AIC	AIC$_c$	AIC$_u$	BIC	AIC	AIC$_c$	AIC$_u$	BIC
Aromatic Hydrogen	-6.8	-5.8	-4.7	-7	-6.4	-1.4	3.4	-4.1
α-Aromatic Hydrogen	-1.4	-0.4	0.7	-1.6	-14.4	-9.4	-4.6	-12.1
Aliphatic Hydrogen	-7.7	-3.7	-1.3	-8.1	-14.4	-9.4	-4.7	-12.2
Aromatic Hydrogen Conversion	-10.3	1.7	5.9	-10.9	-6.4	-1.4	3.4	-4.1
Total Aromatic Hydrogen Conversion	-11.2	0.8	5	-11.8	-14.5	-9.5	-4.7	-12.2

Table 4.17. AIC weighted results for PLSR calibration models.

Measured Property	First Data Set (34)			Second Data Set (25)		
	AIC	AIC$_c$	AIC$_u$	AIC	AIC$_c$	AIC$_u$
Carbon	0	0	0	0	0	0
Hydrogen	0	0	0	0	0	0
H/C	0	0	0	0	0	0
Sulfur	45.3	48.4	49.7	0	0	0
Nitrogen	0	0	0	0	0	0
Density	0	0	0	0	0	0
IBP-300°C	0	0	0	0	0	0
300-400°C	11	6	3	100	99	95
400-500°C	0	0	0	0	0	0
+500°C	0	0	0	0	0	0
+343°C	0	0	0	0	0	0
Sulfur Conversion	43	46.1	47.3	0	1	5
Nitrogen Conversion	0	0	0	0	0	0
+343°C Conversion	0	0	0	0	0	0

Measured Property	Third Data Set (14)			Fourth Data Set (11)		
	AIC	AIC$_c$	AIC$_u$	AIC	AIC$_c$	AIC$_u$
Carbon	0	0	0	0	0	0
Hydrogen	0	0	0	0	0	0
H/C	0	0	0	0	0	0
Sulfur	0	0	0	0	0	0
Nitrogen	0	0	0	0	0	2
Density	0	1	1	0	0	2
IBP-300°C	79	62	47	0	3	30
300-400°C	0	0	0	0	0	0
400-500°C	0.1	0.3	0	100	92	7
+500°C	7	27	43	0	0	0
+343°C	7	5	4	0	3	27
Sulfur Conversion	0	0	0	0	0	0
Nitrogen Conversion	0	0	0	0	0	2
+343°C Conversion	6	5	4	0	3	30

Measured Property	Fifth Data Set (6)			Sixth Data Set (13)		
	AIC	AIC$_c$	AIC$_u$	AIC	AIC$_c$	AIC$_u$
Aromatic Hydrogen	5.7	67.7	79.2	0.6	0.6	0.6
α-Aromatic Hydrogen	0.4	4.5	5.3	32.4	32.4	31.9
Aliphatic Hydrogen	9	23.7	14.5	32.4	32.4	33.5
Aromatic Hydrogen Conversion	33	1.6	0.4	0.6	0.6	0.6
Total Aromatic Hydrogen Conversion	52	2.5	0.6	34	34	33.5

First Data Set

Sulfur and sulfur conversion were the best physicochemical properties calibrated in the first data set. The PLSR model resulted in the best model selection criterion results compared to the other three calibration methods. Overall, the PLSR method is favored for the first data set that calibrated 34 samples.

Second Data Set

Nitrogen concentration was the best property calibrated in the second data set using MLR. The stepwise method included 23 absorbance wavelength channels as all significant variables in the calibration model. The IBP-300°C and 300-400°C fractional concentrations were the second and third best calibration models using MLR and PLSR, respectively. Overall, the MLR stepwise method is favored for the second data set that calibrated 25 samples.

Third Data Set

The 400-500°C fractional concentration was the best property calibrated in the third data set using MLR. Sulfur and nitrogen concentrations were the second and third best calibration models using MLR. Overall, the MLR stepwise method is favored for the third data set that calibrated 14 samples.

Fourth Data Set

Density was the best property calibrated in the fourth data set using MLR. Nitrogen and the 400-500°C fractional concentrations were the second and third best calibration models using PCR and PLSR, respectively. Overall, the MLR stepwise method is favored for the fourth data set that calibrated 11 samples.

Fifth Data Set

Total aromatic hydrogen conversion was the best property calibrated in the fifth data set using PLSR. Overall, the MLR stepwise method is favored for the fifth data set that calibrated 6 samples.

Sixth Data Set

Total aromatic hydrogen conversion was the best property calibrated in the sixth data set using MLR. Overall, the MLR stepwise method is favored for the sixth data set that calibrated 13 samples.

Simple Least Squares

Selection criteria results for SLS calibration models are shown in *Table 4.10*. Corresponding AIC weights are shown in *Table 4.11*. Carbon, sulfur, sulfur conversion, and +343°C conversion resulted in the best calibration model selections for the first four data sets. Aromatic hydrogen and conversion are favored models for the fifth set. The α-aromatic hydrogen is favored for the sixth data set. There were no discrepancies between each model selection criterion result. These results are corroborated by the AIC weights shown in *Table 4.11*. The fourth data had similar model selection probabilities for the IBP-300°C, 400-500°C, +343°C, and +343°C conversion. Aliphatic and total aromatic hydrogen conversion had comparable model selection probabilities to α-aromatic hydrogen.

Multiple Linear Regression

Selection criteria results for MLR calibration models are shown in *Table 4.12*. Corresponding AIC weights are shown in *Table 4.13*. Sulfur, sulfur conversion, nitrogen, nitrogen conversion, IBP-300°C, and 400-500°C fractions resulted in the best calibration model selections for the first four data sets. Aromatic hydrogen and conversion are favored models for the fifth set. Total aromatic hydrogen is favored for the sixth data set. The unbiased AIC favored IBP-300°C and sulfur conversion compared to nitrogen in the second data set. Sulfur, nitrogen, and nitrogen conversion models were preferred by the unbiased AIC in the third data set. These results are corroborated by the AIC weights shown in *Table 4.13*. Nitrogen conversion in the third data set had over 50% model selection probability, compared to sulfur and nitrogen concentrations at 18 and 31%, respectively.

Principal Component Regression

Selection criteria results for PCR calibration models are shown in *Table 4.14*. Corresponding AIC weights are shown in *Table 4.15*. Sulfur, sulfur conversion, nitrogen, IBP-300°C, +500°C, and

+343°C conversion resulted in the best calibration model selections for the first four data sets. Mixed results were obtained for the fifth data set depending on the selection criteria used. The sixth data set favored aliphatic hydrogen and total aromatic hydrogen conversion. The 300-400°C and +500°C calibration models were favored by the unbiased AIC in the second data set. AIC and BIC favored sulfur conversion rather than the IBP-300°C calibration models from AIC_c and AIC_u results in the third data set. The corrected and unbiased AIC favored the IBP-300°C compared to nitrogen in the fourth data set. These results are corroborated by the AIC weights shown in *Table 4.15*. The corrected and unbiased AIC resulted in the best model selection probabilities for aromatic hydrogen conversion in the fifth data set.

Partial Least Squares Regression

Selection criteria results for PLSR calibration models are shown in *Table 4.16*. Corresponding AIC weights are shown in *Table 4.17*. Sulfur, sulfur conversion, IBP-300°C, 300-400°C, 400-500°C, +343°C, and +343°C conversion resulted in the best calibration model selections for the first four data sets. Aromatic hydrogen and total aromatic hydrogen conversion are favored models for the fifth set. Mixed results were obtained for the sixth data set. The unbiased AIC in the fourth data set favored IBP-300°C, +343°C, and +343°C conversion compared to the remaining selection criterions for the 400-500°C calibration model. These results are corroborated by the AIC weights shown in *Table 4.17*. The AIC_c and AIC_u had higher probabilities for the aromatic hydrogen calibration model in the fifth data set. Total aromatic hydrogen conversion had the best probability for model selection in the sixth data set.

Selection Criteria of Boiling Point Distribution Models

Table 4.18. Selection criteria results of optimal boiling point fractional calibration models.

	SLS				MLR			
MSC	**First Set (34)**	**Second Set (25)**	**Third Set (14)**	**Fourth Set (11)**	**First Set (34)**	**Second Set (25)**	**Third Set (14)**	**Fourth Set (11)**
AIC	-8.6	-20	-19.9	-20.6	-29.1	-883	-442.9	-309.9
AIC$_c$	-8.5	-19.8	-19.5	-20.1	-28.3	-89.2	-130.9	-129.9
AIC$_u$	-7.5	-18.8	-18.5	-19.1	-25.2	-76.5	-103.7	-111.2
BIC	-7.1	-18.8	-19.2	-20.2	-24.6	-855	-435.3	-306.3
	PCR				PLSR			
MSC	**First Set (34)**	**Second Set (25)**	**Third Set (14)**	**Fourth Set (11)**	**First Set (34)**	**Second Set (25)**	**Third Set (14)**	**Fourth Set (11)**
AIC	-59.7	-34.2	-45.4	-170.3	-79.9	-72.9	-50.5	-95.7
AIC$_c$	-50.1	-31	-34.8	-16.9	-72.4	-57.2	-45.5	-45.8
AIC$_u$	-38.2	-25.4	-30.1	-15.9	-62	-44.4	-36.8	-34.7
BIC	-44.4	-28.1	-40.9	-166.7	-66.2	-60.7	-47.3	-92.6

Table 4.19. Optimal boiling point fractional calibration models from selection criterions.

	AIC				AIC$_c$			
Method	**First Set (34)**	**Second Set (25)**	**Third Set (14)**	**Fourth Set (11)**	**First Set (34)**	**Second Set (25)**	**Third Set (14)**	**Fourth Set (11)**
SLS	1	95	95	30	1	95	95	30
MLR	95	57	81	77	95	94	81	77
PCR	72	74	97	76	72	74	79	25
PLSR	71	37	95	74	71	37	95	39
	AIC$_u$				BIC			
Method	**First Set (34)**	**Second Set (25)**	**Third Set (14)**	**Fourth Set (11)**	**First Set (34)**	**Second Set (25)**	**Third Set (14)**	**Fourth Set (11)**
SLS	1	95	95	30	1	95	95	30
MLR	95	94	81	77	95	57	81	77
PCR	72	74	79	25	72	74	97	76
PLSR	71	37	95	39	71	37	95	74

Values are cumulative mass fraction off from distribution curve (wt.%)

Selection criteria results for the first four data sets and all calibration models for boiling point distribution fractions are presented in *Tables H7 to H22* in *Appendix H*. Optimal or minimum selection criteria results for boiling point fractional calibration models are shown in *Table 4.18*. Corresponding mass fraction boiled off calibration model to these selection criteria results are highlighted in *Table 4.19*.

217

The second data set using MLR is the optimal model based on the AIC and BIC selection criteria results. This corresponded to the 57wt.% fraction off in the boiling point distribution curve in *Table 4.19*. The AIC_c and AIC_u favored 81 and 77wt.% fractions off in the third and fourth data sets, respectively. The SLS and MLR models resulted in comparable selection values for each criterion for each data set. The PCR and PLSR methods had differences in optimal calibration model selections for AIC_u and BIC criterions. The 95wt.% fraction off in the boiling point distribution curve in *Table 4.19* is the most common calibration model selected from all data sets and methods.

Chapter 5: Discussion

5.1 Hydrotreating Reactions

Hydrotreating reactions are often not conducted using a batch reactor at the pilot or industrial scale. A fixed bed catalytic reactor is used in other hydrotreating studies [1-6]. The disadvantages of batch reactors are undistributed gas-liquid phase transport, limited gas-to-oil ratio, non-trickle flow, liquid product filtering issues, and correlations to process parameters. The advantages of the current batch microreactor used is low cost, robust temperature control, and simple maintenance or replacement. To assess the chemometric calibration in the fourth objective, the microbatch reactor is sufficient.

The NiMo/γ-Al$_2$O$_3$ catalyst used was an industrial catalyst that executed mild hydrotreating reactions. Nickel and molybdenum contents were comparable to literature values in *Table 3.2*. The combined sulfidation procedure from Marroquin and Criterion Catalyst was successfully implemented [7-8]. Sulfidation of nickel and molybdenum to sulfided form was successfully verified by the elemental sulfur analysis in section 4.2 and *Table E2*. Although the sulfur concentrations of both sulfided catalysts were not comparable, successful HDS, HDN, and HDA reactions were achieved with each catalyst. For this reason, a comparison of the liquid product results could not be adequate for the sulfided catalyst pellet versus <45μm solids of the third objective.

The batch microreactor design provided adequate pressure and temperature requirements for all mild hydrotreating reactions. The internal volume was successfully verified assuming the ideal gas law to approximately 20cm^3. The use of nitrogen gas at low pressure provided validity of the law to estimate the internal reactor volume accurately. This was important to determine the gas to oil ratio and complete a valid mass balance for each hydrotreating reaction.

Fluidized baths and agitators provided adequate temperature control and agitation for all experimental reactions. Previous research studies at the University of Alberta were successful in using this equipment [9-11]. The BOSCH agitator had a wide range in agitations speeds. The

second agitator had a fixed agitation speed. The average agitation speed was reported for each reaction. This agitation is important to improve the gas-liquid phase transport and avoid solid suspension in the batch system. The gas-liquid phase transport directly affects product quality. The high variability may not provide an accurate assessment of the mixing effects in the third objective.

The disadvantage of the microbatch reactor was pressure testing, reactor maintenance, and replacement. Approximately every seven to ten reactions, the reactor was replaced because of a failed pressure test. Thermal cycles of the stainless steel wear down the ability to hold pressure. This is uncommon for fixed bed pilot units. However, this challenge was addressed through using multiple low cost microreactors and careful maintenance of the stainless steel fittings after each reaction. This was advantageous for testing the compositional transformations of the third objective and obtaining satisfactory liquid products to calibrate in the fourth objective.

Table 5.1. Comparison of operating conditions.

	Table 2.2 (VGO)	Literature Studies from *Table A1*[1-5,12-14]	Current Study
Operation Temperature (°C)	360 - 400	300 - 450	290 - 390
Hydrogen Pressure (MPa)	3.2 -13.9	7 - 12.5	4.5MPa at lab temperature 10.4MPa at 390°C, Appendix B
Liquid Hourly Space Velocity (h^{-1})	0.8 - 3	0.5 - 4	2.3 - 25.2 Appendix B
Hydrogen Rate (Sm^3/m^3 feed)	170 - 680	400 - 1270	30 - 32 Appendix B
Catalyst Use (m^3 feed / kg catalyst)	20 - 120	-	0.006 Appendix B Average

Comparison of operating conditions from *Table 2.2*, literature studies, and the current study are shown in *Table 5.1*. The reaction temperatures tested in the current study are comparable to industrial and literature studies. Severe hydrotreatment, reactions >400°C, introduce additional cracking and coking reactions to that reported in section 2.3. This was avoided to limit the study to HDS, HDN, and HDA reactions. Temperatures started as low as 290°C to examine the third objective and obtain intermediate liquid products for calibration.

In a fixed bed catalytic reactor, as in other studies reported in *Table A1* of *Appendix A*, liquid feed and hydrogen gas are mixed prior at an elevated temperature. This ensured gas-liquid mass transfer prior to hydrotreatment. The current study was limited to mixing liquid feed and hydrogen gas (4500kPa(g)) at lab temperature in the microreactor in *Table 5.1*. This step may limit hydrotreating reactions from a solubility perspective. The internal pressure at reaction temperature was calculated by VMGSim. This modelled internal pressure was comparable to the ranges reported by others in *Table 5.1*. However, for the current study in assessing the fourth objective, this solubility is not significant. The liquid product properties and colour are obtained after the reaction. This was advantageous in completing reactions faster and at a lower cost compared to the fixed bed method.

The current study was limited in LHSV and hydrogen rate compared to industrial and other studies using fixed bed reactors. The LHSV is important in kinetic models and provided an understanding of feed contact time with the catalyst. The lower the LHSV, the longer the contact time with catalyst. Longer time ensures the reactions are completed efficiently. The hydrogen rate is important to ensure enough is stoichiometrically required to saturate the reactions from section 2.3. The lower rate in the current study was sufficient in obtaining mildly treated liquid products. Compared to other studies, excess hydrogen is normal to ensure stoichiometric requirement for all hydrotreating reactions. The catalyst use in this study was 3330 times the normal amount compared to others. This ensured excess catalyst surface to complete the hydrotreating reactions. For the current study, the incomparable LHSV and hydrogen rate to other studies using a fixed bed reactor, does not impact the assessment of the third and fourth objectives. The liquid products in this study are mildly treated compared to literature.

A verification reaction ensured the internal reactor temperature reached the setpoint of the fluidized bath. This was important to validate the heat transfer of the fluidized bath and complete accurate reaction times and temperatures. Unlike in the fixed bed and industrial cases, ramp up to reaction temperature is in the order of hours. The pressure was measured on colder gas above the fluidized bed and not directly at 390°C. Industrial units measure this pressure on the vessel itself, but for the microbatch reactor, this was sufficient.

Total mass recovery was successful for the experimental reaction matrix in *Table 3.5*. Nearly all mass was accounted for. This provided good validity of the procedure. Liquid product collection was a disadvantage of the microbatch reactor. The addition of a solvent and evaporation overnight, was effective in collecting a liquid product without a catalyst. The solvent evaporation loss was successfully modelled in *Appendix D*. This was important for the analytical characterizations completed. However, liquid product recovery was reduced to an average of 83%. Thus, 17% of the liquid was lost in solvent evaporation, microreactor cleaning, and/or absorbed inside the catalyst itself. In the fixed bed reactor case, liquid product recovery is nearly 100% without catalyst separation from the liquid product. The liquid product trickles out at high temperature through a filtered mesh system. Solvent and filtration are avoided altogether. A few other studies used a continuous stirred tanked reactor (CSTR) with a spinning basket to encompass the catalyst in the vessel [15-16]. This avoided liquid product filtration from the catalyst. Although this dilution effect is not important when assessing the fourth objective because of consistency, product quality and compositional transformation comparisons could be limited.

5.2 Analytical Methods to Assess Product Quality

To assess product quality, the hydrotreated liquid products are characterized by several analytical methods to understand the chemical complexity.

Carbon and Hydrogen

The carbon and hydrogen measurements were validated with an internal standard with low percent differences in *Table 3.7*. This was important to ensure a valid characterization. Unfortunately, the sulfur and nitrogen measurements were non-repeatable with large confidence intervals using this analyzer. The analyzer provided repeatable results for the sulfided catalyst characterization. This was optimal for the <45µm size. The carbon and hydrogen confidence intervals ranged from 0.1 to as high as high as 2wt.% in *Table E1*. These large confidence intervals could limit comparison and deduce trends of the third objectives.

Sulfur and Nitrogen

Internal standards were used to create calibration curves for sulfur and nitrogen analysis of the hydrotreated liquid products. From *Table E3*, sulfur and nitrogen confidence intervals ranged as high as 0.18wt.% and 0.026wt.%, respectively. In comparison to carbon and hydrogen, these measurements had higher repeatability. These results could provide adequate comparison and assessment of the third objectives.

Density

Density measurement was limited to a 25µL syringe and balance scale method. This reduced the density results to two decimal places with confidence intervals as high as 0.01g/ml from *Table E4*. Acetone and HVGO were validated with an Anton Paar 4500M to provide confidence to the syringe and balance scale method. Of all the analytical measurements, density has the lowest relative accuracy in comparison. These large confidence intervals could limit comparison and deduce trends of the third objectives.

Boiling Point Distribution

Liquid product boiling point distribution results were characterized with a well establish standard method. An internal reference gas oil provided validity for all liquid products measured. A limited number of replicates were completed for the HVGO and liquid products. However, these results were repeatable. Solvent dilution with evaporation likely impact these results as in the initial boiling point to 300°C. However, these results used for fractional model assessment of the fourth objective should be sufficient.

Hydrogen Proton Nuclear Magnetic Resonance

Two ^{1}H NMR spectrometers, 400MHz and 60MHz, provided a comparison of molecular hydrogen distribution in the HVGO and its liquid products. Compared to the 60MHz, the 400MHz was optimal because of a low signal to noise ratio. A limited number of samples were characterized with the 400MHz spectrometer because of sample size, cost, and time. The 60MHz was used for a sub-set of remaining samples. An important step of the analysis was a consistent mass and dilution ratio of the samples inside the glass tubes. An internal spike of tetramethylsilane in the

dilution solvent (CDCL₃) validated the spectra obtained. The 60MHz spectrometer used a Bernstein polynomial baseline correction compared to a spline method for the 400MHz results. The molecular hydrogen classification from *Table 2.12* is debated in literature, however it provided adequate fractional molecular hydrogen concentrations. Differences are expected for each spectrometer when compared because of their respective resolution. As such, this could limit comparison and deduce trends of the third and fourth objectives.

Table 5.2. Analytical characterization comparison for the HVGO.

Property	*Table 2.1*	*Table 2.7* [17]	Current Study
Density (kg/m³)	967 - 971	965	967±6
Carbon (wt.%)	-	85.33	86.4±0.3
Hydrogen (wt.%)	-	10.44	11.3±0.1
H/C	1.53 - 1.56	1.47	1.57
Sulfur (wt.%)	2.92 - 3.59	3.48	3.3±0.01
Nitrogen (wt.%)	0.14 - 0.19	0.14	0.1762±0.0016
Boiling Point Range (°C)	244 - 623	-	299 - 643
Saturates (wt.%)	28.7 - 31.2	-	-
Aromatics (wt.%)	59.7 - 65.6	-	-
Total Aromatic Hydrogen (mol%)	-	-	20.2[*] 24.1[**]
Total Aliphatic Hydrogen (mol%)	-	-	79.8[*] 75.9[**]

*400MHz Spectrometer
**60MHz Spectrometer

Analytical characterization results from literature and this study for the HVGO are compared in *Table 5.2*. All properties measured for the HVGO are comparable to literature samples. These results are expected as different instruments, technicians, and procedures were used to measure the properties. Overall, based on the characterization methods from the current study, results for the HVGO appear valid in this comparison. No characterization results appear significantly different.

Visible Absorption Spectrum

The visible absorption measurement is crucial to development of an online spectroscopic analysis tool. As previously mentioned, samples were not diluted in solvent. The first reason was to avoid solvent effects as describe by Evdokimov and Losev [18]. The second reason was to have measurements that could be completed in a process stream directly as developed by Mullins and Insight Analytical [19-20]. This is counter intuitive to the beer-lambert relationship. However, because of the multicomponent nature of the liquid products, the distribution of chromophoric material is of importance for assessing the fourth objective. The results obtained corroborated the trends described in section 2.4.1 with hypsochromic shifts in adsorption spectra to smaller wavelengths due to hydrotreatment. The deconjugation and disentanglement of pi-conjugated material was seen in the brown HVGO to yellow hydrotreated liquid products in *Figure 3.15*. For the visible portion, results from Mullins and Shoute corroborated these results shown in section 4.6 [19-22].

5.3 Compositional Transformations

Evaluation of the dynamic compositional transformations tested are discussed in section 5.3.

What are the experimental control effects?

Two experimental controls, reactor wall and solvent filtration effects, were studied on product quality.

Reactor Wall Effect

A non-catalytic reactor yielded enhanced product quality compared to the HVGO. All characterization results suggested hydrotreating reactions were evident. The catalytic effects were seen from the stainless steel reactor walls. A previous hydrotreating reaction that generated H_2S sulfided the iron, nickel, and molybdenum in the 316 stainless steel walls. The sulfided layer was active enough to complete hydrotreating reactions of the HVGO and enhance product quality. Schmidt et al. found similar results for hydrocracking model compounds in a batch reactor [23]. Non-catalytic reactors that had previously sulfided walls yielded better conversion results compared to the new reactors tested. As a result, to minimize wall effects and compare reactions

to a similar control in the current study, the reactor walls were mechanically sanded, solvent washed, and maintained after each reaction. This is a disadvantage to using microbatch reactors for hydrotreating reactions. However, this control provided better assessment of the remaining objectives.

Solvent Filtration

As discussed in section 5.1, the disadvantage of the microbatch reactor is separation of the solid catalyst from the liquid product following hydrotreatment. The HVGO and three catalytic reactions were evaluated to determine the dichloromethane solvent filtration and overnight evaporation effect. The HVGO after solvent filtration shifted to lower temperatures for the IBP-300°C fraction. Dichloromethane had limited evaporation from this sample causing lighter fractions to appear in the distribution curve.

Three unfiltered and filtered catalytic reactions are compared. Total liquid recovery was lower after product filtration. Heavier fractions with higher density, sulfur, nitrogen, and +343°C fractions were evident in the filtered liquids. However, this contradicts the higher H/C results measured in the filtered compared to non-filtered liquid products. Large procedural errors in measurement could explain the high variability in the mixed results. One unfiltered liquid product had significant visible absorbance interference from solid catalyst in *Figure 4.36*. To avoid this interference, remaining liquid products were filtered with solvent and evaporated overnight. Additional reactions are required to assess the effects of the solvent filtration on product quality using the microbatch reactor. However, for the remaining objectives, and consistency, comparisons were made with filtered liquid products.

What is the effect of using a catalyst on product quality?

Liquid products from catalytic and non-catalytic reactions using unsulfided pellets are compared to address this question. Through extensive knowledge, it is well known that a catalyst is required to complete hydrotreating reactions effectively. This was evident by the significantly different property results obtained in chapter 4. What was interesting are the liquid product spectral colour changes from these two types of reactions in *Figure 4.35*. The visible absorption spectra of the catalytic reactions were all hypsochromically shifted compared to the non-catalytic reactions. A

non-catalytic reactor assumed mild thermal cracking reactions took place. Which could limit a proper model calibration assessment. Without a catalyst, HDS, HDN, and HDA reactions are avoided. These results are directionally correct, with the presence of a catalyst, hydrogenation, sulfur and nitrogen removal are all evident in this comparison. These intermediate spectra are used to address the fourth objective.

What is the effect of mixing on product quality?

The study of mixing effects was important for the microbatch reactor to assess external mass transfer. To ensure the catalyst contacted all liquid and hydrogen, this comparison was completed. Calais et al. found that mixing greater than 1000RPM did not impact the catalyst activity using a continuous stirred tank reactor [24]. The current study did not reach this level of agitation and used significantly less volume of feed. This question could be difficult to assess for that reason. Scarce literature is found on this question because fixed bed reactors are commonly used. In the fixed bed catalytic reactor, the feed trickles down with hydrogen contacting all the catalyst pellets, external mass transfer is not limited. Catalytic reactors at 360 and >800RPM agitation are compared.

Liquid product carbon and hydrogen are significantly different at higher agitations speeds. These H/C values were enhanced compared to 360RPM reactions. However, sulfur and nitrogen concentrations were reduced significantly at 360RPM compared to >800RPM agitation. Visible spectra did not indicate significant differences except for one liquid product at a high mixing case. This liquid product had a significantly lower sulfur and a higher H/C value suggesting additional hydrotreatment was completed. These results provided difficulty in deducing whether mixing impacted product quality and external mass transfer. In certain cases, lower mixing improved product quality for sulfur and nitrogen. In other cases, no significant changes were seen. Additional hydrotreating reactions could be completed to assess agitation and external mass transfer effects with catalyst pellets using the microbatch reactor. However, these liquid products generated intermediate visible adsorption spectra that are used for the calibration models in the fourth objective.

What is the effect of using a unsulfided catalyst versus Sulfided catalyst pellets on product quality?

For enhanced activity, hydrotreating catalysts are sulfided prior to use to optimize HDS, HDN, and HDA reactions [7-8]. Active metal sulfides are known to improve sulfur, nitrogen, and aromatic conversion [7-8]. In the current study, the catalyst was sulfided with Dimethyl Disulfide (DMDS) in the liquid phase as per the Marroquin et al. procedure [7]. Different sulfur precursors and procedures are known to impact activity as reported by others in section 2.1.5. The comparison before and after catalyst sulfidation of S424 pellets is assessed.

Carbon, hydrogen, density, and most of the boiling fractions in the liquid product did not change significantly when using the different pellets. Sulfur, nitrogen, and the 500°C-FBP concentrations changed significantly with the sulfided catalyst pellets. Visible spectra of sulfided pellet liquid products were significantly different apart from one in *Figure 4.38*. Sulfided catalyst pellet liquid products were hypsochromically shifted compared to unsulfided catalyst. The results suggest catalyst sulfidation improved sulfur and nitrogen removal. Reduction in the heaviest boiling fraction and heteroatom removal explains the increase in chromophoric deconjugation to lower wavelength absorbances. This assessment was limited to three reactions for each case. Additional reactions and product assessment could be completed to address this question when using the batch microreactor. These liquid products generated provided additional visible adsorption spectra that are used for calibration in the fourth objective.

What is the effect of reaction temperature and time on product quality?

To generate a broad range of liquid products, a set of reaction temperatures and times were tested. As highlighted in the literature review and in *Table 5.1*, temperature and LHSV impacted the product quality. Of the studies reviewed in *Appendix A*, increasing reaction temperature and reducing LHSV have a positive effect on HDS, HDN, and HDA reactions. This is corroborated by the sulfur and nitrogen trends shown in section 4.2. Further validation was completed for sulfur and nitrogen kinetic assessment in *Appendix F*. The HDA reactions were seen by the H/C increases and the aromatic hydrogen decreases from ^{1}H NMR results. The increasing aliphatic nature of the liquid products with reaction time and temperature is directionally correct. On a conversion basis, agreement is seen for aromatic hydrogen. Data overlap from the 400MHz and 60MHz

spectrometers are seen in the comparisons of *Figures 4.32* and *4.33*. Short reaction times, 0.25h, limited comparisons of temperature effects for characterizations except for sulfur and nitrogen concentrations. Longer reactions are preferred to study broader temperature effects on product quality for the microbatch case. The visible absorption spectra showed increasing hypsochromic nature of the liquid products with increasing reaction temperature and time. This provides validation to the deconjugation and aromatic saturation caused by HDA reactions from *Figures 2.30 to 2.31*. Temperature effects on the visible absorption spectra were significant in *Figure 4.40* compared to reaction time effects in *Figures 4.39* and *4.41*. Several of the adsorption spectra overlapped at similar reaction times. Temperature effects were difficult to assess on the adsorption spectra at low reaction times because of large confidence intervals and significant overlap in *Figure 4.42*. These liquid products provided a diverse visible adsorption spectrum data set that is used for chemometric calibration in the fourth objective.

What is the effect of catalyst size, trilobed pellets versus <45μm solids, on product quality?

Apart from slight H/C and sulfur concentration reduction enhancements from the <45μm solids, characterization results were nearly identical in the catalyst size comparison. The visible adsorption spectrum of the <45μm solids at 2h and 390°C were hypsochromically shifted compared to the catalyst pellet liquid products. The differences seen in the visible spectrum are not confirmed by the characterization results apart from the improved H/C. As previously discussed, the sulfided <45μm solids had a higher sulfur content compared to the pellets. This likely affected the HDS reaction trends. However, at 2h and 390°C, the results for both catalyst sizes had no significant differences from each other. This provides validation that no significant internal diffusion limitations affected the catalyst pellet reactions, apart from the HDS reactions using the batch microreactors. The kinetic results from *Appendix F* corroborate these findings by an evaluation of effectiveness factors at these two catalyst sizes using the Gray method in section 11.8.4 of [25]. The third and fourth visible adsorption spectra data sets separated the liquid product results based on the catalyst pellet and <45μm solids reactions, respectively. This provided a diverse spectral set for the chemometric calibration models in the fourth objective.

5.4 Chemometric Analysis

To address the fourth objective, the visible spectra and measured physicochemical properties of the liquid products are used to calibrate or train chemometric models.

Can the visible spectrum of the liquid products be calibrated to their physicochemical properties measured in objective two?

The visible adsorption spectra of the liquid products were successfully calibrated to their physicochemical properties as demonstrated by the results from section 4.7. Other studies in literature have completed similar calibrations and validations to physicochemical properties using UV-Vis and other forms of EMR interactions as reviewed in section 2.5.5 [26-27]. The study is limited to a training or calibration set, additional liquid products within similar operating conditions are required to validate the models presented in section 4.7. In addition, other studies used a solvent to dilute their liquid products, however, the current study avoided solvent interactions seen by Evdokimov and Losev [18]. The advantage of this control is for efficient development of an online spectroscopic tool that is installed inline following a hydrotreater vessel. The liquid product avoids dilution for an external measurement as in technologies developed by Mullins et al. and Insight Analytical [19-20, 28-30].

Which data sets and modelling methods provided the best calibration results for each property?

Data sets

To ensure a valid comparison, the HVGO and six reacted products were removed in analysis. These spectra are far outside the range of absorbance wavelengths in the calibration set. From the adjusted coefficient of determinations, the third data set, reactions with sulfided catalyst pellets, resulted in the best calibration of the first four sets. Including the complete boiling point distribution calibration models, the third data set with 14 liquid product samples was the best. The fourth data set, reactions with sulfided <45μm solids was the second best data set for the calibration models overall. Of the ^{1}H NMR data sets, the fifth data set with six samples was the optimal calibration set compared to the sixth data set with 13 samples. Similar to the first and second data sets, the sixth set contained samples with different initial conditions and catalyst.

These results are justified as the reactions were similar initial conditions, pressure, and catalyst. The difference was that the fourth data set had a small set of 11 samples rather than 14. The first and second data sets combined reactions with different initial conditions, temperature, time, and catalyst. The broader distribution of initial conditions lowered the visible spectra to their physicochemical properties. Ideally, robust models account for a broader distribution of the initial conditions. However, as mentioned by Chen et al., fluctuations in process conditions are inevitable and some of these variations are non-linear in nature [31]. Overall, the sample selection is important for each data set. Use of the same catalyst and initial conditions is required to create effective calibration data sets.

Modelling Methods

For specific cases, the PLSR method was optimal in calibration of physicochemical properties in the first four data sets. This included the boiling point distribution models. In close comparison, the MLR method had optimal results for molecular hydrogen in the fifth and sixth data sets. The stepwise method did not limit the variable selection to 10 parameters as in PCR and PLSR methods. The MLR method used as high as the sample size for the absorbance wavelength variable selection. In certain cases, this yielded calibration models with a perfect fit and no residual error. Several studies from section 2.5.5 found PLSR as the optimal method for their calibration model because the covariance is maximized between measured spectra and property. However, MLR was advantageous when a high number of variables are included in the calibrated model. These results resemble what Pinheiro et al. suggested, each modelling method is tailored to their specific property of interest [32].

Through model selection criterion, which models are the best calibration results?

As the root mean squared error and the adjusted coefficient of determination are reported throughout literature, the model selection criterion is an alternative approach to selecting the best model result. The current study used the relative square error (RSE) as opposed to the sum of square errors to compare models with different property units. The sum of squares limits the comparison to similar property units. This leads to difficulty in determining the best calibration result overall. The RSE is advantageous for the current study because of the broad collection of physicochemical properties measured.

231

From *Table 4.12*, the second data set using MLR, had the lowest average of values of AIC and BIC selections compared to the remaining data sets. AIC_c and AIC_u selections favoured the first data set using PLSR. In the fifth data set, AIC and BIC selections favoured the PLSR models. The AIC_c and AIC_u selections favoured the SLS and MLR models in the fifth set. The sixth data set favoured MLR models by all model selection criterions. These results corroborated the adjusted coefficient of determination results for optimal modelling methods. However, the first and second data set selections are conflicted to what was previously suggested from the adjusted coefficients. The selection criterions use the RSE in natural logarithm based function and penalizes free parameters differently from the formulas in section 4.7.6. This led to favourable selections in the first and second data sets.

Table 5.3. Summary of the best calibration models to predict physicochemical properties.

Description	All Catalytic Reactions	Sulfided Catalytic Reactions	Sulfided Pellet Reactions	Sulfided <45µm Solids	^{1}H NMR 400MHz Data	^{1}H NMR 60MHz Data
Data Set (m)	First Set (34)	Second Set (25)	Third Set (14)	Fourth Set (11)	Fifth Set (6)	Sixth Set (13)
Optimal Method	PLSR	MLR	MLR	MLR	PLSR* SLS/MLR**	MLR
Best Properties Calibrated	Sulfur	Nitrogen* IBP-300°C**	400-500°C* Nitrogen Conversion**	Density	Total Aromatic Hydrogen Conversion* Aromatic Hydrogen**	Total Aromatic Hydrogen Conversion
Parameters (k)	8	23* 17**	12* 7**	5	3* 1**	4
R^2_{adj}	0.92	1	1	1	0.86* 0.75**	0.86
AIC	-80.8	-796.8*	-380*	-78.5	-11.2*	-22.8
AIC_c	-75	-126.6**	-77.6**	-66.5	-6.6	-17.8
AIC_u	-65.9	-98.2**	-67.9**	-59.8	-5.5	-13
BIC	-68.6	-768.7*	-372.3*	-76.5	-11.8*	-20.5

A summary of the best calibration results to predict physicochemical properties is shown in *Table 5.3*. The minimum AIC and BIC values suggest the nitrogen concentration using the MLR stepwise method with the second data set is the optimal model in the comparison. The minimum AIC_c and AIC_u values suggest the IBP-300°C fraction model using MLR with the second data is optimal. These models had low RSE's and a relatively high number of parameters included in their

calibration models. Sulfur, 400-500°C, nitrogen conversion, and density correlated well with their respective data sets. Total aromatic hydrogen conversion and aromatic hydrogen were the best calibration results from the fifth and sixth data sets.

Successful calibration of aromatic hydrogen and total aromatic hydrogen conversion in the fifth and sixth sets provide validity to the hypsochromic visible spectra shifts seen from HDA reactions from hydrotreatment. This is seen for sulfur and nitrogen concentrations in the first three data sets. This confirms the HDS and HDN reactions impact the visible adsorption spectra. The reduction in sulfur and nitrogen, and their respective conversions are successfully calibrated to their liquid product visible adsorption spectra.

The boiling point distribution calibration models for the second to fourth data sets were optimal compared to the best properties in *Table 5.3*. As highlighted in *Table 4.18*, the 57wt.%, 81wt.%, and the 77wt.% fractions off using the MLR method were the best calibration results overall. These specific fractions correlated well to the liquid product visible absorption spectra and is confirmed by similar results presented in *Figure 2.34* by Shoute et al. [22].

Chapter 6: Conclusion and Recommendations

Online analytical tools are needed to optimize the upgrading process. This technology could reduce environmental impacts, reduce costs, and enhance quality control. One of the challenges of online analytical tools discussed was the chemical complexity of heavy oil feeds and their dynamic compositional transformations. Visible spectroscopy was an example of an analytical method that could be developed as an online analytical tool. The current study focused on this method as an application in the hydrotreating process.

Part of the upgrading process, the current study focused on hydrotreating reactions of an intermediate Heavy Vacuum Gas Oil (HVGO) feed derived from Athabasca Bitumen. Reactions included hydrodesulfurization (HDS), hydrodenitrogenation (HDN), and hydrodearomatization (HDA).

The first objective consisted of a broad set of experimental reactions that used a batch microreactor with sulfided Ni-Mo/γ-Al$_2$O$_3$ catalyst pellets and <45μm solids.

The second objective completed ex-situ observation and characterization of the hydrotreated liquid products generated to assess product quality. Several analytical methods were assessed:

- Carbon and Hydrogen
- Sulfur and Nitrogen
- Density
- Boiling Point Distribution
- Hydrogen Proton Nuclear Magnetic Resonance
- Visible Absorption Spectrum

A visible spectroscope was developed to observed and measure the color of mild hydrotreated liquid products in a 2mm absorption cuvette.

The third objective addressed the dynamic compositional transformations of six experimental effects. Of the broad set of experimental reactions, controls, catalyst use, mixing, and catalyst sulfidation were assessed. A range of reaction temperatures, 290-390°C, and times, 0.25-2h, and catalyst size effects were tested. This broad experimental matrix provided a data set for the fourth objective.

The fourth objective calibrated the visible spectra of liquid products to respective analytical characterization results through chemometric analysis. Six data sets were created, and four modelling methods were assessed:

- Simple Least Squares
- Multiple Linear Regression
- Principal Component Regression
- Partial Least Squares Regression

Model selection criteria, Akaike and Bayesian, were used to determined which modelling methods and physicochemical property were optimally calibrated to their visible absorption spectra.

6.1 Conclusion

Mild hydrotreating reactions were successfully completed on a HVGO industrial feed using batch microreactors. Two sizes of industrial Ni-Mo/γ-Al$_2$O$_3$ pellets and <45µm solids catalyst were successfully activated through sulfidation reactions. A broad experimental matrix was completed to collect a diverse set of liquid products. The operating conditions reported were similar to hydrotreating literature with the exception of hydrogen rate. The internal reaction temperature of the batch microreactor was successfully verified. The mass balance for each reaction was successful for each experimental run. The challenge of liquid product and catalyst separation was solved by solvent dilution, filtration, and evaporation overnight. This step reduced liquid recovery and limited the product quality assessment, however remained consistent for all reactions. This provided a successful set of colored liquid products for characterization.

The analytical methods were completed on the liquid products to provide a broad set of physicochemical properties. Carbon and hydrogen were used to calculate the hydrogen to carbon ratio (H/C). Errors were as high as 2wt.%. Sulfur and nitrogen were repeatable with errors as high as 0.18wt.%. Density measurements were validated with an external method to that of the syringe and balance scaled used. Accuracy was limited to 0.01g/ml. Boiling point distribution for all samples were measured successfully. Two nuclear magnetic resonance spectrometers, 400MHz and 60MHz, were used to measure molecular hydrogen concentration of select liquid products. These results were comparable on an aromatic hydrogen conversion basis. The visible absorption

spectra of the liquid products were measured on the developed spectrophotometer and successfully validated with an external device. The absorption data collected is successfully implemented in the chemometric analysis objective.

Compositional transformations were tested to enhance the knowledge of the mild hydrotreating reactions completed. The reactor wall effect was found catalytically active if not maintained properly prior to loading. Liquid products were found contaminated with catalyst solids following reaction in the visible adsorption spectrum. Solvent filtration separated catalyst from the liquid product and provided a consist control. The use of a catalyst altered the liquid product composition significantly. The HDS, HDN, and HDA reactions were completed successfully when a catalyst was used. Mixing effects were difficult to assess in the current study. The use of a sulfided catalyst impacted sulfur, nitrogen, the 500°C to final boiling point fraction, and the visible adsorption spectra significantly. Increasing reaction temperature and time had a positive effect on HDS, HDN, and HDA reactions. Temperature effects were significant on the liquid product visible adsorption spectra compared to reaction time. Catalyst size impacted the H/C and sulfur concentrations, however, the comparison was limited as total sulfur contents found in each catalyst was different.

Chemometric analysis used the visible spectra of the liquid products to successfully calibrate the physicochemical properties characterized. The study was limited to a training data set. Six data sets and four modeling methods were compared to determine which provided the best calibration result. From an initial assessment, data sets with similar reactor loading conditions provided the highest average of adjusted coefficient of determination results. The partial least square regression and multiple linear regression through stepwise variable selection were the best methods to use for calibration. Model selection criteria corroborated these results. Depending on the data set used, sulfur, nitrogen, initial boiling point to 300°C fraction, 400 to 500°C fraction, density, total aromatic hydrogen and its conversion, were found as the best properties calibrated from their respective visible spectra. The 57, 81, and 77wt.% fractions off from the boiling point distribution curve using multiple linear regression were determined optimal out of 527,715 calibration models overall.

6.2 Recommendations

Future hydrotreating reactions completed with a continuous fixed catalytic bed reactor should be considered. Data obtained can then be easily compared to literature and industrial studies. Replicable operating conditions are needed provide better assessment of the dynamic compositional transformations. This system is predicted to provide better mass balance and avoid solvent dilution, filtration, and evaporation steps.

A larger range of operating conditions could obtain a broader set of liquid products. A spectrometer developed for a continuous unit, temperature, flow rate, and other operating conditions will directly impact the spectra. These liquid products could produce spectra in the visible to ultra-violent adsorption spectrum which provides additional knowledge on the significant hypsochromic color change of the brown HVGO to a yellow-clear liquid product.

For analytical characterizations collecting a large volume of liquid product is recommended as this could provide duplicate measurements, error assessment, and validation. The density measurement should use a calibrated instrument to improve accuracy. Carbon nuclear magnetic resonance and gas chromatography-mass spectrometry could provide additional insight into the complexity of the chemistry. This speciation could provide knowledge on how color is related to the chemical structure changes from hydrotreatment.

Other dynamic transformations such as catalyst type, hydrogen pressure, and feed to catalyst ratio could provide a broader liquid product data set for calibration.

Another recommendation is model validation. Additional reactions could be used to validate the models presented. A predicted response as a function of the measured property on generated liquid products could complete this validation. Assessing other modeling methods such as artificial neural networks is recommended.

It is recommended to assess other forms of electromagnetic radiation spectra from different interactions (i.e. reflectance, fluorescence etc.), such as infrared and NMR as these are common for industrial application.

In conclusion, from the current study and these recommendations, chemometric models implemented in online analytical tools would optimize hydrotreating processes, reduce costs, and enhanced quality control. This technology is advantageous for all upgrader and refinery facilities.

References

Chapter 1 References

[1] IEA, *Medium-Term Oil Market Report 2016.* Organisation for Economic Co-operation and Development, 2016.

[2] IEA, *World Energy Outlook 2017.* Organisation for Economic Co-operation and Development, 2016.

[3] IEA, *World Energy Outlook 2016.* Organisation for Economic Co-operation and Development, 2015.

[4] IEA, *World Energy Outlook 2014.* Organisation for Economic Co-operation and Development, 2014.

[5] AER, *ST98-2016: Alberta's Energy Reserves 2015 and Supply/Demand Outlook 2016-2025.* Calgary: Alberta Energy Regulator, 2016.

[6] AER, *ST98:2017: Alberta's Energy Reserves & Supply/Demand Outlook.* Calgary: Alberta Energy Regulator, 2017.

[7] G. Moritis. ERCB update expects bitumen production doubling by 2017. *Oil & Gas Journal* pp. 51-52,54-56. 2008.

[8] M. R. Gray, *Upgrading Oilsands Bitumen and Heavy Oil.* Edmonton, Alberta: Pica Pica Press, An Imprint of The University of Alberta Press, 2015.

[9] C. S. Hsu and P. R. Robinson, *Practical Advances in Petroleum Processing.* New York: Springer, 2006.

[10] J. G. Speight and J. Ancheyta Jurez, *Hydroprocessing of Heavy Oils and Residua.* Boca Raton: CRC Press, 2007.

[11] N. S. El-Gendy and J. G. Speight, *Handbook of Refinery Desulfurization.* Boca Raton: CRC Press, 2016.

[12] J. G. Speight, *The Chemistry and Technology of Petroleum.* Boca Raton: CRC Press, 2014.

[13] Environment and Climate Change Canada, "Consolidation Sulphur in Gasoline Regulations SOR/99-236", Minister of Justice, 2015. Available: https://www.ec.gc.ca/lcpe-cepa/eng/regulations/detailReg.cfm?intReg=18.

[14] Environment and Climate Change Canada, "Consolidation Sulphur in Diesel Regulations SOR/2002-254", Minister of Justice, 2012. Available: https://www.ec.gc.ca/lcpe-cepa/eng/regulations/detailReg.cfm?intReg=63.

[15] Jacobs Consultancy Canada Inc., "Technology opportunities to improve the competitiveness of Alberta's oil sands for U.S. refineries," Alberta Innovates - Energy and Environment Solutions, Calgary, Alberta, October 2012. Available: http://eipa.alberta.ca/.

[16] ASTM International, *Journal of ASTM International.* West Conshohocken, PA: ASTM International, 2017. Available: https://www.astm.org/.

[17] J. G. Speight, *Handbook of Petroleum Product Analysis.* Hoboken: John Wiley & Sons, 2014.

[18] S. Badoga *et al*, "Hydrotreating of heavy gas oil on mesoporous zirconia supported NiMo catalyst with EDTA," *Fuel,* vol. 128, pp. 30-38, 2014.

[19] Y. Long, T. Dabros and H. Hamza, "Analysis of Solvent-Diluted Bitumen from Oil Sands Froth Treatment Using NIR Spectroscopy," *Can. J. Chem. Eng.,* vol. 82, pp. 776-781, 2004.

[20] T. Chatterjee and D. N. Saraf, "On-line estimation of product properties for crude distillation units," *J. Process Control,* vol. 14, pp. 61, 2004.

[21] M. Bassbasi *et al*, "Study of motor oil adulteration by infrared spectroscopy and chemometrics methods," *Fuel,* vol. 104, pp. 798-804, 2013.

[22] C. T. Pinheiro *et al*, "Assessment and Prediction of Lubricant Oil Properties Using Infrared Spectroscopy and Advanced Predictive Analytics," *Energy Fuels,* vol. 31, pp. 179-187, 2017.

[23] E. Feng, E. Domlan and R. Kadali, "Spectroscopic Measurements in Oil Sands Industry-From Laboratories to Real-time Applications," *IFAC-PapersOnLine,* vol. 48, pp. 199-204, 2015.

[24] K. A. Bakeev, *Process Analytical Technology: Spectroscopic Tools and Implemented Strategies for the Chemical and Pharmaceutical Industries.* Chichester, West Sussex: Wiley, 2010.

[25] Andrews, John, Beck, Gary, Castelijns, Kees, Chen, Andy, Cribbs, Myrt, Fadnes, Finn, Irvine-Fortescue, Jamie, Williams, Stephen, Hashem, Mohamed, Jamaluddin, A., Kurkjian, Andrew, Sass, Bill, Mullins, Oliver, Rylander, Erik, Van Dusen, Alexandra, "Quantifying Contamination Using Color of Crude and Condensate," pp. 24-43, Autumn. 2001.

[26] Betancourt, Soraya, Fujisawa, Go, Mullins, Oliver, Carnegie, Andrew, Dong, Chengli, Kurkjian, Andrew, Otto Eriksen, Kare, Haggag, Mostafa, Jaramillo, Antonio, Terabayashi, Harry, "Analyzing Hydrocarbons in the Borehole," pp. 54-61, Autumn. 2003.

[27] O. C. Mullins, *Asphaltenes, Heavy Oils, and Petroleomics.* New York: Springer, 2007.

[28] Schlumberger, "InSitu Fluid Analyzer Quantitative Fluid Measurements at reservoir conditions, in real time," *Schlumberger,* 2008.

[29] J. Creek *et al*, "Downhole Fluids Laboratory," pp. 38-54, Winter. 2009.

[30] P. Harris, "Applying Near Infrared Spectroscopy to the Online Determination of Composition and Physical Properties of Crudes and Condensates," *Optical Solutions to Process Automation*, Insight Analytical. Proceedings of Joint CCQTA-COQA Meeting 7-10 June, 2016. Edmonton, AB. http://www.coqa-inc.org/meeting-archives. http://www.insight-analytical.com/.

Chapter 2 References

[1] D. S. J. Jones and P. R. Pujad, *Handbook of Petroleum Processing.* Dordrecht: Springer, 2006.

[2] J. H. Gary, M. J. Kaiser and G. E. Handwerk, *Petroleum Refining: Technology and Economics.* (5th ed.) Boca Raton: Taylor & Francis, 2007.

[3] H. Topsøe, B. S. Clausen and F. E. Massoth, "Hydrotreating catalysis," in *Catalysis: Science and Technology*, J. R. Anderson and M. Boudart, Eds. Berlin, Heidelberg: Springer Berlin Heidelberg, 1996, pp. 1-269.

[4] L. Mapiour, "Kinetics and Effects of H_2 Partial Pressure on Hydrotreating of Heavy Gas Oil," University of Saskatchewan, 2009.

[5] A. Owusu-Boakye, "Two-Stage Aromatics Hydrogenation of Bitumen-Derived Light Gas Oil," University of Saskatchewan, 2005.

[6] S. M. Yui and E. C. Sanford, "Kinetics of aromatics hydrogenation of bitumen-derived gas oils," *The Canadian Journal of Chemical Engineering,* vol. 69, *(5),* pp. 1087-1095, 1991.

[7] S. Yui, N. Matsumoto and Y. Sasaki, "Athabasca oil sands produce quality FCC feeds," *Oil & Gas Journal,* pp. 43-51, 1998.

[8] S. Yui, "Removing diolefins from coker naphtha necessary before hydrotreating," *Oil & Gas Journal,* pp. 64-68, 1999.

[9] S. Yui, "Athabasca oilsands produce quality diesel and jet fuels," *Oil & Gas Journal,* pp. 58-66, 2000.

[10] S. Yui and K. H. Chung. "Processing oilsands bitumen is Syncrude's R&D focus," *Oil & Gas Journal* pp. 46-53. 2001.

[11] S. K. Bej, A. K. Dalai and J. Adjaye, "Comparison of Hydrodenitrogenation of Basic and Nonbasic Nitrogen Compounds Present in Oil Sands Derived Heavy Gas Oil," *Energy Fuels,* vol. 15, *(2),* pp. 377-383, 2001.

[12] S. Yui, "Producing Quality Synthetic Crude Oil from Canadian Oil Sands Bitumen," *Journal of the Japan Petroleum Institute,* vol. 51, pp. 1-13, 2008.

[13] A. Owusu-Boakye *et al*, "Experimental and Kinetic Studies of Aromatic Hydrogenation, Hydrodesulfurization, and Hydrodenitrogenation of Light Gas Oils Derived from Athabasca Bitumen," *Ind. Eng. Chem. Res.,* vol. 44, *(21),* pp. 7935-7944, 2005.

[14] J. Chen, H. Farooqi and C. Fairbridge, "Experimental Study on Co-hydroprocessing Canola Oil and Heavy Vacuum Gas Oil Blends," *Energy Fuels,* vol. 27, *(6),* pp. 3306-3315, 2013.

[15] M. R. Gray, *Upgrading Oilsands Bitumen and Heavy Oil.* Edmonton, Alberta: Pica Pica Press, An Imprint of The University of Alberta Press, 2015.

[16] M. R. Gray, "New technique defines the limits of upgrading heavy oils, bitumens," *Oil & Gas Journal,* vol. 100, pp. 50-54, 2002.

[17] S. Yui and K. H. Chung. "Syncrude upgrader revamp improves product quality," *Oil & Gas Journal,* pp. 52-54,56-59. 2007.

[18] C. S. Hsu and P. R. Robinson, *Practical Advances in Petroleum Processing.* New York: Springer, 2006.

[19] J. G. Speight and B. Ozum, *Petroleum Refining Processes.* New York, NY: Marcel Dekker, Inc., 2002.

[20] M. H. Al-Dahhan and M. P. Duduković, "Catalyst wetting efficiency in trickle-bed reactors at high pressure," *Chemical Engineering Science,* vol. 50, *(15),* pp. 2377-2389, 1995.

[21] A. Kundu, K. D. P. Nigam and R. P. Verma, "Catalyst wetting characteristics in trickle-bed reactors," *AIChE J.,* vol. 49, *(9),* pp. 2253-2263, 2003.

[22] R. C. Patil *et al*, "Effect of reactor configuration on performance of vacuum gas oil (VGO) hydrotreater: Modelling studies," *Computers & Chemical Engineering,* vol. 104, pp. 89-106, 2017.

[23] J. G. Speight, *The Chemistry and Technology of Petroleum.* Boca Raton: CRC Press, 2014.

[24] S. Yui and J. Adjaye, "Determining average bed temperature of nonisothermal fixed-bed hydrotreater," *Fuel,* vol. 83, *(14),* pp. 1929-1937, 2004.

[25] C. H. Bartholomew, "Mechanisms of catalyst deactivation," *Applied Catalysis A: General,* vol. 212, *(1),* pp. 17-60, 2001.

[26] H. Y. Cai, J. M. Shaw and K. H. Chung, "Hydrogen solubility measurements in heavy oil and bitumen cuts," *Fuel,* vol. 80, *(8),* pp. 1055-1063, 2001.

[27] M. R. Gray, N. Srinivasan and J. H. Masliyah, "Pressure buildup in gas-liquid flow through packed beds due to deposition of fine particles," *The Canadian Journal of Chemical Engineering,* vol. 80, *(3),* pp. 346-354, 2002.

[28] R. Rana *et al*, "The Impact of Process Parameters on the Deposition of Fines Present in Bitumen-Derived Gas Oil on Hydrotreating Catalyst," *Energy Fuels,* vol. 31, *(6),* pp. 5969-5981, 2017.

[29] K. K. Soni *et al*, "Hydrotreating of coker light gas oil on SBA-15 supported nickel phosphide catalysts," *Catalysis Today,* vol. 207, pp. 119-126, 2013.

[30] I. Chorkendorff and J. W. Niemantsverdriet, *Concepts of Modern Catalysis and Kinetics.* Weinheim Germany: Wiley-VCH, 2003.

[31] M. Trueba and S. P. Trasatti, "γ-Alumina as a Support for Catalysts: A Review of Fundamental Aspects," *European Journal of Inorganic Chemistry,* vol. 2005, *(17),* pp. 3393-3403, 2005.

[32] S. Badoga *et al*, "Synthesis and characterization of mesoporous aluminas with different pore sizes: Application in NiMo supported catalyst for hydrotreating of heavy gas oil," *Applied Catalysis A: General,* vol. 489, pp. 86-97, 2015.

[33] J. M. Herrera *et al*, "New hydrotreating NiMo catalysts supported on MCM-41 modified with phosphorus," *Microporous and Mesoporous Materials,* vol. 83, *(1-3),* pp. 283-291, 2005.

[34] R. C. Ryan *et al*, "Stacking of Molybdenum Disulfide Layers in Hydrotreating Catalysts," *Studies in Surface Science and Catalysis,* vol. 50, pp. 21-40, 1989.

[35] D. Ferdous, A. K. Dalai and J. Adjaye, "A series of NiMo/Al$_2$O$_3$ catalysts containing boron and phosphorus," *Applied Catalysis A: General,* vol. 260, *(2),* pp. 153-162, 2004.

[36] T. ZHOU *et al*, "Influences of different phosphorus contents on NiMoP/Al2O3 hydrotreating catalysts," *Journal of Fuel Chemistry and Technology,* vol. 37, *(3),* pp. 330-334, 2009.

[37] H. S. Fogler, *Elements of Chemical Reaction Engineering.* (4th ed.) Upper Saddle River, NJ: Prentice Hall PTR, 2006.

[38] E. Furimsky, *Catalysts for Upgrading Heavy Petroleum Feeds.* Amsterdam, NL: Elsevier, vol. 169, pp. 1-387, 2007.

[39] S. Eijsbouts *et al*, "Nickel sulfide crystals in Ni-Mo and Ni-W catalysts: Eye-catching inactive feature or an active phase in its own right?" *Catalysis Today,* 2016.

[40] R. Prins, De Beer, V H J and G. A. Somorjai, "Structure and Function of the Catalyst and the Promoter in Co—Mo Hydrodesulfurization Catalysts," *Catalysis Reviews,* vol. 31, pp. 1-41, 1989.

[41] J. V. Lauritsen *et al*, "Atomic-Scale Structure of Co–Mo–S Nanoclusters in Hydrotreating Catalysts," *Journal of Catalysis,* vol. 197, *(1),* pp. 1-5, 2001.

[42] G. Marroquín, J. Ancheyta and J.A.I. Díaz, "On the effect of reaction conditions on liquid phase sulfiding of a NiMo HDS catalyst," *Catalysis Today,* vol. 98, pp. 75-81, 2004.

[43] S. Blashka, G. Bond and D. Ward, "New presulfurized catalyst reduces exotherm potential in hydrocrackers," *Oil & Gas Journal,* vol. 96, (1), pp. 36-40, 1998.

[44] J. S. Magee and G. E. Dolbear, *Petroleum Catalysis in Nontechnical Language.* Tulsa, OK: PennWell, 1998.

[45] Criterion Catalyst & Technologies, "Criterion* Hydrotreating Catalyst In-situ Presulphiding Guidelines," Criterion Catalyst & Technologies, 1998.

[46] V. I. Prvulescu and E. Kemnitz, *New Materials for Catalytic Applications.* Amsterdam: Elsevier, 2016.

[47] S. Texier *et al*, "Activation of alumina-supported hydrotreating catalysts by organosulfides: comparison with H_2S and effect of different solvents," *Journal of Catalysis,* vol. 223, *(2),* pp. 404-418, 2004.

[48] S. Texier *et al*, "Activation of alumina-supported hydrotreating catalysts by organosulfides or H_2S: Effect of the H_2S partial pressure used during the activation process," *Applied Catalysis A: General,* vol. 293, pp. 105-119, 2005.

[49] C. Yin and Y. Wang, "Effect of sulfidation process on catalytic performance over unsupported Ni-Mo-W hydrotreating catalysts," *Korean Journal of Chemical Engineering,* vol. 34, *(4),* pp. 1004-1012, 2017.

[50] C. Glasson *et al*, "Beneficial Effect of Carbon on Hydrotreating Catalysts," *Journal of Catalysis,* vol. 212, *(1),* pp. 76-85, 2002.

[51] A. C. Vicente da Silva, "Study of the liquid activation of CoMo and NiMo catalysts," Tecnico Lisboa, 2014.

[52] Echard M (2001) Contribution à la connaissance des catalyseurs d'hydrotraitement CoMo/Al_2O_3: étudede la sulfuration et de l'adsorption d'H_2S sous flux, PhD thesis, University of Caen.

[53] H. Toulhoat and P. Raybaud, *Catalysis by Transition Metal Sulphides: From Molecular Theory to Industrial Application.* Paris, France: Technip, 2013. Pg. 286, Figure 2.99, Chapter 2.4, Section 2.4.2.2.

[54] E. Laurent and B. Delmon, "Influence of water in the deactivation of a sulfided NiMo γ-Al_2O_3 catalyst during hydrodeoxygenation," *Journal of Catalysis, vol 146(1),* pp. 281-291. 1994.

[55] O. P. Strausz, E. M. Lown and Alberta Energy Research Institute, *The Chemistry of Alberta Oil Sands, Bitumens and Heavy Oils.* Calgary: Alberta Energy Research Institute, 2003.

[56] R. H. Perry and D. W. Green, *Perry's Chemical Engineers' Handbook.* (8th ed.) New York: McGraw-Hill, 2008.

[57] D. J. Luning Prak, E. K. Brown and P. C. Trulove, "Density, Viscosity, Speed of Sound, and Bulk Modulus of Methyl Alkanes, Dimethyl Alkanes, and Hydrotreated Renewable Fuels," *J. Chem. Eng. Data,* vol. 58, *(7),* pp. 2065-2075, 2013.

[58] I. A. McLure and J. Barbarin-Castillo, "Density of cyclodecane from 25 to 192.degree.C," *J. Chem. Eng. Data,* vol. 30, *(3),* pp. 253-254, 1985.

[59] National Institute of Standards and Technology, "NIST chemistry webbook," Available: http://webbook.gov/chemistry/.

[60] ASTM Standard D3279, 1973 (2012), "Standard Test Method for n-Heptane Insolubles," ASTM International, West Conshohocken, PA, 2012, DOI: 10.1520/D3279-12E01, www.astm.org.

[61] ASTM Standard D6560, 2000 (2012), "Standard Test Method for Determination of Asphaltenes (Heptane Insolubles) in Crude Petroleum and Petroleum Products," ASTM International, West Conshohocken, PA, 2012, DOI: 10.1520/D6560-12, www.astm.org.

[62] O. C. Mullins, *Asphaltenes, Heavy Oils, and Petroleomics.* New York: Springer, 2007.

[63] S. S. Betancourt *et al*, "Nanoaggregates of Asphaltenes in a Reservoir Crude Oil and Reservoir Connectivity," *Energy Fuels,* vol. 23, *(3),* pp. 1178-1188, 2009.

[64] M. R. Gray *et al*, "Supramolecular Assembly Model for Aggregation of Petroleum Asphaltenes," *Energy Fuels,* vol. 25, *(7),* pp. 3125-3134, 2011.

[65] K. Ghosh *et al*, "Review on aggregation of asphaltene vis-a-vis spectroscopic studies," *Fuel,* vol. 185*,* pp. 541-554, 2016.

[66] H. Altgelt and M. M. Boduszynski, *Composition and Analysis of Heavy Petroleum Fractions.* Boca Raton, Fla.: CRC Press, 1993.

[67] D. F. Smith *et al*, "Characterization of Athabasca Bitumen Heavy Vacuum Gas Oil Distillation Cuts by Negative/Positive Electrospray Ionization and Automated Liquid Injection Field Desorption Ionization Fourier Transform Ion Cyclotron Resonance Mass Spectrometry," *Energy Fuels,* vol. 22, *(5),* pp. 3118-3125, 2008.

[68] A. M. McKenna *et al*, "Heavy Petroleum Composition. 1. Exhaustive Compositional Analysis of Athabasca Bitumen HVGO Distillates by Fourier Transform Ion Cyclotron Resonance Mass

Spectrometry: A Definitive Test of the Boduszynski Model," *Energy Fuels,* vol. 24, *(5),* pp. 2929-2938, 2010.

[69] D. F. Smith *et al*, "Characterization of Acidic Species in Athabasca Bitumen and Bitumen Heavy Vacuum Gas Oil by Negative-Ion ESI FT−ICR MS with and without Acid−Ion Exchange Resin Prefractionation," *Energy Fuels,* vol. 22, *(4),* pp. 2372-2378, 2008.

[70] D. F. Smith *et al*, "Effect of Thermal Treatment on Acidic Organic Species from Athabasca Bitumen Heavy Vacuum Gas Oil, Analyzed by Negative-Ion Electrospray Fourier Transform Ion Cyclotron Resonance (FT-ICR) Mass Spectrometry," *Energy Fuels,* vol. 23, *(1),* pp. 314-319, 2009.

[71] R. Javadli and A. de Klerk, "Desulfurization of heavy oil," *Applied Petrochemical Research,* vol. 1, *(1),* pp. 3-19, 2012.

[72] G. Brons and J. M. Yu, "Solvent Deasphalting Effects on Whole Cold Lake Bitumen," *Energy Fuels,* vol. 9, *(4),* pp. 641-647, 1995.

[73] G. H. C. Prado, Y. Rao and A. de Klerk, "Nitrogen Removal from Oil: A Review," *Energy Fuels,* vol. 31, *(1),* pp. 14-36, 2017.

[74] J. R. Katzer and R. Sivasubramanian, "Process and Catalyst Needs for Hydrodenitrogenation," *Catalysis Reviews,* vol. 20, *(2),* pp. 155-208, 1979.

[75] J. G. Speight, *High Acid Crudes.* Waltham, MA: Gulf Professional Publishing, an imprint of Elsevier, 2014.

[76] M. M. Ramrez-Corredores, *The Science and Technology of Unconventional Oils: Finding Refining Opportunities.* London, UK: Elsevier Inc., 2017.

[77] Rita Giovannetti ED1, Jamal Uddin, "The use of spectrophotometry UV-vis for the study of porphyrins," in *Macro to Nano Spectroscopy,* 2012.

[78] M. Thompson and J. N. Walsh, *Handbook of Inductively Coupled Plasma Spectrometry.* 2nd ed. New York, NY: Chapman and Hall, Blackie & Son Ltd., 1989.

[79] H. E. Taylor, *Inductively Coupled Plasma-Mass Spectrometry.* San Diego, USA: Academic Press, 2001.

[80] M. Houalla *et al*, "Hydrodesulfurization of dibenzothiophene catalyzed by sulfided CoO-MoO$_3\gamma$-Al$_2$O$_3$: The reaction network," *AIChE J.,* vol. 24, *(6),* pp. 1015-1021, 1978.

[81] N. S. El-Gendy and J. G. Speight, *Handbook of Refinery Desulfurization.* Boca Raton*:* CRC Press, 2016.

[82] J.G. Speight, *The Desulfurization of Heavy Oils and Residua.* New York, NY: Marcel Dekker Inc., 2000.

[83] M. J. Girgis and B. C. Gates, "Reactivities, reaction networks, and kinetics in high-pressure catalytic hydroprocessing," *Ind. Eng. Chem. Res.,* vol. 30, *(9),* pp. 2021-2058, 1991.

[84] T. Kabe, W. Qian and A. Ishihara, *Hydrodesulfurization and Hydrodenitrogenation: Chemistry and Engineering.* Tokyo: Kodansha, Wiley, 1999.

[85] T. Kabe, A. Ishihara and H. Tajima, "Hydrodesulfurization of sulfur-containing polyaromatic compounds in light oil," *Ind. Eng. Chem. Res.,* vol. 31, *(6),* pp. 1577-1580, 1992.

[86] X. Ma, K. Sakanishi and I. Mochida, "Hydrodesulfurization Reactivities of Various Sulfur Compounds in Vacuum Gas Oil," *Ind. Eng. Chem. Res.,* vol. 35, *(8),* pp. 2487-2494, 1996.

[87] J. H. Kim *et al*, "Kinetic Study of 4,6-Dimethyldibenzothiophene Hydrodesulfurization over Ni Phosphide," *Fuel Chemistry Division Preprints,* vol. 48, *(1),* pp. 40, 2003.

[88] S. K. Bej, S. K. Maity and U. T. Turaga, "Search for an Efficient 4,6-DMDBT Hydrodesulfurization Catalyst: A Review of Recent Studies," *Energy Fuels,* vol. 18, *(5),* pp. 1227-1237, 2004.

[89] F. Bataille *et al*, "Alkyldibenzothiophenes Hydrodesulfurization-Promoter Effect, Reactivity, and Reaction Mechanism," *Journal of Catalysis,* vol. 191, *(2),* pp. 409-422, 2000.

[90] J. Fu *et al*, "Comprehensive Compositional Analysis of Hydrotreated and Untreated Nitrogen-Concentrated Fractions from Syncrude Oil by Electron Ionization, Field Desorption Ionization, and Electrospray Ionization Ultrahigh-Resolution FT-ICR Mass Spectrometry," *Energy Fuels,* vol. 20, *(3),* pp. 1235-1241, 2006.

[91] R. T. Hanlon, "Effects of P_{H2S}, P_{H2}, and P_{H2S}/P_{H2} on the hydrodenitrogenation of pyridine," *Energy Fuels,* vol. 1, *(5),* pp. 424-430, 1987.

[92] C. N. Satterfield and S. H. Yang, "Catalytic hydrodenitrogenation of quinoline in a trickle-bed reactor. Comparison with vapor phase reaction," *Ind. Eng. Chem. Proc. Des. Dev.,* vol. 23, *(1),* pp. 11-19, 1984.

[93] J. R. Katzer and R. Sivasubramanian, "Process and Catalyst Needs for Hydrodenitrogenation," *Catalysis Reviews,* vol. 20, *(2),* pp. 155-208, 1979.

[94] T. C. Ho, "Hydrodenitrogenation Catalysis," *Catalysis Reviews,* vol. 30, *(1),* pp. 117-160, 1988.

[95] R. Prins, "Catalytic hydrodenitrogenation," *Advances in Catalysis,* vol. 46, *(Supplement C),* pp. 399-464, 2001.

[96] E. Furimsky and F. E. Massoth, "Hydrodenitrogenation of Petroleum," *Catalysis Reviews,* vol. 47, *(3),* pp. 297-489, 2005.

[97] P. L. Jokuty and M. R. Gray, "Resistant nitrogen compounds in hydrotreated gas oil from Athabasca bitumen," *Energy Fuels,* vol. 5, *(6),* pp. 791-795, 1991.

[98] D. Ferdous, A. K. Dalai and J. Adjaye, "Comparison of Hydrodenitrogenation of Model Basic and Nonbasic Nitrogen Species in a Trickle Bed Reactor Using Commercial NiMo/Al$_2$O$_3$ Catalyst," *Energy Fuels,* vol. 17, *(1),* pp. 164-171, 2003.

[99] S. M. Yui and S. H. Ng, "Hydrotreating of a Bitumen-Derived Coker HGO and Evaluation of Hydrotreated HGOs as Potential FCC Feeds Using Microactivity Test Unit," *Energy Fuels,* vol. 9, *(4),* pp. 665-672, 1995.

[100] T. Zhang *et al*, "Transformation of Nitrogen Compounds in Deasphalted Oil Hydrotreating: Characterized by Electrospray Ionization Fourier Transform-Ion Cyclotron Resonance Mass Spectrometry," *Energy Fuels,* vol. 27, *(6),* pp. 2952-2959, 2013.

[101] M. Liu *et al*, "Transformation of Nitrogen Compounds through Hydrotreatment of Saudi Arabia Atmospheric Residue and Supercritical Fluid Extraction Subfractions," *Energy Fuels,* vol. 30, *(1),* pp. 740-747, 2016.

[102] A. Stanislaus and B. H. Cooper, "Aromatic Hydrogenation Catalysis: A Review," *Catalysis Reviews,* vol. 36, *(1),* pp. 75-123, 1994.

[103] S. Albertazzi *et al*, "Hydrogenation and hydrogenolysis/ring-opening of naphthalene on Pd/Pt supported on zirconium-doped mesoporous silica catalysts," *Journal of Catalysis,* vol. 228, *(1),* pp. 218-224, 2004.

[104] E. Furimsky, "Catalytic hydrodeoxygenation," *Applied Catalysis A: General,* vol. 199, *(2),* pp. 147-190, 2000.

[105] E. Furimsky, "Catalytic deoxygenation of heavy gas oil," *Fuel,* vol. 57, *(8),* pp. 494-496, 1978.

[106] V. LaVopa and C. N. Satterfield, "Catalytic hydrodeoxygenation of dibenzofuran," *Energy Fuels,* vol. 1, *(4),* pp. 323-331, 1987.

[107] V. Blacus, "File:Electromagnetic-Spectrum.svg," October 2012. [Online]. Available: http://commons.wikimedia.org/wiki/File:Electromagnetic-Spectrum.svg. [Accessed 7 June 2015].

[108] M. S. Silberberg, *Chemistry The Molecular Nature of Matter and Change*, New York: McGraw-Hill Companies, Inc., 5th, 2009.

[109] R. J. D. Tilley, *Colour and the Optical Properties of Materials*, 2nd edition, West Sussex, UK: John Wiley & Sons, Ltd., 2011.

[110] D. Harvey, *Analytical Chemistry 2.0*, 2nd edition, McGraw-Hill Companies, Inc., David Harvey, 2008.

[111] R. G. Kuehni, *Color An Introducion to Practice and Principles*, 2nd edition, Hoboken, New Jersey: John Wiley & Sons, Inc., 2005.

[112] R. A. Friedel and M. Orchin, *Ultraviolet Spectra of Aromatic Compounds.* New York: Wiley, 1951.

[113] Photoelectric Spectrometry Group and Institut fr Spektrochemie und Angewandte Spektroskopie, *UV Atlas of Organic Compounds. [UV Atlas] Organischer Verbindungen.* London: Butterworths, 1966.

[114] Siedlecki, Piotr, Light Bulb. Available: http://www.publicdomainpictures.net/view-image.php?image=155227&picture=light-bulb

[115] ASTM Standard D156, 1923 (2015), "Standard Test Method for Saybolt Color of Petroleum Products (Saybolt Chromometer Method)," ASTM International, West Conshohocken, PA, 2015, DOI: 10.1520/D0156-15, www.astm.org.

[116] ASTM Standard D1209, 1952 (2011), "Standard Test Method for Color of Clear Liquids (Platinum-Cobalt Scale)," ASTM International, West Conshohocken, PA, 2011, DOI: 10.1520/D1209-05, www.astm.org.

[117] ASTM Standard D1500, 1957 (2012), "Standard Test Method for ASTM Color of Petroleum Products (ASTM Color Scale)," ASTM International, West Conshohocken, PA, 2012, DOI: 10.1520/D1500-12, www.astm.org.

[118] ASTM Standard D1544, 1958 (2010), "Standard Test Method for Color of Transparent Liquids (Gardner Color Scale)," ASTM International, West Conshohocken, PA, 2010, DOI: 10.1520/D1544-04, www.astm.org.

[119] ASTM Standard D2392, 1965 (2015). "Standard Test Method for Color of Dyed Aviation Gasolines," ASTM International, West Conshohocken, PA, 2015, DOI: 10.1520/D2392-15, www.astm.org.

[120] ASTM Standard D5386, 1993 (2010), "Standard Test Method for Color of Liquids Using Tristimulus Colorimetry," ASTM International, West Conshohocken, PA, 2010, DOI: 10.1520/D5386-10, www.astm.org.

[121] ASTM Standard D6045, 1996 (2012), "Standard Test Method for Color of Petroleum Products by the Automatic Tristimulus Method," ASTM International, West Conshohocken, PA, 2012, DOI: 10.1520/D6045-12, www.astm.org.

[122] ASTM Standard D1840, 2013 (2013), "Standard Test Method for Naphthalene Hydrocarbons in Aviation Turbine Fuels by Ultraviolet Spectrophotometry," ASTM International, West Conshohocken, PA, 2013, DOI: 10.1520/D1840-07, www.astm.org.

[123] ASTM Standard D2008, 1962 (2012), "Standard Test Method for Ultraviolet Absorbance and Absorptivity of Petroleum Products," ASTM International, West Conshohocken, PA, 2012, DOI: 10.1520/D2008-12, www.astm.org.

[124] ASTM Standard E169, 1960 (2016), "Standard Test Method for General Techniques of Ultraviolet-Visible Quantitative Analysis," ASTM International, West Conshohocken, PA, 2016, DOI: 10.1520/E0169-16, www.astm.org.

[125] ASTM Standard E275, 1965 (2013), "Standard Test Method for Describing and Measuring Performance of Ultraviolet and Visible Spectrophotometers," ASTM International, West Conshohocken, PA, 2013, DOI: 10.1520/E0275-08R13, www.astm.org.

[126] ASTM Standard E925, 1983 (2014), "Standard Test Method for Monitoring the Calibration of Ultraviolet-Visible Spectrophotometers whose Spectral Bandwidth does not Exceed 2nm," ASTM International, West Conshohocken, PA, 2014, DOI: 10.1520/E0925-09R14, www.astm.org.

[127] O. C. Mullins, S. Mitra-Kirtley and Y. Zhu, "The Electronic Absorption Edge of Petroleum," *Appl. Spectrosc.,* vol. 46, *(9),* pp. 1405-1411, 1992.

[128] Y. Ruiz-Morales and O. C. Mullins, "Polycyclic Aromatic Hydrocarbons of Asphaltenes Analyzed by Molecular Orbital Calculations with Optical Spectroscopy," *Energy Fuels,* vol. 21, *(1),* pp. 256-265, 2007.

[129] A. R. Shukla, *Analytical Characterization Methods for Crude Oil and Related Products*, 2nd edition, West Sussex, UK: John Wiley & Sons Ltd., 2018.

[130] S. Yoon, S. D. Bhatt, W. Lee, H. Y. Lee, S. Y. Jeong, J. Baeg and C. W. Lee, "Separation and characterization of bitumen from Athabasca oil sand," *Korean Journal of Chemical Engineering,* vol. 26, pp. 64-71, 2009.

[131] I. N. Evdokimov, N. Y. Eliseev and B. R. Akhmetov, "Assembly of asphaltene molecular aggregates as studied by near-UV/visible spectroscopy: I. Structure of the absorbance spectrum," *Journal of Petroleum Science and Engineering,* vol. 37, pp. 135-143, 2003.

[132] C. T. Shoute *et al*, "UV Raman Spectroscopy of Oilsands-Derived Bitumen and Commercial Petroleum Products," *Appl. Spectrosc.,* vol. 56, *(10),* pp. 1308-1313, 2002.

[133] I. N. Evdokimov and A. P. Losev, "Suggested "New Method for Determination of Dispersity in Petroleum Systems" Is Based on Trivial Experimental Artifacts," *Energy Fuels,* vol. 22, *(4),* pp. 2470-2473, 2008.

[134] O. C. Mullins, "Method of distinguishing between crude oils," United States Patent 5266800, 30 November 1993.

[135] J.I. Haberman, R.E. Overfield and W. K. Robbins, "Method for spectroscopic analysis of hydrocarbons," United States Patent 4988446, 29 January 1991.

[136] R.E. Overfield, W. K. Robbins and J.I. Haberman, " Method for refining or upgrading hydrocarbons with analysis," United States Patent 5076909, 31 December 1991.

[137] O. R. Koseoglu, A. Al-Hajji and G. Jamieson, "Characterization of crude oil by ultraviolet visible spectroscopy," United States Patent 9778240, 3 October 2017.

[138] S. Japanwala *et al.*, "Quality of Distillates from Repeated Recycle of Residue," *Energy Fuels,* vol. 16, pp. 477-484, 2002.

[139] J. M. Sheremata *et al*, "Quantitative Molecular Representation and Sequential Optimization of Athabasca Asphaltenes," *Energy Fuels,* vol. 18, pp. 1377-1384, 2004.

[140] T.W. Graham Solomons and C. B. Fryhle, *Organic Chemistry*, Hoboken, New Jersey: John Wiley & Sons, Inc., 9th, 2008.

[141] J. G. Speight., "A structural investigation of the constituents of Athabasca bitumen by proton magnetic resonance spectroscopy," *Fuels, vol. 49,* pp. 76-90. 1970.

[142] J. Mühl and V. Srića, "Determination of fluid catalytic cracking gasoline octane number by n.m.r. spectrometry," *Fuel,* vol. 66, *(8),* pp. 1146-1149, 1987.

[143] Y. Yang *et al*, "Study on relationship between the concentration of hydrocarbon groups in heavy oils and their structural parameter from 1H NMR spectra☆," *Fuel,* vol. 82, *(6),* pp. 721-727, 2003.

[144] F. Ali, Z. H. Khan and N. Ghaloum, "Structural Studies of Vacuum Gas Oil Distillate Fractions of Kuwaiti Crude Oil by Nuclear Magnetic Resonance," *Energy Fuels,* vol. 18, *(6),* pp. 1798-1805, 2004.

[145] G. S. Kapur, A. Chopra and A. S. Sarpal, "Estimation of Total Aromatic Content of Vacuum Gas Oil (VGO) Fractions (370−560 °C) by 1H NMR Spectroscopy," *Energy Fuels,* vol. 19, *(3),* pp. 1065-1071, 2005.

[146] V. Bansal *et al*, "Estimation of Total Aromatics and Their Distribution as Mono and Global Di-Plus Aromatics in Diesel-Range Products by NMR Spectroscopy," *Energy Fuels,* vol. 12, *(6),* pp. 1223-1227, 1998.

[147] K. A. Bakeev, *Process Analytical Technology: Spectroscopic Tools and Implemented Strategies for the Chemical and Pharmaceutical Industries.* Chichester, West Sussex: Wiley, 2010.

[148] P. Gemperline, *Practical Guide to Chemometrics.* Boca Raton: CRC/Taylor & Francis, 2006.

[149] R. G. Brereton, *Chemometrics: Data Analysis for the Laboratory and Chemical Plant.* Chichester, West Sussex, England; Hoboken, NJ: Wiley, 2003.

[150] J. Duckworth H., *Spectroscopic Quantitative Analysis.* Chapter 4 *in* J. Workman and A. Springsteen, *Applied Spectroscopy: A Compact Reference for Practitioners.* 1998.

[151] P. D. Wentzell *et al*, "Estimation of hydrocarbon types in light gas oils and diesel fuels by ultraviolet absorption spectroscopy and multivariate calibration," *Can. J. Chem.,* vol. 77, *(3),* pp. 391-400, 1999.

[152] The MathWorks, Inc., *Stepwise Regression: stepwisefit.* MathWorks Website, 2019. Available: https://www.mathworks.com/help/stats/stepwisefit.html.

[153] The MathWorks, Inc., *Partial Least Squares Regression and Principal Components Regression.* MathWorks Website, 2019. Available: https://www.mathworks.com/help/stats/examples/partial-least-squares-regression-and-principal-components-regression.html.

[154] W. R. Gilbert, de Lima, Flavio S Gusmão, and A. F. Bueno, "Comparison of NIR and NMR spectra chemometrics for FCC feed online characterization," in *Studies in Surface Science and Catalysis* Anonymous 2004.

[155] Molina, U. N. Uribe and J. Murgich, "Partial Least-Squares (PLS) Correlation between Refined Product Yields and Physicochemical Properties with the [1]H Nuclear Magnetic Resonance (NMR) Spectra of Colombian Crude Oils," *Energy Fuels,* vol. 21, *(3),* pp. 1674-1680, 2007.

[156] K. E. Nielsen *et al*, "Quantitative Analysis of Constituents in Heavy Fuel Oil by 1H Nuclear Magnetic Resonance (NMR) Spectroscopy and Multivariate Data Analysis," *Energy Fuels,* vol. 22, *(6),* pp. 4070-4076, 2008.

[157] C. R. Souza *et al*, "Cetane Number Assessment in Diesel Fuel by ^{1}H or Hydrogen Nuclear Magnetic Resonance-Based Multivariate Calibration," *Energy Fuels,* vol. 28, *(8),* pp. 4958-4962, 2014.

[158] L. M. Duarte *et al*, "Study of Distillation Temperature Curves from Brazilian Crude Oil by 1H Nuclear Magnetic Resonance Spectroscopy in Association with Partial Least Squares Regression," *Energy Fuels,* vol. 31, *(4),* pp. 3892-3897, 2017.

[159] H. Chung and M. Ku, "Comparison of near-infrared, infrared, and Raman spectroscopy for the analysis of heavy petroleum products," *Appl. Spectrosc.,* vol. 54, *(2),* pp. 239-245, 2000.

[160] S. Satya *et al*, "Estimation of Properties of Crude Oil Residual Fractions Using Chemometrics," *Energy Fuels,* vol. 21, *(2),* pp. 998-1005, 2007.

[161] L. Jingyan, C. Xiaoli and T. Songbai, "Research on Determination of Total Acid Number of Petroleum Using Mid-infrared Attenuated Total Reflection Spectroscopy," *Energy Fuels,* vol. 26, *(9),* pp. 5633-5637, 2012.

[162] M. Chen *et al*, "Recursive Wavelength-Selection Strategy to Update Near-Infrared Spectroscopy Model with an Industrial Application," *Ind Eng Chem Res,* vol. 52, *(23),* pp. 7886-7895, 2013.

[163] C. T. Pinheiro *et al*, "Assessment and Prediction of Lubricant Oil Properties Using Infrared Spectroscopy and Advanced Predictive Analytics," *Energy Fuels,* vol. 31, *(1),* pp. 179-187, 2017.

[164] R. Chakravarthy *et al*, "Sulfur and Total Carboxylic Acid Number Determination in Vacuum Gas Oil by Attenuated Total Reflectance Fourier Transform Infrared Spectroscopy," *Energy Fuels,* vol. 32, *(2),* pp. 2128-2136, 2018.

[165] C. Baldrich Ferrer and L. Novoa Mantilla, "Detailed chemical characterization of petroleum middle fractions by chemometrics analysis of their ultraviolet spectrum," *CT&F-Ciencia, Tecnología Y Futuro,* vol. 3, *(3),* pp. 173-190, 2007.

[166] C. Baldrich Ferrer, "Prediction of physicochemical properties of FCC feedstock by chemometric analysis of their ultraviolet spectrum," *CT&F-Ciencia, Tecnología Y Futuro,* vol. 3, *(4),* pp. 143-156, 2008.

[167] C. N. C. Corgozinho, O. C. de and P. J. S. Barbeira, "Spectrophotometric and Chemometric Determination of the ASTM Color of Automotive Diesel," *Energy and Fuels,* vol. 23, pp. 2136-2142, 2009.

[168] C. Baldrich, L. Novoa and A. Bueno, "Comparison between NIR and UVVIS spectra chemometrics for predicting FCC feedstocks properties," *CT&F-Ciencia, Tecnologa Y Futuro,* vol. 4, pp. 113-125, 2010.

[169] A. M. Kharrat, K. Indo and F. Mostowfi, "Asphaltene Content Measurement Using an Optical Spectroscopy Technique," *Energy Fuels,* vol. 27, *(5),* pp. 2452-2457, 2013.

[170] S. Wu, K. B. McAuley and T. J. Harris, "Selection of simplified models: I. Analysis of model-selection criteria using mean-squared error," *The Canadian Journal of Chemical Engineering,* vol. 89, *(1),* pp. 148-158, 2011.

[171] K. P. Burnham and D. R. Anderson, "Multimodel inference: understanding AIC and BIC in model selection," *Sociological Methods & Research,* vol. 33, *(2),* pp. 261-304, 2004.

[172] S. Sánchez, J. Ancheyta and W. C. McCaffrey, "Comparison of probability distribution functions for fitting distillation curves of petroleum," *Energy Fuels,* vol. 21, *(5),* pp. 2955-2963, 2007.

Chapter 3 References

[1] A. F. de Vries and W. H. J. Stork, "Process for the Preparation of Light Hydrocarbon Distillates by Hydrocracking and Catalytic Cracking". United States Patent 4859309, 22 August 1989.

[2] J. R. Butler and W. P. Licht, "Catalytic Dewaxing Process". United States Patent 4917789, 17 April 1990.

[3] Z.-S. Ying, B. Gevert and J.-E. Otterstedt, "Large-Pore Catalysts for Hydroprocessing of Residual Oils," *Industrial & Engineering Chemistry Research,* vol. 34, no. 5, pp. 1566-1571, 1995.

[4] Commission of the European Communities *energy*, "Secondary co-refining of petroleum and coal distillates," R. Loring, Luxembourg, 1991.

[5] L. D. R. P. Galvis, "Removal of Nitrogen Compounds from Bitumen-Derived Gas Oil and its Impact on Hydrotreating," University of Alberta, 2012.

[6] J. M. B. Mierau, "Patterns and Pathways of Hydrogenation of Asphaltene Model Compounds," University of Alberta, 2011.

[7] D. Solis *et al*, "NiMo/Al$_2$O$_3$–MgO (x) catalysts: the effect of the prolonged exposure to ambient air on the textural and catalytic properties," *Catalysis Today,* vol. 98, pp. 99-108, 2004.

[8] Criterion Catalyst & Technologies, "Criterion* Hydrotreating Catalyst In-situ Presulphiding Guidelines," Criterion Catalyst & Technologies, 1998. Available: http://www.criterioncatalysts.com.

[9] S. Eijsbouts *et al*, "Nickel sulfide crystals in Ni-Mo and Ni-W catalysts: Eye-catching inactive feature or an active phase in its own right?" *Catalysis Today,* 2016.

[10] R. Prins, De Beer, V H J and G. A. Somorjai, "Structure and Function of the Catalyst and the Promoter in Co—Mo Hydrodesulfurization Catalysts," *Catalysis Reviews,* vol. 31, pp. 1-41, 1989.

[11] M. R. Gray, *Upgrading Oilsands Bitumen and Heavy Oil.* Edmonton, Alberta: Pica Pica Press, An Imprint of The University of Alberta Press, 2015.

[12] *Swagelok®*. Swagelok Company. Available: https://www.swagelok.com/en.

[13] *Swagelok Fluid System Technologies*. Swagelok Company. Available: http://oem.cadregister.com/asp/PPOW_Entry.asp?company=SwagelokCo&elementID=6339650 1/VAR/FINE/Y70340/3&orderedResponses=0|1|0|0|0|0|0&language=GB&oem=true.

[14] W.S. Kanda, "Quinoline Conversion in the Presence of Athabasca Derived Heavy Gas Oil Fractions," University of Alberta, 2003.

[15] S. D. C. D'Armas, "Addition Reactions of Olefins to Asphaltene Model Compounds," University of Alberta, 2014.

[16] M. A. Medina, "Online Characterization of Particle Based Reactions by Laser Backscattering," University of Alberta, 2016.

[17] P. Nhieu, "Role of Water and Fine Solids in Onset of Coke Formation During Bitumen Cracking," University of Alberta, 2014.

[18] B. J. Olson, "The Role of Sulfur during the Cracking of N-Hexadecane and Cold Lake Bitumen with Alpha-Fe_2O_3 and Steam," University of Alberta, 2013.

[19] S. M. Richardson, "Initial Coking of a NiMo/γ-$A1_2O_3$ Bitumen Hydroprocessing Catalyst," University of Alberta, 1996.

[20] F. J. Callahan, *Swagelok Tube Fitting and Installation Manual.* Solon, Ohio: Swagelok Marketing Co., 1998.

[21] T. R. Bednar, R. D. Neitzell and M. S. Steele, "Reciprocating saw," US6851193 B2, 2005.

[22] G. Marroquín, J. Ancheyta and J. A. I. Díaz, "On the effect of reaction conditions on liquid phase sulfiding of a NiMo HDS catalyst," *Catalysis Today,* vol. 98, pp. 75-81, 2004.

[23] T. L. Bergman and F. P. Incropera, *Fundamentals of Heat and Mass Transfer.* Hoboken, NJ: Wiley, 2011.

[24] ASTM Standard D5291, 1992 (2016), "Standard Test Method for Instrumental Determination of Carbon, Hydrogen, and Nitrogen in Petroleum Products and Lubricants," ASTM International, West Conshohocken, PA, 2016, DOI: 10.1520/D5291-16, www.astm.org.

[25] Antek by Pac, "MultiTekTM Operation Manual," Houston, Texas: Petroleum Analyzer Company, L.P., 2009.

[26] ASTM Standard D4294, 1983 (2016), "Standard Test Method for Sulfur in Petroleum and Petroleum Products by Energy Dispersive X-ray Fluorescence Spectrometry," ASTM International, West Conshohocken, PA, 2016, DOI: 10.1520/D4294-16, www.astm.org.

[27] ASTM Standard D5762, 1995 (2012), "Standard Test Method for Nitrogen in Petroleum and Petroleum Products by Boat-Inlet Chemiluminescence," ASTM International, West Conshohocken, PA, 2012, DOI: 10.1520/D5762-12, www.astm.org.

[28] ASTM Standard D4052, 1981 (2016), "Standard Test Method for Density, Relative Density, and API Gravity of Liquids by Digital Density Meter," ASTM International, West Conshohocken, PA, 2016, DOI: 10.1520/D4052-16, www.astm.org.

[29] B. G. Liptak, *Instrument Engineers' Handbook, Fourth Edition, Volume One: Process Measurement and Analysis. Chapter 6.8,* Boca Raton: CRC Press, 2003.

[30] Anton Paar, "Instruction Manual DMA 4500/5000 Density/Specific Gravity/Concentration Meter," Graz, Austria: Anton Paar GmbH, 2005.

[31] Design Institute for Physical Properties, Sponsored by AIChE, *DIPPR Project 801 - Full Version.* Design Institute for Physical Property Research/AIChE, 2017. Available: http://app.knovel.com/web/toc.v/cid:kpDIPPRPF7.

[32] D. F. Smith *et al*, "Characterization of Athabasca Bitumen Heavy Vacuum Gas Oil Distillation Cuts by Negative/Positive Electrospray Ionization and Automated Liquid Injection Field Desorption Ionization Fourier Transform Ion Cyclotron Resonance Mass Spectrometry," *Energy Fuels,* vol. 22, *(5),* pp. 3118-3125, 2008.

[33] J. Chen, H. Farooqi and C. Fairbridge, "Experimental Study on Co-hydroprocessing Canola Oil and Heavy Vacuum Gas Oil Blends," *Energy Fuels,* vol. 27, *(6),* pp. 3306-3315, 2013.

[34] S. Yui and T. Dodge, "Catalyst Deactivation, Kinetics, and Product Quality of Mild Hydrocracking of Bitumen-Derived Heavy Gas Oils," *Petrol. Sci. Technol.,* vol. 24, *(3-4),* pp. 351-365, 2006.

[35] S. Yui and K. H. Chung. "Processing oilsands bitumen is Syncrude's R&D focus," *Oil & Gas Journal,* pp. 46-53. 2001.

[36] S. Yui, N. Matsumoto and Y. Sasaki, "Athabasca oil sands produce quality FCC feeds," *Oil & Gas Journal,* pp. 43-51, 1998.

[37] ASTM Standard D7169, 2005 (2011), "Standard Test Method for Boiling Point Distribution of Samples with Residues Such as Crude Oils and Atmospheric and Vacuum Residues by High Temperature Gas Chromatography," ASTM International, West Conshohocken, PA, 2011, DOI: 10.1520/D7169-05, www.astm.org.

[38] Bruker, "450-GC User Manual," The Netherlands: Bruker Chemical Analysis, 2010.

[39] Nanalysis, "NMReady User's Manual Version 0.9," Calgary, Canada: Nanalysis Corp., 2013.

[40] Avantes, Apeldoorn, The Netherlands: Avantes BV, 2018. https://www.avantes.com.

[41] Thorlabs, Newton, New Jersey: Thorlabs, Inc., 2018. https://www.thorlabs.com/.

[42] ASTM Standard D2008, 1962 (2012), "Standard Test Method for Ultraviolet Absorbance and Absorptivity of Petroleum Products," ASTM International, West Conshohocken, PA, 2012, DOI: 10.1520/D2008-12, www.astm.org.

[43] ASTM Standard E169, 1960 (2016), "Standard Practices for General Techniques of Ultraviolet Quantitative Analysis," ASTM International, West Conshohocken, PA, 2016, DOI: 10.1520/E0169-16, www.astm.org.

[44] ASTM Standard E275, 1965 (2013), "Standard Practice for Describing and Measuring Performance of Ultraviolet and Visible Spectrophotometers," ASTM International, West Conshohocken, PA, 2013, DOI: 10.1520/E0275-08R13, www.astm.org.

Chapter 4 References

[1] M. R. Gray. New technique defines the limits of upgrading heavy oils, bitumens. *Oil & Gas Journal* pp. 50-54. 2002.

[2] The MathWorks, Inc., *Partial Least Squares Regression and Principal Components Regression*. MathWorks Website, 2019. Available: https://www.mathworks.com/help/stats/examples/partial-least-squares-regression-and-principal-components-regression.html.

[3] J. Duckworth H., *Spectroscopic Quantitative Analysis*. Chapter 4 *in* J. Workman and A. Springsteen, *Applied Spectroscopy: A Compact Reference for Practitioners*. 1998.

[4] P. Gemperline, *Practical Guide to Chemometrics*. Boca Raton: CRC/Taylor & Francis, 2006.

[5] R. G. Brereton, *Chemometrics: Data Analysis for the Laboratory and Chemical Plant*. Chichester, West Sussex, England; Hoboken, NJ: Wiley, 2003.

[6] P. D. Wentzell *et al*, "Estimation of hydrocarbon types in light gas oils and diesel fuels by ultraviolet absorption spectroscopy and multivariate calibration," *Can. J. Chem.,* vol. 77, *(3),* pp. 391-400, 1999.

[7] S. Wu, K. B. McAuley and T. J. Harris, "Selection of simplified models: I. Analysis of model-selection criteria using mean-squared error," *The Canadian Journal of Chemical Engineering,* vol. 89, *(1),* pp. 148-158, 2011.

[8] S. Sánchez, J. Ancheyta and W. C. McCaffrey, "Comparison of probability distribution functions for fitting distillation curves of petroleum," *Energy Fuels,* vol. 21, *(5),* pp. 2955-2963, 2007.

[9] F. J. Fabozzi *et al*, *The Basics of Financial Econometrics: Tools, Concepts, and Asset Management Applications. Appendix E Model Selection Criterion: AIC and BIC,* 2014.

Chapter 5 References

[1] S. Yui, "Hydrotreating of Bitumen-Derived Gas Oil: Kinetics of Hydrodesulfurization, Hydrodenitrogenation, and Mild Hydrocracking, and Correlations to Predict Product Yields and Properties," *AOSTRA Journal of Research,* vol. 5, pp. 211-224, 1989.

[2] S. K. Bej, A. K. Dalai and J. Adjaye, "Kinetics of Hydrodesulfurization of Heavy Gas Oil Derived from Oil-Sands Bitumen," *Petroleum Science & Technology,* vol. 20, *(7),* pp. 867, 2002.

[3] C. Botchwey, A. K. Dalai and J. Adjaye, "Kinetics of Bitumen-Derived Gas Oil Upgrading Using a Commercial NiMo/Al2O3 Catalyst," *Can. J. Chem. Eng.,* vol. 82, *(3),* pp. 478-487, 2004.

[4] M. Mapiour *et al*, "Effect of Hydrogen Purity on Hydroprocessing of Heavy Gas Oil Derived from Oil-Sands Bitumen," *Energy Fuels,* vol. 23, *(4),* pp. 2129-2135, 2009.

[5] S. Yui and T. Dodge, "Catalyst Deactivation, Kinetics, and Product Quality of Mild Hydrocracking of Bitumen-Derived Heavy Gas Oils," *Petrol Sci Technol,* vol. 24, *(3-4),* pp. 351-365, 2006.

[6] A. Owusu-Boakye *et al*, "Maximizing Aromatic Hydrogenation of Bitumen-Derived Light Gas Oil: Statistical Approach and Kinetic Studies," *Energy Fuels,* vol. 19, *(5),* pp. 1763-1773, 2005.

[7] G. Marroquín, J. Ancheyta and J.A.I. Díaz, "On the effect of reaction conditions on liquid phase sulfiding of a NiMo HDS catalyst," *Catalysis Today,* vol. 98, pp. 75-81, 2004.

[8] Criterion Catalyst & Technologies, "Criterion* Hydrotreating Catalyst In-situ Presulphiding Guidelines," Criterion Catalyst & Technologies, 1998.

[9] W.S. Kanda, "Quinoline Conversion in the Presence of Athabasca Derived Heavy Gas Oil Fractions," University of Alberta, 2003.

[10] S. D. C. D'Armas, "Addition Reactions of Olefins to Asphaltene Model Compounds," University of Alberta, 2014.

[11] B. J. Olson, "The Role of Sulfur during the Cracking of N-Hexadecane and Cold Lake Bitumen with Alpha-Fe2O3 and Steam," University of Alberta, 2013.

[12] A. Owusu-Boakye, "Two-Stage Aromatics Hydrogenation of Bitumen-Derived Light Gas Oil," University of Saskatchewan, 2005.

[13] A. Owusu-Boakye *et al*, "Experimental and Kinetic Studies of Aromatic Hydrogenation, Hydrodesulfurization, and Hydrodenitrogenation of Light Gas Oils Derived from Athabasca Bitumen," *Ind. Eng. Chem. Res.,* vol. 44, *(21),* pp. 7935-7944, 2005.

[14] R. S. Mann, I. S. Sambi and K. C. Khulbe, "Catalytic hydrofining of heavy gas oil," *Ind. Eng. Chem. Res.,* vol. 26, *(3),* pp. 410-414, 1987.

[15] F. Khorasheh *et al*, "Interactions between thermal and catalytic reactions in mild hydrocracking of gas oil," *Energy Fuels,* vol. 3, *(6),* pp. 716-722, 1989.

[16] T. A. Pecoraro and R. R. Chianelli, "Hydrodesulfurization catalysis by transition metal sulfides," *Journal of Catalysis,* vol. 67, *(2),* pp. 430-445, 1981.

[17] D. F. Smith *et al*, "Characterization of Athabasca Bitumen Heavy Vacuum Gas Oil Distillation Cuts by Negative/Positive Electrospray Ionization and Automated Liquid Injection

Field Desorption Ionization Fourier Transform Ion Cyclotron Resonance Mass Spectrometry," *Energy Fuels,* vol. 22, *(5),* pp. 3118-3125, 2008.

[18] I. N. Evdokimov and A. P. Losev, "Suggested "New Method for Determination of Dispersity in Petroleum Systems" Is Based on Trivial Experimental Artifacts," *Energy Fuels,* vol. 22, *(4),* pp. 2470-2473, 2008.

[19] Andrews, John, Beck, Gary, Castelijns, Kees, Chen, Andy, Cribbs, Myrt, Fadnes, Finn, Irvine-Fortescue, Jamie, Williams, Stephen, Hashem, Mohamed, Jamaluddin, A., Kurkjian, Andrew, Sass, Bill, Mullins, Oliver, Rylander, Erik, Van Dusen, Alexandra, "Quantifying Contamination Using Color of Crude and Condensate," pp. 24-43, Autumn. 2001.

[20] P. Harris, "Applying Near Infrared Spectroscopy to the Online Determination of Composition and Physical Properties of Crudes and Condensates," *Optical Solutions to Process Automation*, Insight Analytical. Proceedings of Joint CCQTA-COQA Meeting 7-10 June, 2016. Edmonton, AB. http://www.coqa-inc.org/meeting-archives. http://www.insight-analytical.com/.

[21] Y. Ruiz-Morales and O. C. Mullins, "Polycyclic Aromatic Hydrocarbons of Asphaltenes Analyzed by Molecular Orbital Calculations with Optical Spectroscopy," *Energy Fuels,* vol. 21, *(1),* pp. 256-265, 2007.

[22] C. T. Shoute *et al*, "UV Raman Spectroscopy of Oilsands-Derived Bitumen and Commercial Petroleum Products," *Appl. Spectrosc.,* vol. 56, *(10),* pp. 1308-1313, 2002.

[23] E. Schmidt, C. Song and H. H. Schobert, "Influence of sulfur addition and S-induced wall catalytic effects on CC bond cleavage and aromatics hydrogenation," *Preprints of Papers, American Chemical Society, Division of Fuel Chemistry,* vol. 40, *(CONF-950801-),* 1995.

[24] C. Calais *et al*, "Selective Reduction of Diphenyldisulfides Catalyzed by Sulfides-Influence of the Nature of the Catalyst," *Journal of Catalysis,* vol. 144, *(1),* pp. 160-174, 1993.

[25] M. R. Gray, *Upgrading Oilsands Bitumen and Heavy Oil.* Edmonton, Alberta: Pica Pica Press, An Imprint of The University of Alberta Press, 2015.

[26] P. D. Wentzell *et al*, "Estimation of hydrocarbon types in light gas oils and diesel fuels by ultraviolet absorption spectroscopy and multivariate calibration," *Can. J. Chem.,* vol. 77, *(3),* pp. 391-400, 1999.

[27] C. Baldrich Ferrer and L. Novoa Mantilla, "Detailed chemical characterization of petroleum middle fractions by chemometrics analysis of their ultraviolet spectrum," *CT&F-Ciencia, Tecnología Y Futuro,* vol. 3, *(3),* pp. 173-190, 2007.

[28] Betancourt, Soraya, Fujisawa, Go, Mullins, Oliver, Carnegie, Andrew, Dong, Chengli, Kurkjian, Andrew, Otto Eriksen, Kare, Haggag, Mostafa, Jaramillo, Antonio, Terabayashi, Harry, "Analyzing Hydrocarbons in the Borehole," pp. 54-61, Autumn. 2003.

[29] Schlumberger, "InSitu Fluid Analyzer Quantitative Fluid Measurements at reservoir conditions, in real time," *Schlumberger,* 2008.

[30] J. Creek *et al*, "Downhole Fluids Laboratory," pp. 38-54, Winter. 2009.
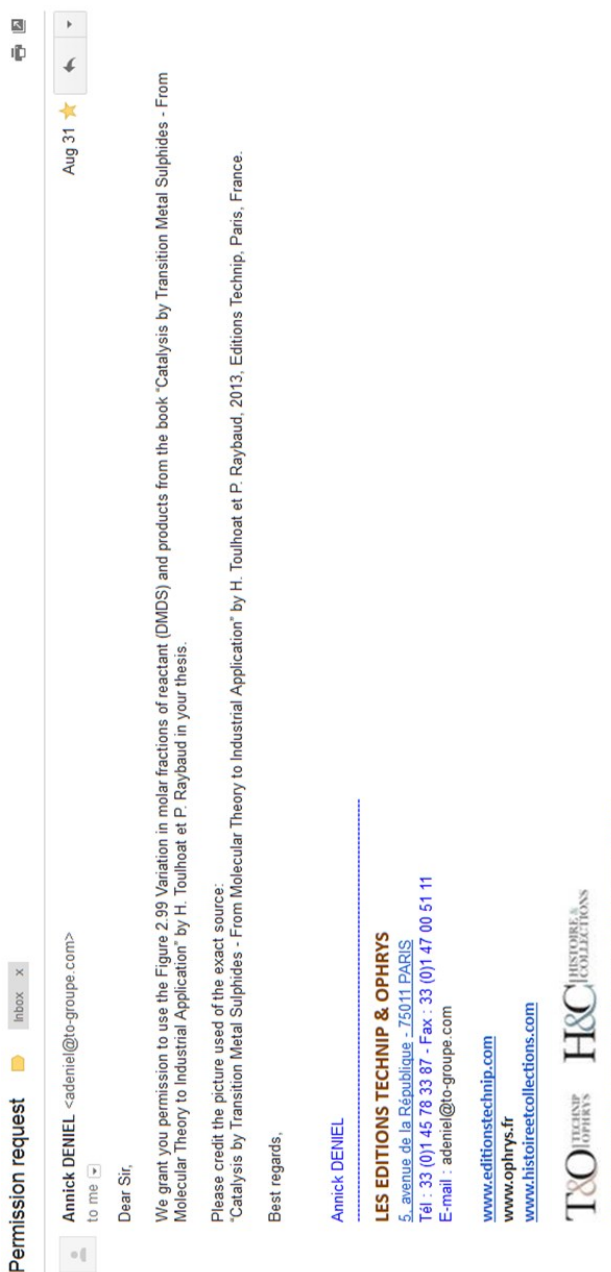
[31] M. Chen *et al*, "Recursive Wavelength-Selection Strategy to Update Near-Infrared Spectroscopy Model with an Industrial Application," *Ind Eng Chem Res,* vol. 52, *(23),* pp. 7886-7895, 2013.

[32] C. T. Pinheiro *et al*, "Assessment and Prediction of Lubricant Oil Properties Using Infrared Spectroscopy and Advanced Predictive Analytics," *Energy Fuels,* vol. 31, *(1),* pp. 179-187, 2017.

Permissions

Figure 2.4. Decomposition of Dimethyl Disulfide (DMDS) reactants and products as a function of temperature.

H. Toulhoat and P. Raybaud, *Catalysis by Transition Metal Sulphides: From Molecular Theory to Industrial Application.* Paris, France: Technip, 2013. Pg. 286, Figure 2.99, Chapter 2.4, Section 2.4.2.2.

Figure 2.5. Decomposition of Dimethyl Disulfide (DMDS) products and temperature profile as a function of time.

S. Texier *et al*, "Activation of alumina-supported hydrotreating catalysts by organosulfides: comparison with H$_2$S and effect of different solvents," *Journal of Catalysis,* vol. 223, *(2),* pp. 404-418, 2004.

Figure 2.6. Altgelt's and Boduszynski's distribution of molecular structures found in petroleum (with carbon number and paraffin molecular weight) as a function of boiling point.

H. Altgelt and M. M. Boduszynski, *Composition and Analysis of Heavy Petroleum Fractions.* Boca Raton, Fla.: CRC Press, 1993.

Specified additional information	Minor Editing Privileges. This figure has been modified slightly and published by others in the journal: Energy Fuels 2010, 24, pg. 2929-2938. Figure 1.
The requesting person/organization is:	Daniel Palys, University of Alberta
Order reference number	
Author/Editor	Daniel Palys
The standard identifier of New Work	Master's Thesis
The proposed price	0
Title of New Work	Ex-situ observation and characterization of hydrotreated liquid products
Publisher of New Work	University of Alberta
Expected publication date	Jan 2018
Estimated size (pages)	200
Total (may include CCC user fee)	0.00 USD
Terms and Conditions	

Figure 2.7. Contoured plots of double bond equivalent as a function of carbon number for each distillate cut fraction of HVGO.

Figure 2.8. Combined contoured plot of double bond equivalent as a function of carbon number for the HVGO.

Figure 2.10. Combined contoured plot of double bond equivalent as a function of carbon number of single thiophenic sulfur (S_1 class) in HVGO.

A. M. McKenna *et al*, "Heavy Petroleum Composition. 1. Exhaustive Compositional Analysis of Athabasca Bitumen HVGO Distillates by Fourier Transform Ion Cyclotron Resonance Mass Spectrometry: A Definitive Test of the Boduszynski Model," *Energy Fuels,* vol. 24, *(5),* pp. 2929-2938, 2010.

Figure 2.12. Positive ion isoabundance contour plots of double bond equivalent as a function of carbon number for the N_1 class of HVGO.

D. F. Smith *et al*, "Characterization of Athabasca Bitumen Heavy Vacuum Gas Oil Distillation Cuts by Negative/Positive Electrospray Ionization and Automated Liquid Injection Field Desorption Ionization Fourier Transform Ion Cyclotron Resonance Mass Spectrometry," *Energy Fuels,* vol. 22, *(5),* pp. 3118-3125, 2008.

Figure 2.13. Negative ion isoabundance contour plots of double bond equivalent as a function of carbon number for the N_1 class of HVGO.

D. F. Smith *et al*, "Characterization of Acidic Species in Athabasca Bitumen and Bitumen Heavy Vacuum Gas Oil by Negative-Ion ESI FT−ICR MS with and without Acid−Ion Exchange Resin Prefractionation," *Energy Fuels,* vol. 22, *(4),* pp. 2372-2378, 2008.

Figure 2.19. Distribution of the monosulfur class before and after hydrotreating of a coker gas oil.

Figure 2.22. Distribution of mononitrogen class before and after hydrotreating of a coker gas oil HDS, HDN and HDA reactions of syncrude heavy cut

Figure 2.25. Relative isoabundance contour plot of double bond equivalent as a function of carbon number for the untreated and hydrotreated coker gas oil cut

J. Fu *et al*, "Comprehensive Compositional Analysis of Hydrotreated and Untreated Nitrogen-Concentrated Fractions from Syncrude Oil by Electron Ionization, Field Desorption Ionization, and Electrospray Ionization Ultrahigh-Resolution FT-ICR Mass Spectrometry," *Energy Fuels,* vol. 20, *(3),* pp. 1235-1241, 2006.

Figure 2.33. Absorption spectra of 22 crude oil samples.

Y. Ruiz-Morales and O. C. Mullins, "Polycyclic Aromatic Hydrocarbons of Asphaltenes Analyzed by Molecular Orbital Calculations with Optical Spectroscopy," *Energy Fuels,* vol. 21, *(1),* pp. 256-265, 2007.

Figure 2.34. Adsorption spectra of oil distillation cuts.

C. T. Shoute *et al*, "UV Raman Spectroscopy of Oilsands-Derived Bitumen and Commercial Petroleum Products," *Appl. Spectrosc.,* vol. 56, *(10),* pp. 1308-1313, 2002.

Figure 2.35. Solvent diluted and neat crude oil UV-Vis absorption spectra.

I. N. Evdokimov and A. P. Losev, "Suggested "New Method for Determination of Dispersity in Petroleum Systems" Is Based on Trivial Experimental Artifacts," *Energy Fuels,* vol. 22, *(4),* pp. 2470-2473, 2008.

Appendix A

A review of conversion and kinetic studies for heavy oil feeds is found in *Table A1*. Calculations for stoichiometric sulfidation reactions, batch microreactor volume and theoretical air flow rate verification are found in *Appendix A*.

Table A1. A review of conversion and kinetic studies of hydrotreating industrials feedstocks.

Feed	Conditions	Catalyst	Conversion/Kinetics	Reference
Middle distillate from synthetic oil (Athabasca)	340-440°C 7-17.3MPa 0.75-2.25h^{-1} LHSV 530m^3 H$_2$ /m^3 feed	CoMo/γ-Al$_2$O$_3$ NiMo/γ-Al$_2$O$_3$ NiW/ γ-Al$_2$O$_3$	HDA, n=1, lnA=10-15, E$_a$=60-83kJ/mol Aromatic ^{13}C Conversion, <16%	Wilson & Kriz 1984 [1]
Heavy gas oil derived from Athabasca bitumen	300-450°C 4.24-12.5MPa 0.5-4h^{-1} LHSV	NiMo/Al$_2$O$_3$ NiW/Al$_2$O$_3$ CoMo/Al$_2$O$_3$	NiMo catalyst best for HDN. NiW catalyst best for cracking, HDA, and HDS. Increase temperature (300-450°C), increase sulfur (20-90%) & nitrogen (5-45%) conversion with all catalysts. Increase pressure (4.2-12.5MPa), decrease density, increase H/C ratio, increase nitrogen conversion (30-70%), increase in sulfur conversion (80-90%).	Mann et al. 1987 [2]
Heavy gas oil derived from Athabasca bitumen	350-425°C 7MPa 1-4h^{-1} LHSV 890m^3 H$_2$ /m^3 feed	NiMo/Al$_2$O$_3$ on zeolite NiMo/γ-Al$_2$O$_3$	Zeolite based catalyst had higher sulfur and nitrogen conversion compared to commercial NiMo catalyst. Power law model for zeolite based catalyst: HDS: n=1.5, lnA=18, E$_a$=87kJ/mol HDN: n=2, lnA=21, E$_a$=105kJ/mol	Mann et al. 1988 [3]
Synthetic crude distillate from delayed and fluid coking	340-440°C 17.2MPa 0.75-2.25h^{-1} LHSV 530m^3 H$_2$ /m^3 feed	CoMo/γ-Al$_2$O$_3$ NiMo/γ-Al$_2$O$_3$ NiW/ γ-Al$_2$O$_3$	Up flow mode reactor. Examined kinetics of aromatic molecules: alkylbenzenes, benzocycloparaffins, and benzodicycloparaffins. NiMo & CoMo for delayed coking distillate NiW for fluid coking distillate HDA kinetics for forward reaction: CoMo: n=1, lnA=10-14, E$_a$=63-84kJ/mol NiMo: n=1, lnA=25-26, E$_a$=138-142kJ/mol NiW: n=1, lnA=6-10, E$_a$=38-59kJ/mol	Fisher & Wilson 1988 [4]
Coker gas oil derived from Athabasca bitumen	Fixed Bed 340-400°C 7-11MPa 0.7-1.5h^{-1} LHSV 600Sm^3 H$_2$ /m^3 feed	NiMo/Al$_2$O$_3$	HDS, n=1.5, lnA=25, E$_a$=138kJ/mol HDN, n=1, lnA=15, E$_a$=92kJ/mol +343°C Conversion, n=1, lnA=13, E$_a$=82kJ/mol α: 0.7 for HDS, 0.64 for HDN, 0.29 for +343°C β: 0.78 for HDS, 1.39 for HDN, 0.32 for +343°C	Yui 1989 [5]
Coker gas oil derived from Athabasca bitumen	340-400°C 7-11MPa 0.7-1.5h^{-1} LHSV 600Sm^3 H$_2$ /m^3 feed	NiMo/Al$_2$O$_3$	HDS, n=1.5, lnA=18-22, E$_a$=90-110kJ/mol HDN, n=1, lnA=15-19, E$_a$=81-101kJ/mol +343°C Conversion, n=1, lnA=13-14, E$_a$=82-83kJ/mol α: 0.9	Kirchen & Sanford 1989 [6]
Coker & hydrocracker gas oils derived from Athabasca bitumen	350-400°C 7-11MPa 0.7-1.5h^{-1} LHSV 600Sm^3 H$_2$ /m^3 feed	NiMo/γ-Al$_2$O$_3$	Hydrocracker gas oil higher reaction rates for HDS & HDN compared to coker gas oil. HDS, n=1.5, lnA=23-25, E$_a$=131-132kJ/mol HDN, n=1, lnA=12-19, E$_a$=76-98kJ/mol α: 1 for HDS, 1 for HDN β: 0.6-1.8 for HDS & HDN	Yui & Stanford 1989 [7]
Coker gas oil derived from Athabasca bitumen	380-450°C 13.9MPa 12.5ml/h·g catalyst 8g of catalyst 1-1.1L/min (STP) 800RPM	NiMo/Al$_2$O$_3$ In 150ml CSTR	Seven gas oil fractions. Kinetics for 300-350°C (2) cut and 450-500°C(5) cut. Apparent Activation Energies for power law model: HDS: n=1, E$_{a(2)}$=109kJ/mol, E$_{a(5)}$=149kJ/mol HDN: n=1, E$_{a(2)}$=78kJ/mol, E$_{a(5)}$=109kJ/mol	Trytten et al. 1990 [8]

Coker gas oil derived from Athabasca bitumen	380-420°C 13.9MPa 12.5-23.5ml/h·g catalyst (8g of catalyst) 1-1.1L/min (STP) 800RPM	NiMo/Al$_2$O$_3$ In 150ml CSTR	Use of ^{1}H and ^{13}C NMR, For reactions with catalyst, all first order reactions: HDS: E$_a$=89±15kJ/mol O,N,S: E$_a$=103±16kJ/mol Aromatic Carbon (O,N,S): E$_a$=63±5kJ/mol Total Aromatic Carbon: E$_a$=67±8kJ/mol	Gray 1990 [9]
Gas oils (light, heavy and coker) derived from Athabasca bitumen	320-400°C 7-11MPa 0.7-1.5h^{-1} LHSV 600Sm^3 H$_2$ /m^3 feed	NiMo/Al$_2$O$_3$	HDA reactions, reversible, first order, partial pressure with β exponential factor. Forward and reverse rate constants are reported. -HDA increases with increasing temperature to maximum, then decreases. -HDA increases with increasing hydrogen pressure and decreasing LHSV. -Equilibrium limit increases as hydrogen pressure increases. -Decreasing LHSV, decreases maximum temperature for HDA reactions. Forward reactions reported: Case 1: HDA, n=1, lnA=9-17, E$_a$=53-100kJ/mol Case 2: HDA, n=1, lnA=8-17, E$_a$=46-98kJ/mol α: Case 1: 0.34-1, Case 2: 0.28-1 β: 0.5 for all models	Yui & Stanford 1991 [10]
Gas oil derived from Athabasca bitumen	350-425°C 6.89MPa 1-4h^{-1} LHSV 890m^3 H$_2$ /m^3 feed	CoMo, NiMo, & NiW all on zeolite Al$_2$O$_3$ CoMo/γ-Al$_2$O$_3$ NiMo/γ-Al$_2$O$_3$ NiW/ γ-Al$_2$O$_3$	Zeolite support catalysts enhanced conversion for HDS & HDN compared to γ-Al$_2$O$_3$ catalysts For zeolite support catalysts: HDS, pseudo 1st, *E$_a$=200-209kJ/mol HDN, pseudo 1st, *E$_a$=160-242kJ/mol *Corrected from log to ln in calculation.	Diaz-Real et al. 1993 [11]
Coker heavy gas oil derived from Athabasca bitumen	340-410°C 7-11MPa 0.6-1.3h^{-1} LHSV 600m^3 H$_2$ /m^3 feed	NiMo/Al$_2$O$_3$	HDS, n=1.5, lnA=16, E$_a$=94kJ/mol HDN, n=1 (for all), TN: lnA=11, E$_a$=79kJ/mol, BN: lnA=15, E$_a$=93kJ/mol, NBN: lnA=11, E$_a$=78kJ/mol, α: 0.53 for HDS, HDN: 0.65 TN, 0.72 BN, 0.62 NBN β: 0.97 for HDS, HDN: 1.56 TN, 1.47 BN, 1.64 NBN	Yui & Ng 1995 [12]
Middle distillate from synthetic oil (Athabasca)	200-360°C 7MPa 0.75-2h^{-1} LHSV 530m^3 H$_2$ /m^3 feed	Pt pillared clay Pt/Y-zeolite NiMo/Al$_2$O$_3$	^{13}C and aromatic mass spec. kinetics (HDA): Pt clay, lnA=37-53, E$_a$=90-130kJ/mol Pt/Y-zeolite, lnA=76-150, E$_a$=160-320kJ/mol NiMo/Al$_2$O$_3$, lnA=35, E$_a$=80kJ/mol	Kimbara et al. 1996 [13]
Heavy gas oil derived from Athabasca bitumen	365-415°C 6.5-8.8MPa 0.5-2h^{-1} LHSV 400-1000m^3 H$_2$ /m^3 feed	NiMo/Al$_2$O$_3$	Basic nitrogen (BN) highest conversion Total nitrogen conversion: 50-80% HDN, n=1.5 (optimal), lnA=15 (all HDN reactions) BN: E$_a$=74kJ/mol, NBN: E$_a$=80kJ/mol, TN: E$_a$=80kJ/mol	Bej et al. 2001 [14]
Heavy gas oil derived from Athabasca bitumen	365-415°C 6.5-8.8MPa 0.5-2h^{-1} LHSV 400-1000m^3 H$_2$ /m^3 feed	NiMo/Al$_2$O$_3$	To increase 370-500°C conversion, +500°C conversion, & micro carbon residue (MCR) conversion (for all): increase temperature, pressure, H$_2$ /m^3 feed, and decrease LHSV Kinetics: MCR (n=2), lnA=19, E$_a$=91kJ/mol +500°C fraction (n=2), lnA=15, E$_a$=87kJ/mol - 370°C fraction, lnA=-12, E$_a$=92kJ/mol	Bej et al. 2001 [15]
Heavy gas oil derived from Athabasca bitumen	365-415°C, 8.8MPa 0.5-1.9h^{-1} LHSV 400-1000m^3 H$_2$ /m^3 feed	NiMo/Al$_2$O$_3$	Sulfur conversion: 96-86% as LHSV increases 0.5-1.9h^{-1} 84-96% as temperature increases 365-415°C 88-93% as H$_2$ /m^3 feed increases 400-1000 HDS, n=2 (optimal), lnA=22, E$_a$=115kJ/mol	Bej et al. 2002 [16]
Heavy gas oil & coker gas oil from Middle east & Athabasca bitumen	363-380°C 13.8MPa 0.75h^{-1} LHSV 4.5mL/h feed rate 400m^3 H$_2$ /m^3 feed	NiMo/γ-Al$_2$O$_3$ for hydrotreating NiMo on boria zeolite Y for hydrocracking	Two-stage hydrotreating and hydrocracking in series for polycyclic aromatics. Langmuir–Hinshelwood model used from hydrocracking. Gas oil conversion dependent on sulfur and polyaromatic content. Hydrocracking dependent on nitrogen content.	Aoyagi et al. 2003 [17]

Feed	Conditions	Catalyst	Results	Reference
Gas oil derived from Athabasca bitumen	340-420°C 6.5-11MPa 0.5-2h⁻¹ LHSV 600m³ H₂ /m³ feed	NiMo/Al₂O₃	S conversion: 86-99% N conversion: TN 38-92%, BN 47-99%, NBN 33-88% Increase T & P increases S & N conversion Decrease LHSV & increase temperature, increases S & N conversion. Increase T & P, decrease aromatic wt.% in product.	Botchwey et al. 2003 [18]
Gas oil derived from Athabasca bitumen	340-420°C 8.8MPa 1h⁻¹ LHSV 600m³ H₂ /m³ feed	NiMo/γ-Al₂O₃	Three T regimes: 340-370°C, 370-400°C, and 400-420°C. Kinetic models for boiling fractions. HDS, n=1.5, 340-370°C: lnA=17, E_a=85kJ/mol 370-400°C: lnA=24, E_a=122kJ/mol 400-420°C: lnA=12, E_a=57kJ/mol HDN, n=1, 340-370°C: lnA=14-27, E_a=75-120kJ/mol 370-400°C: lnA=18-37, E_a=96-193kJ/mol 400-420°C: lnA=8-33, E_a=41-167kJ/mol	Botchwey et al. 2004 [19]
Gas oil derived from Athabasca bitumen	340-420°C 6.5-11MPa 0.5-2h⁻¹ LHSV 600m³ H₂ /m³ feed	NiMo/γ-Al₂O₃	H₂S inhibition on HDS and HDN reactions NBN conversion gain highest with H₂S removal at all temperature, catalyst loading and pressure. Optimal conditions: 380°C, 7.6MPa, and 1:3 w/w catalyst load. Langmuir-Hinshelwood kinetics. HDS: lnA=19-23, E_a=101-114kJ/mol, HDN: lnA=13-16, E_a=93-116kJ/mol	Botchwey et al. 2004 [20]
Gas oil derived from Athabasca bitumen	385°C 8.8MPa 1h⁻¹ LHSV 600m³ H₂ /m³ feed	NiMo/γ-Al₂O₃ NiMoB/γ-Al₂O₃ NiMoP/γ-Al₂O₃ B & P metal loadings	Phosphorus and born enhance HDN As boron increased, 0-1.7wt.%, total nitrogen conversion increased from 62-78% Sulfur conversion constant for all B & P loadings, 96-98%.	Ferdous et al. 2004 [21]
Light gas oil derived from Athabasca bitumen	340-390°C 6.9-12.4MPa 0.5-2h⁻¹ LHSV 550m³ H₂ /m³ feed	NiMo/Al₂O₃	Models were developed to determine effect of process variables on HDS, HDN, & HDA. Temperature and LHSV significant factors for HDS & HDN. Temperature and pressure significant factors for HDA. Increase temperature, increase gasoline yield. Optimal conditions for HDA: 379°C, 11MPa, 0.6h⁻¹, gives 63% conversion. Langmuir-Hinshelwood kinetics for HDA HDA, n=1, lnA=15, E_a=81kJ/mol Power law kinetics for HDS & HDN HDS, n=1, lnA=9, E_a=43kJ/mol HDN, n=1, lnA=7, E_a=28kJ/mol	Owusu-Boakye et al. 2005 [22]
Light gas oils, vacuum, atmospheric, hydrotreated (Athabasca)	340-390°C 11MPa 0.6h⁻¹ LHSV 550m³ H₂ /m³ feed	NiMo/Al₂O₃ NiW/Al₂O₃	HDS, n=1.2-1.4, lnA=4-11, E_a=29-53kJ/mol HDN, n=1, lnA=9-20, E_a=44-112kJ/mol HDA, n=1-1.3, lnA=10-16, E_a=52-91kJ/mol S Conversion: 87-98%, N Conversion: 89-99%, Aromatic Conversion: 12-83%	Owusu-Boakye et al. 2005 [23-24]
Gas oil derived from Athabasca bitumen	340-420°C 6.1-10.2MPa 0.5-2h⁻¹ LHSV 50ml/min H₂ flow 5cm³ catalyst	NiMo/Al₂O₃ NiMoP/Al₂O₃ 2.7wt.% Phosphorus	Surface repose of nitrogen conversion. Increase temperature & pressure, decrease LHSV, increase nitrogen conversion. LHSV and temperature have interactive effects on HDN and HDS reactions. Langmuir–Hinshelwood model: HDS: n=1, lnA=27, E_a=137±8kJ/mol HDN: n=1, lnA=20, E_a=113±10kJ/mol Power law kinetic model: HDS: n=1, lnA=19, E_a=96±4kJ/mol HDN: n=1, lnA=14, E_a=94±4kJ/mol	Ferdous et al. 2005 [25]
Gas oil derived from Athabasca bitumen	340-420°C 6.1-10.2MPa 0.5-2h⁻¹ LHSV 600m³ H₂ /m³ feed	NiMoB/γ-Al₂O₃ with 0-1.7wt.% boron (B)	Continued work from [15] Power law model: HDS, n=1.5, lnA=17, E_a=87kJ/mol HDN, n=1, lnA=14, E_a=75kJ/mol Langmuir-Hinshelwood model: HDS: lnA=31, E_a=159kJ/mol, HDN: lnA=20, E_a=110kJ/mol	Ferdous et al. 2006 [26]
Coker gas oils & HVGO derived from Athabasca bitumen	361-398°C 8.96MPa 0.5-1h⁻¹ LHSV 620m³ H₂ /m³ feed	NiMo/Al₂O₃	Severe hydrotreatment of HVGO. Up to 36% +343°C conversion. Included extra γ parameter to incorporate catalyst deactivation. Power law model for HVGO feed: HDS: n=1.5, lnA=31, E_a=151kJ/mol HDN: n=1, lnA=26, E_a=131kJ/mol HDA: n=1, lnA=13, E_a=72kJ/mol +343°C: n=1, lnA=30, E_a=169kJ/mol	Yui & Dodge 2006 [27]

Heavy gas oil derived from oil sand bitumen	380°C 7.2-10.1MPa 1h^{-1} LHSV 400-1270m^3 H$_2$ /m^3 feed H$_2$ purity 0-100%	NiMo/γ-Al$_2$O$_3$	Increasing hydrogen purity increases HDS, HDN, & HDA reactions. Higher improvement on nitrogen and aromatic conversion compared to sulfur. +343°C conversion increases with hydrogen purity. Lower density and viscosity of liquid product with increasing hydrogen purity. Increasing pressure at lower purity (9MPa at 80%) had similar results for higher purity and lower pressure (7.2MPa at 100%).	Mapiour et al. 2009 [28]
Heavy gas oil derived from Athabasca bitumen	360-400°C 7-11MPa 0.65-2h^{-1} LHSV 400-1200m^3 H$_2$ /m^3 feed H$_2$ purity 75-100%	NiMo/γ-Al$_2$O$_3$	Continue from [21]. Increasing LHSV, decrease sulfur, nitrogen and aromatic conversion. Increase temperature, increase sulfur (>90%) and nitrogen (60-80%) conversion, while aromatic conversion peaks at 380°C (54%). Models developed based on experimental design for sulfur, nitrogen and aromatic conversion: H$_2$ purity and pressure affect HDN and HDA more significantly compared to gas to oil ratio	Mapiour et al. 2009 [29]
Heavy gas oil derived from Athabasca bitumen	360-400°C 7-11MPa 0.65-2h^{-1} LHSV 400-1200m^3 H$_2$ /m^3 feed H$_2$ purity 75-100%	NiMo/γ-Al$_2$O$_3$	Increasing H$_2$ partial pressure had higher significant effect on HDN and HDA compared to HDS reactions. Aromatic conversion peaks around 380°C as H$_2$ dissolved in the liquid decreased, oil feed becomes increasingly vaporized at higher temperatures and H$_2$ consumption decreases. Power law model HDS: n=2, lnA=20, E$_a$=101kJ/mol, HDN: n=1.5, lnA=16, E$_a$=79kJ/mol, HDA: n=1.5, lnA=4, E$_a$=30kJ/mol Langmuir-Hinshelwood model, all pseudo-first order HDS: lnA=20, E$_a$=99kJ/mol, HDN: lnA=14, E$_a$=69kJ/mol HDA: lnA=13, E$_a$=62kJ/mol Multi-parameter model HDS: n=2.68, E$_a$=119kJ/mol, HDN: n=2.02, E$_a$=112kJ/mol, HDA: n=1, E$_a$=34kJ/mol	Mapiour et al. 2010 [30-31]
Chinese coker gas oil from Liaohe oil field	360-420°C 5-8MPa 0.5-2h^{-1} LHSV 400-1200m^3 H$_2$ /m^3 feed	NiW Citric Treated Y zeolite with titania-silica	Total nitrogen (TN), Basic nitrogen (BN) and Nonbasic nitrogen (NBN). Increase temperature & pressure, increase nitrogen conversion. BN had higher conversion for both conditions. 800m^3 H$_2$ /m^3 feed highest nitrogen conversion for all. Decrease LHSV, increase nitrogen conversion. Power law kinetic model. TN & BN first order. NBN 0.5-1 reaction order. BN: lnA=18, E$_a$=100kJ/mol NBN: lnA=13, E$_a$=74kJ/mol TN: lnA=15, E$_a$=82kJ/mol	Wei et al. 2015 [32]
+360°C Atmospheric Kuwait crude	370-410°C 12MPa 1h^{-1} LHSV 680m^3 H$_2$ /m^3 feed	NiMo/γ-Al$_2$O$_3$	HDS, n=2, lnA=23-27, E$_a$=131-153kJ/mol HDM, n=2, lnA=11-20, E$_a$=71-119kJ/mol Sulfur Conversion, 25-84% V Conversion, 44-82%, Ni Conversion 23-57%	Alfadli et al. 2016 [33]

Stoichiometric Sulfidation Reactions

Criterion Catalyst & Technologies guidelines were used to sulfide the dried catalyst pellets and particles [34]. The following reactions were assumed to occur in sulfiding:

$$C_2H_6S_2 + 3H_2 \rightarrow 2CH_4 + 2H_2S$$
$$3NiO + H_2 + 2H_2S \rightarrow Ni_3S_2 + 3H_2O$$
$$MoO_3 + H_2 + 2H_2S \rightarrow MoS_2 + 3H_2O$$
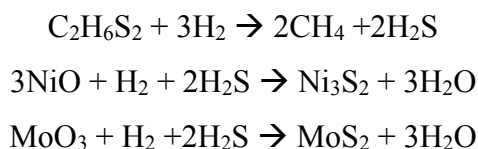
Molybdenum and nickel contents were assumed to range from 12.9-16.7wt.% and 2.8-3.2wt.%, respectively.

Assume a 1g basis of catalyst is sulfided:

Nickel (wt.%)	2.8	3	3.2
Ni (g)	0.028	0.03	0.032
Ni (mmol) 58.69g/mol	0.48	0.51	0.55
NiO (g) 74.69g/mol	0.036	0.038	0.041
NiO (mmol)	0.48	0.51	0.55
Molybdenum (wt.%)	12.9	15.7	16.7
Mo (g)	0.129	0.157	0.167
Mo (mmol) 95.94g/mol	1.34	1.64	1.74
MoO_3 (g) 143.94g/mol	0.19	0.24	0.25
MoO_3 (mmol)	1.34	1.64	1.74
MoS_2 (g) 160.08g/mol	0.22	0.26	0.28
Ni_3S_2 (g) 240.21g/mol (1:3)	0.038	0.041	0.044
S from MoS_2 (g)	0.086	0.105	0.112
S from Ni_3S_2 (g)	0.010	0.011	0.012
Total S (g)	0.096	0.116	0.123
Total S (mmol) 32.07g/mol	3.01	3.61	3.84
H_2S (mmol)	3.01	3.61	3.84
$C_2H_6S_2$ (mmol) (1:2)	1.50	1.81	1.92
H_2 (mmol) (3:2) 2.02g/mol	4.51	5.42	5.77
H_2 for MoS_2 (g)	0.0027	0.0033	0.0035
H_2 for Ni_3S_2 (g)	0.0003	0.0003	0.0004
H_2 for $C_2H_6S_2$ (g)	0.0091	0.0109	0.0116
Total H_2 (g)	0.012	0.015	**0.016**
Total $C_2H_6S_2$ (g) 94.21g/mol	0.142	0.17	**0.181**

From the first sulfidation reactions (S1 and S3), 1.32g and 1.4g of dried catalyst was loaded in the microreactor, respectively.

Pellets

$1.32g \cdot 0.181 = 0.24g$ of DMDS

$1.32g \cdot 0.016 = 0.02g$ of H_2

<45µm Particles

$1.40g \cdot 0.181 = 0.25g$ of DMDS

$1.40g \cdot 0.016 = 0.02g$ of H_2

Mass of DMDS and H_2 loaded over <u>two</u> sulfidation reactions for each catalyst:

Pellets

$0.34g + 0.46g = 0.80g$ of DMDS

$0.05g + 0.04g = 0.09g$ of H_2

<45µm Particles

$0.50g + 0.30g = 0.80g$ of DMDS

$0.05g + 0.05g = 0.10g$ of H_2

A 330% excess DMDS and circa 450% excess H_2 was used from what was stoichiometrically required for the catalyst pellets loaded in the microreactor. For the <45µm catalyst particles loaded in the microreactor, circa 320% excess DMDS and circa 500% excess H_2 was used from what was stoichiometrically required.

Batch Microreactor Volume

Measured using 150mm Mastercraft® electronic caliper:

1/4" Tubing

Wall thickness = 0.065in.

Internal diameter = 0.25 - 0.065 - 0.065 = 0.12in.

0.12in. = 3.048mm

Length = 20cm = 200mm

Assume cylinder shape in 1/4" straight tube:

$V = 0.25 \cdot \pi \cdot D^2 \cdot L$

$V = 0.25 \cdot \pi \cdot (3.048mm)^2 \cdot 200mm =$ ~**1459mm³**

3/4" Tubing (reactor portion)

Wall thickness = 0.083in.

Internal diameter = 0.75 - 0.083 - 0.083 = 0.584in.

0.584in. = 14.834mm

Length = 10cm = 100mm

Assume cylinder shape in 3/4" straight tube:

$V = 0.25 \cdot \pi \cdot D^2 \cdot L$

$V = 0.25 \cdot \pi \cdot (14.834mm)^2 \cdot 100mm = $ **~17282mm³**

$V_T = 17282mm^3 + 1459mm^3 = 18741mm^3 = 18.74 \ cm^3 = $ **~18.7cm³**

From the slope of *Figure 3.4*, 4433.672 kPa / g N_2 was used to calculate the volume at 298K.

$$V = n \cdot R \cdot T \cdot P^{-1}$$

$$slope = P \cdot n^{-1} \cdot M_w^{-1}$$

Combine both equations

$$V = R \cdot T \cdot slope^{-1} \cdot M_w^{-1}$$

$$V = 8314 \ cm^3 \ kPa \ mol^{-1} \ K^{-1} \cdot 298K \cdot (4433.672 \ kPa \ / \ g \ N_2)^{-1} \cdot (28.02g \ N_2 \ / \ mol)^{-1}$$

V = ~19.94cm³

Percent difference:

$$[((18.7cm^3 + 19.94cm^3) \cdot 0.5)^{-1} \cdot (19.94cm^3 - 18.7cm^3)] \cdot 100\% = \textbf{6.4\%}$$

Assume 20cm³ was the approximate volume of the batch microreactor.

Theoretical Air Flow Rate Verification

A force balance on the floating glass sphere inside the rotameter is shown in *Figure A.1*. The rotameter diagram is shown in *Figure A.2*. The scale reading as a function of glass float height is shown in *Figure A.3*. Air flow rate as a function of scale reading is shown in *Figure A.4*. The Gilmont manufacture reported the rotameter air flow rate ranged 1-36NL/min for the GF-1460 model [35]. However, the graduated scale ranged 0-100 with no units. To verify the reported air flow rate, the height (m) of the floating glass sphere was measured on the 0-100 scale. The air flow rate was varied and controlled by the needle valve on the fluidized bath.

Assumptions:

Equations for forces and drag on a single rigid sphere were found Masliyah et al. [36]. The glass float was assumed as a perfect sphere with no friction. Density and viscosity of the air was based on the inlet air pressure, 108kPa(g), when measuring the glass float height. The density and viscosity were obtained from VMGSim. With ideal gas property package, 0.78 nitrogen, 0.21 oxygen and 0.01 argon volume fractions at 20°C, the density and viscosity were predicted: 2.5kg/m^3 and 0.000018kg·m^{-1}·s^{-1}, respectively.
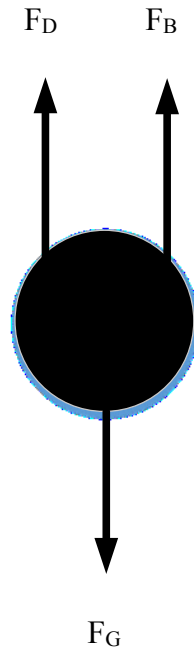
Figure A.1. Force balance on the floating glass sphere inside the rotameter.

From *Figure A.1*, the equations for the force balance on the floating glass sphere:

$$F_G = F_D + F_B \tag{A1}$$

$$F_G = mg \tag{A2}$$

$$F_D = \frac{1}{2}C_D\rho_{fl}A_FV_e^2 \tag{A3}$$

$$F_B = m_{fl}g \tag{A4}$$

$$m = V_F\rho_F \tag{A5}$$

$$A_F = \frac{\pi D^2}{4} \tag{A6}$$

$$V_F = \frac{\pi D^3}{6} \tag{A7}$$

$$m_{fl} = V_F\rho_{fl} \tag{A8}$$

279

Where

F_D = drag force (N)

F_G = force of gravity (N)

F_B = buoyancy force (N)

C_D = drag coefficient (dimensionless)

m = mass of glass float

m_{fl} = mass of fluid (air) in place of glass float

ρ_{fl} = density of fluid (Air at 20°C and 108kPa(g) pressure, 2.5kg/m^3)

μ_{fl} = viscosity of fluid (Air at 20°C and 108kPa(g) pressure, 0.000018 kg·m^{-1}·s^{-1})

ρ_F = density of glass float (2530kg/m^3)

V_F = volume of glass float (m^3)

A_F = cross sectional area of glass float (m^2)

D = diameter of glass float (0.009525m)

V_e = velocity of air flowing around the glass float (m/s)

g = gravity constant (9.81m/s^2)

Substitute equations A2-A8 into equation A1:

$$\frac{\pi D^3}{6}\rho_F g = \frac{1}{2}C_D\rho_{fl}\frac{\pi D^2}{4}V_e^2 + \frac{\pi D^3}{6}\rho_{fl}g \qquad (A9)$$

Solve for velocity of air flowing around the glass float:

$$V_e = \sqrt{\frac{4Dg(\rho_F-\rho_{fl})}{3C_D\rho_{fl}}} \qquad (A10)$$

Assume a drag coefficient of one to calculate initial air velocity:

$$V_e = \sqrt{\frac{4\cdot(0.009525m)\cdot(9.81\frac{m}{s^2})\cdot(2530\frac{kg}{m^3}-2.5\frac{kg}{m^3})}{3\cdot 1\cdot 2.5\frac{kg}{m^3}}}$$

$$V_e = 11.22\text{m/s}$$

Drag coefficient for a sphere depends on the Reynolds number:

$$Re = \frac{\rho_{fl}DV_e}{\mu_{fl}} \qquad (A11)$$

$$Re = \frac{2.5\frac{kg}{m^3}\cdot 0.009525m\cdot 11.22\frac{m}{s}}{0.000018\frac{kg}{m\cdot s}}$$

$$Re = 14843$$

From *Figure 3.2* (pg. 132) of Masliyah et al. and *Figure 8.19* (pg. 278) of Introductory Fluid Mechanics, the flow was turbulent, and the drag coefficient was in the Newton regime [36-37]. At Re=14843, the drag coefficient was 0.44. The new velocity:

$$V_e = \sqrt{\frac{4 \cdot (0.009525m) \cdot (9.81\frac{m}{s^2}) \cdot (2530\frac{kg}{m^3} - 2.5\frac{kg}{m^3})}{3 \cdot 0.44 \cdot 2.5\frac{kg}{m^3}}}$$

$$V_e = 16.92 m/s$$

$$Re = \frac{2.5\frac{kg}{m^3} \cdot 0.009525m \cdot 16.92\frac{m}{s}}{0.000018\frac{kg}{m \cdot s}}$$

$$Re = 22384$$

From *Figure 3.2* (pg. 132) of Masliyah et al. and *Figure 8.19* (pg. 278) of Introductory Fluid Mechanics, the flow was turbulent, and the drag coefficient was in the Newton regime [36-37]. At Re=22384, the drag coefficient remains at 0.44. Stop iteration. The air velocity was circa 16.9m/s.
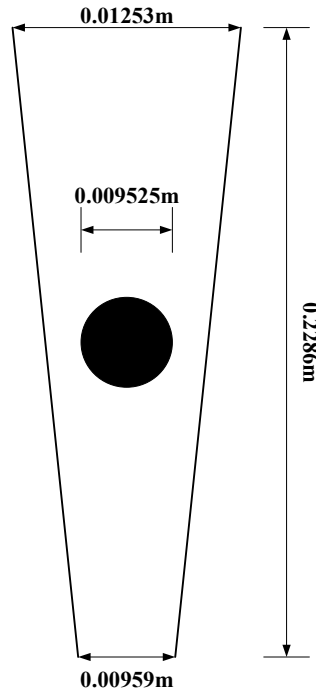
Figure A.2. Rotameter diagram.

From *Figure A.2*, the dimensions of the rotameter glass tube were measured using a 150mm Mastercraft® electronic caliper and measuring tape. The area of air flow varies as a function of glass float height inside the rotameter:

$$A_a = \frac{\pi}{4} \cdot [(D_B + b \cdot h)^2 - D^2] \qquad (A12)$$

Where

D_B = inner diameter at the bottom of the rotameter (0.00959m)

b = slope of rotameter wall

h = height of glass float (m)

D = diameter of glass float (0.009525m)

From *Figure A.2*, the slope of the rotameter wall:

$$b = \frac{(0.01253m - 0.00959m)}{0.2286m} = 0.01286$$
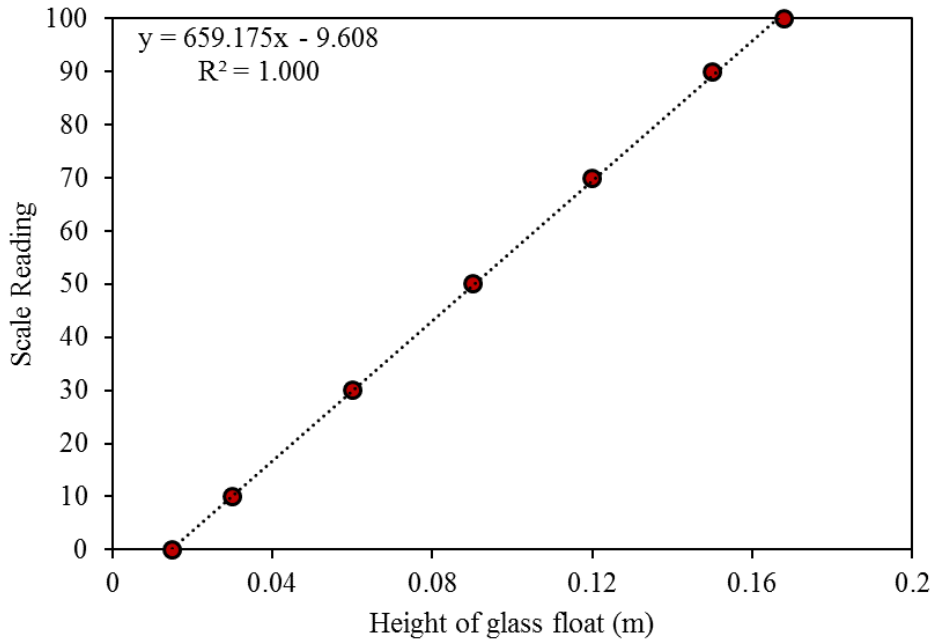
Figure A.3. Scale reading as a function of glass float height.

From *Figure A.3*, the height of the glass float depends linearly on the scale reading (SR). Therefore, the area of flow around the glass float is solved in terms of scale reading:

$$A_a = \frac{\pi}{4} \cdot \left[\left(D_B + 77.76 \cdot [\frac{(SR+9.608)}{659.175}] \right)^2 - D^2 \right] \qquad (A13)$$

Assuming a constant air flow velocity, the air flow rate is solved in terms of scale reading:

$$Q = V_e \cdot A_a = 16.9 \frac{m}{s} \cdot \frac{\pi}{4} \cdot \left[\left((0.00959m) + 0.01286 \cdot \left[\frac{(SR + 9.608)}{659.175} \right] \right)^2 - (0.009525m)^2 \right] \cdot \frac{1000L}{m^3} \cdot \frac{60s}{min}$$
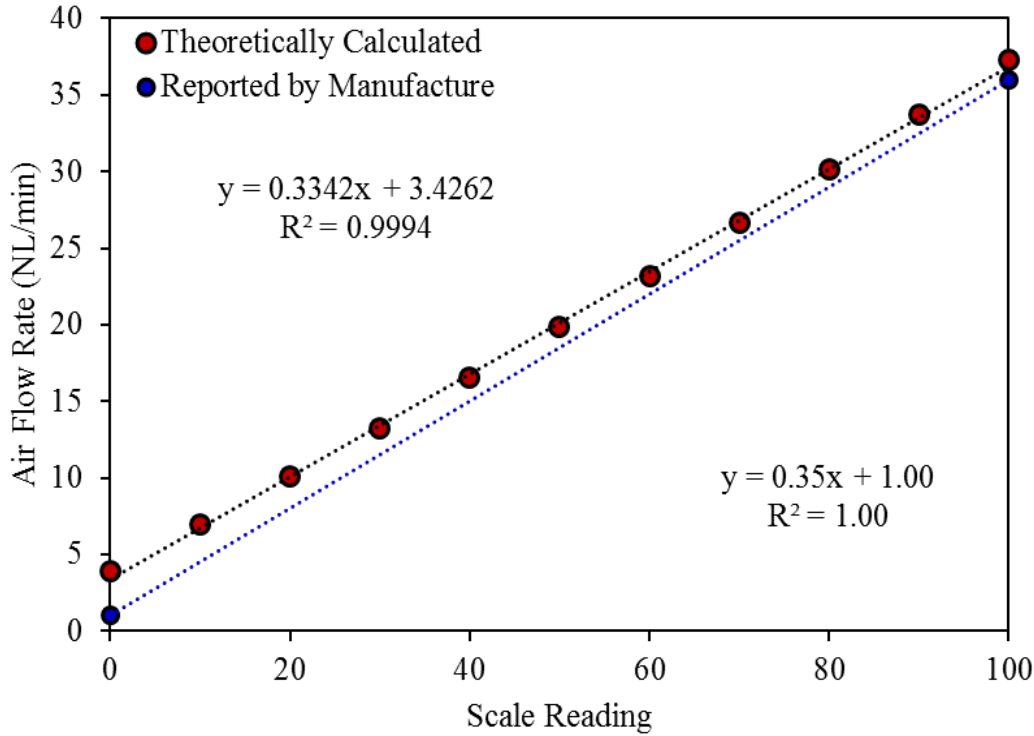
Figure A.4. Air flow rate as a function of scale reading.

The slopes of the linear fitted equations differed by 4.6%. The error was attributed to the assumptions and physical measurements (caliper, measuring tape and scale reading) throughout the theoretical calculations. The linear scale reported by the manufacture was used for all flow rate measurements. To convert the normal flow rate to flow rates at the inlet air pressure:

$$Q_{actual} = Q \cdot \sqrt{\frac{P}{100kPa}} \tag{A14}$$

Where

Q = Air flow rate at normal conditions (20°C and 1atm) from the scale reading (0.35·SR+1)

P = Intel air pressure (kPa(a))

The inlet pressure was measured, 108kPa(g), therefore from equation A14, a factor of 1.44 on the normal flow rate was used to calculate the flow rate at the inlet air pressure.

Appendix A References

[1] M. F. Wilson and J. F. Kriz, "Upgrading of middle distillate fractions of a syncrude from Athabasca oil sands," *Fuel,* vol. 63, *(2),* pp. 190-196, 1984.

[2] R. S. Mann, I. S. Sambi and K. C. Khulbe, "Catalytic hydrofining of heavy gas oil," *Ind. Eng. Chem. Res.,* vol. 26, *(3),* pp. 410-414, 1987.

[3] R. S. Mann, I. S. Sambi and K. C. Khulbe, "Hydrofining of heavy gas oil on zeolite-alumina supported nickel-molybdenum catalyst," *Ind. Eng. Chem. Res.,* vol. 27, *(10),* pp. 1788-1792, 1988.

[4] I. P. Fisher and M. F. Wilson, "Kinetics and thermodynamics of aromatics hydrogenation in distillates from Athabasca syncrudes," *Energy Fuels,* vol. 2, *(4),* pp. 548-555, 1988.

[5] S. Yui, "Hydrotreating of Bitumen-Derived Gas Oil: Kinetics of Hydrodesulfurization, Hydrodenitrogenation, and Mild Hydrocracking, and Correlations to Predict Product Yields and Properties," *AOSTRA Journal of Research,* vol. 5, pp. 211-224, 1989.

[6] R. P. Kirchen and E. C. Sanford, "Kinetics of Ni-Mo/Al$_2$O$_3$, Co-Mo/Al$_2$O$_3$ and Layered Catalyst Charges for Hydrotreating of Athabasca Bitumen-Derived Coker Gas Oil," *AOSTRA Journal of Research,* vol. 5, pp. 287-301, 1989.

[7] S. M. Yui and E. C. Sanford, "Mild hydrocracking of bitumen-derived coker and hydrocracker heavy gas oils: kinetics, product yields, and product properties," *Ind. Eng. Chem. Res.,* vol. 28, *(9),* pp. 1278-1284, 1989.

[8] L. C. Trytten, M. R. Gray and E. C. Sanford, "Hydroprocessing of narrow-boiling gas oil fractions: dependence of reaction kinetics on molecular weight," *Ind. Eng. Chem. Res.,* vol. 29, *(5),* pp. 725-730, 1990.

[9] M. R. Gray, "Lumped kinetics of structural groups: hydrotreating of heavy distillate," *Ind. Eng. Chem. Res.,* vol. 29, *(4),* pp. 505-512, 1990.

[10] S. M. Yui and E. C. Sanford, "Kinetics of aromatics hydrogenation of bitumen-derived gas oils," *The Canadian Journal of Chemical Engineering,* vol. 69, *(5),* pp. 1087-1095, 1991.

[11] R. Diaz-Real, R. S. Mann and I. S. Sambi, "Hydrotreatment of Athabasca bitumen derived gas oil over nickel-molybdenum, nickel-tungsten, and cobalt-molybdenum catalysts," *Ind. Eng. Chem. Res.,* vol. 32, *(7),* pp. 1354-1358, 1993.

[12] S. M. Yui and S. H. Ng, "Hydrotreating of a Bitumen-Derived Coker HGO and Evaluation of Hydrotreated HGOs as Potential FCC Feeds Using Microactivity Test Unit," *Energy Fuels,* vol. 9, *(4),* pp. 665-672, 1995.

[13] N. Kimbara, J. Charland and M. F. Wilson, "Hydrogenation of Aromatics in Synthetic Crude Distillates Catalyzed by Platinum Supported in Molecular Sieves," *Ind. Eng. Chem. Res.,* vol. 35, *(11),* pp. 3874-3883, 1996.

[14] S. K. Bej, A. K. Dalai and J. Adjaye, "Comparison of Hydrodenitrogenation of Basic and Nonbasic Nitrogen Compounds Present in Oil Sands Derived Heavy Gas Oil," *Energy Fuels,* vol. 15, *(2),* pp. 377-383, 2001.

[15] S. K. Bej, A. K. Dalai and J. Adjaye, "Effect of Hydrotreating Conditions on the Conversion of Residual Fraction and Microcarbon Residue Present in Oil Sands Derived Heavy Gas Oil," *Energy Fuels,* vol. 15, *(5),* pp. 1103-1109, 2001.

[16] S. K. Bej, A. K. Dalai and J. Adjaye, "Kinetics of Hydrodesulfurization of Heavy Gas Oil Derived from Oil-Sands Bitumen," *Petroleum Science & Technology,* vol. 20, *(7),* pp. 867, 2002.

[17] K. Aoyagi, W. C. McCaffrey and M. R. Gray, "Kinetics of Hydrocracking and Hydrotreating of Coker and Oilsands Gas Oils," *Petrol. Sci. Technol.,* vol. 21, *(5-6),* pp. 997-1015, 2003.

[18] C. Botchwey, A. K. Dalai and J. Adjaye, "Product Selectivity during Hydrotreating and Mild Hydrocracking of Bitumen-Derived Gas Oil," *Energy Fuels,* vol. 17, *(5),* pp. 1372-1381, 2003.

[19] C. Botchwey, A. K. Dalai and J. Adjaye, "Kinetics of Bitumen-Derived Gas Oil Upgrading Using a Commercial NiMo/Al2O3 Catalyst," *Can. J. Chem. Eng.,* vol. 82, *(3),* pp. 478-487, 2004.

[20] C. Botchwey, A. K. Dalai and J. Adjaye, "Two-Stage Hydrotreating of Athabasca Heavy Gas Oil with Interstage Hydrogen Sulfide Removal: Effect of Process Conditions and Kinetic Analyses," *Ind. Eng. Chem. Res.,* vol. 43, *(18),* pp. 5854-5861, 2004.

[21] D. Ferdous, A. K. Dalai and J. Adjaye, "A series of NiMo/Al$_2$O$_3$ catalysts containing boron and phosphorus," *Applied Catalysis A: General,* vol. 260, *(2),* pp. 153-162, 2004.

[22] A. Owusu-Boakye *et al*, "Maximizing Aromatic Hydrogenation of Bitumen-Derived Light Gas Oil: Statistical Approach and Kinetic Studies," *Energy Fuels,* vol. 19, *(5),* pp. 1763-1773, 2005.

[23] A. Owusu-Boakye, "Two-Stage Aromatics Hydrogenation of Bitumen-Derived Light Gas Oil," University of Saskatchewan, 2005.

[24] A. Owusu-Boakye *et al*, "Experimental and Kinetic Studies of Aromatic Hydrogenation, Hydrodesulfurization, and Hydrodenitrogenation of Light Gas Oils Derived from Athabasca Bitumen," *Ind. Eng. Chem. Res.,* vol. 44, *(21),* pp. 7935-7944, 2005.

[25] D. Ferdous, A. K. Dalai and J. Adjaye, "Hydrodenitrogenation and Hydrodesulphurization of Heavy Gas Oil Using NiMo/Al2O3 Catalyst Containing Phosphorus: Experimental and Kinetic Studies," *The Canadian Journal of Chemical Engineering,* vol. 83, *(5),* pp. 855-864, 2005.

[26] D. Ferdous, A. K. Dalai and J. Adjaye, "Hydrodenitrogenation and Hydrodesulfurization of Heavy Gas Oil Using NiMo/Al$_2$O$_3$ Catalyst Containing Boron: Experimental and Kinetic Studies," *Ind. Eng. Chem. Res.,* vol. 45, *(2),* pp. 544-552, 2006.

[27] S. Yui and T. Dodge, "Catalyst Deactivation, Kinetics, and Product Quality of Mild Hydrocracking of Bitumen-Derived Heavy Gas Oils," *Petrol Sci Technol,* vol. 24, *(3-4),* pp. 351-365, 2006.

[28] M. Mapiour *et al*, "Effect of Hydrogen Purity on Hydroprocessing of Heavy Gas Oil Derived from Oil-Sands Bitumen," *Energy Fuels,* vol. 23, *(4),* pp. 2129-2135, 2009.

[29] M. Mapiour *et al*, "Effects of the operating variables on hydrotreating of heavy gas oil: Experimental, modeling, and kinetic studies," *Fuel,* vol. 89, *(9),* pp. 2536-2543, 2010.

[30] L. Mapiour, "Kinetics and Effects of H$_2$ Partial Pressure on Hydrotreating of Heavy Gas Oil," University of Saskatchewan, 2009.

[31] M. Mapiour *et al*, "Effects of Hydrogen Partial Pressure on Hydrotreating of Heavy Gas Oil Derived from Oil-Sands Bitumen: Experimental and Kinetics," *Energy Fuels,* vol. 24, *(2),* pp. 772-784, 2010.

[32] Q. Wei *et al*, "Hydrodenitrogenation of basic and non-basic nitrogen-containing compounds in coker gas oil," *Fuel Processing Technology,* vol. 129, *(Supplement C),* pp. 76-84, 2015.

[33] J. Alfadhli *et al*, "Performance assessment of NiMo/γ-Al2O3 catalysts for upgrading KEC-AR: An assessment of selected apparent kinetic parameters of selected hydrotreating reactions," *Fuel,* vol. 164, pp. 38-45, 2016.

[34] Criterion Catalyst & Technologies, "Criterion* Hydrotreating Catalyst In-situ Presulphiding Guidelines," Criterion Catalyst & Technologies, 1998.

[35] Gimont® Instruments, "Flowmeters Shielded Type Calibrated and Correlated." Gilmont® Instruments, Inc., Barrington, USA, 2009.

[36] J. H. Masliyah *et al*, *Handbook on Theory and Practice of Bitumen Recovery from Athabasca Oil Sands Volume I: Theoretical Basis.* Cochrane, Alta.: Kingsley Knowledge Pub., 2011.

[37] J. Katz, *Introductory Fluid Mechanics.* New York: Cambridge University Press, 2010.

Appendix B

Reactor loading verification, gas to oil ratio, liquid hourly space velocity approximation, bulk density and hydrogen solubility, as well as predicted pressures at reaction temperatures are found in *Appendix B*. Dimethyl disulfide, catalyst, and hydrogen gas masses loaded in microreactor (from *Table 3.5*) are presented in *Table B1*. Average HVGO, catalyst, and hydrogen gas masses loaded in microreactor (from *Table 3.6*) are presented in *Table B2*.

Table B1. Dimethyl disulfide, catalyst, and hydrogen gas masses loaded in microreactor.

#	Liquid Feed Loaded (g)	Catalyst Loaded (g)	H_2 Gas Loaded (g)
16	0.34	1.32	0.05
17	0.46	1.39	0.04
18	0.5	1.4	0.05
19	0.3	1.24	0.05

Table B2. Average HVGO, catalyst, and hydrogen gas masses loaded in microreactor.

	HVGO Loaded (g)	Catalyst Loaded (g)	H_2 Gas Loaded (g)
Average	0.614	0.103	0.072
Standard Deviation	0.009	0.005	0.005
95% Confidence Interval	0.003	0.001	0.001

Reactor Loading Verification

From *Appendix A*, the microreactor volume was determined at approximately 20cm^3. To ensure the total volume was maintained for all reactions, verification calculations were completed. Additionally, the average gas to oil ratio and approximate liquid hourly space velocities were calculated.

Sulfidation Reactions

Dimethyl disulfide density: 1.06g/cm^3

$0.34 \text{g} / 1.06 \text{g/cm}^3 = 0.32 \text{cm}^3$

$0.46 \text{g} / 1.06 \text{g/cm}^3 = 0.43 \text{cm}^3$

$0.5 \text{g} / 1.06 \text{g/cm}^3 = 0.47 \text{cm}^3$

$0.3 \text{g} / 1.06 \text{g/cm}^3 = 0.28 \text{cm}^3$

Catalyst density (from *Table 3.2*): $0.75\text{-}0.83 \text{g/cm}^3$

$1.32 \text{g} / 0.75 \text{g/cm}^3 = 1.75 \text{cm}^3$

$1.32 \text{g} / 0.83 \text{g/cm}^3 = 1.59 \text{cm}^3$

$1.4 \text{g} / 0.75 \text{ g/cm}^3 = 1.87 \text{cm}^3$

$1.4 \text{g} / 0.83 \text{g/cm}^3 = 1.69 \text{cm}^3$

For initial sulfided catalyst (reactions 17 and 19), assume a density of $0.8\text{-}1 \text{g/cm}^3$

$1.39 \text{g} / 0.8 \text{g/cm}^3 = 1.74 \text{cm}^3$

$1.39 \text{g} / 1 \text{g/cm}^3 = 1.39 \text{cm}^3$

$1.24 \text{g} / 0.8 \text{ g/cm}^3 = 1.55 \text{cm}^3$

$1.24 \text{g} / 1 \text{g/cm}^3 = 1.24 \text{cm}^3$

The hydrogen gas was loaded at 3000kPa(g) into the microreactor for sulfidation reactions 16 to 19. Using VMGSim, Advanced Peng-Robinson property package, the density of hydrogen was predicted at 20 and 25°C (at 3000kPa(g)).

$\rho(20°C) = 0.0025277 \text{g/cm}^3$

$\rho(25°C) = 0.0024854 \text{g/cm}^3$

$0.04 \text{g} / 0.0025277 \text{g/cm}^3 = 15.82 \text{cm}^3$

$0.04 \text{g} / 0.0024854 \text{g/cm}^3 = 16.09 \text{cm}^3$

$0.05 \text{g} / 0.0025277 \text{g/cm}^3 = 19.78 \text{cm}^3$

$0.05 \text{g} / 0.0024854 \text{g/cm}^3 = 20.12 \text{cm}^3$

Reaction 16

Minimum: $0.32 \text{cm}^3 + 1.59 \text{cm}^3 + 19.78 \text{cm}^3 = 21.69 \text{cm}^3$

Maximum: $0.32 \text{cm}^3 + 1.75 \text{cm}^3 + 20.12 \text{cm}^3 = 22.19 \text{cm}^3$

Reaction 17

Minimum: $0.43cm^3 + 1.39cm^3 + 15.82cm^3 = 17.64cm^3$

Maximum: $0.43cm^3 + 1.74cm^3 + 16.09cm^3 = 18.26cm^3$

Reaction 18

Minimum: $0.47cm^3 + 1.69cm^3 + 19.78cm^3 = 21.94cm^3$

Maximum: $0.47cm^3 + 1.87cm^3 + 20.12cm^3 = 22.46cm^3$

Reaction 19

Minimum: $0.28cm^3 + 1.24cm^3 + 19.78cm^3 = 21.3cm^3$

Maximum: $0.28cm^3 + 1.55cm^3 + 20.12cm^3 = 21.95cm^3$

The average calculated volume for all sulfidation reactions was $20.92cm^3$, a 4.5% difference from $20cm^3$. Reasons for the error included mass measurements from the balance scale, potential DMDS evaporation loses (high volatility), and the catalyst density assumption. If the mass of hydrogen gas was measured to 3 decimal places, volumes can be predicted more accurately.

Hydrotreating Reactions

HVGO density: $0.967g/cm^3$

$0.6g / 0.967g/cm^3 = 0.62cm^3$

$0.614g / 0.967g/cm^3 = 0.63cm^3$

$0.63g / 0.967g/cm^3 = 0.65cm^3$

Catalyst density: $0.75g/cm^3$ to $1g/cm^3$ for sulfided catalyst

$0.103g / 0.75g/cm^3 = 0.14cm^3$

$0.103g / 1g/cm^3 = 0.10cm^3$

The hydrogen gas was loaded at 4500kPa(g) into the microreactor for sulfidation reactions 2 to 15, and 20 to 44. Using VMGSim, Advanced Peng-Robinson property package, the density of hydrogen was predicted at 20 and 25°C (at 4500kPa(g)).

$\rho(20°C) = 0.0037219g/cm^3$

$\rho(25°C) = 0.0036598g/cm^3$

At 20°C

$0.06g / 0.0037219g/cm^3 = 16.12cm^3$

$0.072g / 0.0037219g/cm^3 = 19.34cm^3$

$0.08g / 0.0037219g/cm^3 = 21.49cm^3$

At 25°C

$0.06g / 0.0036598g/cm^3 = 16.39cm^3$

$0.072g / 0.0036598g/cm^3 = 19.67cm^3$

$0.08g / 0.0036598g/cm^3 = 21.86cm^3$

Total volume loaded:

Minimum

$16.12cm^3 + 0.10cm^3 + 0.62cm^3 = 16.84cm^3$

Average (1)

$19.34cm^3 + 0.14cm^3 + 0.63cm^3 = 20.11cm^3$

Average (2)

$19.67cm^3 + 0.1cm^3 + 0.63cm^3 = 20.4cm^3$

Maximum

$21.86cm^3 + 0.14cm^3 + 0.65cm^3 = 22.65cm^3$

The average calculated volume for all hydrotreating reactions ranged between 20.11-20.4cm^3, a 0.55-1.98% difference from 20cm^3. Reasons for the error included mass measurements from the balance scale and the catalyst density assumption. The average of minimum, average (1), average (2), and maximum was 20cm^3.

Gas to Oil Ratio

As discussed in section 2.1.4, the gas to oil ratio (hydrogen to HVGO feed) was calculated for comparison to other hydrotreating reactor systems reported in literature.

Minimum

$H_2 / HVGO = 19.34cm^3 / 0.65cm^3 = 29.8 \ cm^3 \ H_2 / cm^3 \ HVGO$

Average (1)

$H_2 / HVGO = 19.34cm^3 / 0.63cm^3 = 30.7 \ cm^3 \ H_2 / cm^3 \ HVGO$

Average (2)

H_2 / HVGO = 19.67 cm^3 / 0.63 cm^3 = 31.2 cm^3 H_2 / cm^3 HVGO

Maximum

H_2 / HVGO = 19.67 cm^3 / 0.62 cm^3 = 31.7 cm^3 H_2 / cm^3 HVGO

The average calculated gas to oil ratio for all hydrotreating reactions ranged between 30.7 to 31.2. Such loading ratios were mild compared to packed bed reactors or industrial reactors (>400 Sm^3/m^3, dimensionless ratio). The average of minimum, average (1), average (2), and maximum was 30.9 cm^3 H_2 / cm^3 HVGO.

Approximate Liquid Hourly Space Velocity (LHSV) Calculations

As discussed in section 2.1.4, the LHSV was calculated for comparison to other hydrotreating reactor systems reported in literature.

$$LHSV\ (h^{-1}) = \frac{Feed\ Flowrate\ (\frac{m^3}{h})}{Volume\ of\ Catalyst\ (m^3)} \qquad (B1)$$

As the microreactor was a batch system, a continuous flow rate was not possible. However, the reaction time was known for each experiment (*Table 3.4*). Using the volume of feed loaded (cm^3) and the reaction time (h), and the volume of catalyst loaded (cm^3), an approximate LHSV was calculated for each reaction in the current study.

Reactions times varied from 0.25h to 2h.

HVGO was assumed constant at 0.63 cm^3

Reaction time (h)	0.25	0.5	1	1.5	2
Catalyst volume 0.10 cm^3	25.2 h^{-1}	12.6 h^{-1}	6.3 h^{-1}	4.2 h^{-1}	3.2 h^{-1}
Catalyst volume 0.14 cm^3	18 h^{-1}	9 h^{-1}	4.5 h^{-1}	3 h^{-1}	2.3 h^{-1}

The approximate LHSV ranged anywhere from 2.3 to 25.2 h^{-1}, depending on the catalyst density assumption. The LHSV values calculated for the current study were higher compared to packed bed reactors or industrial reactors reported in literature for hydrotreating reactions (0.5 to 2 h^{-1}).

Bulk Density and Hydrogen Solubility Predictions using VMGSim

VMGSim thermodynamic software was used to predict bulk density and hydrogen solubility for both sulfidation and hydrotreating reactions. All thermodynamic modeling was completed at a couple of loading ratios and conditions prior to microreactor reactions in the lab to ensure the pressure did not exceed 22.9MPa.

Sulfidation Reactions

Material stream and property table in VMGSim flowsheet is shown in *Figure B1*. Predicted bulk density as a function of pressure for DMDS loadings and hydrogen are presented in *Figures B2 to B4.* Predicted hydrogen solubility in DMDS liquid as a function of pressure is shown in *Figure B5*. The Advanced Peng-Robinson property package was used. Hydrogen and dimethyl disulfide components were installed. A material stream and property table were installed into the main flowsheet as shown in *Figure B1*.
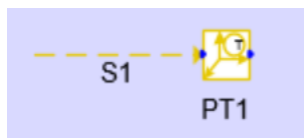
Figure B1. Material stream and property table in VMGSim flowsheet.

A rate of 0.05g/h of H_2 gas and 0.3 to 0.5g/h for DMDS were used. Values were entered in mass flow rates. Technically, these are not flow rates for the batch system, but the ratios were used in the prediction of bulk density and hydrogen solubility. In the property table interface, under variables, the temperature (X-variable) was plotted as a function of pressure (Y-variable). Bulk mass density was the dependent variable. Temperature ranged from 0 to 400°C with 400 points and pressure ranged from 0 to 15000kPa(a) with 1500 points. Results were obtained from the "Table" tab.

The software calculated the bulk mass density of the mixture based on the sum of the vapor and liquid molar volume fractions divided by the average molecular weight of the vapor and liquid fractions. The total vapor molar volume was calculated from the Peng-Robinson equation of state at each condition (dependent on the DMDS vapor pressure (Antoine equation) and hydrogen partial pressure). The liquid molar volume was calculated from the mass density of the liquid (a

built-in correlation for DMDS as a function temperature). The decomposition reaction with a catalyst was not included in modeling. Critical caution is important with such predictions. Three sets of data tables were obtained for 0.3, 0.4 and 0.5g of DMDS. Hydrogen was kept constant at 0.05g. Results are highlighted in *Figures B2 to B4*.
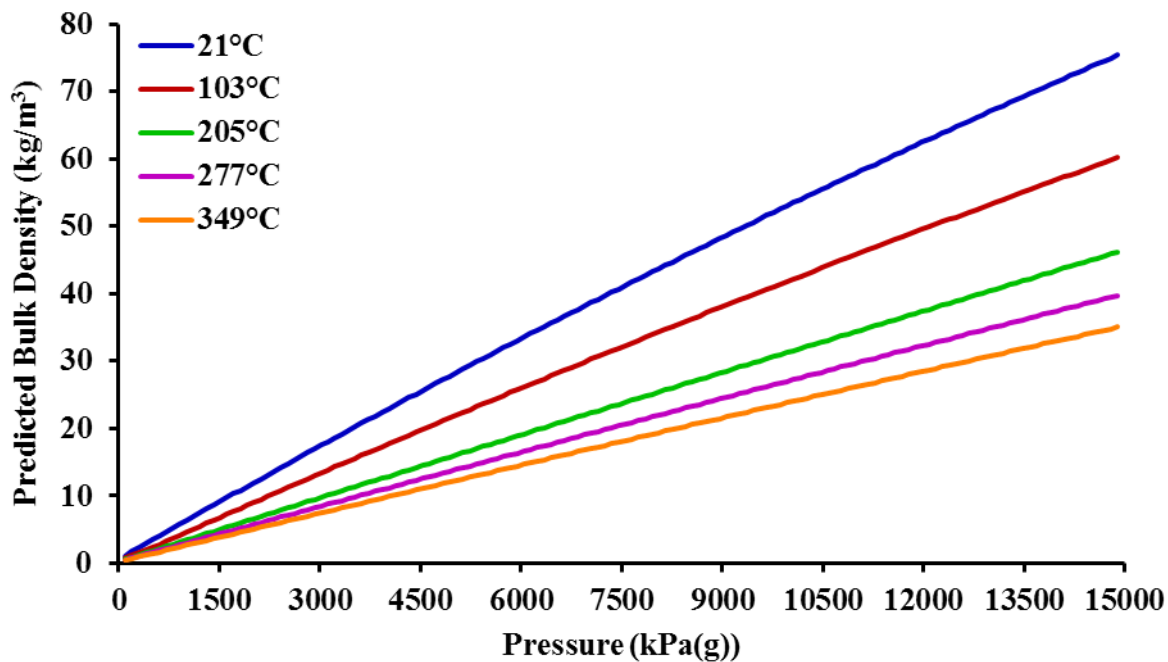
Figure B2. Predicted bulk density as a function of pressure for 0.3g of DMDS and 0.05g of hydrogen.
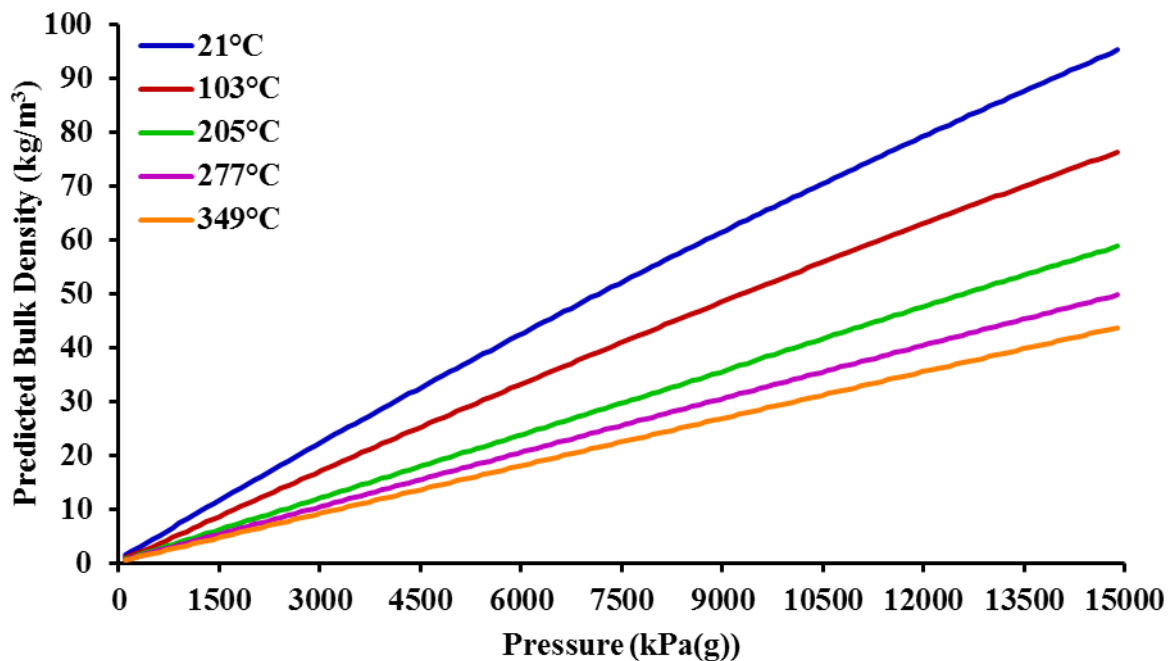
Figure B3. Predicted bulk density as a function of pressure for 0.4g of DMDS and 0.05g of hydrogen.
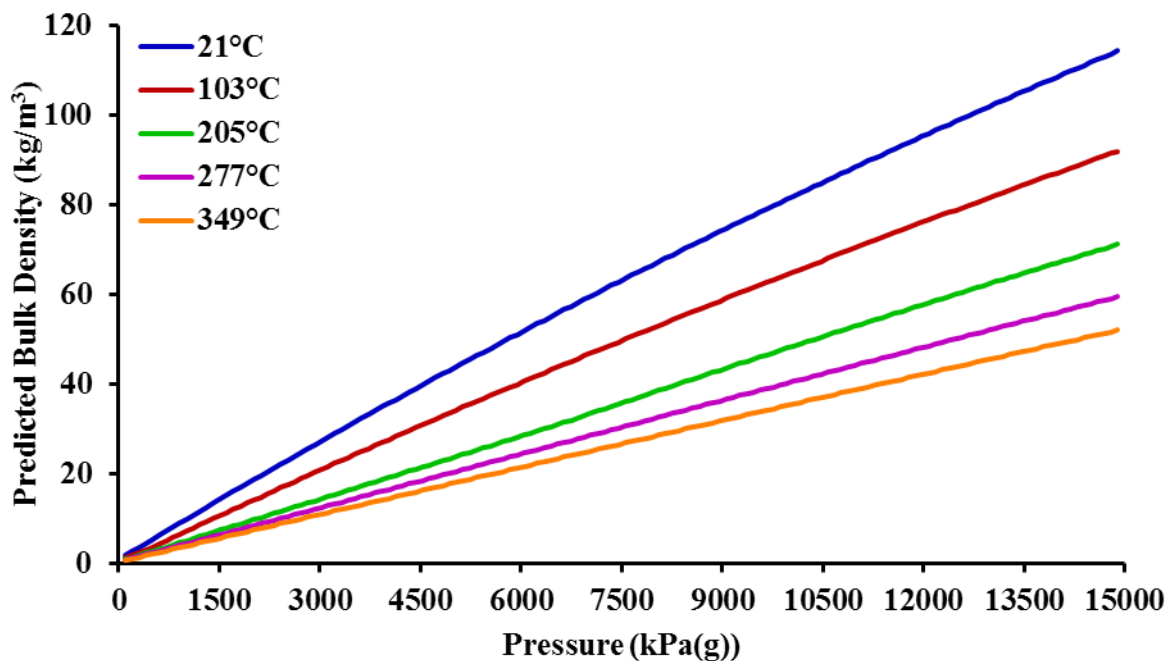
Figure B4. Predicted bulk density as a function of pressure for 0.5g of DMDS and 0.05g of hydrogen.

As seen in *Figures B2 to B4*, select temperatures (21°C, 103°C, 205°C, 277°C, and 349°C) were plotted. If all data was included, a 3-dimensional mesh grid could visually highlight these trends:

- As the pressure increases, the bulk density increases.
- As the temperature increases, the bulk density decreases.
- Decreasing the DMDS loading from 0.5g to 0.3g, decreases the predicted bulk densities.

ExcelUnitOp and signal streams were added to the VMGSim flowsheet to complete rapid hydrogen solubility predictions at different temperatures and pressures. Similar to the bulk density plots, the temperature and pressure varied from 20 to 200°C and 0 to 12000kPa(g), respectively. Hydrogen was kept constant at 0.05g. The hydrogen solubility in the liquid phase was reported as mol per kilogram of liquid (mol H_2 / kg liq.). Results are highlighted in *Figure B5*.
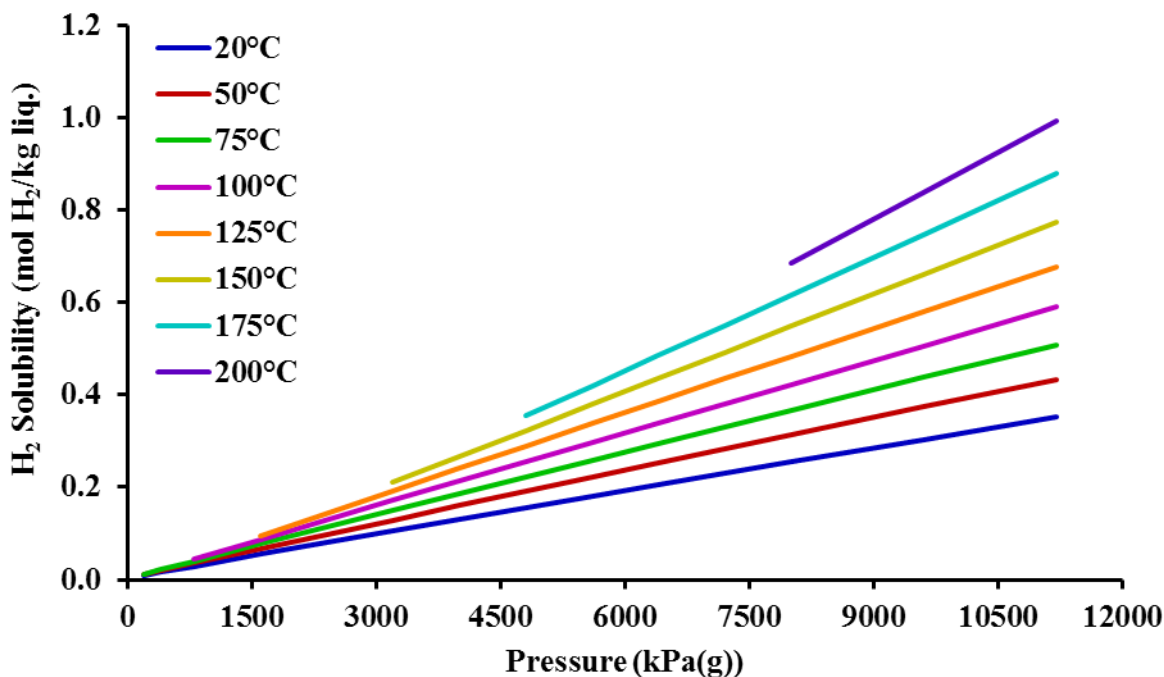
Figure B5. Predicted hydrogen solubility in DMDS liquid as a function of pressure.

From *Figure B5*, the predicted hydrogen solubility in the liquid (mainly DMDS) increases with temperature and pressure. As the temperature increases, the start of the predicted hydrogen solubility shifts to higher pressure as the mixture becomes a complete vapor (partial DMDS vapor pressure curve). Caution is important with these predicted values. Decomposition reaction of

295

DMDS and hydrogen sulfide formation could affect hydrogen solubility in the liquid phase at higher temperatures.

Hydrotreating Reactions

The boiling point distribution of the HVGO is presented in *Table B3*. Material streams, mixer, and property table in VMGSim flowsheet are shown in *Figure B6*. Predicted bulk density as a function of pressure for HVGO and hydrogen loadings are presented in *Figures B7 to B12*. Predicted hydrogen solubility in HVGO liquid as a function of pressure is shown in *Figure B13*. Comparison of predicted hydrogen solubility in HVGO to Cai et al. [1] data is found in *Figure B14*. Comparison of predicted hydrogen solubility in HVGO coefficients to Cai et al. [1] data is found in *Table B4*. The Advanced Peng-Robinson property package was used. Hydrogen and HVGO were installed in the software. The HVGO was installed as an oil mixture component. Measured HVGO oil property data was installed into the oil component mixture assay. The software predicted properties based on built in thermodynamic correlations to estimate critical properties and molecular weights of specific boiling fractions (a few examples are found in Gray [2]). For the current study, the boiling point distribution, measured density (967kg/m^3 at 60°F), and molecular weight (345g/mol from *Table 2.7*) were used. The boiling point distribution of the HVGO used in the VMGSim model is present in *Table B3*.

Table B3. Boiling point distribution of the HVGO.

wt.%	T (°C)	wt.%	T (°C)	wt.%	T (°C)	wt.%	T (°C)
0.5	298.6	26	393	51	428.2	76	462.8
1	309.5	27	394.5	52	429.9	77	465.4
2	322.3	28	396	53	430.7	78	467.2
3	330.6	29	397.9	54	432.1	79	468.9
4	337.3	30	399	55	433.4	80	470.3
5	343.1	31	400.5	56	434.1	81	472.3
6	347.7	32	402	57	435.4	82	474.4
7	351.5	33	403.5	58	436.7	83	476.1
8	355.7	34	404.7	59	437.4	84	478.5
9	359.1	35	406.6	60	438.7	85	480.6
10	362.5	36	408.1	61	440	86	482.8
11	365	37	409.2	62	441.4	87	485.1
12	367.6	38	410.3	63	442	88	487.6
13	370.5	39	411.8	64	443.3	89	490.2
14	372.6	40	413.5	65	444.7	90	493.4
15	374.3	41	414.7	66	445.7	91	496
16	376.6	42	415.9	67	447.3	92	500.4
17	378	43	417.6	68	448.6	93	504.9
18	380	44	418.4	69	450.2	94	509.7
19	382	45	420.4	70	451.9	95	514.2
20	383.3	46	421.7	71	453.6	96	520.3
21	384.7	47	422.5	72	455.7	97	530.5
22	386.7	48	424.1	73	456.9	98	544.1
23	388.1	49	425.4	74	458.6	99	587.7
24	389.4	50	426.6	75	460.7	99.5	643.3
25	391.5						

Once the data was entered, the HVGO oil was "cut" into pseudo components based on the boiling fraction specified in the range section (default). Each pseudo component had estimated critical constants, acentric factors, heat capacity, density, etc. Critical caution is important for these predicted values. Other correlations exist and could be used for further comparison (not an objective for the current study). The HVGO was installed into the component list. Two material streams, a mixer, and property table were installed into the main flowsheet as shown in *Figure B6*.
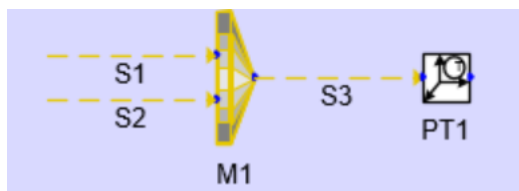
Figure B6. Two material streams, mixer, and property table in VMGSim flowsheet.

A rate of 0.06 to 0.08g/h of H_2 gas (stream 1) and 0.6 to 0.65g/h for HVGO (stream 2) were used. Values were entered in mass flow rates. Technically, these are not flow rates for the batch system, but the ratios were used in predictions of bulk density and hydrogen solubility. In the property table interface, under variables, the temperature (X-variable) was plotted as a function of pressure (Y-variable). Bulk mass density was the dependent variable. Temperature ranged from 0 to 450°C with 450 points and pressure ranged from 0 to 15000kPa(a) with 150 points. Results were obtained from the "Table" tab.

The software calculated the bulk mass density of the mixture based on the sum of the vapor and liquid molar volume fractions divided by the average molecular weight of the vapor and liquid fractions. The total vapor molar volume was calculated from the Peng-Robinson equation of state at each condition (dependent on the predicted vapor pressure of HVGO and the hydrogen partial pressure). The liquid molar volume was calculated from the summation of predicted mass densities and estimated molecular weights of each pseudo component (from built in oil correlations). Six sets of data tables were obtained for three hydrogen loadings and two HVGO loadings. Hydrogen was 0.06, 0.07, and 0.08g/h. HVGO was 0.6 and 0.65g/h. Results are highlighted in *Figures B7 to B12*.
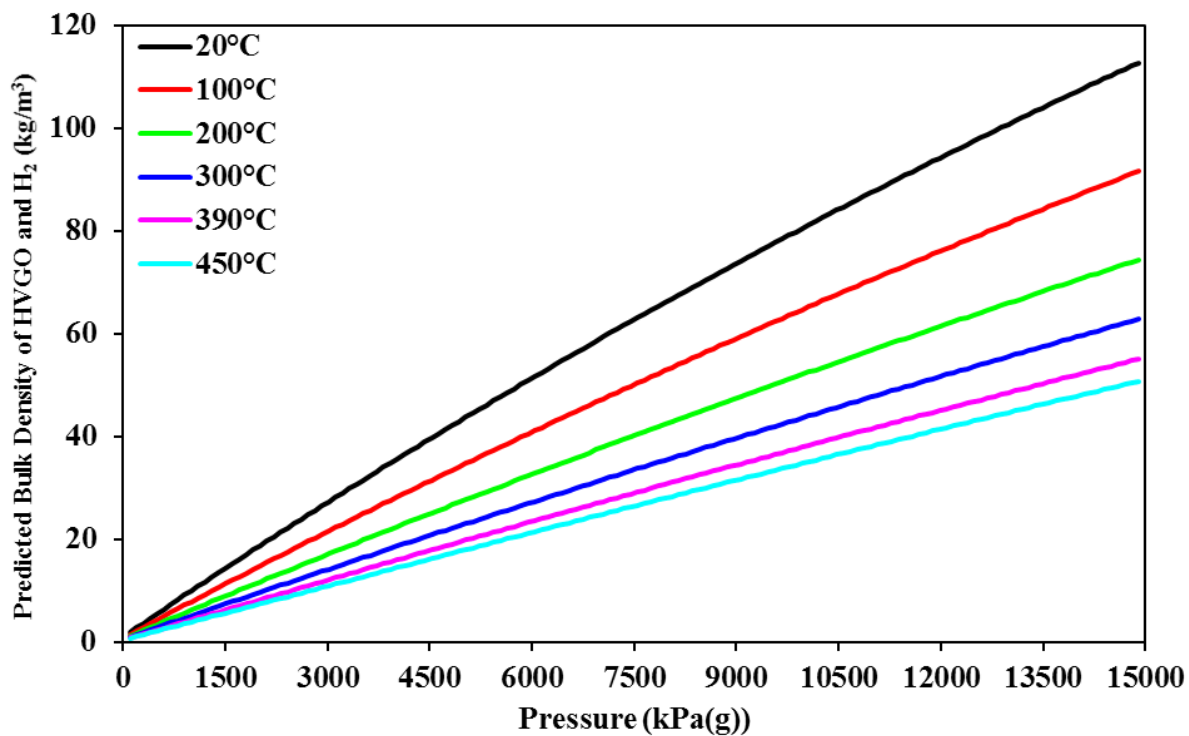
Figure B7. Predicted bulk density as a function of pressure for 0.6g of HVGO and 0.06g of hydrogen.
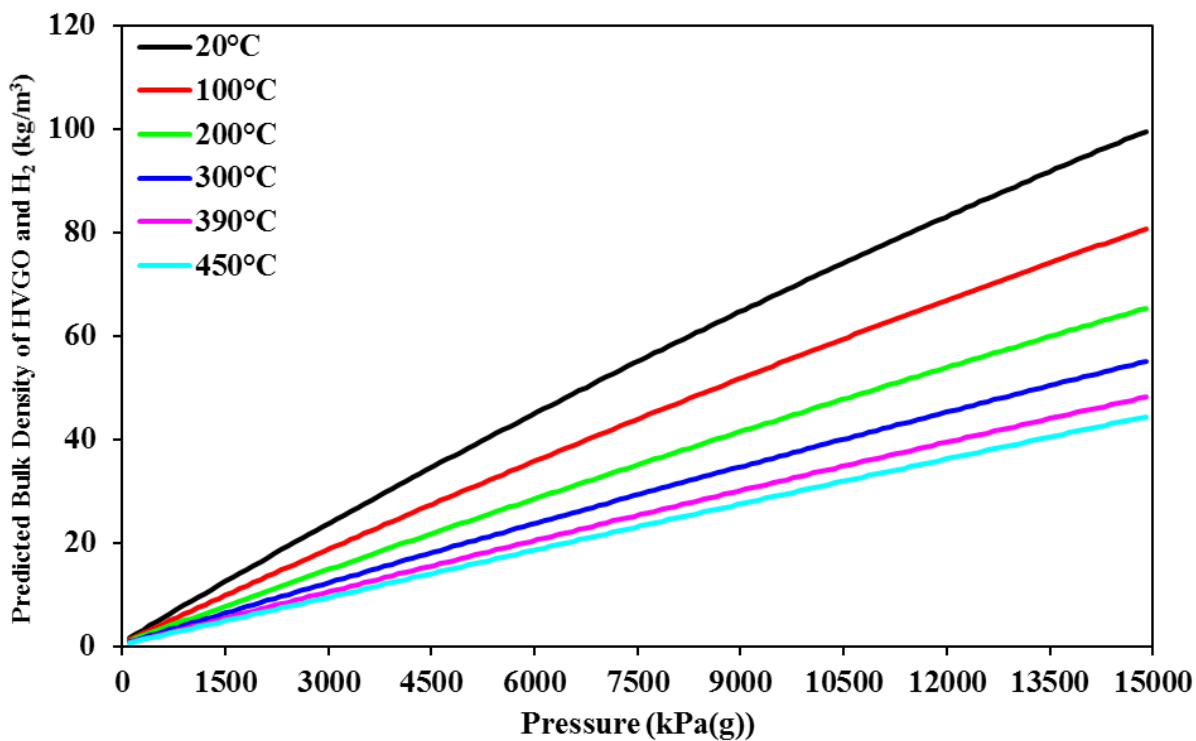
Figure B8. Predicted bulk density as a function of pressure for 0.6g of HVGO and 0.07g of hydrogen.
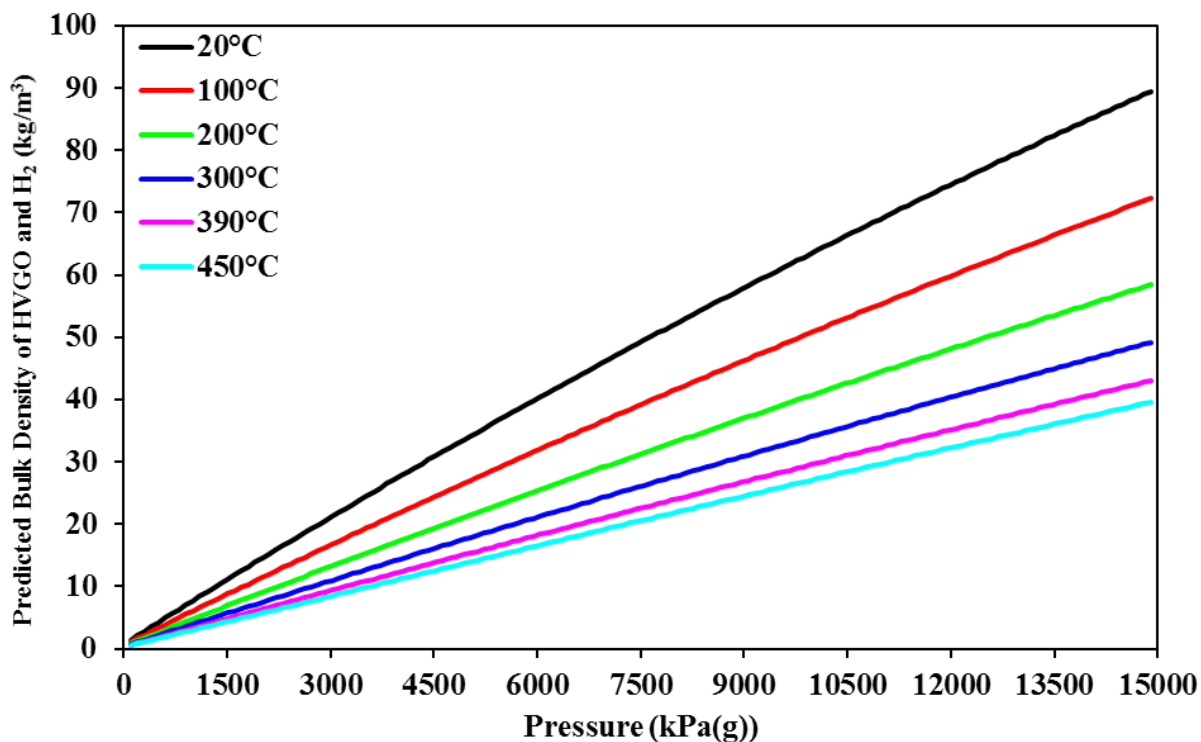
Figure B9. Predicted bulk density as a function of pressure for 0.6g of HVGO and 0.08g of hydrogen.
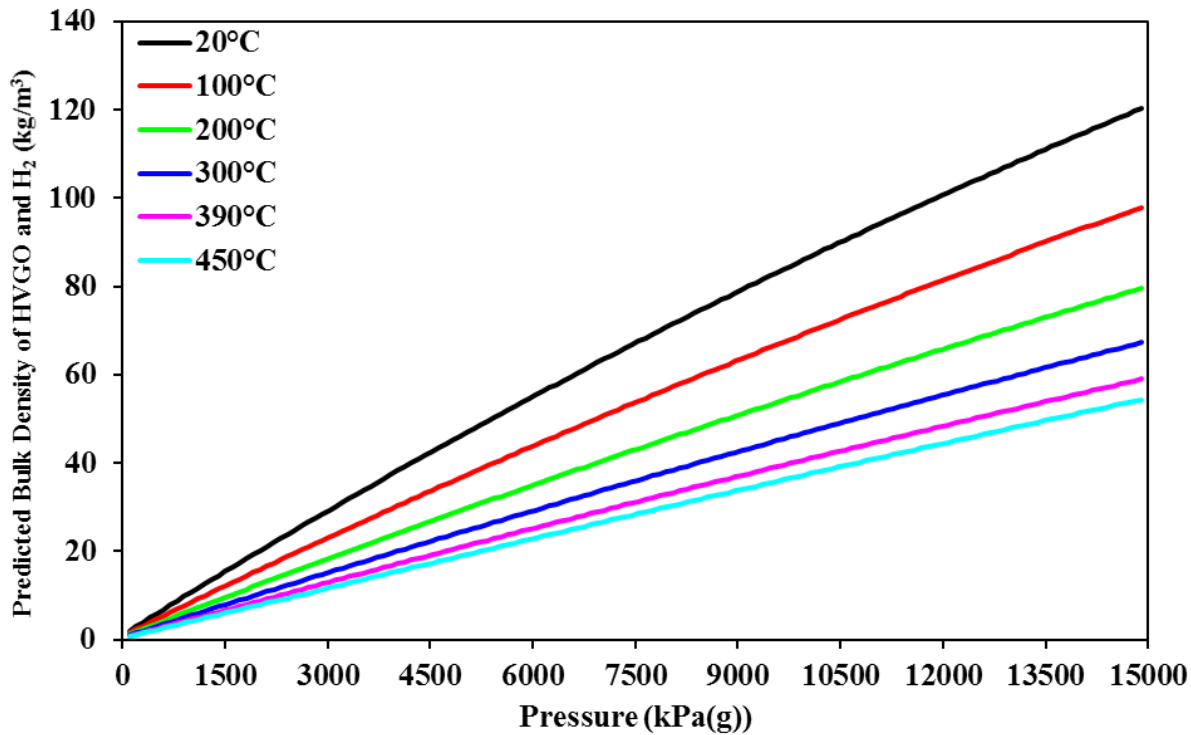
Figure B10. Predicted bulk density as a function of pressure for 0.65g of HVGO and 0.06g of hydrogen.
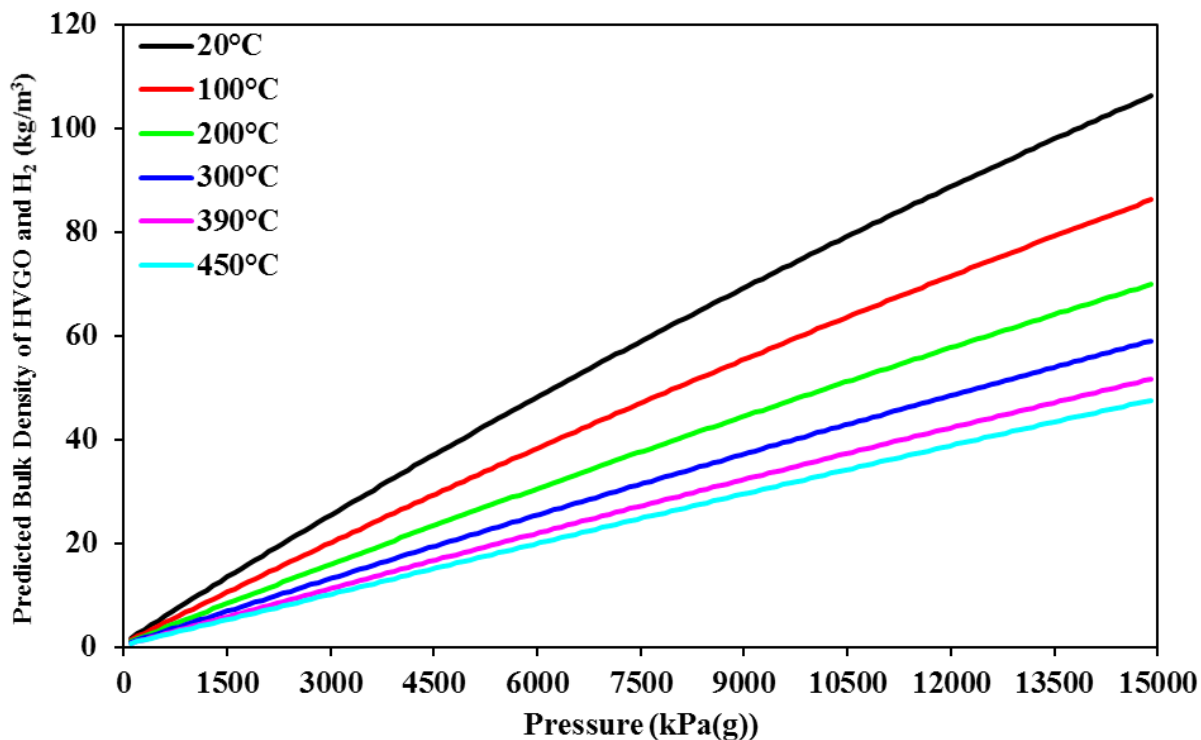
Figure B11. Predicted bulk density as a function of pressure for 0.65g of HVGO and 0.07g of hydrogen.
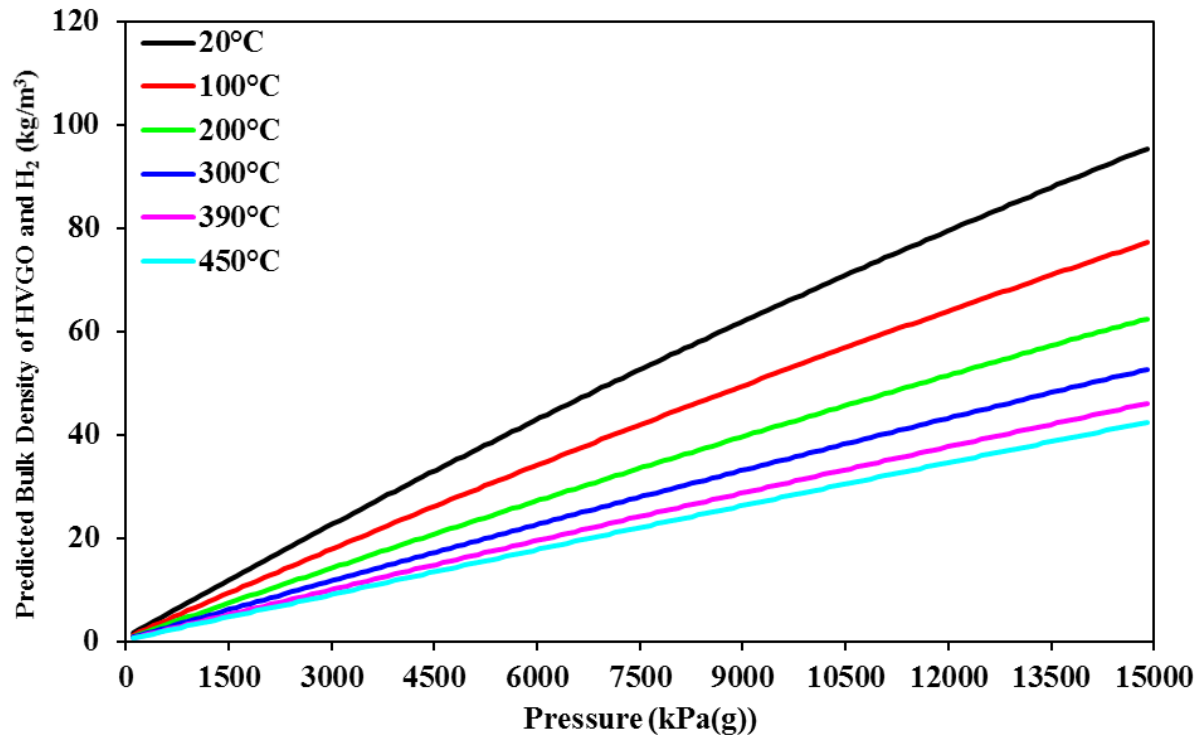
Figure B12. Predicted bulk density as a function of pressure for 0.65g of HVGO and 0.08g of hydrogen.

As seen in *Figures B7 to B12*, select temperatures (20°C, 100°C, 200°C, 300°C, 390°C, and 450°C) were plotted. If all data was included, a 3-dimensional mesh grid could visually highlight these trends:

- As the pressure increases, the bulk density increases.
- As the temperature increases, the bulk density decreases.
- Decreasing the HVGO loading from 0.65g to 0.6g, decreases the predicted bulk densities.
- Increasing the hydrogen loading from 0.06 to 0.08, decreases the predicted bulk densities.

ExcelUnitOp and signal streams were added to the VMGSim flowsheet to complete rapid hydrogen solubility predictions at different temperatures and pressures. Similar to the bulk density plots, the temperature and pressure varied from 20 to 450°C and 0 to 14000kPa(g), respectively. The hydrogen solubility in the liquid phase was reported as mol per kilogram of liquid (mol H_2 / kg liq.). Results are highlighted in *Figure B13*.
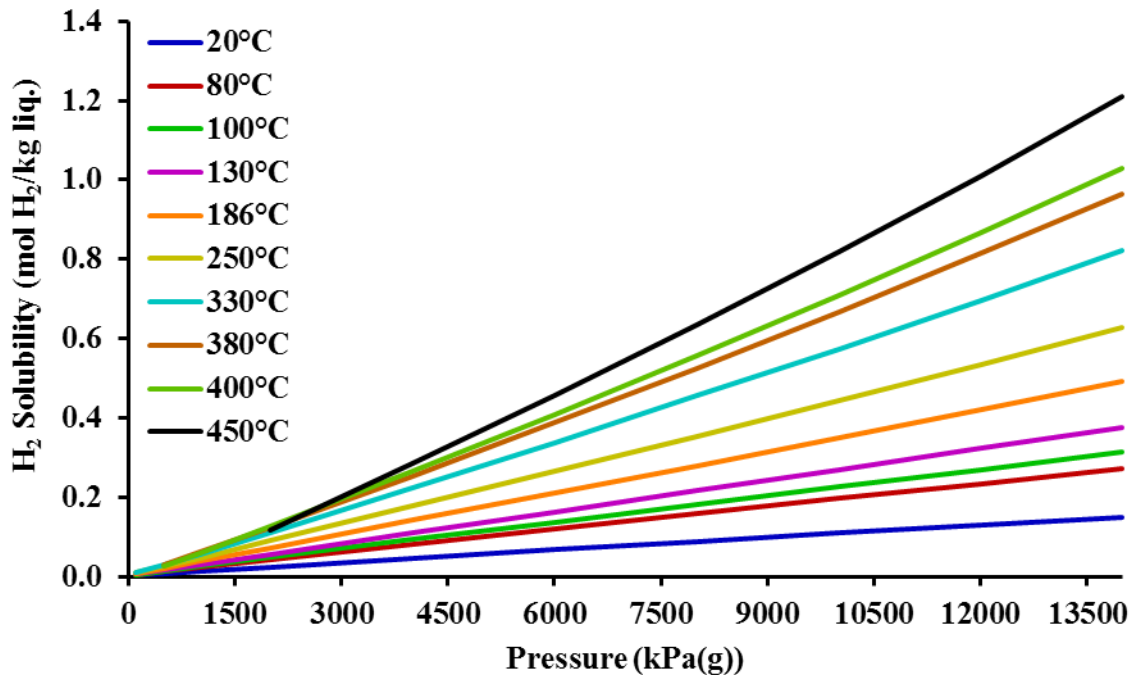
Figure B13. Predicted hydrogen solubility in HVGO liquid as a function of pressure.

From *Figure B13*, the predicted hydrogen solubility in the liquid (HVGO) increases with temperature and pressure. As the temperature increases, the start of the predicted hydrogen

solubility shifts to higher pressure as the mixture becomes a complete vapor (partial HVGO vapor pressure curve). The simulated results were compared to experimental data from Cai et al. [2]. Comparison of hydrogen solubility in HVGO as function of hydrogen partial pressure is shown in *Figure B14*. Comparison of hydrogen solubility coefficients in HVGO is presented in *Table B4*.
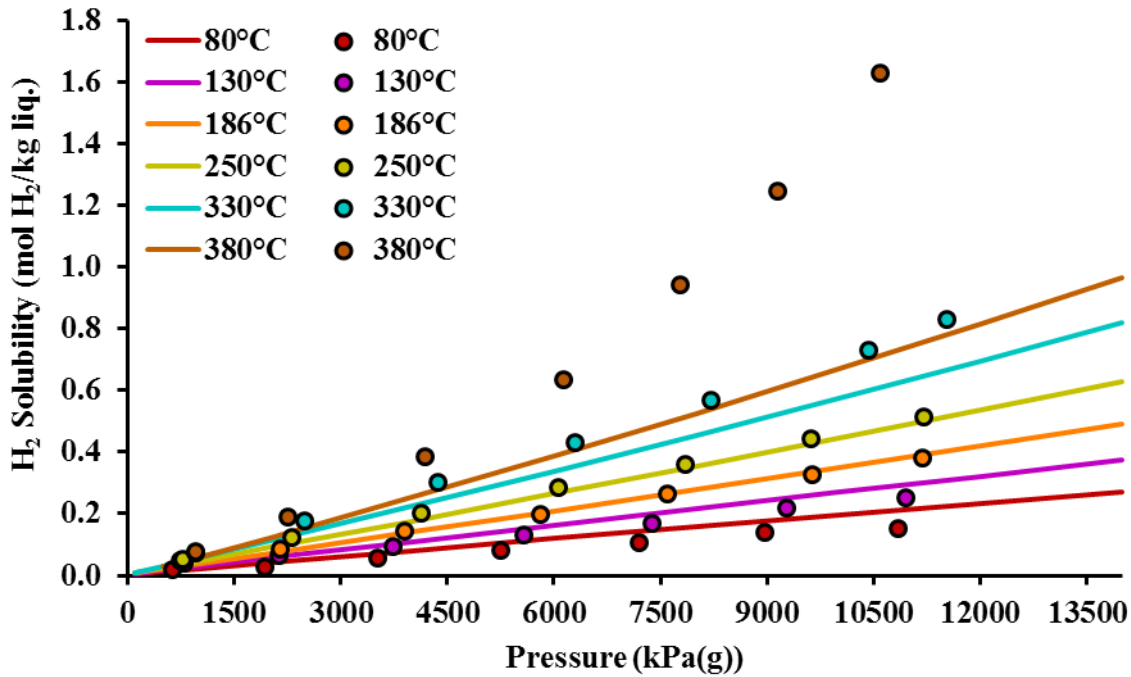
Figure B14. Comparison of predicted hydrogen solubility in HVGO to Cai et al. [1] data.

As seen in *Figure B14*, the data points represent experimental results from Cai et al. [1]. The VMGSim predictions (lines) were in good agreement to experimental results till about 250°C. Higher temperatures resulted in deviations of experimental results from the predictions at higher pressures. The authors suggested, chemical reactions (hydrotreating reactions) were the reason for the deviations above 330°C. The VMGSim predictions did not account for such chemical reactions in the vapor-liquid equilibrium calculations at such temperatures.

Table B4. Comparison of predicted hydrogen solubility coefficients in HVGO to Cai et al. [1] data.

Temperature (°C)	Cai et al. [1] (mol / kg liq. / MPa)	VMGSim Result (mol / kg liq. / MPa)	Difference (%)
80	0.014	0.019	30.3
130	0.023	0.027	16
186	0.034	0.035	2.9
250	0.047	0.044	6.6
330	<0.072	0.057	23.3

From *Table B4*, the hydrogen solubility coefficients were the slopes of the data points and lines from *Figure B14*. The percent difference between experimental and predicted averaged 15.8%. Between 130 to 250°C, the average decreased to 8.5%.

Predicted Pressures at Reaction Temperatures

All experimental loading conditions and operating conditions were simulated in VMGSim to ensure the closed system did not exceed 22.9MPa pressure at 427°C (theoretical limit of microreactor). The initial lab temperature pressures (3000kPa(g) and 4500kPa(g)), mass of liquid feeds and mass of hydrogen gas were simulated in VMGSim. The microreactor was assumed to behave as a closed system, therefore the bulk mass density was assumed to remain constant at any temperature. The maximum predicted pressure of the system was determined at maximum temperatures, 349°C for sulfidation reactions and 390°C for hydrotreating reactions.

Sulfidation Reactions

Second degree polynomials were fitted to simulated data from *Figures B2 to B4* at 21°C and 349°C.

0.3g of DMDS loading at 21°C:

$$\rho = (-4.9 \cdot 10^{-8}) \cdot (P)^2 + 0.005756 \cdot (P) + 0.5901 \tag{B2}$$

0.4g of DMDS loading at 21°C:

$$\rho = (-7.0 \cdot 10^{-8}) \cdot (P)^2 + 0.007376 \cdot (P) + 0.7865 \tag{B3}$$

0.5g of DMDS loading at 21°C:

$$\rho = (-9.3 \cdot 10^{-8}) \cdot (P)^2 + 0.008983 \cdot (P) + 0.9977 \tag{B4}$$

0.3g of DMDS loading at 349°C:

$$\rho = (-6.0 \cdot 10^{-9}) \cdot (P)^2 + 0.002429 \cdot (P) + 0.2312 \tag{B5}$$

0.4g of DMDS loading at 349°C:

$$\rho = (-7.0 \cdot 10^{-9}) \cdot (P)^2 + 0.003016 \cdot (P) + 0.2783 \tag{B6}$$

0.5g of DMDS loading at 349°C:

$$\rho = (-6.0 \cdot 10^{-9}) \cdot (P)^2 + 0.003565 \cdot (P) + 0.3177 \tag{B7}$$

Where ρ is the bulk mass density (kg/m^3) and P is the gauge pressure (kPa(g)). The coefficient of determination (R^2) for all fitted polynomials were one. The bulk mass density was solved at 3000kPa(g) (loaded hydrogen pressure for all sulfidation reactions) from equations B2 to B4:

0.3g of DMDS loading at 21°C and 3000kPa(g): 17.42kg/m^3

0.4g of DMDS loading at 21°C and 3000kPa(g): 22.28kg/m^3

0.5g of DMDS loading at 21°C and 3000kPa(g): 27.11kg/m^3

The bulk mass densities at 21°C were used to predict the gauge pressure at 349°C (constant at any temperature in a closed system). The quadratic formula was solved for equations B5 to B7 (lower numerical value for the predicted pressure):

0.3g of DMDS loading at 349°C and 17.42kg/m^3: 7203kPa(g)

0.4g of DMDS loading at 349°C and 22.28kg/m^3: 7424kPa(g)

0.5g of DMDS loading at 349°C and 27.11kg/m^3: 7624kPa(g)

The predicted maximum pressure ranged from 7200 to 7600kPa(g) for all sulfidation reactions for hydrogen and DMDS. Caution should be used for such predictions. Reactions of DMDS

decomposition and formation of hydrogen sulfide were not included in such pressure predictions. The average predicted maximum pressure for all three DMDS loadings was 7400kPa(g).

Hydrotreating Reactions

Second degree polynomials were fitted to simulated data from *Figures B7 to B12* at 20°C and 390°C.

0.6g of HVGO and 0.06g of hydrogen loading at 20°C:
$$\rho = (-9.9 \cdot 10^{-8}) \cdot (P)^2 + 0.008965 \cdot (P) + 1.0601 \tag{B8}$$
0.6g of HVGO and 0.07g of hydrogen loading at 20°C:
$$\rho = (-8.1 \cdot 10^{-8}) \cdot (P)^2 + 0.007826 \cdot (P) + 0.8941 \tag{B9}$$
0.6g of HVGO and 0.08g of hydrogen loading at 20°C:
$$\rho = (-6.8 \cdot 10^{-8}) \cdot (P)^2 + 0.006966 \cdot (P) + 0.7759 \tag{B10}$$
0.65g of HVGO and 0.06g of hydrogen loading at 20°C:
$$\rho = (-1.1 \cdot 10^{-7}) \cdot (P)^2 + 0.009625 \cdot (P) + 1.1614 \tag{B11}$$
0.65g of HVGO and 0.07g of hydrogen loading at 20°C:
$$\rho = (-9.0 \cdot 10^{-8}) \cdot (P)^2 + 0.008396 \cdot (P) + 0.9759 \tag{B12}$$
0.65g of HVGO and 0.08g of hydrogen loading at 20°C:
$$\rho = (-7.6 \cdot 10^{-8}) \cdot (P)^2 + 0.007468 \cdot (P) + 0.8442 \tag{B13}$$
0.6g of HVGO and 0.06g of hydrogen loading at 390°C:
$$\rho = (-2.1 \cdot 10^{-8}) \cdot (P)^2 + 0.003980 \cdot (P) + 0.2794 \tag{B14}$$
0.6g of HVGO and 0.07g of hydrogen loading at 390°C:
$$\rho = (-1.7 \cdot 10^{-8}) \cdot (P)^2 + 0.003465 \cdot (P) + 0.2511 \tag{B15}$$
0.6g of HVGO and 0.08g of hydrogen loading at 390°C:
$$\rho = (-1.4 \cdot 10^{-8}) \cdot (P)^2 + 0.003078 \cdot (P) + 0.2295 \tag{B16}$$
0.65g of HVGO and 0.06g of hydrogen loading at 390°C:
$$\rho = (-2.3 \cdot 10^{-8}) \cdot (P)^2 + 0.004281 \cdot (P) + 0.2958 \tag{B17}$$
0.65g of HVGO and 0.07g of hydrogen loading at 390°C:
$$\rho = (-1.9 \cdot 10^{-8}) \cdot (P)^2 + 0.003723 \cdot (P) + 0.2653 \tag{B18}$$
0.65g of HVGO and 0.08g of hydrogen loading at 390°C:
$$\rho = (-1.5 \cdot 10^{-8}) \cdot (P)^2 + 0.003303 \cdot (P) + 0.2422 \tag{B19}$$

Where ρ is the bulk mass density (kg/m^3) and P is the gauge pressure (kPa(g)). The coefficient of determination (R^2) for all fitted polynomials were one. The bulk mass density was solved at 4500kPa(g) (loaded hydrogen pressure for all hydrotreating reactions) from equations B8 to B13:

0.6g of HVGO and 0.06 of hydrogen loading at 20°C and 4500kPa(g): 39.4kg/m^3

0.6g of HVGO and 0.07 of hydrogen loading at 20°C and 4500kPa(g): 34.47kg/m^3

0.6g of HVGO and 0.08 of hydrogen loading at 20°C and 4500kPa(g): 30.75kg/m^3

0.65g of HVGO and 0.06 of hydrogen loading at 20°C and 4500kPa(g): 42.25kg/m^3

0.65g of HVGO and 0.07 of hydrogen loading at 20°C and 4500kPa(g): 36.94kg/m^3

0.65g of HVGO and 0.08 of hydrogen loading at 20°C and 4500kPa(g): 32.91kg/m^3

The bulk mass densities at 20°C were used to predict the gauge pressure at 390°C (constant at any temperature in a closed system). The quadratic formula was solved for equations B14 to B19 (lower numerical value for the predicted pressure):

0.6g of HVGO and 0.06 of hydrogen loading at 390°C and 39.4kg/m^3: 10399kPa(g)

0.6g of HVGO and 0.07 of hydrogen loading at 390°C and 34.47kg/m^3: 10407kPa(g)

0.6g of HVGO and 0.08 of hydrogen loading at 390°C and 30.75kg/m^3: 10407kPa(g)

0.65g of HVGO and 0.06 of hydrogen loading at 390°C and 42.25kg/m^3: 10378kPa(g)

0.65g of HVGO and 0.07 of hydrogen loading at 390°C and 36.94kg/m^3: 10402kPa(g)

0.65g of HVGO and 0.08 of hydrogen loading at 390°C and 32.91kg/m^3: 10380kPa(g)

The predicted maximum pressure ranged from 10378 to 10407kPa(g) for the maximum temperature (390°C) hydrotreating reactions of hydrogen and HVGO. Hydrotreating reactions were not included in such pressure predictions (hydrogen partial pressure changes with reaction time). Lower temperatures could result in lower predicted pressures. The average predicted maximum pressure for all loading ratios at 390°C was 10396kPa(g). The assumptions were for the hydrogen pressure inside the batch microreactor submerged in the fluidized alundum. The verification hydrotreating reaction (reaction 12) measured the external stainless-steel tubing temperature around the pressure gauge at circa 80-100°C (positioned well above the 390°C fluidized alundum). The predicted pressure assuming 0.6-0.65g HVGO and 0.08g hydrogen (reaction 12 loading) was circa 5500-5800kPa(g). The measured pressure reached a maximum of 8000kPa(g) when microreactor was submerged. At 8000kPa(g), the vapor inside the tubing was

hotter at 235-240°C (vapor cooled in temperature up in the tube section near the pressure gauge) from *Figures B9* & *B12*.

Appendix B References

[1] H. Y. Cai, J. M. Shaw and K. H. Chung, "Hydrogen solubility measurements in heavy oil and bitumen cuts," *Fuel,* vol. 80, *(8),* pp. 1055-1063, 2001.

[2] M. R. Gray, *Upgrading Oilsands Bitumen and Heavy Oil.* Edmonton, Alberta: Pica Pica Press, An Imprint of The University of Alberta Press, 2015.

Appendix C

Agitation, temperature and fluidization profiles for all experimental reactions are found in *Appendix C (Figures C1 to C43)*. All experimental reactions, feed, catalyst size, pressure, temperature, agitation, and reaction times are presented in *Table C1* (*Table 3.4*).

Table C1. Experimental reactions, feed, catalyst size, pressure, temperature, agitation, and reaction times.

#	Reaction	Feed	Catalyst Size	Pressure (kPa(g))	Temperature (°C)	Agitation (RPM)	Time (h)
1	No Reaction	HVGO	-	-	-	-	-
2	Hydrotreating	HVGO^	-	4500	390	360**	2
3	Hydrotreating	HVGO^	-	4500	390	708	2
4	Hydrotreating	HVGO^	-	4500	390	862	2
5	Hydrotreating	HVGO^	-	4500	390	850	2
6	Hydrotreating	HVGO^	-	4500	390	873	2
7	Hydrotreating	HVGO^	Pellets	4500	390	848	2
8	Hydrotreating	HVGO^	Pellets	4500	390	868	2
9	Hydrotreating	HVGO^	Pellets	4500	390	878	2
10	Hydrotreating	HVGO	Pellets	4500	390	360**	2
11	Hydrotreating	HVGO	Pellets	4500	390	360**	2
12	Hydrotreating	HVGO	Pellets	4500	390	360*	2.25
13	Hydrotreating	HVGO	Pellets	4500	390	884	2
14	Hydrotreating	HVGO	Pellets	4500	390	882	2
15	Hydrotreating	HVGO	Pellets	4500	390	866	2
16	Sulfiding Catalyst	DMDS	Dried Pellets	3000	20 - 360	360**	4.5
17	Sulfiding Catalyst	DMDS	Dried Pellets	3000	20 - 360	360**	4.2
18	Sulfiding Catalyst	DMDS	Dried < 45μm	3300	20 - 360	880	4.2
19	Sulfiding Catalyst	DMDS	Dried < 45μm	3000	20 - 360	863	4.2
20	Hydrotreating	HVGO	Sulfided Pellet	4500	390	878	2
21	Hydrotreating	HVGO	Sulfided Pellet	4500	390	886	2
22	Hydrotreating	HVGO	Sulfided Pellet	4500	390	892	2
23	Hydrotreating	HVGO	Sulfided Pellet	4500	390	896	1.5
24	Hydrotreating	HVGO	Sulfided Pellet	4500	390	889	1
25	Hydrotreating	HVGO	Sulfided Pellet	4500	390	875	1
26	Hydrotreating	HVGO	Sulfided Pellet	4500	370	888	1
27	Hydrotreating	HVGO	Sulfided Pellet	4500	350	900	1
28	Hydrotreating	HVGO	Sulfided Pellet	4500	330	891	1
29	Hydrotreating	HVGO	Sulfided Pellet	4500	310	893	1
30	Hydrotreating	HVGO	Sulfided Pellet	4500	290	898	1
31	Hydrotreating	HVGO	Sulfided Pellet	4500	390	867	0.5
32	Hydrotreating	HVGO	Sulfided Pellet	4500	390	859	0.5
33	Hydrotreating	HVGO	Sulfided Pellet	4500	390	850	0.25
34	Hydrotreating	HVGO	Sulfided < 45μm	4500	390	888	2
35	Hydrotreating	HVGO	Sulfided < 45μm	4500	390	874	2
36	Hydrotreating	HVGO	Sulfided < 45μm	4500	390	879	1
37	Hydrotreating	HVGO	Sulfided < 45μm	4500	390	870	1
38	Hydrotreating	HVGO	Sulfided < 45μm	4500	390	870	0.5
39	Hydrotreating	HVGO	Sulfided < 45μm	4500	390	859	0.5
40	Hydrotreating	HVGO	Sulfided < 45μm	4500	370	894	0.5
41	Hydrotreating	HVGO	Sulfided < 45μm	4500	390	880	0.25
42	Hydrotreating	HVGO	Sulfided < 45μm	4500	390	890	0.25
43	Hydrotreating	HVGO	Sulfided < 45μm	4500	370	900	0.25
44	Hydrotreating	HVGO	Sulfided < 45μm	4500	350	900	0.25

*Modified microreactor design I.
**Modified microreactor design II.
^No liquid product filtration.

Figure C1. Agitation, temperature, and fluidization air flow rate profiles for hydrotreating reaction 2.
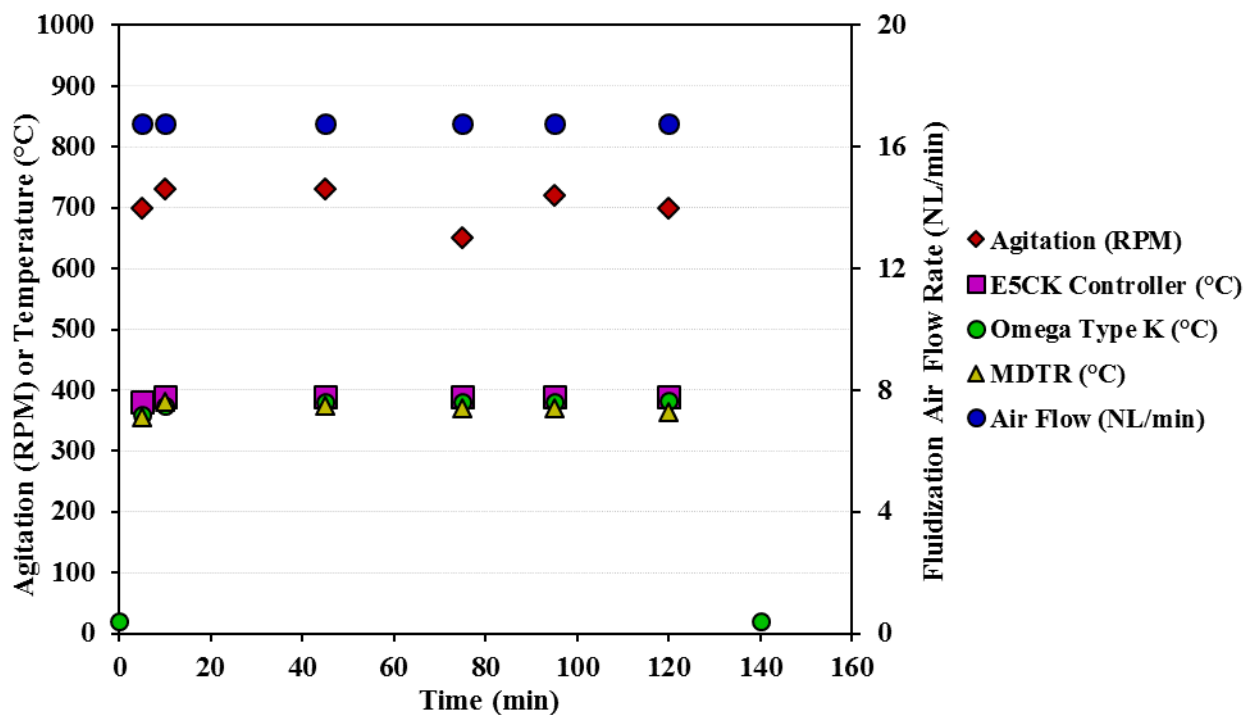
Figure C2. Agitation, temperature, and fluidization air flow rate profiles for hydrotreating reaction 3.

310
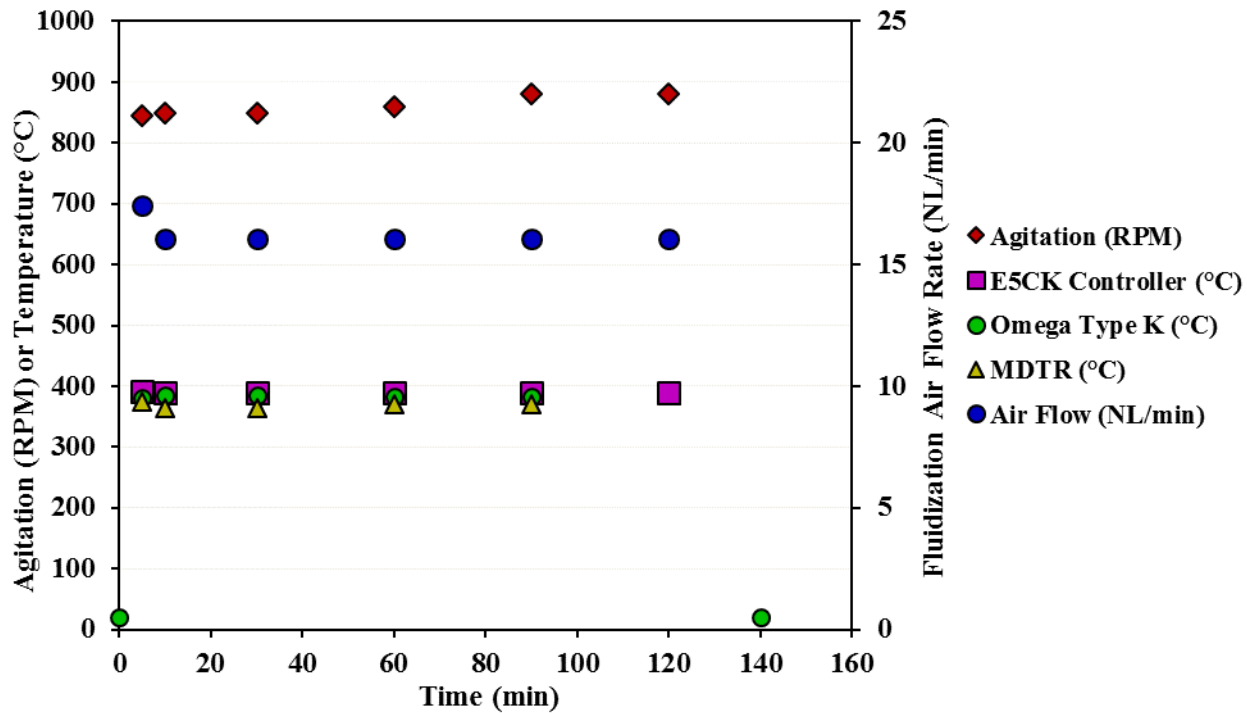
Figure C3. Agitation, temperature, and fluidization air flow rate profiles for hydrotreating reaction 4.
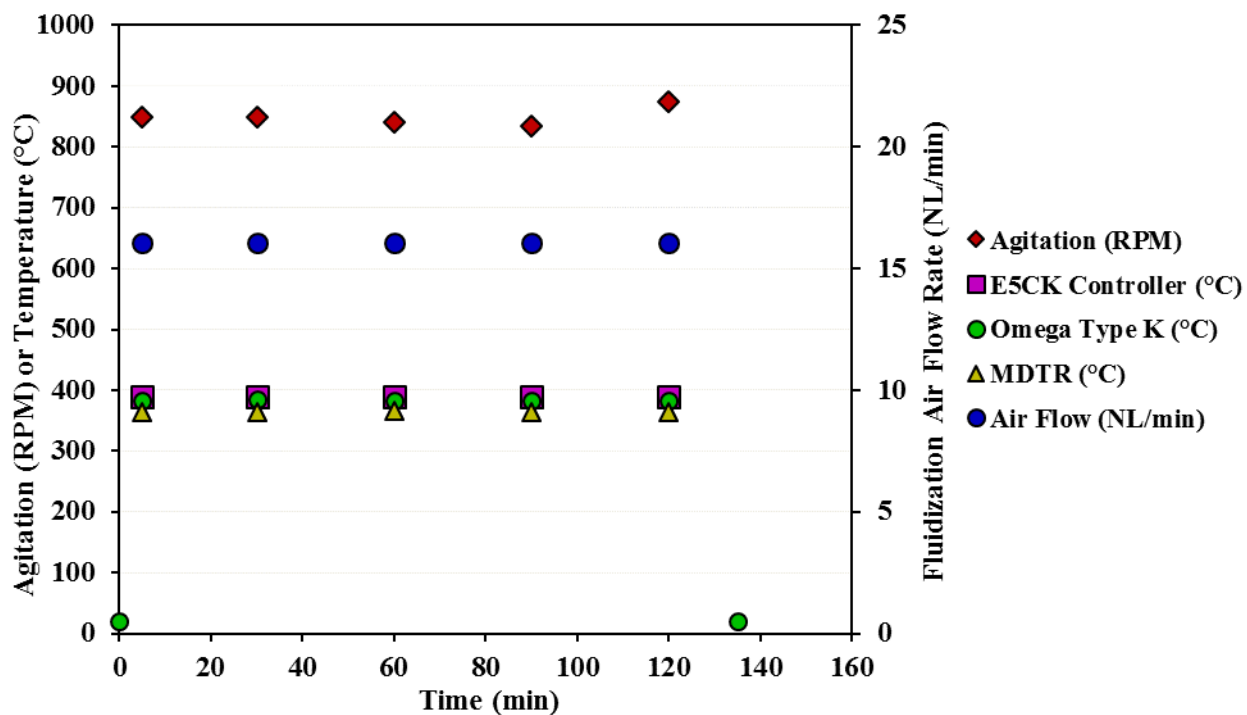
Figure C4. Agitation, temperature, and fluidization air flow rate profiles for hydrotreating reaction 5.

311
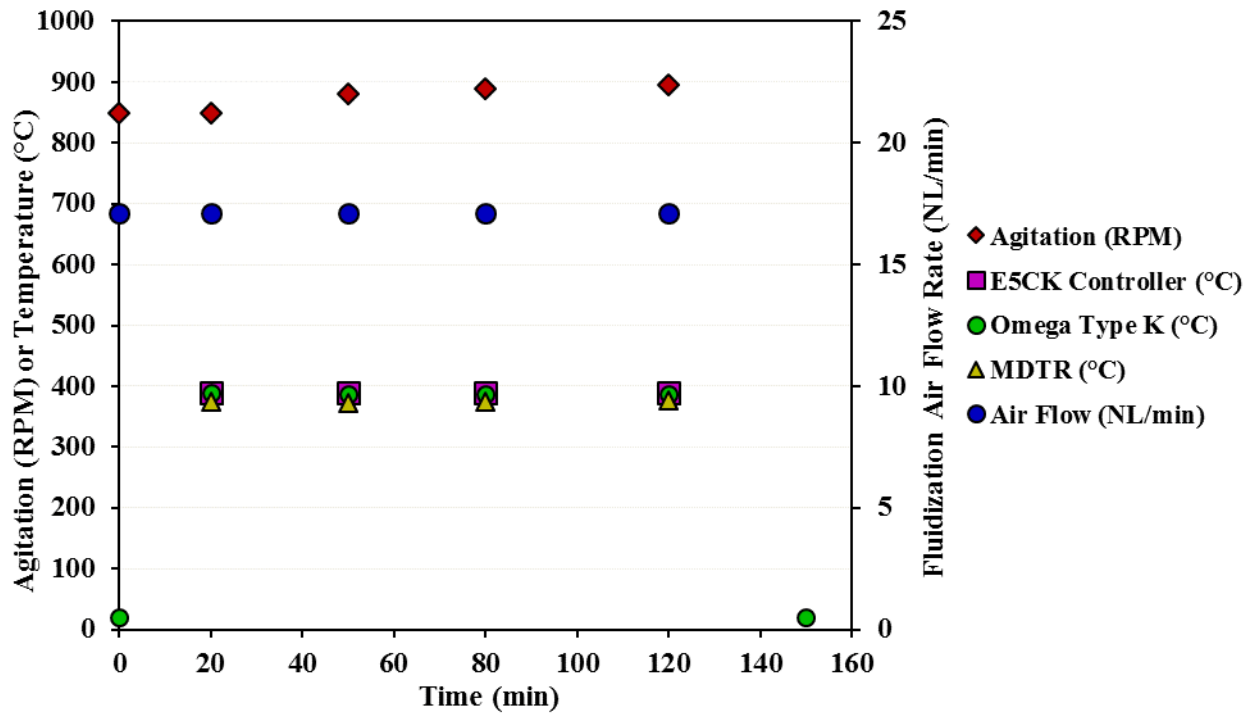
Figure C5. Agitation, temperature, and fluidization air flow rate profiles for hydrotreating reaction 6.
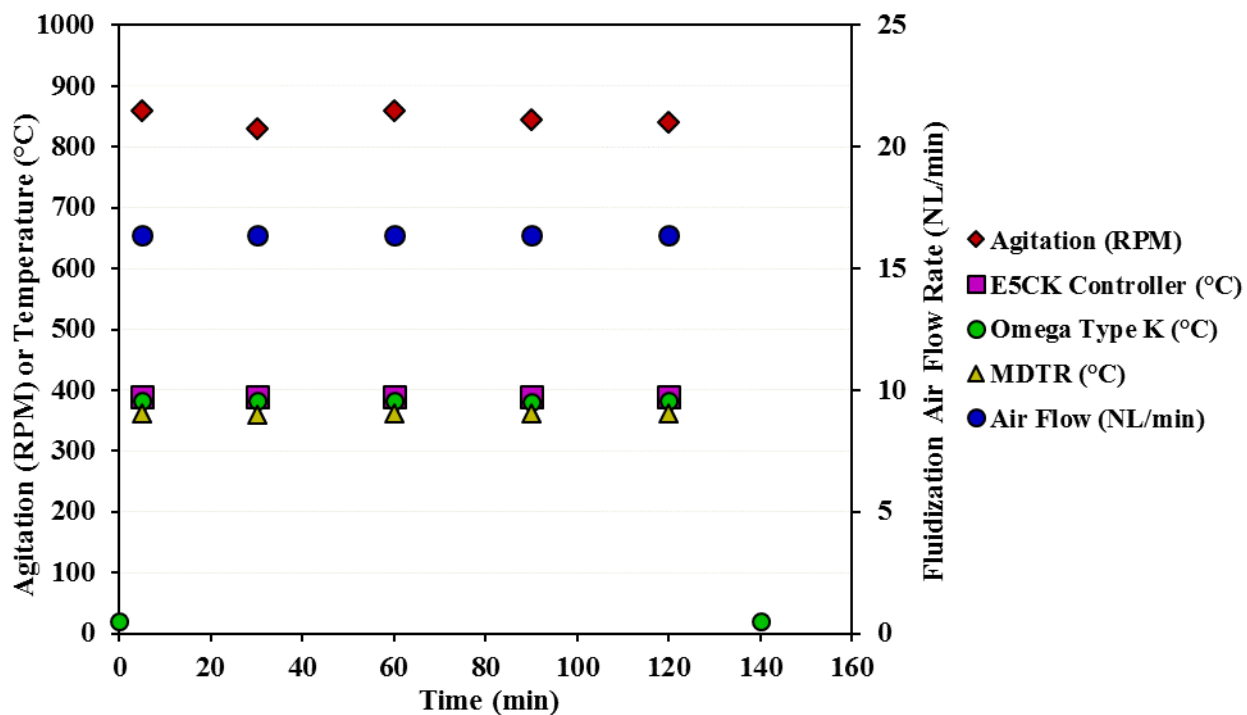
Figure C6. Agitation, temperature, and fluidization air flow rate profiles for hydrotreating reaction 7.

312
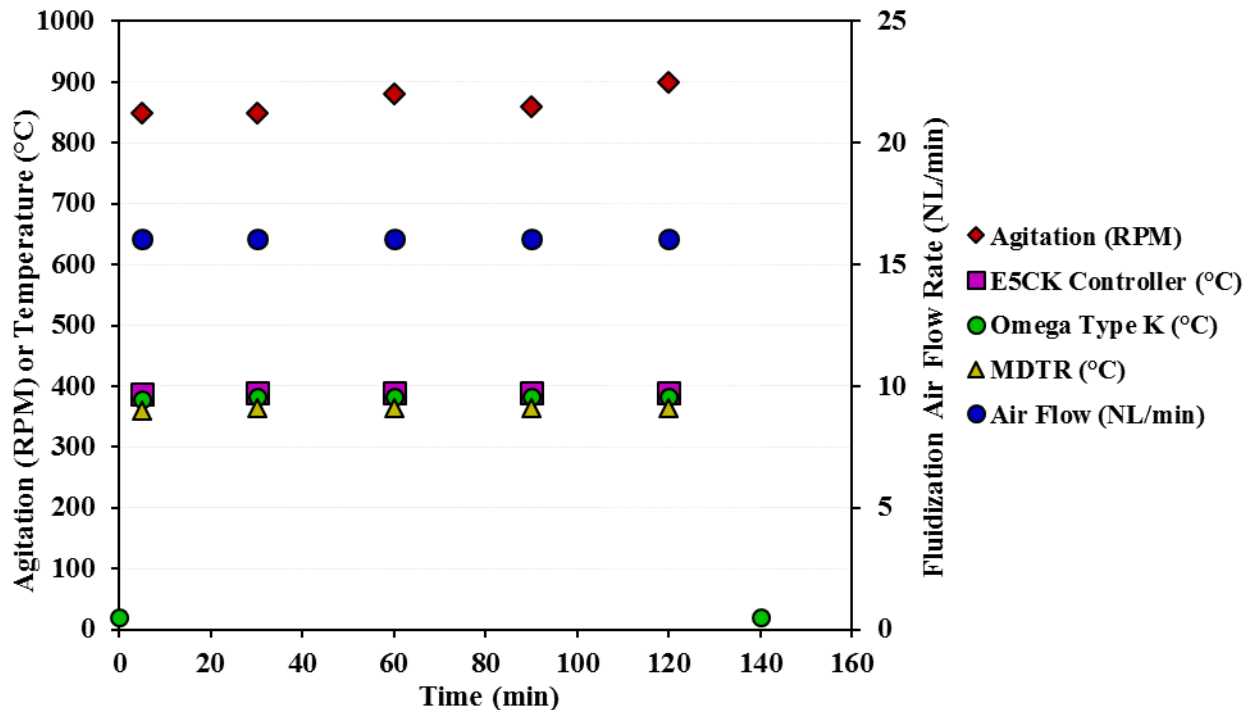
Figure C7. Agitation, temperature, and fluidization air flow rate profiles for hydrotreating reaction 8.
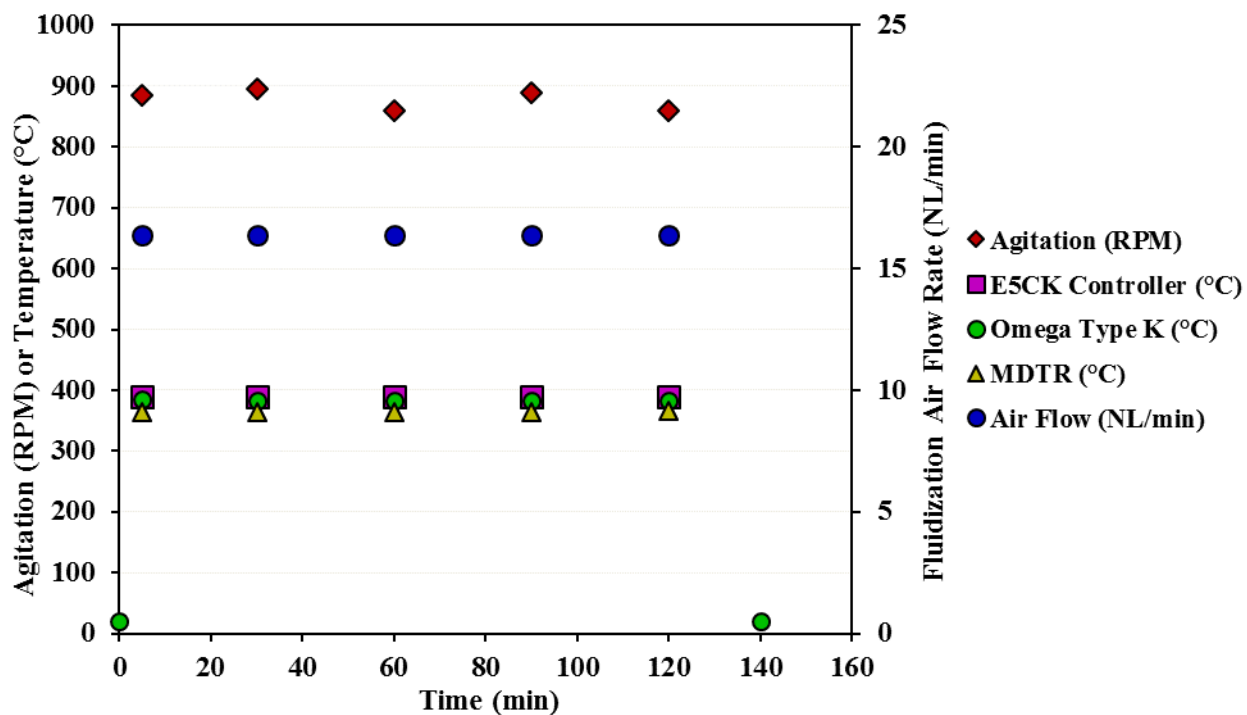
Figure C8. Agitation, temperature, and fluidization air flow rate profiles for hydrotreating reaction 9.
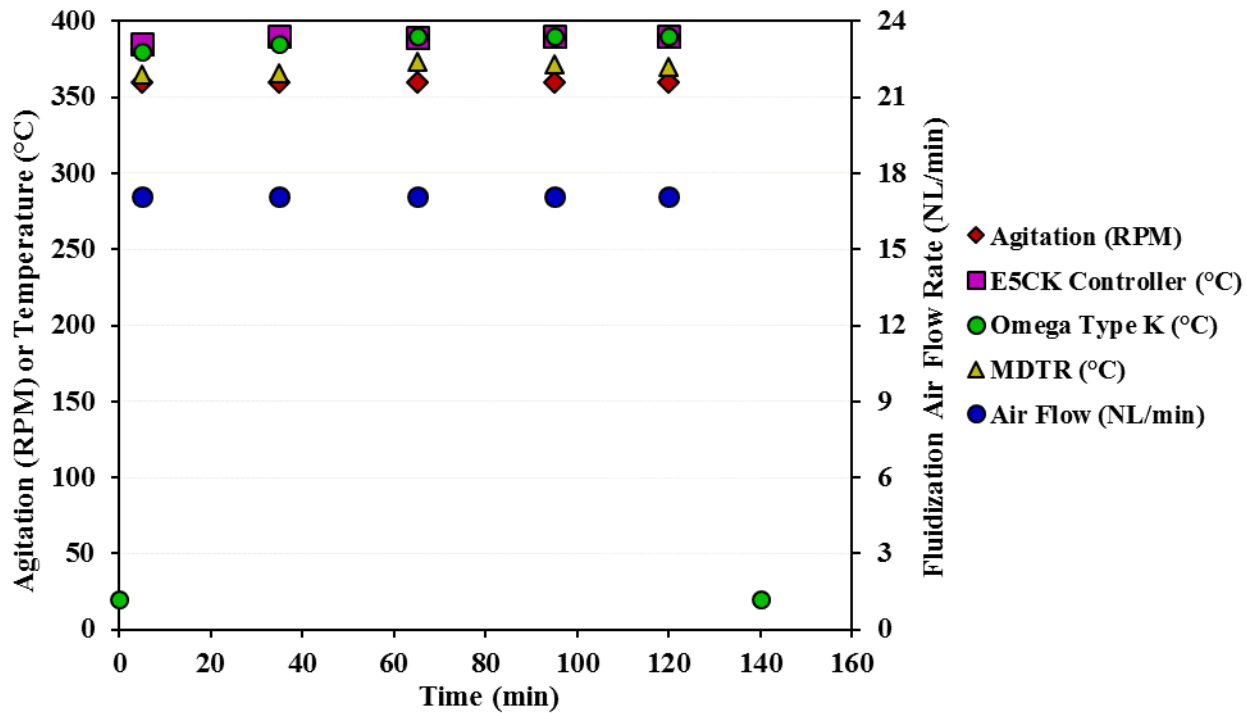
Figure C9. Agitation, temperature, and fluidization air flow rate profiles for hydrotreating reaction 10.
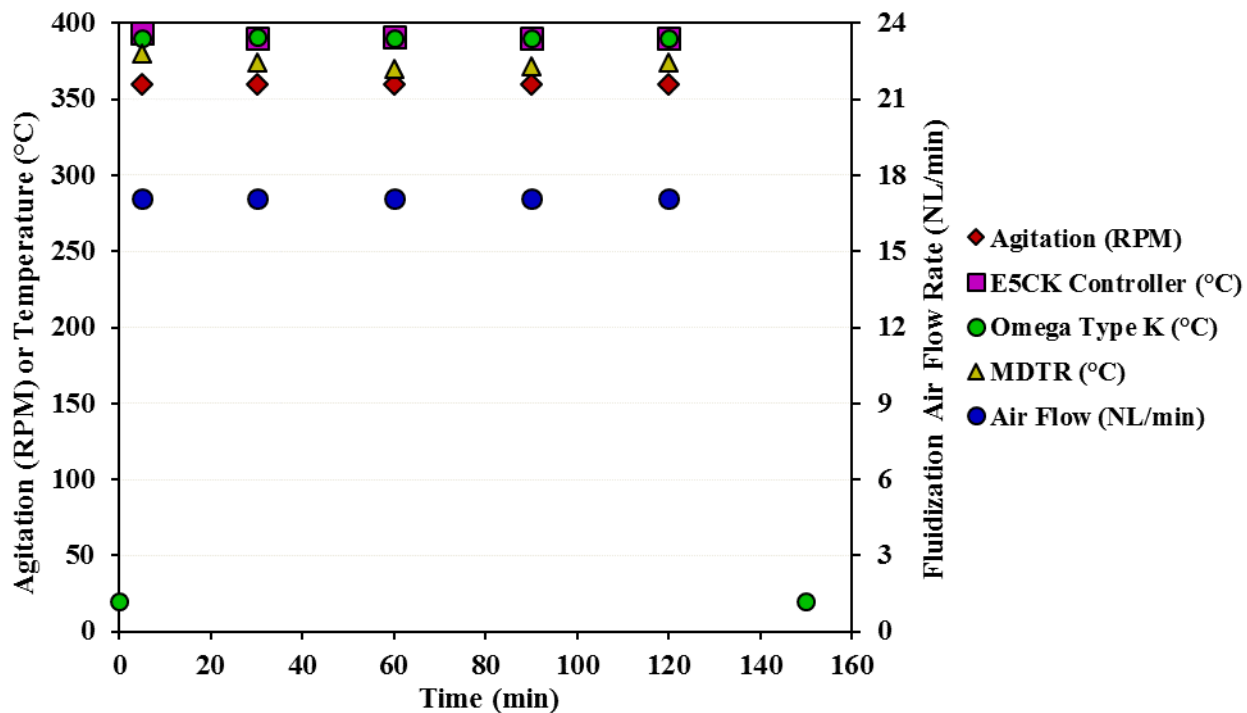
Figure C10. Agitation, temperature, and fluidization air flow rate profiles for hydrotreating reaction 11.

314
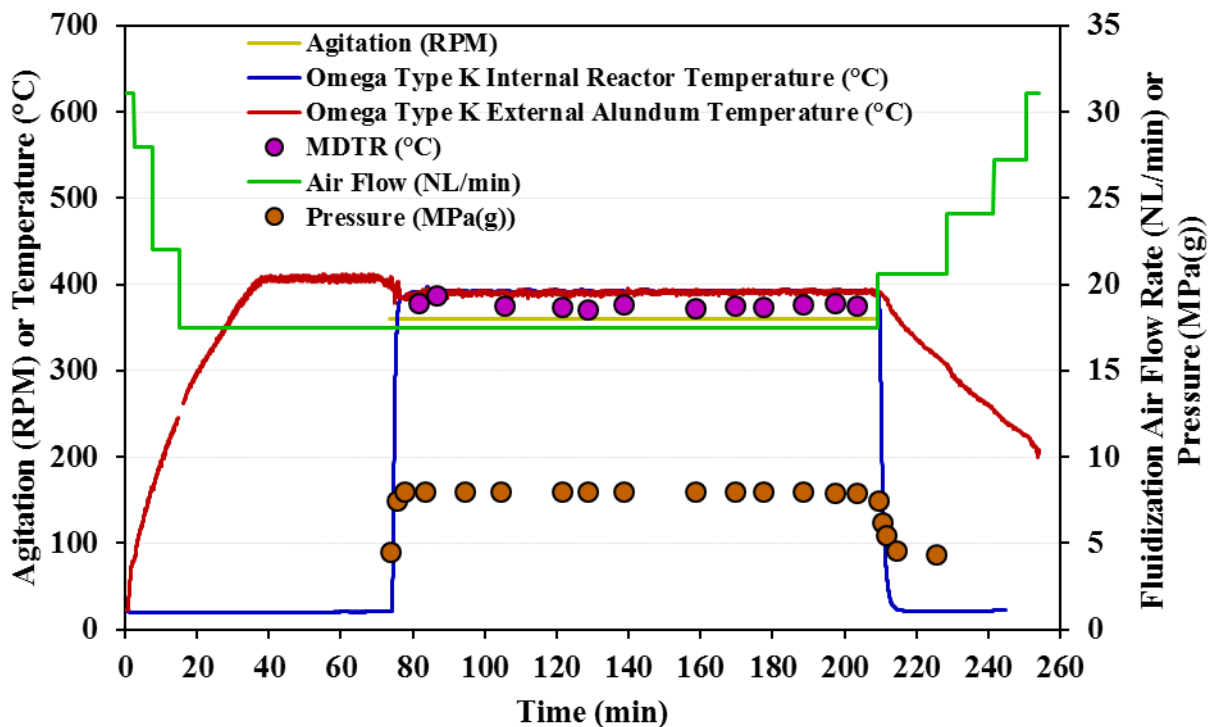
Figure C11. Agitation, internal reactor temperature, external alundum temperature, fluidization air flow rate, and internal gauge pressure profiles for the verification hydrotreating reaction 12.
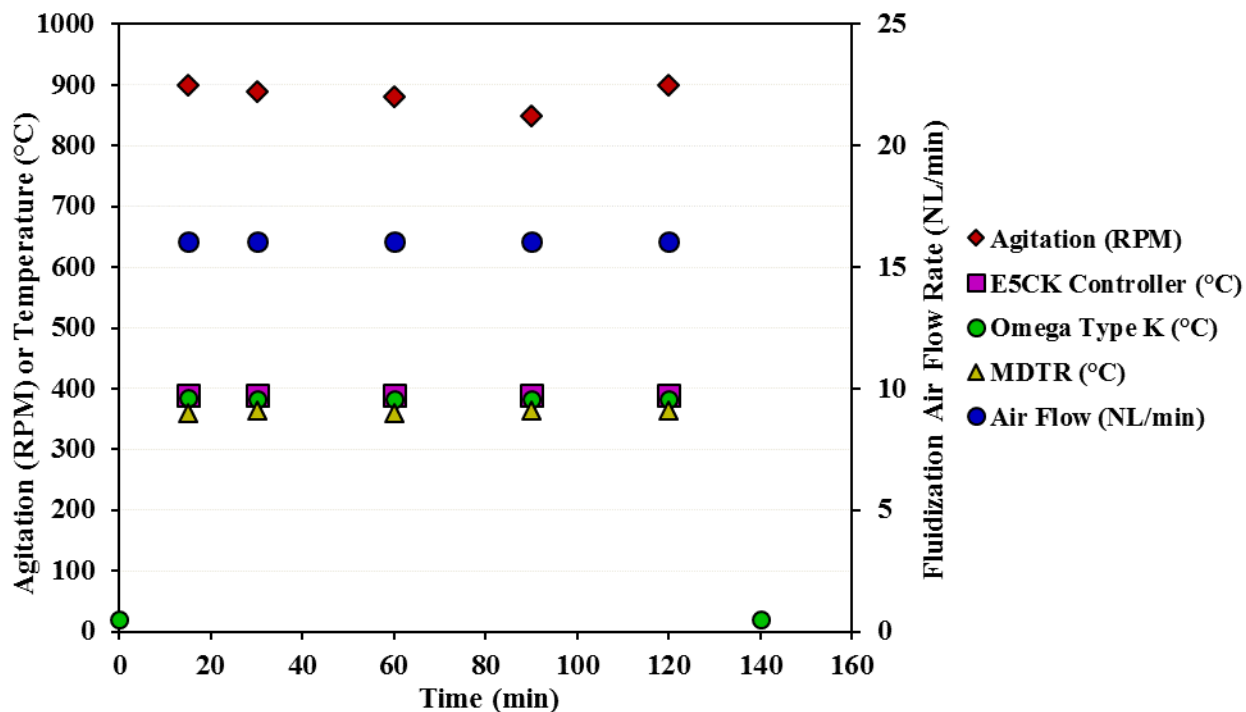
Figure C12. Agitation, temperature, and fluidization air flow rate profiles for hydrotreating reaction 13.
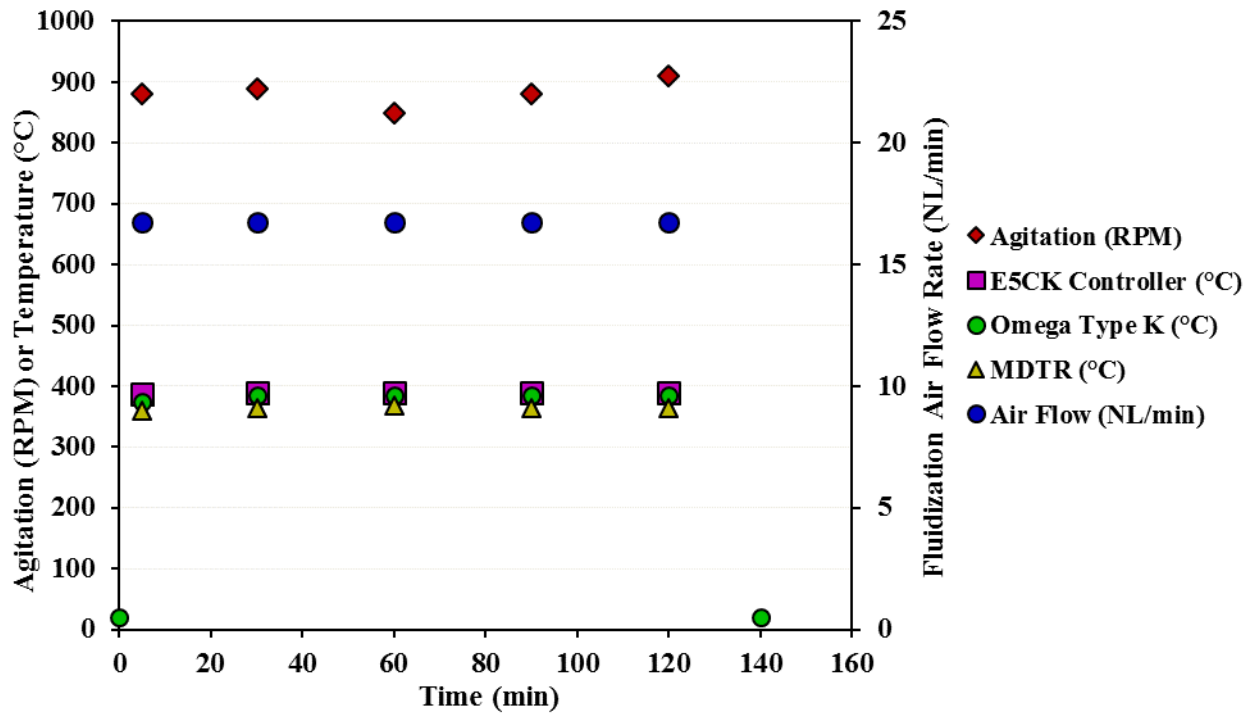
Figure C13. Agitation, temperature, and fluidization air flow rate profiles for hydrotreating reaction 14.
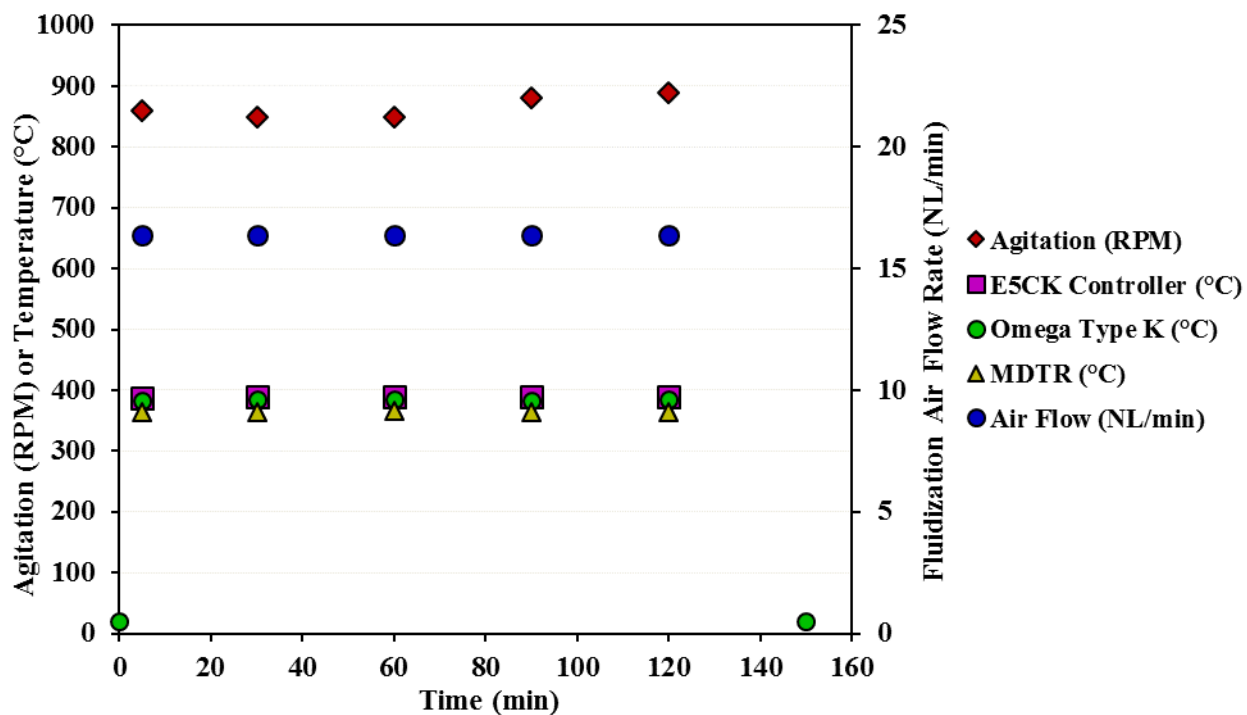
Figure C14. Agitation, temperature, and fluidization air flow rate profiles for hydrotreating reaction 15.
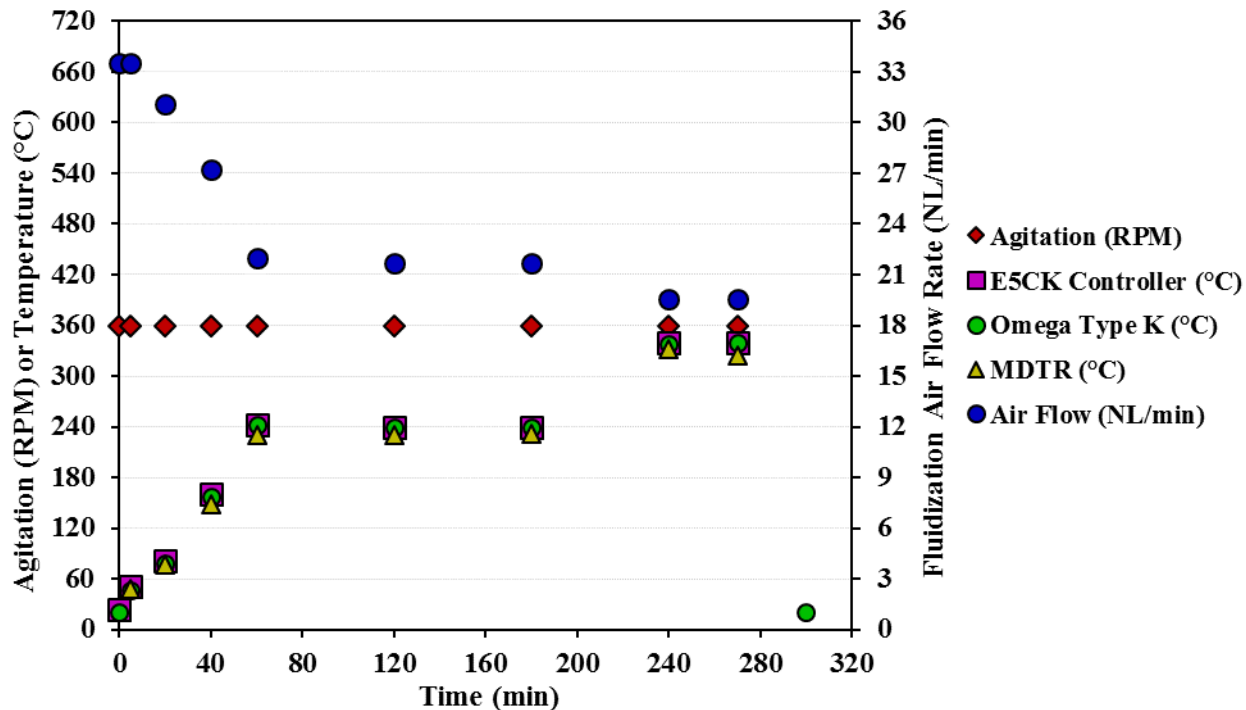
Figure C15. Agitation, temperature, and fluidization air flow rate profiles for the sulfidation reaction of catalyst pellets (reaction 16).
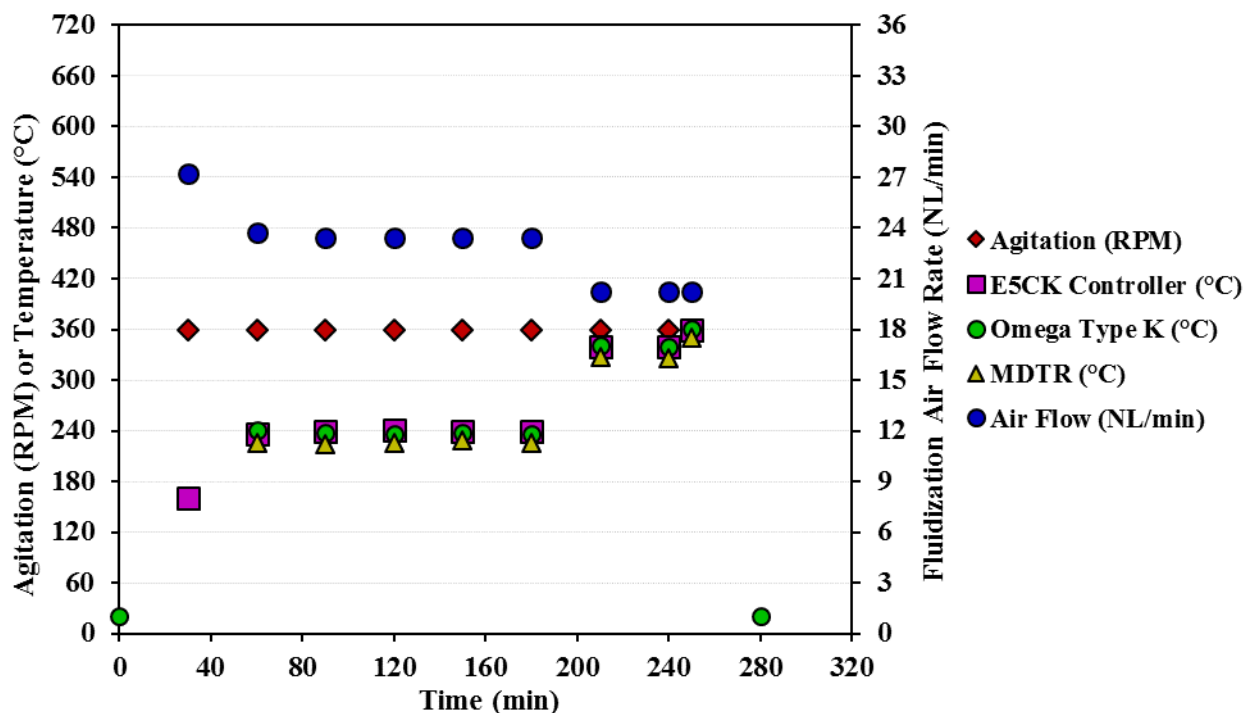
Figure C16. Agitation, temperature, and fluidization air flow rate profiles for the sulfidation reaction of catalyst pellets (reaction 17).
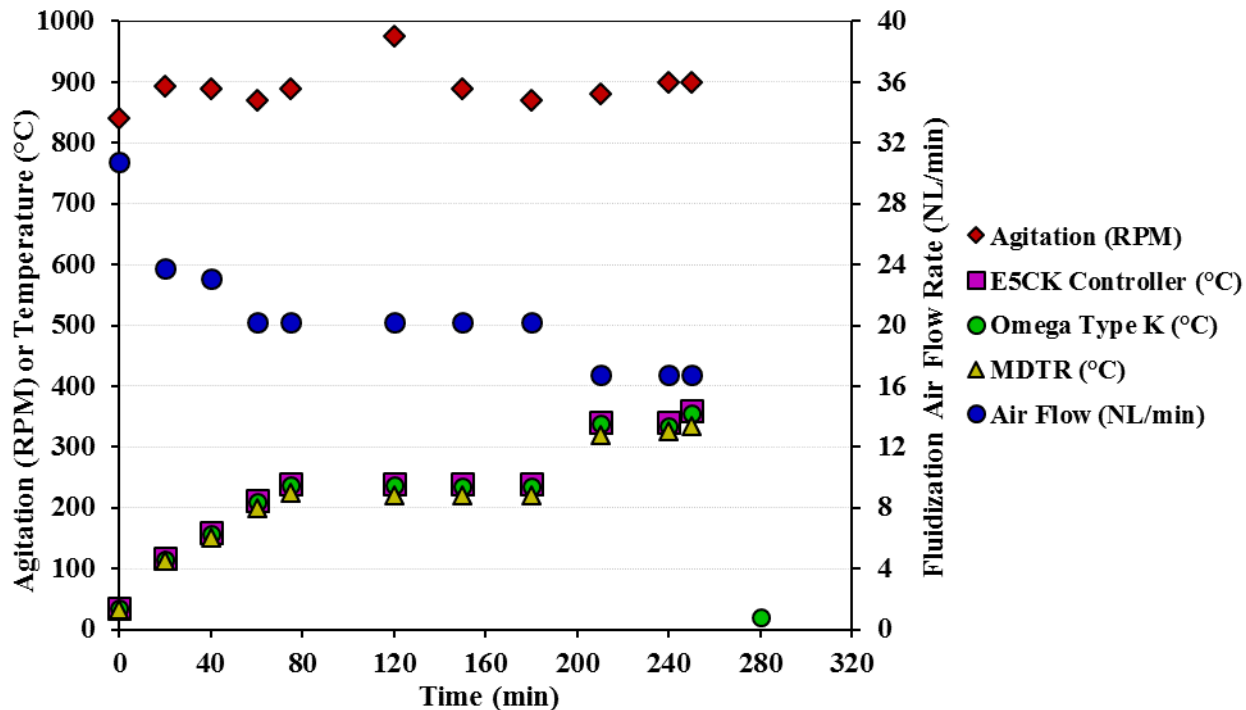
Figure C17. Agitation, temperature, and fluidization air flow rate profiles for the sulfidation reaction of catalyst particles (reaction 18).
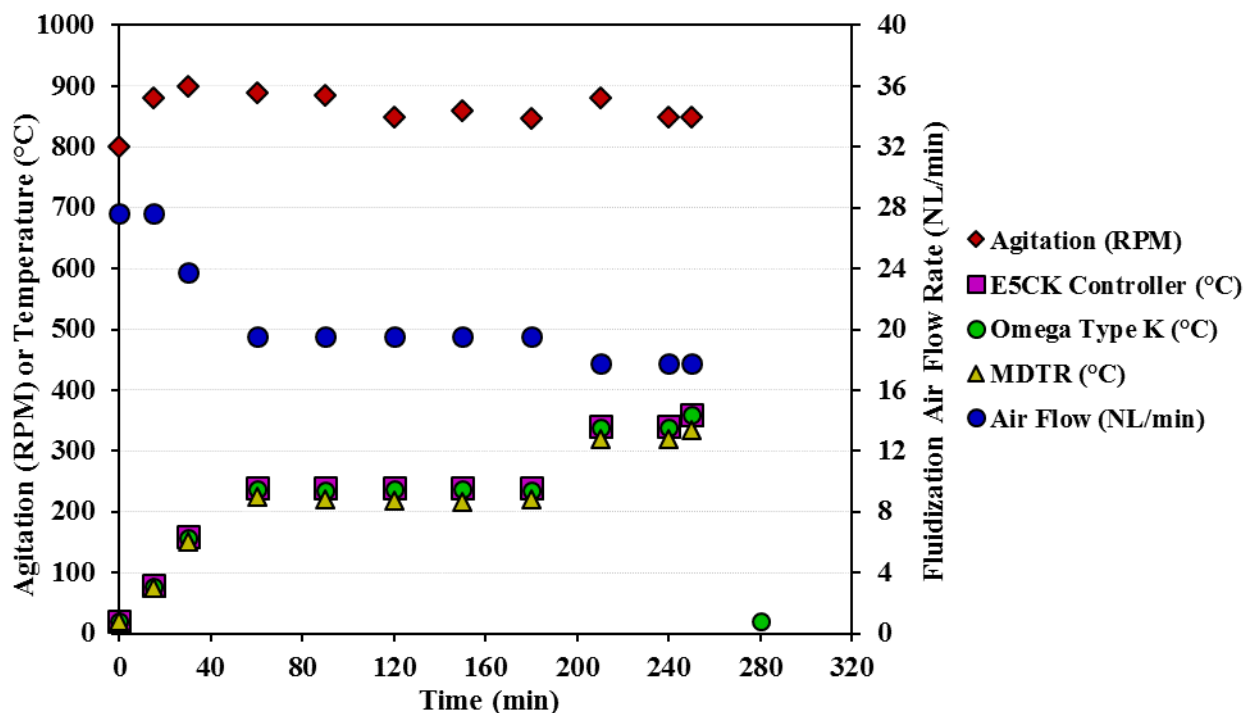
Figure C18. Agitation, temperature, and fluidization air flow rate profiles for the sulfidation reaction of catalyst particles (reaction 19).
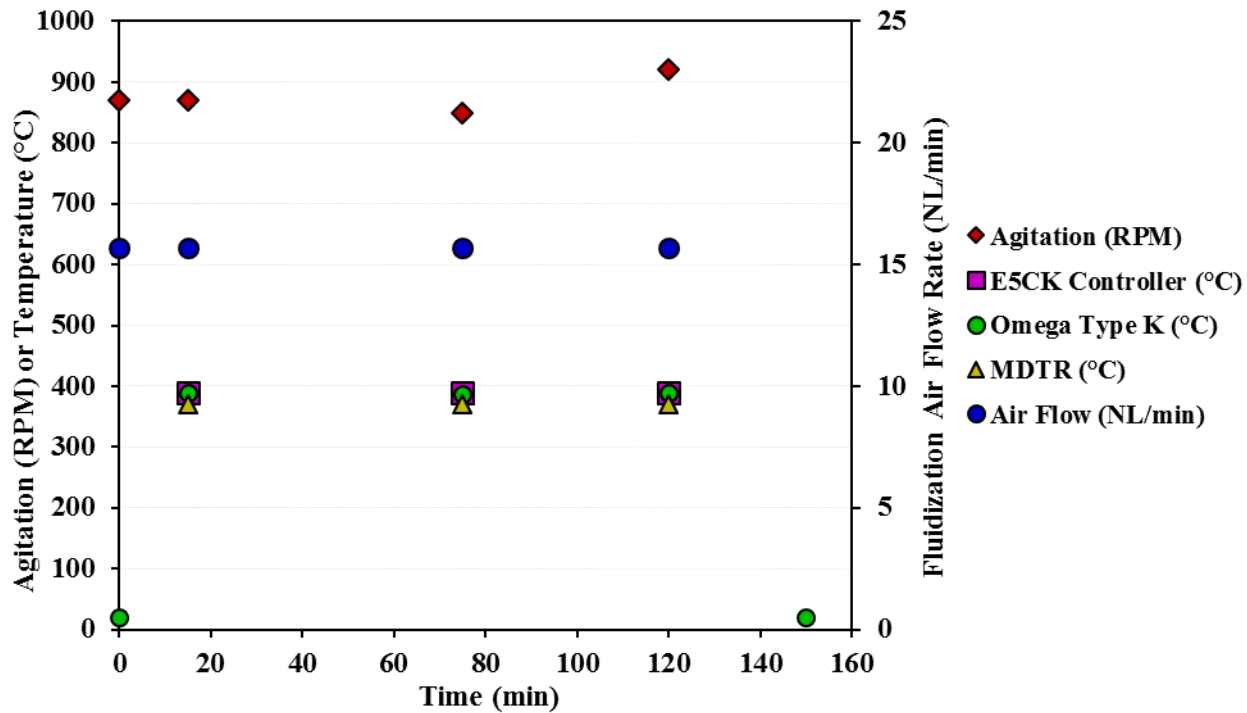
Figure C19. Agitation, temperature, and fluidization air flow rate profiles for hydrotreating reaction 20.
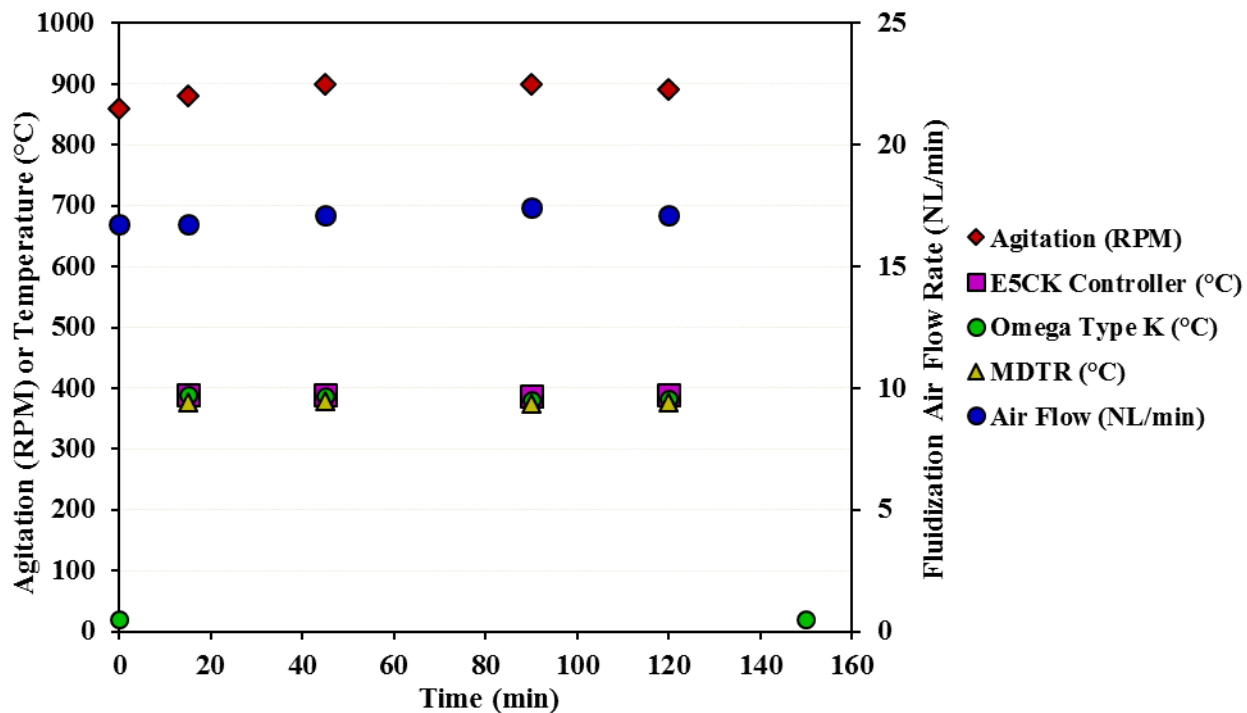
Figure C20. Agitation, temperature, and fluidization air flow rate profiles for hydrotreating reaction 21.
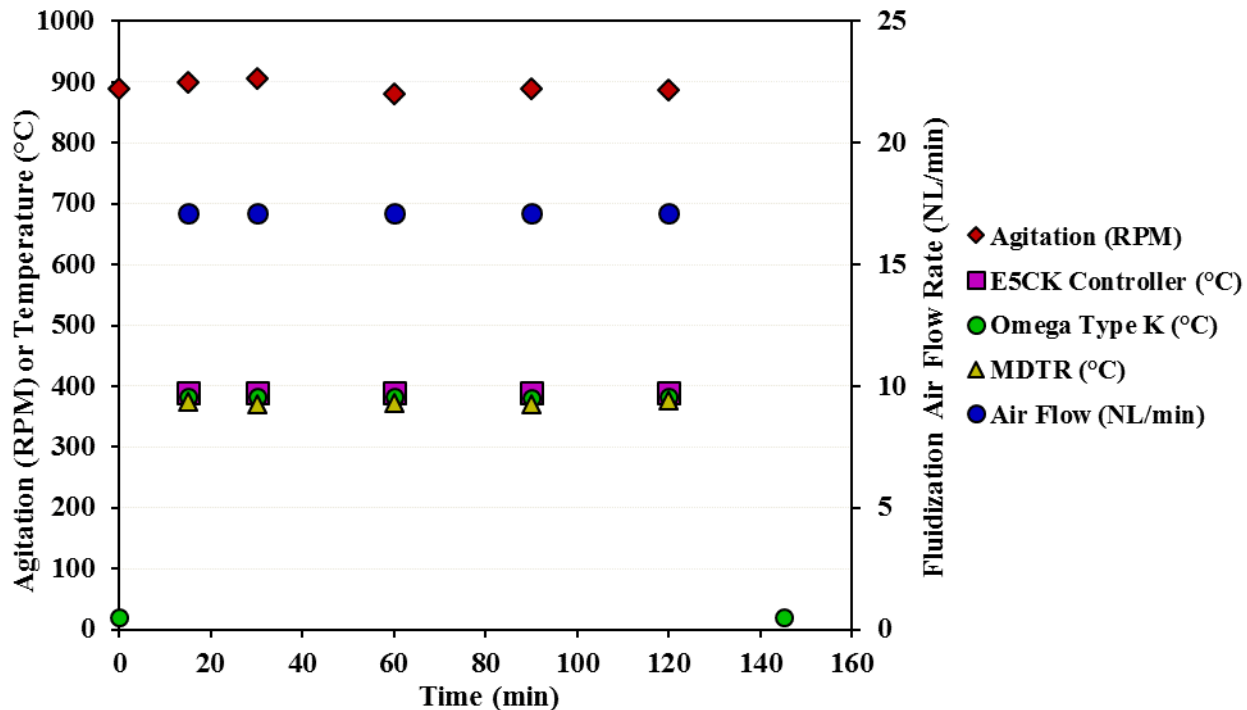
Figure C21. Agitation, temperature, and fluidization air flow rate profiles for hydrotreating reaction 22.
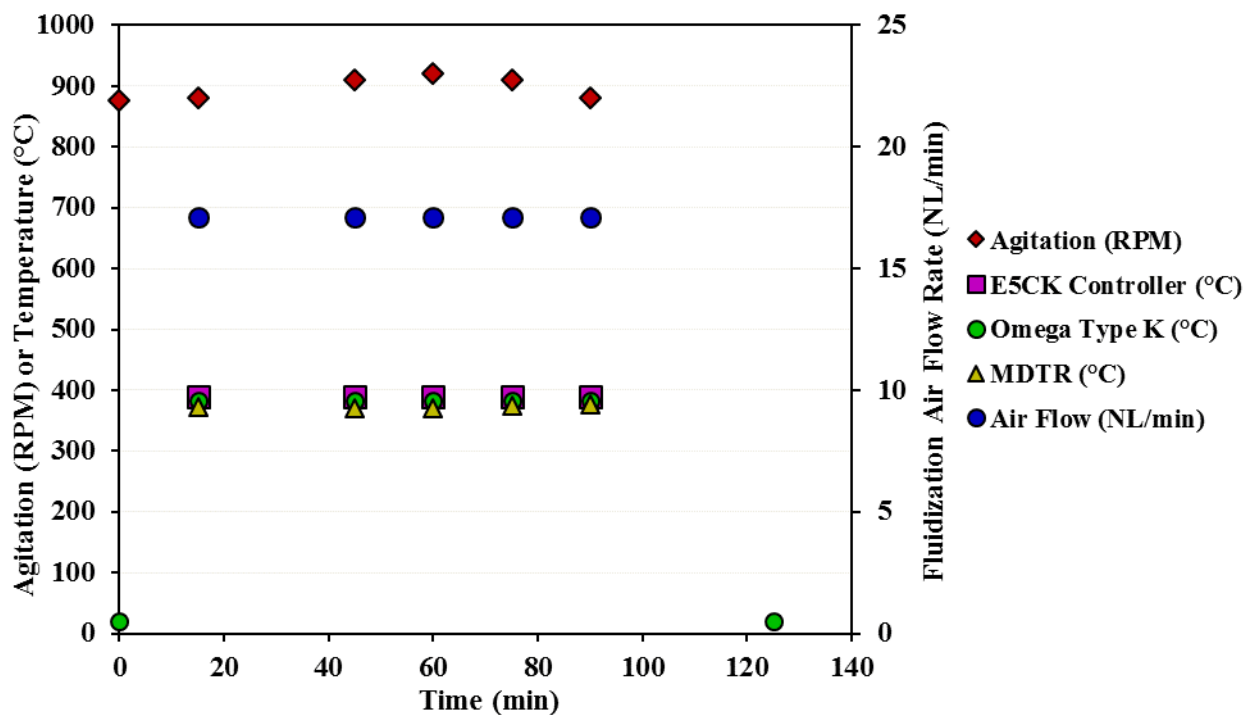
Figure C22. Agitation, temperature, and fluidization air flow rate profiles for hydrotreating reaction 23.
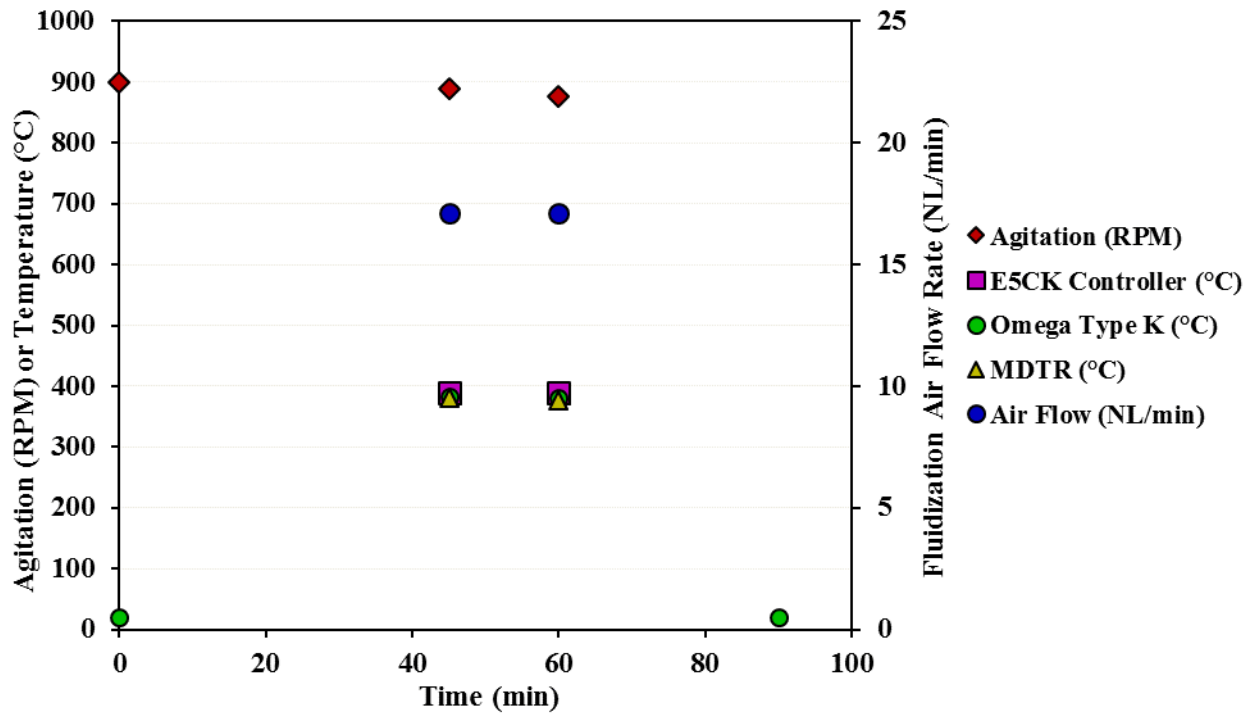
Figure C23. Agitation, temperature, and fluidization air flow rate profiles for hydrotreating reaction 24.
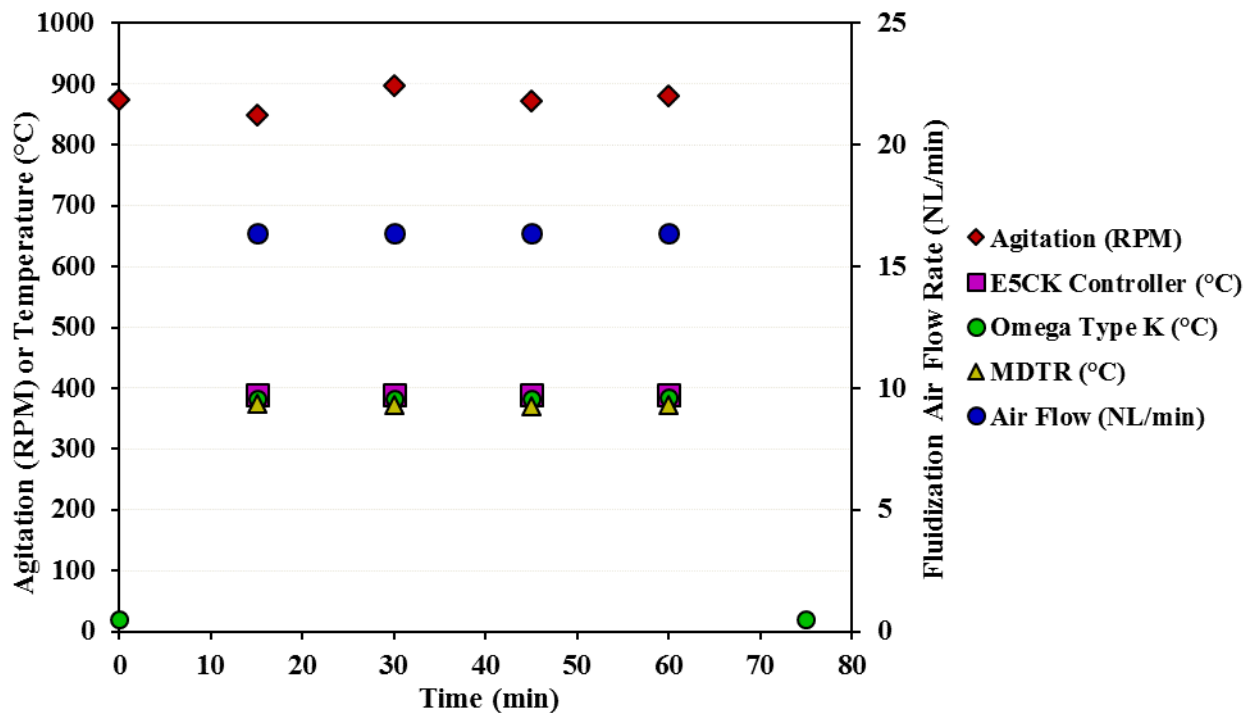
Figure C24. Agitation, temperature, and fluidization air flow rate profiles for hydrotreating reaction 25.
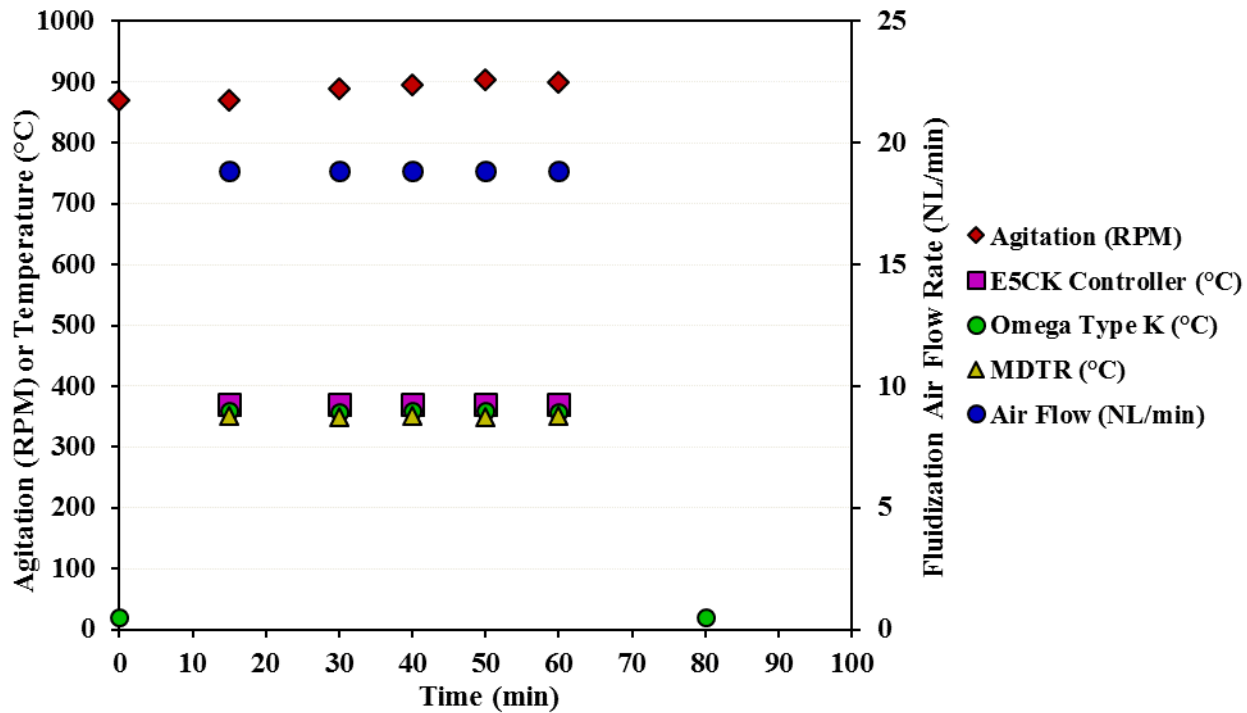
Figure C25. Agitation, temperature, and fluidization air flow rate profiles for hydrotreating reaction 26.
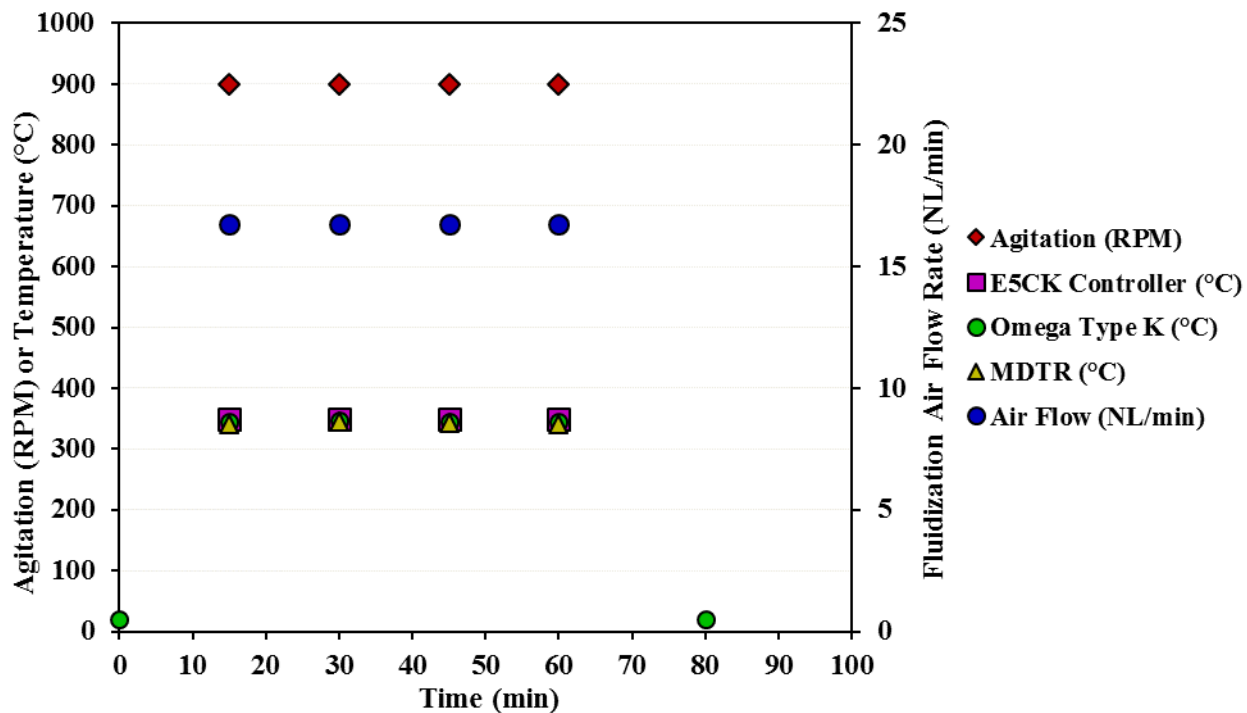
Figure C26. Agitation, temperature, and fluidization air flow rate profiles for hydrotreating reaction 27.
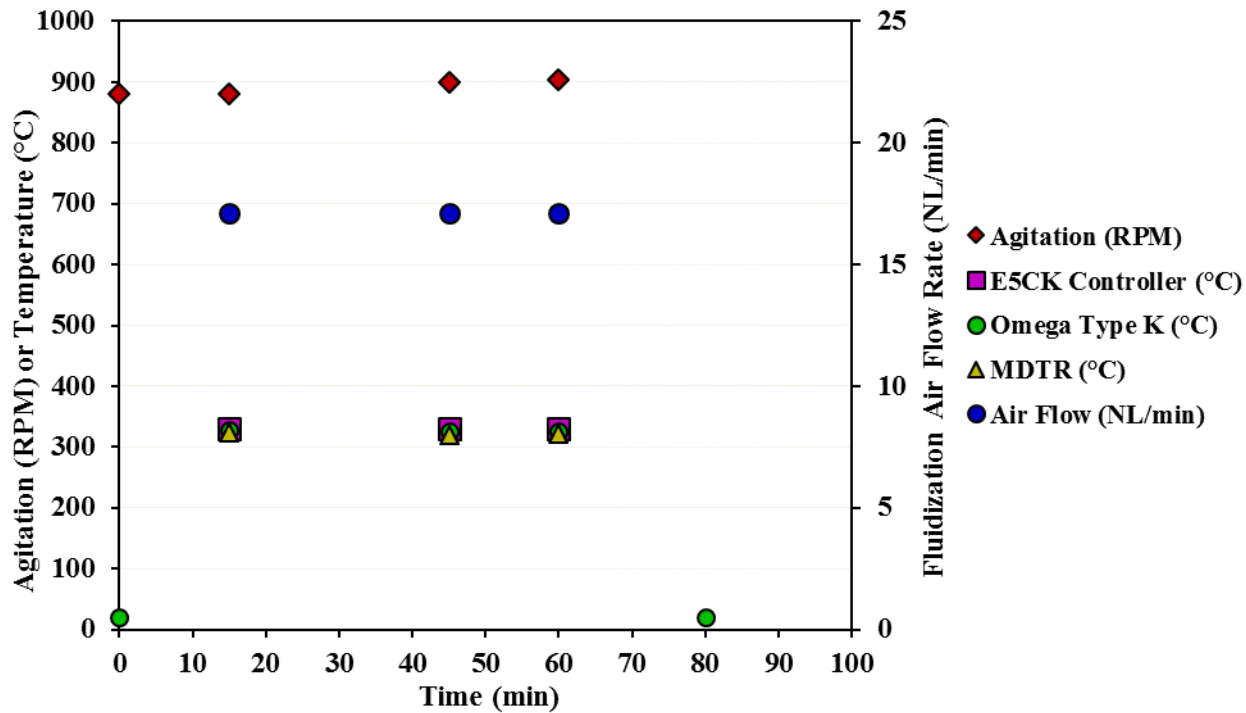
Figure C27. Agitation, temperature, and fluidization air flow rate profiles for hydrotreating reaction 28.
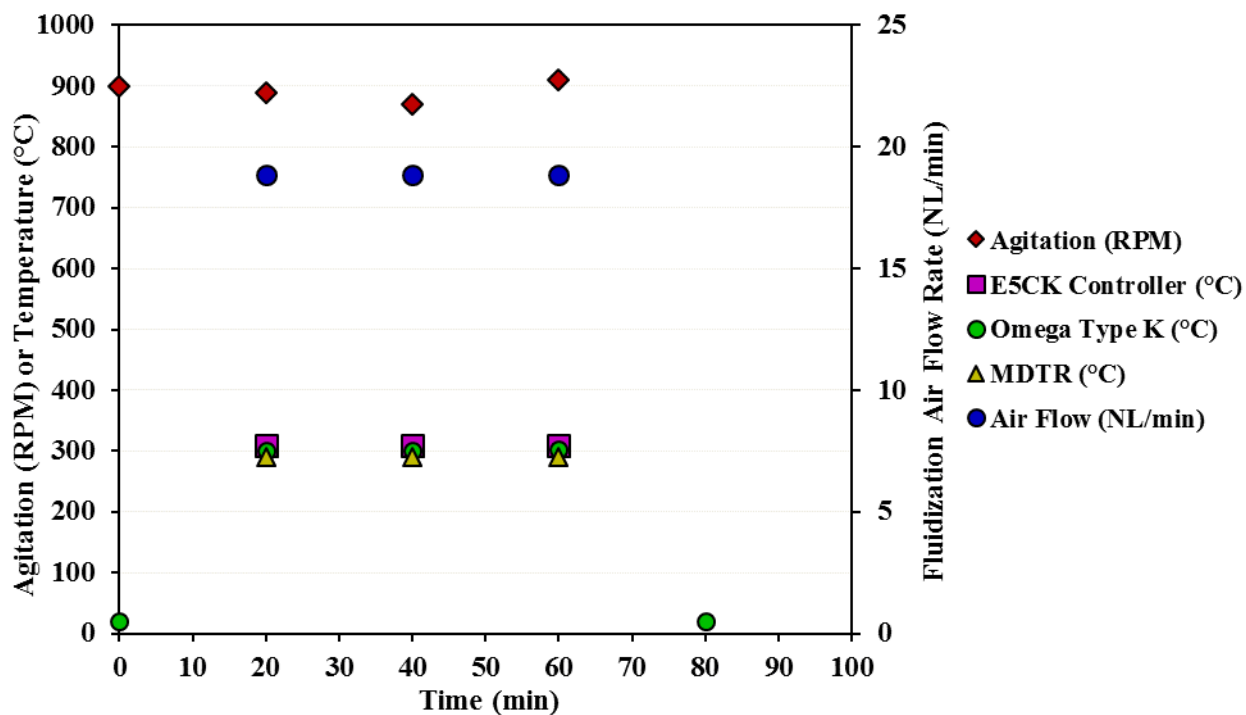
Figure C28. Agitation, temperature, and fluidization air flow rate profiles for hydrotreating reaction 29.
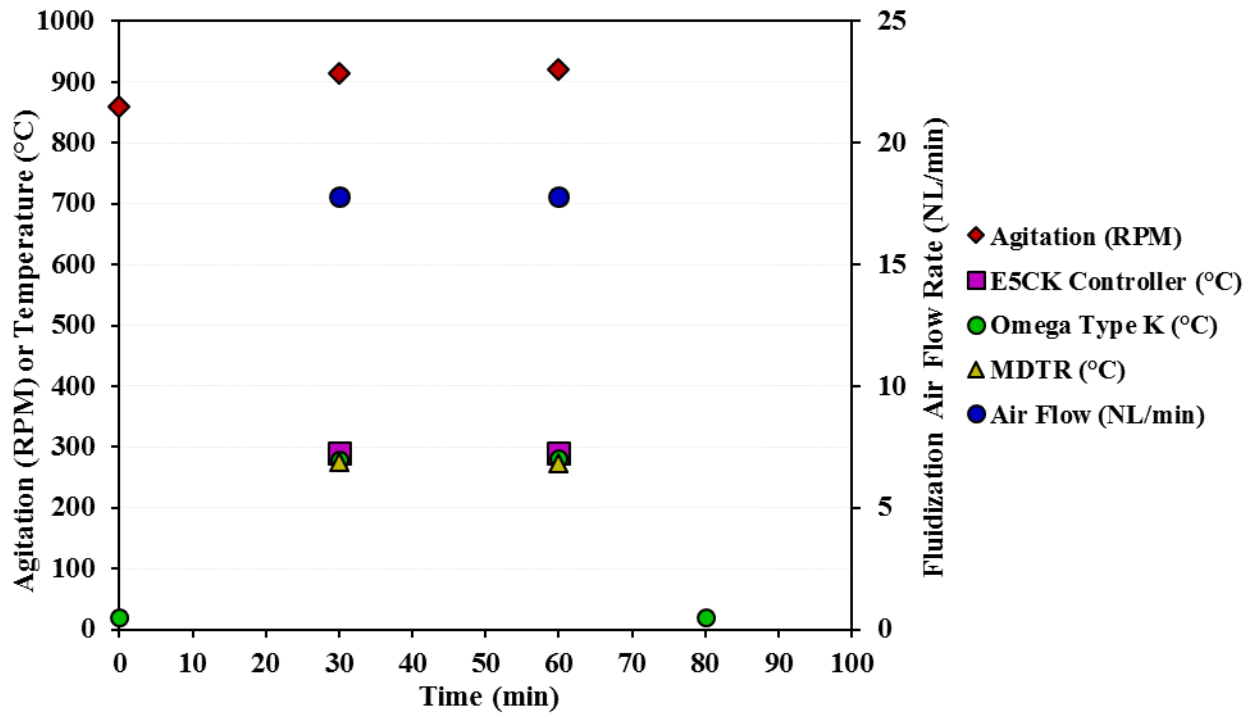
Figure C29. Agitation, temperature, and fluidization air flow rate profiles for hydrotreating reaction 30.
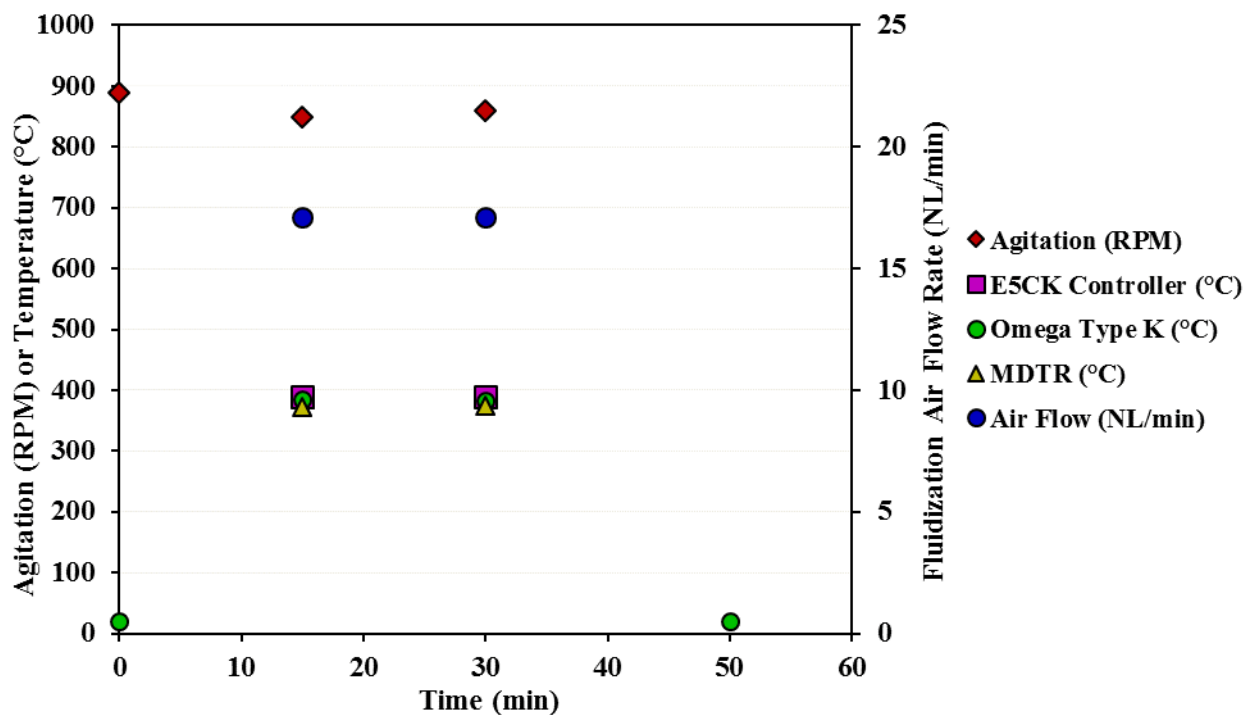
Figure C30. Agitation, temperature, and fluidization air flow rate profiles for hydrotreating reaction 31.
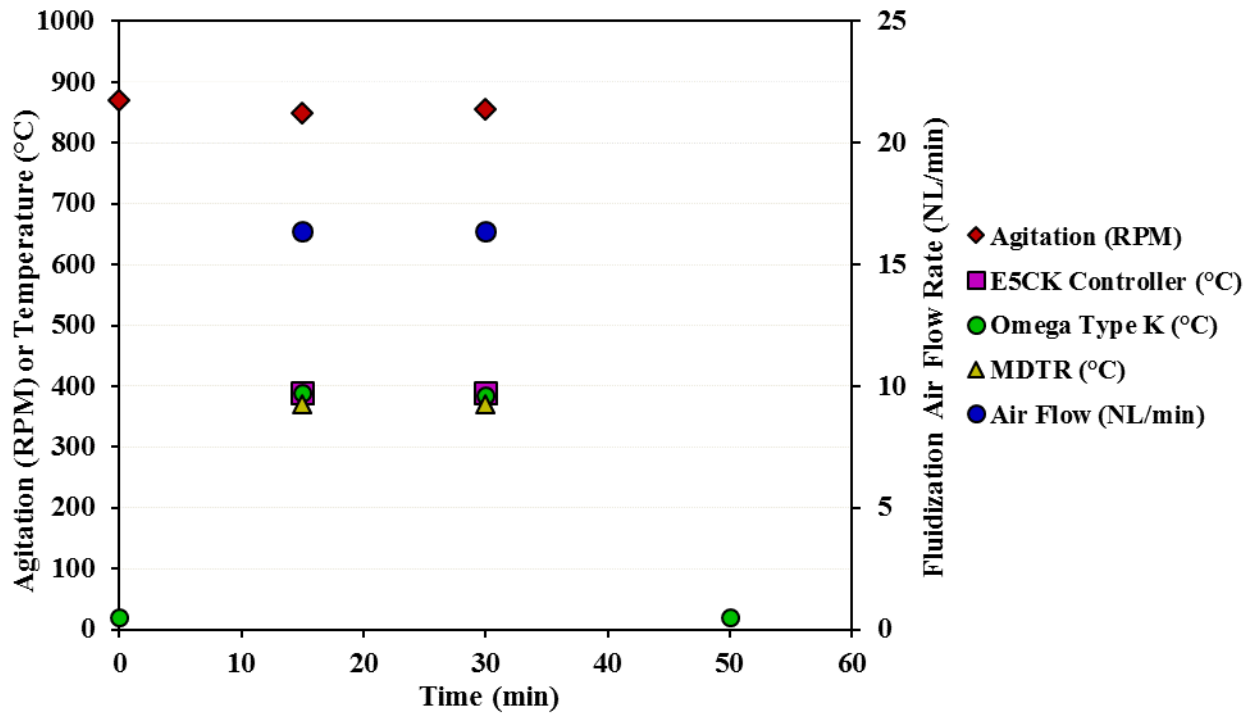
Figure C31. Agitation, temperature, and fluidization air flow rate profiles for hydrotreating reaction 32.
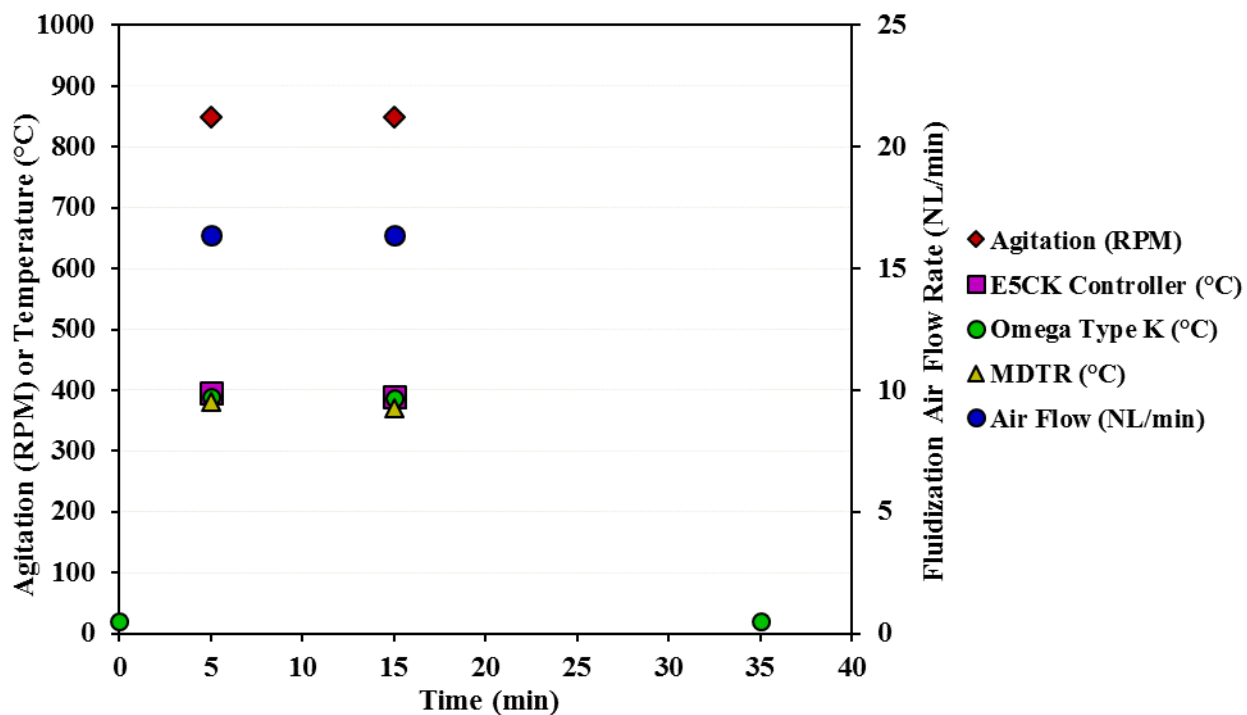
Figure C32. Agitation, temperature, and fluidization air flow rate profiles for hydrotreating reaction 33.
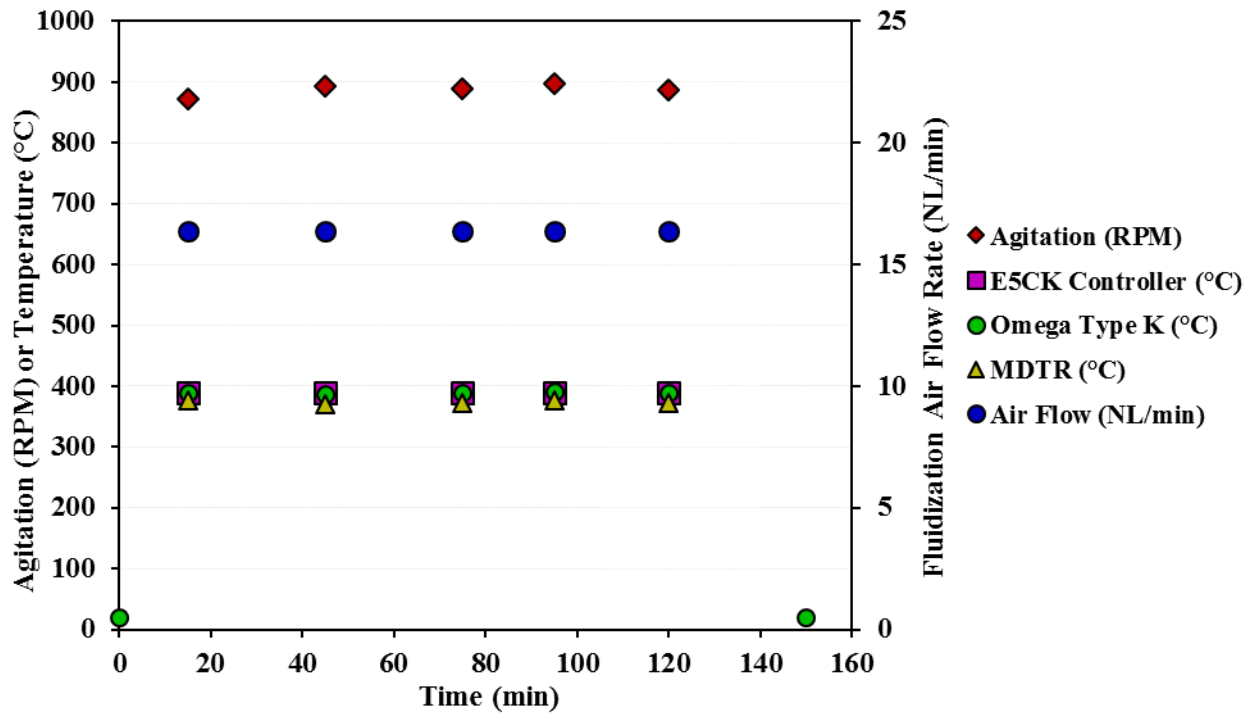
Figure C33. Agitation, temperature, and fluidization air flow rate profiles for hydrotreating reaction 34.
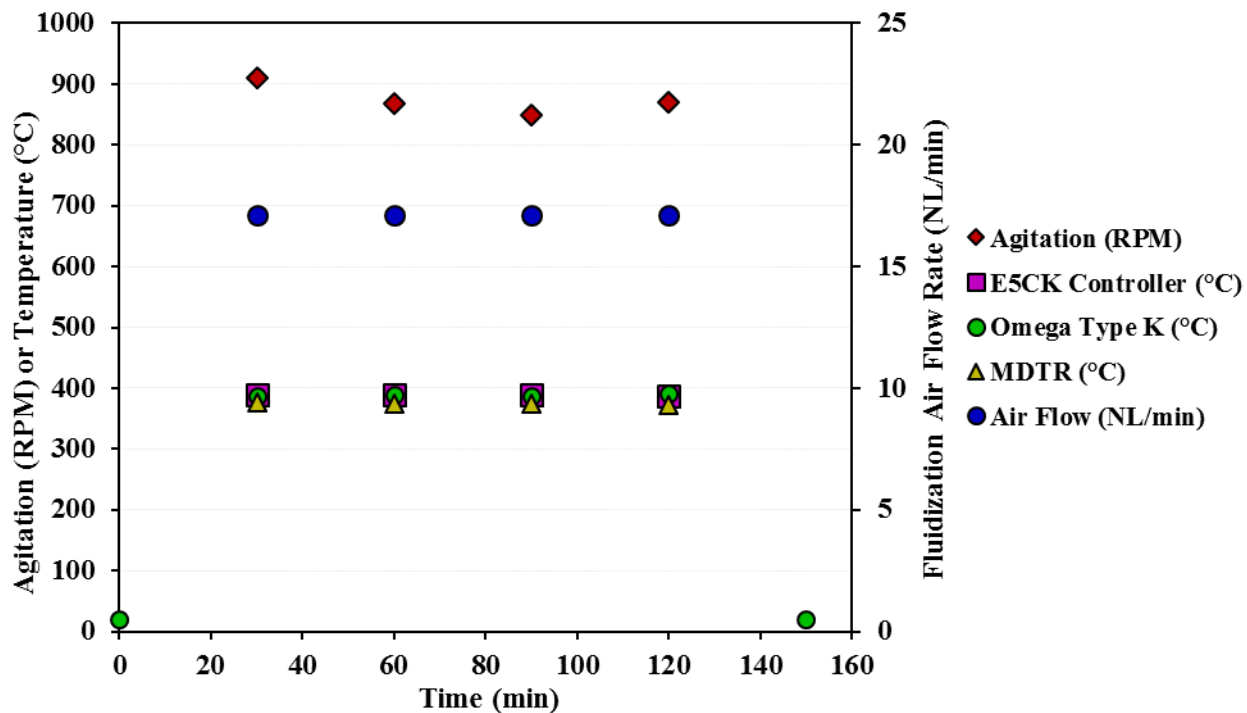
Figure C34. Agitation, temperature, and fluidization air flow rate profiles for hydrotreating reaction 35.
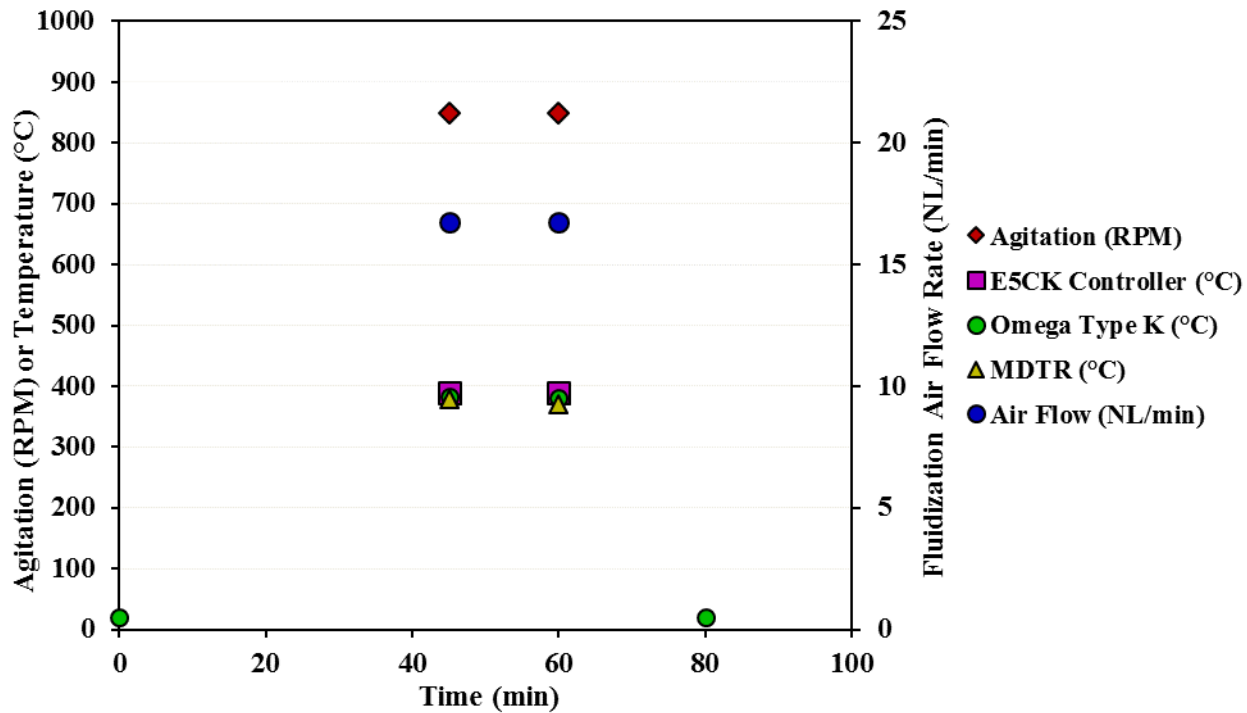
Figure C35. Agitation, temperature, and fluidization air flow rate profiles for hydrotreating reaction 36.
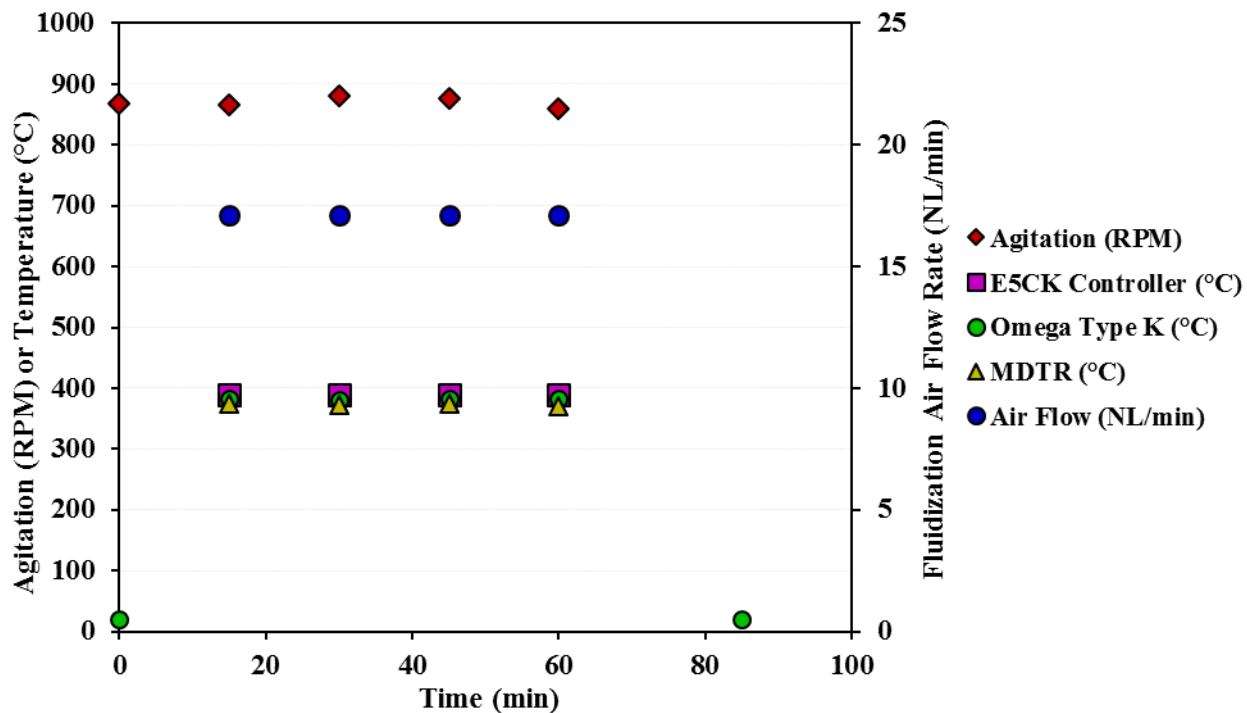
Figure C36. Agitation, temperature, and fluidization air flow rate profiles for hydrotreating reaction 37.
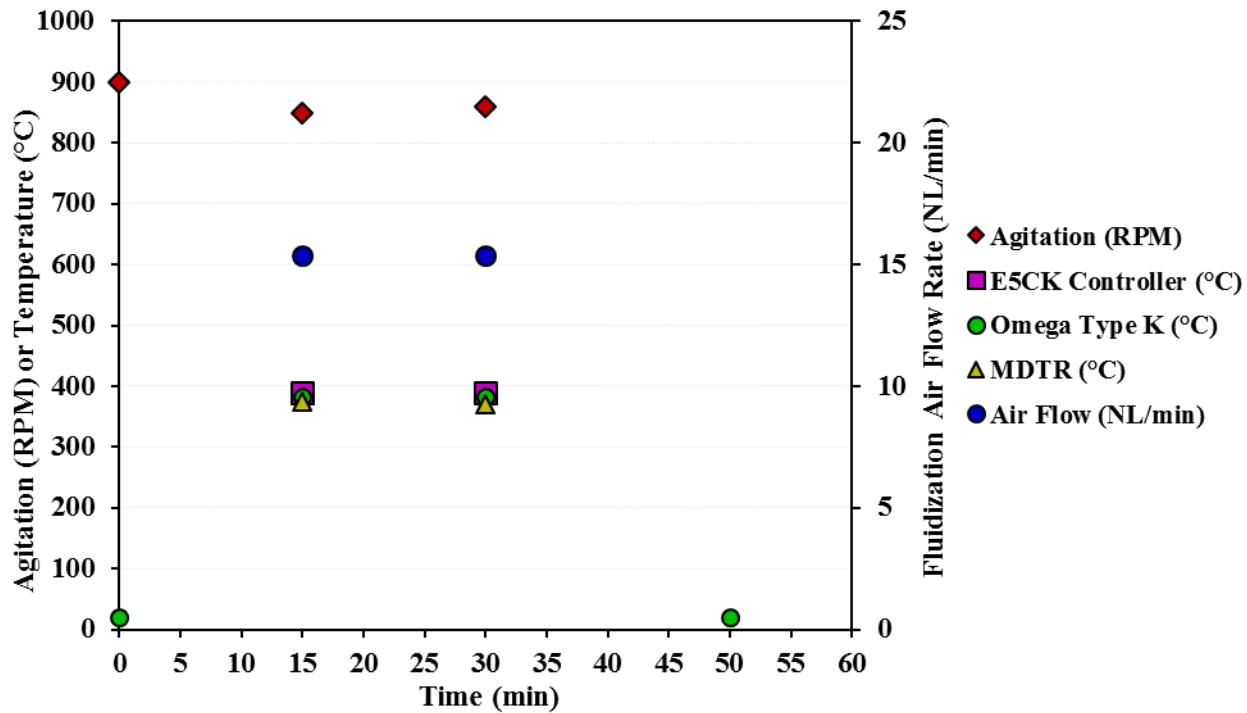
Figure C37. Agitation, temperature, and fluidization air flow rate profiles for hydrotreating reaction 38.
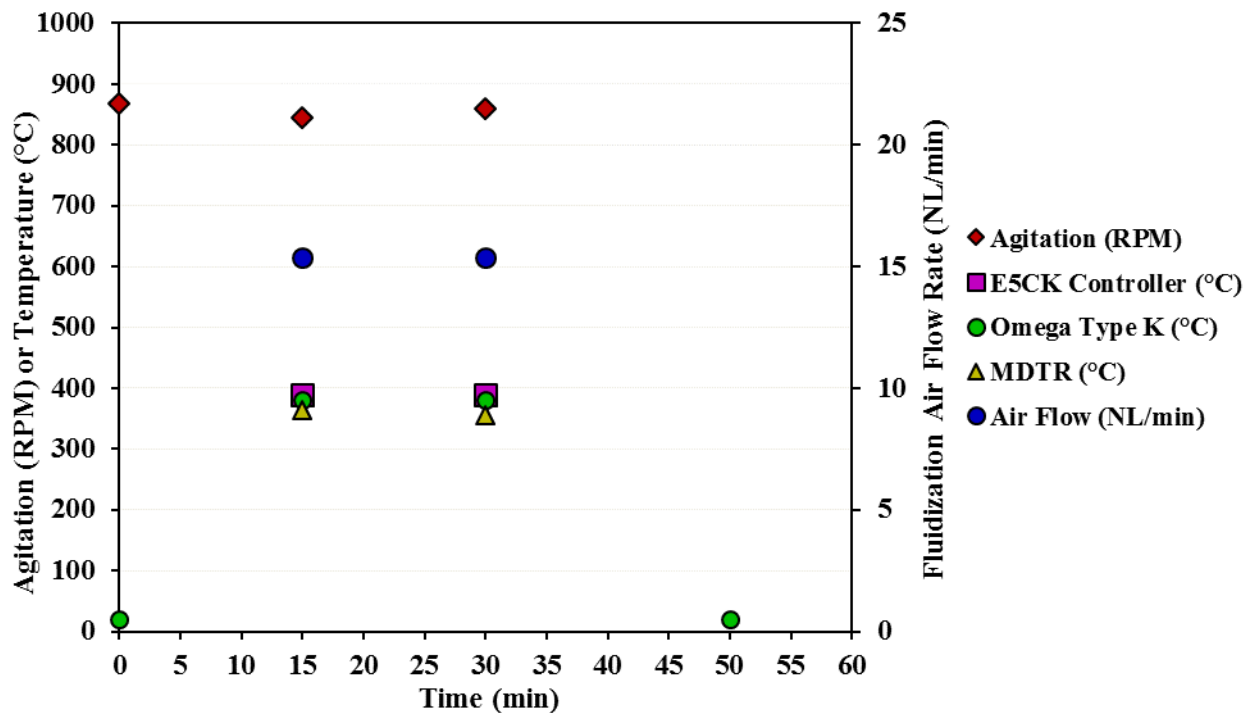
Figure C38. Agitation, temperature, and fluidization air flow rate profiles for hydrotreating reaction 39.

328
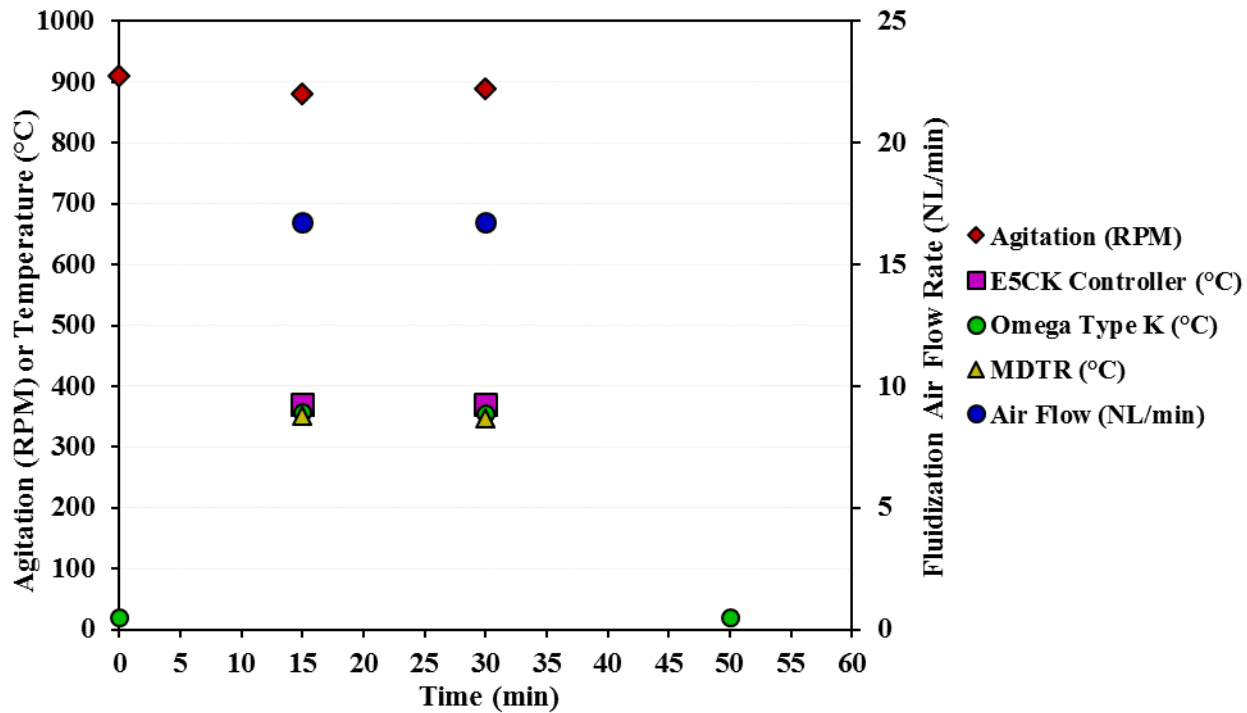
Figure C39. Agitation, temperature, and fluidization air flow rate profiles for hydrotreating reaction 40.
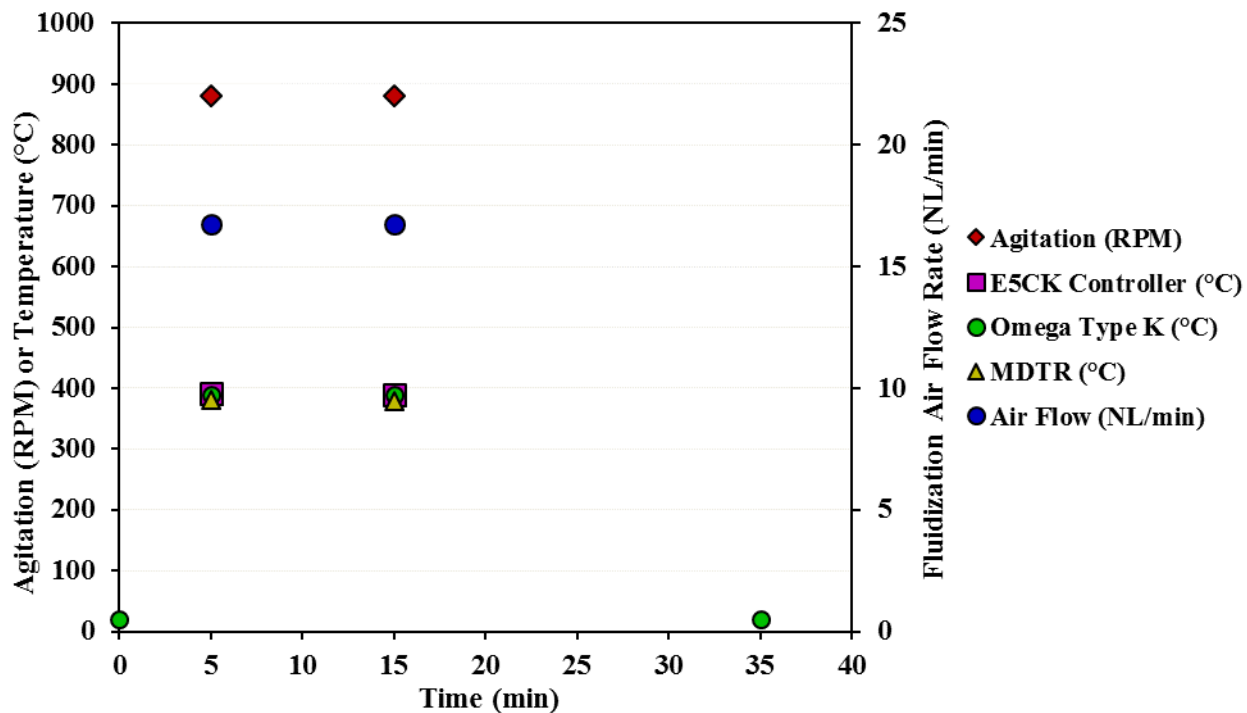
Figure C40. Agitation, temperature, and fluidization air flow rate profiles for hydrotreating reaction 41.

329
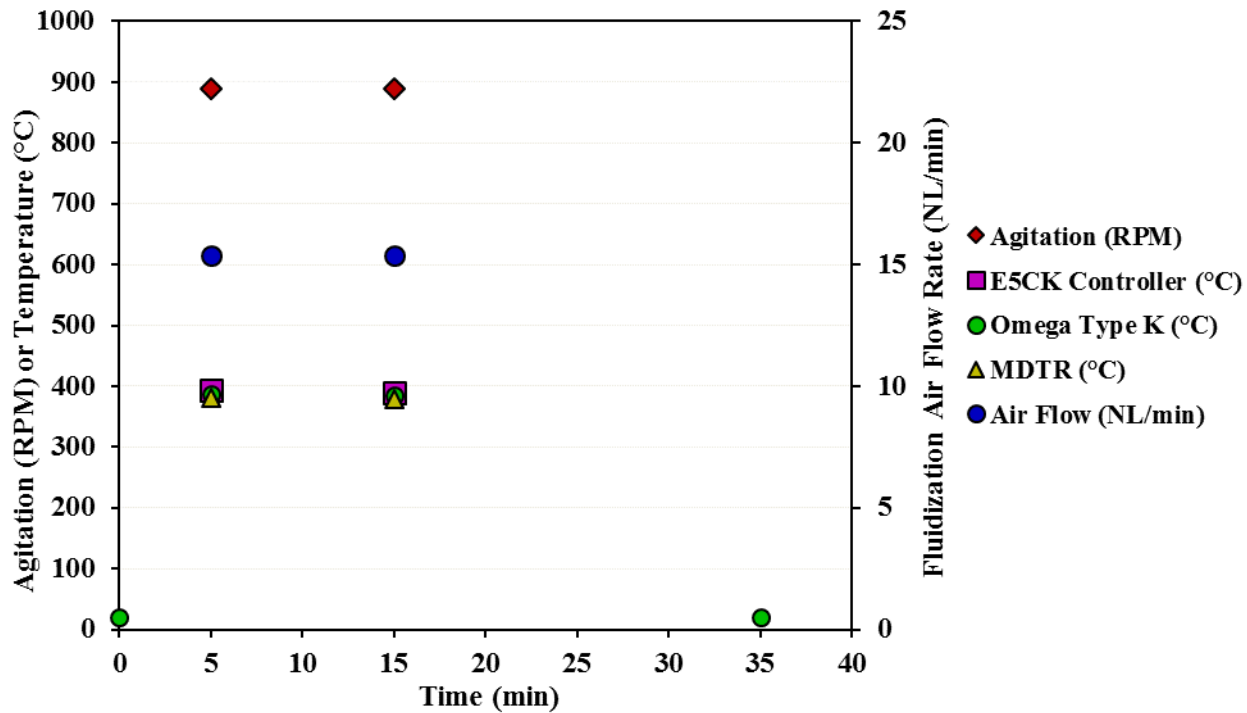
Figure C41. Agitation, temperature, and fluidization air flow rate profiles for hydrotreating reaction 42.
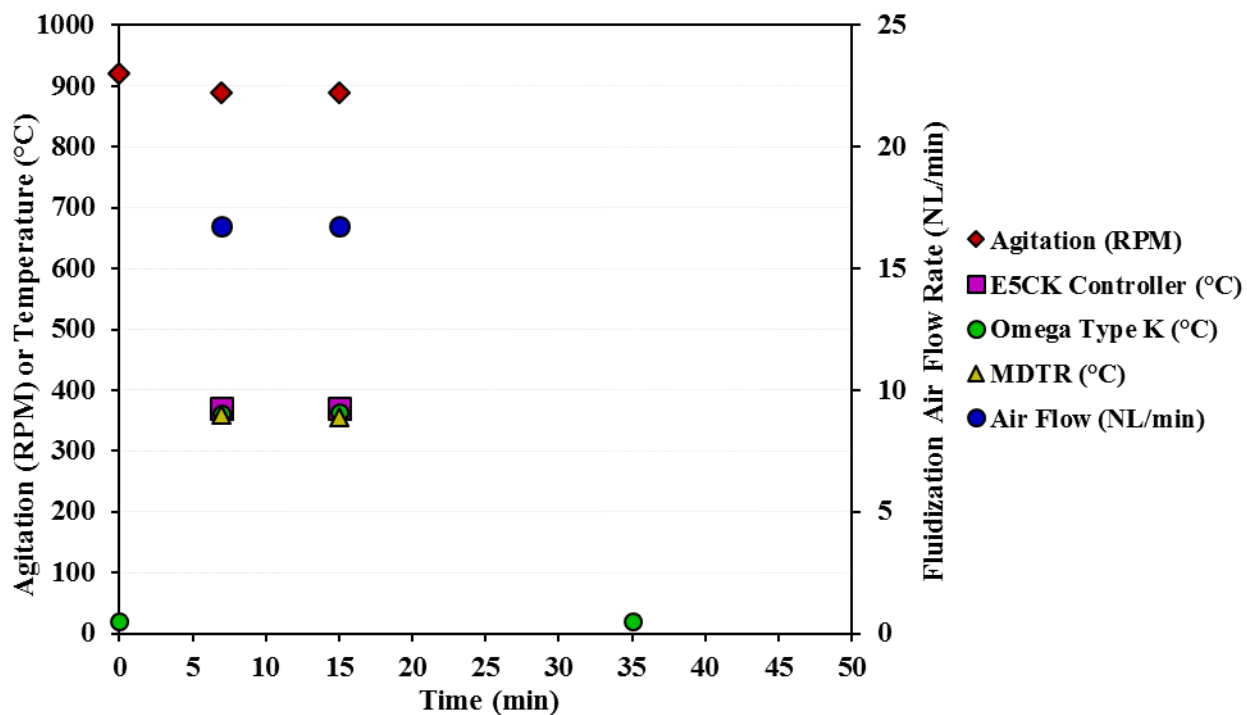
Figure C42. Agitation, temperature, and fluidization air flow rate profiles for hydrotreating reaction 43.
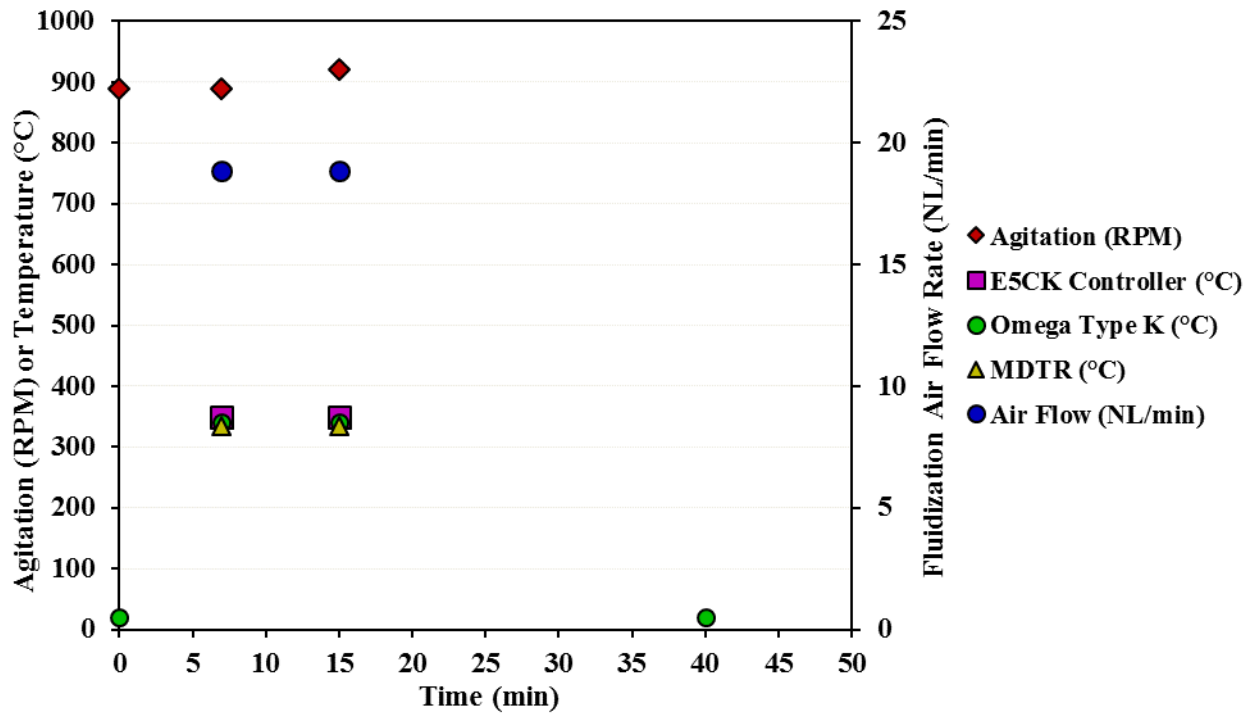
Figure C43. Agitation, temperature, and fluidization air flow rate profiles for hydrotreating reaction 44.

Appendix D

Theoretical evaporation calculations of dichloromethane, with mass measurements, and recovery calculations are found in *Appendix D*. A visual diagram of dichloromethane evaporation from a glass vial in the fume hood is presented in *Figure D1*. Predicted mass of dichloromethane evaporated as a function of time is presented in *Table D1*. All experimental reactions, feed, catalyst size, pressure, temperature, agitation, and reaction times are presented in *Table D2* (*Table 3.4*). All feed and product masses measured with percent recovery are presented in the extended *Table D3*. A summary of feed and product masses measured with recovery for all reactions is presented in *Table D4* (*Table 3.5*).

Theoretical Dichloromethane Evaporation

The mass of dichloromethane (DCM) evaporated from the hydrotreated liquid product was calculated based on a simple mass balance:

$$m_{DCM(E)} = m_{DCM(0)} - m_{DCM(t)} \tag{D1}$$

Where $m_{DCM(E)}$ is the mass of DCM evaporated from the glass vial, $m_{DCM(0)}$ is the initial mass of DCM in the vial (measured), and $m_{DCM(t)}$ is the mass of DCM with time. The mass is written in terms of the height in the glass vial:

$$m_{DCM} = V_{DCM} \cdot \rho_{DCM} = A_{vial} \cdot h_{DCM} \cdot \rho_{DCM} \tag{D2}$$

Where V_{DCM} is the volume of DCM (cm^3), ρ_{DCM} is the density of DCM (g/cm^3), A_{vial} is the cross-sectional area of the glass vial (cm^2), and h_{DCM} is the height of DCM in the glass vial (cm). The cross-sectional area was calculated from the approximate internal diameter of a standard Fisherbrand™ 20ml glass vial measured with a Mastercraft® electronic caliper:

$$A_{vial} = 0.25 \cdot \pi \cdot (0.5 \cdot (2.4cm))^2 = 4.52cm^2 \tag{D3}$$

The total height (h_t) of the internal glass vial (minus bottom glass thickness) was measured with the caliper at approximately 4.3cm. The total height of the internal glass vial and the height of DCM in the glass vial were related:

$$h_t = h_{ft} + h_{DCM} \tag{D4}$$

Where h_{ft} was the height of DCM from the top of the glass vial. See *Figure D1* for a visual diagram. The height of DCM from the top (h_{ft}) was solved in terms of total height, mass of DCM, cross-sectional area, and density ($1.33 g/cm^3$ at 20°C):

$$h_{ft} = 4.3cm - \frac{m_{DCM}}{A_{vial} \cdot \rho_{DCM}} = 4.3cm - \frac{m_{DCM}}{6.01 g/cm} \tag{D5}$$
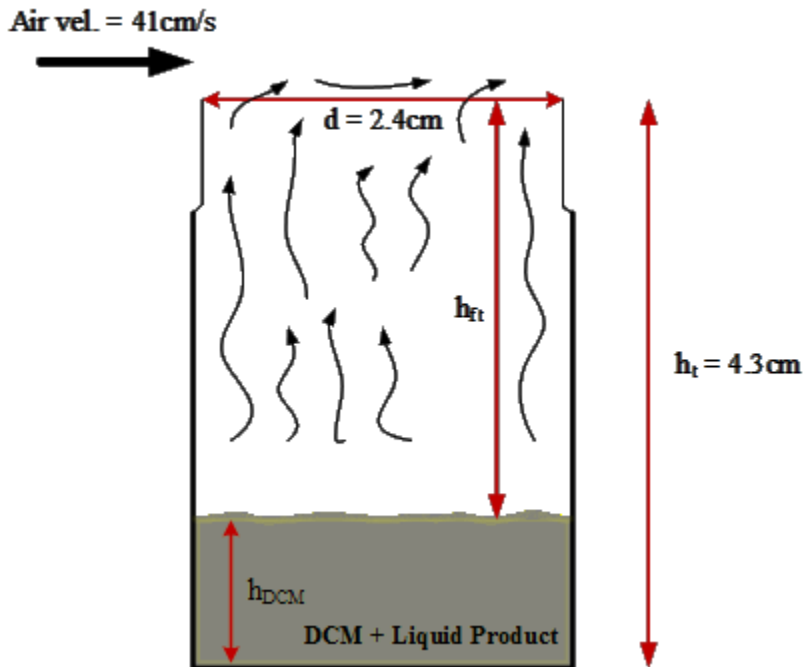
Figure D1. Visual diagram of dichloromethane evaporation from a glass vial in the fume hood.

The evaporation rate was expressed as a change in height rate in terms of diffusion and concentration of DCM evaporating from a tube. The equation was recently published by Mitrovic based on the "the Stefan diffusion problem" in Chemical Engineering Science [1]. Mitrovic derived what Stefan originally published for an evaporating interface in a tube:

$$h(t)_{ft}^2 - h(0)_{ft}^2 = 2 \cdot \frac{MW_{DCM} \cdot P}{\rho_{DCM} \cdot R \cdot T} \cdot D_{AB} \cdot (t - t_o) \cdot \ln\left[\frac{P - P_o}{P - P_{DCM}}\right] \tag{D6}$$

Where D_{AB} is the diffusion coefficient (cm^2/s) of DCM, MW_{DCM} is the molecular weight of DCM (84.93g/mol), P_{DCM} is the vapor pressure of DCM (kPa), P is the pressure of the bulk (air,

101.325kPa), t is the time (s), R is the gas constant (8314kPa cm^3 mol^{-1} K^{-1}), $h(t)_{ft}$ is the height of DCM from the top as a function of time, and $h(0)_{ft}$ is the initial height from the top. Equation D5 was written in terms of initial and final mass of DCM:

$$h(t)_{ft} = 4.3cm - \frac{m_{DCM(t)}}{6.01g/cm} \tag{D7}$$

$$h(0)_{ft} = 4.3cm - \frac{m_{DCM(0)}}{6.01g/cm} \tag{D8}$$

Equations D7 and D8 were used to solve $m_{DCM(E)}$ in equation D1:

$$m_{DCM(E)} = \frac{6.01g}{cm} \cdot \left[h(t)_{ft} - h(0)_{ft} \right] \tag{D9}$$

The height of DCM from the top as a function of time, $h(t)_{ft}$, was solved for in equation D6 and combined into equation D9:

$$m_{DCM(E)} = \frac{6.01g}{cm} \cdot \left[\sqrt{2 \cdot \frac{MW_{DCM} \cdot P}{\rho_{DCM} \cdot R \cdot T} \cdot D_{AB} \cdot (t - t_o) \cdot \ln\left[\frac{P - P_o}{P - P_{DCM}} \right] + h(0)_{ft}^2} - h(0)_{ft} \right] \tag{D10}$$

Assumptions:

MW_{DCM} = 84.93g/mol
P = 101.325kPa
ρ_{DCM} = 1.33g/cm^3 (at 20°C)
R = 8314 kPa cm^3 mol^{-1} K^{-1}
T = 293K (20°C, lab temperature)
t_o = 0 (start time)
P_o = 0 (initial pressure of air at DCM interface)
P_{DCM} = Vapor pressure of DCM (kPa) (10^(4.53691-(1327.016/(293K-20.474)))) [2]
P_{DCM} = 47kPa
$h(0)_{ft}$ = 4.3cm – $m_{DCM(0)}$ / (6.01g/cm) where $m_{DCM(0)}$ = 12.16g (measured 24h after the start of evaporation for hydrotreating reaction 12)
$h(0)_{ft}$ = 4.3cm – 12.16g / (6.01g/cm) = 2.277cm
D_{AB} = 0.00002522·T$^{1.462}$ [3] or 0.00000867·T$^{1.66}$ [4] diffusion coefficient correlations reported for DCM and air.
D_{AB} = 0.00002522·(293K)$^{1.462}$ = 0.1019cm^2/s, 0.00000867·(293K)$^{1.66}$ = 0.1079cm^2/s, the average of the two results are used.
D_{AB} = 0.1049cm^2/s
t=time (×3600s / h)

Assumed convective mass transfer at the top of the vial was negligible. Low Reynolds number with circa 41cm/s air velocity across the 2.4cm vial diameter (Re=642, laminar region).

The mass of DCM evaporated ($m_{DCM(E)}$) is calculated (equation D10) as a function time. Results were compared with the measured mass of DCM evaporated ($m_{DCM(A)}$) for the verification reaction liquid product in _Table D1_.

Table D1. Predicted and measured mass of dichloromethane evaporated with time.

Time (h)	$m_{DCM(E)}$ (g)	$m_{DCM(A)}$ (g)	Time (h)	$m_{DCM(E)}$ (g)	$m_{DCM(A)}$ (g)	Time (h)	$m_{DCM(E)}$ (g)	$m_{DCM(A)}$ (g)
0	0	0	3.25	4.59		6.25	7.98	
0.25	0.41		3.5	4.90		6.5	8.24	
0.5	0.8	0.9621	3.75	5.20		6.75	8.50	
1	1.56		4	5.50	5.5062	7	8.75	8.5133
1.25	1.93	2.0506	4.25	5.79		7.25	9.00	
1.5	2.28		4.5	6.08		7.5	9.25	
1.75	2.63		4.75	6.36		7.75	9.50	
2	2.98		5	6.64		8	9.74	
2.25	3.31		5.25	6.92		8.25	9.98	
2.5	3.64		5.5	7.19		8.5	10.22	
2.75	3.96		5.75	7.46		8.75	10.45	
3	4.28	4.6697	6	7.72		9	10.68	10.15

From _Table D1_, the results were plotted in _Figure 3.13_. For the first 9 hours, the predicted mass loss agreed with the measured mass of DCM evaporated (measured with the balance scale). The complete evaporation of DCM occurred between 9 to 11 hours. The following day, the hydrotreated liquid product was measured with <0.001g change in mass. The vial was capped and store on average 24 to 28 hours after the start of DCM evaporation. Approximately 13 to 19 hours was the light end fraction evaporation time in the fume hood.

Table D2. Experimental reactions, feed, catalyst size, pressure, temperature, agitation, and reaction times.

#	Reaction	Feed	Catalyst Size	Pressure (kPa(g))	Temperature (°C)	Agitation (RPM)	Time (h)
1	No Reaction	HVGO	-	-	-	-	-
2	Hydrotreating	HVGO^	-	4500	390	360**	2
3	Hydrotreating	HVGO^	-	4500	390	708	2
4	Hydrotreating	HVGO^	-	4500	390	862	2
5	Hydrotreating	HVGO^	-	4500	390	850	2
6	Hydrotreating	HVGO^	-	4500	390	873	2
7	Hydrotreating	HVGO^	Pellets	4500	390	848	2
8	Hydrotreating	HVGO^	Pellets	4500	390	868	2
9	Hydrotreating	HVGO^	Pellets	4500	390	878	2
10	Hydrotreating	HVGO	Pellets	4500	390	360**	2
11	Hydrotreating	HVGO	Pellets	4500	390	360**	2
12	Hydrotreating	HVGO	Pellets	4500	390	360*	2.25
13	Hydrotreating	HVGO	Pellets	4500	390	884	2
14	Hydrotreating	HVGO	Pellets	4500	390	882	2
15	Hydrotreating	HVGO	Pellets	4500	390	866	2
16	Sulfiding Catalyst	DMDS	Dried Pellets	3000	20 - 360	360**	4.5
17	Sulfiding Catalyst	DMDS	Dried Pellets	3000	20 - 360	360**	4.2
18	Sulfiding Catalyst	DMDS	Dried < 45μm	3300	20 - 360	880	4.2
19	Sulfiding Catalyst	DMDS	Dried < 45μm	3000	20 - 360	863	4.2
20	Hydrotreating	HVGO	Sulfided Pellet	4500	390	878	2
21	Hydrotreating	HVGO	Sulfided Pellet	4500	390	886	2
22	Hydrotreating	HVGO	Sulfided Pellet	4500	390	892	2
23	Hydrotreating	HVGO	Sulfided Pellet	4500	390	896	1.5
24	Hydrotreating	HVGO	Sulfided Pellet	4500	390	889	1
25	Hydrotreating	HVGO	Sulfided Pellet	4500	390	875	1
26	Hydrotreating	HVGO	Sulfided Pellet	4500	370	888	1
27	Hydrotreating	HVGO	Sulfided Pellet	4500	350	900	1
28	Hydrotreating	HVGO	Sulfided Pellet	4500	330	891	1
29	Hydrotreating	HVGO	Sulfided Pellet	4500	310	893	1
30	Hydrotreating	HVGO	Sulfided Pellet	4500	290	898	1
31	Hydrotreating	HVGO	Sulfided Pellet	4500	390	867	0.5
32	Hydrotreating	HVGO	Sulfided Pellet	4500	390	859	0.5
33	Hydrotreating	HVGO	Sulfided Pellet	4500	390	850	0.25
34	Hydrotreating	HVGO	Sulfided < 45μm	4500	390	888	2
35	Hydrotreating	HVGO	Sulfided < 45μm	4500	390	874	2
36	Hydrotreating	HVGO	Sulfided < 45μm	4500	390	879	1
37	Hydrotreating	HVGO	Sulfided < 45μm	4500	390	870	1
38	Hydrotreating	HVGO	Sulfided < 45μm	4500	390	870	0.5
39	Hydrotreating	HVGO	Sulfided < 45μm	4500	390	859	0.5
40	Hydrotreating	HVGO	Sulfided < 45μm	4500	370	894	0.5
41	Hydrotreating	HVGO	Sulfided < 45μm	4500	390	880	0.25
42	Hydrotreating	HVGO	Sulfided < 45μm	4500	390	890	0.25
43	Hydrotreating	HVGO	Sulfided < 45μm	4500	370	900	0.25
44	Hydrotreating	HVGO	Sulfided < 45μm	4500	350	900	0.25

*Modified microreactor design I.
**Modified microreactor design II.
^No liquid product filtration.

Table D3. All feed and product masses measured with percent recovery.

#	Reactor Bottom Before Reaction (g)	Liquid Feed Loaded (g)	Catalyst Type	Catalyst Loaded (g)	Loaded Reactor Bottom + Top (g)	Reactor Top Before Reaction (g)
Experiment 1	217.539	0.61	Sulfided Pellets	0.101	524.069	305.819
	Loaded Reactor Bottom + Top + Neever·Seez (g)	**Mass of Neever·Seez (g)**	**Pressure Test (MPa(g))**	**Loaded Reactor Bottom + Top + Neever·Seez + H₂ at Atmosphere (g)**	**Loaded Reactor Bottom + Top + Neever·Seez + H₂ at Pressure (g)**	**H₂ Gas Loaded (g)**
	524.075	0.006	12	-	-	-
	Liquid + Catalyst + H₂ Loaded Before Reaction (g)	**After Reaction Mass (g)**	**Difference of Before & After Reaction (g)**	**After Reaction Mass - Product Gas Released (g)**	**Product Gas Released (g)**	**Reactor Bottom After Reaction (g)**
	0.711	-	-	-	-	-
	Reactor Top After Reaction (g)	**Liquid Product + Catalyst Recovered (g)**	**Liquid + Gas Products + Catalyst Recovered (g)**	**Total Mass Recovery (%)**	**Empty Filter Paper (g)**	**Full Filter Paper (g)**
	-	-	0.665	93*	1.0480	1.1575
	Spent Catalyst Recovered (g)	**Empty Vial (g)**	**Full Vial (g)**	**Liquid Product After DCM Evaporation (g)**	**Liquid Product Recovery After DCM Evaporation (%)**	
	0.1095*	17.4919	18.0469	0.555*	91	

#	Reactor Bottom Before Reaction (g)	Liquid Feed Loaded (g)	Catalyst Type	Catalyst Loaded (g)	Loaded Reactor Bottom + Top (g)	Reactor Top Before Reaction (g)
Reaction 2, HVGO, 4500kPa(g) H₂, 390°C, 2h, 360RPM, 30min Cool Time	217.452	0.602	-	-	640.837	430.783
	Loaded Reactor Bottom + Top + Neever·Seez (g)	**Mass of Neever·Seez (g)**	**Pressure Test (MPa(g))**	**Loaded Reactor Bottom + Top + Neever·Seez + H₂ at Atmosphere (g)**	**Loaded Reactor Bottom + Top + Neever·Seez + H₂ at Pressure (g)**	**H₂ Gas Loaded (g)**
	648.843	0.006	12.5	640.838	640.900	0.062
	Liquid + Catalyst + H₂ Loaded Before Reaction (g)	**After Reaction Mass (g)**	**Difference of Before & After Reaction (g)**	**After Reaction Mass - Product Gas Released (g)**	**Product Gas Released (g)**	**Reactor Bottom After Reaction (g)**
	0.664	640.911	-0.011	648.832	0.079	218.003
	Reactor Top After Reaction (g)	**Liquid Product + Catalyst Recovered (g)**	**Liquid + Gas Products + Catalyst Recovered (g)**	**Total Mass Recovery (%)**	**Empty Filter Paper (g)**	**Full Filter Paper (g)**
	430.799	0.567	0.646	97	-	-
	Spent Catalyst Recovered (g)	**Empty Vial (g)**	**Full Vial (g)**	**Liquid Product After DCM Evaporation (g)**	**Liquid Product Recovery After DCM Evaporation (%)**	
	-	17.4236	17.8936	0.47	78	

Reaction 3, HVGO, 4500kPa(g) H$_2$, 390°C, 2h, 708RPM, 20min Cool Time

#	Reactor Bottom Before Reaction (g)	Liquid Feed Loaded (g)	Catalyst Type	Catalyst Loaded (g)	Loaded Reactor Bottom + Top (g)	Reactor Top Before Reaction (g)
	217.282	0.603	-	-	523.406	305.512

Loaded Reactor Bottom + Top + Neever·Seez (g)	Mass of Neever·Seez (g)	Pressure Test (MPa(g))	Loaded Reactor Bottom + Top + Neever·Seez + H$_2$ at Atmosphere (g)	Loaded Reactor Bottom + Top + Neever·Seez + H$_2$ at Pressure (g)	H$_2$ Gas Loaded (g)
523.428	0.022	13	523.418	523.493	0.075

Liquid + Catalyst + H$_2$ Loaded Before Reaction (g)	After Reaction Mass (g)	Difference of Before & After Reaction (g)	After Reaction Mass - Product Gas Released (g)	Product Gas Released (g)	Reactor Bottom After Reaction (g)
0.678	523.459	0.034	523.372	0.087	217.803

Reactor Top After Reaction (g)	Liquid Product + Catalyst Recovered (g)	Liquid + Gas Products + Catalyst Recovered (g)	Total Mass Recovery (%)	Empty Filter Paper (g)	Full Filter Paper (g)
305.550	0.55	0.637	94	-	-

Spent Catalyst Recovered (g)	Empty Vial (g)	Full Vial (g)	Liquid Product After DCM Evaporation (g)	Liquid Product Recovery After DCM Evaporation (%)	
-	17.7504	18.1500	0.40	66	

Reaction 4, HVGO, 4500kPa(g) H$_2$, 390°C, 2h, 862RPM, 20min Cool Time

#	Reactor Bottom Before Reaction (g)	Liquid Feed Loaded (g)	Catalyst Type	Catalyst Loaded (g)	Loaded Reactor Bottom + Top (g)	Reactor Top Before Reaction (g)
	217.176	0.614	-	-	523.262	305.472

Loaded Reactor Bottom + Top + Neever·Seez (g)	Mass of Neever·Seez (g)	Pressure Test (MPa(g))	Loaded Reactor Bottom + Top + Neever·Seez + H$_2$ at Atmosphere (g)	Loaded Reactor Bottom + Top + Neever·Seez + H$_2$ at Pressure (g)	H$_2$ Gas Loaded (g)
523.274	0.012	13	523.264	523.336	0.072

Liquid + Catalyst + H$_2$ Loaded Before Reaction (g)	After Reaction Mass (g)	Difference of Before & After Reaction (g)	After Reaction Mass - Product Gas Released (g)	Product Gas Released (g)	Reactor Bottom After Reaction (g)
0.686	523.325	0.011	523.243	0.082	217.75

Reactor Top After Reaction (g)	Liquid Product + Catalyst Recovered (g)	Liquid + Gas Products + Catalyst Recovered (g)	Total Mass Recovery (%)	Empty Filter Paper (g)	Full Filter Paper (g)
305.503	0.605	0.687	100	-	-

Spent Catalyst Recovered (g)	Empty Vial (g)	Full Vial (g)	Liquid Product After DCM Evaporation (g)	Liquid Product Recovery After DCM Evaporation (%)	
-	17.753	18.2222	0.47	76	

Reaction 5, HVGO, 4500kPa(g) H$_2$, 390°C, 2h, 850RPM, 15min Cool Time

#	Reactor Bottom Before Reaction (g)	Liquid Feed Loaded (g)	Catalyst Type	Catalyst Loaded (g)	Loaded Reactor Bottom + Top (g)	Reactor Top Before Reaction (g)
	218.354	0.604	-	-	524.747	305.789
	Loaded Reactor Bottom + Top + Neever·Seez (g)	Mass of Neever·Seez (g)	Pressure Test (MPa(g))	Loaded Reactor Bottom + Top + Neever·Seez + H$_2$ at Atmosphere (g)	Loaded Reactor Bottom + Top + Neever·Seez + H$_2$ at Pressure (g)	H$_2$ Gas Loaded (g)
	524.761	0.014	13	524.751	524.82	0.069
	Liquid + Catalyst + H$_2$ Loaded Before Reaction (g)	After Reaction Mass (g)	Difference of Before & After Reaction (g)	After Reaction Mass - Product Gas Released (g)	Product Gas Released (g)	Reactor Bottom After Reaction (g)
	0.673	524.842	-0.022	524.769	0.073	218.962
	Reactor Top After Reaction (g)	Liquid Product + Catalyst Recovered (g)	Liquid + Gas Products + Catalyst Recovered (g)	Total Mass Recovery (%)	Empty Filter Paper (g)	Full Filter Paper (g)
	305.821	0.64	0.713	106	-	-
	Spent Catalyst Recovered (g)	Empty Vial (g)	Full Vial (g)	Liquid Product After DCM Evaporation (g)	Liquid Product Recovery After DCM Evaporation (%)	
	-	17.6701	18.1356	0.47	77	

Reaction 6, HVGO, 4500kPa(g) H$_2$, 390°C, 2h, 873RPM, 30min Cool Time

#	Reactor Bottom Before Reaction (g)	Liquid Feed Loaded (g)	Catalyst Type	Catalyst Loaded (g)	Loaded Reactor Bottom + Top (g)	Reactor Top Before Reaction (g)
	217.806	0.616	-	-	524.289	305.867
	Loaded Reactor Bottom + Top + Neever·Seez (g)	Mass of Neever·Seez (g)	Pressure Test (MPa(g))	Loaded Reactor Bottom + Top + Neever·Seez + H$_2$ at Atmosphere (g)	Loaded Reactor Bottom + Top + Neever·Seez + H$_2$ at Pressure (g)	H$_2$ Gas Loaded (g)
	524.308	0.019	12	524.281	524.36	0.079
	Liquid + Catalyst + H$_2$ Loaded Before Reaction (g)	After Reaction Mass (g)	Difference of Before & After Reaction (g)	After Reaction Mass - Product Gas Released (g)	Product Gas Released (g)	Reactor Bottom After Reaction (g)
	0.695	524.363	-0.003	524.272	0.091	218.419
	Reactor Top After Reaction (g)	Liquid Product + Catalyst Recovered (g)	Liquid + Gas Products + Catalyst Recovered (g)	Total Mass Recovery (%)	Empty Filter Paper (g)	Full Filter Paper (g)
	305.846	0.592	0.683	98	-	-
	Spent Catalyst Recovered (g)	Empty Vial (g)	Full Vial (g)	Liquid Product After DCM Evaporation (g)	Liquid Product Recovery After DCM Evaporation (%)	
	-	17.6013	18.0802	0.48	78	

Reaction 7, HVGO, 4500kPa(g) H₂, 390°C, 2h, 848RPM, 20min Cool Time — H_2, $390°C$

#	Reactor Bottom Before Reaction (g)	Liquid Feed Loaded (g)	Catalyst Type	Catalyst Loaded (g)	Loaded Reactor Bottom + Top (g)	Reactor Top Before Reaction (g)
	218.39	0.61	Pellets	0.101	524.89	305.789
	Loaded Reactor Bottom + Top + Neever·Seez (g)	Mass of Neever·Seez (g)	Pressure Test (MPa(g))	Loaded Reactor Bottom + Top + Neever·Seez + H₂ at Atmosphere (g)	Loaded Reactor Bottom + Top + Neever·Seez + H₂ at Pressure (g)	H₂ Gas Loaded (g)
	524.902	0.012	13	524.882	524.956	0.074
	Liquid + Catalyst + H₂ Loaded Before Reaction (g)	After Reaction Mass (g)	Difference of Before & After Reaction (g)	After Reaction Mass - Product Gas Released (g)	Product Gas Released (g)	Reactor Bottom After Reaction (g)
	0.785	524.981	-0.025	524.898	0.083	219.024
	Reactor Top After Reaction (g)	Liquid Product + Catalyst Recovered (g)	Liquid + Gas Products + Catalyst Recovered (g)	Total Mass Recovery (%)	Empty Filter Paper (g)	Full Filter Paper (g)
	305.862	0.707	0.79	101	-	-
	Spent Catalyst Recovered (g)	Empty Vial (g)	Full Vial (g)	Liquid Product After DCM Evaporation (g)	Liquid Product Recovery After DCM Evaporation (%)	
	-	17.7368	18.2582	0.52	85	

Reaction 8, HVGO, 4500kPa(g) H₂, 390°C, 2h, 868RPM, 20min Cool Time

#	Reactor Bottom Before Reaction (g)	Liquid Feed Loaded (g)	Catalyst Type	Catalyst Loaded (g)	Loaded Reactor Bottom + Top (g)	Reactor Top Before Reaction (g)
	218.383	0.618	Pellets	0.107	524.895	305.787
	Loaded Reactor Bottom + Top + Neever·Seez (g)	Mass of Neever·Seez (g)	Pressure Test (MPa(g))	Loaded Reactor Bottom + Top + Neever·Seez + H₂ at Atmosphere (g)	Loaded Reactor Bottom + Top + Neever·Seez + H₂ at Pressure (g)	H₂ Gas Loaded (g)
	524.906	0.011	13	524.88	524.957	0.077
	Liquid + Catalyst + H₂ Loaded Before Reaction (g)	After Reaction Mass (g)	Difference of Before & After Reaction (g)	After Reaction Mass - Product Gas Released (g)	Product Gas Released (g)	Reactor Bottom After Reaction (g)
	0.802	524.967	-0.01	524.883	0.084	219.069
	Reactor Top After Reaction (g)	Liquid Product + Catalyst Recovered (g)	Liquid + Gas Products + Catalyst Recovered (g)	Total Mass Recovery (%)	Empty Filter Paper (g)	Full Filter Paper (g)
	305.815	0.714	0.798	100	-	-
	Spent Catalyst Recovered (g)	Empty Vial (g)	Full Vial (g)	Liquid Product After DCM Evaporation (g)	Liquid Product Recovery After DCM Evaporation (%)	
	-	17.7725	18.342	0.57	92	

#	Reactor Bottom Before Reaction (g)	Liquid Feed Loaded (g)	Catalyst Type	Catalyst Loaded (g)	Loaded Reactor Bottom + Top (g)	Reactor Top Before Reaction (g)
	218.346	0.607	Pellets	0.103	524.84	305.784
	Loaded Reactor Bottom + Top + Neever·Seez (g)	**Mass of Neever·Seez (g)**	**Pressure Test (MPa(g))**	**Loaded Reactor Bottom + Top + Neever·Seez + H$_2$ at Atmosphere (g)**	**Loaded Reactor Bottom + Top + Neever·Seez + H$_2$ at Pressure (g)**	**H$_2$ Gas Loaded (g)**
	524.861	0.021	13	524.84	524.914	0.074
	Liquid + Catalyst + H$_2$ Loaded Before Reaction (g)	**After Reaction Mass (g)**	**Difference of Before & After Reaction (g)**	**After Reaction Mass - Product Gas Released (g)**	**Product Gas Released (g)**	**Reactor Bottom After Reaction (g)**
	0.784	524.919	-0.005	524.837	0.082	218.986
	Reactor Top After Reaction (g)	**Liquid Product + Catalyst Recovered (g)**	**Liquid + Gas Products + Catalyst Recovered (g)**	**Total Mass Recovery (%)**	**Empty Filter Paper (g)**	**Full Filter Paper (g)**
	305.85	0.706	0.788	101	-	-
	Spent Catalyst Recovered (g)	**Empty Vial (g)**	**Full Vial (g)**	**Liquid Product After DCM Evaporation (g)**	**Liquid Product Recovery After DCM Evaporation (%)**	
	-	17.7738	18.2637	0.49	81	

Reaction 9, HVGO, 4500kPa(g) H$_2$, 390°C, 2h, 878RPM, 20min Cool Time

#	Reactor Bottom Before Reaction (g)	Liquid Feed Loaded (g)	Catalyst Type	Catalyst Loaded (g)	Loaded Reactor Bottom + Top (g)	Reactor Top Before Reaction (g)
	218.261	0.619	Pellets	0.104	648.181	429.197
	Loaded Reactor Bottom + Top + Neever·Seez (g)	**Mass of Neever·Seez (g)**	**Pressure Test (MPa(g))**	**Loaded Reactor Bottom + Top + Neever·Seez + H$_2$ at Atmosphere (g)**	**Loaded Reactor Bottom + Top + Neever·Seez + H$_2$ at Pressure (g)**	**H$_2$ Gas Loaded (g)**
	648.19	0.009	13	648.183	648.253	0.07
	Liquid + Catalyst + H$_2$ Loaded Before Reaction (g)	**After Reaction Mass (g)**	**Difference of Before & After Reaction (g)**	**After Reaction Mass - Product Gas Released (g)**	**Product Gas Released (g)**	**Reactor Bottom After Reaction (g)**
	0.793	648.221	0.032	648.143	0.078	218.897
	Reactor Top After Reaction (g)	**Liquid Product + Catalyst Recovered (g)**	**Liquid + Gas Products + Catalyst Recovered (g)**	**Total Mass Recovery (%)**	**Empty Filter Paper (g)**	**Full Filter Paper (g)**
	429.23	0.669	0.747	94	1.0274	1.174
	Spent Catalyst Recovered (g)	**Empty Vial (g)**	**Full Vial (g)**	**Liquid Product After DCM Evaporation (g)**	**Liquid Product Recovery After DCM Evaporation (%)**	
	0.1466	17.6886	18.1052	0.42	67	

Reaction 10, HVGO, 4500kPa(g) H$_2$, 390°C, 2h, 360RPM, 20min Cool Time

Reaction 11, HVGO, 4500kPa(g) H₂, 390°C, 2h, 360RPM, 30min Cool Time

#	Reactor Bottom Before Reaction (g)	Liquid Feed Loaded (g)	Catalyst Type	Catalyst Loaded (g)	Loaded Reactor Bottom + Top (g)	Reactor Top Before Reaction (g)
	218.28	0.609	Pellets	0.112	648.178	429.177
	Loaded Reactor Bottom + Top + Neever·Seez (g)	Mass of Neever·Seez (g)	Pressure Test (MPa(g))	Loaded Reactor Bottom + Top + Neever·Seez + H₂ at Atmosphere (g)	Loaded Reactor Bottom + Top + Neever·Seez + H₂ at Pressure (g)	H₂ Gas Loaded (g)
	648.191	0.013	13	648.171	648.241	0.07
	Liquid + Catalyst + H₂ Loaded Before Reaction (g)	After Reaction Mass (g)	Difference of Before & After Reaction (g)	After Reaction Mass - Product Gas Released (g)	Product Gas Released (g)	Reactor Bottom After Reaction (g)
	0.791	648.264	-0.023	648.186	0.078	218.963
	Reactor Top After Reaction (g)	Liquid Product + Catalyst Recovered (g)	Liquid + Gas Products + Catalyst Recovered (g)	Total Mass Recovery (%)	Empty Filter Paper (g)	Full Filter Paper (g)
	429.192	0.698	0.776	98	1.062	1.1873
	Spent Catalyst Recovered (g)	Empty Vial (g)	Full Vial (g)	Liquid Product After DCM Evaporation (g)	Liquid Product Recovery After DCM Evaporation (%)	
	0.1253	17.5971	18.078	0.48	79	

Reaction 12, HVGO, 4500kPa(g) H₂, 390°C, 2.25h, 360RPM, 35min Cool Time

#	Reactor Bottom Before Reaction (g)	Liquid Feed Loaded (g)	Catalyst Type	Catalyst Loaded (g)	Loaded Reactor Bottom + Top (g)	Reactor Top Before Reaction (g)
	217.887	0.624	Pellets	0.104	1028.06	817.29
	Loaded Reactor Bottom + Top + Neever·Seez (g)	Mass of Neever·Seez (g)	Pressure Test (MPa(g))	Loaded Reactor Bottom + Top + Neever·Seez + H₂ at Atmosphere (g)	Loaded Reactor Bottom + Top + Neever·Seez + H₂ at Pressure (g)	H₂ Gas Loaded (g)
	1028.08	0.02	12.5	1035.59	1035.67	0.08
	Liquid + Catalyst + H₂ Loaded Before Reaction (g)	After Reaction Mass (g)	Difference of Before & After Reaction (g)	After Reaction Mass - Product Gas Released (g)	Product Gas Released (g)	Reactor Bottom After Reaction (g)
	0.808	1035.66	0.01	1035.57	0.09	218.58
	Reactor Top After Reaction (g)	Liquid Product + Catalyst Recovered (g)	Liquid + Gas Products + Catalyst Recovered (g)	Total Mass Recovery (%)	Empty Filter Paper (g)	Full Filter Paper (g)
	817.29	0.693	0.783	97	1.0457	1.1741
	Spent Catalyst Recovered (g)	Empty Vial (g)	Full Vial (g)	Liquid Product After DCM Evaporation (g)	Liquid Product Recovery After DCM Evaporation (%)	
	0.1284	18.2889	18.7904	0.50	80	

#	Reactor Bottom Before Reaction (g)	Liquid Feed Loaded (g)	Catalyst Type	Catalyst Loaded (g)	Loaded Reactor Bottom + Top (g)	Reactor Top Before Reaction (g)
	217.869	0.613	Pellets	0.101	524.394	305.811
	Loaded Reactor Bottom + Top + Neever·Seez (g)	Mass of Neever·Seez (g)	Pressure Test (MPa(g))	Loaded Reactor Bottom + Top + Neever·Seez + H$_2$ at Atmosphere (g)	Loaded Reactor Bottom + Top + Neever·Seez + H$_2$ at Pressure (g)	H$_2$ Gas Loaded (g)
	524.396	0.002	13	524.368	524.444	0.076
	Liquid + Catalyst + H$_2$ Loaded Before Reaction (g)	After Reaction Mass (g)	Difference of Before & After Reaction (g)	After Reaction Mass - Product Gas Released (g)	Product Gas Released (g)	Reactor Bottom After Reaction (g)
	0.79	524.478	-0.034	524.396	0.082	218.503
	Reactor Top After Reaction (g)	Liquid Product + Catalyst Recovered (g)	Liquid + Gas Products + Catalyst Recovered (g)	Total Mass Recovery (%)	Empty Filter Paper (g)	Full Filter Paper (g)
	305.877	0.7	0.782	99	1.0454	1.1582
	Spent Catalyst Recovered (g)	Empty Vial (g)	Full Vial (g)	Liquid Product After DCM Evaporation (g)	Liquid Product Recovery After DCM Evaporation (%)	
	0.1128	17.68	18.1267	0.45	73	

Reaction 13, HVGO, 4500kPa(g) H$_2$, 390°C, 2h, 884RPM, 20min Cool Time

#	Reactor Bottom Before Reaction (g)	Liquid Feed Loaded (g)	Catalyst Type	Catalyst Loaded (g)	Loaded Reactor Bottom + Top (g)	Reactor Top Before Reaction (g)
	217.867	0.607	Pellets	0.106	524.396	305.816
	Loaded Reactor Bottom + Top + Neever·Seez (g)	Mass of Neever·Seez (g)	Pressure Test (MPa(g))	Loaded Reactor Bottom + Top + Neever·Seez + H$_2$ at Atmosphere (g)	Loaded Reactor Bottom + Top + Neever·Seez + H$_2$ at Pressure (g)	H$_2$ Gas Loaded (g)
	524.404	0.008	13	524.375	524.454	0.079
	Liquid + Catalyst + H$_2$ Loaded Before Reaction (g)	After Reaction Mass (g)	Difference of Before & After Reaction (g)	After Reaction Mass - Product Gas Released (g)	Product Gas Released (g)	Reactor Bottom After Reaction (g)
	0.792	524.485	-0.031	524.405	0.08	218.524
	Reactor Top After Reaction (g)	Liquid Product + Catalyst Recovered (g)	Liquid + Gas Products + Catalyst Recovered (g)	Total Mass Recovery (%)	Empty Filter Paper (g)	Full Filter Paper (g)
	305.873	0.714	0.794	100	1.0263	1.164
	Spent Catalyst Recovered (g)	Empty Vial (g)	Full Vial (g)	Liquid Product After DCM Evaporation (g)	Liquid Product Recovery After DCM Evaporation (%)	
	0.1377	17.7185	18.1409	0.42	70	

Reaction 14, HVGO, 4500kPa(g) H$_2$, 390°C, 2h, 882RPM, 20min Cool Time

Reaction 15, HVGO, 4500kPa(g) H$_2$, 390°C, 2h, 866RPM, 30min Cool Time

#	Reactor Bottom Before Reaction (g)	Liquid Feed Loaded (g)	Catalyst Type	Catalyst Loaded (g)	Loaded Reactor Bottom + Top (g)	Reactor Top Before Reaction (g)
	217.88	0.603	Pellets	0.103	524.401	305.815
	Loaded Reactor Bottom + Top + Neever·Seez (g)	Mass of Neever·Seez (g)	Pressure Test (MPa(g))	Loaded Reactor Bottom + Top + Neever·Seez + H$_2$ at Atmosphere (g)	Loaded Reactor Bottom + Top + Neever·Seez + H$_2$ at Pressure (g)	H$_2$ Gas Loaded (g)
	524.406	0.005	13	524.387	524.468	0.081
	Liquid + Catalyst + H$_2$ Loaded Before Reaction (g)	After Reaction Mass (g)	Difference of Before & After Reaction (g)	After Reaction Mass - Product Gas Released (g)	Product Gas Released (g)	Reactor Bottom After Reaction (g)
	0.787	524.468	0	524.387	0.081	218.512
	Reactor Top After Reaction (g)	Liquid Product + Catalyst Recovered (g)	Liquid + Gas Products + Catalyst Recovered (g)	Total Mass Recovery (%)	Empty Filter Paper (g)	Full Filter Paper (g)
	305.864	0.681	0.762	97	1.0419	1.1539
	Spent Catalyst Recovered (g)	Empty Vial (g)	Full Vial (g)	Liquid Product After DCM Evaporation (g)	Liquid Product Recovery After DCM Evaporation (%)	
	0.112	17.5365	17.9454	0.41	68	

Reaction 16, DMDS, 3000kPa(g) H$_2$, 20-360°C, 4.5h, 360RPM, 30min Cool Time

#	Reactor Bottom Before Reaction (g)	Liquid Feed Loaded (g)	Catalyst Type	Catalyst Loaded (g)	Loaded Reactor Bottom + Top (g)	Reactor Top Before Reaction (g)
	218.257	0.338	Dried Pellets	1.317	649.092	429.18
	Loaded Reactor Bottom + Top + Neever·Seez (g)	Mass of Neever·Seez (g)	Pressure Test (MPa(g))	Loaded Reactor Bottom + Top + Neever·Seez + H$_2$ at Atmosphere (g)	Loaded Reactor Bottom + Top + Neever·Seez + H$_2$ at Pressure (g)	H$_2$ Gas Loaded (g)
	649.103	0.011	12	649.073	649.122	0.049
	Liquid + Catalyst + H$_2$ Loaded Before Reaction (g)	After Reaction Mass (g)	Difference of Before & After Reaction (g)	After Reaction Mass - Product Gas Released (g)	Product Gas Released (g)	Reactor Bottom After Reaction (g)
	1.704	649.124	-0.002	648.873	0.25	219.702
	Reactor Top After Reaction (g)	Liquid Product + Catalyst Recovered (g)	Liquid + Gas Products + Catalyst Recovered (g)	Total Mass Recovery (%)	Empty Filter Paper (g)	Full Filter Paper (g)
	429.192	1.46	1.708	100	-	-
	Spent Catalyst Recovered (g)	Empty Vial (g)	Full Vial (g)	Liquid Product After DCM Evaporation (g)	Liquid Product Recovery After DCM Evaporation (%)	
	1.39	17.6243	19.0143	-	-	

#	Reactor Bottom Before Reaction (g)	Liquid Feed Loaded (g)	Catalyst Type	Catalyst Loaded (g)	Loaded Reactor Bottom + Top (g)	Reactor Top Before Reaction (g)
	217.432	0.464	Dried Pellets	1.385	649.2	429.919
	Loaded Reactor Bottom + Top + Neever·Seez (g)	Mass of Neever·Seez (g)	Pressure Test (MPa(g))	Loaded Reactor Bottom + Top + Neever·Seez + H₂ at Atmosphere (g)	Loaded Reactor Bottom + Top + Neever·Seez + H₂ at Pressure (g)	H₂ Gas Loaded (g)
	649.209	0.009	12	649.285	649.328	0.043
	Liquid + Catalyst + H₂ Loaded Before Reaction (g)	After Reaction Mass (g)	Difference of Before & After Reaction (g)	After Reaction Mass - Product Gas Released (g)	Product Gas Released (g)	Reactor Bottom After Reaction (g)
	1.892	649.35	-0.022	648.93	0.42	218.731
	Reactor Top After Reaction (g)	Liquid Product + Catalyst Recovered (g)	Liquid + Gas Products + Catalyst Recovered (g)	Total Mass Recovery (%)	Empty Filter Paper (g)	Full Filter Paper (g)
	430.035	1.42	1.835	97	-	-
	Spent Catalyst Recovered (g)	Empty Vial (g)	Full Vial (g)	Liquid Product After DCM Evaporation (g)	Liquid Product Recovery After DCM Evaporation (%)	
	1.41	17.5648	18.9797	-	-	

Reaction 17, DMDS, 3000kPa(g) H₂, 20-360°C, 4.2h, 360RPM, 30min Cool Time

#	Reactor Bottom Before Reaction (g)	Liquid Feed Loaded (g)	Catalyst Type	Catalyst Loaded (g)	Loaded Reactor Bottom + Top (g)	Reactor Top Before Reaction (g)
	217.819	0.499	Dried < 45μm	1.404	525.598	305.876
	Loaded Reactor Bottom + Top + Neever·Seez (g)	Mass of Neever·Seez (g)	Pressure Test (MPa(g))	Loaded Reactor Bottom + Top + Neever·Seez + H₂ at Atmosphere (g)	Loaded Reactor Bottom + Top + Neever·Seez + H₂ at Pressure (g)	H₂ Gas Loaded (g)
	525.6	0.002	12	525.57	525.621	0.051
	Liquid + Catalyst + H₂ Loaded Before Reaction (g)	After Reaction Mass (g)	Difference of Before & After Reaction (g)	After Reaction Mass - Product Gas Released (g)	Product Gas Released (g)	Reactor Bottom After Reaction (g)
	1.954	525.637	-0.016	525.235	0.40	218.917
	Reactor Top After Reaction (g)	Liquid Product + Catalyst Recovered (g)	Liquid + Gas Products + Catalyst Recovered (g)	Total Mass Recovery (%)	Empty Filter Paper (g)	Full Filter Paper (g)
	306.039	1.26	1.663	85	-	-
	Spent Catalyst Recovered (g)	Empty Vial (g)	Full Vial (g)	Liquid Product After DCM Evaporation (g)	Liquid Product Recovery After DCM Evaporation (%)	
	1.17	17.5478	18.7203	-	-	

Reaction 18, DMDS, 3300kPa(g) H₂, 20-360°C, 4.2h, 880RPM, 30min Cool Time

#	Reactor Bottom Before Reaction (g)	Liquid Feed Loaded (g)	Catalyst Type	Catalyst Loaded (g)	Loaded Reactor Bottom + Top (g)	Reactor Top Before Reaction (g)
	217.828	0.303	Dried < 45μm	1.242	525.226	305.853
	Loaded Reactor Bottom + Top + Neever·Seez (g)	Mass of Neever·Seez (g)	Pressure Test (MPa(g))	Loaded Reactor Bottom + Top + Neever·Seez + H₂ at Atmosphere (g)	Loaded Reactor Bottom + Top + Neever·Seez + H₂ at Pressure (g)	H₂ Gas Loaded (g)
	525.229	0.003	12.5	525.198	525.25	0.052
	Liquid + Catalyst + H₂ Loaded Before Reaction (g)	After Reaction Mass (g)	Difference of Before & After Reaction (g)	After Reaction Mass - Product Gas Released (g)	Product Gas Released (g)	Reactor Bottom After Reaction (g)
	1.597	525.278	-0.028	524.919	0.36	218.991
	Reactor Top After Reaction (g)	Liquid Product + Catalyst Recovered (g)	Liquid + Gas Products + Catalyst Recovered (g)	Total Mass Recovery (%)	Empty Filter Paper (g)	Full Filter Paper (g)
	305.869	1.18	1.538	96	-	-
	Spent Catalyst Recovered (g)	Empty Vial (g)	Full Vial (g)	Liquid Product After DCM Evaporation (g)	Liquid Product Recovery After DCM Evaporation (%)	
	-	17.5478	18.7203	-	-	

Reaction 19, DMDS, 3000kPa(g) H₂, 20-360°C, 4.2h, 863RPM, 30min Cool Time

#	Reactor Bottom Before Reaction (g)	Liquid Feed Loaded (g)	Catalyst Type	Catalyst Loaded (g)	Loaded Reactor Bottom + Top (g)	Reactor Top Before Reaction (g)
	217.39	0.605	Sulfided Pellets	0.097	452.52	234.428
	Loaded Reactor Bottom + Top + Neever·Seez (g)	Mass of Neever·Seez (g)	Pressure Test (MPa(g))	Loaded Reactor Bottom + Top + Neever·Seez + H₂ at Atmosphere (g)	Loaded Reactor Bottom + Top + Neever·Seez + H₂ at Pressure (g)	H₂ Gas Loaded (g)
	452.531	0.011	12	452.513	452.576	0.063
	Liquid + Catalyst + H₂ Loaded Before Reaction (g)	After Reaction Mass (g)	Difference of Before & After Reaction (g)	After Reaction Mass - Product Gas Released (g)	Product Gas Released (g)	Reactor Bottom After Reaction (g)
	0.765	452.602	-0.026	452.525	0.077	218.064
	Reactor Top After Reaction (g)	Liquid Product + Catalyst Recovered (g)	Liquid + Gas Products + Catalyst Recovered (g)	Total Mass Recovery (%)	Empty Filter Paper (g)	Full Filter Paper (g)
	234.4	0.646	0.723	95	1.0396	1.1282
	Spent Catalyst Recovered (g)	Empty Vial (g)	Full Vial (g)	Liquid Product After DCM Evaporation (g)	Liquid Product Recovery After DCM Evaporation (%)	
	0.0886	17.3509	17.8316	0.48	79	

Reaction 20, HVGO, 4500kPa(g) H₂, 390°C, 2h, 878RPM, 30min Cool Time

#	Reactor Bottom Before Reaction (g)	Liquid Feed Loaded (g)	Catalyst Type	Catalyst Loaded (g)	Loaded Reactor Bottom + Top (g)	Reactor Top Before Reaction (g)
	217.38	0.619	Sulfided Pellets	0.1	452.374	234.275
	Loaded Reactor Bottom + Top + Neever·Seez (g)	**Mass of Neever·Seez (g)**	**Pressure Test (MPa(g))**	**Loaded Reactor Bottom + Top + Neever·Seez + H₂ at Atmosphere (g)**	**Loaded Reactor Bottom + Top + Neever·Seez + H₂ at Pressure (g)**	**H₂ Gas Loaded (g)**
	452.38	0.006	12	452.362	452.43	0.068
	Liquid + Catalyst + H₂ Loaded Before Reaction (g)	**After Reaction Mass (g)**	**Difference of Before & After Reaction (g)**	**After Reaction Mass - Product Gas Released (g)**	**Product Gas Released (g)**	**Reactor Bottom After Reaction (g)**
	0.787	452.47	-0.04	452.387	0.083	218.069
	Reactor Top After Reaction (g)	**Liquid Product + Catalyst Recovered (g)**	**Liquid + Gas Products + Catalyst Recovered (g)**	**Total Mass Recovery (%)**	**Empty Filter Paper (g)**	**Full Filter Paper (g)**
	234.305	0.719	0.802	102	1.0552	1.1498
	Spent Catalyst Recovered (g)	**Empty Vial (g)**	**Full Vial (g)**	**Liquid Product After DCM Evaporation (g)**	**Liquid Product Recovery After DCM Evaporation (%)**	
	0.0946	17.484	18.0232	0.54	87	

Reaction 21, HVGO, 4500kPa(g) H₂, 390°C, 2h, 886RPM, 30min Cool Time

#	Reactor Bottom Before Reaction (g)	Liquid Feed Loaded (g)	Catalyst Type	Catalyst Loaded (g)	Loaded Reactor Bottom + Top (g)	Reactor Top Before Reaction (g)
	217.748	0.611	Sulfided Pellets	0.101	524.276	305.816
	Loaded Reactor Bottom + Top + Neever·Seez (g)	**Mass of Neever·Seez (g)**	**Pressure Test (MPa(g))**	**Loaded Reactor Bottom + Top + Neever·Seez + H₂ at Atmosphere (g)**	**Loaded Reactor Bottom + Top + Neever·Seez + H₂ at Pressure (g)**	**H₂ Gas Loaded (g)**
	524.288	0.012	12	524.266	524.343	0.077
	Liquid + Catalyst + H₂ Loaded Before Reaction (g)	**After Reaction Mass (g)**	**Difference of Before & After Reaction (g)**	**After Reaction Mass - Product Gas Released (g)**	**Product Gas Released (g)**	**Reactor Bottom After Reaction (g)**
	0.789	524.355	-0.012	524.273	0.082	218.407
	Reactor Top After Reaction (g)	**Liquid Product + Catalyst Recovered (g)**	**Liquid + Gas Products + Catalyst Recovered (g)**	**Total Mass Recovery (%)**	**Empty Filter Paper (g)**	**Full Filter Paper (g)**
	305.862	0.705	0.787	100	1.039	1.1286
	Spent Catalyst Recovered (g)	**Empty Vial (g)**	**Full Vial (g)**	**Liquid Product After DCM Evaporation (g)**	**Liquid Product Recovery After DCM Evaporation (%)**	
	0.0896	17.565	18.0611	0.50	81	

Reaction 22, HVGO, 4500kPa(g) H₂, 390°C, 2h, 892RPM, 25min Cool Time

#	Reactor Bottom Before Reaction (g)	Liquid Feed Loaded (g)	Catalyst Type	Catalyst Loaded (g)	Loaded Reactor Bottom + Top (g)	Reactor Top Before Reaction (g)
	217.742	0.619	Sulfided Pellets	0.105	453.687	235.221
	Loaded Reactor Bottom + Top + Neever·Seez (g)	Mass of Neever·Seez (g)	Pressure Test (MPa(g))	Loaded Reactor Bottom + Top + Neever·Seez + H₂ at Atmosphere (g)	Loaded Reactor Bottom + Top + Neever·Seez + H₂ at Pressure (g)	H₂ Gas Loaded (g)
	453.694	0.007	12	453.675	453.744	0.069
	Liquid + Catalyst + H₂ Loaded Before Reaction (g)	After Reaction Mass (g)	Difference of Before & After Reaction (g)	After Reaction Mass - Product Gas Released (g)	Product Gas Released (g)	Reactor Bottom After Reaction (g)
	0.793	453.771	-0.027	453.691	0.08	218.417
	Reactor Top After Reaction (g)	Liquid Product + Catalyst Recovered (g)	Liquid + Gas Products + Catalyst Recovered (g)	Total Mass Recovery (%)	Empty Filter Paper (g)	Full Filter Paper (g)
	235.255	0.709	0.789	99	1.0252	1.132
	Spent Catalyst Recovered (g)	Empty Vial (g)	Full Vial (g)	Liquid Product After DCM Evaporation (g)	Liquid Product Recovery After DCM Evaporation (%)	
	0.1068	17.5858	18.1085	0.52	84	

Reaction 23, HVGO, 4500kPa(g) H₂, 390°C, 1.5h, 896RPM, 35min Cool Time

#	Reactor Bottom Before Reaction (g)	Liquid Feed Loaded (g)	Catalyst Type	Catalyst Loaded (g)	Loaded Reactor Bottom + Top (g)	Reactor Top Before Reaction (g)
	217.364	0.61	Sulfided Pellets	0.097	452.354	234.283
	Loaded Reactor Bottom + Top + Neever·Seez (g)	Mass of Neever·Seez (g)	Pressure Test (MPa(g))	Loaded Reactor Bottom + Top + Neever·Seez + H₂ at Atmosphere (g)	Loaded Reactor Bottom + Top + Neever·Seez + H₂ at Pressure (g)	H₂ Gas Loaded (g)
	452.356	0.002	12	452.331	452.402	0.071
	Liquid + Catalyst + H₂ Loaded Before Reaction (g)	After Reaction Mass (g)	Difference of Before & After Reaction (g)	After Reaction Mass - Product Gas Released (g)	Product Gas Released (g)	Reactor Bottom After Reaction (g)
	0.778	452.412	-0.01	452.329	0.083	218.02
	Reactor Top After Reaction (g)	Liquid Product + Catalyst Recovered (g)	Liquid + Gas Products + Catalyst Recovered (g)	Total Mass Recovery (%)	Empty Filter Paper (g)	Full Filter Paper (g)
	234.308	0.681	0.764	98	1.0364	1.1337
	Spent Catalyst Recovered (g)	Empty Vial (g)	Full Vial (g)	Liquid Product After DCM Evaporation (g)	Liquid Product Recovery After DCM Evaporation (%)	
	0.0973	17.3224	17.849	0.53	86	

Reaction 24, HVGO, 4500kPa(g) H₂, 390°C, 1h, 889RPM, 30min Cool Time

#	Reactor Bottom Before Reaction (g)	Liquid Feed Loaded (g)	Catalyst Type	Catalyst Loaded (g)	Loaded Reactor Bottom + Top (g)	Reactor Top Before Reaction (g)
	217.707	0.625	Sulfided Pellets	0.1	453.677	235.245
	Loaded Reactor Bottom + Top + Neever·Seez (g)	**Mass of Neever·Seez (g)**	**Pressure Test (MPa(g))**	**Loaded Reactor Bottom + Top + Neever·Seez + H$_2$ at Atmosphere (g)**	**Loaded Reactor Bottom + Top + Neever·Seez + H$_2$ at Pressure (g)**	**H$_2$ Gas Loaded (g)**
	453.69	0.013	12	453.661	453.732	0.071
	Liquid + Catalyst + H$_2$ Loaded Before Reaction (g)	**After Reaction Mass (g)**	**Difference of Before & After Reaction (g)**	**After Reaction Mass - Product Gas Released (g)**	**Product Gas Released (g)**	**Reactor Bottom After Reaction (g)**
	0.796	453.754	-0.022	453.673	0.081	218.391
	Reactor Top After Reaction (g)	**Liquid Product + Catalyst Recovered (g)**	**Liquid + Gas Products + Catalyst Recovered (g)**	**Total Mass Recovery (%)**	**Empty Filter Paper (g)**	**Full Filter Paper (g)**
	235.268	0.707	0.788	99	1.0263	1.1363
	Spent Catalyst Recovered (g)	**Empty Vial (g)**	**Full Vial (g)**	**Liquid Product After DCM Evaporation (g)**	**Liquid Product Recovery After DCM Evaporation (%)**	
	0.11	17.3488	17.8852	0.54	86	

Reaction 25, HVGO, 4500kPa(g) H$_2$, 390°C, 1h, 875RPM, 15min Cool Time

#	Reactor Bottom Before Reaction (g)	Liquid Feed Loaded (g)	Catalyst Type	Catalyst Loaded (g)	Loaded Reactor Bottom + Top (g)	Reactor Top Before Reaction (g)
	217.133	0.626	Sulfided Pellets	0.101	452.14	234.28
	Loaded Reactor Bottom + Top + Neever·Seez (g)	**Mass of Neever·Seez (g)**	**Pressure Test (MPa(g))**	**Loaded Reactor Bottom + Top + Neever·Seez + H$_2$ at Atmosphere (g)**	**Loaded Reactor Bottom + Top + Neever·Seez + H$_2$ at Pressure (g)**	**H$_2$ Gas Loaded (g)**
	452.146	0.006	11	452.122	452.192	0.07
	Liquid + Catalyst + H$_2$ Loaded Before Reaction (g)	**After Reaction Mass (g)**	**Difference of Before & After Reaction (g)**	**After Reaction Mass - Product Gas Released (g)**	**Product Gas Released (g)**	**Reactor Bottom After Reaction (g)**
	0.797	452.192	0	452.11	0.082	234.283
	Reactor Top After Reaction (g)	**Liquid Product + Catalyst Recovered (g)**	**Liquid + Gas Products + Catalyst Recovered (g)**	**Total Mass Recovery (%)**	**Empty Filter Paper (g)**	**Full Filter Paper (g)**
	217.832	0.702	0.784	98	1.0453	1.156
	Spent Catalyst Recovered (g)	**Empty Vial (g)**	**Full Vial (g)**	**Liquid Product After DCM Evaporation (g)**	**Liquid Product Recovery After DCM Evaporation (%)**	
	0.1107	17.4071	17.9608	0.55	88	

Reaction 26, HVGO, 4500kPa(g) H$_2$, 370°C, 1h, 888RPM, 20min Cool Time

#	Reactor Bottom Before Reaction (g)	Liquid Feed Loaded (g)	Catalyst Type	Catalyst Loaded (g)	Loaded Reactor Bottom + Top (g)	Reactor Top Before Reaction (g)
	217.924	0.61	Sulfided Pellets	0.099	453.522	234.889
	Loaded Reactor Bottom + Top + Neever·Seez (g)	Mass of Neever·Seez (g)	Pressure Test (MPa(g))	Loaded Reactor Bottom + Top + Neever·Seez + H$_2$ at Atmosphere (g)	Loaded Reactor Bottom + Top + Neever·Seez + H$_2$ at Pressure (g)	H$_2$ Gas Loaded (g)
	453.536	0.014	10.5	453.509	453.583	0.074
	Liquid + Catalyst + H$_2$ Loaded Before Reaction (g)	After Reaction Mass (g)	Difference of Before & After Reaction (g)	After Reaction Mass - Product Gas Released (g)	Product Gas Released (g)	Reactor Bottom After Reaction (g)
	0.783	453.602	-0.019	453.525	0.077	218.597
	Reactor Top After Reaction (g)	Liquid Product + Catalyst Recovered (g)	Liquid + Gas Products + Catalyst Recovered (g)	Total Mass Recovery (%)	Empty Filter Paper (g)	Full Filter Paper (g)
	234.914	0.698	0.775	99	1.031	1.1165
	Spent Catalyst Recovered (g)	Empty Vial (g)	Full Vial (g)	Liquid Product After DCM Evaporation (g)	Liquid Product Recovery After DCM Evaporation (%)	
	0.0855	17.4266	17.9468	0.52	85	

(Reaction 27, HVGO, 4500kPa(g) H$_2$, 350°C, 1h, 900RPM, 20min Cool Time)

#	Reactor Bottom Before Reaction (g)	Liquid Feed Loaded (g)	Catalyst Type	Catalyst Loaded (g)	Loaded Reactor Bottom + Top (g)	Reactor Top Before Reaction (g)
	217.818	0.616	Sulfided Pellets	0.1	453.435	234.901
	Loaded Reactor Bottom + Top + Neever·Seez (g)	Mass of Neever·Seez (g)	Pressure Test (MPa(g))	Loaded Reactor Bottom + Top + Neever·Seez + H$_2$ at Atmosphere (g)	Loaded Reactor Bottom + Top + Neever·Seez + H$_2$ at Pressure (g)	H$_2$ Gas Loaded (g)
	453.451	0.016	10	453.425	453.493	0.068
	Liquid + Catalyst + H$_2$ Loaded Before Reaction (g)	After Reaction Mass (g)	Difference of Before & After Reaction (g)	After Reaction Mass - Product Gas Released (g)	Product Gas Released (g)	Reactor Bottom After Reaction (g)
	0.784	453.49	0.003	453.413	0.077	218.496
	Reactor Top After Reaction (g)	Liquid Product + Catalyst Recovered (g)	Liquid + Gas Products + Catalyst Recovered (g)	Total Mass Recovery (%)	Empty Filter Paper (g)	Full Filter Paper (g)
	234.918	0.695	0.772	98	1.025	1.1362
	Spent Catalyst Recovered (g)	Empty Vial (g)	Full Vial (g)	Liquid Product After DCM Evaporation (g)	Liquid Product Recovery After DCM Evaporation (%)	
	0.1112	17.5303	18.0805	0.55	89	

(Reaction 28, HVGO, 4500kPa(g) H$_2$, 330°C, 1h, 891RPM, 20min Cool Time)

Reaction 29, HVGO, 4500kPa(g) H₂, 310°C, 1h, 893RPM, 20min Cool Time

#	Reactor Bottom Before Reaction (g)	Liquid Feed Loaded (g)	Catalyst Type	Catalyst Loaded (g)	Loaded Reactor Bottom + Top (g)	Reactor Top Before Reaction (g)
	216.948	0.643	Sulfided Pellets	0.108	451.974	234.275

Loaded Reactor Bottom + Top + Neever·Seez (g)	Mass of Neever·Seez (g)	Pressure Test (MPa(g))	Loaded Reactor Bottom + Top + Neever·Seez + H₂ at Atmosphere (g)	Loaded Reactor Bottom + Top + Neever·Seez + H₂ at Pressure (g)	H₂ Gas Loaded (g)
451.977	0.003	10	451.952	452.02	0.068

Liquid + Catalyst + H₂ Loaded Before Reaction (g)	After Reaction Mass (g)	Difference of Before & After Reaction (g)	After Reaction Mass - Product Gas Released (g)	Product Gas Released (g)	Reactor Bottom After Reaction (g)
0.819	452.042	-0.022	451.966	0.076	217.694

Reactor Top After Reaction (g)	Liquid Product + Catalyst Recovered (g)	Liquid + Gas Products + Catalyst Recovered (g)	Total Mass Recovery (%)	Empty Filter Paper (g)	Full Filter Paper (g)
234.282	0.753	0.829	101	1.03	1.1463

Spent Catalyst Recovered (g)	Empty Vial (g)	Full Vial (g)	Liquid Product After DCM Evaporation (g)	Liquid Product Recovery After DCM Evaporation (%)
0.1163	17.4052	17.9962	0.59	92

Reaction 30, HVGO, 4500kPa(g) H₂, 290°C, 1h, 898RPM, 20min Cool Time

#	Reactor Bottom Before Reaction (g)	Liquid Feed Loaded (g)	Catalyst Type	Catalyst Loaded (g)	Loaded Reactor Bottom + Top (g)	Reactor Top Before Reaction (g)
	217.761	0.632	Sulfided Pellets	0.105	453.383	234.885

Loaded Reactor Bottom + Top + Neever·Seez (g)	Mass of Neever·Seez (g)	Pressure Test (MPa(g))	Loaded Reactor Bottom + Top + Neever·Seez + H₂ at Atmosphere (g)	Loaded Reactor Bottom + Top + Neever·Seez + H₂ at Pressure (g)	H₂ Gas Loaded (g)
453.391	0.008	10	453.366	453.434	0.068

Liquid + Catalyst + H₂ Loaded Before Reaction (g)	After Reaction Mass (g)	Difference of Before & After Reaction (g)	After Reaction Mass - Product Gas Released (g)	Product Gas Released (g)	Reactor Bottom After Reaction (g)
0.805	453.45	-0.016	453.374	0.076	218.468

Reactor Top After Reaction (g)	Liquid Product + Catalyst Recovered (g)	Liquid + Gas Products + Catalyst Recovered (g)	Total Mass Recovery (%)	Empty Filter Paper (g)	Full Filter Paper (g)
234.915	0.737	0.813	101	1.0468	1.1597

Spent Catalyst Recovered (g)	Empty Vial (g)	Full Vial (g)	Liquid Product After DCM Evaporation (g)	Liquid Product Recovery After DCM Evaporation (%)
0.1129	17.418	17.9855	0.57	90

Reaction 31, HVGO, 4500kPa(g) H₂, 390°C, 0.5h, 867RPM, 20min Cool Time

#	Reactor Bottom Before Reaction (g)	Liquid Feed Loaded (g)	Catalyst Type	Catalyst Loaded (g)	Loaded Reactor Bottom + Top (g)	Reactor Top Before Reaction (g)
	217.732	0.612	Sulfided Pellets	0.1	524.272	305.828
	Loaded Reactor Bottom + Top + Neever·Seez (g)	Mass of Neever·Seez (g)	Pressure Test (MPa(g))	Loaded Reactor Bottom + Top + Neever·Seez + H₂ at Atmosphere (g)	Loaded Reactor Bottom + Top + Neever·Seez + H₂ at Pressure (g)	H₂ Gas Loaded (g)
	524.274	0.002	12	524.248	524.318	0.07
	Liquid + Catalyst + H₂ Loaded Before Reaction (g)	After Reaction Mass (g)	Difference of Before & After Reaction (g)	After Reaction Mass - Product Gas Released (g)	Product Gas Released (g)	Reactor Bottom After Reaction (g)
	0.782	524.317	0.001	524.23	0.087	218.393
	Reactor Top After Reaction (g)	Liquid Product + Catalyst Recovered (g)	Liquid + Gas Products + Catalyst Recovered (g)	Total Mass Recovery (%)	Empty Filter Paper (g)	Full Filter Paper (g)
	305.843	0.676	0.763	98	1.0426	1.1482
	Spent Catalyst Recovered (g)	Empty Vial (g)	Full Vial (g)	Liquid Product After DCM Evaporation (g)	Liquid Product Recovery After DCM Evaporation (%)	
	0.1056	17.411	17.9091	0.50	81	

Reaction 32, HVGO, 4500kPa(g) H₂, 390°C, 0.5h, 859RPM, 20min Cool Time

#	Reactor Bottom Before Reaction (g)	Liquid Feed Loaded (g)	Catalyst Type	Catalyst Loaded (g)	Loaded Reactor Bottom + Top (g)	Reactor Top Before Reaction (g)
	217.342	0.614	Sulfided Pellets	0.101	452.356	234.299
	Loaded Reactor Bottom + Top + Neever·Seez (g)	Mass of Neever·Seez (g)	Pressure Test (MPa(g))	Loaded Reactor Bottom + Top + Neever·Seez + H₂ at Atmosphere (g)	Loaded Reactor Bottom + Top + Neever·Seez + H₂ at Pressure (g)	H₂ Gas Loaded (g)
	452.364	0.008	12	452.341	452.408	0.067
	Liquid + Catalyst + H₂ Loaded Before Reaction (g)	After Reaction Mass (g)	Difference of Before & After Reaction (g)	After Reaction Mass - Product Gas Released (g)	Product Gas Released (g)	Reactor Bottom After Reaction (g)
	0.782	452.399	0.009	452.315	0.084	217.991
	Reactor Top After Reaction (g)	Liquid Product + Catalyst Recovered (g)	Liquid + Gas Products + Catalyst Recovered (g)	Total Mass Recovery (%)	Empty Filter Paper (g)	Full Filter Paper (g)
	234.318	0.668	0.752	96	1.0153	1.1284
	Spent Catalyst Recovered (g)	Empty Vial (g)	Full Vial (g)	Liquid Product After DCM Evaporation (g)	Liquid Product Recovery After DCM Evaporation (%)	
	0.1131	17.4005	17.9423	0.54	88	

#	Reactor Bottom Before Reaction (g)	Liquid Feed Loaded (g)	Catalyst Type	Catalyst Loaded (g)	Loaded Reactor Bottom + Top (g)	Reactor Top Before Reaction (g)
	217.714	0.614	Sulfided Pellets	0.105	524.246	305.813
	Loaded Reactor Bottom + Top + Neever·Seez (g)	Mass of Neever·Seez (g)	Pressure Test (MPa(g))	Loaded Reactor Bottom + Top + Neever·Seez + H₂ at Atmosphere (g)	Loaded Reactor Bottom + Top + Neever·Seez + H₂ at Pressure (g)	H₂ Gas Loaded (g)
	524.277	0.031	12	524.256	524.33	0.074
	Liquid + Catalyst + H₂ Loaded Before Reaction (g)	After Reaction Mass (g)	Difference of Before & After Reaction (g)	After Reaction Mass - Product Gas Released (g)	Product Gas Released (g)	Reactor Bottom After Reaction (g)
	0.793	524.334	-0.004	524.249	0.085	218.398
	Reactor Top After Reaction (g)	Liquid Product + Catalyst Recovered (g)	Liquid + Gas Products + Catalyst Recovered (g)	Total Mass Recovery (%)	Empty Filter Paper (g)	Full Filter Paper (g)
	305.841	0.712	0.797	101	1.0404	1.1611
	Spent Catalyst Recovered (g)	Empty Vial (g)	Full Vial (g)	Liquid Product After DCM Evaporation (g)	Liquid Product Recovery After DCM Evaporation (%)	
	0.1207	17.4105	17.9163	0.51	82	

Reaction 33, HVGO, 4500kPa(g) H₂, 390°C, 0.25h, 850RPM, 20min Cool Time

#	Reactor Bottom Before Reaction (g)	Liquid Feed Loaded (g)	Catalyst Type	Catalyst Loaded (g)	Loaded Reactor Bottom + Top (g)	Reactor Top Before Reaction (g)
	217.813	0.612	Sulfided < 45μm	0.104	524.356	305.827
	Loaded Reactor Bottom + Top + Neever·Seez (g)	Mass of Neever·Seez (g)	Pressure Test (MPa(g))	Loaded Reactor Bottom + Top + Neever·Seez + H₂ at Atmosphere (g)	Loaded Reactor Bottom + Top + Neever·Seez + H₂ at Pressure (g)	H₂ Gas Loaded (g)
	524.363	0.007	12.5	524.341	524.414	0.073
	Liquid + Catalyst + H₂ Loaded Before Reaction (g)	After Reaction Mass (g)	Difference of Before & After Reaction (g)	After Reaction Mass - Product Gas Released (g)	Product Gas Released (g)	Reactor Bottom After Reaction (g)
	0.789	524.424	-0.01	524.336	0.088	218.484
	Reactor Top After Reaction (g)	Liquid Product + Catalyst Recovered (g)	Liquid + Gas Products + Catalyst Recovered (g)	Total Mass Recovery (%)	Empty Filter Paper (g)	Full Filter Paper (g)
	305.85	0.694	0.782	99	1.0396	1.127
	Spent Catalyst Recovered (g)	Empty Vial (g)	Full Vial (g)	Liquid Product After DCM Evaporation (g)	Liquid Product Recovery After DCM Evaporation (%)	
	0.0874	17.533	18.0523	0.52	85	

Reaction 34, HVGO, 4500kPa(g) H₂, 390°C, 2h, 888RPM, 30min Cool Time

#	Reactor Bottom Before Reaction (g)	Liquid Feed Loaded (g)	Catalyst Type	Catalyst Loaded (g)	Loaded Reactor Bottom + Top (g)	Reactor Top Before Reaction (g)
	217.388	0.614	Sulfided < 45μm	0.105	452.428	234.321
	Loaded Reactor Bottom + Top + Neever·Seez (g)	Mass of Neever·Seez (g)	Pressure Test (MPa(g))	Loaded Reactor Bottom + Top + Neever·Seez + H₂ at Atmosphere (g)	Loaded Reactor Bottom + Top + Neever·Seez + H₂ at Pressure (g)	H₂ Gas Loaded (g)
	452.43	0.002	12	452.414	452.483	0.069
	Liquid + Catalyst + H₂ Loaded Before Reaction (g)	After Reaction Mass (g)	Difference of Before & After Reaction (g)	After Reaction Mass - Product Gas Released (g)	Product Gas Released (g)	Reactor Bottom After Reaction (g)
	0.788	452.528	-0.045	452.438	0.09	218.109
	Reactor Top After Reaction (g)	Liquid Product + Catalyst Recovered (g)	Liquid + Gas Products + Catalyst Recovered (g)	Total Mass Recovery (%)	Empty Filter Paper (g)	Full Filter Paper (g)
	234.318	0.718	0.808	103	1.0333	1.1172
	Spent Catalyst Recovered (g)	Empty Vial (g)	Full Vial (g)	Liquid Product After DCM Evaporation (g)	Liquid Product Recovery After DCM Evaporation (%)	
	0.0839	17.4468	18.0079	0.56	91	

Reaction 35, HVGO, 4500kPa(g) H₂, 390°C, 2h, 874RPM, 30min Cool Time

#	Reactor Bottom Before Reaction (g)	Liquid Feed Loaded (g)	Catalyst Type	Catalyst Loaded (g)	Loaded Reactor Bottom + Top (g)	Reactor Top Before Reaction (g)
	217.678	0.603	Sulfided < 45μm	0.105	453.611	235.225
	Loaded Reactor Bottom + Top + Neever·Seez (g)	Mass of Neever·Seez (g)	Pressure Test (MPa(g))	Loaded Reactor Bottom + Top + Neever·Seez + H₂ at Atmosphere (g)	Loaded Reactor Bottom + Top + Neever·Seez + H₂ at Pressure (g)	H₂ Gas Loaded (g)
	453.622	0.011	11.5	453.601	453.671	0.07
	Liquid + Catalyst + H₂ Loaded Before Reaction (g)	After Reaction Mass (g)	Difference of Before & After Reaction (g)	After Reaction Mass - Product Gas Released (g)	Product Gas Released (g)	Reactor Bottom After Reaction (g)
	0.778	453.674	-0.003	453.591	0.083	218.343
	Reactor Top After Reaction (g)	Liquid Product + Catalyst Recovered (g)	Liquid + Gas Products + Catalyst Recovered (g)	Total Mass Recovery (%)	Empty Filter Paper (g)	Full Filter Paper (g)
	235.247	0.687	0.77	99	1.0558	1.1403
	Spent Catalyst Recovered (g)	Empty Vial (g)	Full Vial (g)	Liquid Product After DCM Evaporation (g)	Liquid Product Recovery After DCM Evaporation (%)	
	0.0845	17.419	17.9611	0.54	90	

Reaction 36, HVGO, 4500kPa(g) H₂, 390°C, 1h, 879RPM, 20min Cool Time

Reaction 37, HVGO, 4500kPa(g) H_2, 390°C, 1h, 870RPM, 25min Cool Time

#	Reactor Bottom Before Reaction (g)	Liquid Feed Loaded (g)	Catalyst Type	Catalyst Loaded (g)	Loaded Reactor Bottom + Top (g)	Reactor Top Before Reaction (g)
	217.649	0.618	Sulfided < 45μm	0.102	524.186	305.817
	Loaded Reactor Bottom + Top + Neever·Seez (g)	Mass of Neever·Seez (g)	Pressure Test (MPa(g))	Loaded Reactor Bottom + Top + Neever·Seez + H_2 at Atmosphere (g)	Loaded Reactor Bottom + Top + Neever·Seez + H_2 at Pressure (g)	H_2 Gas Loaded (g)
	524.202	0.016	11.5	524.182	524.259	0.077
	Liquid + Catalyst + H_2 Loaded Before Reaction (g)	After Reaction Mass (g)	Difference of Before & After Reaction (g)	After Reaction Mass - Product Gas Released (g)	Product Gas Released (g)	Reactor Bottom After Reaction (g)
	0.797	524.28	-0.021	524.196	0.084	218.346
	Reactor Top After Reaction (g)	Liquid Product + Catalyst Recovered (g)	Liquid + Gas Products + Catalyst Recovered (g)	Total Mass Recovery (%)	Empty Filter Paper (g)	Full Filter Paper (g)
	305.852	0.732	0.816	102	1.0186	1.1097
	Spent Catalyst Recovered (g)	Empty Vial (g)	Full Vial (g)	Liquid Product After DCM Evaporation (g)	Liquid Product Recovery After DCM Evaporation (%)	
	0.0911	17.4246	17.9519	0.53	85	

Reaction 38, HVGO, 4500kPa(g) H_2, 390°C, 0.5h, 870RPM, 20min Cool Time

#	Reactor Bottom Before Reaction (g)	Liquid Feed Loaded (g)	Catalyst Type	Catalyst Loaded (g)	Loaded Reactor Bottom + Top (g)	Reactor Top Before Reaction (g)
	217.629	0.619	Sulfided < 45μm	0.105	453.586	235.233
	Loaded Reactor Bottom + Top + Neever·Seez (g)	Mass of Neever·Seez (g)	Pressure Test (MPa(g))	Loaded Reactor Bottom + Top + Neever·Seez + H_2 at Atmosphere (g)	Loaded Reactor Bottom + Top + Neever·Seez + H_2 at Pressure (g)	H_2 Gas Loaded (g)
	453.599	0.013	11	453.57	453.64	0.07
	Liquid + Catalyst + H_2 Loaded Before Reaction (g)	After Reaction Mass (g)	Difference of Before & After Reaction (g)	After Reaction Mass - Product Gas Released (g)	Product Gas Released (g)	Reactor Bottom After Reaction (g)
	0.794	453.641	-0.001	453.559	0.082	218.314
	Reactor Top After Reaction (g)	Liquid Product + Catalyst Recovered (g)	Liquid + Gas Products + Catalyst Recovered (g)	Total Mass Recovery (%)	Empty Filter Paper (g)	Full Filter Paper (g)
	235.232	0.684	0.766	96	1.0427	1.1487
	Spent Catalyst Recovered (g)	Empty Vial (g)	Full Vial (g)	Liquid Product After DCM Evaporation (g)	Liquid Product Recovery After DCM Evaporation (%)	
	0.106	17.319	17.8568	0.54	87	

#	Reactor Bottom Before Reaction (g)	Liquid Feed Loaded (g)	Catalyst Type	Catalyst Loaded (g)	Loaded Reactor Bottom + Top (g)	Reactor Top Before Reaction (g)
	217.167	0.609	Sulfided < 45μm	0.103	452.164	234.285
	Loaded Reactor Bottom + Top + Neever·Seez (g)	Mass of Neever·Seez (g)	Pressure Test (MPa(g))	Loaded Reactor Bottom + Top + Neever·Seez + H₂ at Atmosphere (g)	Loaded Reactor Bottom + Top + Neever·Seez + H₂ at Pressure (g)	H₂ Gas Loaded (g)
	452.171	0.007	11	452.151	452.215	0.064
	Liquid + Catalyst + H₂ Loaded Before Reaction (g)	After Reaction Mass (g)	Difference of Before & After Reaction (g)	After Reaction Mass - Product Gas Released (g)	Product Gas Released (g)	Reactor Bottom After Reaction (g)
	0.776	452.216	-0.001	452.134	0.082	217.861
	Reactor Top After Reaction (g)	Liquid Product + Catalyst Recovered (g)	Liquid + Gas Products + Catalyst Recovered (g)	Total Mass Recovery (%)	Empty Filter Paper (g)	Full Filter Paper (g)
	234.283	0.692	0.774	100	1.0405	1.1318
	Spent Catalyst Recovered (g)	Empty Vial (g)	Full Vial (g)	Liquid Product After DCM Evaporation (g)	Liquid Product Recovery After DCM Evaporation (%)	
	0.0913	17.465	17.9985	0.53	88	

Reaction 39, HVGO, 4500kPa(g) H₂, 390°C, 0.5h, 859RPM, 20min Cool Time

#	Reactor Bottom Before Reaction (g)	Liquid Feed Loaded (g)	Catalyst Type	Catalyst Loaded (g)	Loaded Reactor Bottom + Top (g)	Reactor Top Before Reaction (g)
	217.562	0.619	Sulfided < 45μm	0.104	524.095	305.81
	Loaded Reactor Bottom + Top + Neever·Seez (g)	Mass of Neever·Seez (g)	Pressure Test (MPa(g))	Loaded Reactor Bottom + Top + Neever·Seez + H₂ at Atmosphere (g)	Loaded Reactor Bottom + Top + Neever·Seez + H₂ at Pressure (g)	H₂ Gas Loaded (g)
	524.105	0.01	11	524.089	524.159	0.07
	Liquid + Catalyst + H₂ Loaded Before Reaction (g)	After Reaction Mass (g)	Difference of Before & After Reaction (g)	After Reaction Mass - Product Gas Released (g)	Product Gas Released (g)	Reactor Bottom After Reaction (g)
	0.793	524.164	-0.005	524.076	0.088	218.251
	Reactor Top After Reaction (g)	Liquid Product + Catalyst Recovered (g)	Liquid + Gas Products + Catalyst Recovered (g)	Total Mass Recovery (%)	Empty Filter Paper (g)	Full Filter Paper (g)
	305.832	0.711	0.799	101	1.038	1.129
	Spent Catalyst Recovered (g)	Empty Vial (g)	Full Vial (g)	Liquid Product After DCM Evaporation (g)	Liquid Product Recovery After DCM Evaporation (%)	
	0.091	17.4548	17.9654	0.51	82	

Reaction 40, HVGO, 4500kPa(g) H₂, 370°C, 0.5h, 894RPM, 20min Cool Time

#	Reactor Bottom Before Reaction (g)	Liquid Feed Loaded (g)	Catalyst Type	Catalyst Loaded (g)	Loaded Reactor Bottom + Top (g)	Reactor Top Before Reaction (g)
	217.215	0.62	Sulfided < 45μm	0.101	452.219	234.283
	Loaded Reactor Bottom + Top + Neever·Seez (g)	Mass of Neever·Seez (g)	Pressure Test (MPa(g))	Loaded Reactor Bottom + Top + Neever·Seez + H₂ at Atmosphere (g)	Loaded Reactor Bottom + Top + Neever·Seez + H₂ at Pressure (g)	H₂ Gas Loaded (g)
	452.241	0.022	11.5	452.221	452.288	0.067
	Liquid + Catalyst + H₂ Loaded Before Reaction (g)	After Reaction Mass (g)	Difference of Before & After Reaction (g)	After Reaction Mass - Product Gas Released (g)	Product Gas Released (g)	Reactor Bottom After Reaction (g)
	0.788	452.291	-0.003	452.212	0.079	217.914
	Reactor Top After Reaction (g)	Liquid Product + Catalyst Recovered (g)	Liquid + Gas Products + Catalyst Recovered (g)	Total Mass Recovery (%)	Empty Filter Paper (g)	Full Filter Paper (g)
	234.297	0.713	0.792	101	1.0365	1.1343
	Spent Catalyst Recovered (g)	Empty Vial (g)	Full Vial (g)	Liquid Product After DCM Evaporation (g)	Liquid Product Recovery After DCM Evaporation (%)	
	0.0978	17.2611	17.799	0.54	87	

Reaction 41, HVGO, 4500kPa(g) H₂, 390°C, 0.25h, 880RPM, 20min Cool Time

#	Reactor Bottom Before Reaction (g)	Liquid Feed Loaded (g)	Catalyst Type	Catalyst Loaded (g)	Loaded Reactor Bottom + Top (g)	Reactor Top Before Reaction (g)
	217.609	0.606	Sulfided < 45μm	0.1	524.133	305.818
	Loaded Reactor Bottom + Top + Neever·Seez (g)	Mass of Neever·Seez (g)	Pressure Test (MPa(g))	Loaded Reactor Bottom + Top + Neever·Seez + H₂ at Atmosphere (g)	Loaded Reactor Bottom + Top + Neever·Seez + H₂ at Pressure (g)	H₂ Gas Loaded (g)
	524.147	0.014	11	524.124	524.192	0.068
	Liquid + Catalyst + H₂ Loaded Before Reaction (g)	After Reaction Mass (g)	Difference of Before & After Reaction (g)	After Reaction Mass - Product Gas Released (g)	Product Gas Released (g)	Reactor Bottom After Reaction (g)
	0.774	524.197	-0.005	524.119	0.078	218.299
	Reactor Top After Reaction (g)	Liquid Product + Catalyst Recovered (g)	Liquid + Gas Products + Catalyst Recovered (g)	Total Mass Recovery (%)	Empty Filter Paper (g)	Full Filter Paper (g)
	305.826	0.698	0.776	100	1.0361	1.1337
	Spent Catalyst Recovered (g)	Empty Vial (g)	Full Vial (g)	Liquid Product After DCM Evaporation (g)	Liquid Product Recovery After DCM Evaporation (%)	
	0.0976	17.4613	17.9445	0.48	80	

Reaction 42, HVGO, 4500kPa(g) H₂, 390°C, 0.25h, 890RPM, 20min Cool Time

#	Reactor Bottom Before Reaction (g)	Liquid Feed Loaded (g)	Catalyst Type	Catalyst Loaded (g)	Loaded Reactor Bottom + Top (g)	Reactor Top Before Reaction (g)
	217.91	0.603	Sulfided < 45μm	0.102	453.553	234.938
	Loaded Reactor Bottom + Top + Neever·Seez (g)	**Mass of Neever·Seez (g)**	**Pressure Test (MPa(g))**	**Loaded Reactor Bottom + Top + Neever·Seez + H₂ at Atmosphere (g)**	**Loaded Reactor Bottom + Top + Neever·Seez + H₂ at Pressure (g)**	**H₂ Gas Loaded (g)**
	453.555	0.002	10	453.509	453.582	0.073
	Liquid + Catalyst + H₂ Loaded Before Reaction (g)	**After Reaction Mass (g)**	**Difference of Before & After Reaction (g)**	**After Reaction Mass - Product Gas Released (g)**	**Product Gas Released (g)**	**Reactor Bottom After Reaction (g)**
	0.778	453.574	0.008	453.492	0.082	218.580
	Reactor Top After Reaction (g)	**Liquid Product + Catalyst Recovered (g)**	**Liquid + Gas Products + Catalyst Recovered (g)**	**Total Mass Recovery (%)**	**Empty Filter Paper (g)**	**Full Filter Paper (g)**
	234.908	0.64	0.722	93	1.0296	1.1179
	Spent Catalyst Recovered (g)	**Empty Vial (g)**	**Full Vial (g)**	**Liquid Product After DCM Evaporation (g)**	**Liquid Product Recovery After DCM Evaporation (%)**	
	0.0883	17.418	17.9799	0.56	93	

(Left column label, rotated: Reaction 43, HVGO, 4500kPa(g) H₂, 370°C, 0.25h, 900RPM, 20min Cool Time)

#	Reactor Bottom Before Reaction (g)	Liquid Feed Loaded (g)	Catalyst Type	Catalyst Loaded (g)	Loaded Reactor Bottom + Top (g)	Reactor Top Before Reaction (g)
	217.055	0.606	Sulfided < 45μm	0.098	452.035	234.276
	Loaded Reactor Bottom + Top + Neever·Seez (g)	**Mass of Neever·Seez (g)**	**Pressure Test (MPa(g))**	**Loaded Reactor Bottom + Top + Neever·Seez + H₂ at Atmosphere (g)**	**Loaded Reactor Bottom + Top + Neever·Seez + H₂ at Pressure (g)**	**H₂ Gas Loaded (g)**
	452.041	0.006	10.5	452.018	452.092	0.074
	Liquid + Catalyst + H₂ Loaded Before Reaction (g)	**After Reaction Mass (g)**	**Difference of Before & After Reaction (g)**	**After Reaction Mass - Product Gas Released (g)**	**Product Gas Released (g)**	**Reactor Bottom After Reaction (g)**
	0.778	452.062	0.03	451.982	0.08	217.709
	Reactor Top After Reaction (g)	**Liquid Product + Catalyst Recovered (g)**	**Liquid + Gas Products + Catalyst Recovered (g)**	**Total Mass Recovery (%)**	**Empty Filter Paper (g)**	**Full Filter Paper (g)**
	234.282	0.66	0.740	95	1.0335	1.1279
	Spent Catalyst Recovered (g)	**Empty Vial (g)**	**Full Vial (g)**	**Liquid Product After DCM Evaporation (g)**	**Liquid Product Recovery After DCM Evaporation (%)**	
	0.0944	17.546	18.0923	0.55	90	

(Left column label, rotated: Reaction 44, HVGO, 4500kPa(g) H₂, 350°C, 0.25h, 900RPM, 25min Cool Time)

Table D4. A summary of feed and product masses measured with percent recovery.

#	Liquid Feed Loaded (g)	Catalyst Loaded (g)	H₂ Gas Loaded (g)	Product Gas Released (g)	Liquid Product + Catalyst Recovered (g)	Total Mass Recovery (%)	Spent Catalyst Recovered (g)	Liquid Product After DCM Evaporation (g)	Liquid Product Recovery After DCM Evaporation (%)
1	0.61	0.1				93	0.11	0.56	91
2	0.6		0.06	0.08	0.57	97		0.47	78
3	0.6		0.08	0.09	0.55	94		0.4	66
4	0.61		0.07	0.08	0.61	100		0.47	76
5	0.6		0.07	0.07	0.64	106		0.47	77
6	0.62		0.08	0.09	0.59	98		0.48	78
7	0.61	0.1	0.07	0.08	0.71	101		0.52***	85
8	0.62	0.11	0.08	0.08	0.71	100		0.57***	92
9	0.61	0.1	0.07	0.08	0.71	101		0.49***	81
10	0.62	0.1	0.07	0.08	0.67	94	0.15	0.42	67
11	0.61	0.11	0.07	0.08	0.7	98	0.13	0.48	79
12	0.62	0.1	0.08	0.09	0.69	97	0.13	0.5	80
13	0.61	0.1	0.08	0.08	0.7	99	0.11	0.45	73
14	0.61	0.11	0.08	0.08	0.71	100	0.14	0.42	70
15	0.6	0.1	0.08	0.08	0.68	97	0.11	0.41	68
16	0.34	1.32	0.05	0.25	1.46	100	1.39	-	-
17	0.46	1.39*	0.04	0.42	1.42	97	1.41	-	-
18	0.5	1.4	0.05	0.4**	1.26	85	1.24	-	-
19	0.3	1.24*	0.05	0.36	1.17	96	1.17	-	-
20	0.61	0.1	0.06	0.08	0.65	95	0.09	0.48	79
21	0.62	0.1	0.07	0.08	0.72	102	0.09	0.54	87
22	0.61	0.1	0.08	0.08	0.71	100	0.09	0.5	81
23	0.62	0.11	0.07	0.08	0.71	99	0.11	0.52	84
24	0.61	0.1	0.07	0.08	0.68	98	0.1	0.53	86
25	0.63	0.1	0.07	0.08	0.71	99	0.11	0.54	86
26	0.63	0.1	0.07	0.08	0.7	98	0.11	0.55	88
27	0.61	0.1	0.07	0.08	0.7	99	0.09	0.52	85
28	0.62	0.1	0.07	0.08	0.7	98	0.11	0.55	89
29	0.64	0.11	0.07	0.08	0.75	101	0.12	0.59	92
30	0.63	0.11	0.07	0.08	0.74	101	0.11	0.57	90
31	0.61	0.1	0.07	0.09	0.68	98	0.11	0.5	81
32	0.61	0.1	0.07	0.08	0.67	96	0.11	0.54	88
33	0.61	0.11	0.07	0.08	0.71	101	0.12	0.51	82
34	0.61	0.1	0.07	0.09	0.69	99	0.09	0.52	85
35	0.61	0.11	0.07	0.09	0.72	103	0.08	0.56	91
36	0.6	0.11	0.07	0.08	0.69	99	0.08	0.54	90
37	0.62	0.1	0.08	0.08	0.73	102	0.09	0.53	85
38	0.62	0.11	0.07	0.08	0.68	96	0.11	0.54	87
39	0.61	0.1	0.06	0.08	0.69	100	0.09	0.53	88
40	0.62	0.1	0.07	0.09	0.71	101	0.09	0.51	82
41	0.62	0.1	0.07	0.08	0.71	101	0.1	0.54	87
42	0.61	0.1	0.07	0.08	0.7	100	0.1	0.48	80
43	0.6	0.1	0.07	0.08	0.64	93	0.09	0.56	93
44	0.61	0.1	0.07	0.08	0.66	95	0.09	0.55	90

*Sulfided catalyst.
**<45μm catalyst was lost in fume hood.
***Liquid product poured out into vial, catalyst pellets remained in the microreactor.

Appendix D References

[1] J. Mitrovic, "Josef Stefan and his evaporation–diffusion tube—the Stefan diffusion problem," *Chemical Engineering Science,* vol. 75, *(Supplement C),* pp. 279-281, 2012.

[2] National Institute of Standards and Technology, "NIST chemistry webbook," Available: http://webbook.gov/chemistry/.

[3] H. Watts, "Temperature Dependence of the Diffusion of Carbon Tetrachloride, Chloroform, and Methylene Chloride Vapors in Air by a Rate of Evaporation Method," *Can. J. Chem.,* vol. 49, *(1),* pp. 67-73, 1971.

[4] N. Matsunaga, "Gaseous Diffusion Coefficients of Dichloromethane, Trichloromethane and Tetrachloromethane into Air, Nitrogen and Oxygen," *Netsu Bussei,* vol. 26, *(4),* pp. 187-195, 2014.

Appendix E

The numerical results for all characterizations results, except the visible spectra results, are found in *Appendix E*. Measured carbon, hydrogen, and the calculated H/C ratio results for HVGO feed and all hydrotreated liquid products are presented in *Table E1*. Measured carbon, sulfur, and nitrogen results of sulfided catalysts are presented in *Table E2*. Measured sulfur and nitrogen results for HVGO feed and all hydrotreated liquid products are presented in *Table E3*. Measured density results for acetone, HVGO feed, and all hydrotreated liquid products are presented in *Table E4*. Measured boiling point distribution results for HVGO feed and all hydrotreated liquid products are presented in *Table E5*. A summary of select boiling point fractions from simulated distillation results (*Table E5*) for HVGO feed and all hydrotreated liquid products are shown in *Table E6*. Hydrogen nuclear magnetic resonance chemical shift spectra results using the 400MHz spectrometer for HVGO feed and select hydrotreated liquid products are presented in *Figures E1 to E7*. Hydrogen nuclear magnetic resonance chemical shift spectra results using the 60MHz spectrometer for HVGO feed and select hydrotreated liquid products are presented in *Figures E8 to E22*. A summary of molecular hydrogen concentration results obtained from chemical shift spectra for HVGO feed and select hydrotreated liquid products are shown in *Table E7*.

Table E1. Measured carbon, hydrogen, and the calculated H/C ratio results for HVGO feed and all hydrotreated liquid products.

Reaction #	Carbon (wt.%)	Hydrogen (wt.%)	H/C	Reaction #	Carbon (wt.%)	Hydrogen (wt.%)	H/C
HVGO Feed	86.7 86.1 86.3 **86.4 ± 0.3**	11.2 11.3 11.4 **11.3 ± 0.1**	1.57	Experiment 1	86.3 86 85.9 **86.1 ± 0.2**	11.3 11.4 11.1 **11.3 ± 0.2**	1.58
2	85.8 85.1 85.8 85.1 **85.5 ± 0.4**	11 11.1 11 11 **11 ± 0.05**	1.55	3	85.3 85.5 **85.4 ± 0.2**	10.5 11.1 **10.8 ± 0.6**	1.52
4	85.8 85.8 85.5 **85.7 ± 0.2**	11.3 10.4 10.9 11.1 **10.9 ± 0.4**	1.53	5	84.9 85.1 86 85.8 **85.5 ± 0.5**	10.3 10.9 11.5 10.5 **10.8 ± 0.5**	1.52
6	88.3 88.4 87.3 87 **87.8 ± 0.7**	12.1 12.1 12.3 11.9 **12.1 ± 0.2**	1.66	7	87.1 86.0 85.8 **86.3 ± 0.8**	12 11.5 11.4 11.4 **11.6 ± 0.3**	1.61
8	85.8 88.3 85.3 **86.5 ± 1.8**	12 11.8 11.5 **11.8 ± 0.3**	1.64	9	88.7 86.5 86.5 **87.2 ± 1.4**	12.3 11.5 11.5 11.5 **11.7 ± 0.4**	1.61
10	86.6 86.7 87.2 86.9 **86.9 ± 0.3**	11.9 12.2 12.1 **12.1 ± 0.2**	1.67	11	87.1 87.9 87.8 86.7 **87.4 ± 0.6**	12.1 12.1 **12.1**	1.66
12	87.8 87.5 88.2 88.6 **88 ± 0.5**	12.2 11.9 12.3 **12.1 ± 0.2**	1.65	13	87.4 87.5 88.1 **87.7 ± 0.4**	12.2 12.3 12.2 **12.2 ± 0.1**	1.67
14	89.5 87.9 87.4 **88.3 ± 1.2**	12.2 12.4 12.2 **12.3 ± 0.1**	1.67	15	88 87.5 88.3 **87.9 ± 0.5**	12.2 12.2 12.4 **12.3 ± 0.1**	1.68
20	87.2 88.6 87.9 **87.9 ± 0.8**	12.3 12.1 12.4 **12.3 ± 0.2**	1.68	21	88.9 85.8 87.9 **87.5 ± 1.8**	12.5 12.0 11.9 **12.1 ± 0.4**	1.66
22	87.8 87.4 87.8 **87.7 ± 0.3**	12.3 12.4 11.7 **12.1 ± 0.4**	1.66	23	87.6 87.4 **87.5 ± 0.2**	12.2 12.4 11.7 **12.1 ± 0.4**	1.66
24	87.7 87.8 **87.8 ± 0.1**	12.3 12.1 12.1 **12.2 ± 0.1**	1.67	25	87.8 88.2 88 **88 ± 0.2**	12.1 12.3 12.3 **12.2 ± 0.1**	1.67
26	87.7 86.6 88.4 **87.6 ± 1.0**	11.9 12 11.6 **11.8 ± 0.2**	1.62	27	87.6 87.1 87.4 **87.4 ± 0.3**	11.8 12 11.3 **11.7 ± 0.4**	1.61

Reaction #	Carbon (wt.%)	Hydrogen (wt.%)	H/C	Reaction #	Carbon (wt.%)	Hydrogen (wt.%)	H/C
28	88 86.1 **87.1 ± 1.9**	11.7 11.3 **11.5 ± 0.4**	1.59	29	86.6 87.3 87.2 **87 ± 0.4**	11.7 11.6 11.3 **11.5 ± 0.2**	1.59
30	87 86 85.7 **86.2 ± 0.8**	11.5 11.6 11 **11.4 ± 0.4**	1.59	31	87.6 88.4 87 **87.7 ± 0.8**	12.2 12.2 12 **12.1 ± 0.1**	1.66
32	89.1 88 87.3 **88.1 ± 1**	12.4 12 12.1 **12.2 ± 0.2**	1.66	33	88.5 86.2 87.7 **87.5 ± 1.3**	12.1 11.3 11.5 **11.6 ± 0.5**	1.59
34	87.2 87.8 87.6 87.2 **87.5 ± 0.3**	12.3 12.3 **12.3**	1.69	35	88.4 87.1 85.9 **87.1 ± 1.4**	12.5 12.3 11.7 **12.2 ± 0.5**	1.68
36	88.5 88 **88.3 ± 0.5**	12.3 12.6 11.5 **12.1 ± 0.6**	1.65	37	88.6 87.4 **88 ± 1.2**	12.3 12.5 11.6 **12.1 ± 0.5**	1.65
38	88.2 87.9 87.9 **88 ± 0.2**	12.1 12.3 11.6 11.6 **11.9 ± 0.3**	1.62	39	87.8 87.7 **87.8 ± 0.1**	12.1 12.1 11.1 **11.8 ± 0.7**	1.61
40	88.1 86.2 89.7 **88 ± 2**	12.2 11.9 11.8 **12 ± 0.2**	1.64	41	88.6 87.9 87.7 **88.1 ± 0.5**	12 11.5 **11.8 ± 0.5**	1.61
42	88.1 87.7 87.1 **87.6 ± 0.6**	11.9 12.1 11.2 **11.7 ± 0.5**	1.60	43	87.8 89 87.9 **88.2 ± 0.8**	12.1 11.8 11.4 **11.8 ± 0.4**	1.61
44	87.5 86.7 88.5 **87.6 ± 1**	11.4 11.8 11.2 **11.5 ± 0.3**	1.58				

Table E2. Measured carbon, sulfur, and nitrogen results of sulfided catalysts.

Catalyst Type	Carbon (wt.%)	Sulfur (wt.%)	Nitrogen (wt.%)
Pellets (Reaction 17)	1.86 2.04 2.44 **2.11 ± 0.34**	7.64 7.57 5.71 **6.97 ± 1.24**	0.01 0.02 **0.015 ± 0.01**
< 45µm Particles (Reaction 19)	0.4 0.4 0.39 **0.4 ± 0.01**	9.7 9.72 9.71 **9.71 ± 0.01**	0.01 0.01 **0.01**

Table E3. Measured sulfur and nitrogen results for HVGO feed and all hydrotreated liquid products.

Reaction #	Sulfur (wt.%)	Nitrogen (wt.%)	Reaction #	Sulfur (wt.%)	Nitrogen (wt.%)
HVGO Feed	3.32 3.31 3.29 3.28 3.28 3.29 **3.3 ± 0.01**	0.1784 0.1785 0.1737 0.1746 0.1756 0.1762 **0.1762 ± 0.016**	Experiment 1	3.33 3.33 3.13 3.06 **3.21 ± 0.14**	0.1792 0.1605 0.1671 **0.1689 ± 0.0107**
2	2.88 2.86 2.82 **2.85 ± 0.03**	0.2116 0.2276 0.2247 0.2173 **0.2203 ± 0.0071**	3	2.60 2.53 2.71 2.51 **2.59 ± 0.09**	0.1952 0.1948 0.1899 0.2040 0.1948 **0.1957 ± 0.0045**
4	2.98 3 2.67 2.70 2.96 **2.86 ± 0.14**	0.2040 0.2102 0.1984 0.1944 0.1809 0.19 0.2061 **0.1977 ± 0.0075**	5	2.67 3.07 2.73 3.05 2.91 **2.89 ± 0.16**	0.2177 0.2151 0.2022 0.2078 0.2098 **0.2105 ± 0.0054**
6	0.54 0.51 **0.53 ± 0.03**	0.0987 0.0955 0.0828 0.0748 **0.088 ± 0.0109**	7	0.18 0.17 **0.18 ± 0.01**	0.0379 0.0329 **0.0354 ± 0.0049**
8	0.12 0.11 **0.12 ± 0.01**	0.0333 0.0256 **0.0295 ± 0.0075**	9	0.14 0.14 **0.14**	0.0353 0.0303 **0.0328 ± 0.0049**
10	0.22 0.18 0.24 0.26 0.25 **0.23 ± 0.03**	0.061 0.0688 0.0726 0.0554 0.0517 **0.0619 ± 0.0077**	11	0.18 0.17 **0.18 ± 0.01**	0.0865 0.0645 **0.0755 ± 0.0216**
12	0.12 0.25 0.22 0.19 **0.20 ± 0.05**	0.0788 0.0692 0.0637 0.0521 **0.066 ± 0.0109**	13	0.36 0.38 0.37 0.35 **0.37 ± 0.01**	0.0723 0.0977 0.0847 0.0558 **0.0776 ± 0.0175**
14	0.34 0.32 0.40 0.38 **0.36 ± 0.04**	0.092 0.0852 0.0796 0.0866 **0.0859 ± 0.005**	15	0.21 0.17 0.27 0.24 **0.22 ± 0.04**	0.0668 0.0727 0.0765 **0.0720 ± 0.0055**
20	0.13 0.19 0.18 **0.17 ± 0.04**	0.0585 0.0436 **0.0511 ± 0.0146**	21	0.09 0.22 0.20 **0.17 ± 0.08**	0.0693 0.0526 0.0311 **0.051 ± 0.0217**
22	**0.21**	0.0563 0.0302 **0.0433 ± 0.0256**	23	0.17 0.22 0.22 **0.2 ± 0.03**	0.0546 0.0485 **0.0516 ± 0.006**

Reaction #	Sulfur (wt.%)	Nitrogen (wt.%)	Reaction #	Sulfur (wt.%)	Nitrogen (wt.%)
24	0.39 0.38 **0.39 ± 0.01**	0.0949 0.0867 **0.0908 ± 0.008**	25	0.35 0.34 **0.35 ± 0.01**	0.0727 0.0920 **0.0824 ± 0.0189**
26	0.67 0.73 0.71 **0.7 ± 0.03**	0.1164 0.1054 **0.1109 ± 0.0108**	27	1.03 1.05 1.05 **1.04 ± 0.01**	0.1263 0.1215 **0.1239 ± 0.0047**
28	1.61 1.69 1.63 **1.64 ± 0.05**	0.1569 0.1503 0.1394 **0.1489 ± 0.01**	29	2.31 2.22 2.35 2.23 **2.28 ± 0.06**	0.1708 0.1509 **0.1609 ± 0.0195**
30	2.46 2.75 2.51 **2.57 ± 0.18**	0.1695 0.1662 0.1661 0.1649 **0.1667 ± 0.0019**	31	0.6 0.57 0.7 0.7 **0.64 ± 0.07**	**0.1055**
32	0.6 0.6 **0.6**	0.1053 0.0996 **0.1025 ± 0.0056**	33	0.9 1.12 1.01 1 **1.01 ± 0.09**	0.1278 0.1174 **0.1226 ± 0.0102**
34	0.25 0.23 **0.24 ± 0.02**	0.0481 0.0524 0.022 **0.0408 ± 0.0186**	35	0.12 0.1 0.08 **0.1 ± 0.02**	0.0467 0.0192 **0.033 ± 0.0269**
36	0.24 0.23 **0.24 ± 0.01**	0.07 0.0605 **0.0653 ± 0.0093**	37	0.16 0.28 0.27 **0.24 ± 0.08**	0.0672 0.0662 **0.0667 ± 0.001**
38	0.18 0.36 0.35 **0.3 ± 0.11**	0.0951 0.0956 **0.0954 ± 0.0005**	39	0.31 0.31 0.40 0.41 **0.36 ± 0.05**	0.1064 0.0963 0.1073 **0.1033 ± 0.0069**
40	0.61 0.62 0.70 0.68 **0.65 ± 0.04**	0.1279 0.1225 **0.1252 ± 0.0053**	41	0.61 0.66 0.64 **0.64 ± 0.03**	0.1266 0.1293 0.1207 **0.1255 ± 0.005**
42	0.58 0.56 **0.57 ± 0.02**	0.1277 0.1168 **0.1223 ± 0.0107**	43	0.88 0.87 0.88 0.87 **0.88 ± 0.01**	0.1372 0.1383 0.1378 0.1297 **0.1358 ± 0.004**
44	1.68 1.74 **1.71 ± 0.06**	0.1607 0.1655 0.1566 0.1653 0.1493 **0.1595 ± 0.0059**			

Table E4. Measured density results for acetone, HVGO feed, and all hydrotreated liquid products.

Reaction #	Density (g/ml)	Reaction #	Density (g/ml)	Reaction #	Density (g/ml)
Acetone	0.79, 0.785 0.785, 0.79 0.785, 0.79 0.795, 0.79 0.79 **0.789 ± 0.003**	HVGO Feed	0.976, 0.972 0.958, 0.964 0.969, 0.961 0.968, 0.964 0.952, 0.988 **0.967 ± 0.006**	Experiment 1	0.94 0.965 **0.953 ± 0.017**
2	0.96 0.96 0.955 **0.958 ± 0.003**	3	0.965 0.95 0.955 0.94 **0.953 ± 0.009**	4	0.945 0.955 0.955 0.95 **0.951 ± 0.004**
5	0.945 0.96 0.965 0.95 **0.955 ± 0.008**	6	0.905 0.915 **0.91 ± 0.007**	7	0.9 0.895 0.895 **0.897 ± 0.003**
8	0.895 0.915 0.9 **0.903 ± 0.01**	9	0.91 0.9 0.91 **0.907 ± 0.005**	10	0.895 0.91 0.895 **0.9 ± 0.008**
11	0.895 0.91 0.91 **0.905 ± 0.008**	12	0.905 0.905 0.905 **0.905**	13	0.905 0.91 0.91 **0.908 ± 0.003**
14	0.9 0.91 091 **0.907 ± 0.005**	15	0.91 0.905 **0.908 ± 0.003**	20	0.905 0.91 0.9 **0.905 ± 0.005**
21	0.905 0.9 0.91 **0.905 ± 0.005**	22	0.905 0.895 0.905 **0.902 ± 0.005**	23	0.91 0.905 0.905 **0.907 ± 0.003**
24	0.905 0.915 0.915 **0.912 ± 0.005**	25	0.915 0.91 0.915 **0.913 ± 0.003**	26	0.925 0.925 0.925 **0.925**
27	0.93 0.93 0.94 **0.933 ± 0.005**	28	0.94 0.93 **0.935 ± 0.007**	29	0.94 0.93 0.945 **0.938 ± 0.007**

Reaction #	Density (g/ml)	Reaction #	Density (g/ml)	Reaction #	Density (g/ml)
30	0.95 0.935 0.94 **0.942 ± 0.007**	31	0.92 0.915 0.925 **0.92 ± 0.005**	32	0.905 0.92 0.92 **0.915 ± 0.008**
33	0.92 0.925 0.925 **0.923 ± 0.003**	34	0.895 0.9 0.9 **0.898 ± 0.003**	35	0.9 0.9 0.905 0.905 **0.903 ± 0.002**
36	0.905 0.91 0.91 **0.908 ± 0.003**	37	0.91 0.915 0.915 **0.913 ± 0.003**	38	0.905 0.925 0.92 **0.917 ± 0.01**
39	0.91 0.92 0.915 **0.915 ± 0.005**	40	0.915 0.925 0.92 0.92 **0.92 ± 0.003**	41	0.91 0.935 0.93 **0.925 ± 0.012**
42	0.92 0.92 0.92 **0.92**	43	0.935 0.925 **0.93 ± 0.007**	44	0.935 0.93 **0.933 ± 0.003**

Table E5. Measured boiling point distribution results for the HVGO feed and all hydrotreated liquid products.

HVGO Feed				Experiment 1				Reaction 2			
% Off (wt.%)	BP (°C)	% Off (wt.%)	BP (°C)	% Off (wt.%)	BP (°C)	% Off (wt.%)	BP (°C)	% Off (wt.%)	BP (°C)	% Off (wt.%)	BP (°C)
0.5	298.6	51	428.2	0.5	292.0	51	427.3	0.5	134.6	51	415.6
1	309.5	52	429.9	1	305.7	52	429.5	1	162.9	52	416.8
2	322.3	53	430.7	2	317.3	53	430.8	2	208.4	53	418.5
3	330.6	54	432.1	3	326.5	54	431.8	3	239.2	54	420.2
4	337.3	55	433.4	4	333.4	55	432.8	4	261.7	55	421.0
5	343.1	56	434.1	5	338.6	56	434.1	5	280.8	56	422.7
6	347.7	57	435.4	6	343.8	57	434.7	6	294.6	57	424.4
7	351.5	58	436.7	7	348.3	58	435.7	7	305.4	58	425.7
8	355.7	59	437.4	8	351.9	59	437.3	8	312.4	59	427.8
9	359.1	60	438.7	9	355.9	60	437.9	9	318.8	60	429.4
10	362.5	61	440.0	10	359.5	61	439.2	10	324.4	61	431.1
11	365.0	62	441.4	11	363.1	62	440.1	11	330.4	62	431.8
12	367.6	63	442.0	12	365.8	63	441.7	12	335.1	63	433.1
13	370.5	64	443.3	13	368.9	64	442.7	13	339.3	64	434.4
14	372.6	65	444.7	14	370.9	65	443.7	14	342.8	65	436.1
15	374.3	66	445.7	15	372.9	66	444.9	15	346.6	66	437.1
16	376.6	67	447.3	16	374.6	67	446.5	16	349.7	67	438.4
17	378.0	68	448.6	17	376.2	68	447.5	17	353.6	68	439.4
18	380.0	69	450.2	18	378.2	69	448.8	18	356.2	69	441.1
19	382.0	70	451.9	19	380.2	70	450.0	19	359.7	70	442.4
20	383.3	71	453.6	20	381.9	71	452.3	20	362.3	71	443.8
21	384.7	72	455.7	21	383.2	72	454.1	21	364.9	72	445.8
22	386.7	73	456.9	22	384.9	73	456.3	22	367.5	73	447.1
23	388.1	74	458.6	23	386.2	74	457.6	23	369.9	74	448.1
24	389.4	75	460.7	24	388.2	75	459.4	24	371.6	75	450.0
25	391.5	76	462.8	25	389.5	76	461.7	25	373.3	76	452.5
26	393.0	77	465.4	26	390.9	77	463.9	26	375.7	77	454.2
27	394.5	78	467.2	27	392.4	78	466.5	27	377.1	78	456.7
28	396.0	79	468.9	28	393.9	79	468.3	28	378.8	79	458.4
29	397.9	80	470.3	29	395.8	80	469.7	29	380.9	80	460.9
30	399.0	81	472.3	30	396.9	81	471.4	30	382.2	81	463.4
31	400.5	82	474.4	31	398.5	82	473.5	31	384.3	82	466.0
32	402.0	83	476.1	32	400.4	83	475.7	32	385.7	83	468.4
33	403.5	84	478.5	33	401.5	84	477.8	33	387.0	84	470.8
34	404.7	85	480.6	34	403.0	85	479.9	34	389.1	85	472.9
35	406.6	86	482.8	35	404.9	86	482.2	35	390.1	86	475.4
36	408.1	87	485.1	36	406.1	87	484.3	36	391.9	87	478.5
37	409.2	88	487.6	37	407.2	88	486.1	37	393.4	88	481.0
38	410.3	89	490.2	38	408.4	89	488.6	38	395.4	89	483.9
39	411.8	90	493.4	39	409.9	90	491.6	39	397.3	90	487.1
40	413.5	91	496.0	40	411.4	91	494.0	40	398.4	91	490.6
41	414.7	92	500.4	41	412.7	92	497.4	41	400.3	92	494.2
42	415.9	93	504.9	42	414.0	93	502.1	42	401.9	93	498.7
43	417.6	94	509.7	43	416.2	94	506.9	43	403.4	94	505.0
44	418.4	95	514.2	44	417.5	95	512.1	44	404.5	95	511.2
45	420.4	96	520.3	45	418.9	96	517.3	45	406.4	96	519.2
46	421.7	97	530.5	46	420.2	97	525.6	46	408.0	97	532.5
47	422.5	98	544.1	47	422.0	98	539.0	47	409.5	98	556.9
48	424.1	99	587.7	48	422.8	99	572.9	48	410.3	99	616.2
49	425.4	99.5	643.3	49	424.6	99.5	607.9	49	411.8	99.5	663.8
50	426.6			50	425.9			50	413.5		

Reaction 3				Reaction 4				Reaction 5			
% Off (wt.%)	BP (°C)	% Off (wt.%)	BP (°C)	% Off (wt.%)	BP (°C)	% Off (wt.%)	BP (°C)	% Off (wt.%)	BP (°C)	% Off (wt.%)	BP (°C)
0.5	159.5	51	417.7	0.5	156.8	51	421.0	0.5	142.5	51	420.2
1	197.1	52	418.9	1	203.9	52	422.7	1	181.2	52	421.0
2	242.9	53	420.2	2	258.5	53	424.4	2	233.4	53	422.7
3	272.7	54	421.9	3	287.9	54	425.7	3	267.3	54	424.4
4	291.7	55	423.1	4	305.0	55	426.9	4	290.0	55	425.7
5	304.7	56	425.2	5	314.1	56	428.6	5	305.0	56	426.9
6	313.1	57	426.5	6	321.8	57	429.9	6	313.4	57	428.6
7	320.1	58	427.8	7	328.7	58	431.1	7	321.0	58	430.7
8	326.1	59	429.4	8	333.8	59	432.4	8	327.4	59	431.8
9	331.2	60	431.1	9	339.3	60	433.4	9	332.9	60	433.1
10	336.3	61	431.8	10	343.6	61	435.1	10	338.1	61	434.1
11	340.6	62	433.1	11	347.5	62	436.1	11	342.3	62	435.1
12	344.5	63	434.4	12	351.0	63	437.1	12	346.6	63	436.4
13	348.4	64	435.4	13	354.9	64	438.4	13	349.7	64	437.4
14	351.9	65	437.1	14	358.0	65	439.4	14	353.6	65	439.1
15	354.5	66	437.8	15	360.6	66	441.1	15	356.6	66	440.4
16	357.5	67	439.4	16	364.0	67	441.8	16	359.7	67	441.1
17	361.0	68	440.4	17	366.6	68	443.4	17	363.2	68	442.4
18	363.6	69	441.8	18	369.2	69	444.4	18	365.3	69	443.8
19	365.8	70	443.1	19	371.3	70	445.8	19	368.0	70	445.8
20	368.4	71	444.8	20	373.3	71	447.1	20	370.6	71	447.1
21	370.6	72	445.8	21	374.7	72	448.8	21	372.6	72	448.1
22	372.6	73	447.1	22	376.7	73	450.4	22	374.0	73	450.0
23	374.7	74	448.4	23	378.8	74	452.5	23	376.1	74	451.6
24	376.1	75	450.0	24	380.2	75	454.2	24	378.1	75	453.7
25	378.1	76	452.5	25	382.2	76	455.9	25	379.8	76	455.9
26	379.5	77	454.6	26	383.6	77	458.4	26	381.2	77	458.0
27	381.5	78	455.9	27	385.3	78	460.1	27	382.9	78	460.1
28	382.9	79	458.4	28	387.0	79	462.6	28	384.6	79	462.2
29	384.6	80	460.1	29	388.7	80	464.7	29	386.3	80	463.8
30	386.0	81	462.6	30	389.8	81	466.7	30	387.7	81	466.7
31	387.7	82	465.1	31	391.9	82	468.8	31	389.8	82	468.8
32	389.1	83	467.0	32	393.4	83	470.8	32	391.1	83	470.8
33	390.4	84	469.1	33	394.6	84	472.9	33	392.3	84	472.9
34	392.7	85	471.2	34	396.5	85	475.0	34	394.2	85	475.0
35	394.2	86	474.0	35	398.0	86	477.1	35	395.7	86	477.1
36	395.4	87	475.7	36	399.6	87	479.9	36	397.3	87	479.9
37	397.3	88	478.5	37	401.1	88	481.9	37	399.2	88	482.6
38	398.8	89	481.3	38	402.2	89	484.8	38	400.3	89	485.2
39	399.9	90	483.9	39	404.2	90	487.1	39	401.9	90	487.7
40	401.9	91	486.4	40	405.7	91	490.0	40	403.4	91	491.0
41	403.4	92	489.7	41	407.2	92	493.2	41	405.3	92	494.8
42	404.9	93	492.9	42	408.4	93	497.2	42	406.4	93	498.7
43	406.4	94	496.9	43	409.5	94	502.0	43	408.0	94	503.5
44	407.2	95	502.0	44	411.0	95	507.2	44	409.5	95	509.9
45	408.7	96	507.9	45	412.2	96	513.0	45	411.0	96	516.1
46	410.7	97	514.3	46	414.3	97	520.4	46	412.2	97	525.6
47	411.8	98	523.4	47	416.0	98	533.6	47	414.3	98	541.0
48	413.5	99	540.7	48	416.8	99	562.1	48	415.6	99	580.4
49	414.3	99.5	564.4	49	418.5	99.5	606.8	49	416.8	99.5	629.3
50	416.0			50	420.2			50	418.5		

Reaction 6				Reaction 7				Reaction 8			
% Off (wt.%)	BP (°C)	% Off (wt.%)	BP (°C)	% Off (wt.%)	BP (°C)	% Off (wt.%)	BP (°C)	% Off (wt.%)	BP (°C)	% Off (wt.%)	BP (°C)
0.5	165.1	51	401.9	0.5	108.4	51	395.9	0.5	101.5	51	395.9
1	187.4	52	403.4	1	138.7	52	397.8	1	101.5	52	397.4
2	216.0	53	405.3	2	177.5	53	398.9	2	138.7	53	398.9
3	236.7	54	406.4	3	200.8	54	400.8	3	176.6	54	401.2
4	252.9	55	408.0	4	218.5	55	402.7	4	200.4	55	402.4
5	265.7	56	409.5	5	234.3	56	404.3	5	219.3	56	404.3
6	276.4	57	411.0	6	247.2	57	405.8	6	235.1	57	405.8
7	284.5	58	413.0	7	258.7	58	407.7	7	247.6	58	407.3
8	292.5	59	414.3	8	268.3	59	408.9	8	259.1	59	409.6
9	299.3	60	416.0	9	276.1	60	410.4	9	269.5	60	411.2
10	304.3	61	417.7	10	283.4	61	412.8	10	277.2	61	412.3
11	308.9	62	418.9	11	289.6	62	414.6	11	284.1	62	414.6
12	313.1	63	421.0	12	296.4	63	416.3	12	290.4	63	416.3
13	316.7	64	422.7	13	302.0	64	417.6	13	297.3	64	418.1
14	321.0	65	424.0	14	305.8	65	419.8	14	302.3	65	419.8
15	324.4	66	425.2	15	310.0	66	421.6	15	306.5	66	421.2
16	328.7	67	426.9	16	313.4	67	423.4	16	310.6	67	423.4
17	331.6	68	428.6	17	317.1	68	424.7	17	314.1	68	425.1
18	335.5	69	430.7	18	321.0	69	426.9	18	318.0	69	426.9
19	338.1	70	431.8	19	324.0	70	428.7	19	321.4	70	429.1
20	341.5	71	433.1	20	327.5	71	430.4	20	324.9	71	431.2
21	344.0	72	434.4	21	331.0	72	431.9	21	329.3	72	432.2
22	347.5	73	436.4	22	334.5	73	433.5	22	331.9	73	433.8
23	349.7	74	437.4	23	338.0	74	434.8	23	335.8	74	435.1
24	352.7	75	439.1	24	341.0	75	436.4	24	338.8	75	436.4
25	355.3	76	440.4	25	343.6	76	437.6	25	341.4	76	438.3
26	358.0	77	442.4	26	346.7	77	439.6	26	344.9	77	439.6
27	360.6	78	443.8	27	349.4	78	440.9	27	347.6	78	441.5
28	362.3	79	445.8	28	351.7	79	442.1	28	350.3	79	443.1
29	364.9	80	447.1	29	354.3	80	444.1	29	353.0	80	444.7
30	367.5	81	449.1	30	357.5	81	446.0	30	355.7	81	446.6
31	369.2	82	451.6	31	360.2	82	447.9	31	358.8	82	448.6
32	371.3	83	453.7	32	362.0	83	449.7	32	361.1	83	451.1
33	372.6	84	455.9	33	364.7	84	452.4	33	363.8	84	453.7
34	374.7	85	459.2	34	367.3	85	455.5	34	366.4	85	456.8
35	376.1	86	462.2	35	369.1	86	458.1	35	368.2	86	459.9
36	378.1	87	465.1	36	371.1	87	461.2	36	370.4	87	463.0
37	379.1	88	467.4	37	372.5	88	465.2	37	372.5	88	466.0
38	380.9	89	470.1	38	374.5	89	467.8	38	373.8	89	469.5
39	382.9	90	472.9	39	376.5	90	470.9	39	375.8	90	472.4
40	384.3	91	476.4	40	377.8	91	474.5	40	377.1	91	475.9
41	385.7	92	479.9	41	379.5	92	478.0	41	379.2	92	479.4
42	387.0	93	483.2	42	381.2	93	481.4	42	380.5	93	483.3
43	389.1	94	487.1	43	382.8	94	485.1	43	382.5	94	487.0
44	390.8	95	491.6	44	384.2	95	489.5	44	384.2	95	492.0
45	391.9	96	496.5	45	385.9	96	494.4	45	385.9	96	497.9
46	393.4	97	503.5	46	387.2	97	501.0	46	387.5	97	506.7
47	395.7	98	512.4	47	389.2	98	510.6	47	388.5	98	517.3
48	397.3	99	526.7	48	390.6	99	524.4	48	390.2	99	541.2
49	398.4	99.5	541.0	49	392.0	99.5	538.8	49	392.0	99.5	612.3
50	400.3			50	394.3			50	394.3		

Reaction 9				Reaction 10				Reaction 11			
% Off (wt.%)	BP (°C)	% Off (wt.%)	BP (°C)	% Off (wt.%)	BP (°C)	% Off (wt.%)	BP (°C)	% Off (wt.%)	BP (°C)	% Off (wt.%)	BP (°C)
0.5	98.0	51	395.1	0.5	162.3	51	391.1	0.5	158.4	51	391.5
1	122.2	52	396.6	1	178.5	52	393.4	1	172.9	52	393.4
2	162.6	53	398.5	2	198.7	53	394.6	2	193.6	53	395.0
3	189.9	54	399.7	3	213.2	54	396.5	3	209.2	54	397.3
4	210.3	55	401.6	4	224.7	55	398.4	4	222.2	55	398.8
5	226.0	56	403.5	5	236.3	56	400.3	5	233.8	56	400.3
6	240.1	57	405.0	6	245.4	57	401.9	6	243.8	57	401.9
7	252.2	58	406.6	7	254.1	58	403.4	7	252.9	58	403.4
8	262.7	59	408.5	8	262.9	59	405.3	8	261.3	59	405.7
9	271.8	60	409.6	9	270.5	60	407.2	9	269.7	60	406.8
10	279.0	61	411.5	10	276.4	61	408.4	10	275.7	61	408.7
11	285.2	62	413.7	11	282.3	62	410.3	11	282.3	62	410.7
12	291.7	63	415.4	12	287.5	63	411.8	12	287.0	63	411.8
13	298.1	64	417.2	13	293.4	64	413.5	13	293.4	64	413.5
14	302.7	65	418.5	14	298.9	65	415.6	14	298.0	65	416.0
15	306.8	66	420.7	15	303.3	66	417.7	15	303.3	66	417.2
16	311.0	67	422.5	16	306.8	67	418.9	16	306.8	67	419.4
17	314.4	68	424.2	17	310.3	68	421.0	17	310.6	68	420.6
18	318.0	69	426.5	18	313.4	69	422.7	18	313.4	69	422.7
19	321.9	70	427.8	19	316.7	70	424.4	19	317.1	70	424.8
20	324.9	71	429.5	20	320.1	71	426.5	20	320.5	71	426.1
21	328.4	72	431.9	21	323.5	72	427.8	21	323.9	72	428.6
22	331.9	73	433.1	22	327.4	73	429.9	22	327.4	73	430.3
23	335.3	74	434.4	23	330.4	74	431.8	23	330.8	74	432.1
24	338.0	75	436.0	24	332.9	75	433.1	24	333.4	75	433.1
25	341.0	76	437.6	25	336.3	76	435.1	25	336.3	76	435.1
26	344.5	77	439.3	26	339.3	77	436.4	26	339.8	77	436.4
27	346.7	78	440.2	27	342.3	78	438.4	27	342.3	78	438.4
28	350.3	79	442.5	28	344.9	79	440.1	28	344.9	79	440.1
29	352.6	80	443.8	29	347.5	80	441.8	29	348.0	80	441.8
30	355.2	81	446.0	30	350.6	81	443.8	30	350.1	81	443.8
31	358.4	82	447.6	31	352.7	82	445.8	31	352.7	82	445.4
32	360.6	83	449.3	32	355.3	83	447.8	32	355.3	83	447.8
33	362.9	84	452.8	33	358.0	84	450.0	33	358.4	84	450.0
34	365.5	85	455.5	34	360.6	85	452.9	34	360.6	85	452.5
35	367.8	86	458.5	35	362.3	86	455.9	35	363.2	86	455.9
36	369.8	87	461.6	36	364.9	87	459.2	36	365.3	87	459.2
37	371.8	88	464.7	37	367.5	88	462.6	37	367.5	88	462.2
38	373.1	89	468.1	38	369.2	89	466.0	38	369.2	89	466.0
39	375.1	90	470.9	39	371.3	90	469.4	39	371.6	90	468.8
40	376.8	91	474.8	40	372.6	91	472.9	40	373.3	91	472.2
41	378.5	92	478.3	41	374.7	92	476.4	41	374.7	92	475.7
42	380.2	93	482.0	42	376.1	93	480.6	42	376.4	93	479.9
43	381.8	94	485.8	43	378.1	94	484.8	43	378.1	94	483.9
44	383.5	95	490.7	44	379.8	95	489.7	44	380.2	95	488.4
45	384.5	96	495.7	45	381.2	96	494.8	45	381.5	96	493.5
46	386.5	97	504.4	46	382.9	97	503.5	46	383.6	97	501.3
47	387.9	98	514.8	47	384.6	98	513.6	47	385.0	98	511.2
48	389.9	99	535.3	48	386.3	99	534.0	48	386.3	99	526.3
49	391.3	99.5	594.6	49	388.1	99.5	565.3	49	388.1	99.5	541.9
50	392.8			50	389.8			50	389.8		

Reaction 12				Reaction 13				Reaction 14			
% Off (wt.%)	BP (°C)	% Off (wt.%)	BP (°C)	% Off (wt.%)	BP (°C)	% Off (wt.%)	BP (°C)	% Off (wt.%)	BP (°C)	% Off (wt.%)	BP (°C)
0.5	165.1	51	395.0	0.5	169.6	51	397.3	0.5	160.1	51	395.7
1	183.0	52	397.3	1	186.5	52	399.2	1	177.6	52	397.7
2	203.5	53	398.8	2	208.8	53	400.3	2	201.9	53	398.8
3	218.9	54	400.3	3	225.5	54	401.9	3	218.9	54	400.3
4	232.2	55	402.2	4	239.6	55	404.2	4	233.8	55	402.6
5	243.4	56	403.4	5	251.6	56	405.7	5	246.3	56	403.8
6	253.3	57	405.3	6	261.7	57	407.2	6	256.9	57	405.7
7	262.9	58	407.2	7	271.3	58	408.4	7	266.5	58	407.2
8	271.3	59	408.7	8	278.6	59	410.3	8	274.6	59	408.7
9	277.9	60	410.7	9	285.2	60	411.8	9	281.5	60	410.3
10	284.5	61	411.8	10	291.3	61	413.5	10	287.9	61	412.2
11	290.4	62	413.5	11	297.6	62	415.6	11	293.4	62	413.5
12	296.3	63	415.1	12	302.9	63	416.8	12	299.3	63	415.1
13	301.8	64	417.2	13	306.8	64	418.5	13	304.0	64	417.2
14	305.7	65	418.5	14	310.3	65	420.2	14	308.2	65	418.5
15	309.6	66	420.2	15	314.1	66	421.9	15	311.7	66	421.0
16	313.1	67	422.7	16	317.5	67	424.0	16	314.8	67	422.7
17	316.7	68	424.4	17	321.0	68	425.2	17	318.4	68	424.0
18	320.5	69	425.7	18	325.2	69	426.9	18	322.2	69	426.1
19	323.5	70	427.8	19	328.7	70	428.6	19	326.1	70	427.8
20	327.4	71	429.4	20	331.2	71	431.1	20	329.5	71	429.0
21	330.4	72	431.1	21	335.1	72	432.4	21	332.5	72	431.1
22	334.2	73	432.8	22	338.1	73	433.4	22	335.5	73	432.4
23	337.2	74	434.4	23	340.6	74	435.1	23	338.5	74	434.1
24	339.8	75	435.4	24	343.6	75	436.4	24	341.0	75	435.4
25	342.3	76	437.1	25	346.6	76	438.4	25	344.5	76	437.1
26	345.8	77	439.1	26	349.3	77	440.1	26	347.1	77	439.1
27	348.4	78	440.4	27	351.9	78	441.8	27	349.7	78	440.4
28	351.0	79	442.4	28	354.0	79	443.4	28	352.3	79	442.4
29	353.6	80	444.4	29	356.6	80	445.1	29	354.9	80	444.1
30	356.2	81	446.4	30	359.7	81	447.1	30	357.5	81	446.1
31	358.8	82	447.8	31	361.9	82	449.1	31	360.1	82	447.4
32	361.4	83	450.4	32	364.0	83	451.6	32	361.9	83	449.5
33	363.2	84	452.9	33	366.6	84	454.2	33	364.0	84	452.9
34	365.8	85	456.3	34	368.8	85	456.7	34	366.6	85	455.4
35	368.4	86	459.2	35	370.6	86	460.1	35	369.2	86	458.4
36	369.9	87	461.7	36	372.3	87	462.6	36	370.6	87	460.9
37	371.9	88	465.1	37	374.0	88	466.0	37	372.6	88	464.3
38	373.3	89	468.8	38	375.7	89	469.4	38	374.3	89	467.7
39	375.4	90	471.5	39	377.1	90	472.2	39	375.7	90	470.8
40	376.7	91	475.0	40	378.8	91	475.4	40	377.4	91	474.3
41	378.8	92	478.5	41	380.9	92	479.2	41	379.5	92	477.5
42	380.5	93	482.6	42	382.2	93	483.2	42	380.9	93	481.6
43	381.9	94	487.1	43	383.6	94	487.1	43	382.6	94	485.8
44	383.6	95	491.6	44	385.7	95	492.3	44	383.9	95	490.0
45	385.0	96	497.6	45	387.0	96	497.6	45	385.7	96	495.5
46	387.0	97	506.4	46	388.7	97	505.7	46	387.0	97	503.1
47	388.4	98	518.0	47	390.1	98	516.1	47	389.1	98	512.7
48	389.8	99	544.8	48	391.9	99	535.7	48	390.1	99	529.6
49	391.9	99.5	652.1	49	393.4	99.5	562.7	49	391.9	99.5	547.3
50	393.8			50	395.7			50	394.2		

Reaction 15				Reaction 20				Reaction 21			
% Off (wt.%)	BP (°C)	% Off (wt.%)	BP (°C)	% Off (wt.%)	BP (°C)	% Off (wt.%)	BP (°C)	% Off (wt.%)	BP (°C)	% Off (wt.%)	BP (°C)
0.5	158.4	51	396.1	0.5	174.9	51	396.5	0.5	129.4	51	396.2
1	177.2	52	397.3	1	192.3	52	398.0	1	158.8	52	397.7
2	200.7	53	398.8	2	214.0	53	399.6	2	189.4	53	400.0
3	218.1	54	401.1	3	230.1	54	401.1	3	211.3	54	401.5
4	233.0	55	402.6	4	244.6	55	403.4	4	229.1	55	403.0
5	246.3	56	404.2	5	256.1	56	404.5	5	242.7	56	404.9
6	256.9	57	406.1	6	266.1	57	406.4	6	255.9	57	406.1
7	267.3	58	407.2	7	274.9	58	407.6	7	266.3	58	407.6
8	274.9	59	408.7	8	282.3	59	409.5	8	275.0	59	409.1
9	282.3	60	410.7	9	288.3	60	410.7	9	282.2	60	410.7
10	288.3	61	411.8	10	294.6	61	412.6	10	288.6	61	412.7
11	294.2	62	413.5	11	300.1	62	413.9	11	295.0	62	414.4
12	300.1	63	416.0	12	304.7	63	416.0	12	300.5	63	416.6
13	304.7	64	417.7	13	308.9	64	417.2	13	305.0	64	418.4
14	308.9	65	419.4	14	312.4	65	419.4	14	309.5	65	419.7
15	312.4	66	420.6	15	315.2	66	420.6	15	312.6	66	422.0
16	315.5	67	422.7	16	318.8	67	422.7	16	316.0	67	423.7
17	319.2	68	424.4	17	323.1	68	424.0	17	319.5	68	425.5
18	323.1	69	425.7	18	326.1	69	426.1	18	323.4	69	427.3
19	326.1	70	427.8	19	329.5	70	427.3	19	327.3	70	428.6
20	329.5	71	429.4	20	332.9	71	429.4	20	330.8	71	430.8
21	332.9	72	431.1	21	335.5	72	430.7	21	333.4	72	432.1
22	335.5	73	432.8	22	338.9	73	432.4	22	336.9	73	433.7
23	338.5	74	433.8	23	341.5	74	434.1	23	339.5	74	434.7
24	341.5	75	435.4	24	344.0	75	435.1	24	343.0	75	436.6
25	344.0	76	437.1	25	347.5	76	437.1	25	345.6	76	437.9
26	347.1	77	438.4	26	350.1	77	438.4	26	348.3	77	439.2
27	349.7	78	440.4	27	352.3	78	440.4	27	351.0	78	441.1
28	352.3	79	442.1	28	354.5	79	441.8	28	353.7	79	442.4
29	354.9	80	443.8	29	357.1	80	443.8	29	356.4	80	444.3
30	357.1	81	445.8	30	359.7	81	445.4	30	359.0	81	446.2
31	360.1	82	447.8	31	362.3	82	447.1	31	361.3	82	447.5
32	362.3	83	450.0	32	364.0	83	449.1	32	363.5	83	449.6
33	364.9	84	452.5	33	366.2	84	451.6	33	365.8	84	452.7
34	367.1	85	455.0	34	368.4	85	454.6	34	368.5	85	455.4
35	368.8	86	458.4	35	370.6	86	457.5	35	370.3	86	459.0
36	370.6	87	460.9	36	371.9	87	460.1	36	371.9	87	462.1
37	372.6	88	464.7	37	374.0	88	463.4	37	373.6	88	465.7
38	374.0	89	467.4	38	375.7	89	466.7	38	375.2	89	468.6
39	376.1	90	470.8	39	377.4	90	469.4	39	376.9	90	471.1
40	377.4	91	474.3	40	378.5	91	472.9	40	378.9	91	474.3
41	379.5	92	477.5	41	380.2	92	476.4	41	380.2	92	478.5
42	380.9	93	481.3	42	382.2	93	480.3	42	381.9	93	481.9
43	382.6	94	485.8	43	383.6	94	483.9	43	383.6	94	485.2
44	383.9	95	490.0	44	385.0	95	488.7	44	385.2	95	489.8
45	385.7	96	495.2	45	386.7	96	493.2	45	386.2	96	494.7
46	387.4	97	502.7	46	388.4	97	500.5	46	387.9	97	501.7
47	389.1	98	513.0	47	390.1	98	509.3	47	389.5	98	511.2
48	390.4	99	529.6	48	391.1	99	523.1	48	390.9	99	526.0
49	391.9	99.5	550.2	49	393.4	99.5	536.9	49	393.1	99.5	544.1
50	394.2			50	395.0			50	394.3		

Reaction 22				Reaction 23				Reaction 24			
% Off (wt.%)	BP (°C)	% Off (wt.%)	BP (°C)	% Off (wt.%)	BP (°C)	% Off (wt.%)	BP (°C)	% Off (wt.%)	BP (°C)	% Off (wt.%)	BP (°C)
0.5	153.1	51	395.8	0.5	154.2	51	400.0	0.5	166.9	51	405.3
1	171.5	52	397.7	1	177.5	52	401.5	1	197.1	52	406.9
2	197.5	53	398.8	2	208.1	53	403.0	2	230.3	53	408.4
3	215.4	54	400.8	3	228.2	54	404.2	3	253.1	54	409.5
4	230.7	55	402.3	4	245.2	55	406.1	4	268.7	55	411.4
5	243.6	56	403.8	5	259.1	56	407.6	5	280.4	56	413.1
6	255.1	57	406.1	6	269.9	57	409.1	6	288.6	57	414.4
7	264.7	58	407.6	7	279.0	58	410.7	7	297.1	58	416.6
8	273.2	59	409.1	8	286.2	59	412.7	8	303.6	59	417.5
9	280.4	60	410.7	9	292.9	60	414.0	9	308.1	60	419.7
10	286.2	61	412.2	10	298.8	61	415.8	10	312.6	61	421.1
11	292.9	62	413.5	11	304.3	62	418.0	11	316.5	62	422.8
12	298.8	63	415.8	12	308.4	63	419.3	12	320.4	63	424.6
13	303.6	64	417.5	13	312.6	64	421.1	13	324.7	64	425.9
14	307.7	65	419.3	14	316.0	65	422.8	14	329.1	65	428.2
15	311.2	66	421.1	15	319.5	66	424.2	15	332.1	66	429.0
16	314.7	67	422.8	16	323.4	67	426.4	16	336.0	67	431.2
17	317.8	68	424.6	17	327.3	68	428.2	17	339.0	68	432.1
18	322.1	69	426.8	18	330.8	69	429.9	18	342.1	69	433.4
19	325.6	70	428.2	19	334.3	70	431.2	19	345.6	70	434.7
20	329.1	71	429.9	20	336.9	71	432.8	20	348.3	71	436.3
21	331.7	72	432.1	21	339.9	72	434.1	21	351.4	72	437.3
22	335.1	73	433.4	22	343.0	73	435.0	22	353.7	73	438.5
23	338.6	74	434.7	23	346.5	74	436.6	23	356.4	74	440.1
24	341.2	75	436.0	24	348.7	75	437.9	24	359.0	75	441.7
25	343.8	76	437.3	25	351.4	76	439.8	25	361.7	76	442.7
26	347.4	77	439.2	26	354.1	77	441.1	26	364.4	77	444.3
27	350.1	78	440.5	27	356.8	78	442.4	27	367.1	78	445.9
28	352.3	79	442.4	28	359.9	79	444.3	28	368.9	79	447.5
29	355.5	80	443.7	29	362.2	80	446.2	29	370.9	80	449.6
30	358.2	81	445.6	30	364.4	81	447.5	30	372.3	81	451.4
31	359.9	82	447.2	31	367.1	82	449.6	31	374.2	82	454.1
32	362.6	83	449.6	32	369.3	83	452.3	32	375.9	83	456.8
33	365.3	84	452.3	33	370.9	84	455.0	33	377.2	84	459.4
34	367.1	85	455.0	34	372.6	85	457.6	34	378.9	85	462.6
35	369.9	86	458.1	35	374.2	86	461.2	35	380.2	86	465.3
36	371.6	87	461.2	36	375.9	87	463.9	36	382.2	87	467.9
37	373.3	88	464.8	37	377.2	88	466.8	37	383.6	88	470.7
38	374.9	89	467.9	38	378.9	89	470.0	38	384.9	89	472.8
39	376.2	90	470.7	39	380.9	90	472.8	39	386.9	90	476.0
40	378.2	91	473.5	40	382.2	91	475.7	40	388.2	91	479.2
41	379.6	92	477.1	41	383.6	92	479.2	41	389.9	92	482.5
42	381.6	93	481.3	42	385.5	93	483.1	42	390.9	93	485.5
43	382.9	94	484.9	43	386.9	94	486.7	43	392.4	94	489.2
44	384.2	95	488.6	44	388.5	95	490.7	44	394.7	95	492.8
45	386.2	96	493.4	45	389.5	96	495.3	45	396.2	96	498.2
46	387.5	97	499.8	46	391.6	97	502.1	46	397.3	97	506.1
47	388.9	98	509.2	47	393.1	98	512.1	47	399.2	98	514.4
48	390.9	99	520.3	48	395.0	99	526.4	48	400.8	99	531.5
49	392.4	99.5	533.5	49	396.2	99.5	546.0	49	402.3	99.5	554.0
50	393.9			50	398.1			50	404.2		

Reaction 25				Reaction 26				Reaction 27			
% Off (wt.%)	BP (°C)	% Off (wt.%)	BP (°C)	% Off (wt.%)	BP (°C)	% Off (wt.%)	BP (°C)	% Off (wt.%)	BP (°C)	% Off (wt.%)	BP (°C)
0.5	172.7	51	404.6	0.5	216.4	51	411.8	0.5	229.7	51	415.6
1	198.3	52	406.1	1	242.9	52	413.9	1	257.7	52	416.8
2	229.5	53	407.6	2	272.0	53	415.1	2	282.3	53	418.5
3	251.8	54	408.8	3	286.7	54	416.8	3	295.9	54	419.8
4	267.1	55	409.9	4	297.6	55	418.5	4	305.4	55	421.0
5	279.0	56	411.4	5	305.0	56	419.4	5	312.0	56	422.7
6	286.9	57	413.1	6	311.0	57	421.0	6	317.5	57	424.4
7	295.4	58	414.9	7	315.9	58	422.7	7	322.2	58	425.2
8	302.2	59	416.6	8	321.0	59	424.0	8	327.8	59	426.9
9	307.0	60	418.4	9	325.2	60	425.2	9	332.5	60	428.6
10	311.2	61	420.2	10	329.9	61	427.3	10	336.3	61	429.9
11	315.3	62	422.0	11	333.8	62	428.6	11	339.8	62	431.1
12	319.5	63	423.3	12	338.1	63	430.3	12	343.6	63	432.4
13	323.0	64	424.6	13	341.5	64	431.8	13	346.6	64	433.4
14	327.3	65	426.8	14	344.5	65	432.4	14	349.7	65	435.1
15	330.8	66	428.2	15	347.5	66	433.8	15	352.7	66	436.1
16	334.3	67	430.4	16	350.1	67	435.1	16	356.2	67	437.1
17	337.7	68	431.5	17	353.6	68	436.1	17	358.8	68	438.4
18	341.2	69	432.5	18	356.2	69	437.8	18	361.0	69	440.1
19	343.8	70	434.1	19	358.8	70	439.1	19	364.0	70	441.1
20	347.0	71	435.0	20	361.4	71	440.1	20	366.6	71	442.4
21	350.1	72	436.6	21	364.0	72	441.8	21	368.8	72	443.8
22	352.8	73	438.2	22	365.8	73	443.1	22	370.6	73	445.1
23	355.5	74	439.2	23	368.4	74	444.4	23	372.3	74	446.8
24	357.7	75	440.8	24	370.6	75	445.8	24	374.0	75	447.8
25	360.8	76	442.4	25	371.9	76	447.4	25	376.1	76	449.1
26	362.6	77	443.7	26	374.0	77	448.4	26	377.1	77	451.6
27	364.9	78	444.9	27	375.4	78	450.8	27	378.8	78	453.7
28	368.0	79	446.9	28	377.4	79	452.5	28	380.9	79	455.9
29	369.6	80	448.5	29	378.8	80	455.0	29	382.2	80	458.0
30	371.3	81	450.5	30	380.5	81	457.5	30	383.6	81	460.1
31	372.9	82	453.2	31	381.9	82	459.2	31	385.7	82	462.2
32	374.9	83	455.9	32	383.6	83	461.7	32	387.0	83	464.7
33	376.2	84	458.1	33	385.0	84	464.3	33	388.1	84	466.7
34	377.6	85	461.2	34	386.3	85	466.7	34	389.8	85	468.8
35	379.2	86	463.9	35	388.4	86	469.1	35	391.1	86	471.2
36	380.9	87	467.2	36	389.8	87	471.5	36	393.1	87	473.3
37	382.6	88	469.3	37	390.8	88	474.0	37	394.2	88	476.1
38	384.2	89	472.1	38	392.7	89	476.8	38	396.5	89	478.5
39	385.5	90	475.0	39	394.2	90	479.2	39	398.0	90	481.6
40	386.9	91	478.5	40	396.1	91	482.6	40	399.6	91	484.2
41	388.2	92	481.9	41	397.3	92	485.5	41	401.1	92	487.1
42	389.9	93	484.9	42	398.8	93	488.7	42	402.2	93	490.6
43	391.6	94	488.6	43	400.3	94	492.3	43	403.4	94	494.2
44	393.5	95	492.2	44	401.9	95	496.9	44	405.3	95	498.3
45	394.7	96	497.4	45	403.8	96	502.0	45	406.4	96	504.2
46	396.6	97	504.5	46	404.9	97	509.6	46	408.0	97	511.2
47	397.7	98	513.3	47	406.4	98	517.4	47	409.5	98	519.2
48	399.6	99	528.4	48	408.0	99	534.0	48	411.0	99	535.7
49	401.5	99.5	544.6	49	409.1	99.5	554.8	49	412.2	99.5	557.9
50	403.0			50	411.0			50	413.5		

Reaction 28				Reaction 29				Reaction 30			
% Off (wt.%)	BP (°C)	% Off (wt.%)	BP (°C)	% Off (wt.%)	BP (°C)	% Off (wt.%)	BP (°C)	% Off (wt.%)	BP (°C)	% Off (wt.%)	BP (°C)
0.5	172.4	51	418.5	0.5	266.5	51	422.7	0.5	271.3	51	425.2
1	229.7	52	420.2	1	285.9	52	424.0	1	292.5	52	426.5
2	280.8	53	421.9	2	305.4	53	425.2	2	309.6	53	427.8
3	298.0	54	422.7	3	314.5	54	426.9	3	319.2	54	429.4
4	308.5	55	424.4	4	321.8	55	427.8	4	326.5	55	430.7
5	315.2	56	425.7	5	328.7	56	429.4	5	332.9	56	431.8
6	321.8	57	427.8	6	333.8	57	431.1	6	338.1	57	433.1
7	327.4	58	428.6	7	338.5	58	431.8	7	342.8	58	434.1
8	332.9	59	430.7	8	342.8	59	433.1	8	347.5	59	435.1
9	337.2	60	431.8	9	346.6	60	434.4	9	351.0	60	436.4
10	341.5	61	433.1	10	350.6	61	435.1	10	354.9	61	437.1
11	344.9	62	434.1	11	353.6	62	436.4	11	358.0	62	438.4
12	348.4	63	435.1	12	357.5	63	437.4	12	361.0	63	439.4
13	351.9	64	436.4	13	360.6	64	439.1	13	364.0	64	441.1
14	354.9	65	437.1	14	363.2	65	440.1	14	366.6	65	441.8
15	358.0	66	438.4	15	365.3	66	441.1	15	369.2	66	443.4
16	360.6	67	440.1	16	368.0	67	442.4	16	371.3	67	444.4
17	363.2	68	441.1	17	370.6	68	443.8	17	373.3	68	445.8
18	366.2	69	442.4	18	372.6	69	445.1	18	375.0	69	447.1
19	368.8	70	443.8	19	374.0	70	446.1	19	376.7	70	448.1
20	370.6	71	445.1	20	376.1	71	447.8	20	378.8	71	450.0
21	372.6	72	446.1	21	377.8	72	449.1	21	380.2	72	451.6
22	374.0	73	447.8	22	379.1	73	450.4	22	382.2	73	452.9
23	376.1	74	449.1	23	380.9	74	452.5	23	383.6	74	455.0
24	377.8	75	451.2	24	382.9	75	454.2	24	385.7	75	456.7
25	379.1	76	452.5	25	384.3	76	455.9	25	387.0	76	458.4
26	380.9	77	455.0	26	385.7	77	458.0	26	388.7	77	460.9
27	382.9	78	456.7	27	387.7	78	460.1	27	389.8	78	462.6
28	384.3	79	458.4	28	389.1	79	462.2	28	391.9	79	464.7
29	385.7	80	460.9	29	390.8	80	463.8	29	393.4	80	466.7
30	387.0	81	462.6	30	391.9	81	466.0	30	394.6	81	468.8
31	389.1	82	465.1	31	393.4	82	467.7	31	396.5	82	470.1
32	390.1	83	467.4	32	395.4	83	470.1	32	398.0	83	472.2
33	391.9	84	469.4	33	396.5	84	472.2	33	399.6	84	474.3
34	393.4	85	471.2	34	398.0	85	474.3	34	401.1	85	476.4
35	395.4	86	474.0	35	399.6	86	476.4	35	402.2	86	478.5
36	396.5	87	476.1	36	401.1	87	478.5	36	404.2	87	481.0
37	398.0	88	478.5	37	403.0	88	481.0	37	405.7	88	483.2
38	399.6	89	481.0	38	404.2	89	483.2	38	406.4	89	485.8
39	401.1	90	483.2	39	405.7	90	485.8	39	408.0	90	488.1
40	403.0	91	486.1	40	407.2	91	488.7	40	409.5	91	491.0
41	404.2	92	489.0	41	408.0	92	491.6	41	411.0	92	494.2
42	405.7	93	492.3	42	409.5	93	494.8	42	412.2	93	497.6
43	407.2	94	496.1	43	411.0	94	498.7	43	413.5	94	502.0
44	408.4	95	500.5	44	412.2	95	503.5	44	415.6	95	507.2
45	410.3	96	506.1	45	414.3	96	509.3	45	416.8	96	512.4
46	411.8	97	512.4	46	415.6	97	515.2	46	417.7	97	518.6
47	413.0	98	520.4	47	416.8	98	523.8	47	419.8	98	528.9
48	414.3	99	535.7	48	418.5	99	540.4	48	421.0	99	549.4
49	416.0	99.5	555.2	49	419.8	99.5	565.0	49	421.9	99.5	589.9
50	417.7			50	421.0			50	424.0		

Reaction 31				Reaction 32				Reaction 33			
% Off (wt.%)	BP (°C)	% Off (wt.%)	BP (°C)	% Off (wt.%)	BP (°C)	% Off (wt.%)	BP (°C)	% Off (wt.%)	BP (°C)	% Off (wt.%)	BP (°C)
0.5	196.7	51	409.1	0.5	172.7	51	408.4	0.5	185.8	51	410.3
1	220.4	52	410.7	1	205.6	52	410.3	1	216.2	52	412.2
2	251.0	53	411.8	2	243.6	53	411.4	2	252.7	53	413.5
3	271.1	54	413.1	3	266.7	54	413.1	3	274.7	54	414.9
4	283.7	55	415.3	4	281.2	55	414.4	4	286.9	55	416.6
5	292.9	56	416.6	5	290.7	56	415.8	5	298.0	56	418.4
6	301.4	57	418.4	6	299.7	57	418.0	6	305.0	57	420.2
7	307.7	58	420.2	7	306.4	58	419.3	7	311.2	58	421.5
8	312.2	59	421.1	8	311.2	59	421.1	8	315.3	59	422.8
9	316.9	60	422.8	9	315.3	60	422.4	9	320.4	60	424.6
10	321.3	61	424.6	10	320.4	61	423.7	10	325.2	61	426.4
11	325.6	62	425.9	11	324.7	62	425.9	11	329.5	62	428.2
12	329.5	63	428.2	12	329.1	63	427.3	12	333.8	63	429.5
13	333.4	64	429.9	13	332.5	64	429.0	13	337.3	64	430.8
14	336.9	65	431.2	14	336.9	65	430.4	14	340.8	65	432.5
15	340.4	66	432.1	15	339.5	66	432.1	15	344.3	66	433.4
16	344.3	67	433.4	16	343.0	67	433.1	16	347.4	67	434.4
17	347.4	68	434.7	17	346.1	68	434.1	17	351.0	68	436.0
18	350.1	69	435.7	18	349.6	69	435.3	18	353.7	69	436.9
19	352.8	70	437.3	19	352.3	70	436.9	19	356.4	70	437.9
20	355.9	71	438.5	20	355.5	71	437.9	20	359.0	71	439.2
21	358.6	72	439.5	21	358.2	72	439.2	21	362.2	72	440.8
22	361.3	73	441.1	22	360.8	73	440.5	22	364.4	73	441.7
23	364.0	74	442.4	23	363.1	74	441.7	23	367.1	74	443.7
24	366.2	75	443.7	24	365.8	75	443.3	24	369.3	75	444.9
25	368.5	76	445.6	25	367.6	76	444.9	25	370.9	76	446.2
26	370.3	77	446.9	26	369.6	77	446.2	26	372.9	77	447.5
27	372.3	78	448.5	27	371.6	78	448.1	27	374.6	78	449.6
28	373.9	79	450.0	28	372.9	79	450.0	28	376.2	79	451.8
29	375.2	80	452.3	29	374.9	80	451.8	29	377.2	80	454.1
30	376.9	81	455.0	30	376.6	81	454.1	30	378.9	81	456.3
31	378.2	82	457.2	31	377.9	82	456.8	31	380.9	82	458.5
32	380.2	83	460.3	32	379.6	83	459.4	32	382.2	83	461.2
33	381.6	84	463.0	33	381.6	84	462.1	33	383.6	84	463.9
34	382.9	85	465.7	34	382.9	85	464.8	34	385.2	85	466.5
35	384.9	86	467.9	35	384.6	86	467.2	35	386.9	86	468.6
36	385.9	87	470.7	36	385.5	87	469.7	36	387.9	87	471.1
37	387.5	88	472.8	37	387.5	88	472.5	37	389.5	88	473.2
38	388.9	89	475.7	38	388.9	89	475.0	38	390.9	89	476.0
39	390.9	90	478.8	39	390.2	90	477.8	39	392.4	90	479.2
40	392.4	91	481.6	40	392.0	91	481.3	40	393.9	91	481.9
41	393.9	92	484.3	41	393.1	92	484.0	41	396.2	92	484.3
42	395.0	93	488.0	42	394.7	93	487.4	42	397.3	93	487.4
43	396.9	94	491.0	43	396.6	94	490.4	43	399.2	94	490.7
44	398.5	95	495.3	44	397.7	95	494.4	44	400.4	95	494.7
45	400.4	96	501.3	45	399.2	96	500.6	45	402.3	96	500.2
46	401.5	97	508.8	46	401.1	97	507.7	46	403.4	97	506.9
47	403.0	98	517.3	47	402.3	98	515.9	47	404.6	98	514.7
48	404.6	99	536.1	48	403.8	99	531.5	48	406.1	99	526.8
49	406.1	99.5	569.3	49	405.7	99.5	546.8	49	408.0	99.5	539.8
50	407.2			50	406.9			50	409.1		

Reaction 34				Reaction 35				Reaction 36			
% Off (wt.%)	BP (°C)	% Off (wt.%)	BP (°C)	% Off (wt.%)	BP (°C)	% Off (wt.%)	BP (°C)	% Off (wt.%)	BP (°C)	% Off (wt.%)	BP (°C)
0.5	134.6	51	393.4	0.5	164.6	51	396.2	0.5	172.7	51	403.0
1	154.0	52	395.4	1	183.0	52	398.1	1	199.1	52	404.6
2	178.9	53	396.5	2	207.2	53	399.6	2	231.1	53	406.1
3	201.1	54	398.4	3	224.5	54	401.5	3	251.8	54	408.0
4	218.1	55	400.3	4	238.6	55	403.0	4	267.1	55	409.1
5	232.2	56	401.9	5	251.0	56	404.6	5	278.3	56	410.7
6	244.6	57	403.4	6	261.5	57	406.1	6	286.2	57	412.7
7	255.3	58	405.3	7	270.3	58	408.0	7	294.2	58	414.0
8	264.9	59	407.2	8	277.9	59	409.5	8	300.5	59	415.8
9	272.7	60	408.4	9	284.0	60	411.4	9	305.7	60	417.5
10	280.1	61	410.3	10	290.3	61	413.1	10	310.5	61	418.9
11	285.9	62	411.8	11	296.3	62	414.4	11	314.3	62	420.2
12	292.1	63	413.5	12	301.4	63	416.6	12	317.8	63	422.0
13	297.6	64	414.7	13	305.7	64	418.4	13	322.1	64	424.2
14	302.2	65	416.8	14	309.1	65	420.2	14	325.6	65	425.5
15	306.8	66	418.5	15	312.6	66	422.0	15	329.5	66	427.3
16	310.3	67	420.2	16	315.7	67	423.3	16	333.4	67	429.0
17	313.4	68	421.9	17	319.5	68	425.5	17	336.0	68	430.4
18	316.7	69	424.0	18	323.4	69	427.3	18	339.0	69	432.1
19	320.1	70	425.2	19	326.5	70	429.0	19	342.1	70	433.4
20	324.4	71	427.8	20	330.4	71	431.2	20	345.6	71	434.7
21	327.4	72	429.4	21	333.4	72	432.1	21	348.3	72	435.7
22	330.4	73	431.1	22	336.0	73	433.4	22	351.4	73	437.3
23	333.8	74	432.4	23	339.0	74	435.3	23	353.7	74	438.5
24	337.2	75	434.1	24	342.1	75	436.6	24	356.4	75	439.5
25	339.8	76	435.4	25	344.7	76	438.2	25	359.0	76	441.1
26	342.3	77	437.1	26	348.3	77	439.5	26	361.7	77	442.7
27	345.3	78	439.1	27	350.5	78	441.1	27	364.0	78	444.3
28	348.4	79	440.4	28	353.7	79	442.7	28	366.2	79	445.6
29	351.0	80	442.4	29	356.4	80	444.9	29	368.9	80	447.5
30	353.6	81	444.4	30	358.6	81	446.5	30	370.3	81	449.6
31	356.2	82	446.1	31	361.3	82	448.5	31	372.3	82	451.4
32	358.8	83	448.1	32	364.0	83	450.9	32	373.9	83	454.1
33	360.6	84	450.4	33	366.2	84	453.6	33	375.2	84	456.8
34	363.2	85	452.9	34	368.5	85	456.8	34	376.9	85	459.4
35	365.3	86	455.9	35	370.3	86	459.4	35	378.2	86	463.0
36	367.5	87	459.2	36	371.9	87	463.0	36	380.2	87	465.7
37	369.9	88	462.6	37	373.3	88	466.5	37	381.6	88	468.3
38	371.3	89	466.0	38	374.9	89	469.3	38	382.9	89	471.4
39	373.3	90	468.8	39	376.9	90	472.5	39	384.9	90	473.9
40	374.7	91	472.2	40	378.2	91	475.7	40	385.9	91	477.1
41	376.7	92	476.1	41	380.2	92	479.2	41	387.5	92	480.6
42	378.1	93	479.9	42	381.6	93	483.1	42	388.9	93	483.7
43	380.2	94	483.9	43	383.6	94	486.4	43	390.2	94	487.4
44	381.9	95	488.1	44	384.9	95	491.0	44	392.4	95	491.0
45	383.6	96	493.2	45	386.5	96	495.9	45	393.9	96	495.3
46	385.3	97	500.5	46	388.2	97	504.5	46	395.0	97	502.5
47	386.3	98	510.5	47	389.9	98	514.4	47	396.9	98	511.5
48	388.1	99	524.9	48	390.9	99	536.6	48	398.5	99	524.8
49	389.8	99.5	542.2	49	392.7	99.5	603.8	49	400.4	99.5	540.9
50	391.9			50	394.7			50	401.5		401.5

Reaction 37				Reaction 38				Reaction 39			
% Off (wt.%)	BP (°C)	% Off (wt.%)	BP (°C)	% Off (wt.%)	BP (°C)	% Off (wt.%)	BP (°C)	% Off (wt.%)	BP (°C)	% Off (wt.%)	BP (°C)
0.5	161.1	51	403.0	0.5	216.0	51	409.5	0.5	206.3	51	409.5
1	187.6	52	404.6	1	236.7	52	411.0	1	230.9	52	411.0
2	222.0	53	406.1	2	263.7	53	412.2	2	260.9	53	412.2
3	245.2	54	407.6	3	279.3	54	413.5	3	278.2	54	414.3
4	261.9	55	408.8	4	290.0	55	415.6	4	289.2	55	416.0
5	274.7	56	410.7	5	299.3	56	416.8	5	298.9	56	416.8
6	283.7	57	411.8	6	305.4	57	418.5	6	305.4	57	418.5
7	291.2	58	414.0	7	311.0	58	420.2	7	310.3	58	420.2
8	298.8	59	414.9	8	315.2	59	421.0	8	315.2	59	421.9
9	304.3	60	416.6	9	320.1	60	422.7	9	319.2	60	423.1
10	308.8	61	418.4	10	324.4	61	424.4	10	324.4	61	424.4
11	312.9	62	420.2	11	328.7	62	425.7	11	328.7	62	426.5
12	316.9	63	422.0	12	332.5	63	427.8	12	332.5	63	427.8
13	321.3	64	423.7	13	335.5	64	429.4	13	335.5	64	429.4
14	325.2	65	425.5	14	339.3	65	430.7	14	339.3	65	431.1
15	328.2	66	426.4	15	342.3	66	431.8	15	342.3	66	432.4
16	331.7	67	428.2	16	345.3	67	433.1	16	345.3	67	433.1
17	335.1	68	429.9	17	348.4	68	434.4	17	348.4	68	434.4
18	338.6	69	431.8	18	351.0	69	435.4	18	351.0	69	436.1
19	342.1	70	432.8	19	353.6	70	437.1	19	354.0	70	437.1
20	344.7	71	434.1	20	356.2	71	438.4	20	356.6	71	438.4
21	347.8	72	435.3	21	358.8	72	439.4	21	359.7	72	440.1
22	350.1	73	436.6	22	361.9	73	441.1	22	362.3	73	441.1
23	352.8	74	438.2	23	364.0	74	442.4	23	364.0	74	442.4
24	355.5	75	439.8	24	366.6	75	443.8	24	366.6	75	443.8
25	358.2	76	440.8	25	368.8	76	445.8	25	369.2	76	445.8
26	361.3	77	442.4	26	370.6	77	447.1	26	370.6	77	447.1
27	363.5	78	444.0	27	372.3	78	448.8	27	372.6	78	448.8
28	365.8	79	445.6	28	374.0	79	450.4	28	374.0	79	450.4
29	368.0	80	446.9	29	375.7	80	452.5	29	376.1	80	452.5
30	370.3	81	448.8	30	377.1	81	455.0	30	377.1	81	455.0
31	371.6	82	450.9	31	378.8	82	457.1	31	378.8	82	457.1
32	373.3	83	454.1	32	380.2	83	460.1	32	380.9	83	460.1
33	374.9	84	456.8	33	382.2	84	462.6	33	382.2	84	462.6
34	376.6	85	459.0	34	383.6	85	465.1	34	383.6	85	465.1
35	378.2	86	462.1	35	384.6	86	467.7	35	385.3	86	467.4
36	379.9	87	464.8	36	386.3	87	470.1	36	387.0	87	470.1
37	380.9	88	467.9	37	387.7	88	472.9	37	388.1	88	472.2
38	382.9	89	470.7	38	389.8	89	475.4	38	389.8	89	475.0
39	384.2	90	473.5	39	391.1	90	478.5	39	391.1	90	478.2
40	385.5	91	476.7	40	392.3	91	481.9	40	393.1	91	481.0
41	386.9	92	480.3	41	394.2	92	485.2	41	394.2	92	484.2
42	388.9	93	483.4	42	395.7	93	488.7	42	395.7	93	487.7
43	389.9	94	486.7	43	397.3	94	492.3	43	398.0	94	491.6
44	391.6	95	490.4	44	399.2	95	497.6	44	399.6	95	495.5
45	393.1	96	494.7	45	400.3	96	503.5	45	401.1	96	501.3
46	394.7	97	501.3	46	401.9	97	512.1	46	402.2	97	509.3
47	396.9	98	510.3	47	403.4	98	523.4	47	404.2	98	518.0
48	398.5	99	521.4	48	405.3	99	566.3	48	405.3	99	537.5
49	400.0	99.5	536.1	49	406.4	99.5	658.1	49	406.4	99.5	576.0
50	401.1			50	408.0			50	408.0		

Reaction 40				Reaction 41				Reaction 42			
% Off (wt.%)	BP (°C)	% Off (wt.%)	BP (°C)	% Off (wt.%)	BP (°C)	% Off (wt.%)	BP (°C)	% Off (wt.%)	BP (°C)	% Off (wt.%)	BP (°C)
0.5	233.0	51	413.5	0.5	203.2	51	411.4	0.5	226.6	51	409.5
1	259.7	52	414.7	1	238.2	52	412.2	1	249.4	52	410.7
2	282.3	53	416.8	2	270.7	53	414.4	2	274.0	53	412.2
3	295.1	54	417.7	3	285.5	54	415.8	3	286.2	54	414.0
4	304.0	55	419.8	4	297.1	55	417.1	4	297.1	55	415.8
5	310.3	56	421.0	5	305.0	56	418.4	5	304.3	56	417.1
6	315.5	57	421.9	6	310.5	57	420.2	6	309.5	57	418.4
7	321.0	58	423.6	7	315.3	58	422.0	7	314.0	58	419.7
8	325.7	59	424.8	8	320.4	59	423.7	8	318.6	59	422.0
9	330.4	60	426.9	9	324.7	60	425.1	9	323.9	60	422.8
10	333.8	61	427.8	10	329.1	61	426.4	10	328.2	61	424.6
11	338.1	62	429.4	11	333.4	62	428.2	11	331.7	62	426.4
12	341.5	63	431.4	12	336.9	63	429.9	12	335.1	63	427.7
13	344.9	64	432.4	13	340.4	64	430.8	13	338.6	64	429.9
14	347.5	65	433.1	14	344.3	65	432.1	14	342.1	65	430.8
15	351.0	66	434.8	15	347.4	66	433.4	15	345.6	66	432.5
16	353.6	67	435.8	16	350.1	67	434.7	16	348.7	67	433.4
17	356.6	68	437.1	17	352.8	68	435.7	17	351.0	68	434.7
18	358.8	69	438.4	18	356.4	69	437.3	18	354.6	69	436.0
19	361.4	70	439.8	19	358.6	70	437.9	19	356.8	70	437.3
20	364.0	71	440.8	20	361.7	71	439.5	20	359.0	71	437.9
21	366.6	72	441.8	21	363.5	72	440.5	21	362.2	72	439.2
22	368.8	73	443.1	22	366.2	73	441.7	22	364.4	73	440.5
23	370.6	74	445.1	23	368.9	74	443.0	23	367.1	74	442.1
24	372.6	75	446.4	24	370.3	75	444.6	24	368.9	75	443.7
25	374.3	76	447.8	25	372.3	76	446.2	25	370.9	76	444.6
26	376.1	77	449.1	26	373.6	77	447.2	26	372.3	77	446.2
27	377.4	78	451.2	27	375.6	78	448.8	27	374.2	78	447.5
28	379.1	79	453.3	28	376.9	79	451.4	28	375.6	79	449.6
29	380.9	80	455.4	29	378.2	80	453.2	29	377.2	80	451.4
30	381.9	81	457.5	30	380.2	81	455.9	30	378.9	81	454.1
31	383.6	82	460.1	31	381.6	82	457.6	31	379.9	82	456.3
32	385.0	83	461.7	32	382.9	83	460.3	32	381.6	83	458.5
33	387.0	84	464.3	33	384.9	84	463.5	33	383.2	84	461.2
34	388.4	85	466.7	34	385.9	85	465.7	34	384.9	85	464.4
35	389.8	86	469.1	35	387.5	86	467.9	35	386.2	86	466.5
36	391.1	87	471.5	36	389.2	87	470.4	36	387.5	87	469.3
37	393.1	88	474.0	37	390.2	88	472.8	37	388.9	88	471.4
38	394.2	89	476.4	38	392.0	89	475.7	38	390.2	89	474.3
39	395.7	90	479.2	39	393.1	90	478.5	39	391.6	90	476.7
40	397.3	91	481.9	40	394.7	91	481.3	40	393.1	91	479.9
41	398.8	92	484.5	41	396.2	92	483.7	41	395.0	92	483.1
42	400.3	93	487.7	42	397.7	93	486.7	42	396.2	93	486.1
43	402.2	94	491.6	43	399.6	94	490.4	43	397.7	94	489.2
44	403.4	95	495.5	44	400.8	95	493.7	44	399.2	95	493.1
45	404.9	96	500.5	45	402.3	96	499.0	45	400.8	96	497.4
46	406.4	97	506.4	46	403.8	97	506.1	46	402.7	97	504.5
47	408.0	98	514.3	47	405.3	98	513.3	47	403.8	98	512.7
48	409.5	99	525.3	48	407.2	99	525.6	48	405.3	99	524.4
49	410.3	99.5	536.9	49	408.4	99.5	539.0	49	406.9	99.5	538.5
50	411.8			50	409.9		409.9	50	408.4		

Reaction 43				Reaction 44			
% Off (wt.%)	BP (°C)	% Off (wt.%)	BP (°C)	% Off (wt.%)	BP (°C)	% Off (wt.%)	BP (°C)
0.5	234.6	51	414.7	0.5	261.7	51	420.2
1	261.7	52	416.8	1	280.8	52	421.9
2	284.5	53	417.7	2	300.1	53	423.1
3	297.6	54	419.8	3	309.6	54	424.4
4	306.8	55	421.0	4	316.7	55	426.5
5	312.4	56	422.7	5	323.5	56	427.8
6	318.0	57	424.0	6	329.1	57	428.6
7	323.5	58	425.2	7	334.2	58	430.7
8	328.7	59	426.9	8	338.5	59	431.8
9	332.9	60	428.6	9	342.3	60	433.1
10	336.3	61	429.4	10	346.6	61	434.1
11	340.6	62	431.1	11	349.7	62	435.1
12	344.0	63	432.4	12	352.7	63	436.4
13	347.5	64	433.4	13	356.2	64	437.1
14	350.6	65	434.4	14	358.8	65	438.4
15	353.6	66	436.1	15	362.3	66	439.4
16	356.2	67	437.1	16	364.9	67	441.1
17	358.8	68	438.4	17	367.5	68	441.8
18	361.9	69	439.4	18	369.2	69	443.4
19	364.0	70	441.1	19	371.3	70	444.4
20	366.6	71	441.8	20	373.3	71	445.8
21	368.8	72	443.8	21	375.0	72	447.1
22	370.6	73	445.1	22	376.7	73	448.8
23	372.6	74	446.1	23	378.8	74	450.0
24	374.0	75	447.8	24	380.2	75	451.6
25	376.1	76	449.1	25	381.9	76	454.2
26	377.8	77	451.2	26	383.6	77	455.9
27	378.8	78	452.9	27	385.3	78	458.0
28	380.9	79	455.0	28	386.3	79	460.1
29	382.2	80	457.1	29	388.1	80	462.2
30	383.6	81	459.2	30	389.8	81	463.8
31	385.3	82	461.3	31	391.1	82	466.0
32	387.0	83	463.8	32	392.3	83	468.4
33	388.1	84	466.7	33	394.2	84	470.1
34	389.8	85	468.8	34	395.7	85	472.2
35	391.1	86	470.8	35	397.3	86	474.3
36	393.1	87	473.3	36	399.2	87	476.4
37	394.2	88	476.1	37	400.3	88	479.2
38	395.7	89	478.5	38	401.9	89	481.6
39	397.3	90	481.0	39	403.4	90	483.9
40	399.2	91	483.9	40	404.5	91	487.1
41	400.3	92	487.1	41	406.4	92	489.7
42	401.9	93	490.6	42	408.0	93	492.9
43	403.4	94	494.2	43	409.1	94	496.1
44	405.3	95	498.3	44	410.3	95	501.3
45	406.4	96	504.2	45	411.8	96	506.8
46	408.0	97	511.2	46	413.5	97	512.4
47	409.5	98	520.1	47	414.7	98	520.4
48	411.0	99	539.5	48	416.0	99	535.7
49	411.8	99.5	582.0	49	417.7	99.5	555.2
50	413.5			50	418.9		

Table E6. Summary of select boiling point fractions from simulated distillation results (*Table E5*) for HVGO feed and all hydrotreated liquid products.

Fraction	HVGO Feed (wt.%)	Experiment 1 (wt.%)	Reaction 2 (wt.%)	Reaction 3 (wt.%)
IBP - 300°C	0.5	1	6.5	4.5
300 - 400°C	30	31	34.5	34.5
400 - 500°C	61.5	60.5	52	55.5
500°C - FBP	8	7.5	7	5.5
+343°C	95	94	86	88
Fraction	Reaction 4 (wt.%)	Reaction 5 (wt.%)	Reaction 6 (wt.%)	Reaction 7 (wt.%)
IBP - 300°C	3.5	4.5	9	13
300 - 400°C	32.5	33.5	41	40.5
400 - 500°C	57.5	55.5	46.5	43.5
500°C - FBP	6.5	6.5	3.5	3
+343°C	90	89	79	75
Fraction	Reaction 8 (wt.%)	Reaction 9 (wt.%)	Reaction 10 (wt.%)	Reaction 11 (wt.%)
IBP - 300°C	14	13	14	14.5
300 - 400°C	39.5	41	42	41.5
400 - 500°C	42.5	42.5	40.5	40.5
500°C - FBP	4	3.5	3.5	3.5
+343°C	74.5	74	72.5	72.5
Fraction	Reaction 12 (wt.%)	Reaction 13 (wt.%)	Reaction 14 (wt.%)	Reaction 15 (wt.%)
IBP - 300°C	12.5	11.5	12	12
300 - 400°C	41.5	41.5	42	41.5
400 - 500°C	42.5	43.5	42.5	43
500°C - FBP	3.5	3.5	3.5	3.5
+343°C	75	76	75	75
Fraction	Reaction 20 (wt.%)	Reaction 21 (wt.%)	Reaction 22 (wt.%)	Reaction 23 (wt.%)
IBP - 300°C	11	12	12	10
300 - 400°C	42	41	41.5	41
400 - 500°C	44	44	43.5	46
500°C - FBP	3	3	3	3
+343°C	76	76	75	78

Fraction	Reaction 24 (wt.%)	Reaction 25 (wt.%)	Reaction 26 (wt.%)	Reaction 27 (wt.%)
IBP - 300°C	7.5	8	4	3.5
300 - 400°C	40	40	39	36.5
400 - 500°C	48.5	48.5	52.5	55
500°C - FBP	4	3.5	4.5	5
+343°C	82	81	86	88

Fraction	Reaction 28 (wt.%)	Reaction 29 (wt.%)	Reaction 30 (wt.%)	Reaction 31 (wt.%)
IBP - 300°C	3	2	1.5	6
300 - 400°C	35	33	31.5	39
400 - 500°C	57	59	60.5	51
500°C - FBP	5	6	6.5	4
+343°C	89.5	92	92	84

Fraction	Reaction 32 (wt.%)	Reaction 33 (wt.%)	Reaction 34 (wt.%)	Reaction 35 (wt.%)
IBP - 300°C	6	5	13.5	12
300 - 400°C	39.5	39	41.5	41
400 - 500°C	50.5	52	42	43.5
500°C - FBP	4	4	3	3.5
+343°C	84	85	74	76

Fraction	Reaction 36 (wt.%)	Reaction 37 (wt.%)	Reaction 38 (wt.%)	Reaction 39 (wt.%)
IBP - 300°C	8	8	5	5
300 - 400°C	41	41	40	39
400 - 500°C	48	48	50.5	52
500°C - FBP	3	3	4.5	4
+343°C	81	81	85	85

Fraction	Reaction 40 (wt.%)	Reaction 41 (wt.%)	Reaction 42 (wt.%)	Reaction 43 (wt.%)
IBP - 300°C	3.5	4.5	4.5	3
300 - 400°C	38.5	38.5	40	38
400 - 500°C	54	53	52	54
500°C - FBP	4	4	3.5	5
+343°C	87.5	86	86	88

Fraction	Reaction 44 (wt.%)
IBP - 300°C	2
300 - 400°C	35
400 - 500°C	58
500°C - FBP	5
+343°C	91
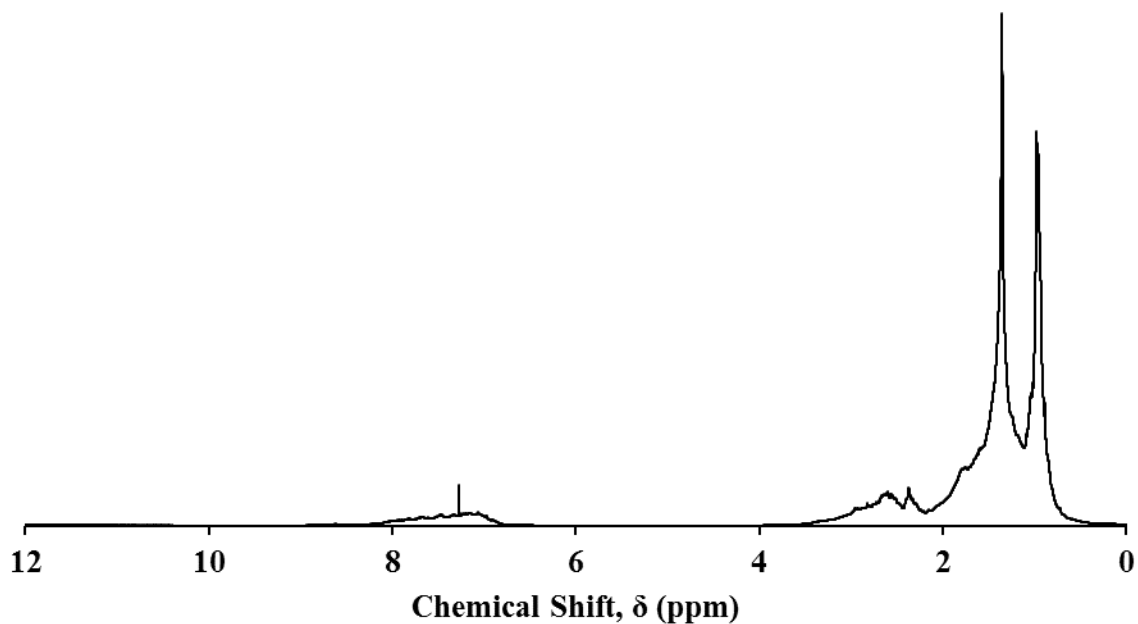
Figure E1. Hydrogen nuclear magnetic resonance chemical shift spectra of HVGO feed using the 400MHz spectrometer.
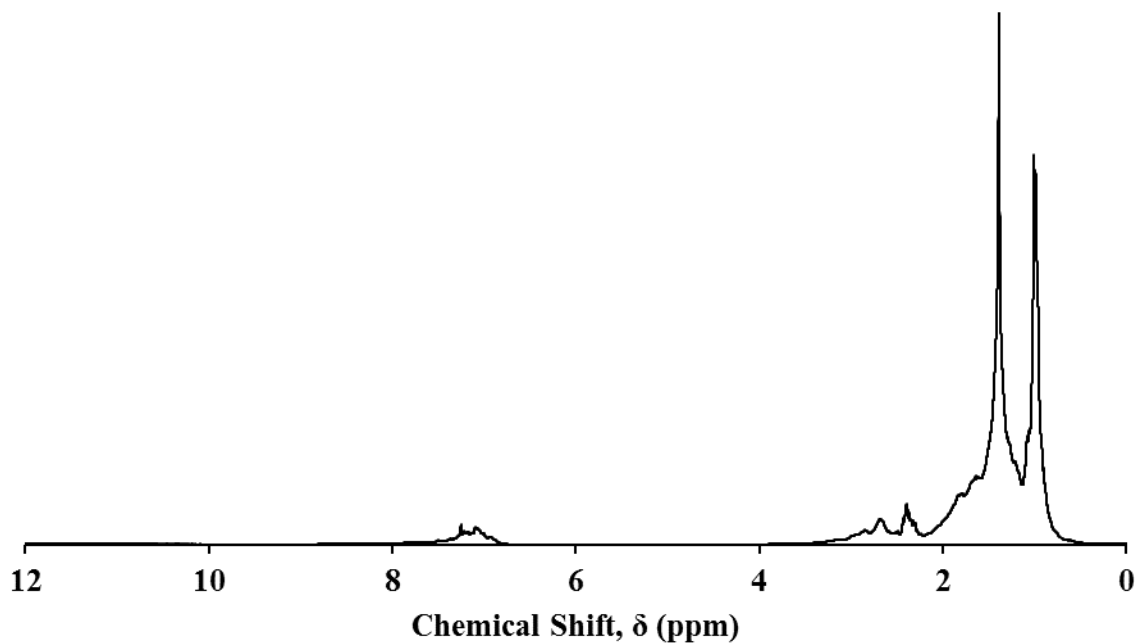
Figure E2. Hydrogen nuclear magnetic resonance chemical shift spectra of reaction 21 (390°C, 2h, and sulfided pellets) liquid product using the 400MHz spectrometer.
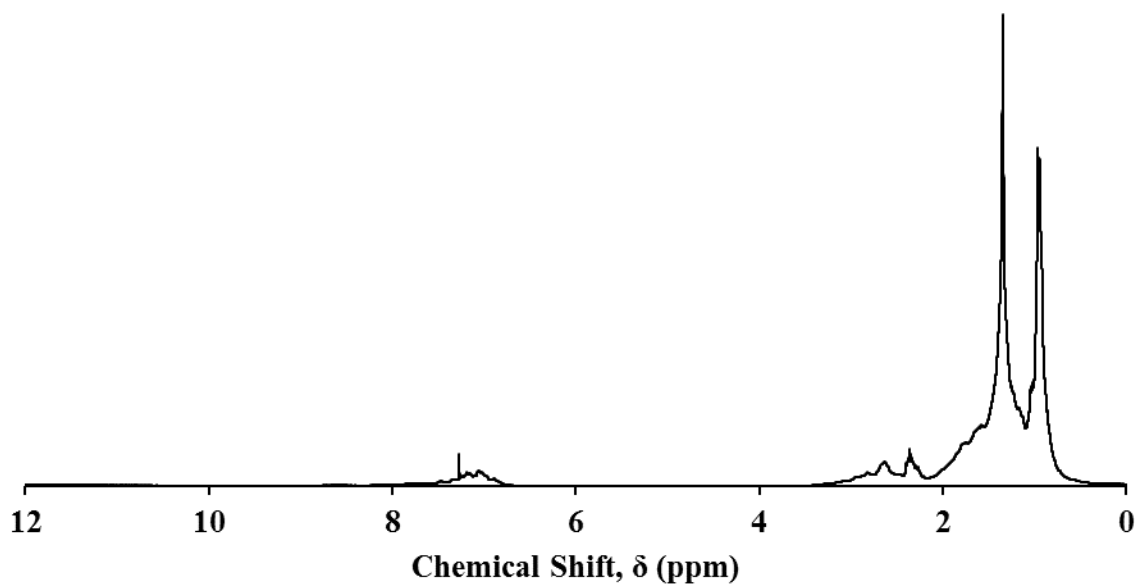
Figure E3. Hydrogen nuclear magnetic resonance chemical shift spectra of reaction 25 (390°C, 1h, and sulfided pellets) liquid product using the 400MHz spectrometer.
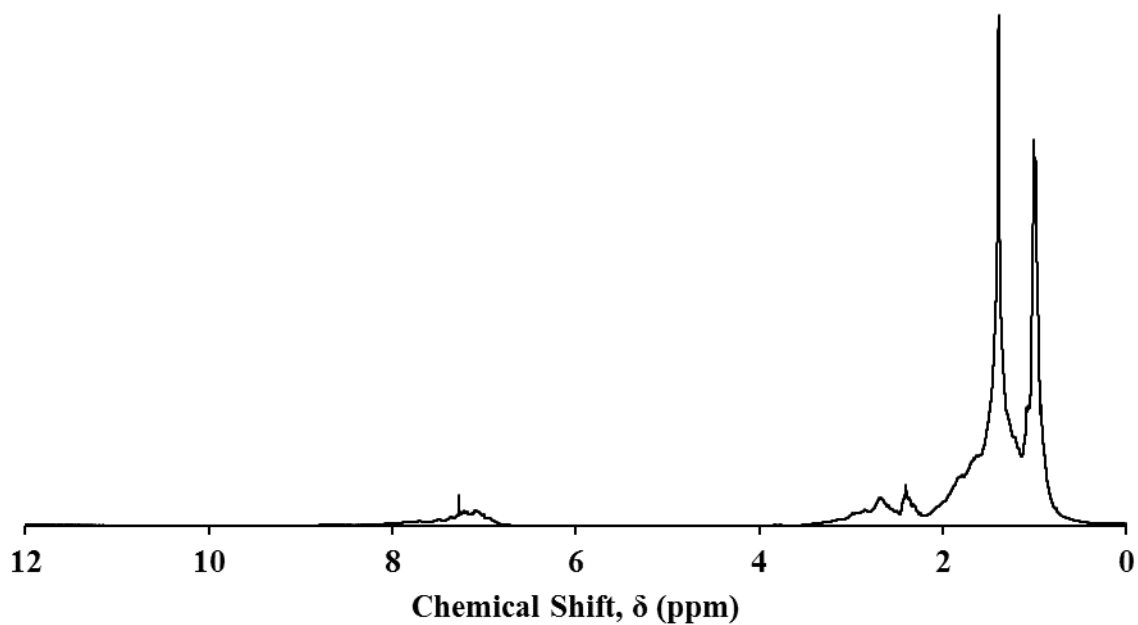
Figure E4. Hydrogen nuclear magnetic resonance chemical shift spectra of reaction 27 (350°C, 2h, and sulfided pellets) liquid product using the 400MHz spectrometer.

385
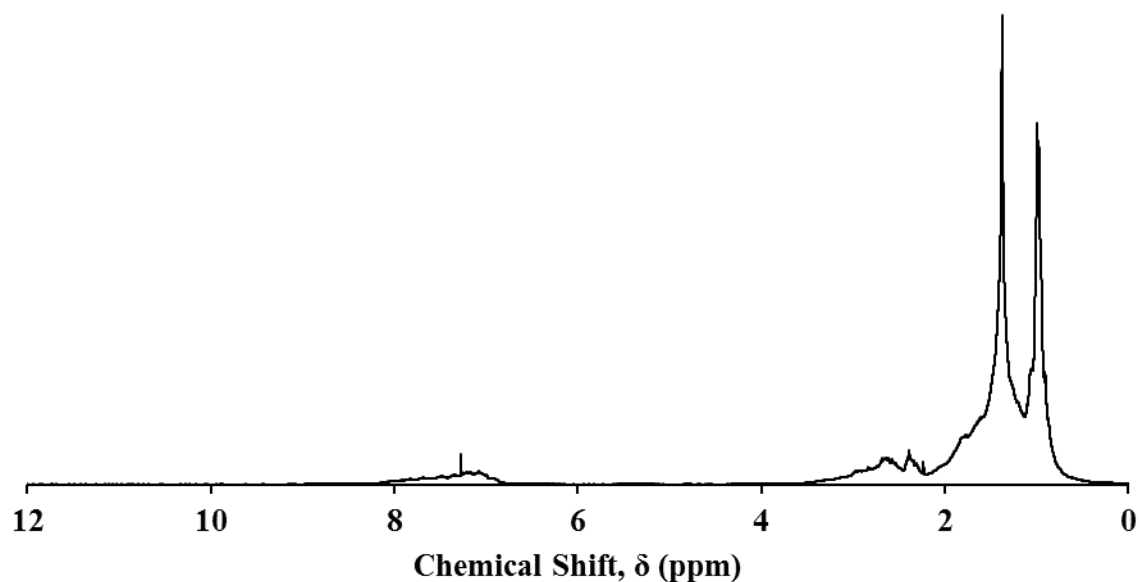
Figure E5. Hydrogen nuclear magnetic resonance chemical shift spectra of reaction 29 (310°C, 2h, and sulfided pellets) liquid product using the 400MHz spectrometer.
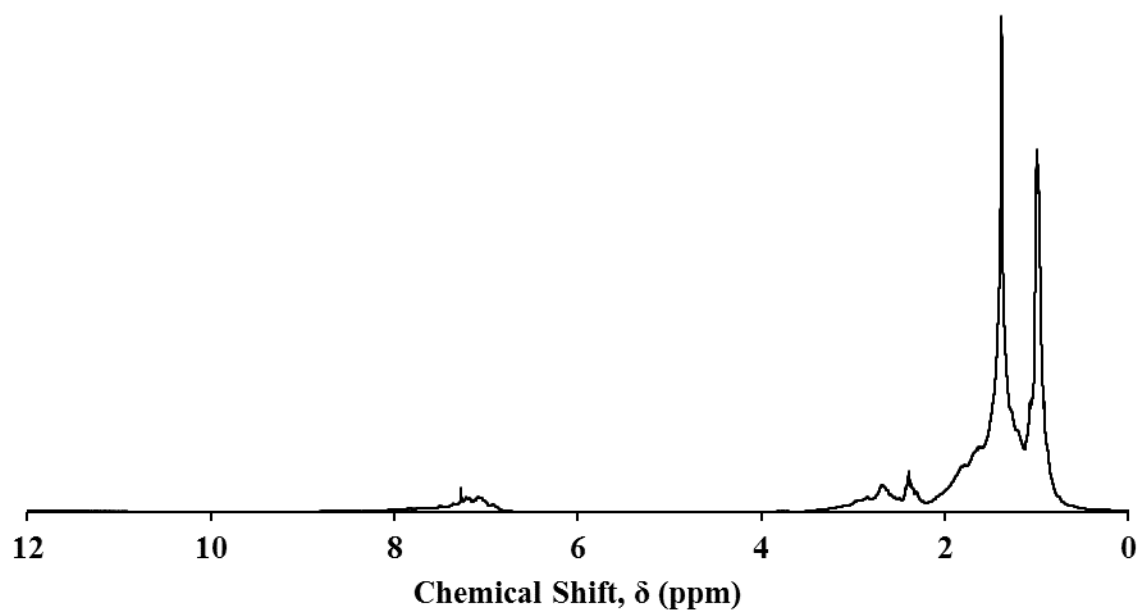
Figure E6. Hydrogen nuclear magnetic resonance chemical shift spectra of reaction 32 (390°C, 0.5h, and sulfided pellets) liquid product using the 400MHz spectrometer.
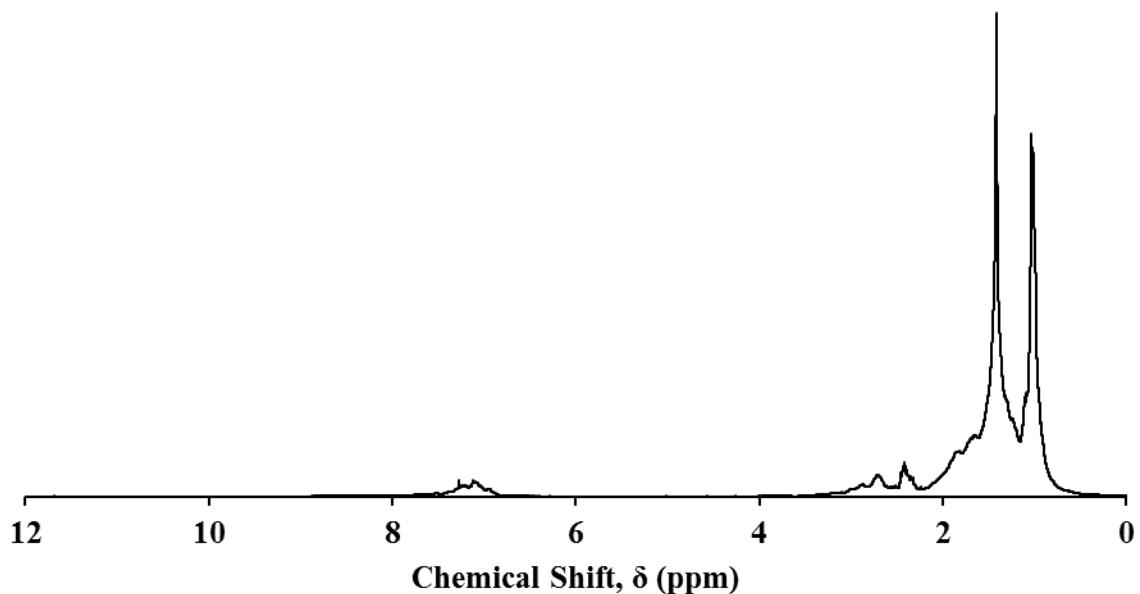
Figure E7. Hydrogen nuclear magnetic resonance chemical shift spectra of reaction 35 (390°C, 2h, and sulfided <45μm particles) liquid product using the 400MHz spectrometer.
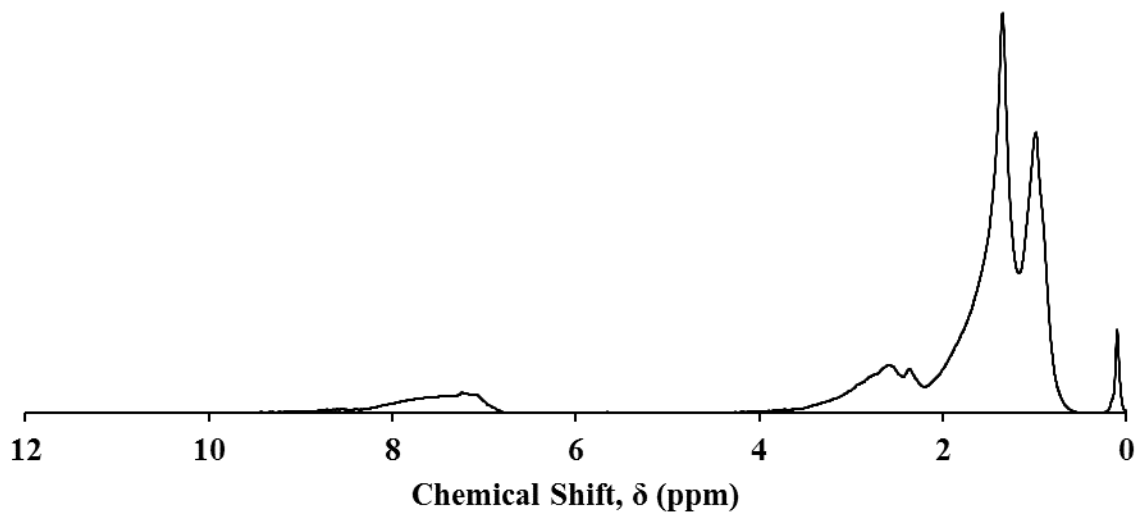
Figure E8. Hydrogen nuclear magnetic resonance chemical shift spectra of HVGO feed using the 60MHz spectrometer.
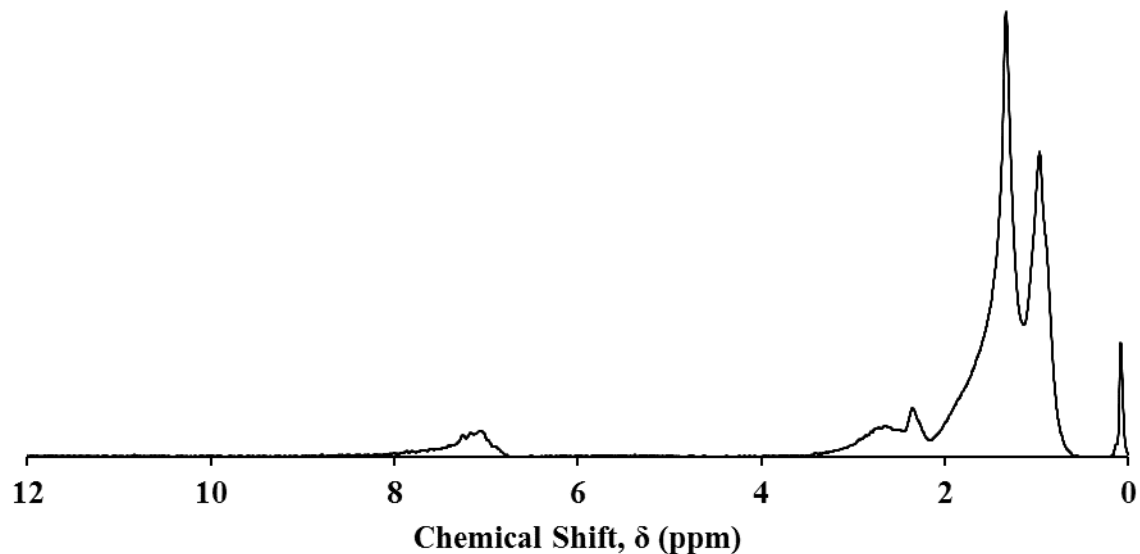
Figure E9. Hydrogen nuclear magnetic resonance chemical shift spectra of reaction 23 (390°C, 1.5h, and sulfided pellets) liquid product using the 60MHz spectrometer.
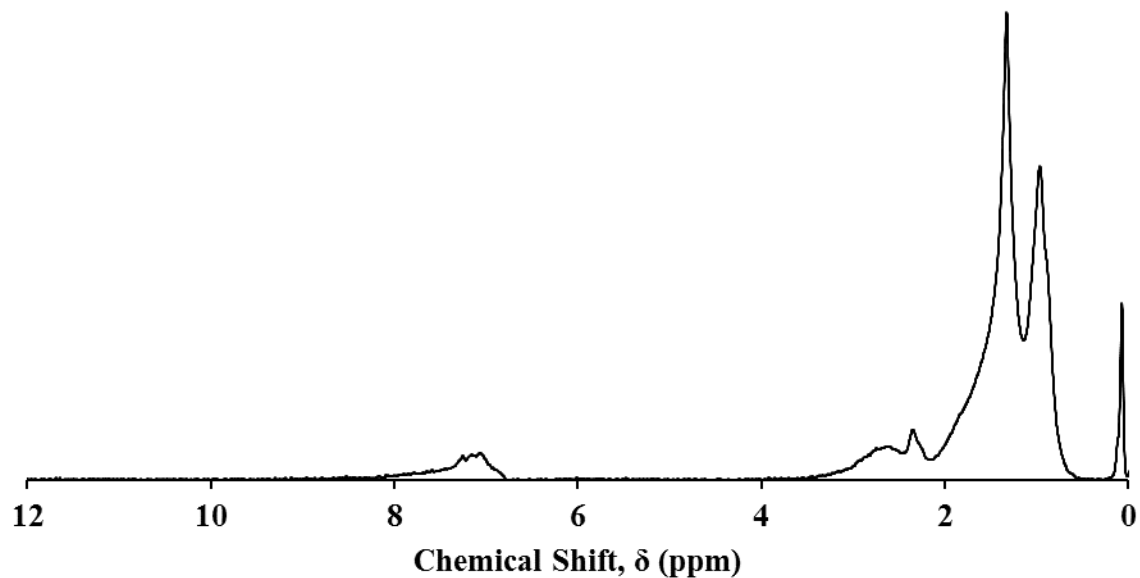
Figure E10. Hydrogen nuclear magnetic resonance chemical shift spectra of reaction 24 (390°C, 1h, and sulfided pellets) liquid product using the 60MHz spectrometer.
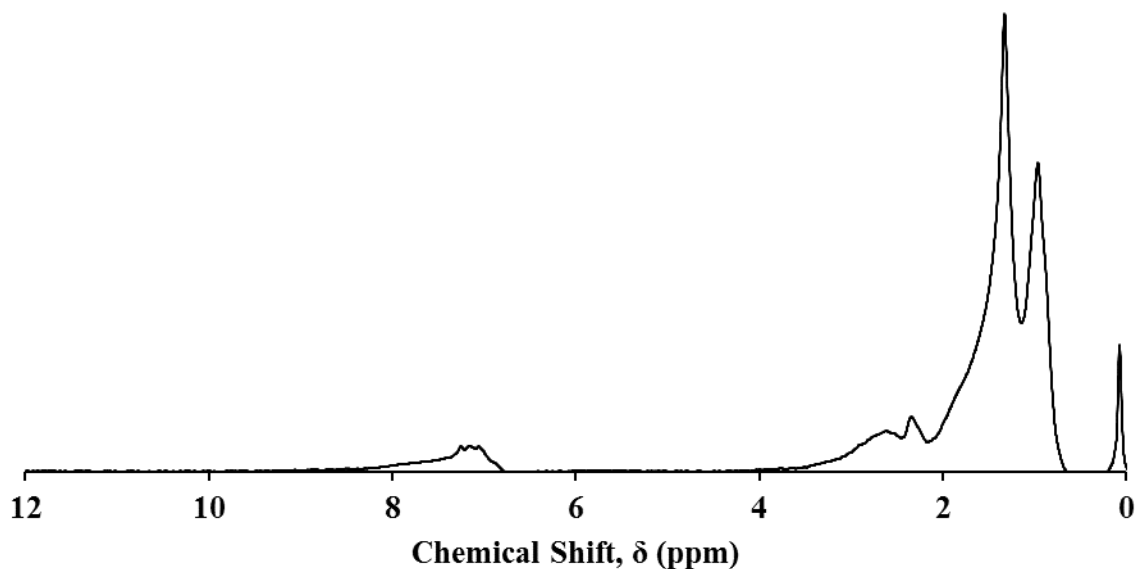
Figure E11. Hydrogen nuclear magnetic resonance chemical shift spectra of reaction 26 (370°C, 1h, and sulfided pellets) liquid product using the 60MHz spectrometer.
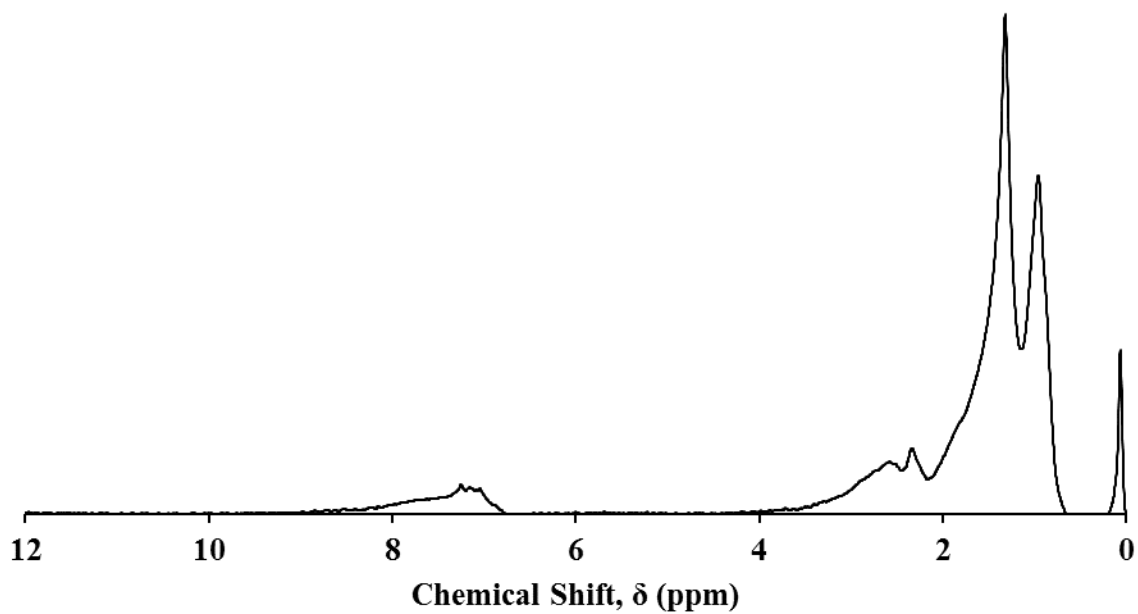
Figure E12. Hydrogen nuclear magnetic resonance chemical shift spectra of reaction 28 (330°C, 1h, and sulfided pellets) liquid product using the 60MHz spectrometer.

389
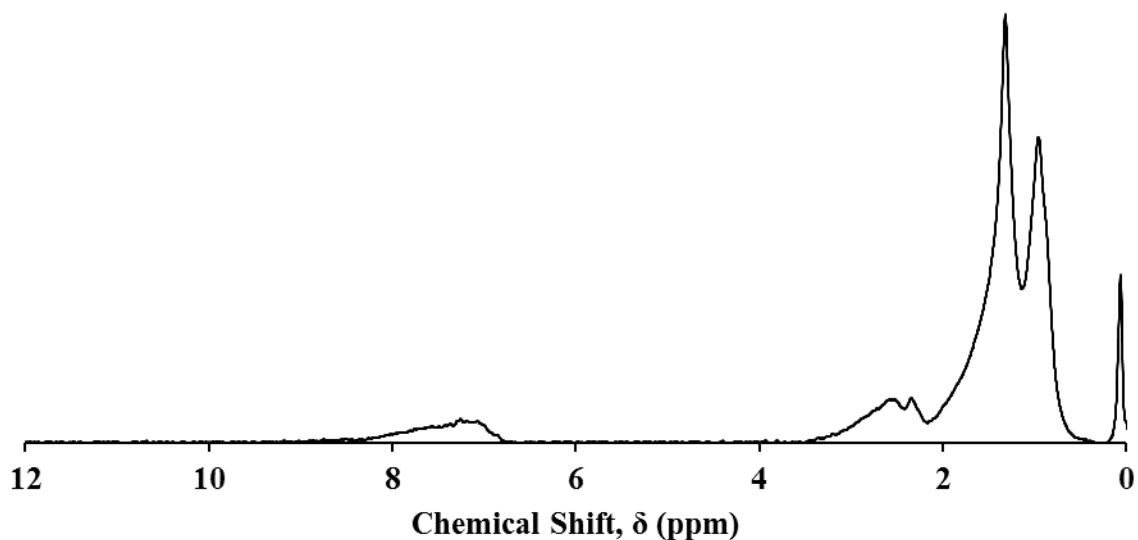
Figure E13. Hydrogen nuclear magnetic resonance chemical shift spectra of reaction 30 (290°C, 1h, and sulfided pellets) liquid product using the 60MHz spectrometer.
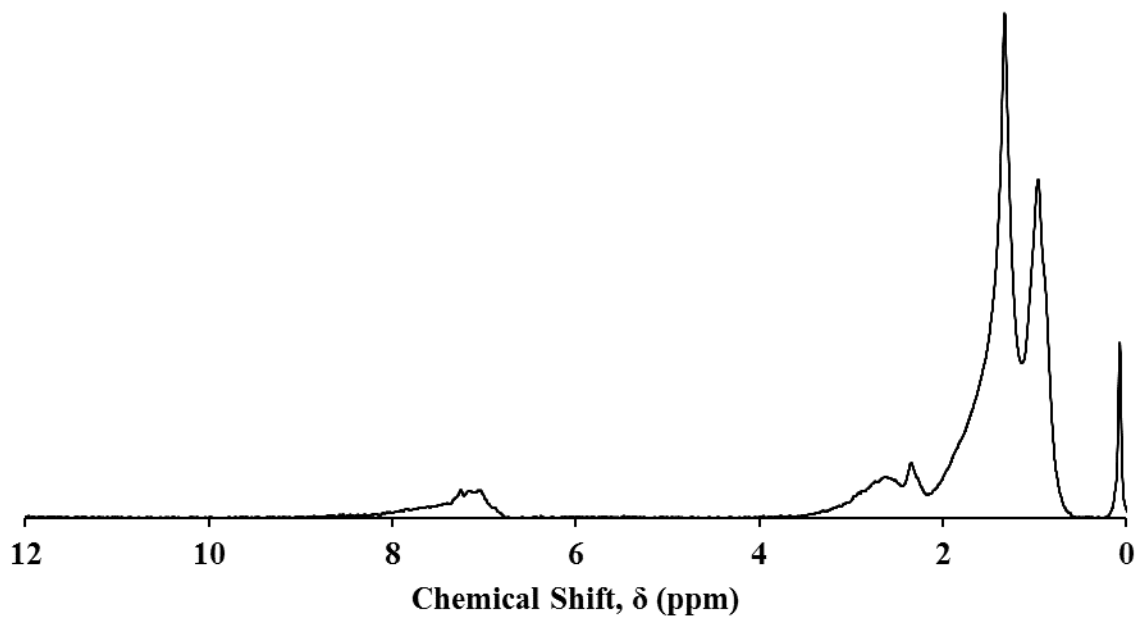
Figure E14. Hydrogen nuclear magnetic resonance chemical shift spectra of reaction 31 (390°C, 0.5h, and sulfided pellets) liquid product using the 60MHz spectrometer.
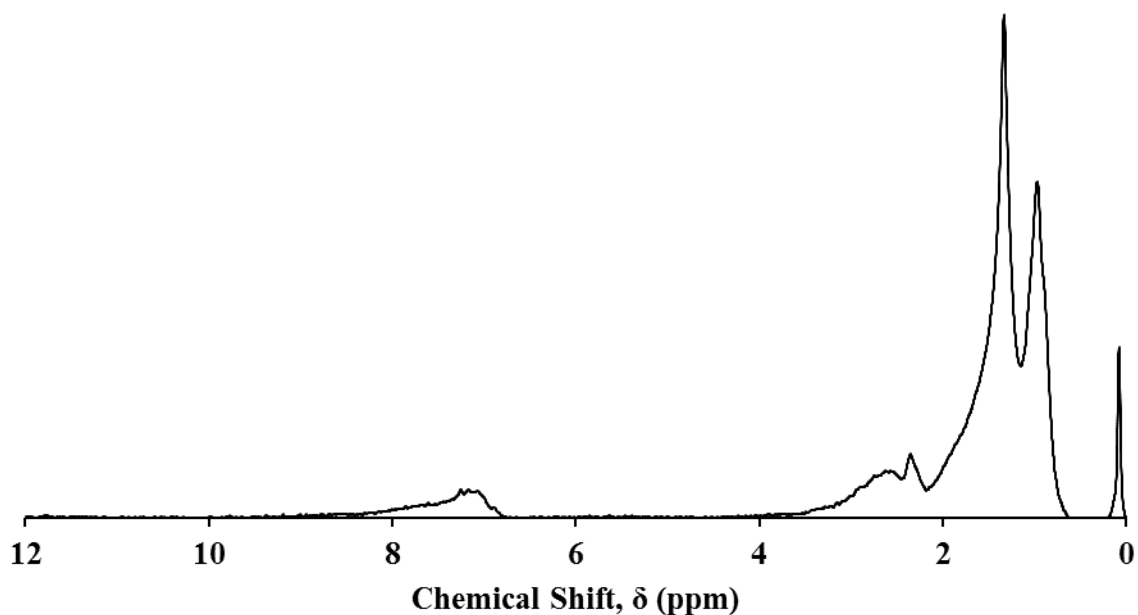
Figure E15. Hydrogen nuclear magnetic resonance chemical shift spectra of reaction 33 (390°C, 0.25h, and sulfided pellets) liquid product using the 60MHz spectrometer.
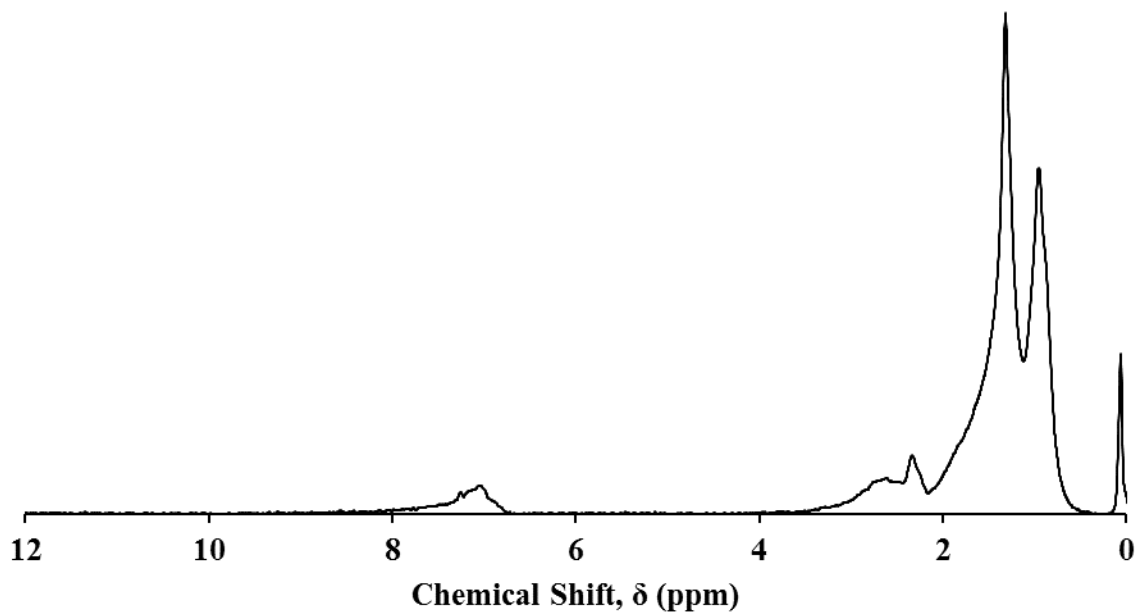
Figure E16. Hydrogen nuclear magnetic resonance chemical shift spectra of reaction 34 (390°C, 2h, and sulfided <45μm particles) liquid product using the 60MHz spectrometer.

391
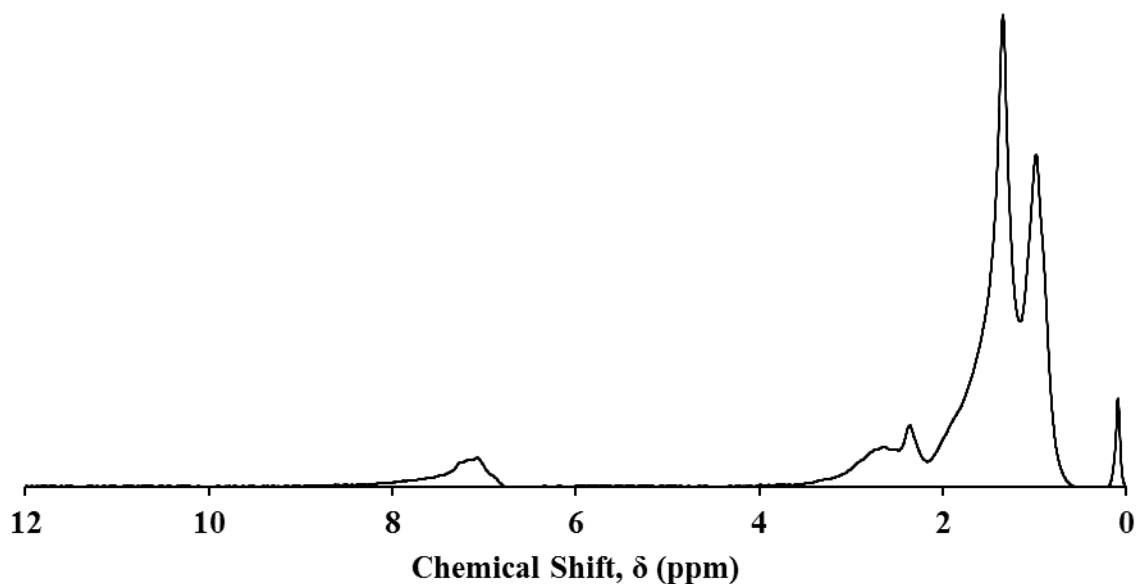
Figure E17. Hydrogen nuclear magnetic resonance chemical shift spectra of reaction 37 (390°C, 1h, and sulfided <45μm particles) liquid product using the 60MHz spectrometer.
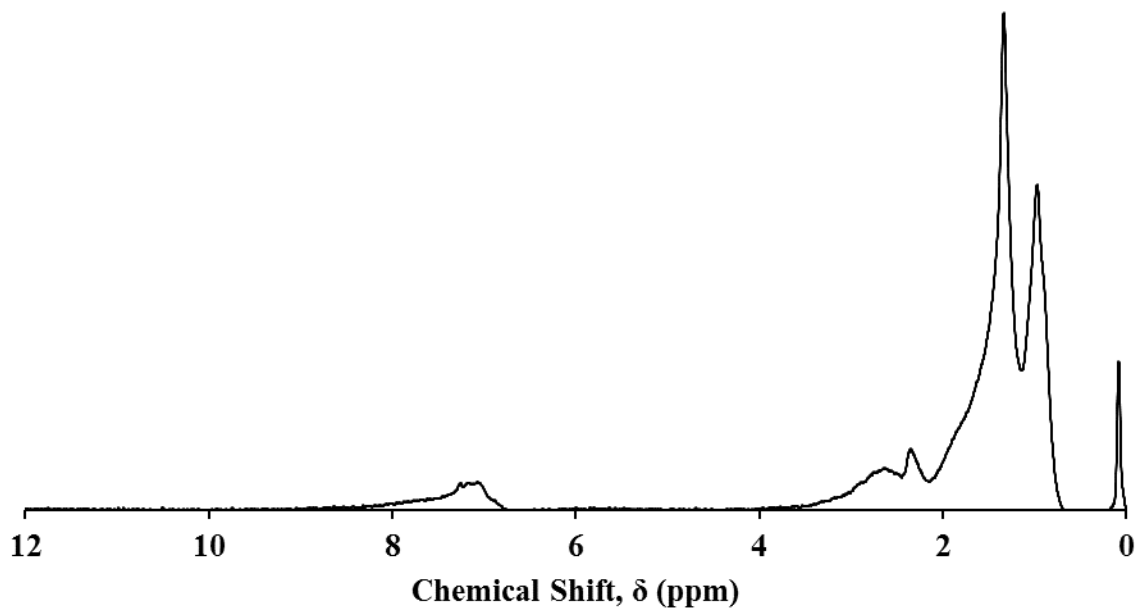
Figure E18. Hydrogen nuclear magnetic resonance chemical shift spectra of reaction 38 (390°C, 0.5h, and sulfided <45μm particles) liquid product using the 60MHz spectrometer.
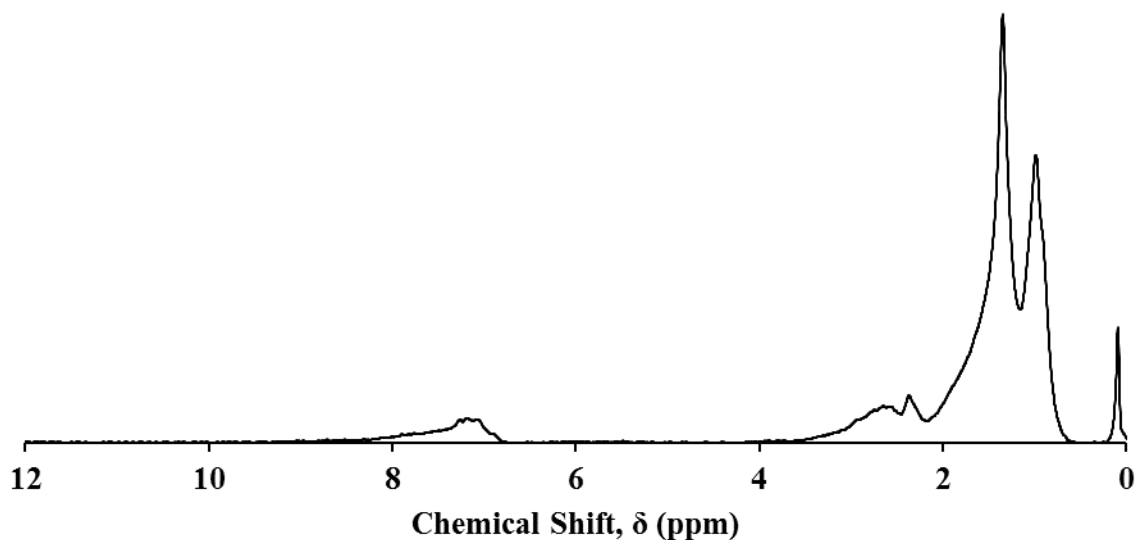
Figure E19. Hydrogen nuclear magnetic resonance chemical shift spectra of reaction 41 (390°C, 0.25h, and sulfided <45μm particles) liquid product using the 60MHz spectrometer.
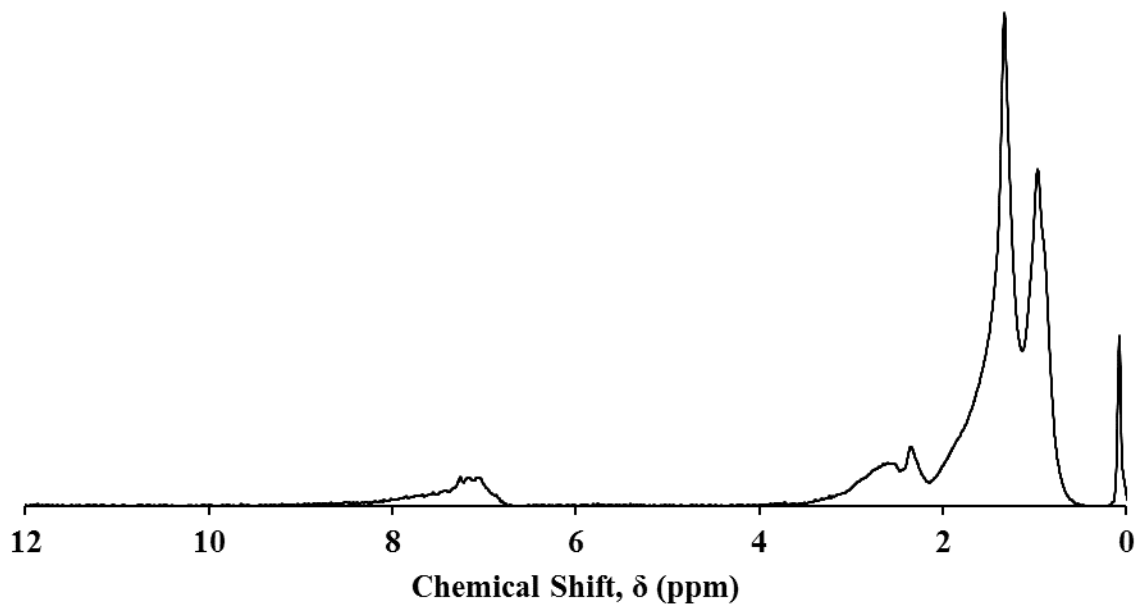
Figure E20. Hydrogen nuclear magnetic resonance chemical shift spectra of reaction 42 (390°C, 0.25h, and sulfided <45μm particles) liquid product using the 60MHz spectrometer.
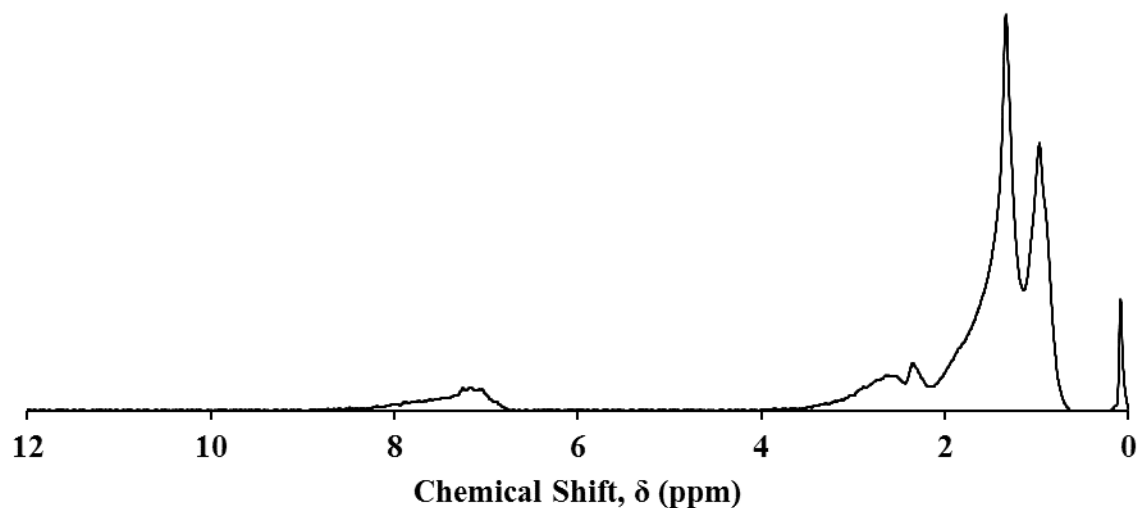
Figure E21. Hydrogen nuclear magnetic resonance chemical shift spectra of reaction 43 (370°C, 0.25h, and sulfided <45µm particles) liquid product using the 60MHz spectrometer.
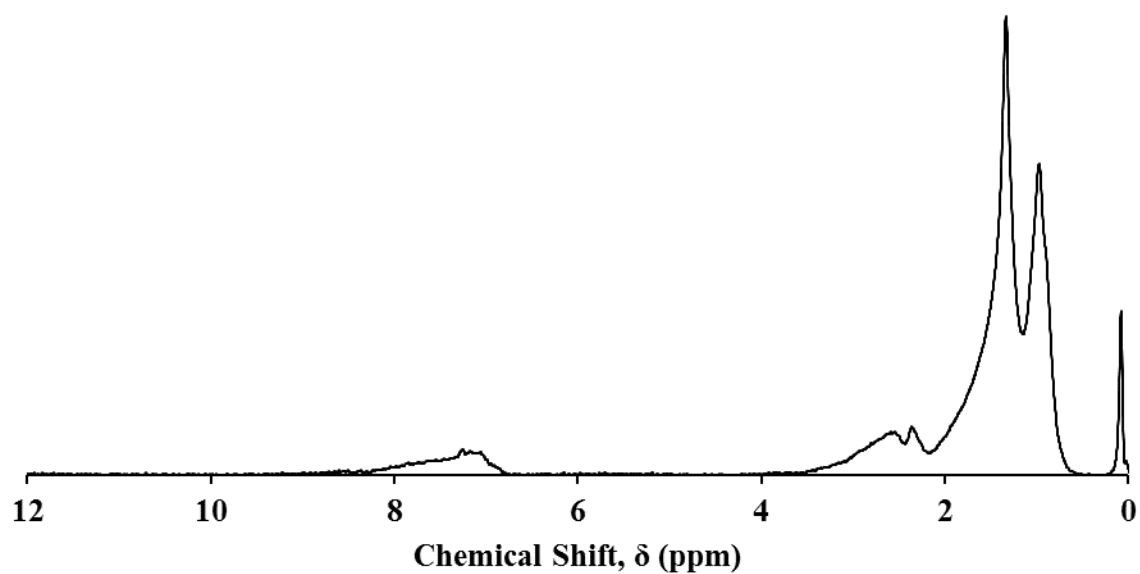
Figure E22. Hydrogen nuclear magnetic resonance chemical shift spectra of reaction 44 (350°C, 0.25h, and sulfided <45µm particles) liquid product using the 60MHz spectrometer.

394

Table E7. Summary of molecular hydrogen concentration results obtained from chemical shift spectra for HVGO feed and select hydrotreated liquid products.

400MHz Spectrometer								
Chemical Shift Region	HVGO Feed mol H %		Reaction 21 mol H %		Reaction 25 mol H %		Reaction 27 mol H %	
Polyaromatic	3.01	6.1	0.52	3.93	1.28	4.94	1.88	5.37
Monoaromatic	3.09		3.41		3.66		3.49	
α-Aromatic (CH$_2$)	9.48	14.07	7.7	12.57	7.51	12.33	8.83	13.67
α-Aromatic (CH$_3$)	4.59		4.87		4.82		4.84	
Aliphatic (CH$_2$)	51.28	79.83	56.72	83.5	53.48	82.73	53.88	80.96
γ-Aliphatic (CH$_3$)	28.22		26.78		29.25		27.08	
Chemical Shift Region	Reaction 29 mol H %		Reaction 32 mol H%		Reaction 35 mol H%			
Polyaromatic	2.67	6.11	1.7	5.36	0.85	4.2		
Monoaromatic	3.44		3.66		3.35			
α-Aromatic (CH$_2$)	8.97	13.29	7.96	12.65	6.91	10.89		
α-Aromatic (CH$_3$)	4.32		4.69		3.98			
Aliphatic (CH$_2$)	52.15	80.6	53.6	81.99	57.24	84.91		
γ-Aliphatic (CH$_3$)	28.45		28.39		27.67			

60MHz Spectrometer								
Chemical Shift Region	HVGO Feed mol H %		Reaction 23 mol H %		Reaction 24 mol H %		Reaction 26 mol H %	
Polyaromatic	4.63	7.65	1.72	5.52	2.15	6.04	2.85	6.39
Monoaromatic	3.02		3.8		3.89		3.54	
α-Aromatic (CH$_2$)	11.34	16.46	6.93	11.6	7.43	12.22	9.36	15.08
α-Aromatic (CH$_3$)	5.12		4.67		4.79		5.72	
Aliphatic (CH$_2$)	53.3	75.89	54.78	82.88	54.99	81.74	55.46	78.53
γ-Aliphatic (CH$_3$)	22.59		28.1		26.75		23.07	
Chemical Shift Region	Reaction 28 mol H %		Reaction 30 mol H %		Reaction 31 mol H %		Reaction 33 mol H %	
Polyaromatic	3.69	7.07	3.94	7.55	2.48	6.28	3.35	6.98
Monoaromatic	3.38		3.61		3.8		3.63	
α-Aromatic (CH$_2$)	10.61	16.6	8.29	12.71	13.11	13.11	10.07	15.73
α-Aromatic (CH$_3$)	5.99		4.42		5.66		5.66	
Aliphatic (CH$_2$)	54.08	76.33	52.46	79.74	54.75	80.61	53.82	77.29
γ-Aliphatic (CH$_3$)	22.25		27.28		25.86		23.47	

60MHz Spectrometer								
Chemical Shift Region	Reaction 28		Reaction 30		Reaction 31		Reaction 33	
	mol H %		mol H %		mol H %		mol H %	
Polyaromatic	3.69	7.07	3.94	7.55	2.48	6.28	3.35	6.98
Monoaromatic	3.38		3.61		3.8		3.63	
α-Aromatic (CH$_2$)	10.61	16.6	8.29	12.71	13.11	13.11	10.07	15.73
α-Aromatic (CH$_3$)	5.99		4.42		5.66		5.66	
Aliphatic (CH$_2$)	54.08	76.33	52.46	79.74	54.75	80.61	53.82	77.29
γ-Aliphatic (CH$_3$)	22.25		27.28		25.86		23.47	
Chemical Shift Region	Reaction 34		Reaction 37		Reaction 38		Reaction 41	
	mol H %		mol H %		mol H %		mol H %	
Polyaromatic	1.61	5.28	1.99	5.76	2.62	6.38	3.09	6.82
Monoaromatic	3.67		0.76		3.76		3.73	
α-Aromatic (CH$_2$)	7.34	12.43	8.58	13.95	9.23	15.14	8.97	13.97
α-Aromatic (CH$_3$)	5.09		5.37		5.91		5	
Aliphatic (CH$_2$)	54.03	82.29	55.95	80.29	56.14	78.48	55.1	79.21
γ-Aliphatic (CH$_3$)	28.26		24.34		22.34		24.11	
Chemical Shift Region	Reaction 42		Reaction 43		Reaction 44			
	mol H %		mol H %		mol H %			
Polyaromatic	2.83	6.87	3.12	7.11	3.59	7.21		
Monoaromatic	4.04		3.99		3.62			
α-Aromatic (CH$_2$)	8.68	13.77	9.11	14.69	9.22	13.99		
α-Aromatic (CH$_3$)	5.09		5.58		4.77			
Aliphatic (CH$_2$)	52.96	79.36	54.49	78.2	53.69	78.8		
γ-Aliphatic (CH$_3$)	26.4		23.71		25.11			

Appendix F

Conversion and kinetic plots for sulfur and nitrogen are found in *Appendix F*. Results from *Table E3* are used to generate comparative plots. The plotted data highlight the reaction time, reaction temperature, and catalyst size trends for the reactions completed in *Table F1*.

Table F1. Experimental reactions, feed, catalyst size, pressure, temperature, agitation, and reaction times.

#	Reaction	Feed	Catalyst Size	Pressure (kPa(g))	Temperature (°C)	Agitation (RPM)	Time (h)
20	Hydrotreating	HVGO	Sulfided Pellet	4500	390	878	2
21	Hydrotreating	HVGO	Sulfided Pellet	4500	390	886	2
22	Hydrotreating	HVGO	Sulfided Pellet	4500	390	892	2
23	Hydrotreating	HVGO	Sulfided Pellet	4500	390	896	1.5
24	Hydrotreating	HVGO	Sulfided Pellet	4500	390	889	1
25	Hydrotreating	HVGO	Sulfided Pellet	4500	390	875	1
26	Hydrotreating	HVGO	Sulfided Pellet	4500	370	888	1
27	Hydrotreating	HVGO	Sulfided Pellet	4500	350	900	1
28	Hydrotreating	HVGO	Sulfided Pellet	4500	330	891	1
29	Hydrotreating	HVGO	Sulfided Pellet	4500	310	893	1
30	Hydrotreating	HVGO	Sulfided Pellet	4500	290	898	1
31	Hydrotreating	HVGO	Sulfided Pellet	4500	390	867	0.5
32	Hydrotreating	HVGO	Sulfided Pellet	4500	390	859	0.5
33	Hydrotreating	HVGO	Sulfided Pellet	4500	390	850	0.25
34	Hydrotreating	HVGO	Sulfided < 45μm	4500	390	888	2
35	Hydrotreating	HVGO	Sulfided < 45μm	4500	390	874	2
36	Hydrotreating	HVGO	Sulfided < 45μm	4500	390	879	1
37	Hydrotreating	HVGO	Sulfided < 45μm	4500	390	870	1
38	Hydrotreating	HVGO	Sulfided < 45μm	4500	390	870	0.5
39	Hydrotreating	HVGO	Sulfided < 45μm	4500	390	859	0.5
40	Hydrotreating	HVGO	Sulfided < 45μm	4500	370	894	0.5
41	Hydrotreating	HVGO	Sulfided < 45μm	4500	390	880	0.25
42	Hydrotreating	HVGO	Sulfided < 45μm	4500	390	890	0.25
43	Hydrotreating	HVGO	Sulfided < 45μm	4500	370	900	0.25
44	Hydrotreating	HVGO	Sulfided < 45μm	4500	350	900	0.25

Sulfur and Nitrogen Conversion Trends

The effect of the reaction time at 390°C with sulfided catalyst pellets on sulfur and nitrogen conversion results of the hydrotreated liquid products are presented in *Figure F1*. The effect of the reaction temperature at 1h with sulfided catalyst pellets on sulfur and nitrogen conversion results of the hydrotreated liquid products are presented in *Figure F2*. The effect of the reaction time at 390°C with <45μm sulfided catalyst solids on sulfur and nitrogen conversion results of the hydrotreated liquid products are presented in *Figure F3*. The effect of the reaction temperature at 0.25 and 0.5h with <45μm sulfided catalyst solids on sulfur plus nitrogen conversion results of the hydrotreated liquid products are presented in *Figure F4*. The effect of the reaction time at 390°C with sulfided catalyst pellets and <45μm solids on sulfur plus nitrogen conversion results of the hydrotreated liquid products are presented in *Figure F5*.
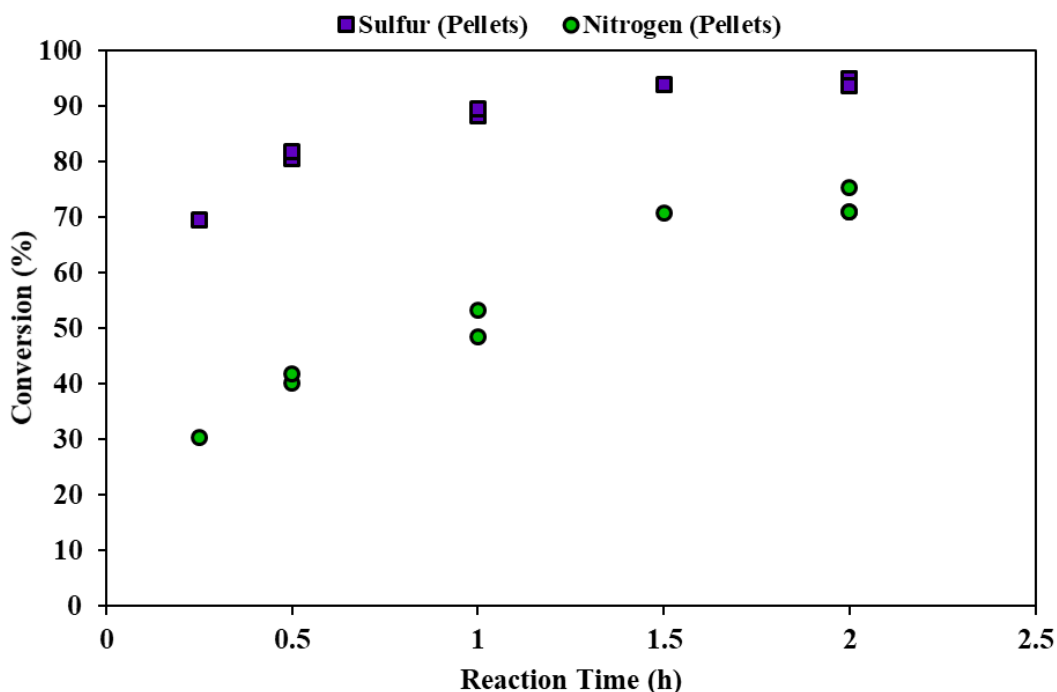
Figure F1. The effect of the reaction time at 390°C with sulfided catalyst pellets on sulfur and nitrogen conversion results of the hydrotreated liquid products.
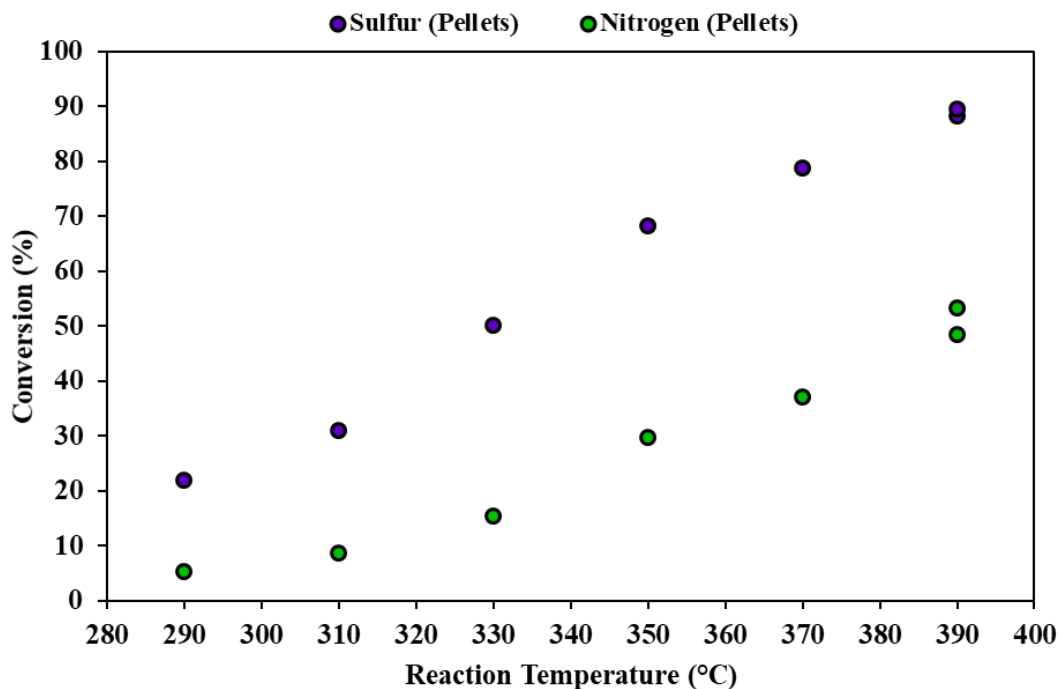
Figure F2. The effect of the reaction temperature at 1h with sulfided catalyst pellets on sulfur and nitrogen conversion results of the hydrotreated liquid products.
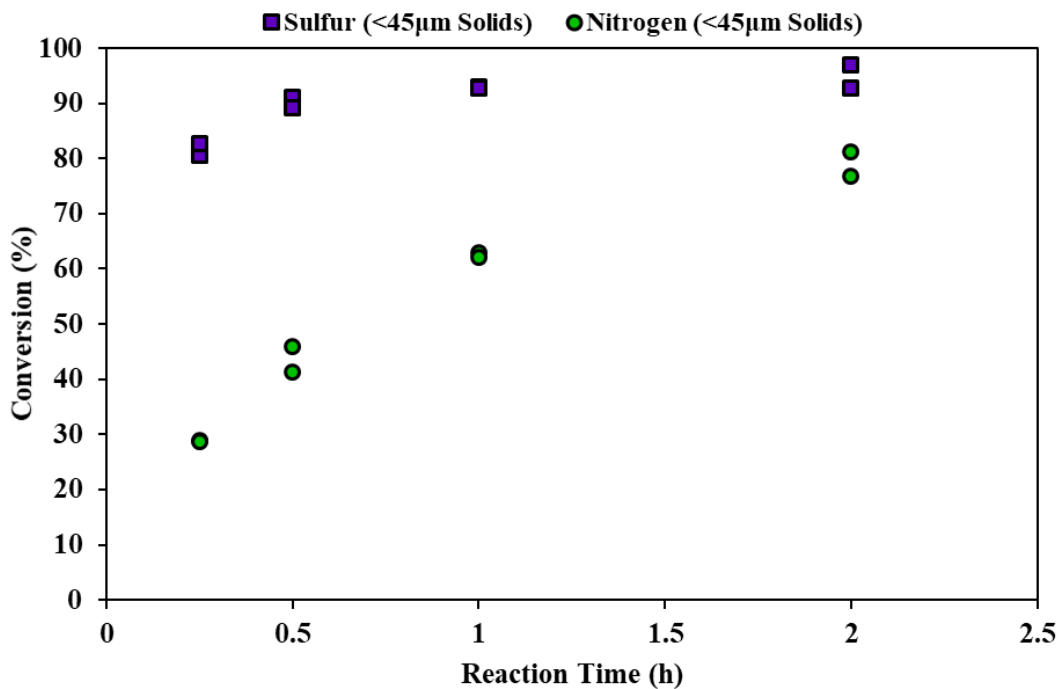
Figure F3. The effect of the reaction time at 390°C with <45μm sulfided catalyst solids on sulfur and nitrogen conversion results of the hydrotreated liquid products.
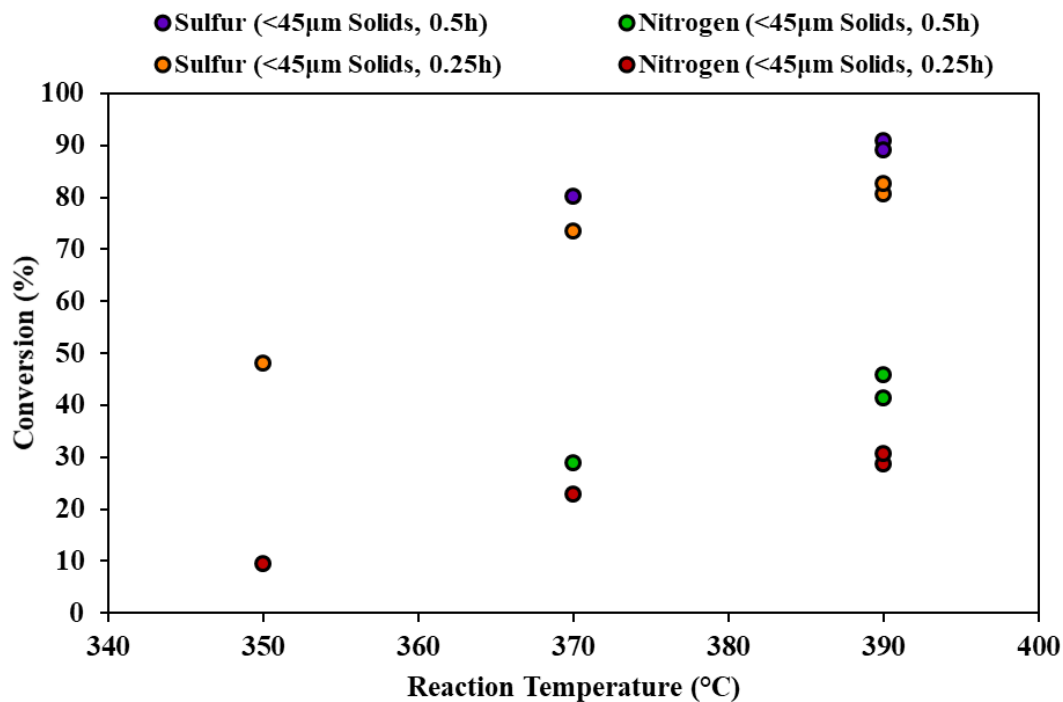
Figure F4. The effect of the reaction temperature at 0.25 and 0.5h with <45μm sulfided catalyst solids on sulfur plus nitrogen conversion results of the hydrotreated liquid products.
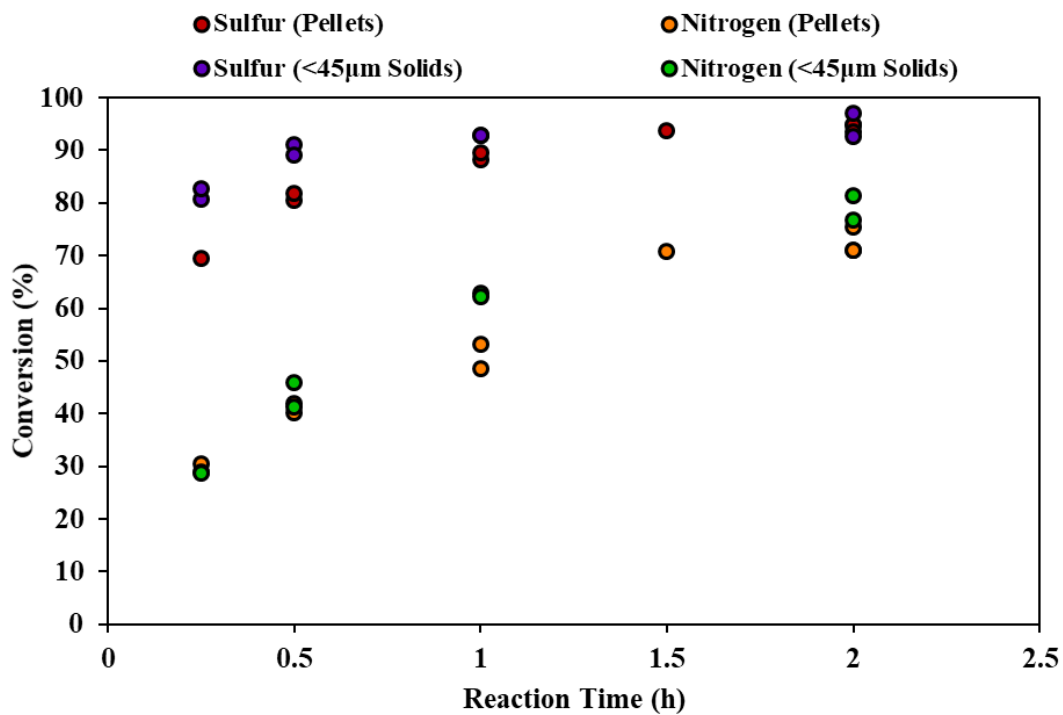
Figure F5. The effect of the reaction time at 390°C with sulfided catalyst pellets and <45μm solids on sulfur plus nitrogen conversion results of the hydrotreated liquid products.

Rate Constants and Optimal Reaction Orders

Sulfur and nitrogen concentration results using sulfided catalysts are used to develop rate law expressions for the hydrodesulfurization (HDS) and hydrodenitrogenation (HDN) reactions, respectively. A power law model for the reaction removal rates of heteroatom sulfur and nitrogen from the HVGO is used to model the concentration data measured in the liquid products.

$$\frac{dC}{dt} = -k \cdot C^n \cdot \frac{V_{cat}}{V_{liq}} \tag{F1}$$

For n=1

$$\frac{V_{liq}}{V_{cat}} \cdot \int_{C_{AO}}^{C_A} \frac{dC}{C} = -k \cdot \int_0^t dt \tag{F2}$$

$$\frac{V_{liq}}{V_{cat}} \cdot \ln\frac{C_A}{C_{AO}} = -k \cdot t \tag{F3}$$

For n≠1

$$\frac{V_{liq}}{V_{cat}} \cdot \int_{C_{AO}}^{C_A} \frac{dC}{C^n} = -k \cdot \int_0^t dt \tag{F4}$$

$$(1 - n)^{-1} \cdot (C_A^{1-n} - C_{AO}^{1-n}) \cdot \frac{V_{liq}}{V_{cat}} = -k \cdot t \tag{F5}$$

The power law expression depends on the reaction rate constant (k) and the concentration of a heteroatom raised to a reaction order exponent (n). The sulfur and nitrogen concentrations, with their 95% confidence intervals, of the HVGO and its respective liquid products are used in the nonlinear regressions. Sulfided catalyst densities, V_{cat}, are assumed to range between 0.75 to 0.85g/ml. The volume of liquid, V_{liq}, was assumed to remain constant at M_{HGVO} (g) loaded over the density (0.967g/ml). Results for each density assumption are compared. The data regression tool in Polymath software (version 6.2) is used to determine the rate constants, confidence intervals, and coefficient of determination (R^2) for four integer reaction orders. The data regression tool, assuming a nonlinear fit, is used to determine the optimal order for HDS and HDN reactions.

Figures F6 to F9 display models using sulfided catalyst pellets at 390°C for HDS (*F6* and *F7)* and HDN (*F8* and *F9*). *Figures F10 to F13* display models using sulfided <45µm catalyst solids at 390°C for HDS (*F10* and *F11*) and HDN (*F12* and *F13*). Summary results of reaction rate constants and their coefficient of determinations for each reaction order are highlighted in *Tables F1* and *F2*.
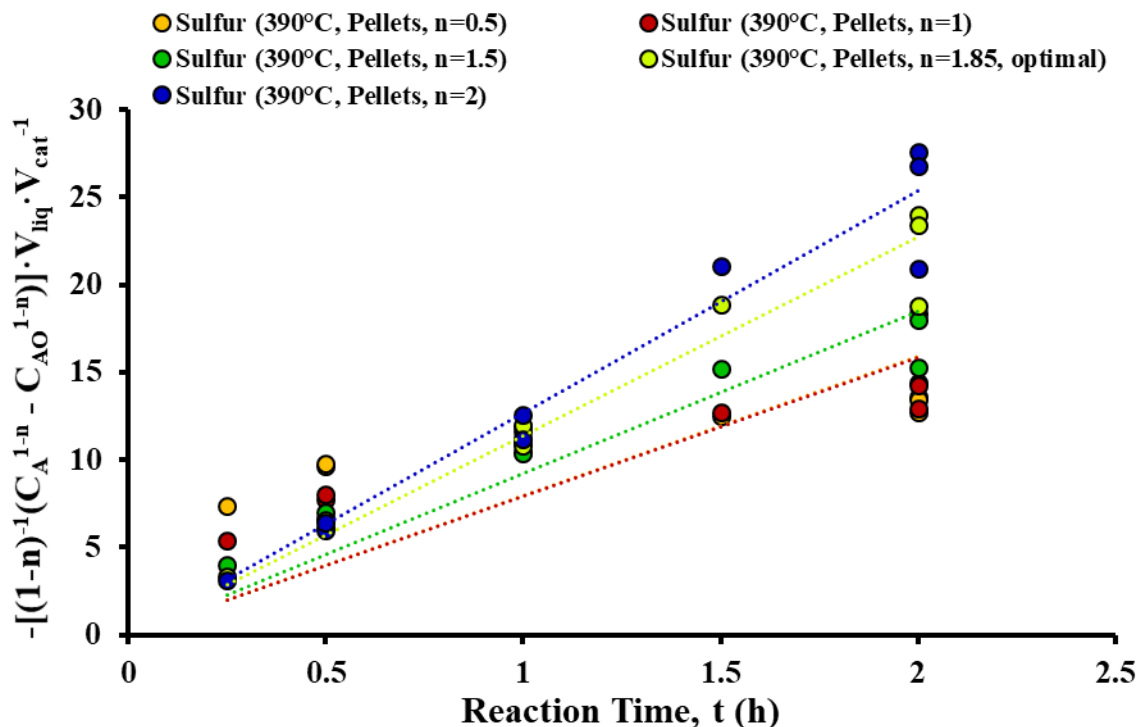
Figure F6. Power law model to fit experimental data to determine optimal reaction order for predicting sulfur concentration in the hydrotreated liquid products (0.75g/ml catalyst pellet density).
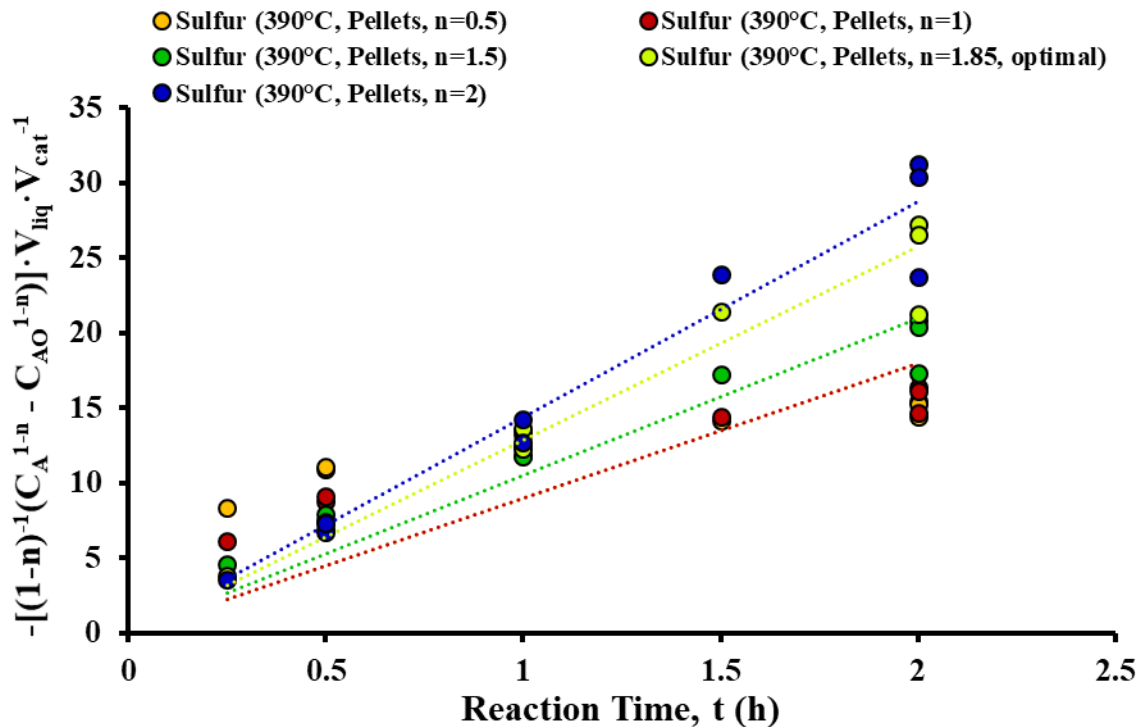
Figure F7. Power law model to fit experimental data to determine optimal reaction order for predicting sulfur concentration in the hydrotreated liquid products (0.85g/ml catalyst pellet density).
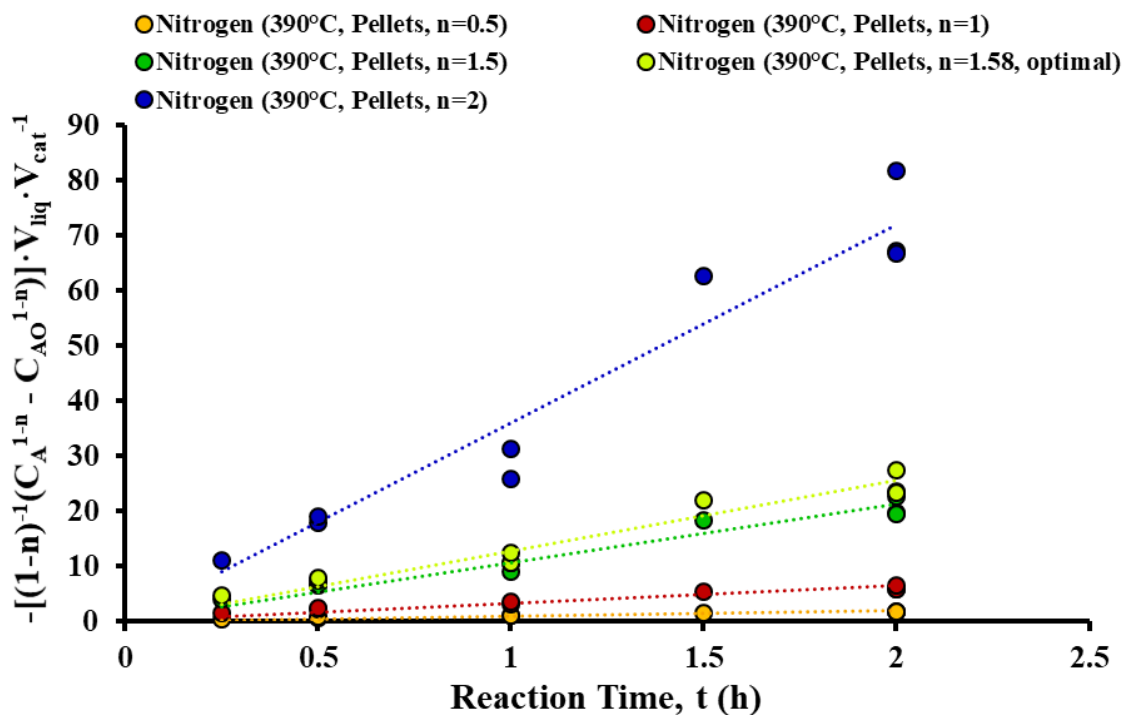
Figure F8. Power law model to fit experimental data to determine optimal reaction order for predicting nitrogen concentration in the hydrotreated liquid products (0.75g/ml catalyst pellet density).
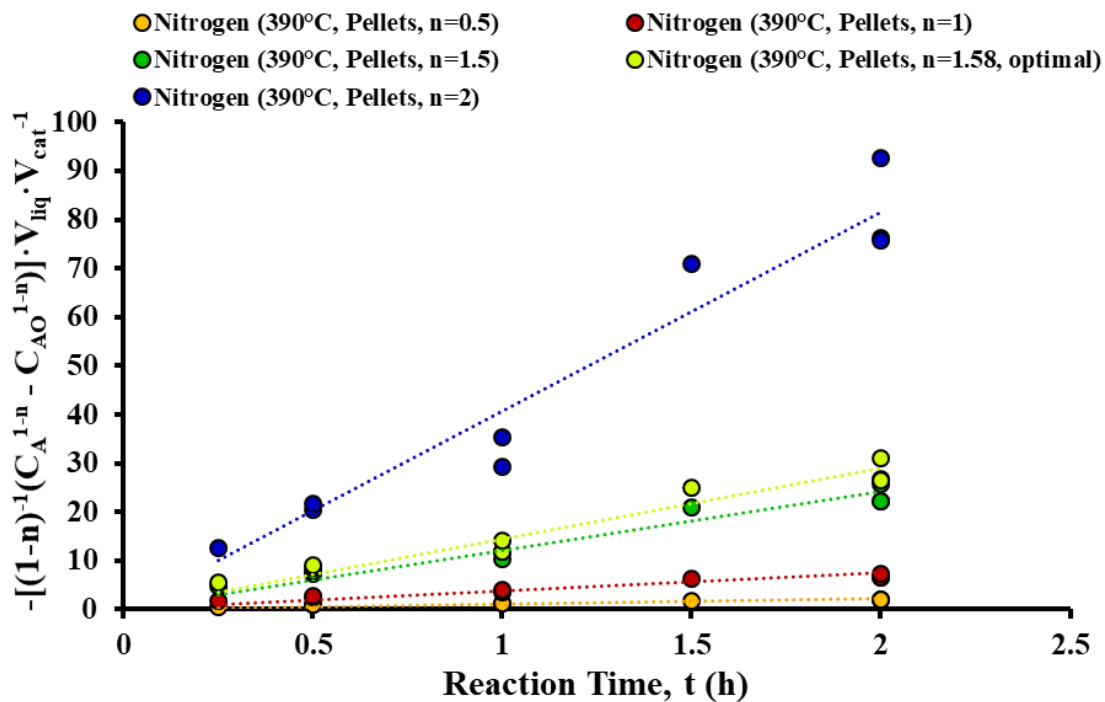
Figure F9. Power law model to fit experimental data to determine optimal reaction order for predicting nitrogen concentration in the hydrotreated liquid products (0.85g/ml catalyst pellet density).

Table F1. Fitted rate constant results at five reaction orders for HDS and HDN reactions at 390°C using sulfided catalyst pellets.

				Hydrodesulfurization (HDS)		
	Reaction Order	n = 0.5	n = 1	n = 1.5	n = 2	**Optimal** **n = 1.85 ± 0.34** 1.4 – 2.07*
	R²	-3.23	0.1	0.86	0.95	0.96
Pellet (0.75g/ml)	**k (h⁻¹ wt.%¹⁻ⁿ)**	7.9 ± 2.4	7.9 ± 1.7	9.25 ± 1.1	**12.7 ± 1.2**	**11.5 ± 2.9**
	95% Confidence Range	7.8 – 8.2	7.5 – 8.5	8.3 – 10.9	10.6 – 17	10.5 – 11.2
Pellet (0.85g/ml)	**k (h⁻¹ wt.%¹⁻ⁿ)**	8.99 ± 2.7	8.96 ± 1.9	10.5 ± 1.2	**14.4 ± 1.3**	**13 ± 0.04**
	95% Confidence Range	8.8 – 9.2	8.5 – 9.6	9.4 – 12.3	12.1 – 19.3	11.9 – 12.7

				Hydrodenitrogenation (HDN)		
	Reaction Order	n = 0.5	n = 1	n = 1.5	n = 2	**Optimal** **n = 1.58 ± 0.66** 0.79 – 1.58*
	R²	0.67	0.87	0.94	0.94	0.95
Pellet (0.75g/ml)	**k (h⁻¹ wt.%¹⁻ⁿ)**	1.1 ± 0.2	3.3 ± 0.4	**10.7 ± 1**	36 ± 3.7	**12.95±0.01**
	95% Confidence Range	0.87 – 1.27	2.6 – 4.4	7.7 – 16.9	23.7 – 70	2.7 – 13
Pellet (0.85g/ml)	**k (h⁻¹ wt.%¹⁻ⁿ)**	1.2 ± 0.2	3.7 ± 0.4	**12.1 ± 1.1**	40.8 ± 4.2	**14.7 ± 0.1**
	95% Confidence Range	1 – 1.4	2.9– 5	8.7 – 19.1	26.8 – 79.1	3 – 14.7

*95% Confidence interval for optimal reaction order

Fitted rate constant results at five orders for HDS and HDN reactions at 390°C using sulfided catalyst pellets are shown in *Table F1*. The 95% range rate constant results used the confidence intervals of the sulfur and nitrogen concentrations reported in section 4.2 and *Appendix E*. A second order model for HDS reactions resulted in the highest coefficient of determination of the four integers fitted. An optimal order for the HDS reactions is fitted to 1.85 with a 0.96 coefficient of determination. This optimal is not significantly different compared to the second order model. The HDS reaction rate constants from the second and the 1.85 order models differ by 10%. A 1.5 order model for HDN reactions resulted in the highest coefficient of determination of the four integers fitted. An optimal order for the HDN reactions is fitted to 1.58 with a 0.95 coefficient of

determination. This optimal is not significantly different compared to the 1.5 order model. The HDN reaction rate constants from the 1.5 and the 1.58 order models differ by 19%.
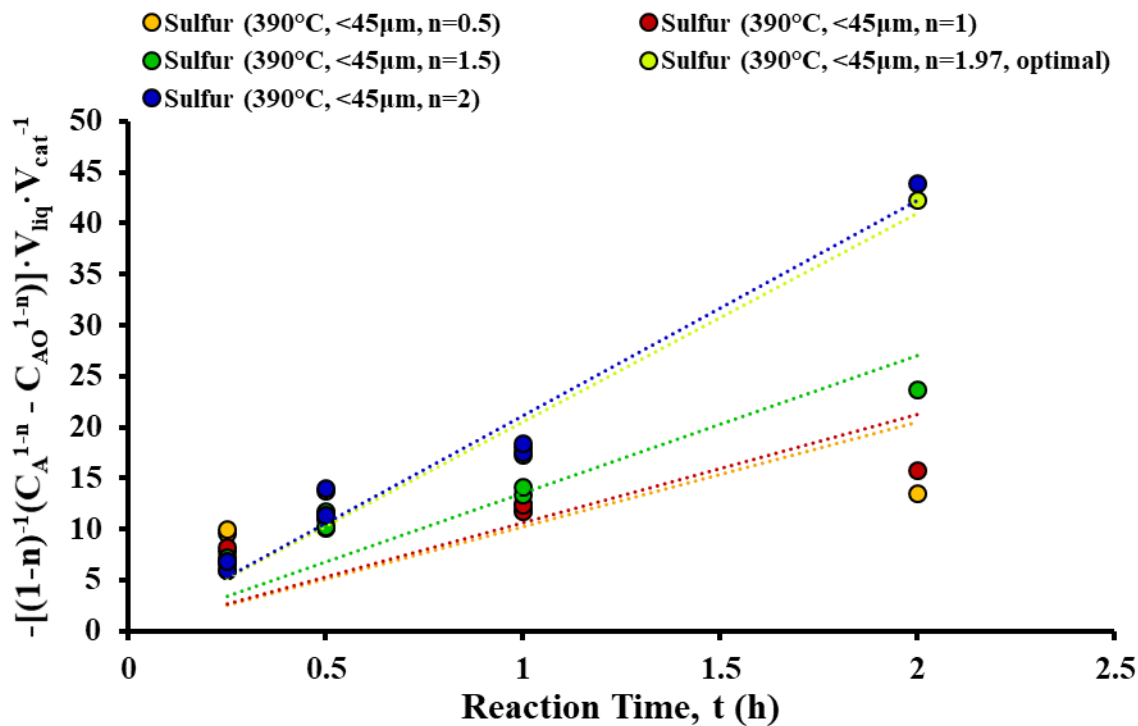
Figure F10. Power law model to fit experimental data to determine optimal reaction order for predicting sulfur concentration in the hydrotreated liquid products (0.75g/ml <45μm catalyst density).
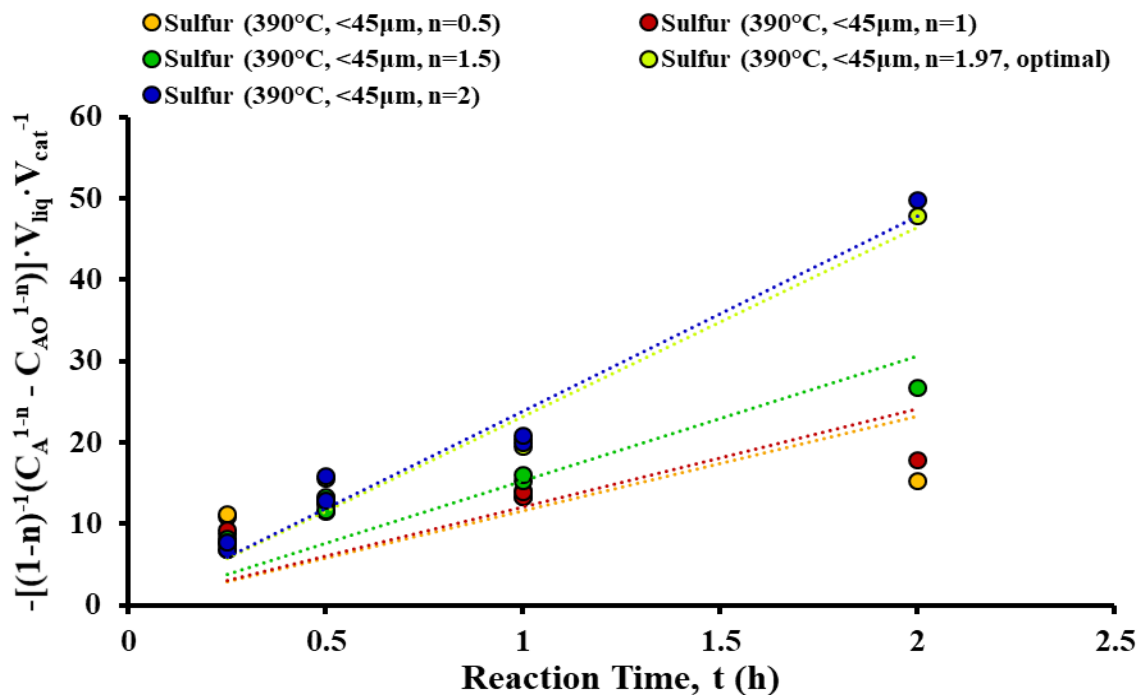
Figure F11. Power law model to fit experimental data to determine optimal reaction order for predicting sulfur concentration in the hydrotreated liquid products (0.85g/ml <45μm catalyst pellet density).
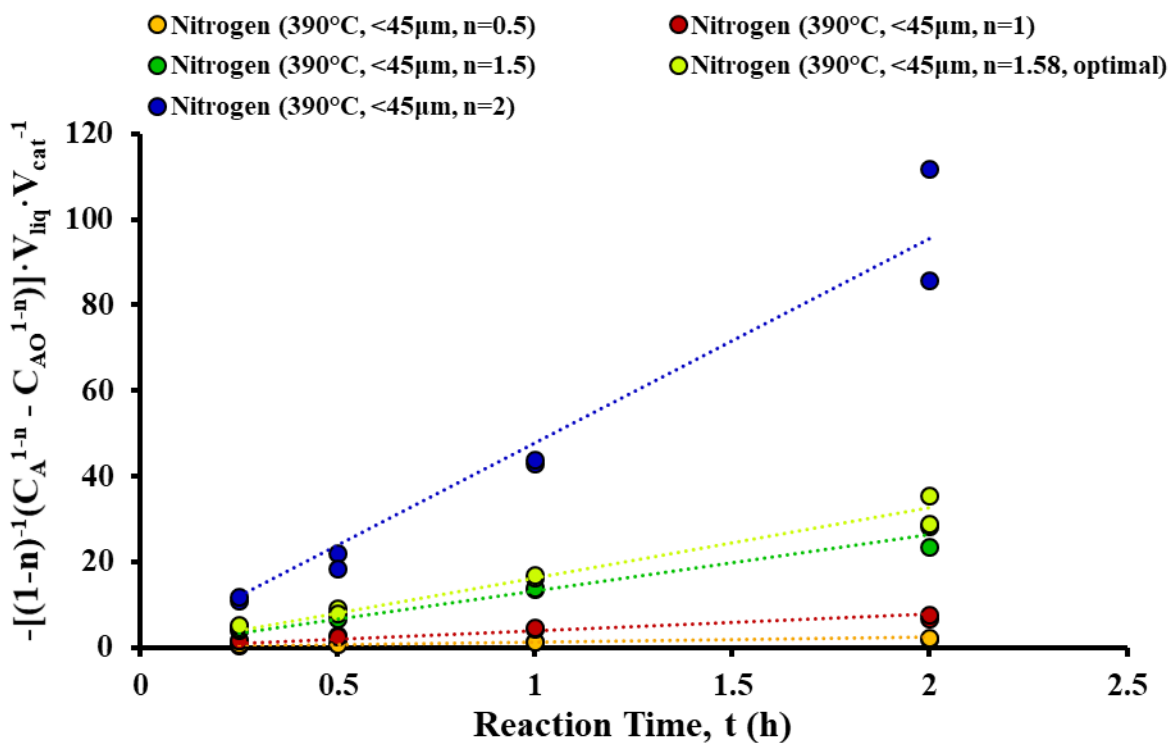
Figure F12. Power law model to fit experimental data to determine optimal reaction order for predicting nitrogen concentration in the hydrotreated liquid products (0.75g/ml <45μm catalyst density).
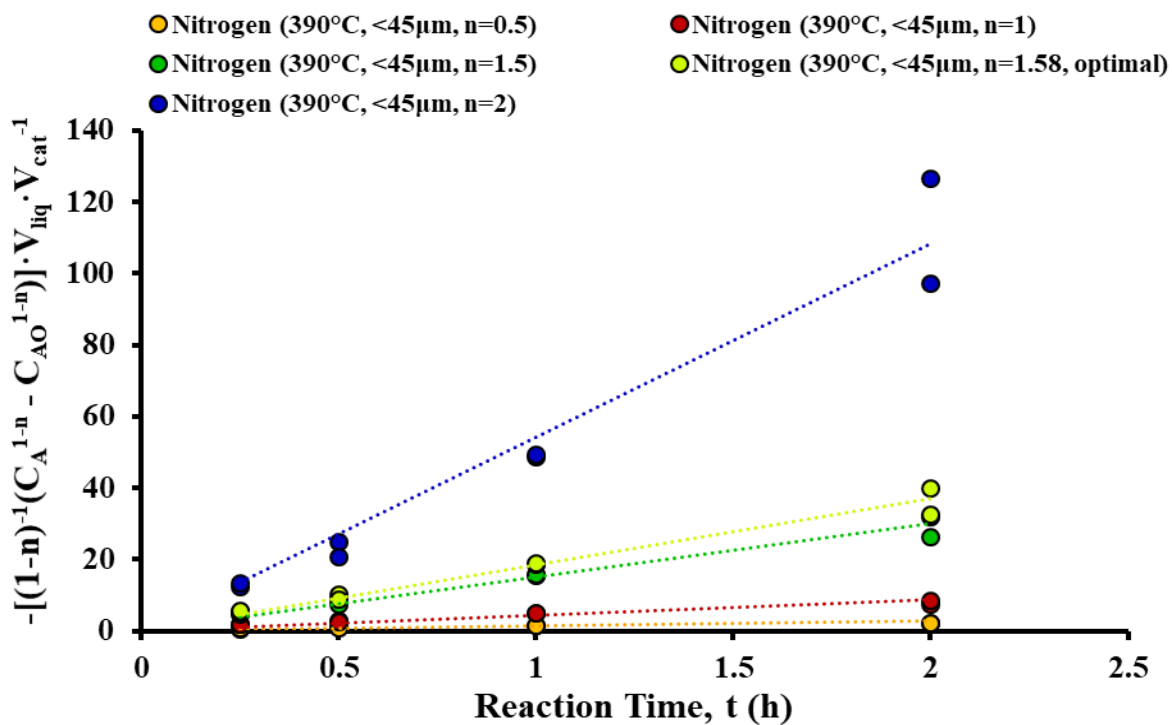
Figure F13. Power law model to fit experimental data to determine optimal reaction order for predicting nitrogen concentration in the hydrotreated liquid products (0.75g/ml <45μm catalyst density).

Table F2. Fitted rate constant results at five reaction orders for HDS and HDN reactions at 390°C using sulfided <45µm catalyst solids.

	Hydrodesulfurization (HDS)					
	Reaction Order	n = 0.5	n = 1	n = 1.5	n = 2	**Optimal n = 1.97 ± 0.29** 1.95 – 2*
	R^2	-20	-2.3	0.62	0.96	0.96
<45µm (0.75g/ml)	**k (h^{-1} wt.%$^{1-n}$)**	10.3 ± 6	10.6 ± 4.7	13.5 ± 3.4	**21.1 ± 2.4**	**20.8 ± 2.2**
	95% Confidence Range	10 – 10.6	10 – 11.5	12 – 15.8	17.3 – 27.6	17.5 – 27
<45µm (0.85g/ml)	**k (h^{-1} wt.%$^{1-n}$)**	11.6 ± 6.8	12.1 ± 5.4	15.3 ± 3.8	**23.9 ± 2.7**	**23.5 ± 7.8**
	95% Confidence Range	11.3 – 12	11.3 – 13.1	13.6 – 17.9	19.6 – 31.3	19.9 – 30.6

	Hydrodenitrogenation (HDN)					
	Reaction Order	n = 0.5	n = 1	n = 1.5	n = 2	**Optimal n = 1.58 ± 0.4** 0.65 – 3.6*
	R^2	0.63	0.89	0.97	0.96	0.97
<45µm (0.75g/ml)	**k (h^{-1} wt.%$^{1-n}$)**	1.2 ± 0.3	3.9 ± 0.5	**13.2 ± 1.1**	47.8 ± 5.7	**16.5 ± 0.2**
	95% Confidence Range	1 – 1.5	3 – 5.9	9.1 – 29.2	29 – 183	2.3 – 16.5
<45µm (0.85g/ml)	**k (h^{-1} wt.%$^{1-n}$)**	1.3 ± 0.3	4.4 ± 0.6	**15 ± 1.3**	54.2 ± 6.5	**18.7 ± 0.06**
	95% Confidence Range	1.1 – 1.7	3.4 – 6.7	10.3 – 33	32.4 – 208	2.6 – 18.7

*95% Confidence interval for optimal reaction order

Fitted rate constant results at five orders for HDS and HDN reactions at 390°C using sulfided <45µm catalyst solids are shown in *Table F2*. The 95% range rate constant results used the confidence intervals of the sulfur and nitrogen concentrations reported in section 4.2 and *Appendix E*. A second order model for HDS reactions resulted in the highest coefficient of determination of the four integers fitted. An optimal order for the HDS reactions is fitted to 1.97 with a 0.96 coefficient of determination. This optimal is not significantly different compared to the second order model. The HDS reaction rate constants from the second and the 1.97 order models differ by 1.5%. A 1.5 order model for HDN reactions resulted in the highest coefficient of determination of the four integers fitted. An optimal order for the HDN reactions is fitted to 1.58 with a 0.97

coefficient of determination. This optimal is not significantly different compared to the 1.5 order model. The HDN reaction rate constants from the 1.5 and the 1.58 order models differ by 19%.

Catalyst Size Effects with Sulfided Pellets and <45µm Solids

To compare rate constants and reaction order results from sulfided catalyst pellets and <45µm solids shown in *Tables F1* and *F2*, percent differences are calculated. The HDS rate constants are significantly different by 50 and 58% for the fitted second and optimal order reactions, respectively. The HDS optimal reaction orders, 1.85 and 1.97, are not significantly different. The HDN rate constants are significantly different by 21 and 24% for the fitted 1.5 and 1.58 order reactions, respectively. The HDN optimal reaction orders are identical at 1.58. To assess internal diffusion limitations, the procedure from section 11.8.4 from Gray [1] is used. The ratio of reaction rates at two different catalyst sizes is proportional to the ratio of effectiveness factors. The ratio of effective catalyst sizes is proportional to the ratio of Thiele moduli. The pellet length and solids were assumed as 1000 and 45µm, respectively. The Thiele moduli and effectiveness factor results for both HDS and HDN reactions are shown in *Table F3*.

Table F3. Rate constants, Thiele moduli, and effectiveness factor results for HDS and HDN reactions.

	Pellet	<45µm Solids
k_{HDS} (h^{-1} wt.%$^{-1}$)	14.4 ± 1.3	23.9 ± 2.7
k_{HDN} (h^{-1} wt.%$^{-0.5}$)	12.1 ± 1.1	15 ± 1.3
η_{HDS}	0.6 0.49 - 0.74	0.99
η_{HDN}	0.85 0.67 - 0.96	1
φ_{HDS}	1.2 0.8 - 1.6	0.05 0.04 - 0.07
φ_{HDN}	0.6 0.3 - 1	0.025 0.01 - 0.05

From *Table F3*, internal diffusions are seen for the HDS reactions using sulfided catalyst pellets as the reaction effectiveness factor is 0.6. The HDN reactions did not see internal diffusion limitations using sulfided catalyst pellets as 0.85 was in the recommend effectiveness factor range [1]. However, this comparison is limited due to different sulfur contents on each of the catalysts. The activity of the 45μm solids had a higher sulfur content with additional active sites and could be a reason why the HDS reactions were limited.

Activation Energies and Preexponential Factors

With known optimal orders for both HDS and HDN reactions of the HVGO, the rate constant is used to determine the temperature dependent Arrhenius parameters. Plotting the natural logarithm of the rate constant against the inverse temperature (K), the activation energy, E_a, and the preexponential factor, $\ln(A)$, are calculated from the slope and intercept, respectively. The rate constant is calculated at each reaction temperature for sulfided catalyst pellets and <45μm solids. The rate constants for the <45μm solids are normalized to 1h reaction time (from 0.5 and 0.25h reaction times) in order compare to sulfided catalyst pellet results.

$$k = A \cdot exp\left[\frac{-E_a}{R \cdot T}\right] \tag{F6}$$

$$\ln(k) = \ln(A) - \frac{E_a}{R \cdot T} \tag{F7}$$

Arrhenius plots for both HDS and HDN reactions are presented in *Appendix F*. *Figures F14 to F17* display Arrhenius models using sulfided catalyst pellets at 1h for HDS (*F14* and *F15)* and HDN (*F16* and *F17*) reactions. *Figures F18 to F21* display models using sulfided <45μm catalyst solids at 1h for HDS (*F18* and *F19*) and HDN (*F20* and *F21*) reactions. Catalyst density assumptions and known optimal reaction orders from *Tables F1* and *F2* are used for comparison. Summary results of activation energies, preexponential factors and their coefficient of determinations are highlighted in *Tables F4* and *F5*.
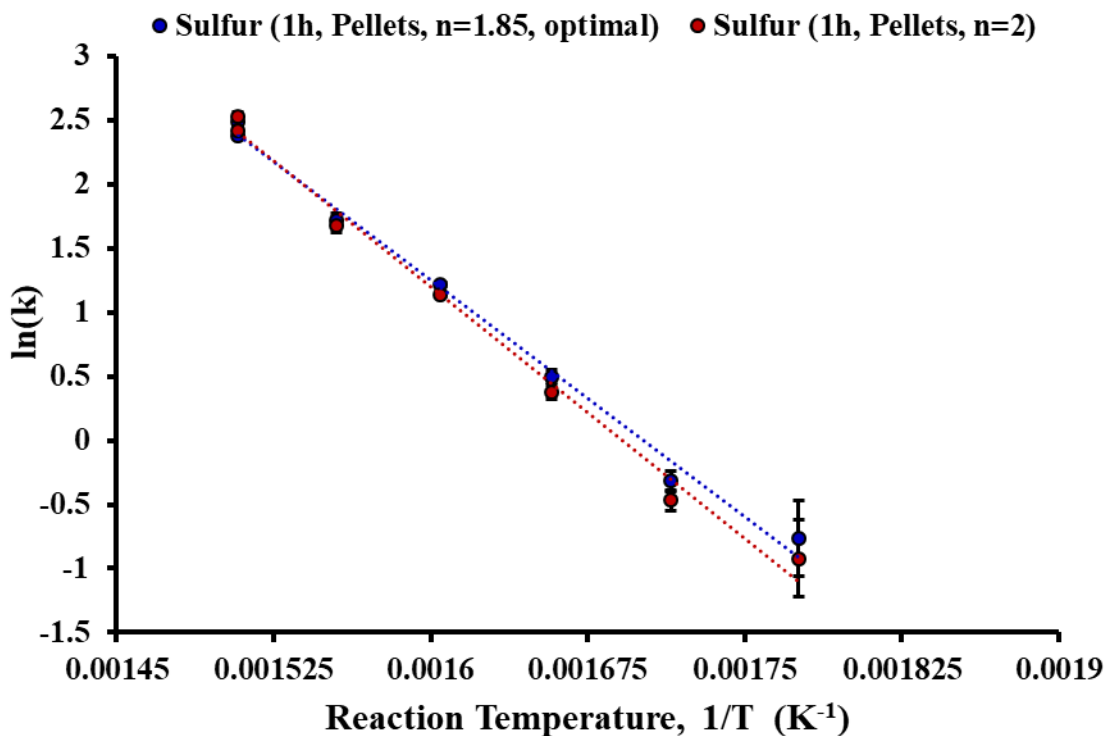
Figure F14. Arrhenius plot to determine activation energy and pre-exponential factor for hydrodesulfurization reactions (0.75g/ml catalyst pellet density).
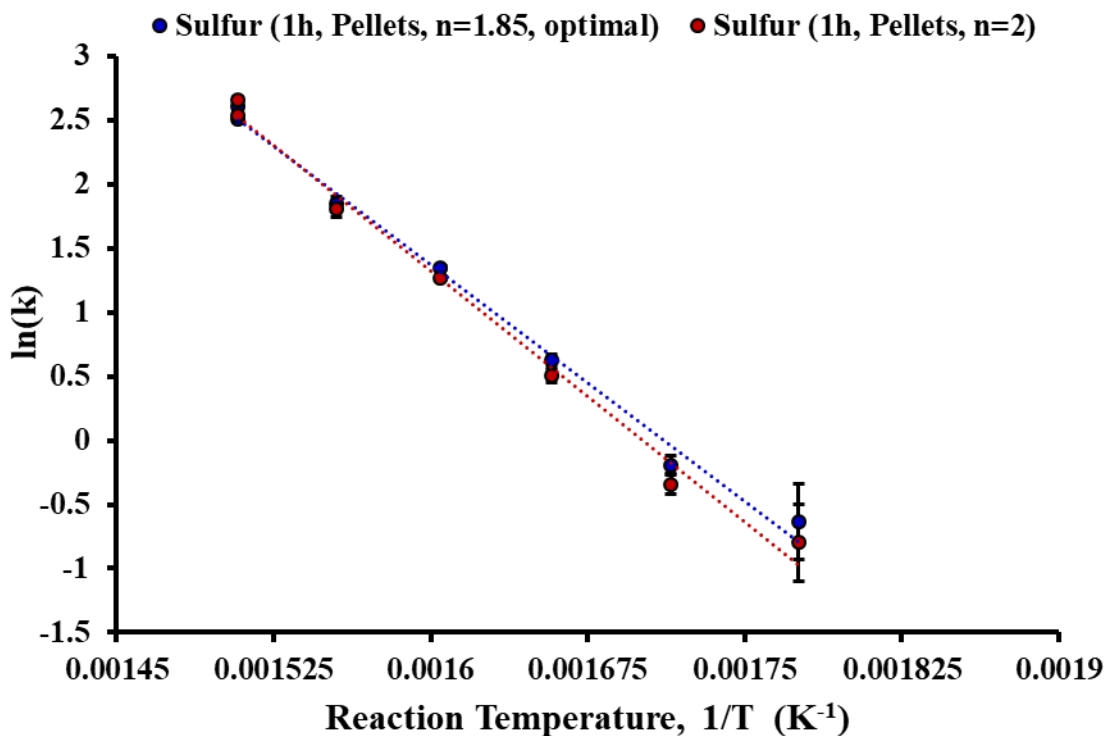
Figure F15. Arrhenius plot to determine activation energy and pre-exponential factor for hydrodesulfurization reactions (0.85g/ml catalyst pellet density).
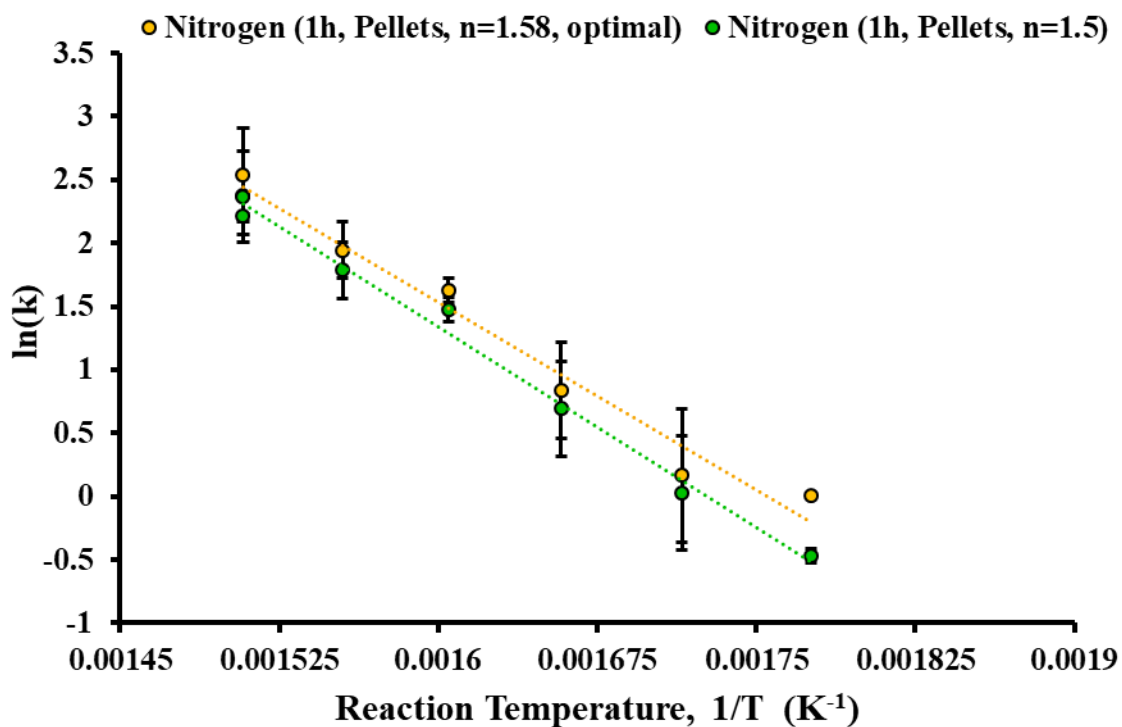
Figure F16. Arrhenius plot to determine activation energy and pre-exponential factor for hydrodenitrogenation reactions (0.75g/ml catalyst pellet density).
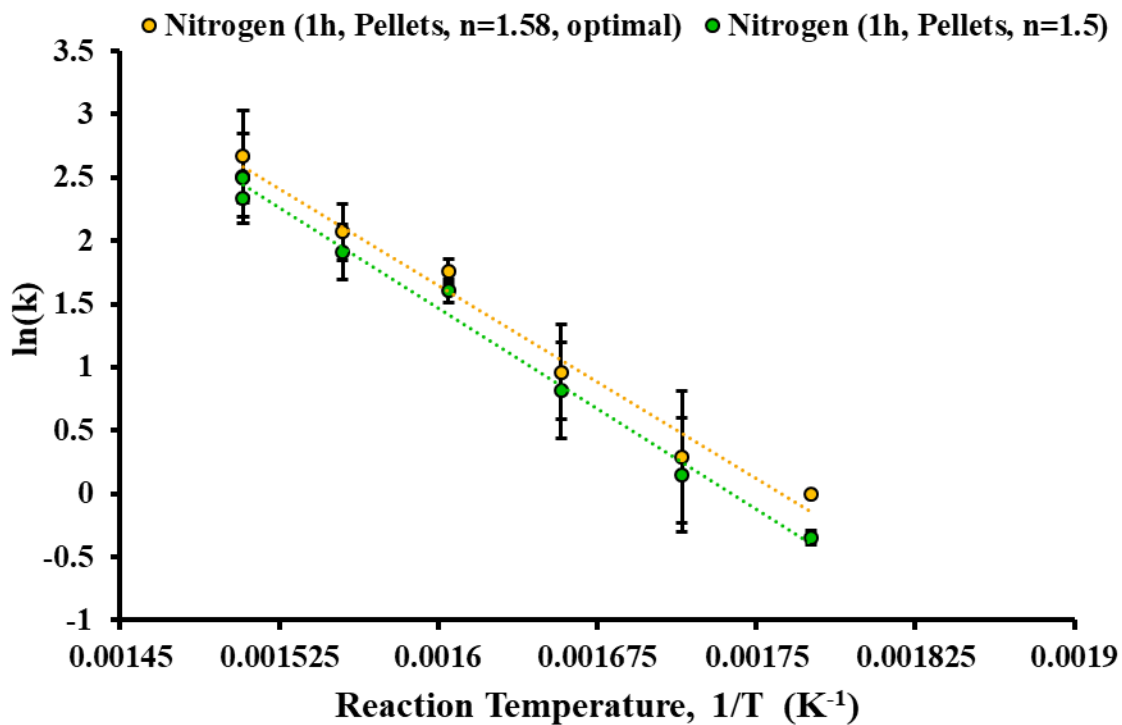
Figure F17. Arrhenius plot to determine activation energy and pre-exponential factor for hydrodenitrogenation reactions (0.85g/ml catalyst pellet density).

413

Table F4. Activation energy and preexponential factor results for HDS plus HDN reactions using sulfided catalyst pellets.

Hydrodesulfurization (HDS)

Assumption	Pellet (0.75g/ml)		Pellet (0.85g/ml)	
Reaction Order	n = 1.85	n = 2	n = 1.85	n = 2
E_a (kJ/mol)	102.3 ± 9.8	108.7 ± 11	102.3 ± 9.8	108.7 ± 11
95% Confidence Range	$96.7 - 108.8$	$103.1 - 115$	$96.7 - 108.8$	$103.2 - 115$
ln(A) $\ln(h^{-1}\ wt.\%^{1-n})$	20.9 ± 1.9	22.1 ± 2.2	21.1 ± 1.9	22.2 ± 2.2
95% Confidence Range	$19.9 - 22.1$	$21.1 - 23.3$	$20.1 - 22.2$	$21.2 - 23.4$
R^2	0.993	0.992	0.993	0.992

Hydrodenitrogenation (HDN)

Assumption	Pellet (0.75g/ml)		Pellet (0.85g/ml)	
Reaction Order	n = 1.5	n = 1.58	n = 1.5	n = 1.58
E_a (kJ/mol)	87.8 ± 9.5	88.7 ± 9.6	87.8 ± 9.5	88.7 ± 9.6
95% Confidence Range	$82.2 - 87.8$	$82.9 - 88.7$	$82.2 - 87.8$	$82.9 - 88.7$
ln(A) $\ln(h^{-1}\ wt.\%^{1-n})$	18.2 ± 1.9	18.6 ± 1.9	18.4 ± 1.9	18.7 ± 1.9
95% Confidence Range	$17 - 18.2$	$17.2 - 18.6$	$17.1 - 18.4$	$17.4 - 18.7$
R^2	0.991	0.991	0.991	0.991

Calculated activation energies (E_a) and preexponential factors (lnA) for both HDS and HDN reactions using sulfided catalyst pellets are shown in *Table F4*. The 95% range results used the confidence intervals of the sulfur and nitrogen concentrations reported in section 4.2 and *Appendix E*. Coefficient of determinations for all linear fits are >0.99 for both HDS and HDN reactions. The catalyst density assumptions affect the calculated rate constants, however, when plotted as a function of inverse temperature, the activation energies and preexponential factors for each reaction are identical. There are no significant differences in activation energies and preexponential factors when comparing optimal (i.e. 1.85 and 1.58) with predetermined orders (i.e. 2 and 1.5) for HDS and HDN reactions, respectively. The activation energies for optimal and predetermined orders differ by 6.1% for HDS and 1% for HDN reactions. The preexponential factors for optimal and predetermined orders differ by 5.6% for HDS and 2.2% for HDN reactions.
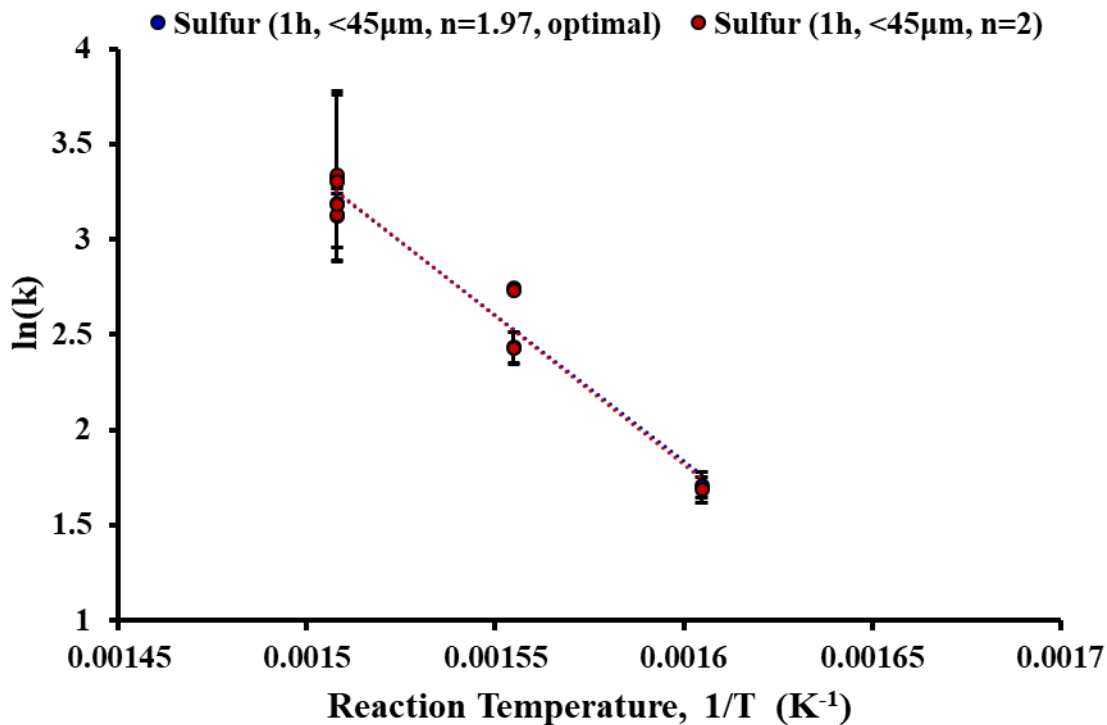
Figure F18. Arrhenius plot to determine activation energy and pre-exponential factor for hydrodesulfurization reactions (0.75g/ml <45μm catalyst density).
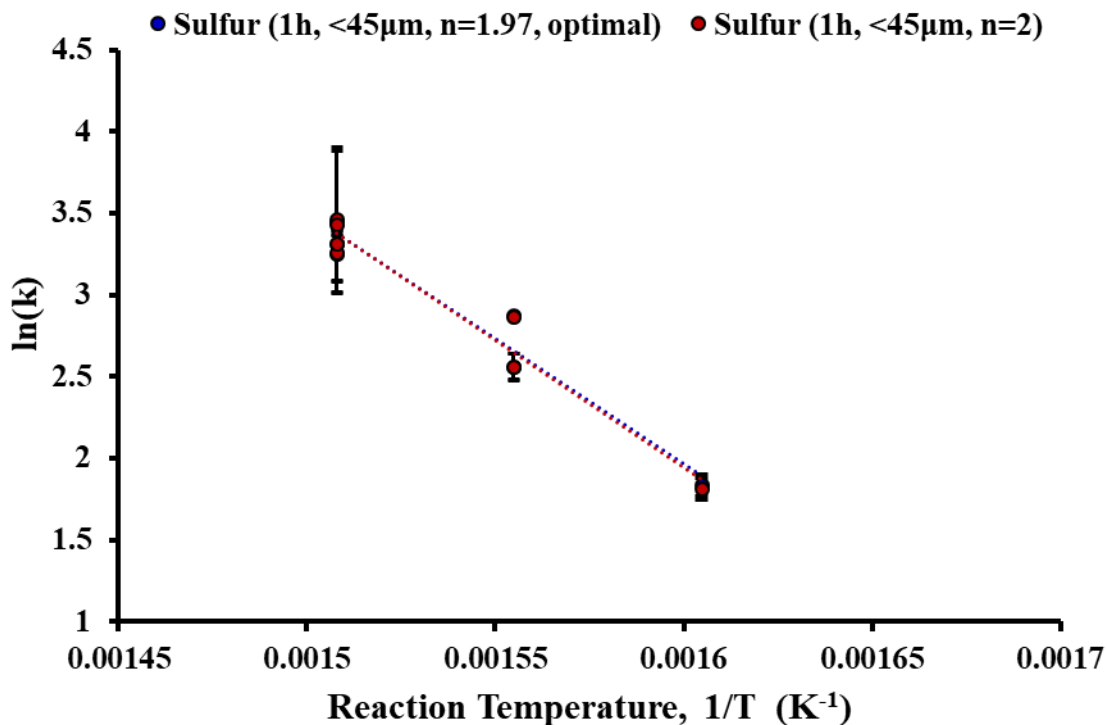
Figure F19. Arrhenius plot to determine activation energy and pre-exponential factor for hydrodesulfurization reactions (0.85g/ml <45μm catalyst density).
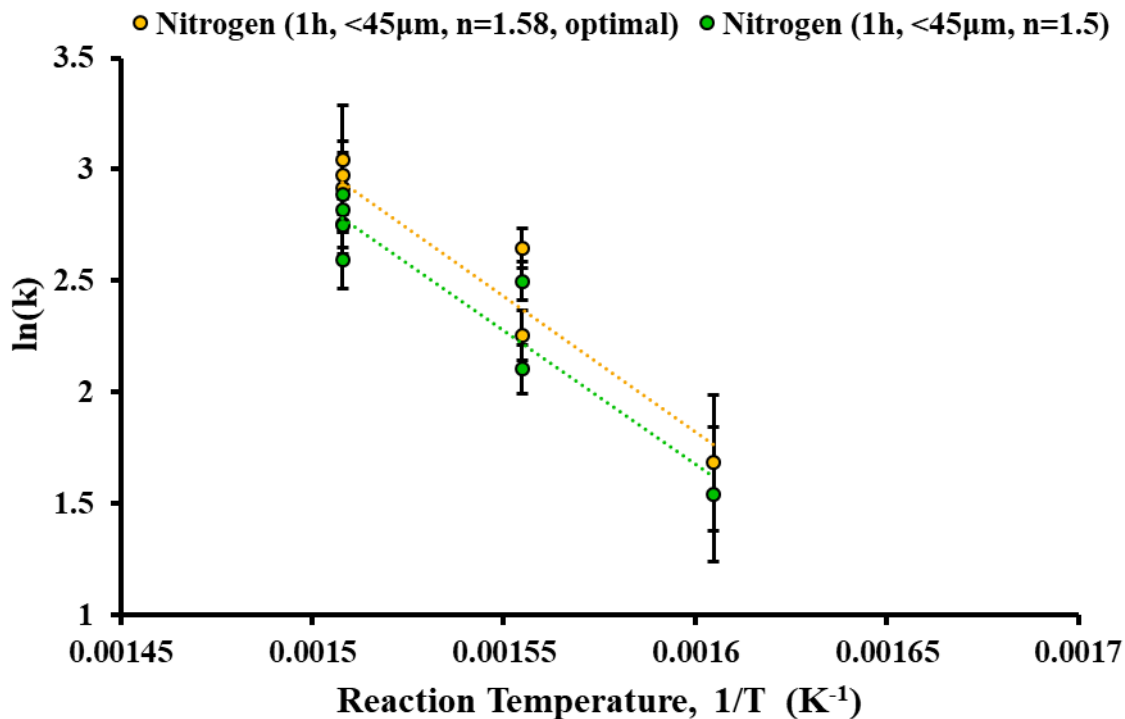
Figure F20. Arrhenius plot to determine activation energy and pre-exponential factor for hydrodenitrogenation reactions (0.75g/ml <45μm catalyst density).
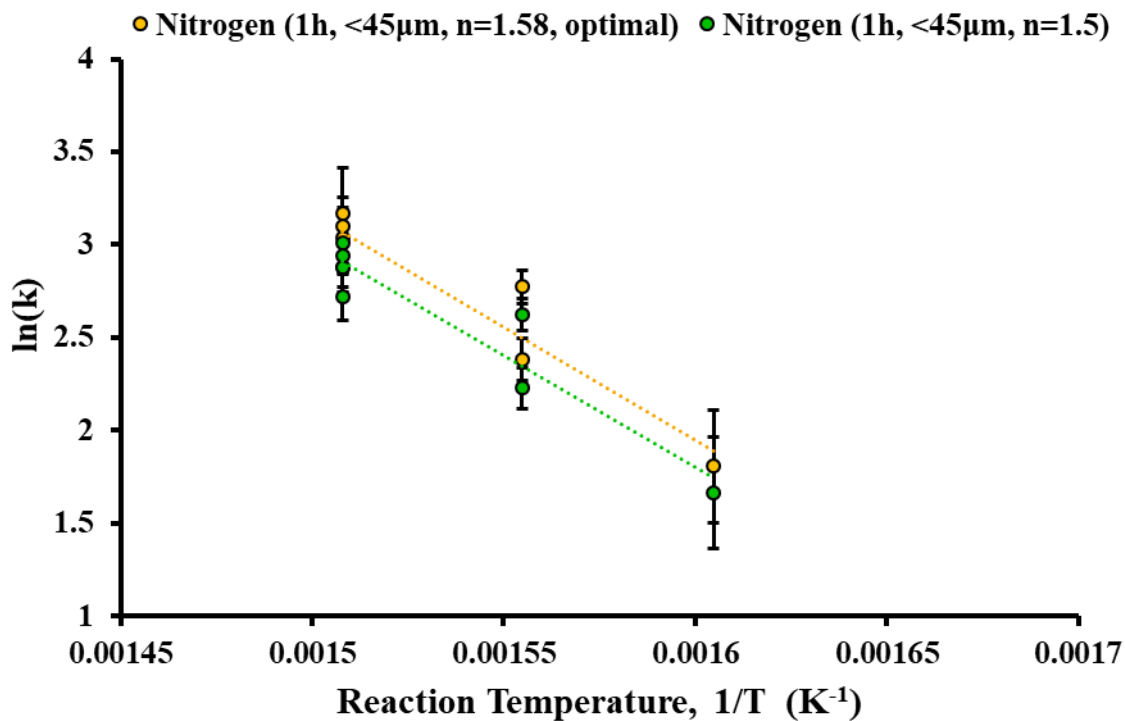
Figure F21. Arrhenius plot to determine activation energy and pre-exponential factor for hydrodenitrogenation reactions (0.85g/ml <45μm catalyst density).

Table F5. Activation energy and preexponential factor results for HDS plus HDN reactions of sulfided <45μm catalyst solids.

Hydrodesulfurization (HDS)

Assumption	<45μm Solids (0.75g/ml)		<45μm Solids (0.85g/ml)	
Reaction Order	n = 1.97	n = 2	n = 1.97	n = 2
E_a (kJ/mol) **95% Confidence Range**	127.1 ± 30 118 – 142	129.4 ± 30 120 – 145	127.1 ± 30 118 – 142	129.4 ± 30 120 – 145
ln(A) **$\ln(h^{-1}\ wt.\%^{1-n})$** **95% Confidence Range**	26.5 ± 5.6 24.4 – 29.2	26.8 ± 5.6 24.8 – 29.7	26.5 ± 5.6 24.5 – 29.3	26.9 ± 5.6 24.9 – 29.8
R^2	0.96	0.96	0.96	0.96

Hydrodenitrogenation (HDN)

Assumption	<45μm Solids (0.75g/ml)		<45μm Solids (0.85g/ml)	
Reaction Order	n = 1.5	n = 1.58	n = 1.5	n = 1.58
E_a (kJ/mol) **95% Confidence Range**	99.6 ± 39.6 90.3 – 114	100.9 ± 39 91.7 – 115	99.8 ± 39 90.3 – 114	101 ± 39 91.7 – 115
ln(A) **$\ln(h^{-1}\ wt.\%^{1-n})$** **95% Confidence Range**	20.9 ± 7.3 19.3 – 23.3	21.3 ± 7.2 19.7 – 23.7	21.1 ± 7.3 19.4 – 23.5	21.4 ± 7.2 19.8 – 23.8
R^2	0.89	0.9	0.89	0.9

Calculated activation energies (E_a) and preexponential factors (lnA) for both HDS and HDN reactions using sulfided catalyst solids are shown in *Table F5*. The 95% range results used the confidence intervals of the sulfur and nitrogen concentrations reported in section 4.2 and *Appendix E*. The calculated rate constants from 0.5 and 0.25h reactions at 350 to 390°C temperatures are normalized to 1h. Coefficient of determinations for all linear fits are >0.88 for both HDS and HDN reactions. The activation energies and preexponential factors for each reaction assuming different catalyst densities are mostly identical. There are no significant differences in activation energies and preexponential factors when comparing optimal (i.e. 1.97 and 1.58) with predetermined orders (i.e. 2 and 1.5) for HDS and HDN reactions, respectively. The activation energies for optimal and predetermined orders differ by 1.8% for HDS and 1.3% for HDN reactions. The preexponential factors for optimal and predetermined orders differ by 1.1% for HDS and 1.9% for HDN reactions.

Catalyst Size Effects with Sulfided Pellets and <45μm Solids

To compare activation energies and preexponential factor results from sulfided catalyst pellets and <45μm solids shown in *Tables F4* and *F5*, percent differences are calculated. The HDS activation energies are significantly different by 17 and 22% for the fitted second and optimal order reactions, respectively. The HDS preexponential factors are significantly different by 19 and 24% for the fitted second and optimal order reactions, respectively. The HDN activation energies are significantly different by 13% for both 1.5 and 1.58 order reactions. The HDN preexponential factors are significantly different by 14% for both 1.5 and 1.58 order reactions. Results reported in *Tables F1* *to* *F5* are comparable to literature values reported in *Appendix A* in *Table A1*.

Density Prediction

Density prediction results are found in *Appendix F*. As discussed in section 2.1.3, the density is predicted from approximate hydrogen, sulfur, and nitrogen compositions. The Gray regression [1] is compared to an optimal linear regression equation fitted to the hydrogen, sulfur, and nitrogen concentrations highlighted in sections 4.1 and 4.2. Both regressions are compared in the predicted versus measured density plot in *Appendix F*.
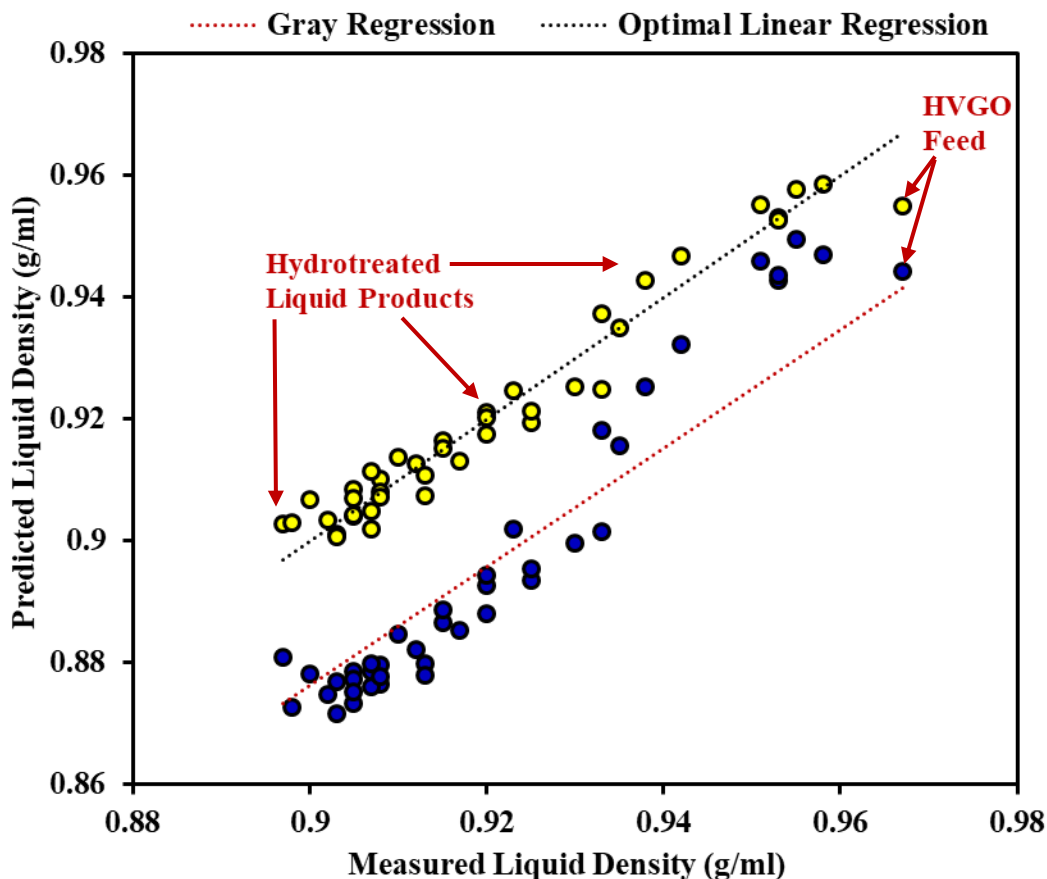
Figure F22. Predicted density versus measured density comparison.

The Gray regression in section 2.1.3 (equation 2.1) is used to calculate the predicted density in *Figure 4.19*. Matlab software is used to regress the measured density with hydrogen, sulfur, and nitrogen concentrations of the HVGO feed and all hydrotreated liquid products. The coefficients and intercept for the fitted linear regression is presented:

$$\rho = 916.6 - 1.846 \cdot H + 9.283 \cdot S + 161.2 \cdot N$$

The results from *Figure F22* are summarized in *Table F5*. The coefficient of determination, slope, as well as coefficients, for the Gray and the fitted regressions are highlighted in *Table F5*.

Table F5. The coefficient of determination, slope, as well as coefficients, with error intervals, for the Gray and the optimal regressions.

	Optimal Linear Regression		Gray Regression
R^2	0.953		0.882
Slope	1		0.9737
Intercept	916.6	906 - 921*	1033
Hydrogen (H)	-1.846	-1.5 to -1.85*	-13.69
Sulfur (S)	9.283	7.2 to 11.3*	13.85
Nitrogen (N)	161.2	144 to 184*	115.7

*95% Confidence Interval

The Gray regression predicted the density of the samples from this study with slight errors. The regression was based on feeds from bitumen, heavy gas oils, and light gas oil feeds. However, the fitted coefficient results obtained are directionally comparable. Hydrogen is negative, while sulfur and nitrogen are positive interactions toward density prediction.

Appendix F References

[1] M. R. Gray, *Upgrading Oilsands Bitumen and Heavy Oil.* Edmonton, Alberta: Pica Pica Press, An Imprint of The University of Alberta Press, 2015.

Appendix G

Matlab code used for the entire study is found in *Appendix G*.

Trimmed to 450nm absorbance data
First Data Set (X1)
34x1122
No feed, no catalyst, no sulfiding reactions, and no reaction 9.
6-8, 10-15, 20-44
Second Data Set (X2)
25x1122
Reactions 20-40
Third Set (X3)
Sulfided Pellet Reactions
14 x1122
20-33
Fourth Set (X4)
Sulfided <45μm Solids
11 x1122
34-44
Fifth NMR Set (X5)
6x1122 400MHz
Reactions 21, 25, 27, 29, 32, 35
Sixth NMR Set (X6)
13x1122 60MHz
Reactions 23, 24, 26, 28, 31, 33, 34, 37, 38, 41, 42, 43, 44

Simple Least Squares
X1M=mean(X1);
X2M=mean(X2);
X3M=mean(X3);
X4M=mean(X4);
X5M=mean(X5);
X6M=mean(X6);
Y1M=mean(Y1);
Y2M=mean(Y2);
Y3M=mean(Y3);
Y4M=mean(Y4);
Y5M=mean(Y5);
Y6M=mean(Y6);
X1C=X1-X1M;
X2C=X2-X2M;
X3C=X3-X3M;
X4C=X4-X4M;
X5C=X5-X5M;
X6C=X6-X6M;
Y1C=Y1-Y1M;
Y2C=Y2-Y2M;
Y3C=Y3-Y3M;
Y4C=Y4-Y4M;
Y5C=Y5-Y5M;
Y6C=Y6-Y6M;

for i=1:115;
for n=1:1122;
K1(i,n)=(((X1C(:,n))'*(X1C(:,n)))^-1)*(X1C(:,n))'*Y1C(:,i);
end
end
for i=1:115;

421

```
for n=1:1122;
K2(i,n)=(((X2C(:,n))'*(X2C(:,n)))^-1)*(X2C(:,n))'*Y2C(:,i);
end
end
for i=1:115;
for n=1:1122;
K3(i,n)=(((X3C(:,n))'*(X3C(:,n)))^-1)*(X3C(:,n))'*Y3C(:,i);
end
end
for i=1:115;
for n=1:1122;
K4(i,n)=(((X4C(:,n))'*(X4C(:,n)))^-1)*(X4C(:,n))'*Y4C(:,i);
end
end
for i=1:5;
for n=1:1122;
K5(i,n)=(((X5C(:,n))'*(X5C(:,n)))^-1)*(X5C(:,n))'*Y5C(:,i);
end
end
for i=1:5;
for n=1:1122;
K6(i,n)=(((X6C(:,n))'*(X6C(:,n)))^-1)*(X6C(:,n))'*Y6C(:,i);
end
end

for n=1:1122;
Y1P1(:,n)=K1(1,n)*X1C(:,n);
Y1P2(:,n)=K1(2,n)*X1C(:,n);
…
Y1P114(:,n)=K1(114,n)*X1C(:,n);
Y1P115(:,n)=K1(115,n)*X1C(:,n);
end

for n=1:1122;
Y2P1(:,n)=K2(1,n)*X2C(:,n);
Y2P2(:,n)=K2(2,n)*X2C(:,n);
…
Y2P114(:,n)=K2(114,n)*X2C(:,n);
Y2P115(:,n)=K2(115,n)*X2C(:,n);
end

for n=1:1122;
Y3P1(:,n)=K3(1,n)*X3C(:,n);
Y3P2(:,n)=K3(2,n)*X3C(:,n);
…
Y3P114(:,n)=K3(114,n)*X3C(:,n);
Y3P115(:,n)=K3(115,n)*X3C(:,n);
end

for n=1:1122;
Y4P1(:,n)=K4(1,n)*X4C(:,n);
Y4P2(:,n)=K4(2,n)*X4C(:,n);
…
Y4P114(:,n)=K4(114,n)*X4C(:,n);
Y4P115(:,n)=K4(115,n)*X4C(:,n);
end

for n=1:1122;
Y5P1(:,n)=K5(1,n)*X5C(:,n);
Y5P2(:,n)=K5(2,n)*X5C(:,n);
Y5P3(:,n)=K5(3,n)*X5C(:,n);
Y5P4(:,n)=K5(4,n)*X5C(:,n);
```

```
Y5P5(:,n)=K5(5,n)*X5C(:,n);
end

for n=1:1122;
Y6P1(:,n)=K6(1,n)*X6C(:,n);
Y6P2(:,n)=K6(2,n)*X6C(:,n);
Y6P3(:,n)=K6(3,n)*X6C(:,n);
Y6P4(:,n)=K6(4,n)*X6C(:,n);
Y6P5(:,n)=K6(5,n)*X6C(:,n);
end

for n=1:1122;
R1(1,n)=1-((sum((Y1P1(:,n)-Y1C(:,1)).^2))./(sum((-Y1C(:,1)).^2)));
R1(2,n)=1-((sum((Y1P2(:,n)-Y1C(:,2)).^2))./(sum((-Y1C(:,2)).^2)));
…
R1(114,n)=1-((sum((Y1P114(:,n)-Y1C(:,114)).^2))./(sum((-Y1C(:,114)).^2)));
R1(115,n)=1-((sum((Y1P115(:,n)-Y1C(:,115)).^2))./(sum((-Y1C(:,115)).^2)));
end

for n=1:1122;
R2(1,n)=1-((sum((Y2P1(:,n)-Y2C(:,1)).^2))./(sum((-Y2C(:,1)).^2)));
R2(2,n)=1-((sum((Y2P2(:,n)-Y2C(:,2)).^2))./(sum((-Y2C(:,2)).^2)));
…
R2(114,n)=1-((sum((Y2P114(:,n)-Y2C(:,114)).^2))./(sum((-Y2C(:,114)).^2)));
R2(115,n)=1-((sum((Y2P115(:,n)-Y2C(:,115)).^2))./(sum((-Y2C(:,115)).^2)));
end

for n=1:1122;
R3(1,n)=1-((sum((Y3P1(:,n)-Y3C(:,1)).^2))./(sum((-Y3C(:,1)).^2)));
R3(2,n)=1-((sum((Y3P2(:,n)-Y3C(:,2)).^2))./(sum((-Y3C(:,2)).^2)));
…
R3(114,n)=1-((sum((Y3P114(:,n)-Y3C(:,114)).^2))./(sum((-Y3C(:,114)).^2)));
R3(115,n)=1-((sum((Y3P115(:,n)-Y3C(:,115)).^2))./(sum((-Y3C(:,115)).^2)));
end

for n=1:1122;
R4(1,n)=1-((sum((Y4P1(:,n)-Y4C(:,1)).^2))./(sum((-Y4C(:,1)).^2)));
R4(2,n)=1-((sum((Y4P2(:,n)-Y4C(:,2)).^2))./(sum((-Y4C(:,2)).^2)));
…
R4(114,n)=1-((sum((Y4P114(:,n)-Y4C(:,114)).^2))./(sum((-Y4C(:,114)).^2)));
R4(115,n)=1-((sum((Y4P115(:,n)-Y4C(:,115)).^2))./(sum((-Y4C(:,115)).^2)));
end

for n=1:1122;
R5(1,n)=1-((sum((Y5P1(:,n)-Y5C(:,1)).^2))./(sum((-Y5C(:,1)).^2)));
R5(2,n)=1-((sum((Y5P2(:,n)-Y5C(:,2)).^2))./(sum((-Y5C(:,2)).^2)));
R5(3,n)=1-((sum((Y5P3(:,n)-Y5C(:,3)).^2))./(sum((-Y5C(:,3)).^2)));
R5(4,n)=1-((sum((Y5P4(:,n)-Y5C(:,4)).^2))./(sum((-Y5C(:,4)).^2)));
R5(5,n)=1-((sum((Y5P5(:,n)-Y5C(:,5)).^2))./(sum((-Y5C(:,5)).^2)));
end

for n=1:1122;
R6(1,n)=1-((sum((Y6P1(:,n)-Y6C(:,1)).^2))./(sum((-Y6C(:,1)).^2)));
R6(2,n)=1-((sum((Y6P2(:,n)-Y6C(:,2)).^2))./(sum((-Y6C(:,2)).^2)));
R6(3,n)=1-((sum((Y6P3(:,n)-Y6C(:,3)).^2))./(sum((-Y6C(:,3)).^2)));
R6(4,n)=1-((sum((Y6P4(:,n)-Y6C(:,4)).^2))./(sum((-Y6C(:,4)).^2)));
R6(5,n)=1-((sum((Y6P5(:,n)-Y6C(:,5)).^2))./(sum((-Y6C(:,5)).^2)));
end
```

Multilinear regression of spectral data sets using stepwise regression.

```
[b1i1,se1i1,pval1i1,inmodel1i1,stats1i1,nextstep1i1,history1i1] = stepwisefit(X1,Y1(:,1));
[b1i2,se1i2,pval1i2,inmodel1i2,stats1i2,nextstep1i2,history1i2] = stepwisefit(X1,Y1(:,2));
…
[b1i114,se1i114,pval1i114,inmodel1i114,stats1i114,nextstep1i114,history1i114] = stepwisefit(X1,Y1(:,114));
[b1i115,se1i115,pval1i115,inmodel1i115,stats1i115,nextstep1i115,history1i115] = stepwisefit(X1,Y1(:,115));

[b2i1,se2i1,pval2i1,inmodel2i1,stats2i1,nextstep2i1,history2i1] = stepwisefit(X2,Y2(:,1));
[b2i2,se2i2,pval2i2,inmodel2i2,stats2i2,nextstep2i2,history2i2] = stepwisefit(X2,Y2(:,2));
…
[b2i114,se2i114,pval2i114,inmodel2i114,stats2i114,nextstep2i114,history2i114] = stepwisefit(X2,Y2(:,114));
[b2i115,se2i115,pval2i115,inmodel2i115,stats2i115,nextstep2i115,history2i115] = stepwisefit(X2,Y2(:,115));

[b3i1,se3i1,pval3i1,inmodel3i1,stats3i1,nextstep3i1,history3i1] = stepwisefit(X3,Y3(:,1));
[b3i2,se3i2,pval3i2,inmodel3i2,stats3i2,nextstep3i2,history3i2] = stepwisefit(X3,Y3(:,2));
…
[b3i114,se3i114,pval3i114,inmodel3i114,stats3i114,nextstep3i114,history3i114] = stepwisefit(X3,Y3(:,114));
[b3i115,se3i115,pval3i115,inmodel3i115,stats3i115,nextstep3i115,history3i115] = stepwisefit(X3,Y3(:,115));

[b4i1,se4i1,pval4i1,inmodel4i1,stats4i1,nextstep4i1,history4i1] = stepwisefit(X4,Y4(:,1));
[b4i2,se4i2,pval4i2,inmodel4i2,stats4i2,nextstep4i2,history4i2] = stepwisefit(X4,Y4(:,2));
…
[b4i114,se4i114,pval4i114,inmodel4i114,stats4i114,nextstep4i114,history4i114] = stepwisefit(X4,Y4(:,114));
[b4i115,se4i115,pval4i115,inmodel4i115,stats4i115,nextstep4i115,history4i115] = stepwisefit(X4,Y4(:,115));

[b5i1,se5i1,pval5i1,inmodel5i1,stats5i1,nextstep5i1,history5i1] = stepwisefit(X5,Y5(:,1));
[b5i2,se5i2,pval5i2,inmodel5i2,stats5i2,nextstep5i2,history5i2] = stepwisefit(X5,Y5(:,2));
[b5i3,se5i3,pval5i3,inmodel5i3,stats5i3,nextstep5i3,history5i3] = stepwisefit(X5,Y5(:,3));
[b5i4,se5i4,pval5i4,inmodel5i4,stats5i4,nextstep5i4,history5i4] = stepwisefit(X5,Y5(:,4));
[b5i5,se5i5,pval5i5,inmodel5i5,stats5i5,nextstep5i5,history5i5] = stepwisefit(X5,Y5(:,5));

[b6i1,se6i1,pval6i1,inmodel6i1,stats6i1,nextstep6i1,history6i1] = stepwisefit(X6,Y6(:,1));
[b6i2,se6i2,pval6i2,inmodel6i2,stats6i2,nextstep6i2,history6i2] = stepwisefit(X6,Y6(:,2));
[b6i3,se6i3,pval6i3,inmodel6i3,stats6i3,nextstep6i3,history6i3] = stepwisefit(X6,Y6(:,3));
[b6i4,se6i4,pval6i4,inmodel6i4,stats6i4,nextstep6i4,history6i4] = stepwisefit(X6,Y6(:,4));
[b6i5,se6i5,pval6i5,inmodel6i5,stats6i5,nextstep6i5,history6i5] = stepwisefit(X6,Y6(:,5));

K1(1,:)=inmodel1i1;
K1(2,:)=inmodel1i2;
…
K1(114,:)=inmodel1i114;
K1(115,:)=inmodel1i115;

K2(1,:)=inmodel2i1;
K2(2,:)=inmodel2i2;
…
K2(114,:)=inmodel2i114;
K2(115,:)=inmodel2i115;

K3(1,:)=inmodel3i1;
K3(2,:)=inmodel3i2;
…
K3(114,:)=inmodel3i114;
K3(115,:)=inmodel3i115;

K4(1,:)=inmodel4i1;
K4(2,:)=inmodel4i2;
…
K4(114,:)=inmodel4i114;
K4(115,:)=inmodel4i115;
```

```
K5(1,:)=inmodel5i1;
K5(2,:)=inmodel5i2;
K5(3,:)=inmodel5i3;
K5(4,:)=inmodel5i4;
K5(5,:)=inmodel5i5;

K6(1,:)=inmodel6i1;
K6(2,:)=inmodel6i2;
K6(3,:)=inmodel6i3;
K6(4,:)=inmodel6i4;
K6(5,:)=inmodel6i5;
```

L is a 1x1122 matrix of numerical wavelengths.

```
for i=1:115;
for n=1:1122;
LL1(i,n)=K1(i,n)*L(1,n);
end
end
for i=1:115;
for n=1:1122;
LL2(i,n)=K2(i,n)*L(1,n);
end
end
for i=1:115;
for n=1:1122;
LL3(i,n)=K3(i,n)*L(1,n);
end
end
for i=1:115;
for n=1:1122;
LL4(i,n)=K4(i,n)*L(1,n);
end
end
for i=1:5;
for n=1:1122;
LL5(i,n)=K5(i,n)*L(1,n);
end
end
for i=1:5;
for n=1:1122;
LL6(i,n)=K6(i,n)*L(1,n);
end
end

M1i1=nonzeros(LL1(1,:))';
M1i2=nonzeros(LL1(2,:))';
…
M1i114=nonzeros(LL1(114,:))';
M1i115=nonzeros(LL1(115,:))';

M2i1=nonzeros(LL2(1,:))';
M2i2=nonzeros(LL2(2,:))';
…
M2i114=nonzeros(LL2(114,:))';
M2i115=nonzeros(LL2(115,:))';

M3i1=nonzeros(LL3(1,:))';
M3i2=nonzeros(LL3(2,:))';
…
M3i114=nonzeros(LL3(114,:))';
M3i115=nonzeros(LL3(115,:))';
```

```
M4i1=nonzeros(LL4(1,:))';
M4i2=nonzeros(LL4(2,:))';
…
M4i114=nonzeros(LL4(114,:))';
M4i115=nonzeros(LL4(115,:))';

M5i1=nonzeros(LL5(1,:))';
M5i2=nonzeros(LL5(2,:))';
M5i3=nonzeros(LL5(3,:))';
M5i4=nonzeros(LL5(4,:))';
M5i5=nonzeros(LL5(5,:))';

M6i1=nonzeros(LL6(1,:))';
M6i2=nonzeros(LL6(2,:))';
M6i3=nonzeros(LL6(3,:))';
M6i4=nonzeros(LL6(4,:))';
M6i5=nonzeros(LL6(5,:))';

N1i1=[nonzeros(history1i1.B(:,stats1i1.df0));stats1i1.intercept];
N1i2=[nonzeros(history1i2.B(:,stats1i2.df0));stats1i2.intercept];
…
N2i114=[nonzeros(history2i114.B(:,stats2i114.df0));stats2i114.intercept];
N2i115=[nonzeros(history2i115.B(:,stats2i115.df0));stats2i115.intercept];

N3i1=[nonzeros(history3i1.B(:,stats3i1.df0));stats3i1.intercept];
N3i2=[nonzeros(history3i2.B(:,stats3i2.df0));stats3i2.intercept];
…
N3i114=[nonzeros(history3i114.B(:,stats3i114.df0));stats3i114.intercept];
N3i115=[nonzeros(history3i115.B(:,stats3i115.df0));stats3i115.intercept];

N4i1=[nonzeros(history4i1.B(:,stats4i1.df0));stats4i1.intercept];
N4i2=[nonzeros(history4i2.B(:,stats4i2.df0));stats4i2.intercept];
…
N4i114=[nonzeros(history4i114.B(:,stats4i114.df0));stats4i114.intercept];
N4i115=[nonzeros(history4i115.B(:,stats4i115.df0));stats4i115.intercept];

N5i1=[nonzeros(history5i1.B(:,stats5i1.df0));stats5i1.intercept];
N5i2=[nonzeros(history5i2.B(:,stats5i2.df0));stats5i2.intercept];
N5i3=[nonzeros(history5i3.B(:,stats5i3.df0));stats5i3.intercept];
N5i4=[nonzeros(history5i4.B(:,stats5i4.df0));stats5i4.intercept];
N5i5=[nonzeros(history5i5.B(:,stats5i5.df0));stats5i5.intercept];

N6i1=[nonzeros(history6i1.B(:,stats6i1.df0));stats6i1.intercept];
N6i2=[nonzeros(history6i2.B(:,stats6i2.df0));stats6i2.intercept];
N6i3=[nonzeros(history6i3.B(:,stats6i3.df0));stats6i3.intercept];
N6i4=[nonzeros(history6i4.B(:,stats6i4.df0));stats6i4.intercept];
N6i5=[nonzeros(history6i5.B(:,stats6i5.df0));stats6i5.intercept];

Y1P(:,1)=X1*history1i1.B(:,end)+stats1i1.intercept;
Y1P(:,2)=X1*history1i2.B(:,end)+stats1i2.intercept;
…
Y1P(:,114)=X1*history1i114.B(:,end)+stats1i114.intercept;
Y1P(:,115)=X1*history1i115.B(:,end)+stats1i115.intercept;

Y2P(:,1)=X2*history2i1.B(:,end)+stats2i1.intercept;
Y2P(:,2)=X2*history2i2.B(:,end)+stats2i2.intercept;
…
Y2P(:,114)=X2*history2i114.B(:,end)+stats2i114.intercept;
Y2P(:,115)=X2*history2i115.B(:,end)+stats2i115.intercept;

Y3P(:,1)=X3*history3i1.B(:,end)+stats3i1.intercept;
```

Y3P(:,2)=X3*history3i2.B(:,end)+stats3i2.intercept;
…
Y3P(:,114)=X3*history3i114.B(:,end)+stats3i114.intercept;
Y3P(:,115)=X3*history3i115.B(:,end)+stats3i115.intercept;

Y4P(:,1)=X4*history4i1.B(:,end)+stats4i1.intercept;
Y4P(:,2)=X4*history4i2.B(:,end)+stats4i2.intercept;
…
Y4P(:,114)=X4*history4i114.B(:,end)+stats4i114.intercept;
Y4P(:,115)=X4*history4i115.B(:,end)+stats4i115.intercept;

Y5P(:,1)=X5*history5i1.B(:,end)+stats5i1.intercept;
Y5P(:,2)=X5*history5i2.B(:,end)+stats5i2.intercept;
Y5P(:,3)=X5*history5i3.B(:,end)+stats5i3.intercept;
Y5P(:,4)=X5*history5i4.B(:,end)+stats5i4.intercept;
Y5P(:,5)=X5*history5i5.B(:,end)+stats5i5.intercept;

Y6P(:,1)=X6*history6i1.B(:,end)+stats6i1.intercept;
Y6P(:,2)=X6*history6i2.B(:,end)+stats6i2.intercept;
Y6P(:,3)=X6*history6i3.B(:,end)+stats6i3.intercept;
Y6P(:,4)=X6*history6i4.B(:,end)+stats6i4.intercept;
Y6P(:,5)=X6*history6i5.B(:,end)+stats6i5.intercept;

Root Mean Squared Error
RMSE(:,1)=sqrt(((sum((((Y1)-Y1P).^2))))./34);
RMSE(:,2)=sqrt(((sum((((Y2)-Y2P).^2))))./25);
RMSE(:,3)=sqrt(((sum((((Y3)-Y3P).^2))))./14);
RMSE(:,4)=sqrt(((sum((((Y4)-Y4P).^2))))./11);
RMSE=RMSE';
RMSE5=sqrt(((sum((((Y5)-Y5P).^2))))./6);
RMSE6=sqrt(((sum(((((Y5)-Y5P).^2))))./13);

Relative Squared Error
RSE(1,:)=(sum((Y1P-Y1).^2))./(sum(((mean(Y1))-Y1).^2));
RSE(2,:)=(sum((Y2P-Y2).^2))./(sum(((mean(Y2))-Y2).^2));
RSE(3,:)=(sum((Y3P-Y3).^2))./(sum(((mean(Y3))-Y3).^2));
RSE(4,:)=(sum((Y4P-Y4).^2))./(sum(((mean(Y4))-Y4).^2));
RSE5=(sum((Y5P-Y5).^2))./(sum(((mean(Y5))-Y5).^2));
RSE6=(sum((Y6P-Y6).^2))./(sum(((mean(Y6))-Y6).^2));

Coefficient of Determination

R2=1-RSE;
R2five=1-RSE5;
R2six=1-RSE6;

Degrees of freedom
D(1,1)=stats1i1.df0;
…
D(1,115)=stats1i115.df0;

D(2,1)=stats2i1.df0;
…
D(2,115)=stats2i115.df0;

D(3,1)=stats3i1.df0;
…
D(3,115)=stats3i115.df0;

DD(1,1)=stats5i1.df0;
DD(1,2)=stats5i2.df0;
DD(1,3)=stats5i3.df0;

```
DD(1,4)=stats5i4.df0;
DD(1,5)=stats5i5.df0;

DD(2,5)=stats6i5.df0;
DD(2,4)=stats6i4.df0;
DD(2,3)=stats6i3.df0;
DD(2,2)=stats6i2.df0;
DD(2,1)=stats6i1.df0;
```

Cross Validation for PLSR and PCR

```
X1i=X1;
X2i=X2;
X3i=X3;
X4i=X4;
X5i=X5;
X6i=X6;
Y1i=Y1;
Y2i=Y2;
Y3i=Y3;
Y4i=Y4;
Y5i=Y5;
Y6i=Y6;
[X1i1,Y1i1,Xs1i1,Ys1i1,beta1i1,pctVar1i1,PLSmsep1i1] = plsregress(X1i,Y1i(:,1),10,'CV',10);
[X1i2,Y1i2,Xs1i2,Ys1i2,beta1i2,pctVar1i2,PLSmsep1i2] = plsregress(X1i,Y1i(:,2),10,'CV',10);
…
[X1i114,Y1i114,Xs1i114,Ys1i114,beta1i114,pctVar1i114,PLSmsep1i114] = plsregress(X1i,Y1i(:,114),10,'CV',10);
[X1i115,Y1i115,Xs1i115,Ys1i115,beta1i115,pctVar1i115,PLSmsep1i115] = plsregress(X1i,Y1i(:,115),10,'CV',10);


PCRmsep1i1 = sum(crossval(@pcrsse,X1i,Y1i(:,1),'KFold',10),1)/34;
PCRmsep1i2 = sum(crossval(@pcrsse,X1i,Y1i(:,2),'KFold',10),1)/34;
…
PCRmsep1i114 = sum(crossval(@pcrsse,X1i,Y1i(:,114),'KFold',10),1)/34;
PCRmsep1i115 = sum(crossval(@pcrsse,X1i,Y1i(:,115),'KFold',10),1)/34;

[X2i1,Y2i1,Xs2i1,Ys2i1,beta2i1,pctVar2i1,PLSmsep2i1] = plsregress(X2i,Y2i(:,1),10,'CV',10);
[X2i2,Y2i2,Xs2i2,Ys2i2,beta2i2,pctVar2i2,PLSmsep2i2] = plsregress(X2i,Y2i(:,2),10,'CV',10);
…
[X2i114,Y2i114,Xs2i114,Ys2i114,beta2i114,pctVar2i114,PLSmsep2i114] = plsregress(X2i,Y2i(:,114),10,'CV',10);
[X2i115,Y2i115,Xs2i115,Ys2i115,beta2i115,pctVar2i115,PLSmsep2i115] = plsregress(X2i,Y2i(:,115),10,'CV',10);


PCRmsep2i1 = sum(crossval(@pcrsse,X2i,Y2i(:,1),'KFold',10),1)/25;
PCRmsep2i2 = sum(crossval(@pcrsse,X2i,Y2i(:,2),'KFold',10),1)/25;
…
PCRmsep2i114 = sum(crossval(@pcrsse,X2i,Y2i(:,114),'KFold',10),1)/25;
PCRmsep2i115 = sum(crossval(@pcrsse,X2i,Y2i(:,115),'KFold',10),1)/25;

[X3i1,Y3i1,Xs3i1,Ys3i1,beta3i1,pctVar3i1,PLSmsep3i1] = plsregress(X3i,Y3i(:,1),10,'CV',10);
[X3i2,Y3i2,Xs3i2,Ys3i2,beta3i2,pctVar3i2,PLSmsep3i2] = plsregress(X3i,Y3i(:,2),10,'CV',10);
…
[X3i114,Y3i114,Xs3i114,Ys3i114,beta3i114,pctVar3i114,PLSmsep3i114] = plsregress(X3i,Y3i(:,114),10,'CV',10);
[X3i115,Y3i115,Xs3i115,Ys3i115,beta3i115,pctVar3i115,PLSmsep3i115] = plsregress(X3i,Y3i(:,115),10,'CV',10);


PCRmsep3i1 = sum(crossval(@pcrsse,X3i,Y3i(:,1),'KFold',10),1)/14;
PCRmsep3i2 = sum(crossval(@pcrsse,X3i,Y3i(:,2),'KFold',10),1)/14;
…
PCRmsep3i114 = sum(crossval(@pcrsse,X3i,Y3i(:,114),'KFold',10),1)/14;
PCRmsep3i115 = sum(crossval(@pcrsse,X3i,Y3i(:,115),'KFold',10),1)/14;

[X4i1,Y4i1,Xs4i1,Ys4i1,beta4i1,pctVar4i1,PLSmsep4i1] = plsregress(X4i,Y4i(:,1),8,'CV',8);
[X4i2,Y4i2,Xs4i2,Ys4i2,beta4i2,pctVar4i2,PLSmsep4i2] = plsregress(X4i,Y4i(:,2),8,'CV',8);
```

…
[X4i114,Y4i114,Xs4i114,Ys4i114,beta4i114,pctVar4i114,PLSmsep4i114] = plsregress(X4i,Y4i(:,114),8,'CV',8);
[X4i115,Y4i115,Xs4i115,Ys4i115,beta4i115,pctVar4i115,PLSmsep4i115] = plsregress(X4i,Y4i(:,115),8,'CV',8);

PCRmsep4i1 = sum(crossval(@pcrsse,X4i,Y4i(:,1),'KFold',8),1)/11;
PCRmsep4i2 = sum(crossval(@pcrsse,X4i,Y4i(:,2),'KFold',8),1)/11;
…
PCRmsep4i114 = sum(crossval(@pcrsse,X4i,Y4i(:,114),'KFold',8),1)/11;
PCRmsep4i115 = sum(crossval(@pcrsse,X4i,Y4i(:,115),'KFold',8),1)/11;

[X5i1,Y5i1,Xs5i1,Ys5i1,beta5i1,pctVar5i1,PLSmsep5i1] = plsregress(X5i,Y5i(:,1),3,'CV',3);
[X5i2,Y5i2,Xs5i2,Ys5i2,beta5i2,pctVar5i2,PLSmsep5i2] = plsregress(X5i,Y5i(:,2),3,'CV',3);
[X5i3,Y5i3,Xs5i3,Ys5i3,beta5i3,pctVar5i3,PLSmsep5i3] = plsregress(X5i,Y5i(:,3),3,'CV',3);
[X5i4,Y5i4,Xs5i4,Ys5i4,beta5i4,pctVar5i4,PLSmsep5i4] = plsregress(X5i,Y5i(:,4),3,'CV',3);
[X5i5,Y5i5,Xs5i5,Ys5i5,beta5i5,pctVar5i5,PLSmsep5i5] = plsregress(X5i,Y5i(:,5),3,'CV',3);

PCRmsep5i1 = sum(crossval(@pcrsse,X5i,Y5i(:,1),'KFold',3),1)/6;
PCRmsep5i2 = sum(crossval(@pcrsse,X5i,Y5i(:,2),'KFold',3),1)/6;
PCRmsep5i3 = sum(crossval(@pcrsse,X5i,Y5i(:,3),'KFold',3),1)/6;
PCRmsep5i4 = sum(crossval(@pcrsse,X5i,Y5i(:,4),'KFold',3),1)/6;
PCRmsep5i5 = sum(crossval(@pcrsse,X5i,Y5i(:,5),'KFold',3),1)/6;

[X6i1,Y6i1,Xs6i1,Ys6i1,beta6i1,pctVar6i1,PLSmsep6i1] = plsregress(X6i,Y6i(:,1),10,'CV',10);
[X6i2,Y6i2,Xs6i2,Ys6i2,beta6i2,pctVar6i2,PLSmsep6i2] = plsregress(X6i,Y6i(:,2),10,'CV',10);
[X6i3,Y6i3,Xs6i3,Ys6i3,beta6i3,pctVar6i3,PLSmsep6i3] = plsregress(X6i,Y6i(:,3),10,'CV',10);
[X6i4,Y6i4,Xs6i4,Ys6i4,beta6i4,pctVar6i4,PLSmsep6i4] = plsregress(X6i,Y6i(:,4),10,'CV',10);
[X6i5,Y6i5,Xs6i5,Ys6i5,beta6i5,pctVar6i5,PLSmsep6i5] = plsregress(X6i,Y6i(:,5),10,'CV',10);

PCRmsep6i1 = sum(crossval(@pcrsse,X6i,Y6i(:,1),'KFold',10),1)/13;
PCRmsep6i2 = sum(crossval(@pcrsse,X6i,Y6i(:,2),'KFold',10),1)/13;
PCRmsep6i3 = sum(crossval(@pcrsse,X6i,Y6i(:,3),'KFold',10),1)/13;
PCRmsep6i4 = sum(crossval(@pcrsse,X6i,Y6i(:,4),'KFold',10),1)/13;
PCRmsep6i5 = sum(crossval(@pcrsse,X6i,Y6i(:,5),'KFold',10),1)/13;

Minimum of Cross Validation Results for PLSR and PCR, if result was zero, used second lowest component result.

[B1(1,1),B1(1,2)] = min(PLSmsep1i1(2,:)); B1(1,2)=B1(1,2)-1;
[B1(2,1),B1(2,2)] = min(PLSmsep1i2(2,:)); B1(2,2)=B1(2,2)-1;
…
[B1(114,1),B1(114,2)] = min(PLSmsep1i114(2,:)); B1(114,2)=B1(114,2)-1;
[B1(115,1),B1(115,2)] = min(PLSmsep1i115(2,:)); B1(115,2)=B1(115,2)-1;

[C1(1,1),C1(1,2)] = min(PCRmsep1i1); C1(1,2)=C1(1,2)-1;
[C1(2,1),C1(2,2)] = min(PCRmsep1i2); C1(2,2)=C1(2,2)-1;
…
[C1(114,1),C1(114,2)] = min(PCRmsep1i114); C1(114,2)=C1(114,2)-1;
[C1(115,1),C1(115,2)] = min(PCRmsep1i115); C1(115,2)=C1(115,2)-1;

[B2(1,1),B2(1,2)] = min(PLSmsep2i1(2,:)); B2(1,2)=B2(1,2)-1;
[B2(2,1),B2(2,2)] = min(PLSmsep2i2(2,:)); B2(2,2)=B2(2,2)-1;
…
[B2(114,1),B2(114,2)] = min(PLSmsep2i114(2,:)); B2(114,2)=B2(114,2)-1;
[B2(115,1),B2(115,2)] = min(PLSmsep2i115(2,:)); B2(115,2)=B2(115,2)-1;

[C2(1,1),C2(1,2)] = min(PCRmsep2i1); C2(1,2)=C2(1,2)-1;
[C2(2,1),C2(2,2)] = min(PCRmsep2i2); C2(2,2)=C2(2,2)-1;
…
[C2(114,1),C2(114,2)] = min(PCRmsep2i114); C2(114,2)=C2(114,2)-1;
[C2(115,1),C2(115,2)] = min(PCRmsep2i115); C2(115,2)=C2(115,2)-1;

[B3(1,1),B3(1,2)] = min(PLSmsep3i1(2,:)); B3(1,2)=B3(1,2)-1;
[B3(2,1),B3(2,2)] = min(PLSmsep3i2(2,:)); B3(2,2)=B3(2,2)-1;

429

…
[B3(114,1),B3(114,2)] = min(PLSmsep3i114(2,:)); B3(114,2)=B3(114,2)-1;
[B3(115,1),B3(115,2)] = min(PLSmsep3i115(2,:)); B3(115,2)=B3(115,2)-1;

[C3(1,1),C3(1,2)] = min(PCRmsep3i1); C3(1,2)=C3(1,2)-1;
[C3(2,1),C3(2,2)] = min(PCRmsep3i2); C3(2,2)=C3(2,2)-1;
…
[C3(114,1),C3(114,2)] = min(PCRmsep3i114); C3(114,2)=C3(114,2)-1;
[C3(115,1),C3(115,2)] = min(PCRmsep3i115); C3(115,2)=C3(115,2)-1;

[B4(1,1),B4(1,2)] = min(PLSmsep4i1(2,:)); B4(1,2)=B4(1,2)-1;
[B4(2,1),B4(2,2)] = min(PLSmsep4i2(2,:)); B4(2,2)=B4(2,2)-1;
…
[B4(114,1),B4(114,2)] = min(PLSmsep4i114(2,:)); B4(114,2)=B4(114,2)-1;
[B4(115,1),B4(115,2)] = min(PLSmsep4i115(2,:)); B4(115,2)=B4(115,2)-1;

[C4(1,1),C4(1,2)] = min(PCRmsep4i1); C4(1,2)=C4(1,2)-1;
[C4(2,1),C4(2,2)] = min(PCRmsep4i2); C4(2,2)=C4(2,2)-1;
..
[C4(114,1),C4(114,2)] = min(PCRmsep4i114); C4(114,2)=C4(114,2)-1;
[C4(115,1),C4(115,2)] = min(PCRmsep4i115); C4(115,2)=C4(115,2)-1;

[B5(1,1),B5(1,2)] = min(PLSmsep5i1(2,:)); B5(1,2)=B5(1,2)-1;
[B5(2,1),B5(2,2)] = min(PLSmsep5i2(2,:)); B5(2,2)=B5(2,2)-1;
[B5(3,1),B5(3,2)] = min(PLSmsep5i3(2,:)); B5(3,2)=B5(3,2)-1;
[B5(4,1),B5(4,2)] = min(PLSmsep5i4(2,:)); B5(4,2)=B5(4,2)-1;
[B5(5,1),B5(5,2)] = min(PLSmsep5i5(2,:)); B5(5,2)=B5(5,2)-1;

[C5(1,1),C5(1,2)] = min(PCRmsep5i1); C5(1,2)=C5(1,2)-1;
[C5(2,1),C5(2,2)] = min(PCRmsep5i2); C5(2,2)=C5(2,2)-1;
[C5(3,1),C5(3,2)] = min(PCRmsep5i3); C5(3,2)=C5(3,2)-1;
[C5(4,1),C5(4,2)] = min(PCRmsep5i4); C5(4,2)=C5(4,2)-1;
[C5(5,1),C5(5,2)] = min(PCRmsep5i5); C5(5,2)=C5(5,2)-1;

[B6(1,1),B6(1,2)] = min(PLSmsep6i1(2,:)); B6(1,2)=B6(1,2)-1;
[B6(2,1),B6(2,2)] = min(PLSmsep6i2(2,:)); B6(2,2)=B6(2,2)-1;
[B6(3,1),B6(3,2)] = min(PLSmsep6i3(2,:)); B6(3,2)=B6(3,2)-1;
[B6(4,1),B6(4,2)] = min(PLSmsep6i4(2,:)); B6(4,2)=B6(4,2)-1;
[B6(5,1),B6(5,2)] = min(PLSmsep6i5(2,:)); B6(5,2)=B6(5,2)-1;

[C6(1,1),C6(1,2)] = min(PCRmsep6i1); C6(1,2)=C6(1,2)-1;
[C6(2,1),C6(2,2)] = min(PCRmsep6i2); C6(2,2)=C6(2,2)-1;
[C6(3,1),C6(3,2)] = min(PCRmsep6i3); C6(3,2)=C6(3,2)-1;
[C6(4,1),C6(4,2)] = min(PCRmsep6i4); C6(4,2)=C6(4,2)-1;
[C6(5,1),C6(5,2)] = min(PCRmsep6i5); C6(5,2)=C6(5,2)-1;

PLS Model with minimum number of variables from CV analysis

[Xloadings1i1,Yloadings1i1,Xscores1i1,Yscores1i1,betaPLS1i1] = plsregress(X1i,Y1i(:,1),B1(1,2));
[Xloadings1i2,Yloadings1i2,Xscores1i2,Yscores1i2,betaPLS1i2] = plsregress(X1i,Y1i(:,2),B1(2,2));
…
[Xloadings1i114,Yloadings1i114,Xscores1i114,Yscores1i114,betaPLS1i114] = plsregress(X1i,Y1i(:,114),B1(114,2));
[Xloadings1i115,Yloadings1i115,Xscores1i115,Yscores1i115,betaPLS1i115] = plsregress(X1i,Y1i(:,115),B1(115,2));

[Xloadings2i1,Yloadings2i1,Xscores2i1,Yscores2i1,betaPLS2i1] = plsregress(X2i,Y2i(:,1),B2(1,2));
[Xloadings2i2,Yloadings2i2,Xscores2i2,Yscores2i2,betaPLS2i2] = plsregress(X2i,Y2i(:,2),B2(2,2));
…
[Xloadings2i114,Yloadings2i114,Xscores2i114,Yscores2i114,betaPLS2i114] = plsregress(X2i,Y2i(:,114),B2(114,2));
[Xloadings2i115,Yloadings2i115,Xscores2i115,Yscores2i115,betaPLS2i115] = plsregress(X2i,Y2i(:,115),B2(115,2));

[Xloadings3i1,Yloadings3i1,Xscores3i1,Yscores3i1,betaPLS3i1] = plsregress(X3i,Y3i(:,1),B3(1,2));
[Xloadings3i2,Yloadings3i2,Xscores3i2,Yscores3i2,betaPLS3i2] = plsregress(X3i,Y3i(:,2),B3(2,2));

…
[Xloadings3i114,Yloadings3i114,Xscores3i114,Yscores3i114,betaPLS3i114] = plsregress(X3i,Y3i(:,114),B3(114,2));
[Xloadings3i115,Yloadings3i115,Xscores3i115,Yscores3i115,betaPLS3i115] = plsregress(X3i,Y3i(:,115),B3(115,2));

[Xloadings4i1,Yloadings4i1,Xscores4i1,Yscores4i1,betaPLS4i1] = plsregress(X4i,Y4i(:,1),B4(1,2));
[Xloadings4i2,Yloadings4i2,Xscores4i2,Yscores4i2,betaPLS4i2] = plsregress(X4i,Y4i(:,2),B4(2,2));
…
[Xloadings4i114,Yloadings4i114,Xscores4i114,Yscores4i114,betaPLS4i114] = plsregress(X4i,Y4i(:,114),B4(114,2));
[Xloadings4i115,Yloadings4i115,Xscores4i115,Yscores4i115,betaPLS4i115] = plsregress(X4i,Y4i(:,115),B4(115,2));

[Xloadings5i1,Yloadings5i1,Xscores5i1,Yscores5i1,betaPLS5i1] = plsregress(X5i,Y5i(:,1), B5(1,2));
[Xloadings5i2,Yloadings5i2,Xscores5i2,Yscores5i2,betaPLS5i2] = plsregress(X5i,Y5i(:,2), B5(2,2));
[Xloadings5i3,Yloadings5i3,Xscores5i3,Yscores5i3,betaPLS5i3] = plsregress(X5i,Y5i(:,3), B5(3,2));
[Xloadings5i4,Yloadings5i4,Xscores5i4,Yscores5i4,betaPLS5i4] = plsregress(X5i,Y5i(:,4), B5(4,2));
[Xloadings5i5,Yloadings5i5,Xscores5i5,Yscores5i5,betaPLS5i5] = plsregress(X5i,Y5i(:,5), B5(5,2));

[Xloadings6i1,Yloadings6i1,Xscores6i1,Yscores6i1,betaPLS6i1] = plsregress(X6i,Y6i(:,1), B6(1,2));
[Xloadings6i2,Yloadings6i2,Xscores6i2,Yscores6i2,betaPLS6i2] = plsregress(X6i,Y6i(:,2), B6(2,2));
[Xloadings6i3,Yloadings6i3,Xscores6i3,Yscores6i3,betaPLS6i3] = plsregress(X6i,Y6i(:,3), B6(3,2));
[Xloadings6i4,Yloadings6i4,Xscores6i4,Yscores6i4,betaPLS6i4] = plsregress(X6i,Y6i(:,4), B6(4,2));
[Xloadings6i5,Yloadings6i5,Xscores6i5,Yscores6i5,betaPLS6i5] = plsregress(X6i,Y6i(:,5), B6(5,2));

PCA

[PCALoadingsX1i,PCAScoresX1i,PCAVarX1i] = pca(X1i);
[PCALoadingsX2i,PCAScoresX2i,PCAVarX2i] = pca(X2i);
[PCALoadingsX3i,PCAScoresX3i,PCAVarX3i] = pca(X3i);
[PCALoadingsX4i,PCAScoresX4i,PCAVarX4i] = pca(X4i);
[PCALoadingsX5i,PCAScoresX5i,PCAVarX5i] = pca(X5i);
[PCALoadingsX6i,PCAScoresX6i,PCAVarX6i] = pca(X6i);

PCR beta prediction with minimum variables from CV analysis

betaPCRX1i1 = regress(Y1i(:,1)-mean(Y1i(:,1)), PCAScoresX1i(:,1:(C1(1,2))));
betaPCRX1i2 = regress(Y1i(:,2)-mean(Y1i(:,2)), PCAScoresX1i(:,1:(C1(2,2))));
…
betaPCRX1i114 = regress(Y1i(:,114)-mean(Y1i(:,114)), PCAScoresX1i(:,1:(C1(114,2))));
betaPCRX1i115 = regress(Y1i(:,115)-mean(Y1i(:,115)), PCAScoresX1i(:,1:(C1(115,2))));

betaPCRX2i1 = regress(Y2i(:,1)-mean(Y2i(:,1)), PCAScoresX2i(:,1:(C2(1,2))));
betaPCRX2i2 = regress(Y2i(:,2)-mean(Y2i(:,2)), PCAScoresX2i(:,1:(C2(2,2))));
…
betaPCRX2i114 = regress(Y2i(:,114)-mean(Y2i(:,114)), PCAScoresX2i(:,1:(C2(114,2))));
betaPCRX2i115 = regress(Y2i(:,115)-mean(Y2i(:,115)), PCAScoresX2i(:,1:(C2(115,2))));

betaPCRX3i1 = regress(Y3i(:,1)-mean(Y3i(:,1)), PCAScoresX3i(:,1:(C3(1,2))));
betaPCRX3i2 = regress(Y3i(:,2)-mean(Y3i(:,2)), PCAScoresX3i(:,1:(C3(2,2))));
…
betaPCRX3i114 = regress(Y3i(:,114)-mean(Y3i(:,114)), PCAScoresX3i(:,1:(C3(114,2))));
betaPCRX3i115 = regress(Y3i(:,115)-mean(Y3i(:,115)), PCAScoresX3i(:,1:(C3(115,2))));

betaPCRX4i1 = regress(Y4i(:,1)-mean(Y4i(:,1)), PCAScoresX4i(:,1:(C4(1,2))));
betaPCRX4i2 = regress(Y4i(:,2)-mean(Y4i(:,2)), PCAScoresX4i(:,1:(C4(2,2))));
…
betaPCRX4i114 = regress(Y4i(:,114)-mean(Y4i(:,114)), PCAScoresX4i(:,1:(C4(114,2))));
betaPCRX4i115 = regress(Y4i(:,115)-mean(Y4i(:,115)), PCAScoresX4i(:,1:(C4(115,2))));

betaPCRX5i1 = regress(Y5i(:,1)-mean(Y5i(:,1)), PCAScoresX5i(:,1:(C5(1,2))));
betaPCRX5i2 = regress(Y5i(:,2)-mean(Y5i(:,2)), PCAScoresX5i(:,1:(C5(2,2))));
betaPCRX5i3 = regress(Y5i(:,3)-mean(Y5i(:,3)), PCAScoresX5i(:,1:(C5(3,2))));
betaPCRX5i4 = regress(Y5i(:,4)-mean(Y5i(:,4)), PCAScoresX5i(:,1:(C5(4,2))));
betaPCRX5i5 = regress(Y5i(:,5)-mean(Y5i(:,5)), PCAScoresX5i(:,1:(C5(5,2))));

betaPCRX6i1 = regress(Y6i(:,1)-mean(Y6i(:,1)), PCAScoresX6i(:,1:(C6(1,2))));
betaPCRX6i2 = regress(Y6i(:,2)-mean(Y6i(:,2)), PCAScoresX6i(:,1:(C6(2,2))));
betaPCRX6i3 = regress(Y6i(:,3)-mean(Y6i(:,3)), PCAScoresX6i(:,1:(C6(3,2))));
betaPCRX6i4 = regress(Y6i(:,4)-mean(Y6i(:,4)), PCAScoresX6i(:,1:(C6(4,2))));
betaPCRX6i5 = regress(Y6i(:,5)-mean(Y6i(:,5)), PCAScoresX6i(:,1:(C6(5,2))));

Transform regression coefficients

betaPCRX1i1 = PCALoadingsX1i(:,1:(C1(1,2)))*betaPCRX1i1;
betaPCRX1i2 = PCALoadingsX1i(:,1:(C1(2,2)))*betaPCRX1i2;
…
betaPCRX1i114 = PCALoadingsX1i(:,1:(C1(114,2)))*betaPCRX1i114;
betaPCRX1i115 = PCALoadingsX1i(:,1:(C1(115,2)))*betaPCRX1i115;

betaPCRX2i1 = PCALoadingsX2i(:,1:(C2(1,2)))*betaPCRX2i1;
betaPCRX2i2 = PCALoadingsX2i(:,1:(C2(2,2)))*betaPCRX2i2;
…
betaPCRX2i114 = PCALoadingsX2i(:,1:(C2(114,2)))*betaPCRX2i114;
betaPCRX2i115 = PCALoadingsX2i(:,1:(C2(115,2)))*betaPCRX2i115;

betaPCRX3i1 = PCALoadingsX3i(:,1:(C3(1,2)))*betaPCRX3i1;
betaPCRX3i2 = PCALoadingsX3i(:,1:(C3(2,2)))*betaPCRX3i2;
…
betaPCRX3i114 = PCALoadingsX3i(:,1:(C3(114,2)))*betaPCRX3i114;
betaPCRX3i115 = PCALoadingsX3i(:,1:(C3(115,2)))*betaPCRX3i115;

betaPCRX4i1 = PCALoadingsX4i(:,1:(C4(1,2)))*betaPCRX4i1;
betaPCRX4i2 = PCALoadingsX4i(:,1:(C4(2,2)))*betaPCRX4i2;
…
betaPCRX4i114 = PCALoadingsX4i(:,1:(C4(114,2)))*betaPCRX4i114;
betaPCRX4i115 = PCALoadingsX4i(:,1:(C4(115,2)))*betaPCRX4i115;

betaPCRX5i1 = PCALoadingsX5i(:,1:(C5(1,2)))*betaPCRX5i1;
betaPCRX5i2 = PCALoadingsX5i(:,1:(C5(2,2)))*betaPCRX5i2;
betaPCRX5i3 = PCALoadingsX5i(:,1:(C5(3,2)))*betaPCRX5i3;
betaPCRX5i4 = PCALoadingsX5i(:,1:(C5(4,2)))*betaPCRX5i4;
betaPCRX5i5 = PCALoadingsX5i(:,1:(C5(5,2)))*betaPCRX5i5;

betaPCRX6i1 = PCALoadingsX6i(:,1:(C6(1,2)))*betaPCRX6i1;
betaPCRX6i2 = PCALoadingsX6i(:,1:(C6(2,2)))*betaPCRX6i2;
betaPCRX6i3 = PCALoadingsX6i(:,1:(C6(3,2)))*betaPCRX6i3;
betaPCRX6i4 = PCALoadingsX6i(:,1:(C6(4,2)))*betaPCRX6i4;
betaPCRX6i5 = PCALoadingsX6i(:,1:(C6(5,2)))*betaPCRX6i5;

Uncenter regression coefficients

betaPCRX1i1 = [mean(Y1i(:,1)) - mean(X1i)*betaPCRX1i1; betaPCRX1i1];
betaPCRX1i2 = [mean(Y1i(:,2)) - mean(X1i)*betaPCRX1i2; betaPCRX1i2];
…
betaPCRX1i114 = [mean(Y1i(:,114)) - mean(X1i)*betaPCRX1i114; betaPCRX1i114];
betaPCRX1i115 = [mean(Y1i(:,115)) - mean(X1i)*betaPCRX1i115; betaPCRX1i115];

betaPCRX2i1 = [mean(Y2i(:,1)) - mean(X2i)*betaPCRX2i1; betaPCRX2i1];
betaPCRX2i2 = [mean(Y2i(:,2)) - mean(X2i)*betaPCRX2i2; betaPCRX2i2];
…
betaPCRX2i114 = [mean(Y2i(:,114)) - mean(X2i)*betaPCRX2i114; betaPCRX2i114];
betaPCRX2i115 = [mean(Y2i(:,115)) - mean(X2i)*betaPCRX2i115; betaPCRX2i115];

betaPCRX3i1 = [mean(Y3i(:,1)) - mean(X3i)*betaPCRX3i1; betaPCRX3i1];
betaPCRX3i2 = [mean(Y3i(:,2)) - mean(X3i)*betaPCRX3i2; betaPCRX3i2];
…

betaPCRX3i114 = [mean(Y3i(:,114)) - mean(X3i)*betaPCRX3i114; betaPCRX3i114];
betaPCRX3i115 = [mean(Y3i(:,115)) - mean(X3i)*betaPCRX3i115; betaPCRX3i115];

betaPCRX4i1 = [mean(Y4i(:,1)) - mean(X4i)*betaPCRX4i1; betaPCRX4i1];
betaPCRX4i2 = [mean(Y4i(:,2)) - mean(X4i)*betaPCRX4i2; betaPCRX4i2];
…
betaPCRX4i114 = [mean(Y4i(:,114)) - mean(X4i)*betaPCRX4i114; betaPCRX4i114];
betaPCRX4i115 = [mean(Y4i(:,115)) - mean(X4i)*betaPCRX4i115; betaPCRX4i115];

betaPCRX5i1 = [mean(Y5i(:,1)) - mean(X5i)*betaPCRX5i1; betaPCRX5i1];
betaPCRX5i2 = [mean(Y5i(:,2)) - mean(X5i)*betaPCRX5i2; betaPCRX5i2];
betaPCRX5i3 = [mean(Y5i(:,3)) - mean(X5i)*betaPCRX5i3; betaPCRX5i3];
betaPCRX5i4 = [mean(Y5i(:,4)) - mean(X5i)*betaPCRX5i4; betaPCRX5i4];
betaPCRX5i5 = [mean(Y5i(:,5)) - mean(X5i)*betaPCRX5i5; betaPCRX5i5];

betaPCRX6i1 = [mean(Y6i(:,1)) - mean(X6i)*betaPCRX6i1; betaPCRX6i1];
betaPCRX6i2 = [mean(Y6i(:,2)) - mean(X6i)*betaPCRX6i2; betaPCRX6i2];
betaPCRX6i3 = [mean(Y6i(:,3)) - mean(X6i)*betaPCRX6i3; betaPCRX6i3];
betaPCRX6i4 = [mean(Y6i(:,4)) - mean(X6i)*betaPCRX6i4; betaPCRX6i4];
betaPCRX6i5 = [mean(Y6i(:,5)) - mean(X6i)*betaPCRX6i5; betaPCRX6i5];

Predict y with PLS regression with minimum number of variables from CV analysis

yfitPLS1i(:,1) = [ones(34,1) X1i]*betaPLS1i1;
yfitPLS1i(:,2) = [ones(34,1) X1i]*betaPLS1i2;
…
yfitPLS1i(:,114) = [ones(34,1) X1i]*betaPLS1i114;
yfitPLS1i(:,115) = [ones(34,1) X1i]*betaPLS1i115;

yfitPLS2i(:,1) = [ones(25,1) X2i]*betaPLS2i1;
yfitPLS2i(:,2) = [ones(25,1) X2i]*betaPLS2i2;
…
yfitPLS2i(:,114) = [ones(25,1) X2i]*betaPLS2i114;
yfitPLS2i(:,115) = [ones(25,1) X2i]*betaPLS2i115;

yfitPLS3i(:,1) = [ones(14,1) X3i]*betaPLS3i1;
yfitPLS3i(:,2) = [ones(14,1) X3i]*betaPLS3i2;
…
yfitPLS3i(:,114) = [ones(14,1) X3i]*betaPLS3i114;
yfitPLS3i(:,115) = [ones(14,1) X3i]*betaPLS3i115;

yfitPLS4i(:,1) = [ones(11,1) X4i]*betaPLS4i1;
yfitPLS4i(:,2) = [ones(11,1) X4i]*betaPLS4i2;
…
yfitPLS4i(:,114) = [ones(11,1) X4i]*betaPLS4i114;
yfitPLS4i(:,115) = [ones(11,1) X4i]*betaPLS4i115;

yfitPLS5i(:,1) = [ones(6,1) X5i]*betaPLS5i1;
yfitPLS5i(:,2) = [ones(6,1) X5i]*betaPLS5i2;
yfitPLS5i(:,3) = [ones(6,1) X5i]*betaPLS5i3;
yfitPLS5i(:,4) = [ones(6,1) X5i]*betaPLS5i4;
yfitPLS5i(:,5) = [ones(6,1) X5i]*betaPLS5i5;

yfitPLS6i(:,1) = [ones(13,1) X6i]*betaPLS6i1;
yfitPLS6i(:,2) = [ones(13,1) X6i]*betaPLS6i2;
yfitPLS6i(:,3) = [ones(13,1) X6i]*betaPLS6i3;
yfitPLS6i(:,4) = [ones(13,1) X6i]*betaPLS6i4;
yfitPLS6i(:,5) = [ones(13,1) X6i]*betaPLS6i5;

Predict y with PC regression with minimum number of variables from CV analysis

yfitPCR1i(:,1) = [ones(34,1) X1i]*betaPCRX1i1;
yfitPCR1i(:,2) = [ones(34,1) X1i]*betaPCRX1i2;
…
yfitPCR1i(:,114) = [ones(34,1) X1i]*betaPCRX1i114;
yfitPCR1i(:,115) = [ones(34,1) X1i]*betaPCRX1i115;

yfitPCR2i(:,1) = [ones(25,1) X2i]*betaPCRX2i1;
yfitPCR2i(:,2) = [ones(25,1) X2i]*betaPCRX2i2;
…
yfitPCR2i(:,114) = [ones(25,1) X2i]*betaPCRX2i114;
yfitPCR2i(:,115) = [ones(25,1) X2i]*betaPCRX2i115;

yfitPCR3i(:,1) = [ones(14,1) X3i]*betaPCRX3i1;
yfitPCR3i(:,2) = [ones(14,1) X3i]*betaPCRX3i2;
…
yfitPCR3i(:,114) = [ones(14,1) X3i]*betaPCRX3i114;
yfitPCR3i(:,115) = [ones(14,1) X3i]*betaPCRX3i115;

yfitPCR4i(:,1) = [ones(11,1) X4i]*betaPCRX4i1;
yfitPCR4i(:,2) = [ones(11,1) X4i]*betaPCRX4i2;
…
yfitPCR4i(:,114) = [ones(11,1) X4i]*betaPCRX4i114;
yfitPCR4i(:,115) = [ones(11,1) X4i]*betaPCRX4i115;

yfitPCR5i(:,1) = [ones(6,1) X5i]*betaPCRX5i1;
yfitPCR5i(:,2) = [ones(6,1) X5i]*betaPCRX5i2;
yfitPCR5i(:,3) = [ones(6,1) X5i]*betaPCRX5i3;
yfitPCR5i(:,4) = [ones(6,1) X5i]*betaPCRX5i4;
yfitPCR5i(:,5) = [ones(6,1) X5i]*betaPCRX5i5;

yfitPCR6i(:,1) = [ones(13,1) X6i]*betaPCRX6i1;
yfitPCR6i(:,2) = [ones(13,1) X6i]*betaPCRX6i2;
yfitPCR6i(:,3) = [ones(13,1) X6i]*betaPCRX6i3;
yfitPCR6i(:,4) = [ones(13,1) X6i]*betaPCRX6i4;
yfitPCR6i(:,5) = [ones(13,1) X6i]*betaPCRX6i5;

Root Mean Squared Error

EPCR1=sqrt(((sum((((Y1i)-yfitPCR1i).^2))))./34);
EPCR2=sqrt(((sum((((Y2i)-yfitPCR2i).^2))))./25);
EPCR3=sqrt(((sum((((Y3i)-yfitPCR3i).^2))))./14);
EPCR4=sqrt(((sum((((Y4i)-yfitPCR4i).^2))))./11);
EPCR5=sqrt(((sum((((Y5i)-yfitPCR5i).^2))))./6);
EPCR6=sqrt(((sum((((Y6i)-yfitPCR6i).^2))))./13);
EPLS1=sqrt(((sum((((Y1i)-yfitPLS1i).^2))))./34);
EPLS2=sqrt(((sum((((Y2i)-yfitPLS2i).^2))))./25);
EPLS3=sqrt(((sum((((Y3i)-yfitPLS3i).^2))))./14);
EPLS4=sqrt(((sum((((Y4i)-yfitPLS4i).^2))))./11);
EPLS5=sqrt(((sum((((Y5i)-yfitPLS5i).^2))))./6);
EPLS6=sqrt(((sum((((Y6i)-yfitPLS6i).^2))))./13);

Relative Squared Error

RSEPCR1=(sum((yfitPCR1i-Y1i).^2))./(sum(((mean(Y1i))-Y1i).^2));
RSEPCR2=(sum((yfitPCR2i-Y2i).^2))./(sum(((mean(Y2i))-Y2i).^2));
RSEPCR3=(sum((yfitPCR3i-Y3i).^2))./(sum(((mean(Y3i))-Y3i).^2));
RSEPCR4=(sum((yfitPCR4i-Y4i).^2))./(sum(((mean(Y4i))-Y4i).^2));
RSEPCR5=(sum((yfitPCR5i-Y5i).^2))./(sum(((mean(Y5i))-Y5i).^2));
RSEPCR6=(sum((yfitPCR6i-Y6i).^2))./(sum(((mean(Y6i))-Y6i).^2));
RSEPLS1=(sum((yfitPLS1i-Y1i).^2))./(sum(((mean(Y1i))-Y1i).^2));

RSEPLS2=(sum((yfitPLS2i-Y2i).^2))./(sum(((mean(Y2i))-Y2i).^2));
RSEPLS3=(sum((yfitPLS3i-Y3i).^2))./(sum(((mean(Y3i))-Y3i).^2));
RSEPLS4=(sum((yfitPLS4i-Y4i).^2))./(sum(((mean(Y4i))-Y4i).^2));
RSEPLS5=(sum((yfitPLS5i-Y5i).^2))./(sum(((mean(Y5i))-Y5i).^2));
RSEPLS6=(sum((yfitPLS6i-Y6i).^2))./(sum(((mean(Y6i))-Y6i).^2));

Coefficient of Determination

R2PCR1=1-RSEPCR1;
R2PCR2=1-RSEPCR2;
R2PCR3=1-RSEPCR3;
R2PCR4=1-RSEPCR4;
R2PCR5=1-RSEPCR5;
R2PCR6=1-RSEPCR6;
R2PLS1=1-RSEPLS1;
R2PLS2=1-RSEPLS2;
R2PLS3=1-RSEPLS3;
R2PLS4=1-RSEPLS4;
R2PLS5=1-RSEPLS5;
R2PLS6=1-RSEPLS6;

Appendix H

Numerical regression coefficients and adjusted coefficient of determinations for all SLS models are found in *Appendix H*. Simple least squares regression parameter as a function of wavelength for all measured properties in the six data sets are presented in *Figures H1 to H14*. Adjusted coefficient of determination as a function of wavelength for simple least square regression results are presented for six data sets in *Figures H15 to H28*. Absorbance wavelength channels and corresponding regressor coefficients for MLR models of cumulative boiling point distribution fractions are highlighted in *Tables H1 to H4*. Variance explained by each principal component for each data set is highlighted in *Figures H29 to H34*. Principal component analysis for all six data sets is presented in *Figures H35 to H40*. Minimum number of cross validated components in the PCR and PLSR models for cumulative boiling point distribution fractions are shown in *Tables H5 and H6*, respectively. Section criteria results for the first four data sets of all modeling methods for cumulative boiling point distribution fractions are shown in *Tables H7 to H22*.
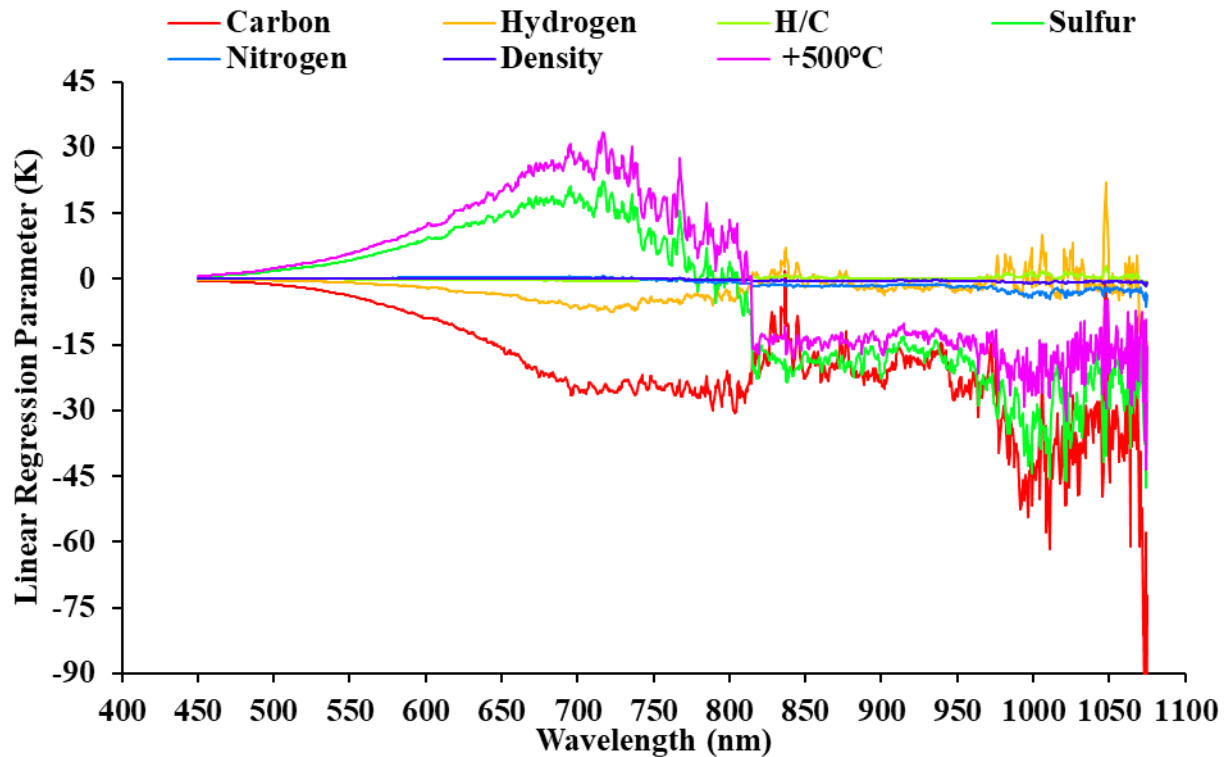
Figure H1. Simple least squares regression parameter as a function of wavelength for the first data set.
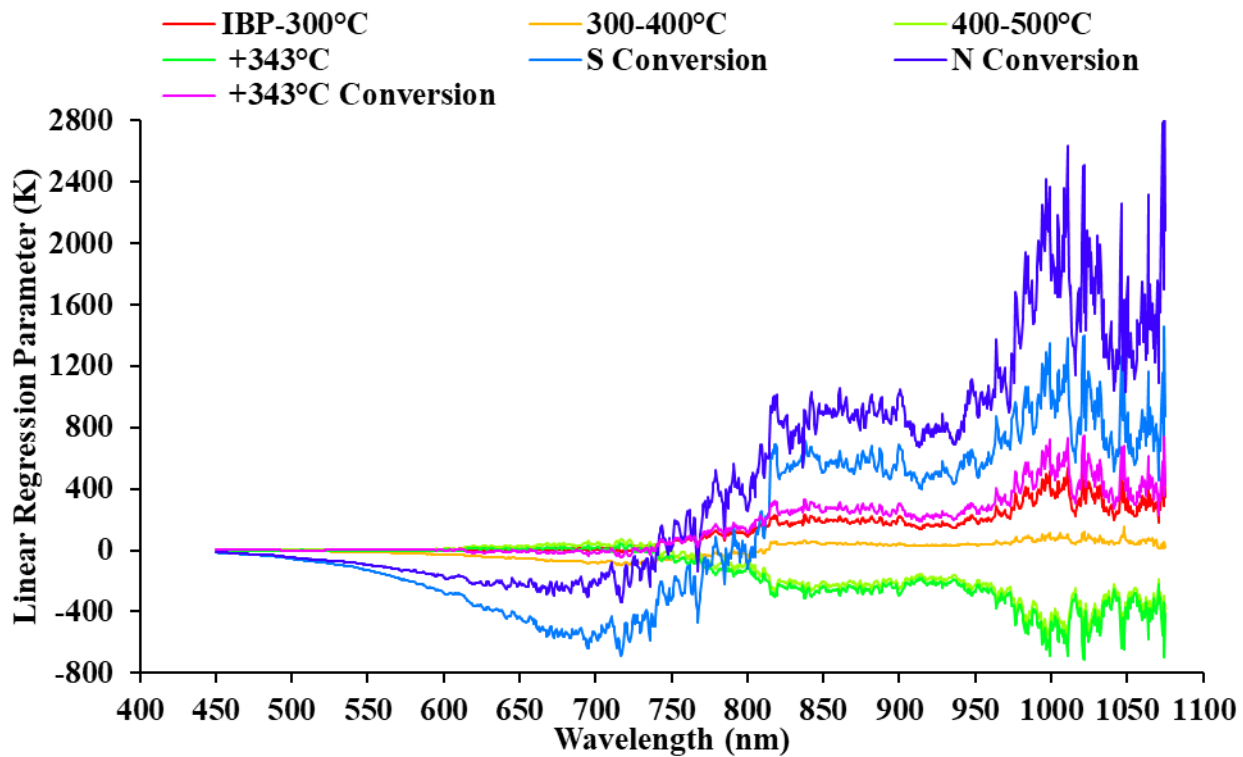
Figure H2. Simple least squares regression parameter as a function of wavelength for the first data set.
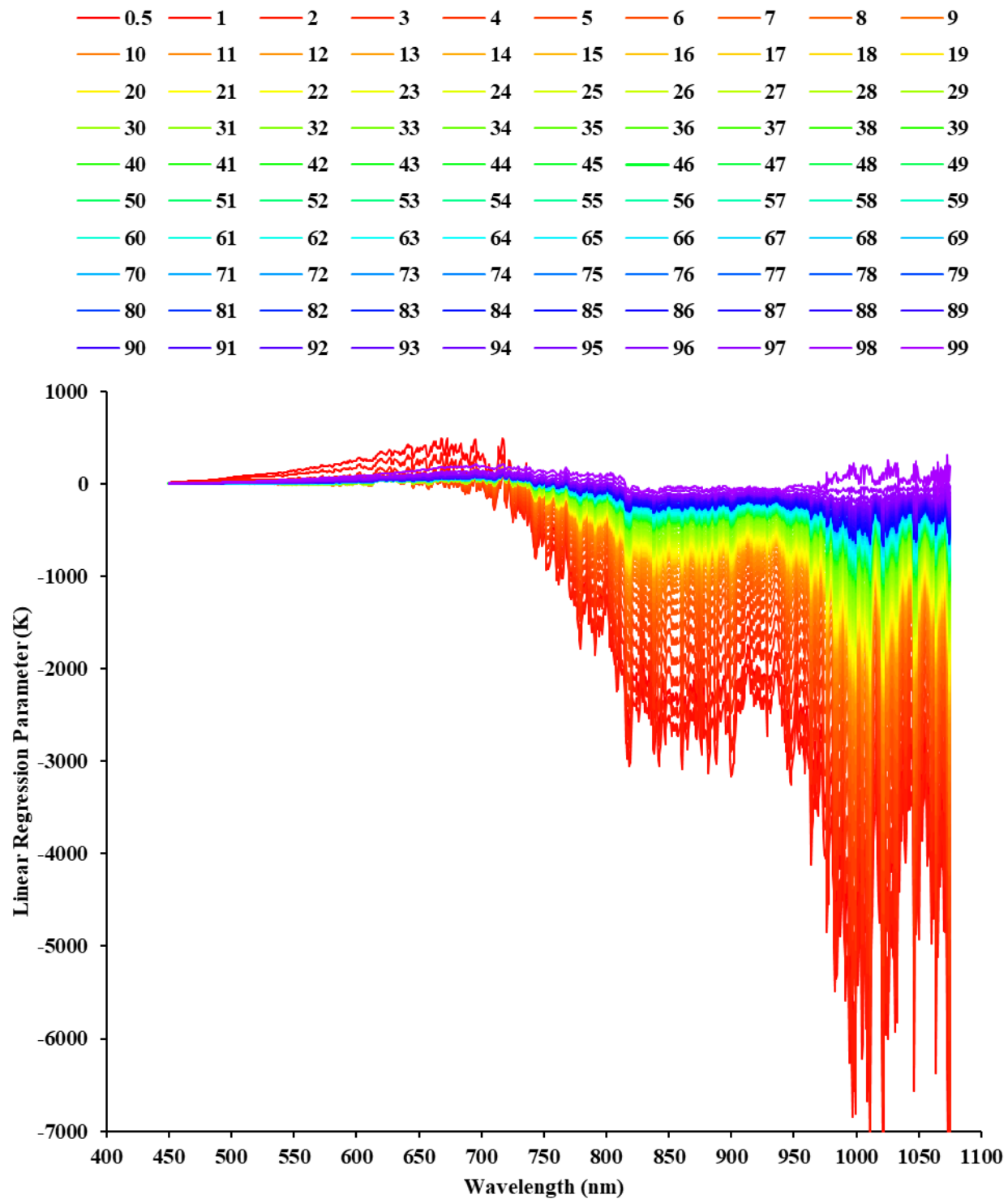
Figure H3. Simple least squares regression parameter as a function of wavelength for the first data set boiling point distribution.
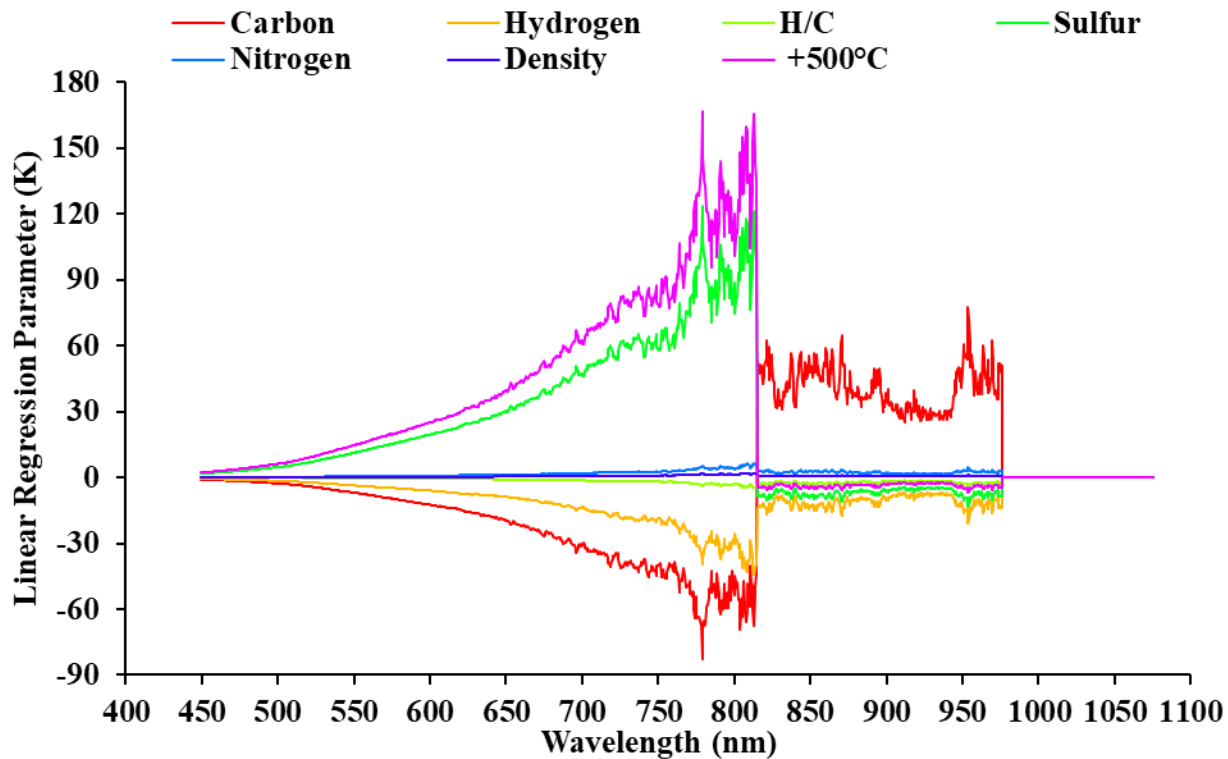
Figure H4. Simple least squares regression parameter as a function of wavelength for the second data set.
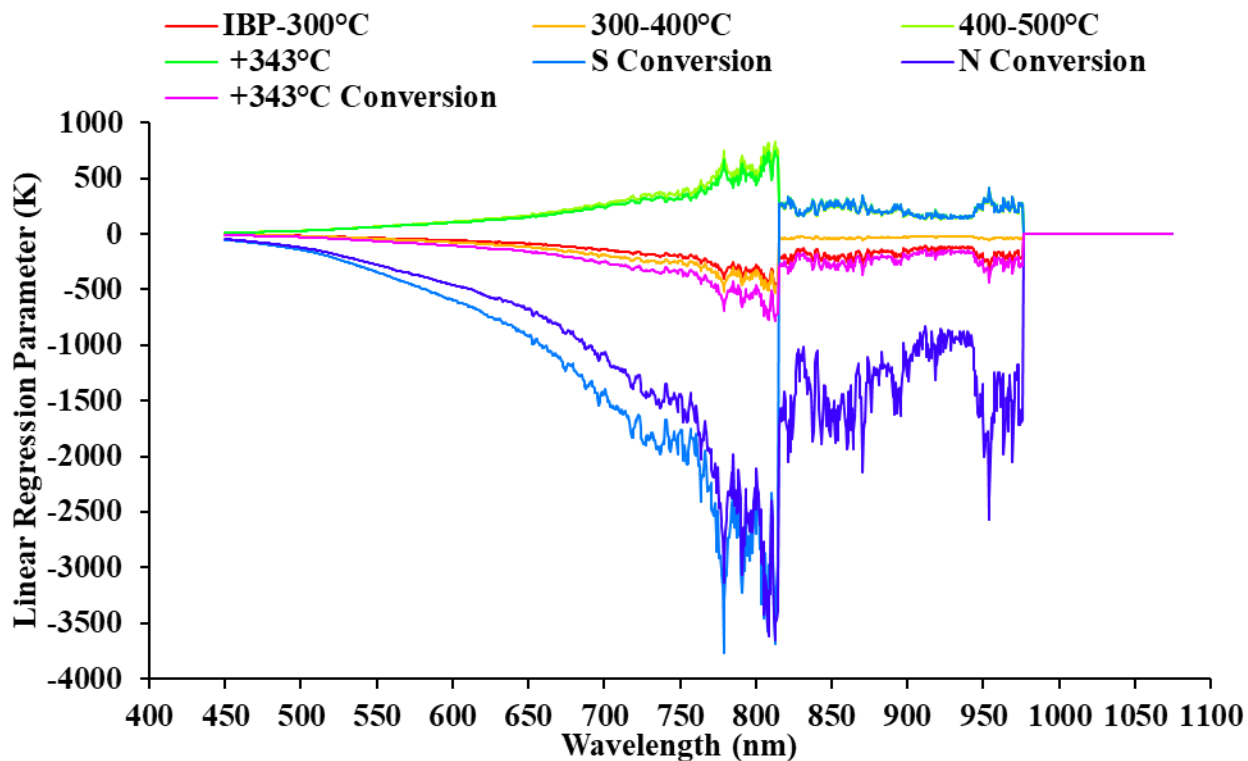
Figure H5. Simple least squares regression parameter as a function of wavelength for the second data set.
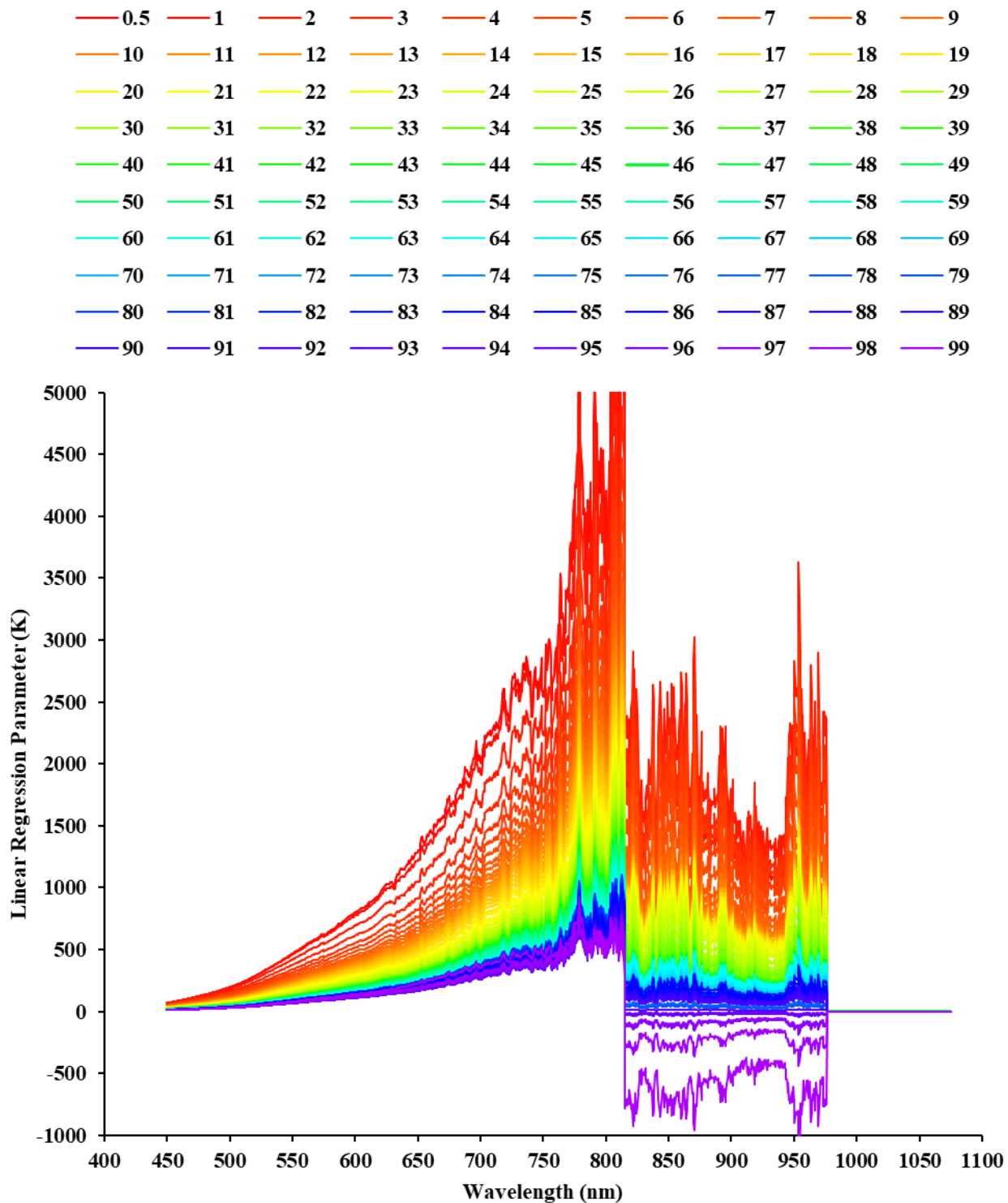
Figure H6. Simple least squares regression parameter as a function of wavelength for the second data set boiling point distribution.
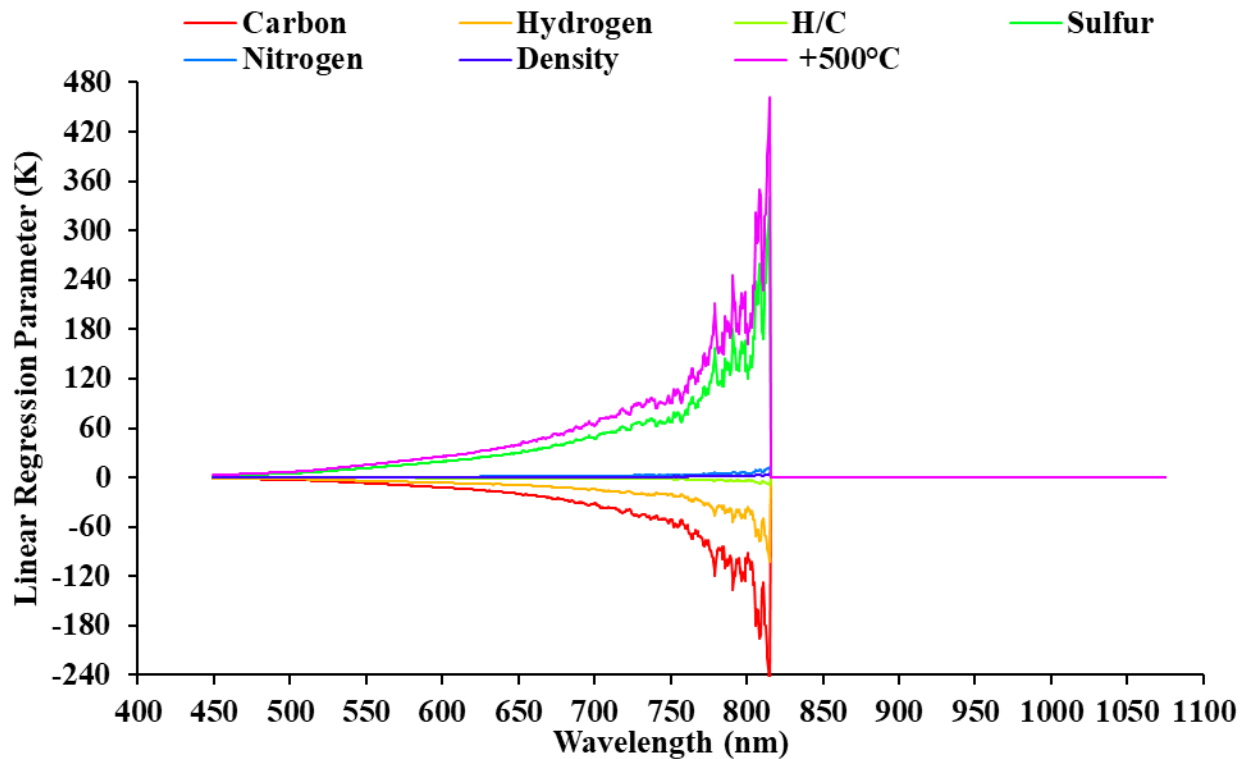
Figure H7. Simple least squares regression parameter as a function of wavelength for the third data set.
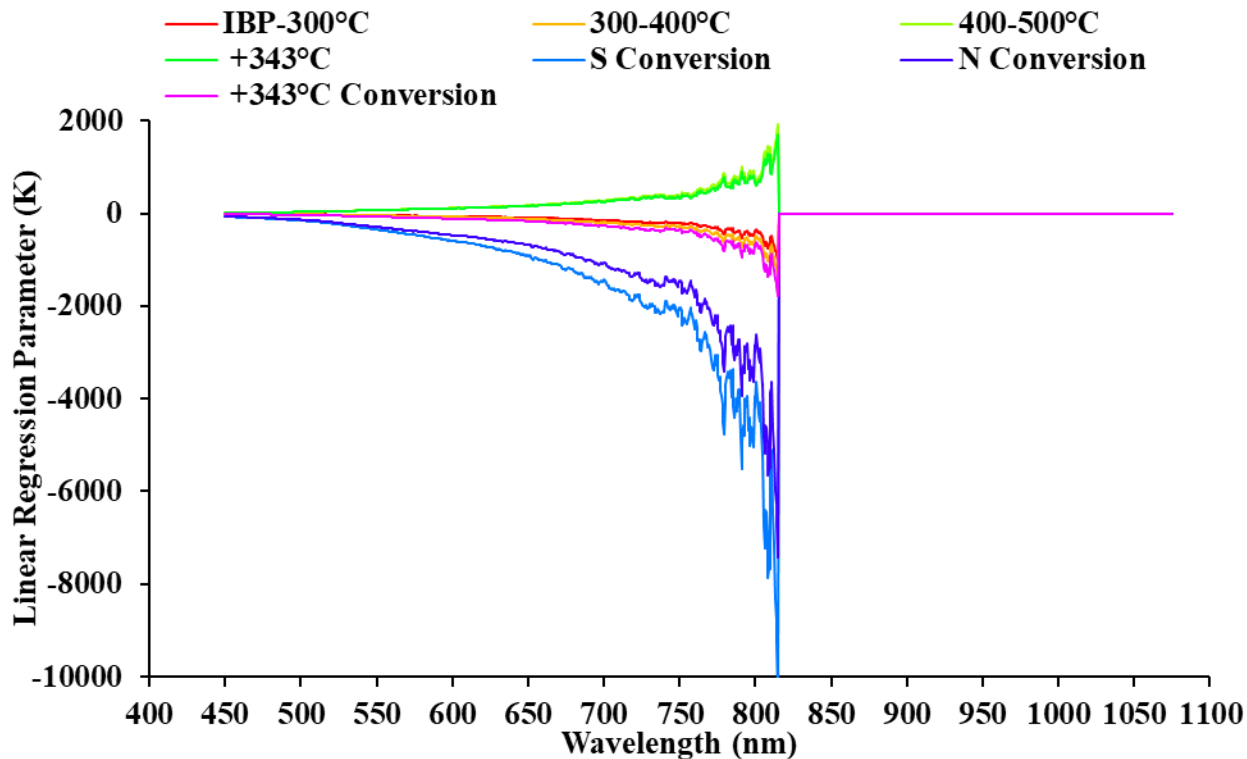
Figure H8. Simple least squares regression parameter as a function of wavelength for the third data set.
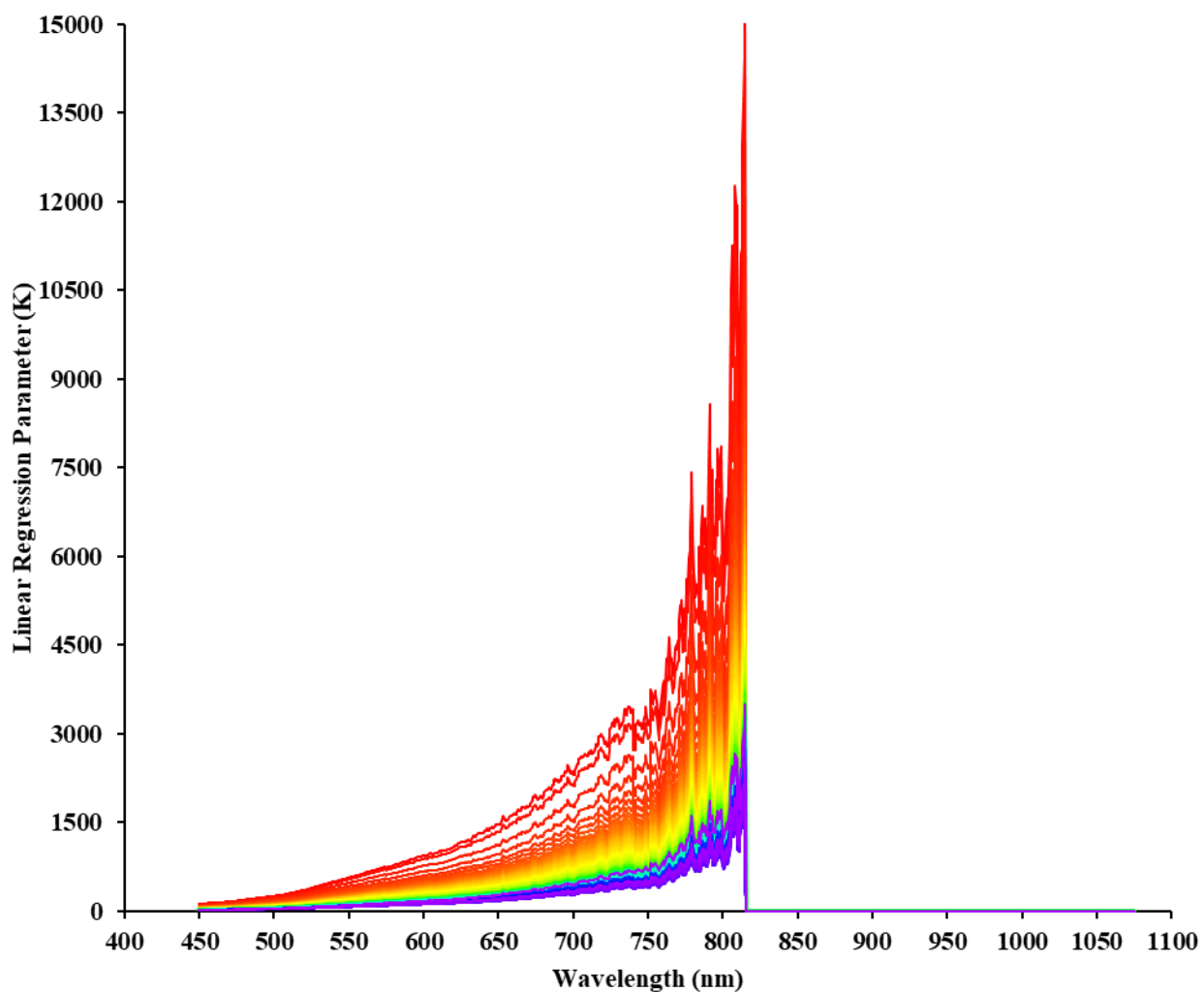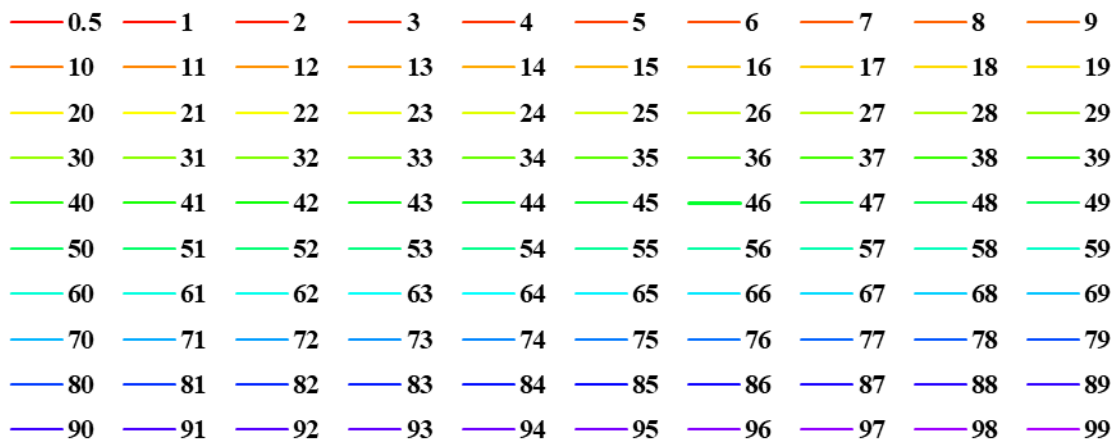
Figure H9. Simple least squares regression parameter as a function of wavelength for the third data set boiling point distribution.
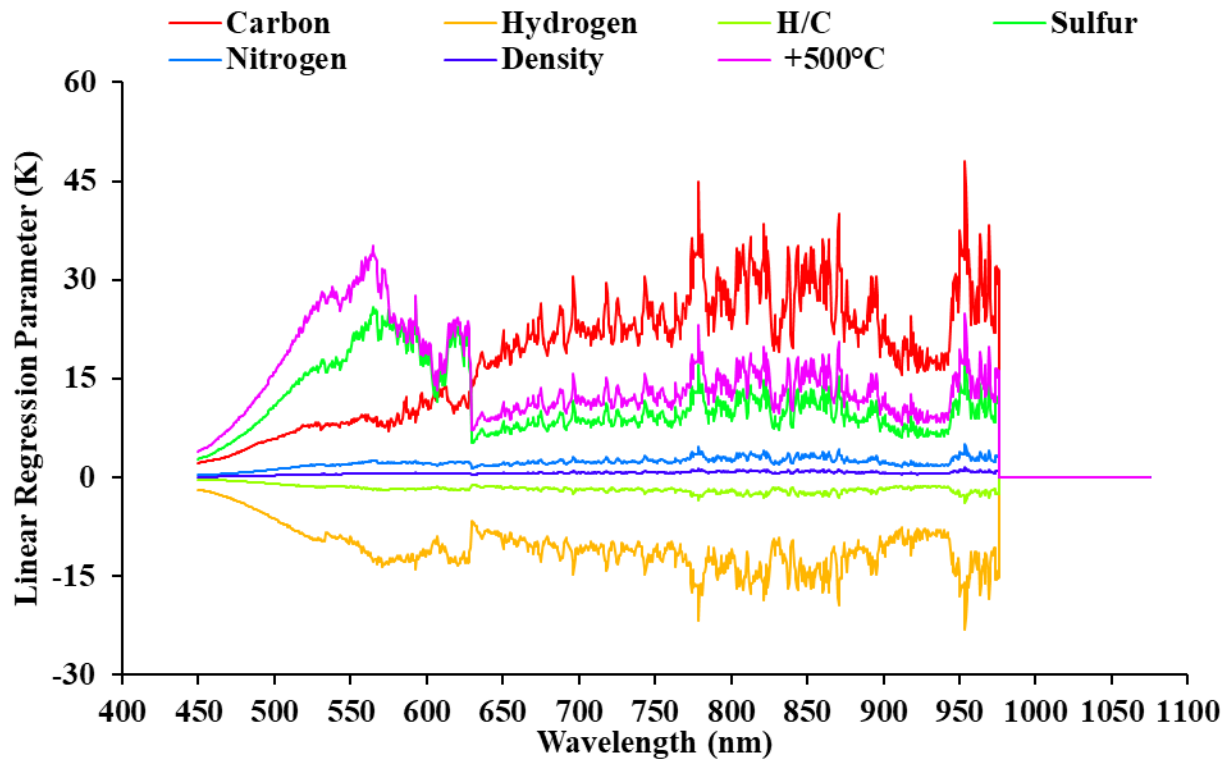
Figure H10. Simple least squares regression parameter as a function of wavelength for the fourth data set.
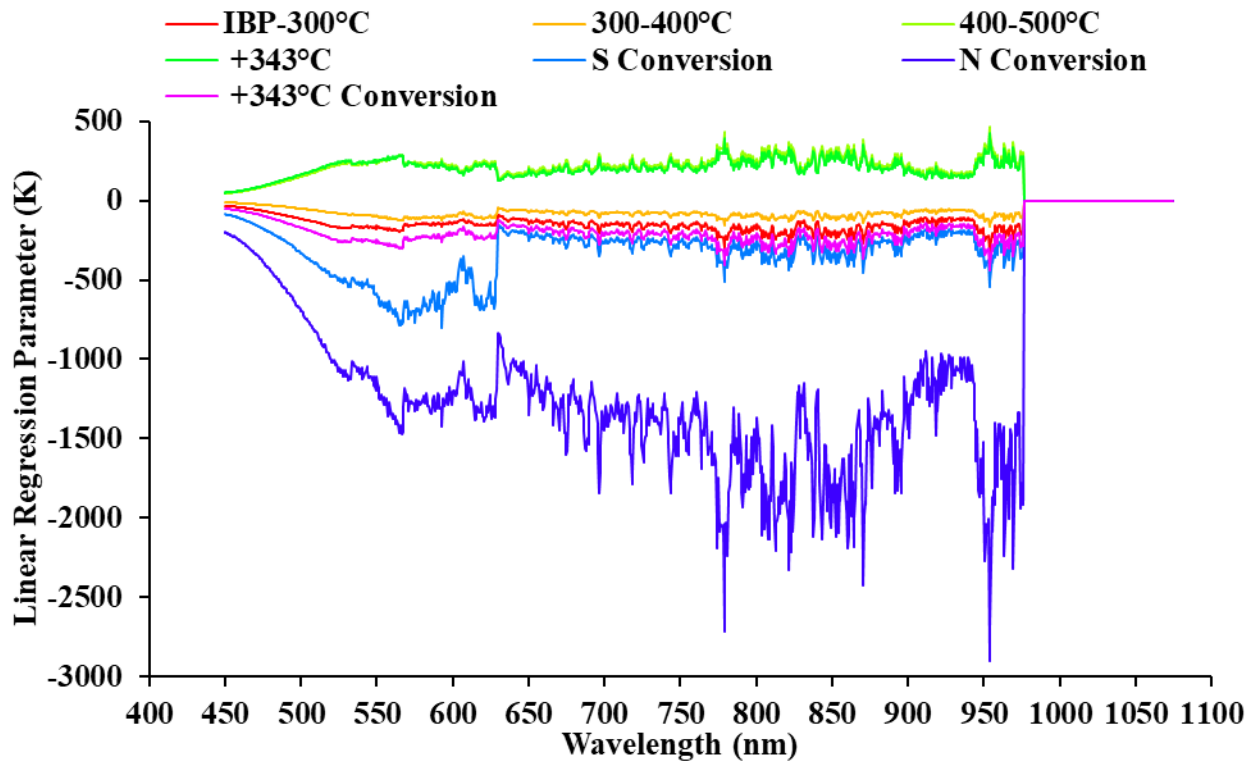
Figure H11. Simple least squares regression parameter as a function of wavelength for the fourth data set.
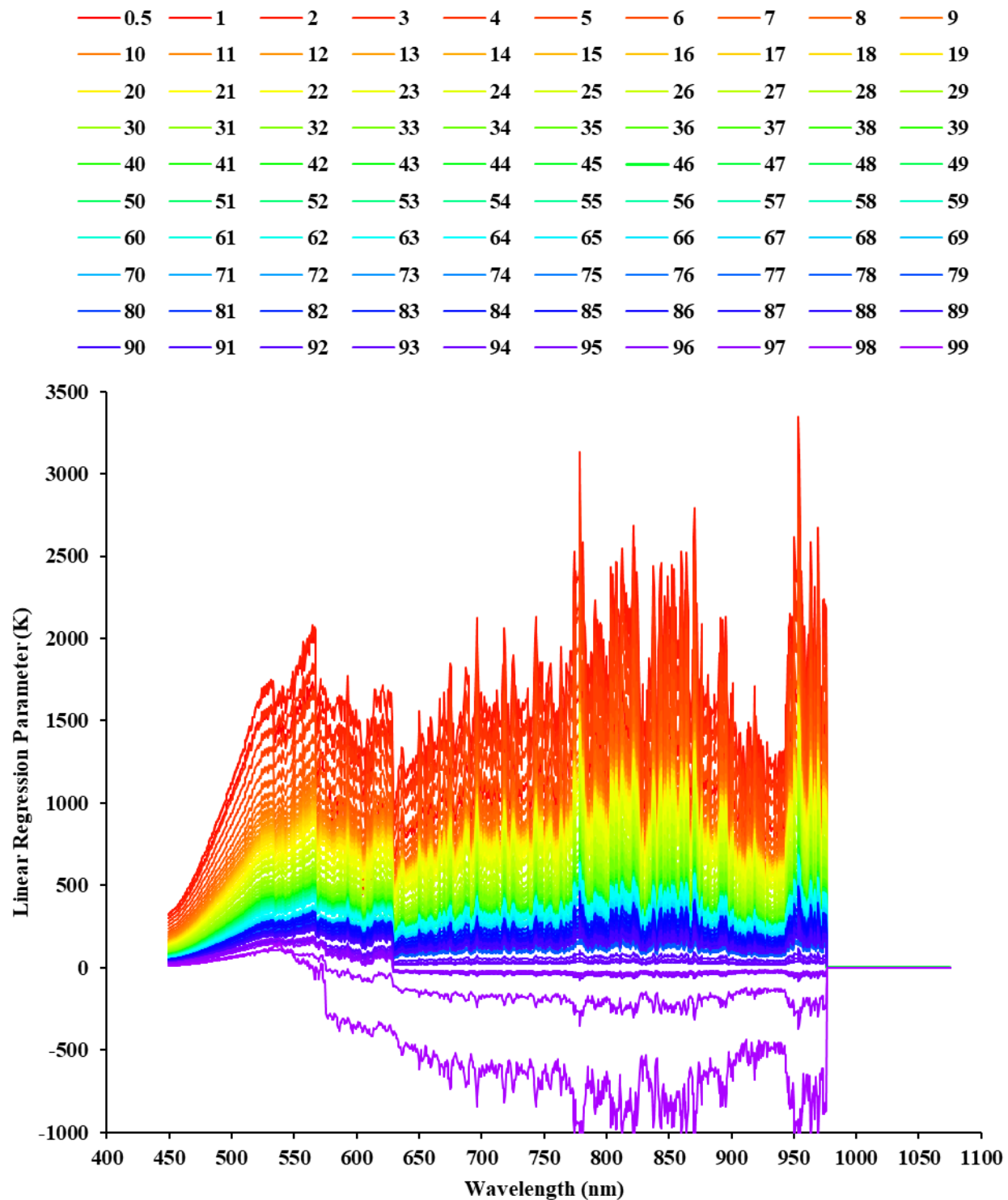
Figure H12. Simple least squares regression parameter as a function of wavelength for the fourth data set boiling point distribution.
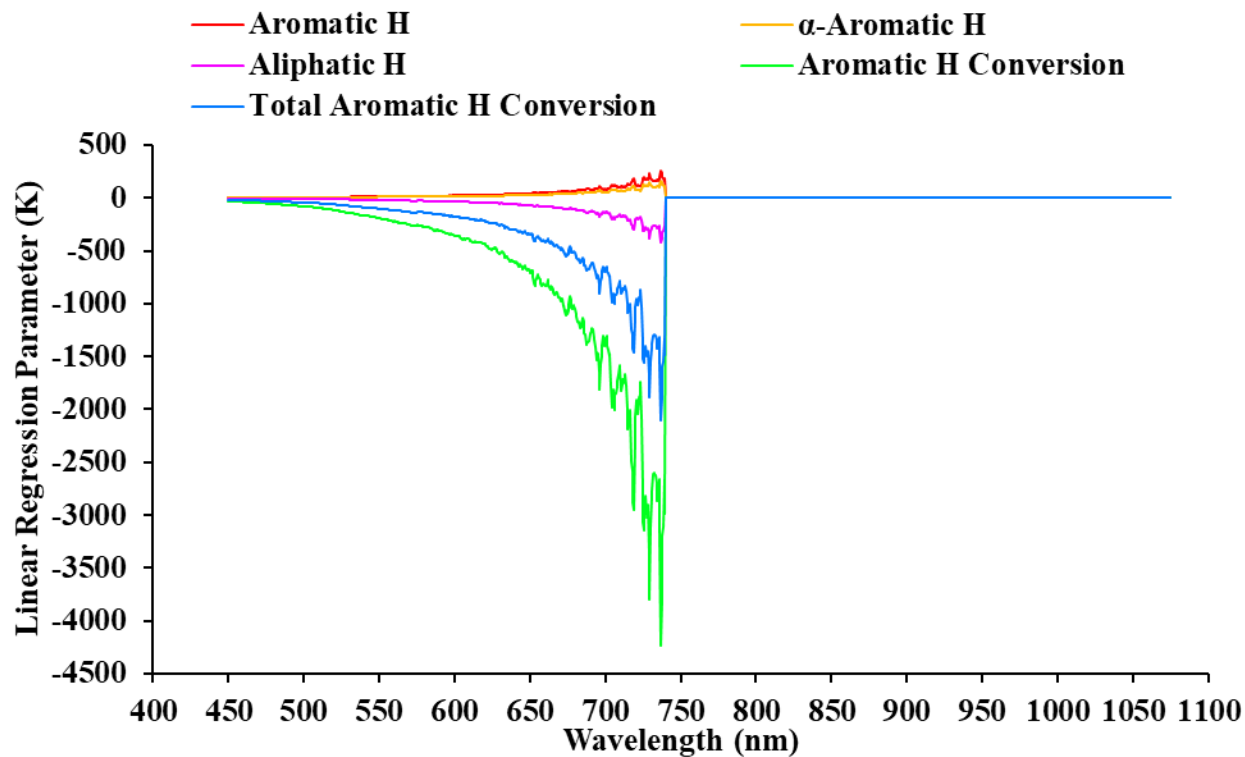
Figure H13. Simple least squares regression parameter as a function of wavelength for the fifth data set.
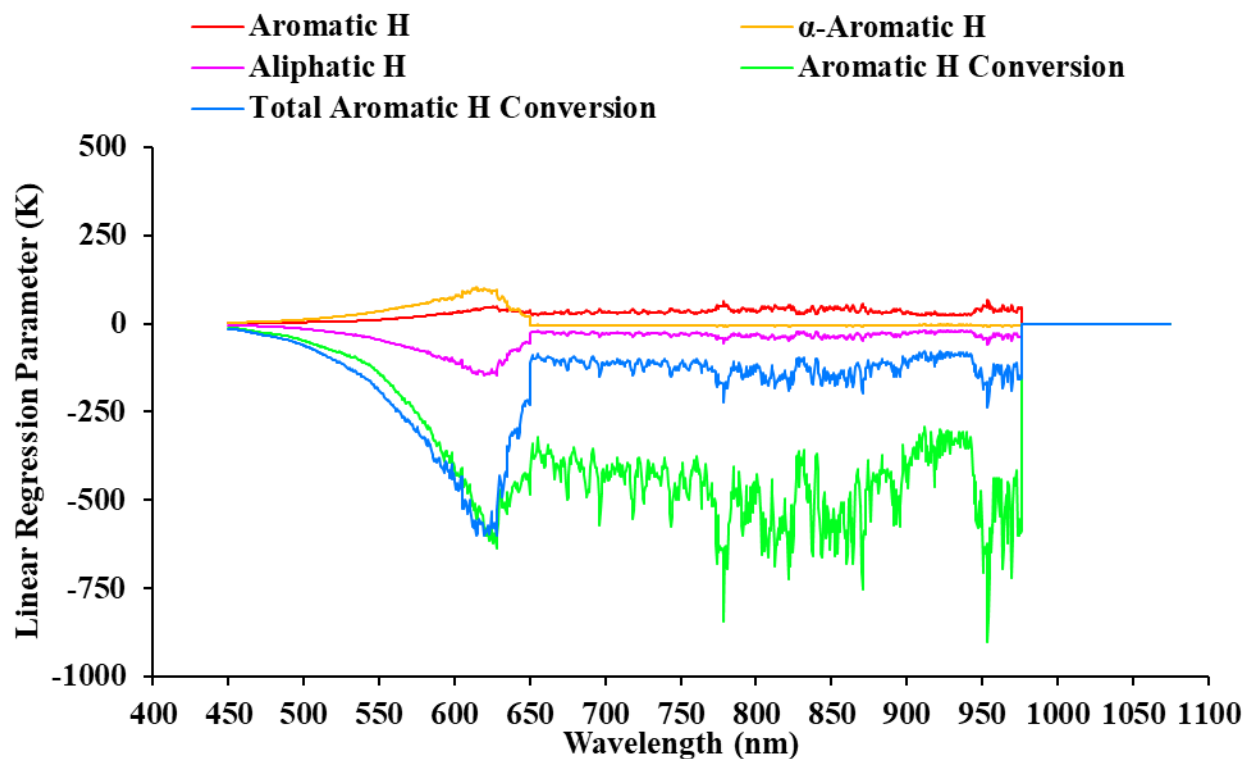
Figure H14. Simple least squares regression parameter as a function of wavelength for the sixth data set.
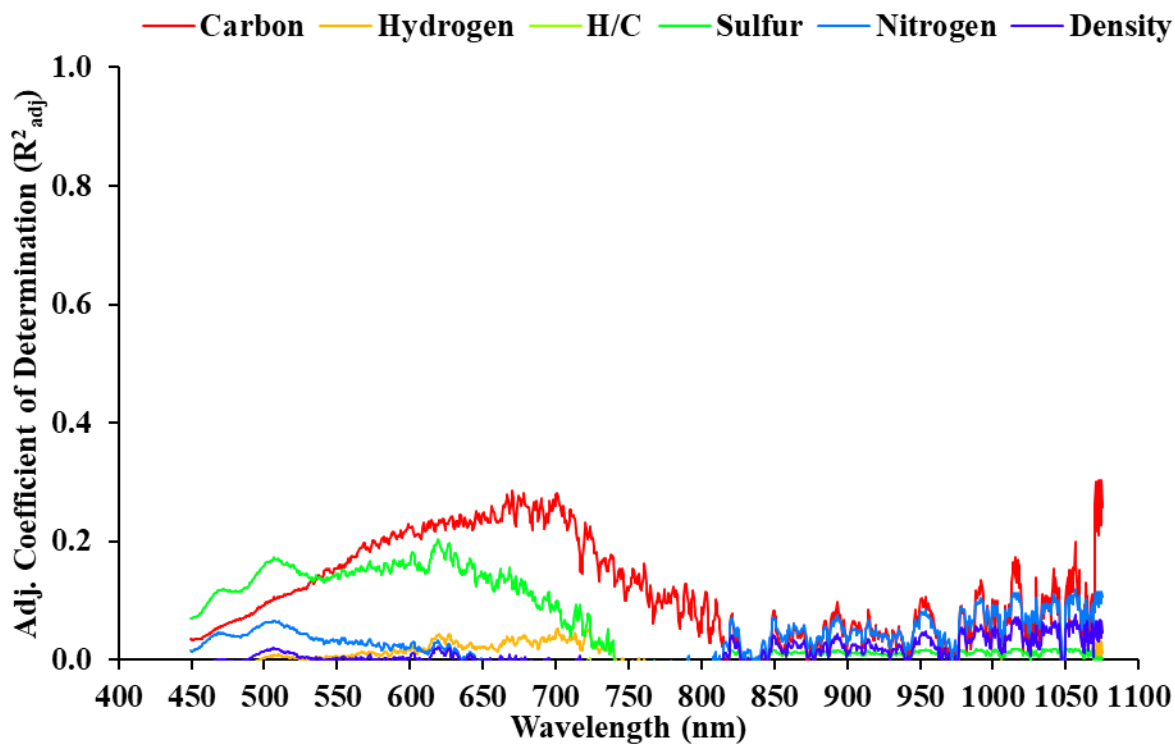
Figure H15. Simple least squares adjusted coefficient of determination as a function of wavelength for the first data set.
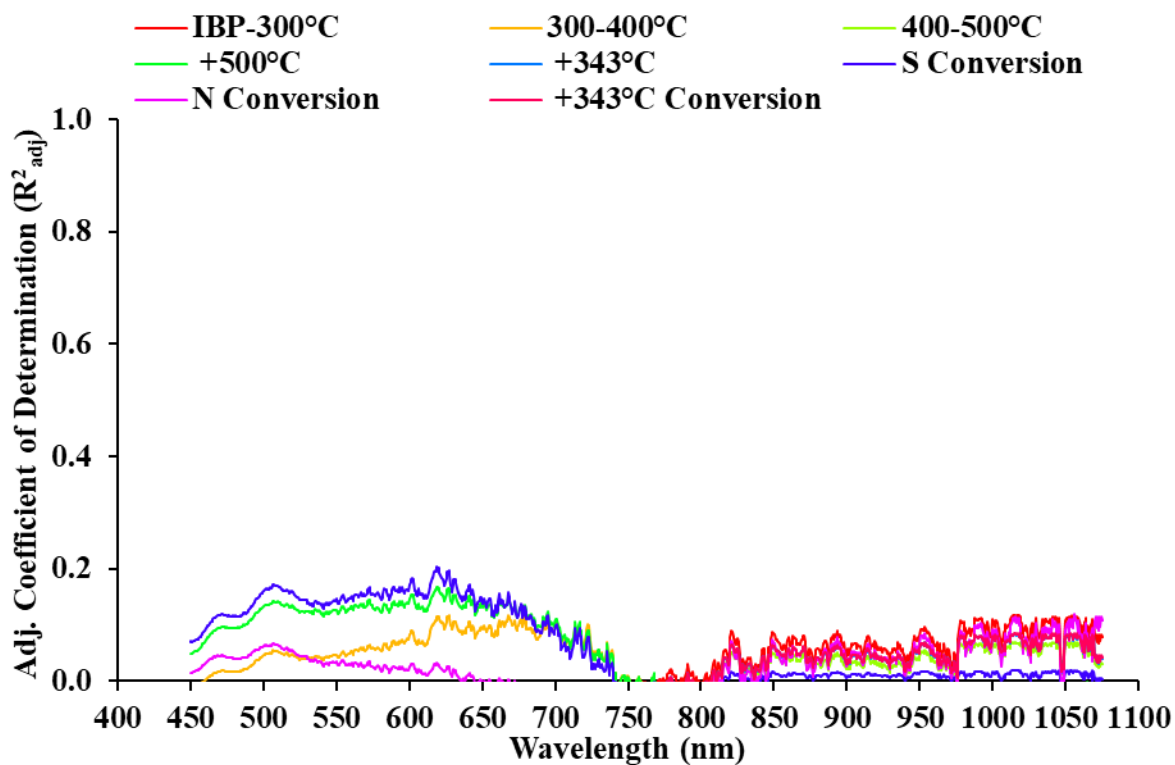
Figure H16. Simple least squares adjusted coefficient of determination as a function of wavelength for the first data set.
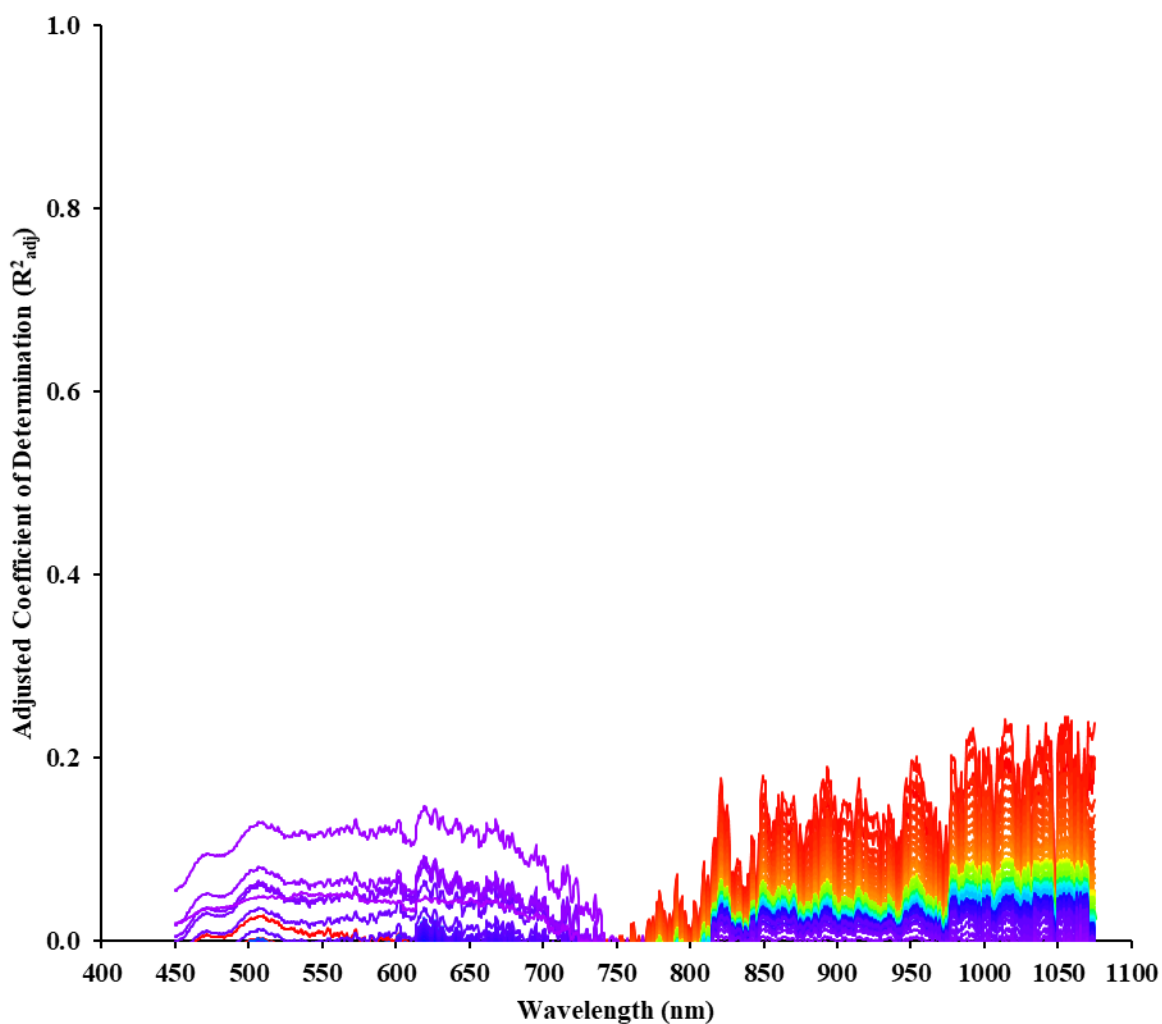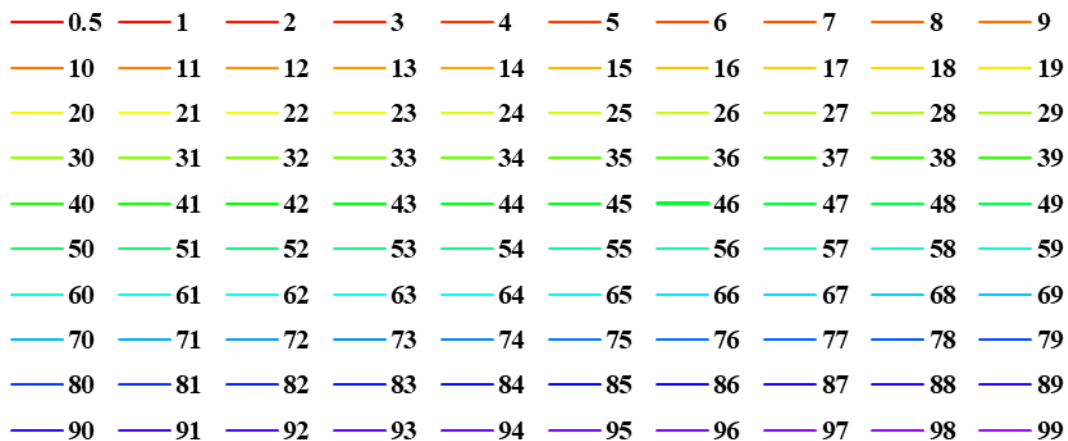
Figure H17. Simple least squares adjusted coefficient of determination as a function of wavelength for the first data set boiling point distribution.
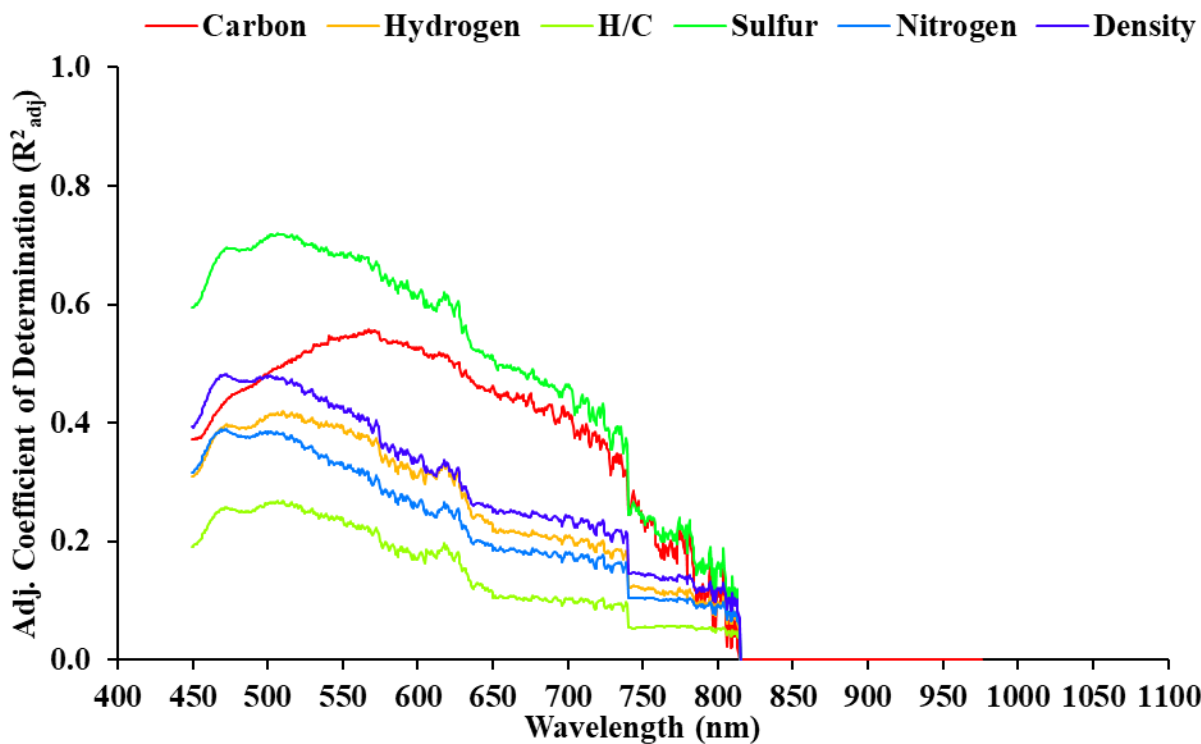
Figure H18. Simple least squares adjusted coefficient of determination as a function of wavelength for the second data set.
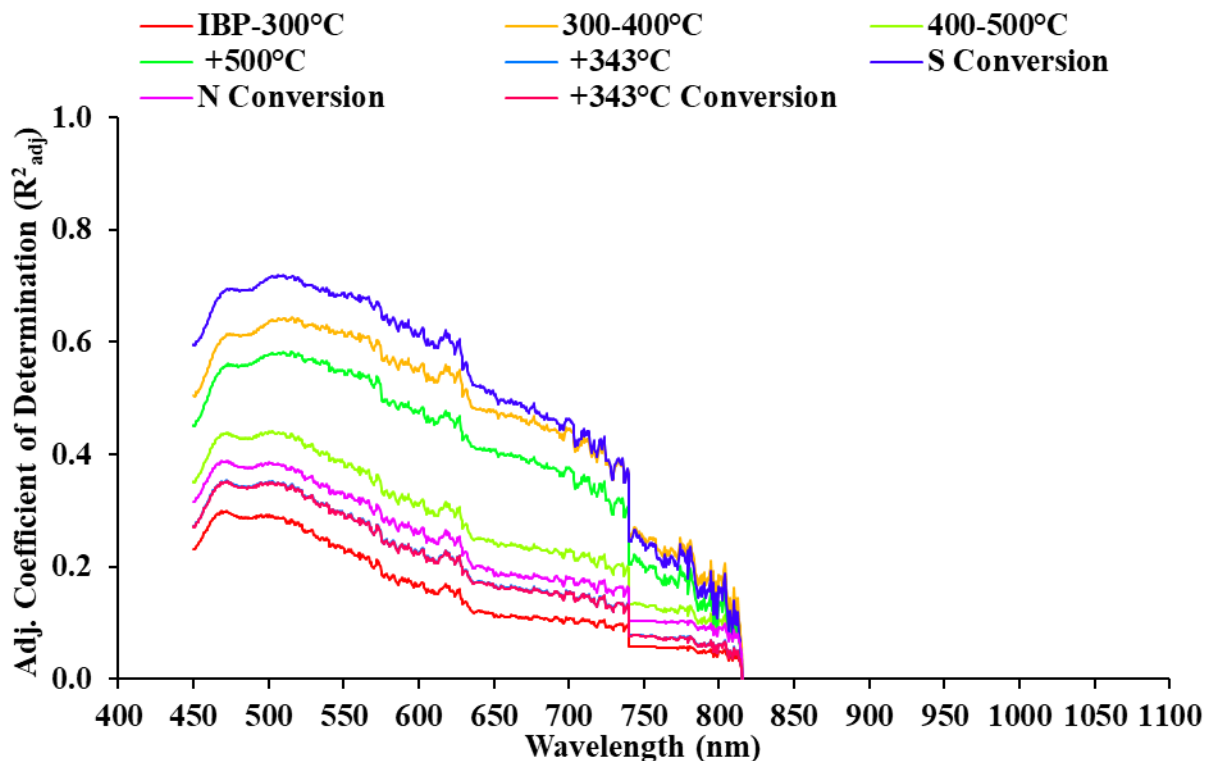
Figure H19. Simple least squares adjusted coefficient of determination as a function of wavelength for the second data set.
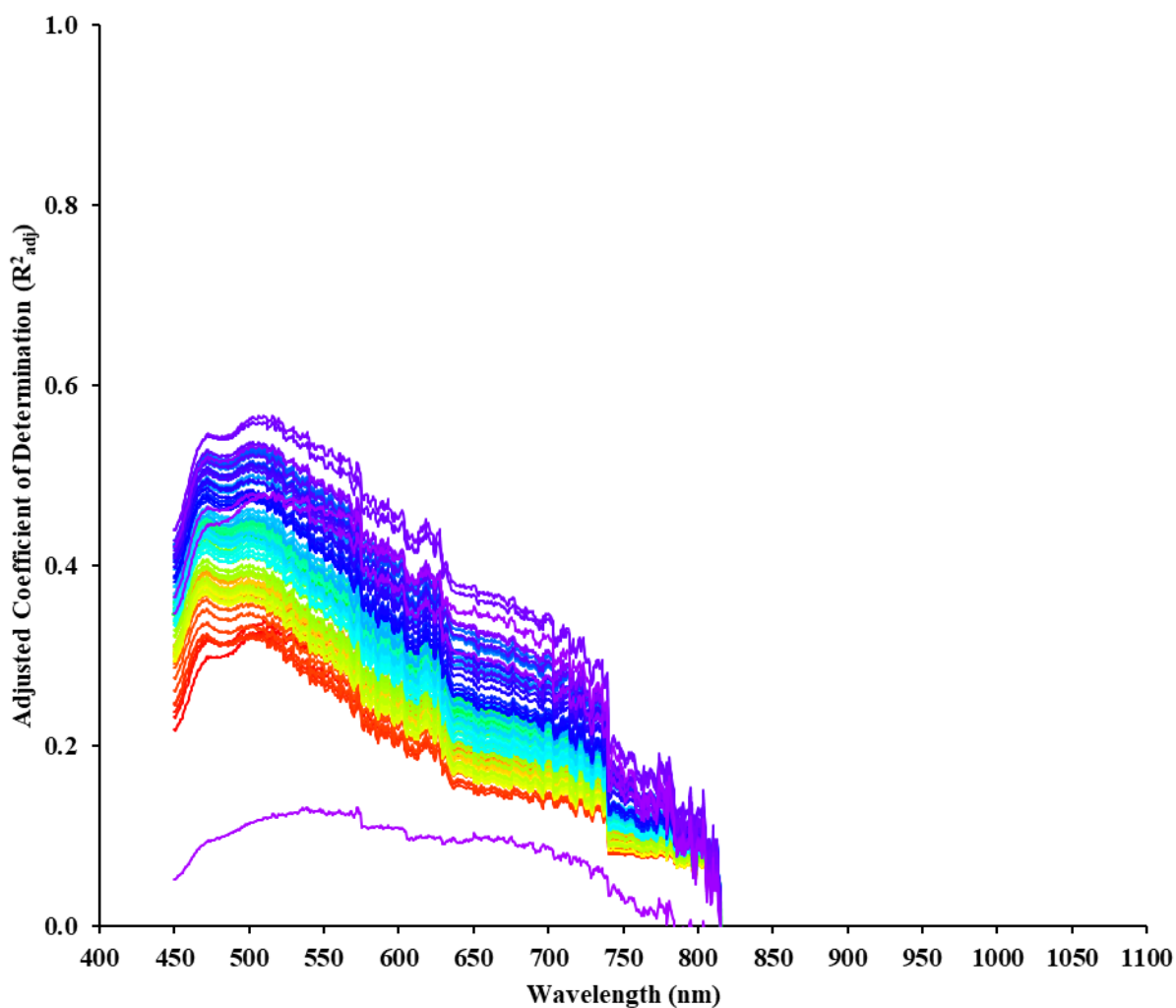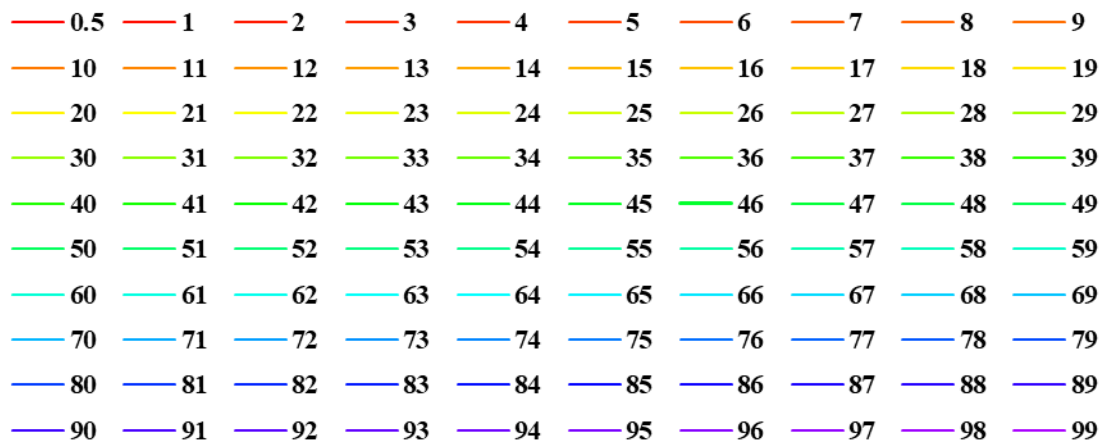
Figure H20. Simple least squares adjusted coefficient of determination as a function of wavelength for the second data set boiling point distribution.
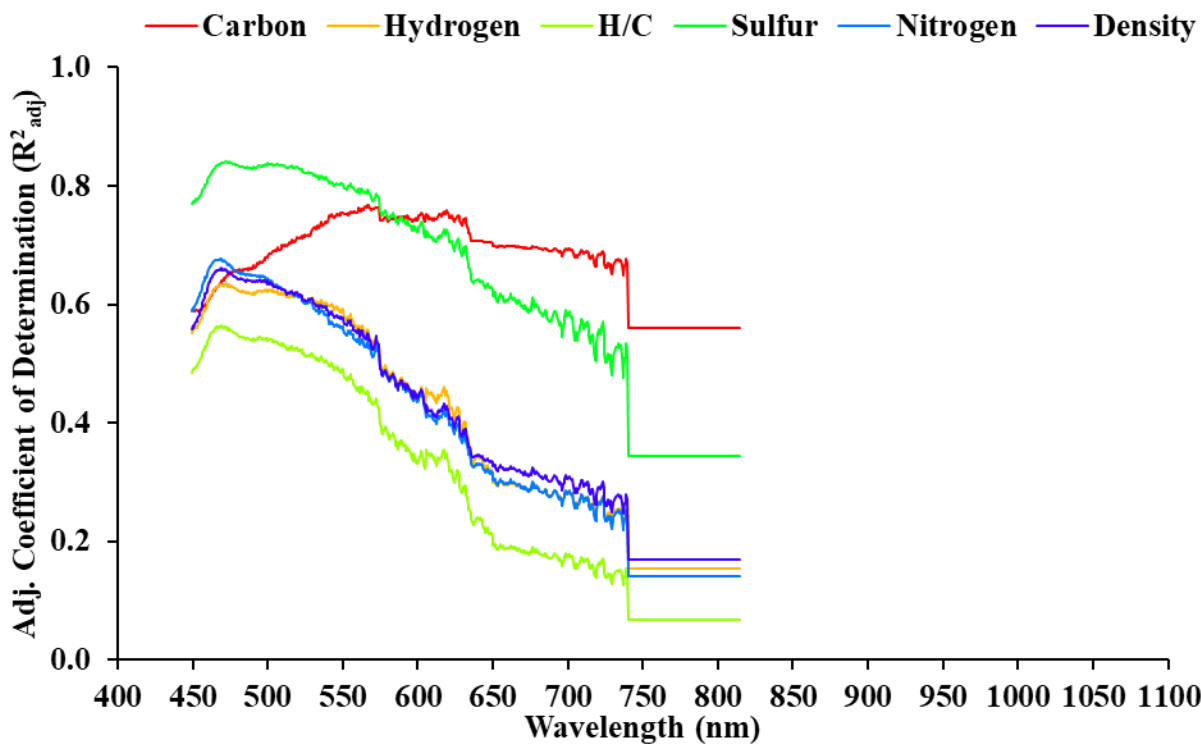
Figure H21. Simple least squares adjusted coefficient of determination as a function of wavelength for the third data set.
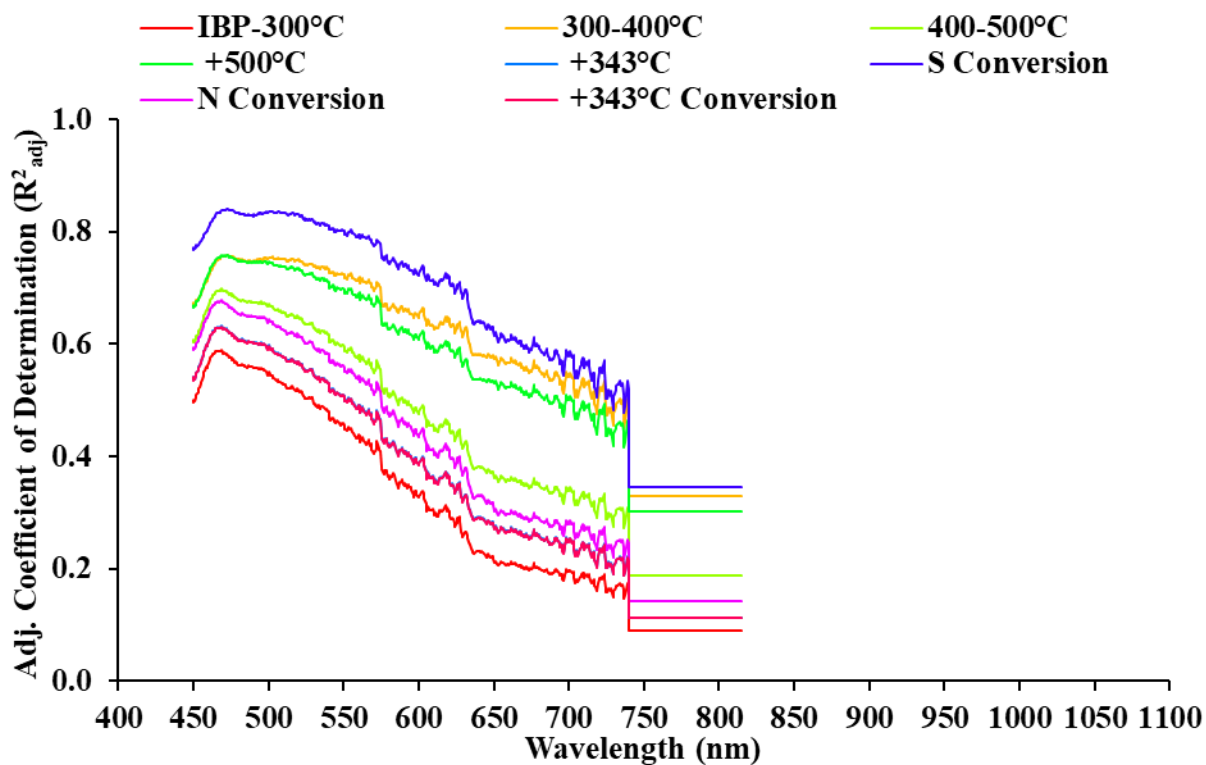
Figure H22. Simple least squares adjusted coefficient of determination as a function of wavelength for the third data set.
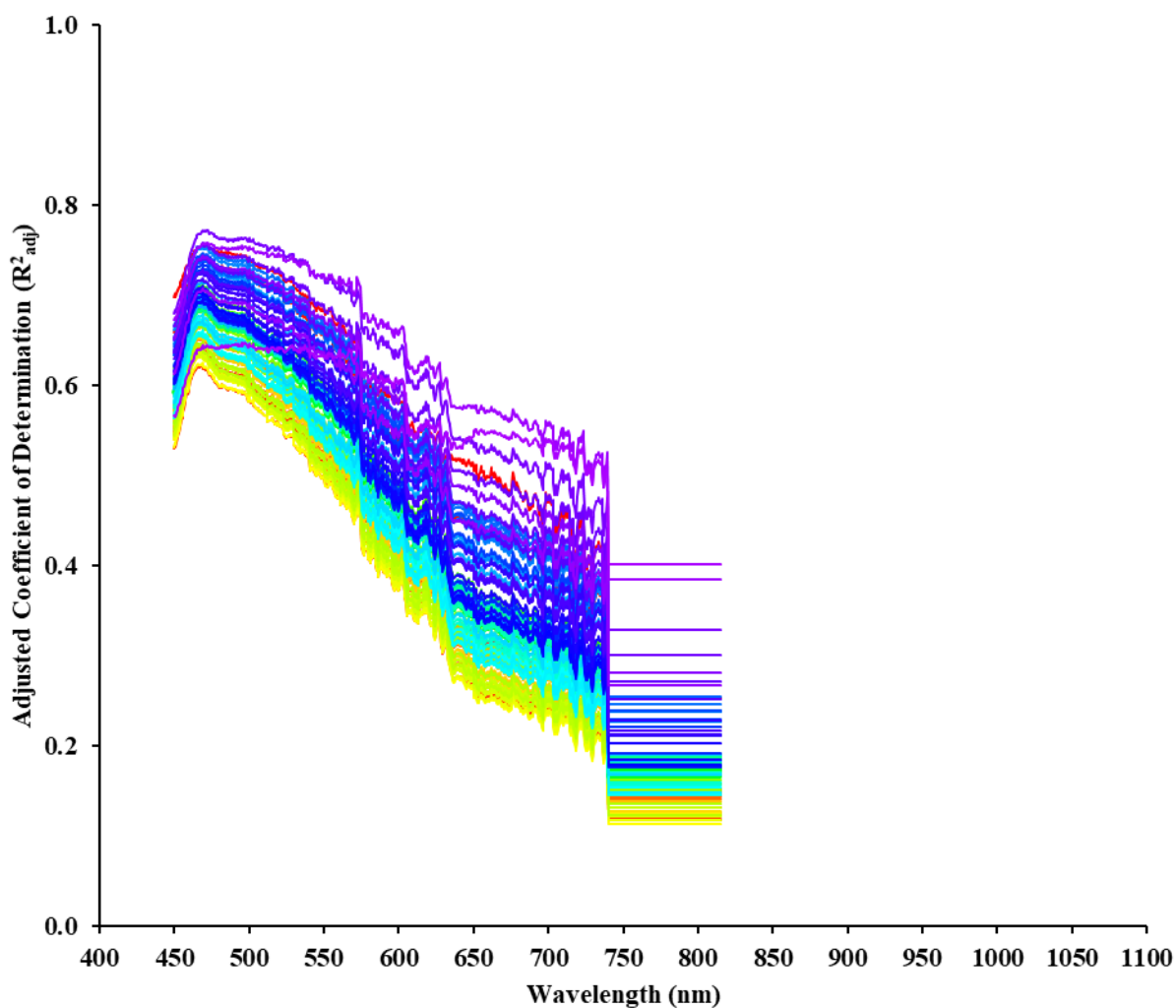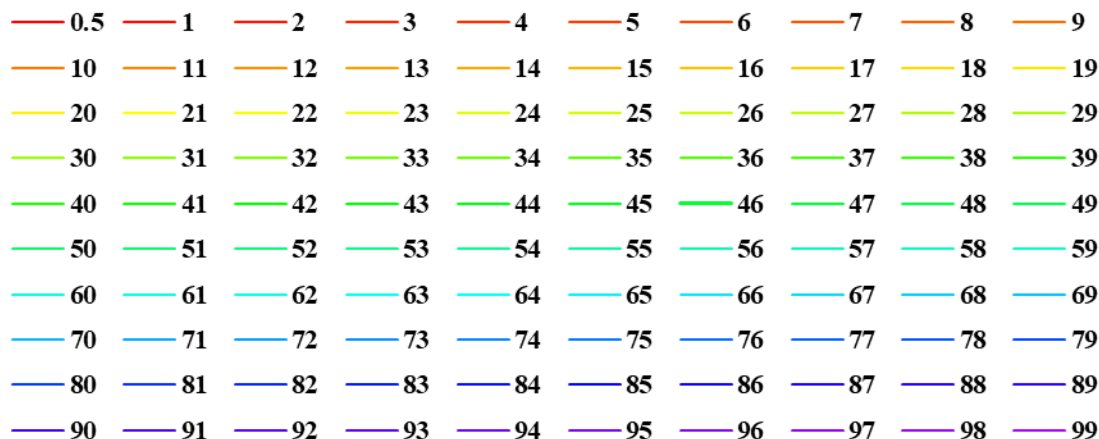
Figure H23. Simple least squares adjusted coefficient of determination as a function of wavelength for the third data set boiling point distribution.
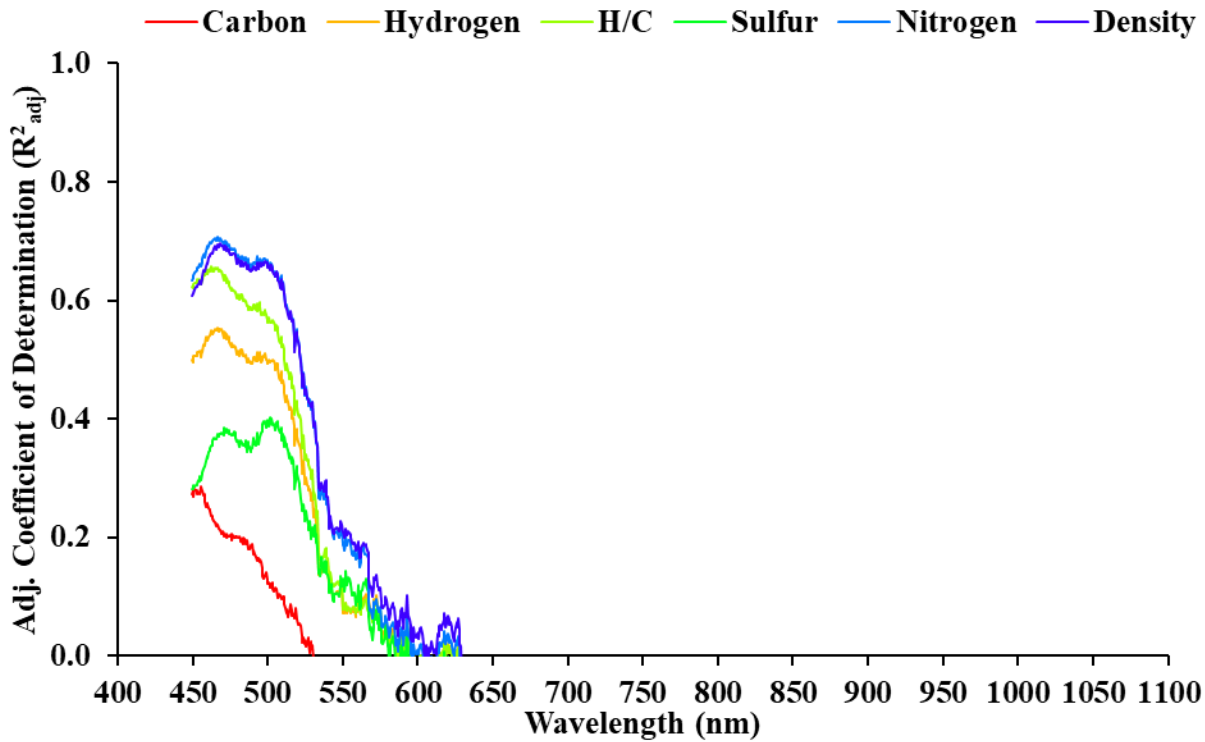
Figure H24. Simple least squares adjusted coefficient of determination as a function of wavelength for the fourth data set.
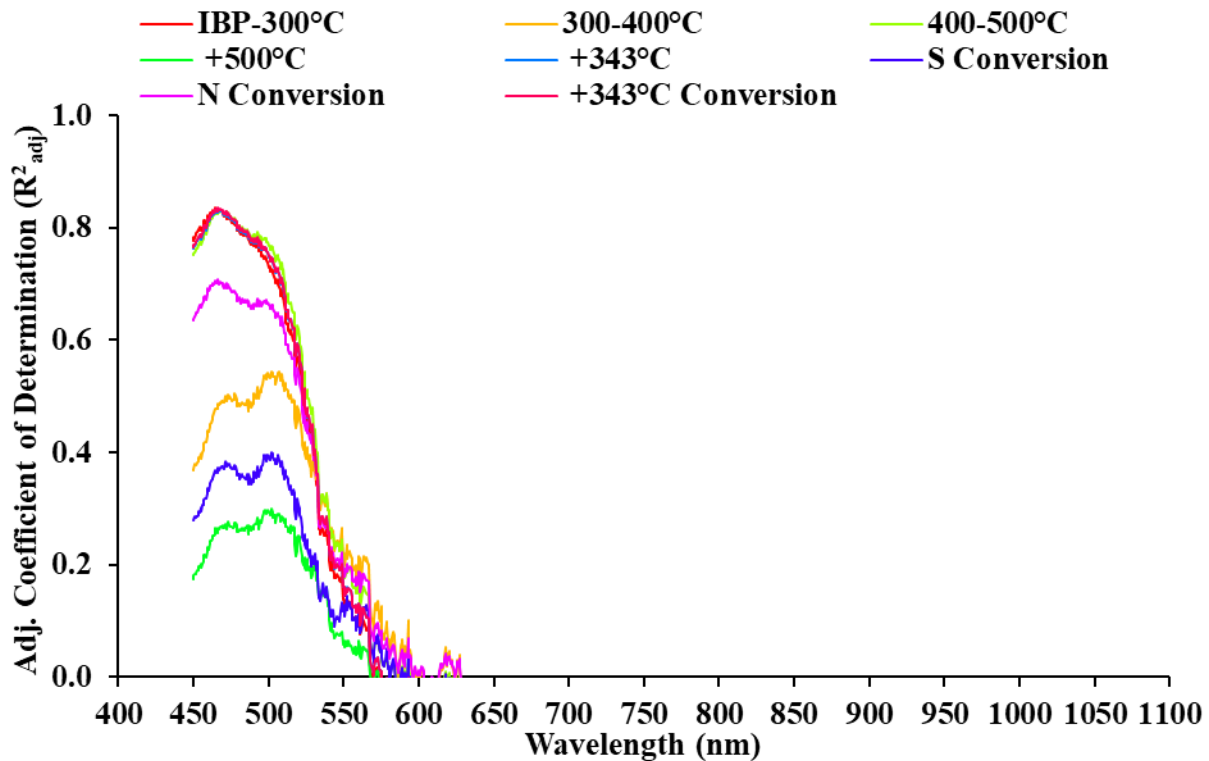
Figure H25. Simple least squares adjusted coefficient of determination as a function of wavelength for the fourth data set.
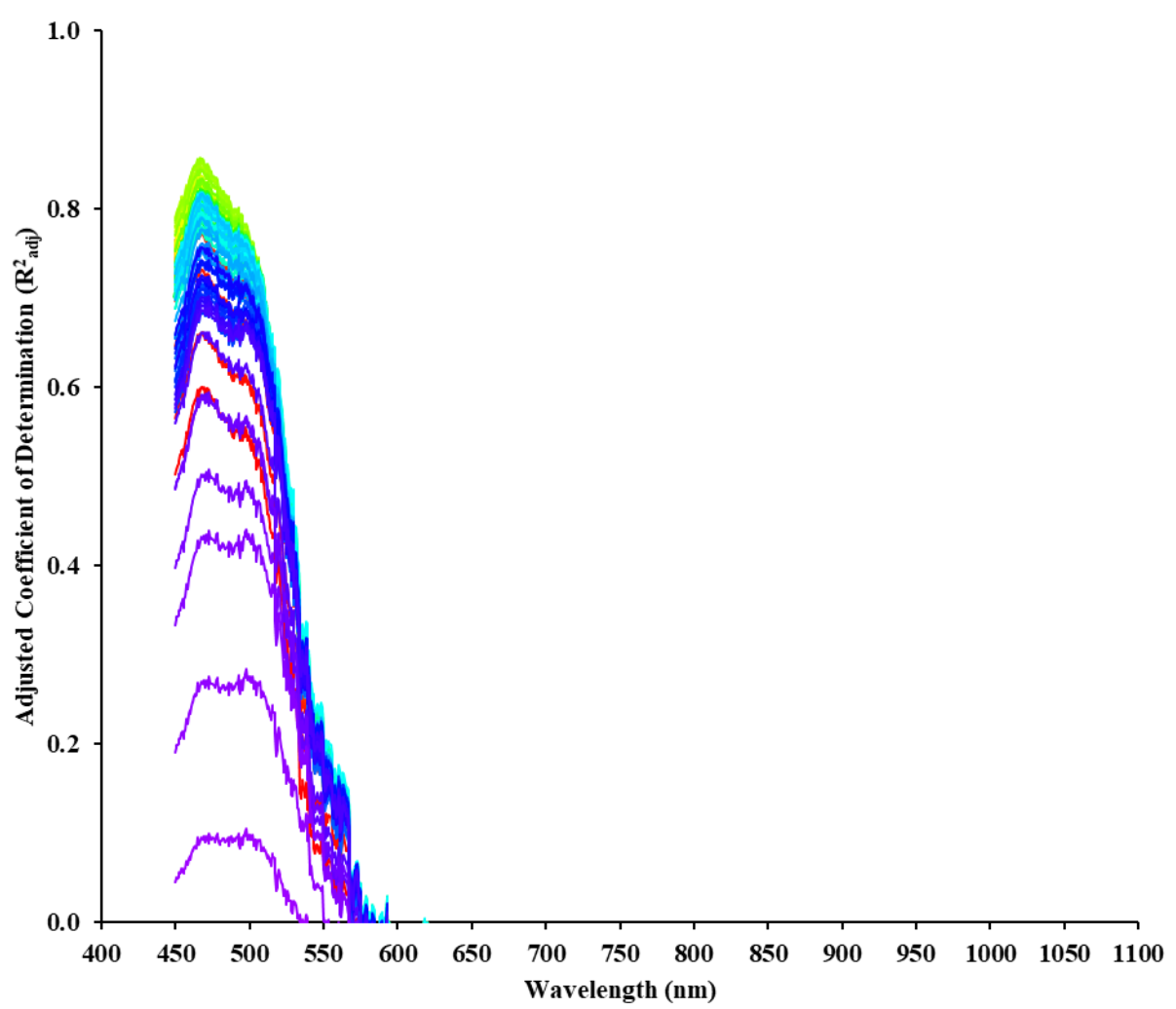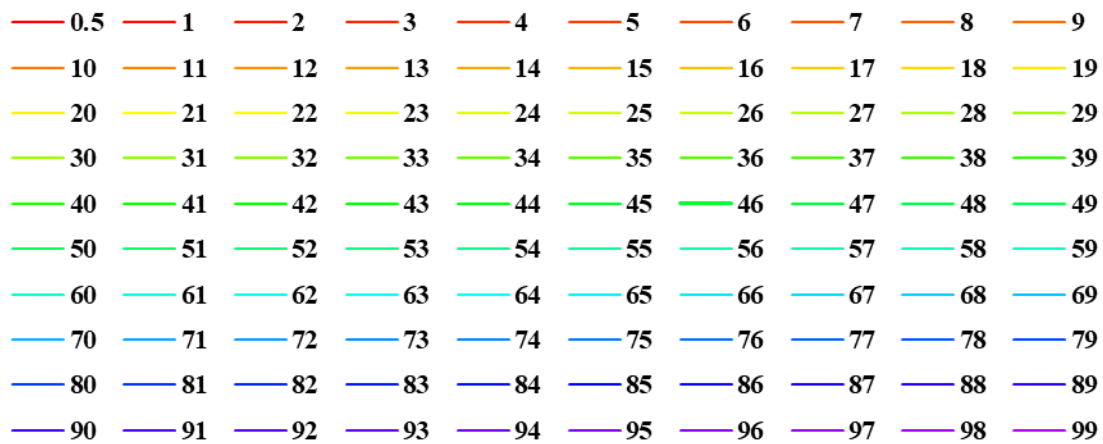
Figure H26. Simple least squares adjusted coefficient of determination as a function of wavelength for the fourth data set boiling point distribution.
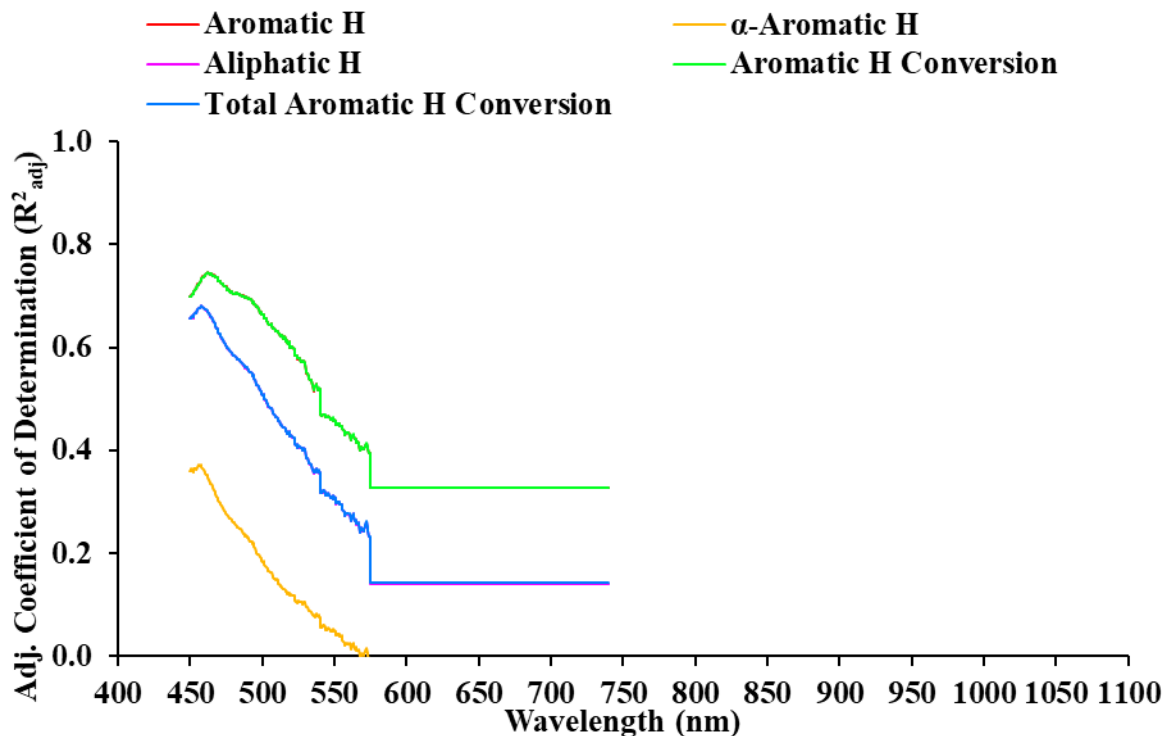
Figure H27. Simple least squares adjusted coefficient of determination as a function of wavelength for the fifth data set.
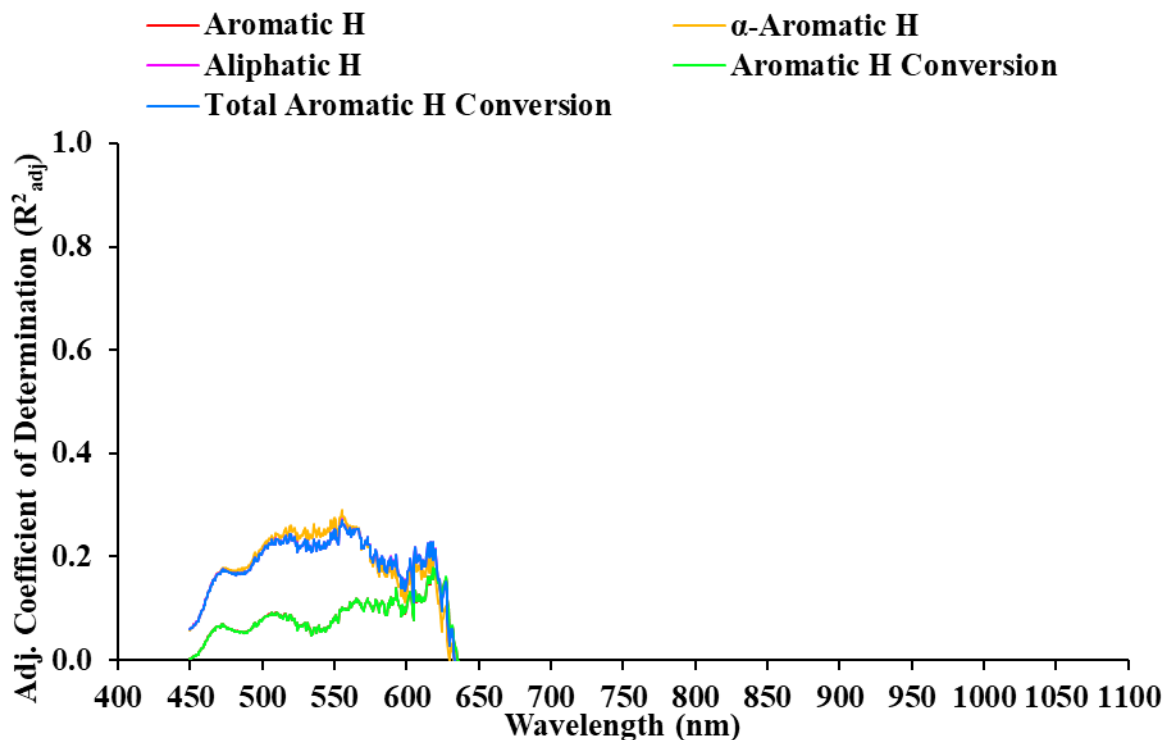
Figure H28. Simple least squares adjusted coefficient of determination as a function of wavelength for the sixth data set.

Table H1. Absorbance wavelength channels and corresponding regressor coefficients for MLR models of cumulative boiling point distribution fractions in the first data set.

		First Data Set (34)			
% Off (wt.%)	**λ**	**β**	**% Off (wt.%)**	**λ**	**β**
0.5	723, 1056	2246, -5092 $\varepsilon = 184$	51	-	-
1	723, 1057	2265, -6811 $\varepsilon = 208$	52	-	-
2	723, 1057	1982, -6152 $\varepsilon = 236$	53	-	-
3	723, 1014	1808, -4764 $\varepsilon = 254$	54	-	-
4	688, 723, 1014	-2670, 4795, -5147 $\varepsilon = 270$	55	-	-
5	688, 723, 1014	-2558, 4536, -4690 $\varepsilon = 280$	56	-	-
6	688, 723, 1014	-2458, 4302, -4295 $\varepsilon = 288$	57	-	-
7	688, 723, 1014	-2324, 4059, -3961 $\varepsilon = 296$	58	-	-
8	688, 723, 1014	-2194, 3837, -3687 $\varepsilon = 302$	59	-	-
9	694, 723, 1017	-3026, 4653, -4180 $\varepsilon = 308$	60	-	-
10	694, 723, 1017	-2936, 4510, -3996 $\varepsilon = 313$	61	-	-
11	694, 723, 1017	-2819, 4331, -3813 $\varepsilon = 317$	62	-	-
12	694, 723, 1018	-2694, 4167, -4217 $\varepsilon = 322$	63	-	-
13	694, 723, 1017	-2608, 4017, -3456 $\varepsilon = 326$	64	-	-
14	694, 723, 1017	-2506, 3874, -3352 $\varepsilon = 329$	65	-	-
15	694, 723, 1017	-2439, 3769, -3262 $\varepsilon = 333$	66	-	-
16	694, 723, 1017	-2426, 3720, -3201 $\varepsilon = 336$	67	-	-
17	694, 723, 1017	-2392, 3655, -3132 $\varepsilon = 339$	68	-	-
18	-	-	69	-	-
19	694, 723, 1017	-2316, 3501, -2972 $\varepsilon = 345$	70	-	-
20	694, 723, 1017	-2298, 3461, -2916 $\varepsilon = 348$	71	-	-
21	-	-	72	-	-
22	694, 723, 1015	-2133, 3261, -2603 $\varepsilon = 354$	73	-	-
23	-	-	74	-	-
24	-	-	75	-	-
25	-	-	76	-	-
26	-	-	77	-	-
27	-	-	78	-	-
28	-	-	79	-	-
29	-	-	80	-	-

30	-	-	**81**	-	-
31	-	-	**82**	-	-
32	-	-	**83**	-	-
33	-	-	**84**	-	-
34	-	-	**85**	-	-
35	-	-	**86**	-	-
36	-	-	**87**	-	-
37	-	-	**88**	-	-
38	-	-	**89**	-	-
39	-	-	**90**	-	-
40	-	-	**91**	-	-
41	-	-	**92**	-	-
42	-	-	**93**	-	-
43	-	-	**94**	-	-
44	-	-	**95**	614, 612, 631	-2126, 2839, -574 $\varepsilon = 492$
45	-	-	**96**	-	-
46	-	-	**97**	614, 619	-1781, 1974 $\varepsilon = 505$
47	-	-	**98**	614, 6120	-1734, 1959 $\varepsilon = 514$
48	-	-	**99**	-	-
49	-	-	**99.5**	-	-
50	-	-			

Table H2. Absorbance wavelength channels and corresponding regressor coefficients for MLR models of cumulative boiling point distribution fractions in the second data set.

Second Data Set (25)					
% Off (wt.%)	λ	β	% Off (wt.%)	λ	β
0.5	514, 514, 516, 518	10419, -21312, 29341, -18756 ε = 150	51	450, 450, 472, 474	691, -839, 2730, -2617 ε = 403
1	451, 511, 514	-209, 15195, -15093 ε = 188	52	450, 450, 472, 474	659, -805, 2703, -2591 ε = 404
2	450, 511, 514	-172, 15202, -15213 ε = 212	53	450, 450, 472, 474	662, -808, 2703, -2591 ε = 406
3	500, 500	-14126, 14440 ε = 253	54	500, 500	-3163, 3245 ε = 408
4	450, 450, 472, 474	2911, -3485, 11299, -10926 ε = 259	55	500, 500	-3178, 3259 ε = 410
5	450, 450, 472, 474	2780, -3300, 10308, -9973 ε = 269	56	500, 500	-3121, 3201 ε = 412
6	450, 450, 472, 474	2517, -2986 9357, -9054 ε = 278	57	450, 453, 463, 465, 469, 470, 472, 472, 476, 477, 479, 496, 500, 505, 509, 511, 515, 517, 518, 520, 522, 548, 549	-108, 1.76, -13, 233, 0.035, -16, 1174, 1905, -3676, -326, 276, -50, -0.262, -2004, 3359, 1373, -1929, 1667, -1153, 208, -1095, 408, -288 ε = 408
7	450, 450, 472, 474	2347, -2778, 8634, -8356 ε = 286	58	450, 450, 472, 476	672, -821, 1594, -1497 ε = 414
8	450, 450, 472, 474	2174, -2582, 8067, -7798 ε = 293	59	450, 450, 472, 476	637, -785, 1587, -1491 ε = 416
9	450, 450, 472, 474	2027, -2415, 7618, -7359 ε = 299	60	450, 450, 472, 476	644, -792, 1587, -1493 ε = 417
10	450, 450, 472, 474	1902, -2273, 7200, -6946 ε = 305	61	450, 450, 472, 476	622, -764, 1553, -1464 ε = 419
11	450, 450, 472, 474	1767, -2119, 6799, -6556 ε = 310	62	450, 450, 472, 476	638, -777, 1540, -1455 ε = 420
12	450, 450, 472, 474	1600, -1937, 6502, -6265 ε = 315	63	450, 450, 472, 476	624, -759, 1496, -1414 ε = 422
13	450, 450, 472, 474	1557, -1885, 6285, -6053 ε = 319	64	450, 450, 472, 476	618, -750, 1454, -1374 ε = 423
14	450, 450, 472, 474	1554, -1874, 6192, -5969 ε = 323	65	450, 450, 472, 476	620, -744, 1403, -1330 ε = 425
15	450, 450, 472, 474	1582, -1902, 6126, -5902 ε = 327	66	450, 450, 472, 476	594, -717, 1349, -1274 ε = 427
16	450, 450, 472, 474	1578, -1890, 6082, -5870 ε = 329	67	450, 450, 472, 476	588, -705, 1308, -1239 ε = 428
17	450, 450, 472, 474	1514, -1816, 5973, -5770 ε = 332	68	450, 450, 472, 474	532, -636, 1979, -1902 ε = 429
18	450, 450, 472, 474	1463, -1756, 5828, -5633 ε = 336	69	450, 450, 472, 476	508, -617, 1162, -1090 ε = 432
19	450, 450, 472, 474	1439, -1723, 5708, -5523 ε = 339	70	450, 450, 472, 476	489, -596, 1157, -1087 ε = 433
20	450, 450, 472, 474	1378, -1655, 5510, -5327 ε = 342	71	500, 500	-2040, 2096 ε = 435

457

21	450, 450, 472, 474	1385, -1656, 5486, -5311 $\varepsilon = 344$	**72**	502	36 $\varepsilon = 435$
22	450, 450, 472, 474	-232, 4327, 630, -4792 $\varepsilon = 347$	**73**	502	36 $\varepsilon = 437$
23	450, 450, 472, 474	-223, 4194, 617, -4653 $\varepsilon = 350$	**74**	501, 502	-2710, 2772 $\varepsilon = 439$
24	450, 450, 472, 474	-217, 4008, 646, -4499 $\varepsilon = 352$	**75**	502	38 $\varepsilon = 440$
25	450, 450, 472, 474	-209, 3934, 572, -4360 $\varepsilon = 355$	**76**	502	38 $\varepsilon = 441$
26	450, 450, 472, 474	-201, 3660, 705, -4224 $\varepsilon = 357$	**77**	501, 502	-2987, 3055 $\varepsilon = 444$
27	450, 450, 472, 474	-193, 3550, 690, -4105 $\varepsilon = 359$	**78**	501, 502	-3182, 3251 $\varepsilon = 446$
28	450, 450, 472, 474	1162, -1371, 4227, -4092 $\varepsilon = 362$	**79**	501, 502	-3263, 3335 $\varepsilon = 447$
29	450, 450, 472, 474	1123, -1324, 4030, -3896 $\varepsilon = 364$	**80**	501, 502	-3362, 3435 $\varepsilon = 449$
30	450, 450, 472, 474	1073, -1266, 3851, -3723 $\varepsilon = 366$	**81**	501, 502	-3253, 3325 $\varepsilon = 451$
31	450, 450, 472, 474	1007, -1194, 3676, -3547 $\varepsilon = 369$	**82**	500, 500	-2486, 2552 $\varepsilon = 453$
32	450, 450, 472, 474	947, -1128, 3506, -3379 $\varepsilon = 371$	**83**	450, 450, 472, 476	485, -606, 1259, -1176 $\varepsilon = 455$
33	450, 450, 472, 474	932, -1109, 3395, -3269 $\varepsilon = 373$	**84**	500, 500	-2457, 2521 $\varepsilon = 458$
34	450, 450, 472, 474	878, -1051, 3261, -3135 $\varepsilon = 375$	**85**	450, 450 472, 476,	488, -600, 1199, -1124 $\varepsilon = 460$
35	450, 450 472, 474	823, -990, 3190, -3069 $\varepsilon = 377$	**86**	450, 450, 472, 476	456, -560, 1120, -1050 $\varepsilon = 463$
36	450, 450, 472, 474	841, -1011, 3148, -3022 $\varepsilon = 379$	**87**	450, 450, 472, 476	448, -547, 1037, -968 $\varepsilon = 466$
37	450, 450, 472, 474	793, -958, 3060, -2937 $\varepsilon = 380$	**88**	500, 500	-1855, 1906 $\varepsilon = 469$
38	450, 450, 472, 474	764, -929, 3100, -2978 $\varepsilon = 382$	**89**	500, 500	-1743, 1793 $\varepsilon = 472$
39	450, 450, 472, 474	753, -916, 3038, -2916 $\varepsilon = 384$	**90**	500, 500	-1716, 1764 $\varepsilon = 475$
40	450, 450, 472, 474	723, -886, 3057, -2936 $\varepsilon = 385$	**91**	500, 500	-1733, 1781 $\varepsilon = 478$
41	450, 450, 472, 474	759, -922, 3018, -2896 $\varepsilon = 387$	**92**	502	29 $\varepsilon = 481$
42	450, 450 472, 474	736, -896, 2970, -2851 $\varepsilon = 388$	**93**	502	29 $\varepsilon = 484$
43	450, 450, 472, 473, 474	639, -783, 1595, 2598, -4090 $\varepsilon = 389$	**94**	450, 450, 504, 505, 506, 507, 508, 510, 511, 514	-196, 136, 749, -925, -1621, 2763, -1092, 3932, -279, -3597 $\varepsilon = 488$
44	500, 500	-3432, 3520 $\varepsilon = 393$	**95**	516, 518, 569, 572	2008, -2078, -1317, 1426 $\varepsilon = 490$
45	450, 450, 472, 474	731, -890, 2946, -2826 $\varepsilon = 393$	**96**	502	33 $\varepsilon = 497$

458

46	450, 450, 472, 474	707, -865, 2933, -2815 ε = 395	97	516, 518, 519, 520	1523, -2916, -1690, 3098 ε = 503
47	500, 500	-3454, 3542 ε = 398	98	516, 518, 520	1270, -3237, 1998 ε = 512
48	450, 450, 472, 474	735, -892, 2899, -2782 ε = 398	99	570, 571	-3115, 3261 ε = 529
49	450, 450, 472, 474	721, -873, 2858, -2746 ε = 399	99.5	-	-
50	500, 500	-3368, 3454 ε = 402			

Table H3. Absorbance wavelength channels and corresponding regressor coefficients for MLR models of cumulative boiling point distribution fractions in the third data set.

% Off (wt.%)	λ	β	% Off (wt.%)	λ	β
		Third Data Set (13)			
0.5	460, 468, 469, 470, 472, 472	-620, 11293, -27175, 15590, 4721, -3721 ε = 190	51	451, 467, 469, 476	-96, -882, 1572, -574 ε = 410
1	451, 469	-546, 815 ε = 245	52	451, 467, 469, 476	-95, -875, 1581, -593 ε = 411
2	450, 451, 469, 535, 538, 541, 542	1504, -2031, 1350, -9747, 6215, -3575, 5868 ε = 197	53	451, 467 469, 472, 476	-91, -776, 1009, 1037, -1174 ε = 413
3	451, 469, 474	-549, 3101, -2522 ε = 258	54	451, 467, 469, 472, 476	-95, -666, 921, 908, -1059 ε = 414
4	451, 469, 474	-502, 2958, -2440 ε = 270	55	451, 469, 472, 473	-156, 648, 1282, -1751 ε = 418
5	451, 469, 472, 474	-387, 1519, 6665, -7911 ε = 264	56	451, 469, 476	-137, 507, -345 ε = 417
6	451, 469, 473	-443, 2865, -2387 ε = 292	57	451, 451, 463, 466, 469, 470, 476, 478, 542, 602, 624, 632	-596, 547, -279, -151, 1133, 24, 155, -883, -4.8, -0.82, -344, 542 ε = 417
7	451, 469, 473	-407, 2618, -2177 ε = 300	58	451, 472, 473, 476	-149, 696, 1280, -1811 ε = 419
8	451, 469, 473	-395, 2337, -1895 ε = 310	59	451, 467, 469, 472, 476	-79, -824, 1122, 909, -1130 ε = 421
9	451, 469, 473	-378, 2161, -1734 ε = 316	60	451, 469, 476	-130, 538, -392 ε = 422
10	451, 469, 473	-365, 2046, -1629 ε = 321	61	450, 451, 469, 471, 472, 472, 476	246, -382, -212, 859, -858, 1537, -1200 ε = 425
11	451, 469, 473	-345, 1898, -1501 ε = 326	62	450, 467, 469, 476	-85, -730, 1412, -590 ε = 425
12	451, 469, 476	-308, 1283, -941 ε = 328	63	451, 469, 472, 473	-134, 716, 1092, -1665 ε = 427
13	451, 466, 467, 467, 469, 476, 630	-283, 2553, -4319, 1398, 2074, -1464, 180 ε = 320	64	451, 469, 472, 473	-131, 694, 1183, -1738 ε = 428
14	451, 467, 469, 476	-213, -1475, 2986, -1277 ε = 335	65	450, 450, 472, 476	339, -456, 552, -440 ε = 427
15	451, 467, 469, 476	-210, -1446, 2957, -1283 ε = 338	66	450, 469, 473	-116, 684, -551 ε = 431
16	450, 451,453, 472, 476	772, -1059, 567, 1889, -2205 ε = 340	67	451, 472, 473, 476	-119, 568, 1432, -1874 ε = 432
17	450, 451,469, 476	674, -973, 1335, -1042 ε = 342	68	451, 469 472, 473	-112, 527, 1270, -1675 ε = 435
18	451, 467, 469, 476	-186, -1467, 2956, -1298 ε = 346	69	451, 469, 472, 473	-112, 459, 1082, -1414 ε = 438
19	450, 451,472, 476	625, -911, 1273, -993 ε = 348	70	451, 469, 472, 473	-112, 477, 1183, -1535 ε = 439

20	450, 451, 451, 469, 476, 502, 504, 509, 523, 523, 531, 632	4.72, -317, -2.53, 1365, -1217, -1755, 2054, 345 -417, 885, -1081 159 ε = 364	**71**	451, 469, 472, 473	-108, 376, 1210, -1460 ε = 441
21	450, 451, 469, 476	597, -864, 1278, -1026 ε = 352	**72**	451, 469, 476	-92, 303, -188 ε = 441
22	451, 469, 473	-256, 1675, -1400 ε = 356	**73**	450, 451,469, 479, 632	223, -322, 429, -358, 109 ε = 440
23	451, 469, 473	-245, 1668, -1409 ε = 357	**74**	450, 451,468, 468, 469, 486, 493, 632	220, -314, 268, -669, 733, 16, -297, 111 ε = 440
24	451, 469, 473	-242, 1620, -1359 ε = 361	**75**	451, 468,469, 487, 489, 492	-86, -928, 1218, -429, -794, 1060 ε = 448
25	451, 469, 473	-228, 1556, -1315 ε = 362	**76**	451, 461, 462, 469, 473	-70, 558, -772, 797, -487 ε = 447
26	451, 469, 473	-219, 1472, -1235 ε = 365	**77**	451, 469	-106, 155 ε = 453
27	451, 469,472, 473, 476	-195, 640, 3128, -2474, -1128 ε = 365	**78**	451, 469, 487, 492	-116, 285, -869, 753 ε = 455
28	451, 469, 472, 473	-217, 1250, 2067, -3097 ε = 370	**79**	450, 451, 469, 487, 630	235, -349, 394, -341, 137 ε = 448
29	451, 453, 456, 458, 469, 472, 473, 476	-696, 530, 737, -875, 696, 2428, -1137, -1730 ε = 370	**80**	450, 451, 469, 482, 630	242, -358, 433, -355, 130 ε = 452
30	451, 469, 472, 473, 476	-177, 524, 2659, -2120, -900 ε = 373	**81**	450, 451, 451, 463, 464, 469, 478, 479, 503, 521, 625, 632	2.61, -371, 315, 11, -314, 728, -240, -94, -58, -0.48, -443, 545 ε = 455
31	451, 469, 472, 473	-199, 994, 1974, -2755 ε = 378	**82**	451, 467, 469, 476	-78, -665, 1199, -440 ε = 458
32	451, 469, 472, 473	-189, 951, 1874, -2622 ε = 380	**83**	450, 451, 472, 476	314, -437, 488, -360 ε = 458
33	451, 469, 472, 473	-184, 891, 1795, -2486 ε = 382	**84**	450, 469, 473	-114, 628, -495 ε = 462
34	451, 451, 469, 476, 624, 632	-797, 661, 712, -587, -1061, 1250 ε = 383	**85**	450, 469, 473	-105, 628, -507 ε = 463
35	451, 469, 473	-169, 897, -698 ε = 385	**86**	451, 469, 472, 473	-111, 488, 1269, -1636 ε = 468
36	451, 467, 469, 476	-112, -866, 1617, -616 ε = 387	**87**	451, 469, 472, 473	-104, 464, 1242, -1591 ε = 471
37	450, 452, 457, 460, 464, 466, 467, 469, 472, 474, 476	-135, 84, -39, -332, 1010, 745, -1674, 334, 1293, 27, -1333 ε = 381	**88**	450, 469, 472	-94, 433, -318 ε = 474
38	451, 467, 469, 472, 476	-102, -790, 1076, 1093, -1273 ε = 390	**89**	450, 469, 472	-88, 403, -294 ε = 476
39	451, 467, 469, 476	-109, -894, 1644, -619 ε = 392	**90**	450, 469, 472	-85, 437, -334 ε = 478
40	451, 467, 469, 476	-115, -853, 1600, -609 ε = 394	**91**	450, 469, 472	-84, 440, -338 ε = 481
41	451, 469, 476	-156, 593, -413 ε = 394	**92**	450, 454, 455, 469, 472, 473, 475, 475, 479, 481, 482, 485	-225, 78, 69, 254, 94, -1678, 24, 1531, 820, -2.1, -395, -556 ε = 493
42	451, 467, 469, 476	-110, -809, 1523, -581 ε = 397	**93**	451, 469, 471, 473, 613, 632	-87, 329, 519, -758, -305, 416 ε = 488
43	451, 467, 469, 476	-105, -847, 1589, -620 ε = 397	**94**	451, 469	-77, 114 ε = 495

44	450, 451, 472, 476	371, -538, 623, -443 $\varepsilon = 398$	95	451, 469	-81, 119 $\varepsilon = 500$
45	450, 451, 472, 476	-106, -831, 1579, -624 $\varepsilon = 399$	96	451, 469	-87, 128 $\varepsilon = 506$
46	451, 467, 469, 472, 476	-92, -862, 1195, 997, -1236 $\varepsilon = 401$	97	451, 453, 469	-382, 346, 72 $\varepsilon = 513$
47	451, 472, 473, 476	-170, 722, 1442, -1971 $\varepsilon = 404$	98	450, 451, 469	336, -426, 121 $\varepsilon = 521$
48	451, 472, 473, 476	-168, 736, 1419, -1966 $\varepsilon = 405$	99	571, 572	-2349, 2504 $\varepsilon = 528$
49	451, 467, 469, 472, 476	-86, -836, 1104, 1094, -1277, $\varepsilon = 406$	99.5	568, 572	-7842, 8384 $\varepsilon = 546$
50	451, 472, 473, 476	-167, 691, 1657, -2160 $\varepsilon = 409$			

Table H4. Absorbance wavelength channels and corresponding regressor coefficients for MLR models of cumulative boiling point distribution fractions in the fourth data set.

% Off (wt.%)	λ	β	% Off (wt.%)	λ	β
		Fourth Data Set (11)			
0.5	468	494 ε = 145	51	465, 467	-2672, 2875 ε = 396
1	468	525 ε = 166	52	465, 467	-2837, 3043 ε = 398
2	467	499 ε = 192	53	465, 467	-2776, 2981 ε = 399
3	467	460 ε = 213	54	465, 467	-2905, 3111 ε = 401
4	467	425 ε = 229	55	465, 467	-2706, 2906 ε = 402
5	467	392 ε = 242	56	465, 467	-2825, 3027 ε = 404
6	467	360 ε = 253	57	465, 467	-2774, 2972 ε = 406
7	467	335 ε = 263	58	467, 468	-4623, 4795 ε = 408
8	465, 467	-6829, 7375 ε = 275	59	465, 467	-2754, 2949 ε = 409
9	465, 467	-6419, 6936 ε = 282	60	465, 467	-2865, 3064 ε = 411
10	465, 467	-6070, 6559 ε = 289	61	465, 467	-2557, 2742 ε = 413
11	465, 467	-6030, 6507 ε = 294	62	465, 467	-2464, 2646 ε = 414
12	465, 467	-5761, 6216 ε = 300	63	465, 467	-2358, 2534 ε = 416
13	465, 467	-5756, 6202 ε = 304	64	465, 467	-2151, 2318 ε = 418
14	465, 467	-5387, 5816 ε = 308	65	464, 467, 467	-2090, 3805, -1533 ε = 420
15	465, 467	-5373, 5797 ε = 312	66	465, 467	-2164, 2324 ε = 421
16	465, 467	-5204, 5619 ε = 316	67	465, 467	-2153, 2311 ε = 423
17	465, 467	-5069, 5476 ε = 319	68	465, 467	-2096, 2248 ε = 425
18	465, 467	-5062, 5462 ε = 323	69	467, 468	-3360, 3487 ε = 427
19	465, 467	-4787, 5172 ε = 326	70	467, 468	-3381, 3506 ε = 428
20	465, 467	-4815, 5192 ε = 330	71	467, 468	-3500, 3621 ε = 431
21	465, 467	-4477, 4838 ε = 333	72	467, 468	-3776, 3900 ε = 432
22	467	205 ε = 333	73	467, 468	-3690, 3813 ε = 433
23	467	199 ε = 336	74	473, 474	2992, -2979 ε = 434
24	467	191 ε = 340	75	473, 474	3008, -2994 ε = 435
25	467	187 ε = 342	76	473, 474	3267, -3257 ε = 436

26	465, 467	-3611, 3913 $\varepsilon = 347$	**77**	450, 457, 460, 463, 468, 469, 471, 472, 550	-330, 17, 583, -267, -73, 499, 1825, -2220, 0.11 $\varepsilon = 446$
27	465, 467	-3337, 3624 $\varepsilon = 350$	**78**	473, 474	3408, -3401 $\varepsilon = 439$
28	465, 467	-3395, 3675 $\varepsilon = 353$	**79**	473, 474	3553, -3544 $\varepsilon = 441$
29	465, 467	-3290, 3561 $\varepsilon = 356$	**80**	473, 474	3901, -3901 $\varepsilon = 443$
30	465, 467	-3230, 3494 $\varepsilon = 356$	**81**	473, 474	4009, -4009 $\varepsilon = 445$
31	465, 467	-3313, 3573 $\varepsilon = 360$	**82**	473, 474	4115, -4116 $\varepsilon = 447$
32	465, 467	-3281, 3533 $\varepsilon = 363$	**83**	473, 474	3816, -3808 $\varepsilon = 449$
33	465, 467	-3162, 3409 $\varepsilon = 365$	**84**	473, 474	3756, -3748 $\varepsilon = 452$
34	465, 467	-3183, 3425 $\varepsilon = 367$	**85**	467, 468	-4196, 4332 $\varepsilon = 456$
35	465, 467	-3178, 3417 $\varepsilon = 369$	**86**	467, 468	-3779, 3906 $\varepsilon = 459$
36	465, 467	-3280, 3522 $\varepsilon = 371$	**87**	467, 468	-3736, 3855 $\varepsilon = 462$
37	465, 467	-3148, 3382 $\varepsilon = 373$	**88**	473, 474	2946, -2940 $\varepsilon = 464$
38	465, 467	-3019, 3249 $\varepsilon = 374$	**89**	473, 474	2798, -2793 $\varepsilon = 467$
39	465, 467	-3149, 3380 $\varepsilon = 376$	**90**	473, 474	2877, -2876 $\varepsilon = 470$
40	465, 467	-3198, 3431 $\varepsilon = 378$	**91**	450, 469, 472, 473, 482	-102, 809, -1600, 1230, -344 $\varepsilon = 478$
41	465, 467	-3096, 3324 $\varepsilon = 379$	**92**	460, 465, 472, 473, 482	-295, 538, -1372, 1539, -461 $\varepsilon = 479$
42	465, 467	-3089, 3317 $\varepsilon = 381$	**93**	460, 465, 469, 472, 473, 482, 483, 502, 507	-320, 673, -269, -1356, 1675, 37, -541, 66, -15 $\varepsilon = 483$
43	465, 467	-3007, 3230 $\varepsilon = 383$	**94**	451, 463, 472, 473	-50, -1751, 2312, -530 $\varepsilon = 491$
44	465, 467	-2998, 3219 $\varepsilon = 384$	**95**	450, 472, 473, 486	-60, -1993, 2456, -422 $\varepsilon = 492$
45	465, 467	-2948, 3166 $\varepsilon = 386$	**96**	498	106 $\varepsilon = 494$
46	465, 467	-2944, 3162 $\varepsilon = 388$	**97**	-	-
47	465, 467	-2906, 3123 $\varepsilon = 389$	**98**	-	-
48	465, 467	-2801, 3015 $\varepsilon = 390$	**99**	-	-
49	465, 467	-2776, 2986 $\varepsilon = 392$	**99.5**	-	-
50	465, 467	-2785, 2992 $\varepsilon = 394$		-	-
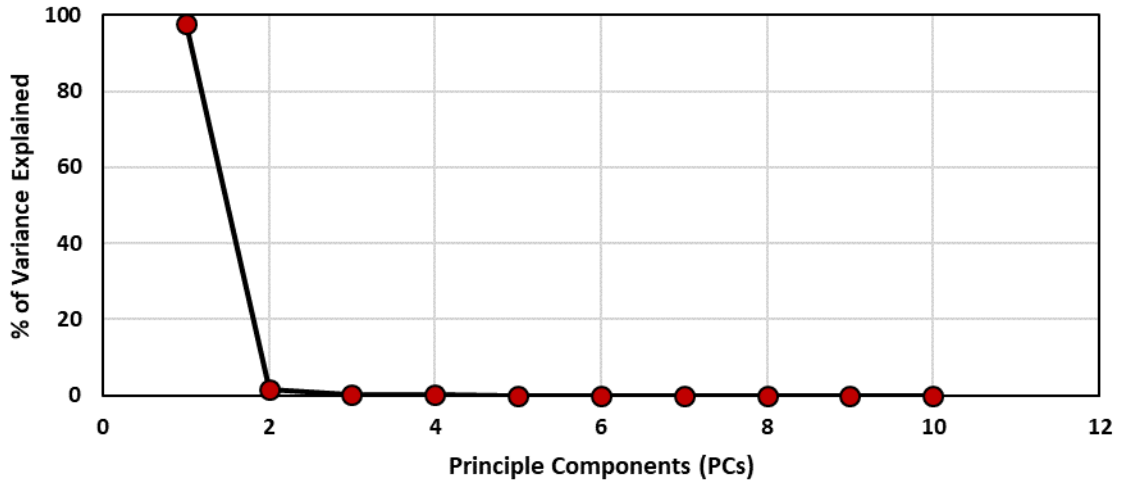
Figure H29. Variance explained by each principal component for the first data set.
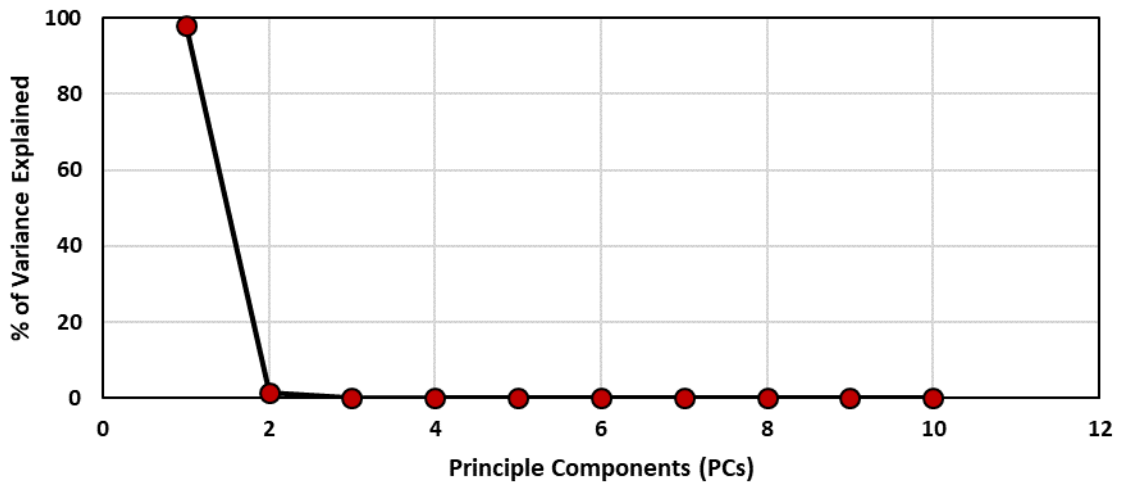
Figure H30. Variance explained by each principal component for the second data set.
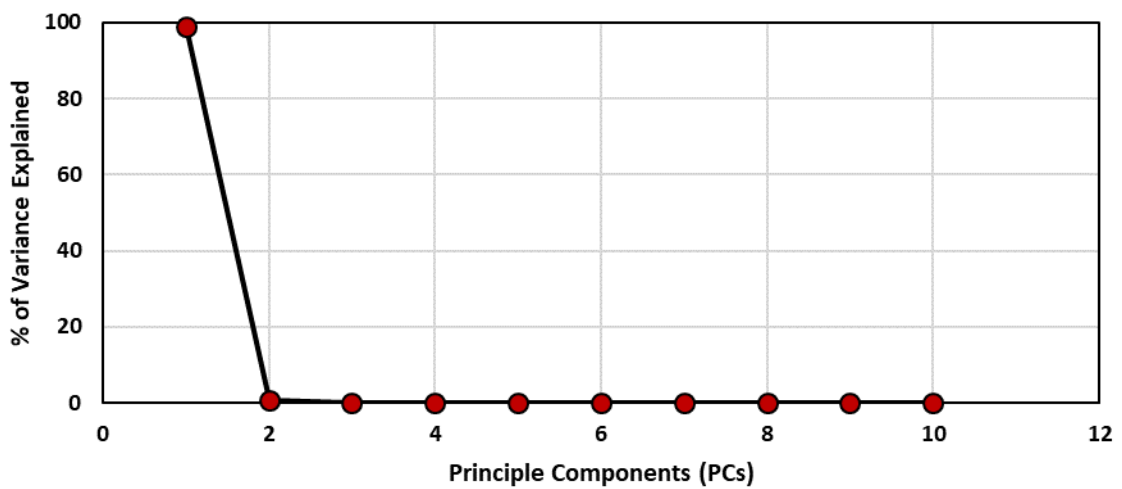
Figure H31. Variance explained by each principal component for the third data set.
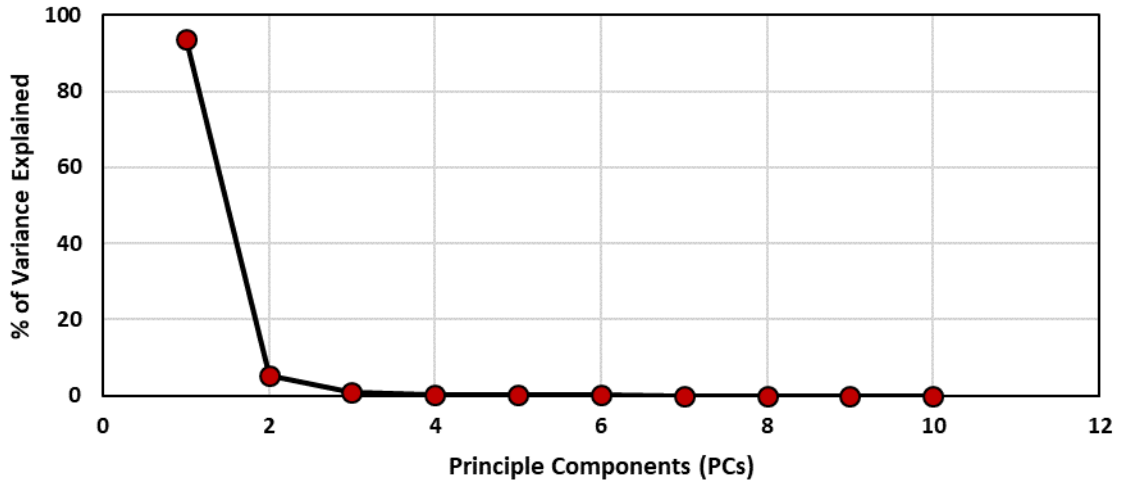
Figure H32. Variance explained by each principal component for the fourth data set.
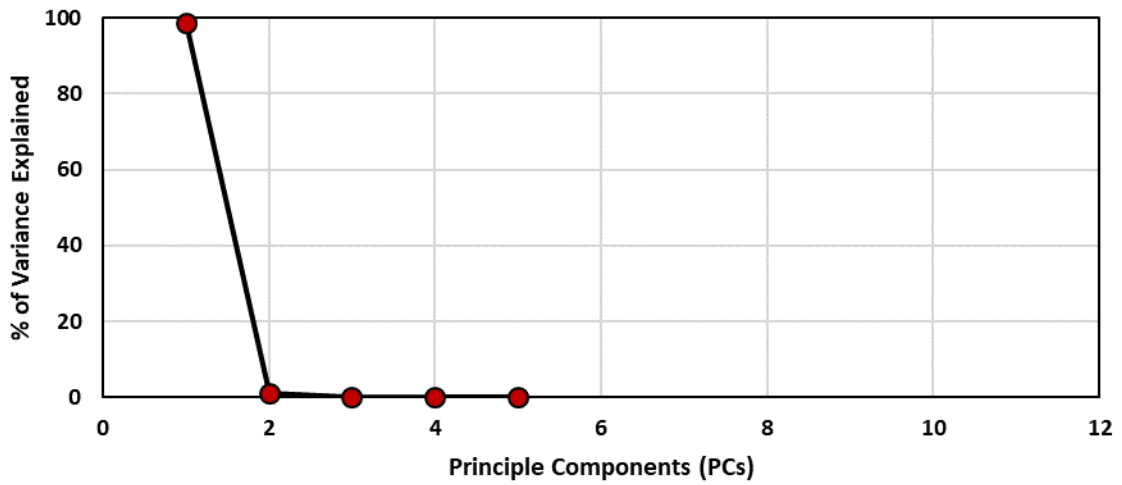
Figure H33. Variance explained by each principal component for the fifth data set.
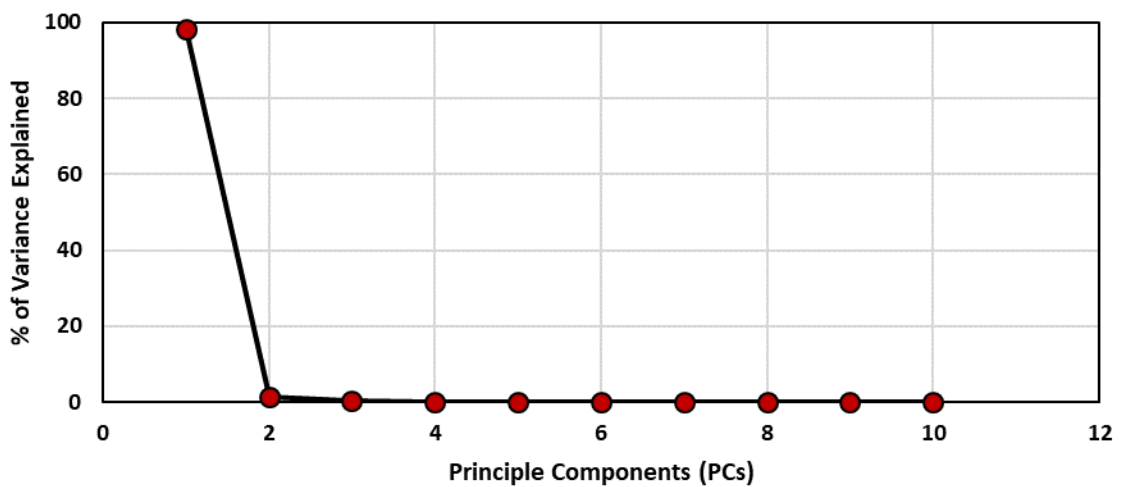
Figure H34. Variance explained by each principal component for the sixth data set.
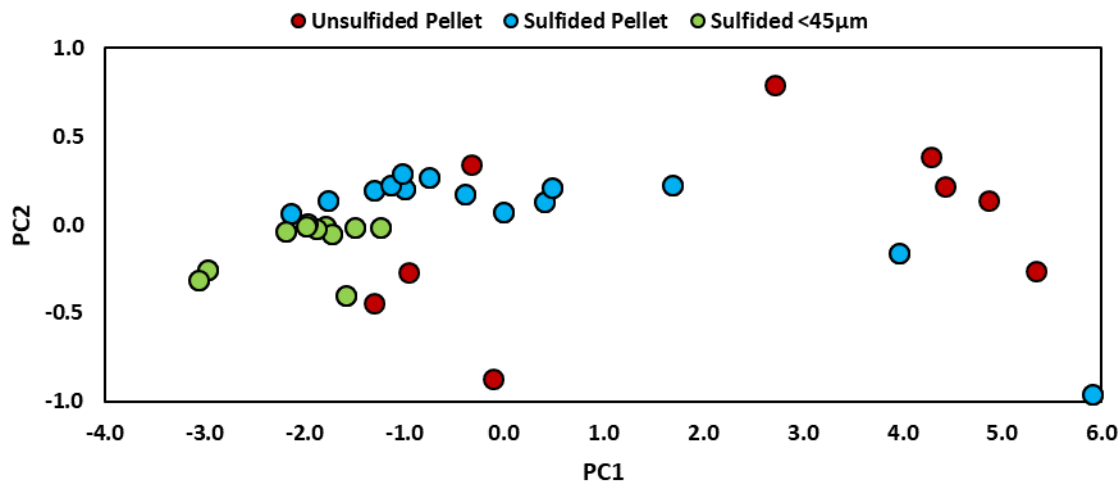
Figure H35. Principal component analysis of the first data set.
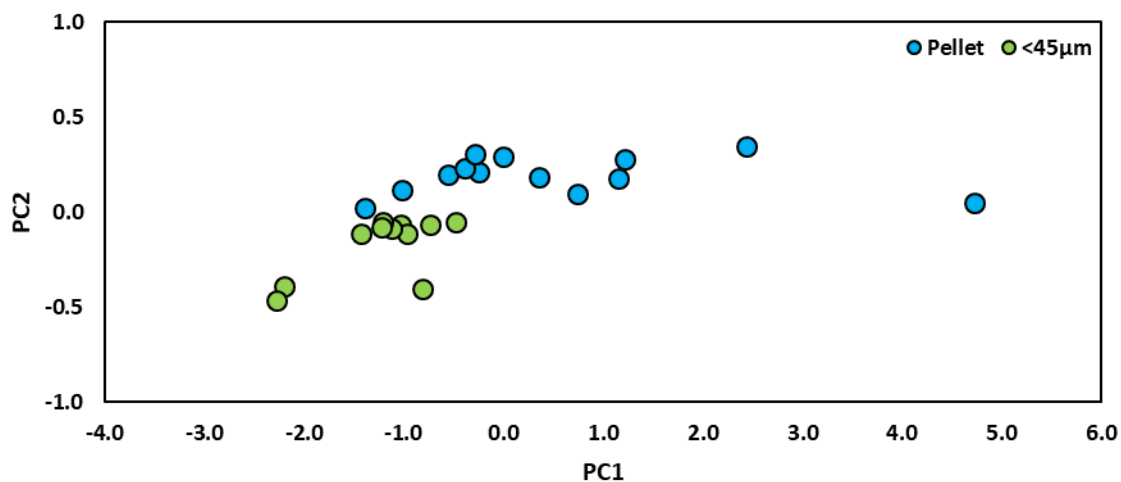
Figure H36. Principal component analysis of the second data set.
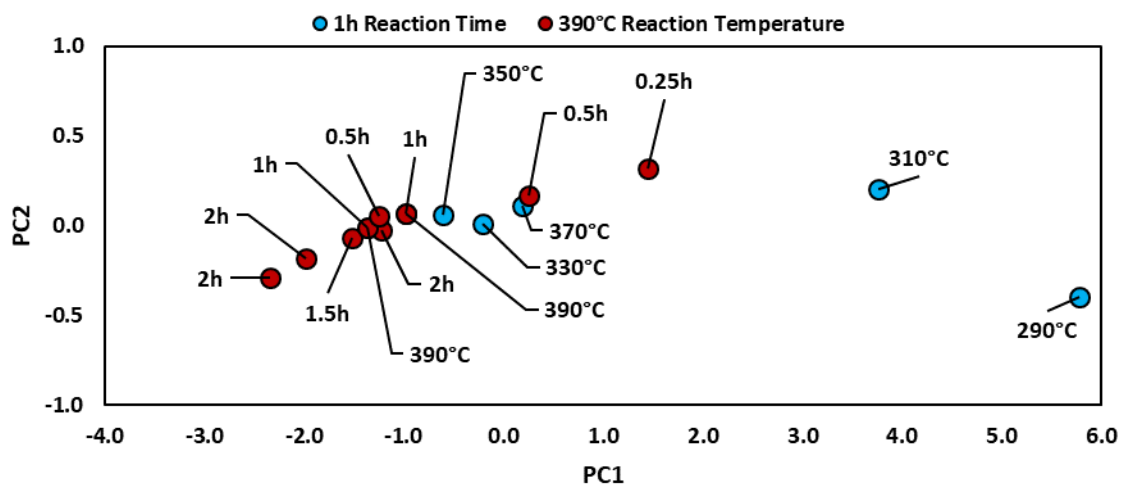
Figure H37. Principal component analysis of the third data set.
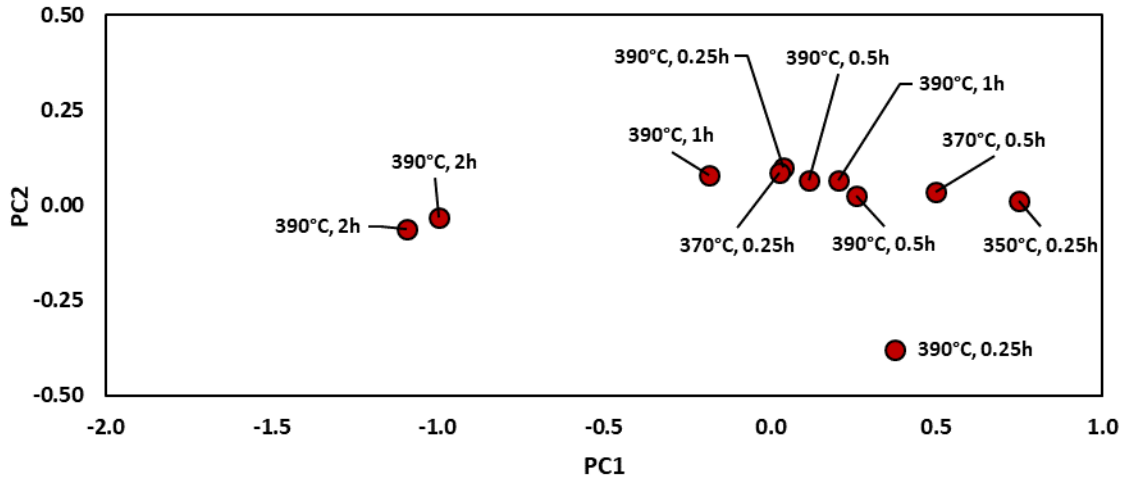
Figure H38. Principal component analysis of the fourth data set.
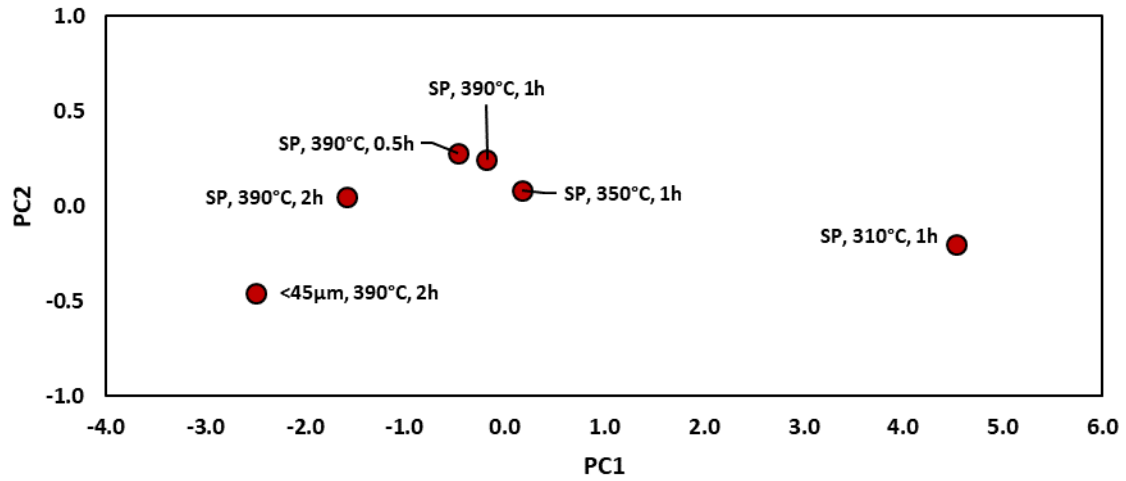
Figure H39. Principal component analysis of the fifth data set.
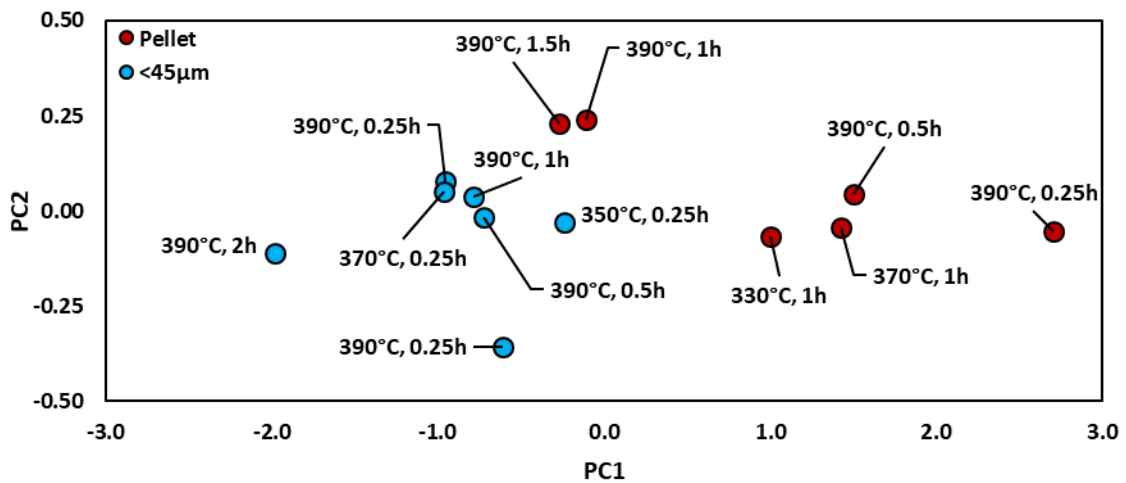
Figure H40. Principal component analysis of the sixth data set.

Table H5. Minimum number of cross validated components in the PCR models for cumulative boiling point distribution fractions.

% Off (wt.%)	1st (34)	2nd (25)	3rd (14)	4th (11)	% Off (wt.%)	1st (34)	2nd (25)	3rd (14)	4th (11)
0.5	9	7	1	4	51	7	5	6	4
1	8	5	7	4	52	7	5	7	4
2	8	6	5	5	53	10	5	6	4
3	10	5	6	4	54	7	5	6	1
4	10	6	6	1	55	10	6	7	9
5	10	5	6	5	56	10	5	6	9
6	10	5	6	1	57	10	5	6	4
7	10	10	6	1	58	7	5	4	4
8	7	6	6	1	59	7	5	6	9
9	7	5	6	4	60	10	6	6	9
10	7	1	6	4	61	7	5	5	4
11	10	5	6	1	62	7	6	6	7
12	7	5	6	4	63	7	5	6	4
13	7	5	6	5	64	10	5	8	4
14	7	5	6	4	65	7	5	6	4
15	10	5	6	4	66	10	5	6	5
16	7	5	6	4	67	7	6	6	4
17	7	5	6	4	68	10	5	6	4
18	7	5	6	1	69	7	6	6	4
19	7	5	4	4	70	7	5	6	4
20	7	6	6	4	71	7	5	6	4
21	10	5	6	4	72	10	5	5	9
22	7	5	6	4	73	7	1	6	9
23	10	5	6	1	74	10	5	6	4
24	7	5	6	1	75	10	5	6	9
25	7	6	6	1	76	10	5	6	9
26	10	6	6	5	77	10	5	6	9
27	10	5	6	4	78	10	5	6	9
28	10	5	6	4	79	7	5	4	9
29	7	5	6	5	80	10	5	6	9
30	10	5	6	4	81	10	5	6	9
31	7	5	6	4	82	10	5	6	9
32	6	5	6	7	83	10	5	6	9
33	7	5	6	5	84	7	5	6	4
34	10	6	6	4	85	7	5	6	4
35	7	5	6	7	86	10	5	9	4
36	7	6	6	4	87	6	7	6	4
37	7	5	6	4	88	7	5	6	5
38	10	5	6	4	89	6	5	6	4
39	7	5	4	4	90	10	5	6	4
40	10	5	6	4	91	6	5	4	4
41	10	5	6	4	92	7	6	6	4
42	10	5	4	4	93	10	5	5	4
43	10	5	6	4	94	10	5	6	3
44	10	5	6	4	95	10	5	6	1
45	7	5	6	4	96	7	5	4	1
46	7	5	6	9	97	6	6	7	1
47	10	5	6	7	98	6	3	8	1
48	7	5	6	1	99	1	2	7	1
49	10	5	6	4	99.5	1	1	2	1
50	7	5	6	4					

Table H6. Minimum number of cross validated components in the PLSR models for cumulative boiling point distribution fractions.

% Off (wt.%)	1st (34)	2nd (25)	3rd (14)	4th (11)	% Off (wt.%)	1st (34)	2nd (25)	3rd (14)	4th (11)
0.5	4	4	1	1	51	9	5	4	8
1	6	4	4	1	52	9	5	4	7
2	8	4	5	1	53	9	5	4	3
3	8	4	4	1	54	8	5	5	7
4	8	4	5	1	55	9	5	4	8
5	8	4	3	1	56	8	5	5	7
6	8	4	5	1	57	9	5	4	7
7	7	4	5	2	58	8	5	5	1
8	9	4	5	1	59	9	10	4	7
9	9	5	4	2	60	8	8	5	7
10	8	4	4	1	61	9	4	4	8
11	9	4	4	1	62	8	4	5	1
12	9	5	5	1	63	9	5	5	3
13	9	4	4	1	64	8	5	4	1
14	8	5	5	1	65	9	4	5	1
15	9	10	4	1	66	9	4	5	3
16	8	5	4	1	67	9	4	4	1
17	9	5	4	3	68	9	5	4	4
18	9	4	5	1	69	9	8	4	1
19	8	5	5	1	70	8	5	4	5
20	9	4	4	1	71	9	4	4	3
21	9	5	5	3	72	8	4	5	7
22	9	8	5	1	73	9	4	3	7
23	9	4	5	1	74	8	4	5	8
24	8	4	5	1	75	8	4	4	7
25	8	4	5	1	76	8	4	4	7
26	9	4	4	3	77	9	4	4	8
27	8	5	3	1	78	8	5	4	7
28	9	5	3	1	79	9	4	4	8
29	9	4	5	1	80	8	4	4	8
30	9	8	4	1	81	8	5	4	7
31	9	5	4	1	82	8	4	4	1
32	9	5	4	1	83	8	5	4	6
33	9	5	5	1	84	8	4	4	4
34	8	5	4	5	85	8	8	5	3
35	8	4	5	5	86	8	5	4	3
36	9	4	4	8	87	8	4	4	5
37	8	10	5	8	88	9	4	4	4
38	8	5	4	7	89	9	4	4	4
39	8	5	5	7	90	9	4	5	4
40	8	4	5	8	91	9	4	4	4
41	8	5	4	1	92	9	5	5	4
42	8	5	5	6	93	9	4	4	4
43	8	4	5	7	94	9	5	4	1
44	8	4	4	7	95	8	5	5	1
45	8	4	4	1	96	8	5	5	1
46	9	4	4	1	97	5	1	5	1
47	8	4	5	8	98	5	4	5	1
48	8	5	5	1	99	1	2	6	1
49	8	4	4	4	99.5	1	2	1	1
50	9	5	4	6					

Table H7. Section criteria results in the first data set of SLS models for cumulative boiling point distribution fractions.

% Off (wt.%)	AIC	AICc	AICu	BIC	% Off (wt.%)	AIC	AICc	AICu	BIC
0.5	-7	-6.9	-5.8	-5.4	51	-1.1	-1	0.1	0.4
1	-8.6	-8.5	-7.5	-7.1	52	-1.3	-1.2	-0.1	0.2
2	-7.5	-7.4	-6.4	-6	53	-1.3	-1.2	-0.2	0.2
3	-6	-5.9	-4.9	-4.5	54	-1	-0.9	0.1	0.5
4	-5.4	-5.3	-4.3	-3.9	55	-1.2	-1.1	0	0.4
5	-4.9	-4.7	-3.7	-3.3	56	-1.1	-0.9	0.1	0.5
6	-4.4	-4.3	-3.2	-2.9	57	-1.1	-1	0.1	0.4
7	-4	-3.8	-2.8	-2.4	58	-1.2	-1.1	-0.1	0.3
8	-3.6	-3.5	-2.5	-2.1	59	-1.2	-1.1	-0.1	0.3
9	-3.2	-3.1	-2.1	-1.7	60	-1.1	-1	0	0.4
10	-3	-2.8	-1.8	-1.4	61	-1.3	-1.2	-0.2	0.2
11	-2.8	-2.7	-1.7	-1.3	62	-1.1	-1	0	0.4
12	-2.5	-2.4	-1.4	-1	63	-1	-0.9	0.1	0.5
13	-2.2	-2.1	-1.1	-0.7	64	-1.1	-0.9	0.1	0.5
14	-2.2	-2.1	-1.1	-0.7	65	-1	-0.9	0.1	0.5
15	-2.2	-2	-1	-0.6	66	-1.2	-1.1	-0.1	0.3
16	-2.2	-2.1	-1.1	-0.7	67	-1	-0.9	0.1	0.5
17	-2.2	-2.1	-1	-0.7	68	-1	-0.9	0.1	0.5
18	-2.1	-2	-1	-0.6	69	-1.1	-0.9	0.1	0.5
19	-2.2	-2.1	-1.1	-0.7	70	-0.6	-0.5	0.5	0.9
20	-2.3	-2.1	-1.1	-0.7	71	-0.6	-0.4	0.6	1
21	-2	-1.9	-0.9	-0.5	72	-0.6	-0.5	0.5	0.9
22	-2.2	-2.1	-1.1	-0.7	73	-0.5	-0.4	0.6	1
23	-2	-1.9	-0.9	-0.5	74	-0.8	-0.6	0.4	0.8
24	-2	-1.8	-0.8	-0.4	75	-0.6	-0.5	0.5	0.9
25	-2.1	-2	-1	-0.6	76	-0.6	-0.5	0.6	0.9
26	-2	-1.9	-0.9	-0.5	77	-0.5	-0.4	0.6	1
27	-2	-1.9	-0.9	-0.5	78	-0.4	-0.3	0.7	1.1
28	-2.1	-1.9	-0.9	-0.5	79	-0.6	-0.5	0.6	1
29	-2.1	-1.9	-0.9	-0.5	80	-0.6	-0.5	0.5	0.9
30	-2	-1.9	-0.9	-0.5	81	-0.7	-0.5	0.5	0.9
31	-1.7	-1.5	-0.5	-0.1	82	-0.6	-0.5	0.5	0.9
32	-1.7	-1.6	-0.6	-0.2	83	-0.8	-0.7	0.3	0.7
33	-1.5	-1.4	-0.3	0	84	-0.8	-0.7	0.3	0.7
34	-1.3	-1.2	-0.2	0.2	85	-0.8	-0.7	0.3	0.7
35	-1.5	-1.4	-0.3	0	86	-0.9	-0.7	0.3	0.7
36	-1.4	-1.2	-0.2	0.2	87	-0.9	-0.8	0.2	0.6
37	-1.3	-1.2	-0.2	0.2	88	-0.4	-0.3	0.7	1.1
38	-1.4	-1.3	-0.3	0.1	89	-0.7	-0.6	0.4	0.8
39	-1.3	-1.1	-0.1	0.3	90	-0.5	-0.4	0.7	1
40	-1.4	-1.3	-0.2	0.1	91	-0.2	-0.1	0.9	1.3
41	-1.2	-1.1	-0.1	0.3	92	-0.3	-0.2	0.8	1.2
42	-1.3	-1.2	-0.2	0.2	93	-0.4	-0.3	0.7	1.1
43	-1.3	-1.1	-0.1	0.3	94	-1.4	-1.2	-0.2	0.2
44	-1.4	-1.3	-0.3	0.1	95	-2.3	-2.2	-1.2	-0.8
45	-1.2	-1.1	-0.1	0.3	96	-2.1	-2	-0.9	-0.5
46	-1.3	-1.2	-0.2	0.2	97	-2.3	-2.2	-1.2	-0.8
47	-1.3	-1.2	-0.2	0.2	98	-4.5	-4.4	-3.3	-3
48	-1.4	-1.3	-0.2	0.1	99	-1	-0.8	0.2	0.6
49	-1.5	-1.4	-0.4	0	99.5	-0.1	0	1	1.4
50	-1.2	-1	0	0.4					

Table H8. Section criteria results in the second data set of SLS models for cumulative boiling point distribution fractions.

% Off (wt.%)	AIC	AICc	AICu	BIC	% Off (wt.%)	AIC	AICc	AICu	BIC
0.5	-9.2	-9	-8	-8	51	-14.2	-14	-13	-13
1	-9.4	-9.3	-8.2	-8.2	52	-14.3	-14.1	-13.1	-13
2	-9	-8.8	-7.8	-7.7	53	-13.9	-13.8	-12.7	-12.7
3	-8.9	-8.7	-7.7	-7.7	54	-14.1	-13.9	-12.9	-12.9
4	-8.9	-8.7	-7.7	-7.7	55	-13.6	-13.5	-12.5	-12.4
5	-9.4	-9.2	-8.2	-8.1	56	-13.7	-13.6	-12.5	-12.5
6	-9.9	-9.7	-8.7	-8.7	57	-14.3	-14.1	-13.1	-13.1
7	-10.4	-10.2	-9.2	-9.1	58	-13.5	-13.4	-12.3	-12.3
8	-10.6	-10.5	-9.4	-9.4	59	-13	-12.8	-11.8	-11.8
9	-10.8	-10.6	-9.6	-9.5	60	-12.9	-12.7	-11.7	-11.7
10	-11	-10.9	-9.8	-9.8	61	-13	-12.8	-11.8	-11.8
11	-11.1	-11	-9.9	-9.9	62	-12.8	-12.6	-11.6	-11.6
12	-11.6	-11.4	-10.4	-10.4	63	-12.6	-12.4	-11.4	-11.3
13	-11.7	-11.5	-10.5	-10.5	64	-13.3	-13.1	-12.1	-12.1
14	-11.6	-11.4	-10.4	-10.3	65	-13.5	-13.3	-12.3	-12.3
15	-11.3	-11.1	-10.1	-10	66	-13.3	-13.2	-12.1	-12.1
16	-11.3	-11.1	-10.1	-10	67	-13.7	-13.6	-12.6	-12.5
17	-11.4	-11.2	-10.2	-10.1	68	-14.6	-14.4	-13.4	-13.4
18	-11.1	-10.9	-9.9	-9.9	69	-14.7	-14.6	-13.5	-13.5
19	-11	-10.8	-9.8	-9.7	70	-14.4	-14.2	-13.2	-13.2
20	-10.9	-10.8	-9.7	-9.7	71	-16.1	-15.9	-14.9	-14.9
21	-10.7	-10.5	-9.5	-9.5	72	-16.8	-16.6	-15.6	-15.6
22	-10.7	-10.5	-9.5	-9.4	73	-16.4	-16.3	-15.2	-15.2
23	-10.7	-10.5	-9.5	-9.5	74	-18	-17.9	-16.8	-16.8
24	-11.1	-10.9	-9.9	-9.8	75	-17.8	-17.7	-16.6	-16.6
25	-10.8	-10.6	-9.6	-9.6	76	-17.6	-17.4	-16.4	-16.4
26	-11.2	-11	-10	-9.9	77	-18	-17.8	-16.8	-16.8
27	-11.3	-11.1	-10.1	-10.1	78	-17.9	-17.8	-16.7	-16.7
28	-11.8	-11.6	-10.6	-10.6	79	-17.8	-17.6	-16.6	-16.5
29	-11.9	-11.7	-10.7	-10.7	80	-17.2	-17	-16	-16
30	-12.2	-12	-11	-10.9	81	-17.1	-16.9	-15.9	-15.9
31	-12.6	-12.4	-11.4	-11.3	82	-15.6	-15.4	-14.4	-14.4
32	-13.1	-12.9	-11.9	-11.9	83	-15.4	-15.2	-14.2	-14.1
33	-13	-12.9	-11.8	-11.8	84	-15.1	-15	-13.9	-13.9
34	-13.2	-13.1	-12	-12	85	-15.3	-15.2	-14.1	-14.1
35	-13.7	-13.5	-12.5	-12.5	86	-15.8	-15.6	-14.6	-14.6
36	-13.5	-13.3	-12.3	-12.3	87	-16.2	-16	-15	-15
37	-14.2	-14	-13	-12.9	88	-16.2	-16	-15	-15
38	-13.5	-13.4	-12.3	-12.3	89	-17	-16.9	-15.9	-15.8
39	-13.8	-13.6	-12.6	-12.6	90	-17	-16.8	-15.8	-15.8
40	-13.8	-13.6	-12.6	-12.6	91	-16.8	-16.6	-15.6	-15.6
41	-13.6	-13.5	-12.5	-12.4	92	-17.6	-17.4	-16.4	-16.4
42	-13.6	-13.4	-12.4	-12.3	93	-18.3	-18.1	-17.1	-17.1
43	-13.4	-13.2	-12.2	-12.2	94	-19.6	-19.4	-18.4	-18.4
44	-13.5	-13.4	-12.4	-12.3	95	-20	-19.8	-18.8	-18.8
45	-14	-13.8	-12.8	-12.8	96	-18.1	-18	-16.9	-16.9
46	-13.3	-13.2	-12.1	-12.1	97	-15.5	-15.3	-14.3	-14.3
47	-13.5	-13.3	-12.3	-12.3	98	-15.5	-15.3	-14.3	-14.3
48	-13.6	-13.4	-12.4	-12.4	99	-2.6	-2.4	-1.4	-1.4
49	-13.8	-13.6	-12.6	-12.6	99.5	0.7	0.9	1.9	2
50	-14	-13.8	-12.8	-12.8					

Table H9. Section criteria results in the third data set of SLS models for cumulative boiling point distribution fractions.

% Off (wt.%)	AIC	AICC	AICU	BIC	% Off (wt.%)	AIC	AICC	AICU	BIC
0.5	-18.9	-18.5	-17.5	-18.2	51	-16	-15.6	-14.6	-15.3
1	-18.2	-17.9	-16.9	-17.6	52	-15.9	-15.5	-14.5	-15.2
2	-14.8	-14.5	-13.4	-14.2	53	-15.3	-15	-14	-14.7
3	-13.5	-13.1	-12.1	-12.8	54	-16.1	-15.8	-14.8	-15.5
4	-12.8	-12.5	-11.4	-12.2	55	-16	-15.7	-14.7	-15.4
5	-13.3	-12.9	-11.9	-12.6	56	-15.9	-15.6	-14.6	-15.3
6	-13.4	-13.1	-12.1	-12.8	57	-15.6	-15.2	-14.2	-14.9
7	-13.7	-13.3	-12.3	-13	58	-15.6	-15.3	-14.2	-15
8	-13.7	-13.4	-12.3	-13	59	-14.7	-14.4	-13.3	-14.1
9	-14	-13.6	-12.6	-13.3	60	-14.7	-14.3	-13.3	-14
10	-14.2	-13.8	-12.8	-13.5	61	-14.2	-13.9	-12.8	-13.6
11	-14.6	-14.2	-13.2	-13.9	62	-14.1	-13.8	-12.8	-13.5
12	-14.7	-14.4	-13.4	-14.1	63	-14.3	-13.9	-12.9	-13.6
13	-14.9	-14.5	-13.5	-14.2	64	-14.9	-14.6	-13.5	-14.3
14	-14.6	-14.3	-13.2	-13.9	65	-14.7	-14.4	-13.3	-14.1
15	-14.5	-14.2	-13.1	-13.9	66	-15.1	-14.7	-13.7	-14.4
16	-14.1	-13.8	-12.8	-13.5	67	-14.8	-14.4	-13.4	-14.1
17	-14	-13.7	-12.7	-13.4	68	-15.9	-15.5	-14.5	-15.2
18	-13.8	-13.4	-12.4	-13.1	69	-16.1	-15.8	-14.7	-15.5
19	-13.2	-12.9	-11.9	-12.6	70	-15.5	-15.2	-14.2	-14.9
20	-13.3	-12.9	-11.9	-12.6	71	-16.8	-16.5	-15.4	-16.1
21	-12.9	-12.5	-11.5	-12.2	72	-18	-17.7	-16.6	-17.4
22	-13.2	-12.9	-11.8	-12.6	73	-17.4	-17.1	-16.1	-16.8
23	-13.2	-12.9	-11.8	-12.6	74	-18.8	-18.5	-17.4	-18.2
24	-13.4	-13	-12	-12.7	75	-18.2	-17.9	-16.9	-17.6
25	-13.3	-12.9	-11.9	-12.6	76	-19	-18.7	-17.6	-18.4
26	-13.7	-13.4	-12.3	-13.1	77	-18.3	-17.9	-16.9	-17.6
27	-13.5	-13.2	-12.1	-12.9	78	-18	-17.7	-16.6	-17.4
28	-13.8	-13.4	-12.4	-13.1	79	-18.4	-18.1	-17	-17.8
29	-14.2	-13.9	-12.9	-13.6	80	-17.5	-17.2	-16.2	-16.9
30	-14.6	-14.2	-13.2	-13.9	81	-17.8	-17.4	-16.4	-17.1
31	-14.6	-14.2	-13.2	-13.9	82	-16.1	-15.7	-14.7	-15.4
32	-15.3	-14.9	-13.9	-14.6	83	-15.7	-15.4	-14.4	-15.1
33	-15.6	-15.3	-14.3	-15	84	-16	-15.7	-14.6	-15.4
34	-15.8	-15.5	-14.4	-15.2	85	-16.2	-15.9	-14.9	-15.6
35	-15.9	-15.6	-14.5	-15.3	86	-15.8	-15.4	-14.4	-15.1
36	-16.2	-15.9	-14.8	-15.6	87	-16.5	-16.2	-15.1	-15.9
37	-16.6	-16.3	-15.2	-15.9	88	-16.4	-16.1	-15	-15.7
38	-15.6	-15.3	-14.2	-15	89	-17.4	-17.1	-16	-16.7
39	-15.6	-15.3	-14.3	-15	90	-17.3	-16.9	-15.9	-16.6
40	-15.4	-15	-14	-14.7	91	-16.9	-16.6	-15.5	-16.3
41	-15.7	-15.4	-14.3	-15	92	-17.4	-17.1	-16	-16.8
42	-15.9	-15.5	-14.5	-15.2	93	-18.1	-17.8	-16.8	-17.5
43	-15.8	-15.5	-14.4	-15.2	94	-19	-18.6	-17.6	-18.3
44	-15.9	-15.5	-14.5	-15.2	95	-19.9	-19.5	-18.5	-19.2
45	-16.1	-15.7	-14.7	-15.4	96	-18.2	-17.9	-16.9	-17.6
46	-15.4	-15.1	-14.1	-14.8	97	-16.3	-16	-15	-15.7
47	-15.8	-15.5	-14.5	-15.2	98	-19	-18.7	-17.7	-18.4
48	-15.9	-15.6	-14.6	-15.3	99	-13.8	-13.4	-12.4	-13.1
49	-15.6	-15.3	-14.2	-14.9	99.5	-13.2	-12.9	-11.9	-12.6
50	-15.7	-15.4	-14.3	-15.1					

Table H10. Section criteria results in the fourth data set of SLS models for cumulative boiling point distribution fractions.

% Off (wt.%)	AIC	AICc	AICu	BIC	% Off (wt.%)	AIC	AICc	AICu	BIC
0.5	-9.2	-8.8	-7.8	-8.8	51	-17.7	-17.2	-16.2	-17.3
1	-11.1	-10.6	-9.6	-10.7	52	-16.5	-16.1	-15.1	-16.1
2	-13.7	-13.2	-12.2	-13.3	53	-17.5	-17.1	-16	-17.1
3	-15.5	-15.1	-14	-15.1	54	-16.3	-15.9	-14.8	-15.9
4	-16.6	-16.2	-15.1	-16.2	55	-16.2	-15.8	-14.7	-15.8
5	-17.9	-17.4	-16.4	-17.5	56	-16.3	-15.8	-14.8	-15.9
6	-18.2	-17.8	-16.7	-17.8	57	-16.2	-15.7	-14.7	-15.8
7	-18.5	-18.1	-17	-18.1	58	-17	-16.5	-15.5	-16.6
8	-18.9	-18.5	-17.4	-18.5	59	-15.6	-15.2	-14.1	-15.2
9	-18.9	-18.5	-17.5	-18.6	60	-15.9	-15.4	-14.4	-15.5
10	-18.7	-18.2	-17.2	-18.3	61	-16.5	-16	-15	-16.1
11	-18	-17.5	-16.5	-17.6	62	-16.7	-16.3	-15.2	-16.3
12	-17.6	-17.2	-16.1	-17.2	63	-17.2	-16.8	-15.7	-16.8
13	-17.8	-17.3	-16.3	-17.4	64	-17.6	-17.2	-16.1	-17.2
14	-18	-17.6	-16.5	-17.6	65	-17.9	-17.5	-16.4	-17.5
15	-17.9	-17.4	-16.4	-17.5	66	-16.4	-15.9	-14.9	-16
16	-18.3	-17.8	-16.8	-17.9	67	-17.7	-17.2	-16.2	-17.3
17	-18.5	-18.1	-17	-18.1	68	-17.1	-16.7	-15.7	-16.7
18	-18	-17.6	-16.5	-17.6	69	-17.8	-17.4	-16.3	-17.4
19	-18.7	-18.3	-17.2	-18.3	70	-16.3	-15.9	-14.8	-15.9
20	-18.3	-17.8	-16.8	-17.9	71	-15.7	-15.2	-14.2	-15.3
21	-18.4	-17.9	-16.9	-18	72	-14.5	-14.1	-13	-14.1
22	-18.7	-18.2	-17.2	-18.3	73	-14.5	-14.1	-13	-14.1
23	-18.6	-18.1	-17.1	-18.2	74	-14.9	-14.5	-13.4	-14.5
24	-19.1	-18.6	-17.6	-18.7	75	-14.7	-14.2	-13.2	-14.3
25	-19.2	-18.8	-17.7	-18.8	76	-14.1	-13.6	-12.6	-13.7
26	-19.8	-19.3	-18.3	-19.4	77	-13.3	-12.8	-11.8	-12.9
27	-20.4	-20	-18.9	-20	78	-13.1	-12.6	-11.6	-12.7
28	-19.9	-19.4	-18.4	-19.5	79	-13.2	-12.7	-11.7	-12.8
29	-20.3	-19.8	-18.8	-19.9	80	-12	-11.6	-10.5	-11.6
30	-20.6	-20.1	-19.1	-20.2	81	-12.7	-12.2	-11.2	-12.3
31	-19.7	-19.3	-18.2	-19.3	82	-12.9	-12.5	-11.4	-12.5
32	-18.7	-18.2	-17.2	-18.3	83	-14	-13.5	-12.5	-13.6
33	-18.9	-18.5	-17.4	-18.5	84	-14.1	-13.6	-12.6	-13.7
34	-18.2	-17.7	-16.7	-17.8	85	-13.2	-12.8	-11.7	-12.8
35	-18	-17.5	-16.5	-17.6	86	-14.7	-14.3	-13.2	-14.3
36	-17.8	-17.3	-16.3	-17.4	87	-13.4	-12.9	-11.9	-13
37	-17.6	-17.1	-16.1	-17.2	88	-12.4	-11.9	-10.9	-12
38	-18.2	-17.7	-16.7	-17.8	89	-12.5	-12	-11	-12.1
39	-17.4	-17	-15.9	-17	90	-12.2	-11.8	-10.7	-11.8
40	-16.9	-16.4	-15.4	-16.5	91	-12	-11.6	-10.5	-11.6
41	-16.7	-16.2	-15.2	-16.3	92	-11.1	-10.7	-9.6	-10.7
42	-17.2	-16.8	-15.7	-16.8	93	-9.1	-8.6	-7.6	-8.7
43	-16.3	-15.9	-14.8	-15.9	94	-9	-8.6	-7.5	-8.6
44	-16.5	-16	-15	-16.1	95	-7	-6.5	-5.5	-6.6
45	-16.6	-16.2	-15.1	-16.2	96	-5.6	-5.1	-4.1	-5.2
46	-16.3	-15.8	-14.8	-15.9	97	-2.8	-2.4	-1.3	-2.4
47	-17.2	-16.8	-15.7	-16.8	98	-0.4	0.1	1.1	0
48	-17.9	-17.5	-16.4	-17.5	99	1.6	2	3.1	2
49	-18.1	-17.6	-16.6	-17.7	99.5	1.3	1.8	2.8	1.7
50	-16.8	-16.3	-15.3	-16.4					

Table H11. Section criteria results in the first data set of MLR models for cumulative boiling point distribution fractions.

% Off (wt.%)	AIC	AICc	AICu	BIC	% Off (wt.%)	AIC	AICc	AICu	BIC
0.5	-14.7	-14.3	-12.2	-11.6	51				
1	-15.9	-15.5	-13.4	-12.8	52				
2	-12.7	-12.3	-10.2	-9.6	53				
3	-10.5	-10.1	-8.1	-7.5	54				
4	-12.1	-11.3	-8.2	-7.5	55				
5	-11.7	-10.9	-7.8	-7.1	56				
6	-11.5	-10.7	-7.6	-6.9	57				
7	-11.3	-10.5	-7.4	-6.7	58				
8	-11.1	-10.3	-7.1	-6.5	59				
9	-11.1	-10.3	-7.2	-6.5	60				
10	-11.1	-10.3	-7.1	-6.5	61				
11	-11.1	-10.3	-7.1	-6.5	62				
12	-10.8	-10	-6.9	-6.3	63				
13	-10.4	-9.6	-6.5	-5.9	64				
14	-10.2	-9.4	-6.3	-5.7	65				
15	-10	-9.2	-6	-5.4	66				
16	-9.8	-9	-5.9	-5.3	67				
17	-9.8	-9	-5.8	-5.2	68				
18					69				
19	-9.8	-9	-5.9	-5.2	70				
20	-10.1	-9.3	-6.2	-5.6	71				
21					72				
22	-10.2	-9.4	-6.3	-5.6	73				
23					74				
24					75				
25					76				
26					77				
27					78				
28					79				
29					80				
30					81				
31					82				
32					83				
33					84				
34					85				
35					86				
36					87				
37					88				
38					89				
39					90				
40					91				
41					92				
42					93				
43					94				
44					95	-29.1	-28.3	-25.2	-24.6
45					96				
46					97	-14.3	-13.9	-11.8	-11.2
47					98	-14.6	-14.2	-12.2	-11.6
48					99				
49					99.5				
50									

Table H12. Section criteria results in the second data set of MLR models for cumulative boiling point distribution fractions.

% Off (wt.%)	AIC	AICc	AICu	BIC	% Off (wt.%)	AIC	AICc	AICu	BIC
0.5	-37.3	-35.3	-31	-32.5	51	-48.8	-46.8	-42.4	-43.9
1	-43	-41.9	-38.7	-39.4	52	-49	-47	-42.6	-44.1
2	-49.6	-48.5	-45.3	-45.9	53	-48.6	-46.6	-42.2	-43.7
3	-14.4	-13.8	-11.7	-11.9	54	-19.3	-18.8	-16.7	-16.9
4	-47.1	-45.1	-40.8	-42.2	55	-19	-18.4	-16.4	-16.5
5	-47.8	-45.8	-41.4	-42.9	56	-19	-18.4	-16.4	-16.5
6	-47.7	-45.7	-41.4	-42.8	57	-883	221	284.1	-855
7	-48.2	-46.2	-41.9	-43.4	58	-49.3	-47.3	-43	-44.4
8	-49.6	-47.6	-43.3	-44.8	59	-47.9	-45.9	-41.5	-43
9	-49	-47	-42.7	-44.2	60	-48.5	-46.5	-42.1	-43.6
10	-48.6	-46.6	-42.3	-43.7	61	-50.2	-48.2	-43.9	-45.4
11	-46.8	-44.8	-40.5	-41.9	62	-47.7	-45.7	-41.3	-42.8
12	-47.3	-45.3	-41	-42.4	63	-48.1	-46.1	-41.7	-43.2
13	-47.7	-45.7	-41.3	-42.8	64	-49.7	-47.7	-43.3	-44.8
14	-47.7	-45.7	-41.4	-42.9	65	-51.2	-49.2	-44.8	-46.3
15	-47.9	-45.9	-41.6	-43.1	66	-49.3	-47.3	-42.9	-44.4
16	-48.5	-46.5	-42.2	-43.7	67	-49.3	-47.3	-42.9	-44.4
17	-48.1	-46.1	-41.8	-43.3	68	-48.7	-46.7	-42.4	-43.9
18	-47.3	-45.3	-40.9	-42.4	69	-50.5	-48.5	-44.1	-45.6
19	-47.7	-45.7	-41.4	-42.8	70	-49.1	-47.1	-42.8	-44.3
20	-48	-46	-41.7	-43.1	71	-21.2	-20.7	-18.6	-18.8
21	-48.8	-46.8	-42.5	-44	72	-16.8	-16.6	-15.6	-15.6
22	-47.3	-45.3	-41	-42.5	73	-16.4	-16.3	-15.2	-15.2
23	-46.8	-44.8	-40.4	-41.9	74	-20.7	-20.1	-18.1	-18.2
24	-47.8	-45.8	-41.4	-42.9	75	-17.8	-17.7	-16.6	-16.6
25	-48.1	-46.1	-41.8	-43.2	76	-17.6	-17.4	-16.4	-16.4
26	-49	-47	-42.6	-44.1	77	-21	-20.4	-18.4	-18.5
27	-49.3	-47.3	-42.9	-44.4	78	-21.4	-20.9	-18.8	-19
28	-50.4	-48.4	-44	-45.5	79	-21.2	-20.6	-18.5	-18.7
29	-50.4	-48.4	-44	-45.5	80	-20.7	-20.1	-18.1	-18.3
30	-49.8	-47.8	-43.4	-44.9	81	-20	-19.4	-17.4	-17.6
31	-49.2	-47.2	-42.8	-44.3	82	-21.2	-20.7	-18.6	-18.8
32	-49.7	-47.7	-43.3	-44.8	83	-50.7	-48.7	-44.3	-45.8
33	-47.9	-45.9	-41.5	-43	84	-20.9	-20.3	-18.2	-18.4
34	-48.3	-46.3	-41.9	-43.4	85	-50.4	-48.4	-44	-45.5
35	-48.5	-46.5	-42.1	-43.6	86	-50.4	-48.4	-44	-45.5
36	-48.9	-46.9	-42.5	-44	87	-50.7	-48.7	-44.4	-45.9
37	-48.7	-46.7	-42.4	-43.8	88	-21	-20.4	-18.3	-18.5
38	-48.6	-46.6	-42.2	-43.7	89	-21.9	-21.3	-19.2	-19.4
39	-49.1	-47.1	-42.7	-44.2	90	-21.9	-21.3	-19.2	-19.4
40	-48.4	-46.4	-42.1	-43.5	91	-22.1	-21.6	-19.5	-19.7
41	-49.1	-47.1	-42.7	-44.2	92	-17.6	-17.4	-16.4	-16.4
42	-47.2	-45.2	-40.9	-42.4	93	-18.3	-18.1	-17.1	-17.1
43	-50.2	-47	-41.5	-44.1	94	-105	-89.2	-76.5	-92.8
44	-18.6	-18	-15.9	-16.1	95	-44.3	-42.3	-38	-39.5
45	-50.3	-48.3	-43.9	-45.4	96	-18.1	-18	-16.9	-16.9
46	-48.1	-46.1	-41.7	-43.2	97	-39.3	-37.3	-33	-34.5
47	-18.8	-18.3	-16.2	-16.4	98	-34.7	-33.5	-30.3	-31
48	-48.5	-46.5	-42.1	-43.6	99	-12.1	-11.5	-9.5	-9.6
49	-49.5	-47.5	-43.2	-44.7	99.5				
50	-19.6	-19.1	-17	-17.2					

Table H13. Section criteria results in the third data set of MLR models for cumulative boiling point distribution fractions.

% Off (wt.%)	AIC	AICc	AICu	BIC	% Off (wt.%)	AIC	AICc	AICu	BIC
0.5	-58.5	-46.5	-38.7	-54.7	51	-51.9	-47.4	-42.7	-49.3
1	-31.5	-30.4	-28.3	-30.2	52	-55.8	-51.4	-46.7	-53.3
2	-84.2	-65.6	-55.9	-79.8	53	-58.8	-51.3	-45.1	-55.6
3	-48.3	-45.9	-42.5	-46.4	54	-61.8	-54.3	-48.1	-58.6
4	-47.4	-45	-41.6	-45.5	55	-56.2	-51.7	-47	-53.6
5	-51.5	-47	-42.3	-48.9	56	-49.3	-46.9	-43.5	-47.3
6	-47.3	-44.9	-41.5	-45.3	57	-387	-75	-47.7	-379.3
7	-45.3	-42.9	-39.5	-43.4	58	-58.4	-53.9	-49.2	-55.8
8	-44.9	-42.5	-39.2	-43	59	-59.8	-52.3	-46.1	-56.6
9	-46.3	-43.9	-40.5	-44.4	60	-47	-44.6	-41.2	-45.1
10	-46.6	-44.2	-40.8	-44.7	61	-96.8	-78.1	-68.4	-92.3
11	-48.5	-46.1	-42.7	-46.6	62	-51.1	-46.6	-41.9	-48.5
12	-51.7	-49.3	-45.9	-49.8	63	-55.3	-50.8	-46.1	-52.7
13	-92	-73.3	-63.6	-87.5	64	-56.2	-51.7	-47	-53.6
14	-55.7	-51.3	-46.6	-53.1	65	-58.3	-53.9	-49.2	-55.8
15	-57.1	-52.7	-48	-54.6	66	-46.2	-43.8	-40.4	-44.3
16	-64.4	-56.9	-50.7	-61.2	67	-54.7	-50.3	-45.6	-52.2
17	-54.4	-49.9	-45.2	-51.8	68	-47.8	-43.4	-38.7	-45.3
18	-55.7	-51.3	-46.5	-53.1	69	-50.6	-46.2	-41.5	-48.1
19	-57.8	-53.3	-48.6	-55.2	70	-50.6	-46.2	-41.5	-48.1
20	-386.8	-74.8	-47.5	-379.1	71	-49.3	-44.9	-40.2	-46.8
21	-55.3	-50.9	-46.2	-52.8	72	-48.3	-45.9	-42.6	-46.4
22	-49.7	-47.3	-43.9	-47.8	73	-69	-61.5	-55.3	-65.8
23	-51.2	-48.8	-45.4	-49.3	74	-112.9	-84.1	-72.3	-107.8
24	-50.2	-47.8	-44.4	-48.3	75	-71.3	-59.3	-51.5	-67.5
25	-47.9	-45.5	-42.1	-46	76	-61.8	-54.3	-48.1	-58.6
26	-48.1	-45.7	-42.3	-46.2	77	-40.3	-39.2	-37.1	-39
27	-57.7	-50.2	-44	-54.5	78	-63.2	-58.7	-54	-60.6
28	-50.5	-46.1	-41.3	-47.9	79	-76.5	-69	-62.8	-73.3
29	-98	-69.2	-57.3	-92.9	80	-71.3	-63.8	-57.6	-68.1
30	-57.2	-49.7	-43.5	-54	81	-442.9	-130.9	-103.7	-435.3
31	-49.5	-45.1	-40.4	-47	82	-52.4	-48	-43.3	-49.9
32	-50.7	-46.3	-41.6	-48.2	83	-58.6	-54.1	-49.4	-56
33	-52.1	-47.7	-43	-49.6	84	-47.5	-45.1	-41.7	-45.6
34	-71.2	-59.2	-51.4	-67.4	85	-46.4	-44	-40.6	-44.5
35	-49.8	-47.4	-44	-47.8	86	-49.4	-44.9	-40.2	-46.8
36	-54.4	-50	-45.3	-51.9	87	-47.5	-43.1	-38.4	-45
37	-236.4	-104.4	-82.9	-229.4	88	-41.7	-39.3	-36	-39.8
38	-60.2	-52.7	-46.5	-57	89	-44.9	-42.5	-39.1	-42.9
39	-52.8	-48.4	-43.6	-50.2	90	-42.9	-40.5	-37.1	-41
40	-55.9	-51.4	-46.7	-53.3	91	-43.9	-41.5	-38.1	-41.9
41	-50.8	-48.4	-45	-48.9	92	-350.4	-38.4	-11.2	-342.7
42	-56.3	-51.9	-47.1	-53.7	93	-69.8	-57.8	-50	-66
43	-56.6	-52.1	-47.4	-54	94	-41.1	-40	-37.8	-39.8
44	-63.4	-58.9	-54.2	-60.8	95	-46.2	-45.1	-43	-45
45	-68.4	-63.9	-59.2	-65.8	96	-39.4	-38.3	-36.1	-38.1
46	-62.6	-55.1	-48.9	-59.4	97	-41.8	-39.4	-36	-39.9
47	-58.1	-53.7	-49	-55.6	98	-38.8	-36.4	-33	-36.9
48	-58.8	-54.3	-49.6	-56.2	99	-23.2	-22.2	-20	-22
49	-62	-54.5	-48.3	-58.8	99.5	-20.9	-19.8	-17.6	-19.6
50	-61.8	-57.3	-52.6	-59.2					

Table H14. Section criteria results in the fourth data set of MLR models for cumulative boiling point distribution fractions.

% Off (wt.%)	AIC	AICc	AICu	BIC	% Off (wt.%)	AIC	AICc	AICu	BIC
0.5	-9.2	-8.8	-7.8	-8.8	51	-22.6	-21.1	-18.9	-21.8
1	-11.1	-10.6	-9.6	-10.7	52	-22	-20.5	-18.2	-21.2
2	-13.7	-13.2	-12.2	-13.3	53	-23.4	-21.9	-19.6	-22.6
3	-15.5	-15.1	-14	-15.1	54	-22.4	-20.9	-18.7	-21.6
4	-16.6	-16.2	-15.1	-16.2	55	-20.5	-19	-16.8	-19.7
5	-17.9	-17.4	-16.4	-17.5	56	-21.8	-20.3	-18.1	-21
6	-18.2	-17.8	-16.7	-17.8	57	-21.7	-20.2	-17.9	-20.9
7	-18.5	-18.1	-17	-18.1	58	-21.7	-20.2	-18	-20.9
8	-23.4	-21.9	-19.7	-22.6	59	-20.8	-19.3	-17.1	-20
9	-23.2	-21.7	-19.5	-22.4	60	-22.3	-20.8	-18.6	-21.5
10	-22.7	-21.2	-19	-21.9	61	-21.9	-20.4	-18.2	-21.1
11	-21.9	-20.4	-18.2	-21.1	62	-21.6	-20.1	-17.9	-20.8
12	-21.3	-19.8	-17.6	-20.5	63	-22.1	-20.6	-18.4	-21.3
13	-22.1	-20.6	-18.4	-21.3	64	-21.9	-20.4	-18.2	-21.1
14	-21.8	-20.3	-18.1	-21	65	-28.2	-24.8	-21.3	-27.1
15	-21.8	-20.3	-18.1	-21	66	-20.9	-19.4	-17.2	-20.2
16	-22.3	-20.8	-18.6	-21.5	67	-23.8	-22.3	-20.1	-23
17	-22.5	-21	-18.8	-21.7	68	-23.4	-21.9	-19.7	-22.6
18	-22	-20.5	-18.3	-21.2	69	-23.1	-21.6	-19.4	-22.3
19	-22.8	-21.3	-19.1	-22	70	-20.6	-19.1	-16.8	-19.8
20	-22.8	-21.3	-19.1	-22	71	-21.6	-20.1	-17.9	-20.8
21	-22.1	-20.6	-18.4	-21.3	72	-20.7	-19.2	-17	-20
22	-18.7	-18.2	-17.2	-18.3	73	-20.3	-18.8	-16.6	-19.5
23	-18.6	-18.1	-17.1	-18.2	74	-21.2	-19.7	-17.5	-20.4
24	-19.1	-18.6	-17.6	-18.7	75	-20.6	-19.1	-16.8	-19.8
25	-19.2	-18.8	-17.7	-18.8	76	-20.3	-18.8	-16.6	-19.5
26	-23.7	-22.2	-20	-22.9	77	-309.9	-129.9	-111.2	-306.3
27	-24.1	-22.6	-20.4	-23.3	78	-18.7	-17.2	-15	-17.9
28	-24.3	-22.8	-20.6	-23.6	79	-18.7	-17.2	-15	-17.9
29	-25.1	-23.6	-21.4	-24.3	80	-18.3	-16.8	-14.6	-17.5
30	-26	-24.5	-22.3	-25.2	81	-20.4	-18.9	-16.7	-19.6
31	-25.7	-24.2	-22	-24.9	82	-21.1	-19.6	-17.3	-20.3
32	-24.3	-22.8	-20.6	-23.5	83	-21.3	-19.8	-17.6	-20.5
33	-24.1	-22.6	-20.4	-23.3	84	-21.4	-19.9	-17.7	-20.6
34	-23.6	-22.1	-19.9	-22.8	85	-18.3	-16.8	-14.6	-17.5
35	-23.6	-22.1	-19.9	-22.8	86	-20.5	-19	-16.8	-19.7
36	-24.1	-22.6	-20.4	-23.3	87	-19.1	-17.6	-15.4	-18.3
37	-23.3	-21.8	-19.6	-22.5	88	-17.4	-15.9	-13.7	-16.6
38	-23.6	-22.1	-19.9	-22.8	89	-17.7	-16.2	-14	-16.9
39	-23.5	-22	-19.8	-22.7	90	-18.5	-17	-14.8	-17.7
40	-22.5	-21	-18.8	-21.7	91	-50.9	-38.9	-32.3	-48.9
41	-21.7	-20.2	-18	-20.9	92	-48.5	-36.5	-29.8	-46.5
42	-22.7	-21.2	-19	-21.9	93	-203.4	-23.4	-4.7	-199.8
43	-20.7	-19.2	-17	-19.9	94	-43	-36.4	-31.4	-41.4
44	-21.2	-19.7	-17.5	-20.4	95	-27.8	-21.1	-16.1	-26.2
45	-21.3	-19.8	-17.6	-20.5	96	-5.6	-5.1	-4.1	-5.2
46	-20.7	-19.2	-17	-19.9	97				
47	-22.3	-20.8	-18.6	-21.5	98				
48	-22.9	-21.4	-19.2	-22.1	99				
49	-23.5	-22	-19.8	-22.7	99.5				
50	-21.5	-20	-17.8	-20.7					

Table H15. Section criteria results in the first data set of PCR models for cumulative boiling point distribution fractions.

% Off (wt.%)	AIC	AICc	AICu	BIC	% Off (wt.%)	AIC	AICc	AICu	BIC
0.5	-21.1	-13.6	-3.1	-7.3	51	-29.4	-25.1	-17.2	-18.7
1	-31.5	-25.7	-16.6	-19.3	52	-29.4	-25.1	-17.3	-18.7
2	-33.4	-27.6	-18.5	-21.2	53	-55.3	-45.7	-33.9	-40
3	-44.1	-34.5	-22.6	-28.8	54	-30.1	-25.8	-18	-19.4
4	-46.2	-36.7	-24.8	-31	55	-52.8	-43.3	-31.4	-37.6
5	-47.3	-37.8	-25.9	-32.1	56	-53.5	-43.9	-32.1	-38.2
6	-49.4	-39.9	-28	-34.2	57	-55.7	-46.1	-34.3	-40.4
7	-50.4	-40.8	-29	-35.1	58	-27.8	-23.5	-15.6	-17.1
8	-30.2	-25.9	-18	-19.5	59	-28.2	-23.9	-16.1	-17.5
9	-29.7	-25.4	-17.6	-19.1	60	-53	-43.4	-31.6	-37.7
10	-29.8	-25.5	-17.7	-19.2	61	-27.9	-23.6	-15.7	-17.2
11	-52.1	-42.5	-30.7	-36.8	62	-26.9	-22.6	-14.8	-16.3
12	-29.4	-25.1	-17.3	-18.7	63	-26.2	-21.9	-14	-15.5
13	-28.9	-24.6	-16.7	-18.2	64	-53.6	-44	-32.2	-38.3
14	-28.4	-24.1	-16.2	-17.7	65	-26.6	-22.3	-14.4	-15.9
15	-51.5	-41.9	-30.1	-36.2	66	-55.2	-45.7	-33.8	-40
16	-28	-23.7	-15.8	-17.3	67	-27.4	-23.1	-15.3	-16.7
17	-27.4	-23.1	-15.3	-16.7	68	-55.1	-45.5	-33.7	-39.8
18	-27.5	-23.2	-15.4	-16.9	69	-29.2	-24.9	-17.1	-18.5
19	-27.7	-23.4	-15.5	-17	70	-28.8	-24.5	-16.7	-18.1
20	-28	-23.7	-15.9	-17.3	71	-29.3	-25	-17.1	-18.6
21	-52.7	-43.1	-31.3	-37.4	72	-59.7	-50.1	-38.2	-44.4
22	-26.8	-22.5	-14.6	-16.1	73	-29.6	-25.3	-17.4	-18.9
23	-52.1	-42.5	-30.7	-36.8	74	-58.8	-49.3	-37.4	-43.6
24	-26.5	-22.2	-14.4	-15.8	75	-58.5	-49	-37.1	-43.3
25	-26.3	-22	-14.2	-15.6	76	-53.6	-44.1	-32.2	-38.4
26	-52.6	-43	-31.1	-37.3	77	-55.9	-46.3	-34.5	-40.6
27	-53.2	-43.6	-31.8	-37.9	78	-55.4	-45.8	-34	-40.1
28	-54.3	-44.7	-32.8	-39	79	-30.6	-26.3	-18.5	-20
29	-28.7	-24.4	-16.6	-18	80	-54.3	-44.8	-32.9	-39.1
30	-55.5	-45.9	-34.1	-40.2	81	-54.8	-45.2	-33.4	-39.5
31	-28.9	-24.6	-16.8	-18.3	82	-53.5	-43.9	-32.1	-38.2
32	-25	-21.9	-15.3	-15.8	83	-53.5	-43.9	-32.1	-38.2
33	-28.6	-24.3	-16.5	-17.9	84	-27.4	-23.1	-15.2	-16.7
34	-55.8	-46.2	-34.4	-40.5	85	-26.7	-22.3	-14.5	-16
35	-28.6	-24.3	-16.5	-17.9	86	-53.1	-43.5	-31.7	-37.8
36	-29.5	-25.2	-17.3	-18.8	87	-23.8	-20.7	-14.1	-14.6
37	-28.8	-24.5	-16.7	-18.2	88	-29.1	-24.8	-17	-18.4
38	-55.7	-46.1	-34.3	-40.4	89	-23.4	-20.3	-13.7	-14.3
39	-29.2	-24.9	-17.1	-18.5	90	-53	-43.4	-31.6	-37.7
40	-55.8	-46.2	-34.4	-40.5	91	-23.7	-20.6	-14	-14.5
41	-54.9	-45.3	-33.4	-39.6	92	-29.9	-25.6	-17.8	-19.2
42	-54.3	-44.8	-32.9	-39.1	93	-48.9	-39.4	-27.5	-33.7
43	-53.9	-44.3	-32.4	-38.6	94	-47.5	-37.9	-26.1	-32.3
44	-53.9	-44.4	-32.5	-38.7	95	-41.3	-31.8	-19.9	-26.1
45	-28.1	-23.8	-16	-17.5	96	-24.7	-20.4	-12.5	-14
46	-28.4	-24.1	-16.3	-17.7	97	-17.5	-14.4	-7.8	-8.3
47	-54	-44.4	-32.6	-38.7	98	-12.3	-9.1	-2.5	-3.1
48	-28.8	-24.4	-16.6	-18.1	99	-0.2	-0.1	0.9	1.3
49	-54.6	-45.1	-33.2	-39.4	99.5	1.5	1.6	2.6	3
50	-29.3	-25	-17.1	-18.6					

Table H16. Section criteria results in the second data set of PCR models for cumulative boiling point distribution fractions.

% Off (wt.%)	AIC	AICc	AICu	BIC	% Off (wt.%)	AIC	AICc	AICu	BIC
0.5	-9.3	-2.7	5.5	-0.7	51	-30.2	-27	-21.4	-24.1
1	-18.3	-15.1	-9.5	-12.2	52	-30.2	-27	-21.5	-24.1
2	-20.5	-15.8	-9	-13.2	53	-30.1	-27	-21.4	-24.1
3	-23.6	-20.4	-14.9	-17.5	54	-30.7	-27.6	-22	-24.6
4	-22	-17.4	-10.5	-14.7	55	-26.2	-21.5	-14.6	-18.9
5	-24.3	-21.1	-15.6	-18.2	56	-28.8	-25.6	-20	-22.7
6	-24.6	-21.4	-15.8	-18.5	57	-30.3	-27.2	-21.6	-24.2
7	-25.5	-9.8	3	-13.3	58	-28.9	-25.7	-20.1	-22.8
8	-24	-19.3	-12.5	-16.7	59	-29.2	-26	-20.5	-23.1
9	-26	-22.8	-17.2	-19.9	60	-27.6	-23	-16.1	-20.3
10	-10	-9.8	-8.8	-8.8	61	-29.5	-26.4	-20.8	-23.4
11	-25.9	-22.7	-17.1	-19.8	62	-27.1	-22.5	-15.6	-19.8
12	-26.8	-23.6	-18	-20.7	63	-27.9	-24.8	-19.2	-21.8
13	-26.9	-23.7	-18.2	-20.8	64	-28.5	-25.3	-19.8	-22.4
14	-26.8	-23.7	-18.1	-20.7	65	-29.2	-26.1	-20.5	-23.1
15	-26.4	-23.2	-17.7	-20.3	66	-28.8	-25.6	-20.1	-22.7
16	-26.5	-23.3	-17.7	-20.4	67	-27.2	-22.5	-15.6	-19.8
17	-26.4	-23.2	-17.6	-20.3	68	-30.1	-26.9	-21.3	-24
18	-26.5	-23.4	-17.8	-20.4	69	-29.6	-25	-18.1	-22.3
19	-26.4	-23.3	-17.7	-20.3	70	-30.5	-27.4	-21.8	-24.4
20	-25	-20.4	-13.5	-17.7	71	-32.4	-29.2	-23.7	-26.3
21	-26.5	-23.3	-17.7	-20.4	72	-32.6	-29.4	-23.8	-26.5
22	-25.4	-22.2	-16.7	-19.3	73	-15	-14.8	-13.8	-13.8
23	-25.6	-22.4	-16.9	-19.5	74	-34.2	-31	-25.4	-28.1
24	-25.8	-22.7	-17.1	-19.7	75	-33.2	-30	-24.4	-27.1
25	-23.2	-18.5	-11.7	-15.9	76	-30.7	-27.5	-21.9	-24.6
26	-23.7	-19	-12.1	-16.3	77	-32.1	-28.9	-23.3	-26
27	-26	-22.9	-17.3	-19.9	78	-32.5	-29.3	-23.8	-26.4
28	-27.2	-24.1	-18.5	-21.2	79	-32.9	-29.8	-24.2	-26.8
29	-27.3	-24.2	-18.6	-21.2	80	-32.1	-28.9	-23.3	-26
30	-27.4	-24.2	-18.7	-21.3	81	-32.4	-29.2	-23.6	-26.3
31	-28.3	-25.1	-19.5	-22.2	82	-31.4	-28.2	-22.7	-25.3
32	-29.1	-25.9	-20.3	-23	83	-31.6	-28.4	-22.8	-25.5
33	-28.3	-25.1	-19.5	-22.2	84	-31	-27.8	-22.2	-24.9
34	-26.5	-21.8	-14.9	-19.1	85	-30.5	-27.4	-21.8	-24.4
35	-28.8	-25.6	-20	-22.7	86	-31.2	-28	-22.5	-25.1
36	-27.2	-22.6	-15.7	-19.9	87	-27.9	-21.4	-13.1	-19.4
37	-29.3	-26.2	-20.6	-23.2	88	-31.7	-28.5	-23	-25.6
38	-29.5	-26.4	-20.8	-23.4	89	-32	-28.8	-23.2	-25.9
39	-29.7	-26.5	-21	-23.6	90	-32.5	-29.3	-23.7	-26.4
40	-29.8	-26.6	-21	-23.7	91	-32.1	-28.9	-23.4	-26
41	-29.1	-26	-20.4	-23.1	92	-30.8	-26.1	-19.3	-23.5
42	-28.6	-25.5	-19.9	-22.5	93	-31.5	-28.3	-22.7	-25.4
43	-28.4	-25.2	-19.6	-22.3	94	-33.6	-30.4	-24.9	-27.5
44	-28.6	-25.5	-19.9	-22.5	95	-30.3	-27.1	-21.5	-24.2
45	-29.5	-26.4	-20.8	-23.4	96	-27	-23.9	-18.3	-21
46	-28.9	-25.7	-20.2	-22.8	97	-22	-17.3	-10.5	-14.7
47	-29	-25.8	-20.3	-22.9	98	-17.9	-16.7	-13.5	-14.2
48	-29.4	-26.2	-20.6	-23.3	99	-1.2	-0.6	1.4	1.2
49	-29.3	-26.2	-20.6	-23.2	99.5	1.7	1.8	2.9	2.9
50	-29.9	-26.7	-21.1	-23.8					

Table H17. Section criteria results in the third data set of PCR models for cumulative boiling point distribution fractions.

% Off (wt.%)	AIC	AICᴄ	AICᵤ	BIC	% Off (wt.%)	AIC	AICᴄ	AICᵤ	BIC
0.5	-17.7	-17.3	-16.3	-17	51	-37.8	-25.8	-17.9	-33.9
1	-30.8	-12.1	-2.4	-26.3	52	-39.1	-20.5	-10.8	-34.7
2	-36.1	-28.6	-22.5	-32.9	53	-38.3	-26.3	-18.5	-34.5
3	-38	-26	-18.1	-34.1	54	-42.2	-30.2	-22.3	-38.3
4	-37.7	-25.7	-17.8	-33.8	55	-40.5	-21.9	-12.2	-36.1
5	-37.9	-25.9	-18.1	-34.1	56	-39.6	-27.6	-19.7	-35.7
6	-37.9	-25.9	-18.1	-34.1	57	-38.1	-26.1	-18.2	-34.2
7	-36.6	-24.6	-16.8	-32.8	58	-31.7	-27.2	-22.5	-29.1
8	-36.7	-24.7	-16.8	-32.8	59	-36.7	-24.7	-16.8	-32.8
9	-37.5	-25.5	-17.7	-33.7	60	-36.4	-24.4	-16.6	-32.6
10	-38.1	-26.1	-18.3	-34.3	61	-32.5	-25	-18.8	-29.3
11	-39.4	-27.4	-19.6	-35.6	62	-37.3	-25.3	-17.4	-33.4
12	-41.8	-29.8	-22	-38	63	-38.3	-26.3	-18.5	-34.5
13	-41.6	-29.6	-21.8	-37.8	64	-41.2	-12.4	-0.5	-36.1
14	-41.4	-29.4	-21.6	-37.6	65	-36.2	-24.2	-16.3	-32.3
15	-40.8	-28.8	-20.9	-37	66	-37.4	-25.4	-17.6	-33.6
16	-39.2	-27.2	-19.4	-35.4	67	-33.6	-21.6	-13.7	-29.7
17	-39.4	-27.4	-19.6	-35.6	68	-34	-22	-14.2	-30.2
18	-39.1	-27.1	-19.3	-35.3	69	-37.6	-25.6	-17.8	-33.8
19	-28.9	-24.5	-19.8	-26.4	70	-35.1	-23.1	-15.2	-31.2
20	-39.6	-27.6	-19.8	-35.8	71	-35.6	-23.6	-15.7	-31.7
21	-39.6	-27.6	-19.7	-35.7	72	-37.5	-30	-23.8	-34.3
22	-39.1	-27.1	-19.3	-35.3	73	-37.9	-25.9	-18	-34
23	-39.1	-27.1	-19.3	-35.3	74	-40.6	-28.6	-20.8	-36.8
24	-40.3	-28.3	-20.5	-36.5	75	-37	-25	-17.2	-33.2
25	-37.8	-25.8	-17.9	-33.9	76	-36.9	-24.9	-17.1	-33.1
26	-38.6	-26.6	-18.8	-34.8	77	-34.5	-22.5	-14.7	-30.7
27	-36.6	-24.6	-16.8	-32.8	78	-39.2	-27.2	-19.4	-35.4
28	-36.6	-24.6	-16.8	-32.8	79	-39.3	-34.8	-30.1	-36.7
29	-37.3	-25.3	-17.5	-33.5	80	-40.2	-28.2	-20.3	-36.3
30	-38.4	-26.4	-18.6	-34.6	81	-42.4	-30.4	-22.5	-38.5
31	-37.2	-25.2	-17.3	-33.3	82	-37.2	-25.2	-17.4	-33.4
32	-38	-26	-18.1	-34.1	83	-35.7	-23.7	-15.9	-31.9
33	-38.4	-26.4	-18.5	-34.5	84	-36.5	-24.5	-16.6	-32.6
34	-39	-27	-19.1	-35.1	85	-36.3	-24.3	-16.5	-32.5
35	-39.2	-27.2	-19.4	-35.4	86	-37.8	7.2	21.7	-32
36	-40.8	-28.8	-21	-37	87	-32.5	-20.5	-12.7	-28.7
37	-39.2	-27.2	-19.4	-35.4	88	-33.9	-21.9	-14.1	-30.1
38	-40.4	-28.4	-20.6	-36.6	89	-34.9	-22.9	-15.1	-31.1
39	-33.6	-29.1	-24.4	-31	90	-34.2	-22.2	-14.4	-30.4
40	-40.2	-28.2	-20.4	-36.4	91	-29.6	-25.2	-20.5	-27.1
41	-40.3	-28.3	-20.5	-36.5	92	-34.8	-22.8	-14.9	-30.9
42	-34.3	-29.8	-25.1	-31.7	93	-32.8	-25.3	-19.1	-29.6
43	-39.7	-27.7	-19.9	-35.9	94	-36.4	-24.4	-16.6	-32.6
44	-40.1	-28.1	-20.2	-36.2	95	-39.4	-27.4	-19.6	-35.6
45	-40.1	-28.1	-20.3	-36.3	96	-32	-27.5	-22.8	-29.4
46	-38.7	-26.7	-18.9	-34.9	97	-45.4	-26.7	-17	-40.9
47	-39.4	-27.4	-19.5	-35.5	98	-41.8	-13	-1.1	-36.7
48	-39.7	-27.7	-19.8	-35.8	99	-38	-19.4	-9.6	-33.5
49	-37.9	-25.9	-18.1	-34.1	99.5	-10.6	-9.5	-7.4	-9.3
50	-38.1	-26.1	-18.3	-34.3					

Table H18. Section criteria results in the fourth data set of PCR models for cumulative boiling point distribution fractions.

% Off (wt.%)	AIC	AICc	AICu	BIC	% Off (wt.%)	AIC	AICc	AICu	BIC
0.5	-9.3	-2.6	2.4	-7.7	51	-18.1	-11.4	-6.4	-16.5
1	-10.6	-3.9	1.1	-9	52	-17.2	-10.5	-5.6	-15.6
2	-11.4	0.6	7.3	-9.4	53	-18.7	-12	-7	-17.1
3	-14.5	-7.8	-2.8	-12.9	54	-14.6	-14.1	-13.1	-14.2
4	-14.9	-14.5	-13.4	-14.5	55	-72.8	107.2	126	-69.2
5	-16.3	-4.3	2.4	-14.3	56	-78.7	101.3	120.1	-75.1
6	-16.3	-15.9	-14.8	-15.9	57	-16.8	-10.1	-5.1	-15.2
7	-16.5	-16	-15	-16.1	58	-17.7	-11.1	-6.1	-16.1
8	-16.8	-16.4	-15.3	-16.4	59	-72.2	107.8	126.5	-68.6
9	-19.8	-13.1	-8.1	-18.2	60	-163	17	35.7	-159.4
10	-19.4	-12.7	-7.7	-17.8	61	-17.4	-10.8	-5.8	-15.8
11	-16.1	-15.6	-14.6	-15.7	62	-27.8	9.5	20.6	-25.1
12	-17.3	-10.6	-5.6	-15.7	63	-17.3	-10.7	-5.7	-15.8
13	-16.2	-4.2	2.5	-14.2	64	-18.1	-11.4	-6.5	-16.5
14	-17.5	-10.8	-5.9	-15.9	65	-18.2	-11.6	-6.6	-16.6
15	-17.5	-10.8	-5.8	-15.9	66	-15.3	-3.3	3.4	-13.3
16	-18.1	-11.5	-6.5	-16.5	67	-19.9	-13.3	-8.3	-18.4
17	-18.2	-11.6	-6.6	-16.6	68	-19.8	-13.1	-8.1	-18.2
18	-16.2	-15.8	-14.7	-15.8	69	-21.7	-15	-10	-20.1
19	-18.7	-12	-7	-17.1	70	-19.9	-13.2	-8.2	-18.3
20	-18.3	-11.7	-6.7	-16.8	71	-19.6	-12.9	-7.9	-18
21	-18	-11.4	-6.4	-16.4	72	-84.1	95.9	114.7	-80.5
22	-17.9	-11.2	-6.3	-16.3	73	-67.3	112.7	131.4	-63.8
23	-16.8	-16.4	-15.3	-16.4	74	-18.2	-11.5	-6.6	-16.6
24	-17.2	-16.8	-15.7	-16.8	75	-64.5	115.5	134.3	-60.9
25	-17.4	-16.9	-15.9	-17	76	-170.3	9.7	28.5	-166.7
26	-18.5	-6.5	0.1	-16.6	77	-59.3	120.7	139.4	-55.7
27	-20.7	-14.1	-9.1	-19.1	78	-55.9	124.1	142.9	-52.3
28	-20.6	-13.9	-8.9	-19	79	-54.9	125.1	143.9	-51.3
29	-20.2	-8.2	-1.6	-18.3	80	-65.8	114.2	133	-62.2
30	-22.7	-16	-11.1	-21.1	81	-162.7	17.3	36.1	-159.1
31	-21.8	-15.2	-10.2	-20.2	82	-97.2	82.8	101.5	-93.6
32	-28.3	9	20.1	-25.5	83	-83.6	96.4	115.2	-80
33	-19	-7	-0.3	-17	84	-14.1	-7.5	-2.5	-12.5
34	-20.2	-13.5	-8.6	-18.6	85	-13.6	-6.9	-1.9	-12
35	-31.5	5.9	17	-28.7	86	-16	-9.3	-4.3	-14.4
36	-20.1	-13.4	-8.5	-18.5	87	-14.9	-8.2	-3.2	-13.3
37	-19	-12.3	-7.4	-17.4	88	-13.1	-1.1	5.6	-11.1
38	-19.3	-12.6	-7.6	-17.7	89	-15.1	-8.4	-3.5	-13.5
39	-19.3	-12.6	-7.6	-17.7	90	-13.5	-6.8	-1.9	-11.9
40	-17.7	-11	-6.1	-16.1	91	-13.4	-6.7	-1.7	-11.8
41	-17.8	-11.1	-6.1	-16.2	92	-11.8	-5.2	-0.2	-10.2
42	-18.5	-11.9	-6.9	-16.9	93	-9.3	-2.7	2.3	-7.7
43	-16.4	-9.7	-4.7	-14.8	94	-5.1	-1.7	1.8	-3.9
44	-16.4	-9.7	-4.7	-14.8	95	-6	-5.5	-4.5	-5.6
45	-16.7	-10	-5.1	-15.1	96	-4.7	-4.3	-3.2	-4.3
46	-76.9	103.1	121.8	-73.3	97	-2.2	-1.8	-0.7	-1.8
47	-27.9	9.4	20.5	-25.1	98	0	0.4	1.5	0.4
48	-16.1	-15.7	-14.6	-15.7	99	1.9	2.3	3.4	2.3
49	-19.3	-12.6	-7.6	-17.7	99.5	1.8	2.3	3.3	2.2
50	-17.1	-10.4	-5.5	-15.5					

Table H19. Section criteria results in the first data set of PLSR models for cumulative boiling point distribution fractions.

% Off (wt.%)	AIC	AIC$_C$	AIC$_U$	BIC	% Off (wt.%)	AIC	AIC$_C$	AIC$_U$	BIC
0.5	-24.9	-23.5	-19.2	-18.8	51	-73.6	-66.1	-55.6	-59.8
1	-41.9	-38.8	-32.2	-32.8	52	-74.2	-66.7	-56.3	-60.5
2	-53.9	-48.2	-39	-41.7	53	-73.2	-65.7	-55.2	-59.5
3	-56.6	-50.8	-41.7	-44.4	54	-69.9	-64.2	-55.1	-57.7
4	-58.6	-52.8	-43.7	-46.4	55	-70.4	-62.9	-52.5	-56.7
5	-59.7	-54	-44.9	-47.5	56	-67.7	-61.9	-52.8	-55.5
6	-61.9	-56.1	-47	-49.7	57	-73.8	-66.3	-55.8	-60
7	-62.5	-58.2	-50.3	-51.8	58	-68.7	-63	-53.9	-56.5
8	-66	-58.5	-48	-52.3	59	-72.5	-65	-54.6	-58.8
9	-65.6	-58.1	-47.6	-51.8	60	-68.1	-62.3	-53.2	-55.9
10	-64.9	-59.2	-50	-52.7	61	-73.1	-65.6	-55.1	-59.4
11	-66.1	-58.6	-48.2	-52.4	62	-67.9	-62.1	-53	-55.7
12	-67.5	-60	-49.5	-53.7	63	-70.5	-63	-52.5	-56.7
13	-67.4	-59.9	-49.4	-53.7	64	-67.6	-61.9	-52.7	-55.4
14	-65.1	-59.4	-50.2	-52.9	65	-72.6	-65.1	-54.6	-58.8
15	-66.2	-58.7	-48.3	-52.5	66	-71.4	-63.9	-53.4	-57.7
16	-64.7	-58.9	-49.8	-52.4	67	-72.5	-65	-54.6	-58.8
17	-66.4	-58.9	-48.4	-52.7	68	-73.6	-66.1	-55.6	-59.8
18	-67	-59.5	-49	-53.2	69	-77.4	-69.9	-59.4	-63.6
19	-65.6	-59.8	-50.7	-53.4	70	-69.9	-64.1	-55	-57.7
20	-68.3	-60.8	-50.4	-54.6	71	-79.9	-72.4	-62	-66.2
21	-67.3	-59.8	-49.4	-53.6	72	-74.7	-69	-59.8	-62.5
22	-65.6	-58.1	-47.7	-51.9	73	-78.3	-70.8	-60.3	-64.6
23	-66.2	-58.7	-48.2	-52.5	74	-75	-69.2	-60.1	-62.7
24	-65.5	-59.7	-50.6	-53.3	75	-74.4	-68.7	-59.5	-62.2
25	-64.3	-58.6	-49.5	-52.1	76	-69.8	-64	-54.9	-57.6
26	-67.1	-59.6	-49.1	-53.3	77	-79.7	-72.2	-61.8	-66
27	-66.1	-60.3	-51.2	-53.9	78	-72.9	-67.2	-58.1	-60.7
28	-69.7	-62.2	-51.8	-56	79	-77.6	-70.1	-59.7	-63.9
29	-70.4	-62.9	-52.4	-56.6	80	-70.8	-65	-55.9	-58.6
30	-70.9	-63.4	-53	-57.2	81	-70.7	-64.9	-55.8	-58.5
31	-71.7	-64.2	-53.7	-57.9	82	-69.3	-63.6	-54.4	-57.1
32	-73	-65.5	-55	-59.2	83	-70.3	-64.5	-55.4	-58
33	-71.6	-64.1	-53.7	-57.9	84	-69.4	-63.7	-54.6	-57.2
34	-69	-63.3	-54.2	-56.8	85	-67.9	-62.1	-53	-55.7
35	-70.7	-65	-55.9	-58.5	86	-69.3	-63.5	-54.4	-57.1
36	-73.2	-65.7	-55.2	-59.5	87	-69.8	-64	-54.9	-57.6
37	-69.8	-64.1	-55	-57.6	88	-75.5	-68	-57.6	-61.8
38	-69.9	-64.1	-55	-57.7	89	-76.1	-68.6	-58.2	-62.4
39	-69.4	-63.6	-54.5	-57.2	90	-74.6	-67.1	-56.6	-60.8
40	-69.9	-64.2	-55.1	-57.7	91	-73.3	-65.8	-55.3	-59.5
41	-68.9	-63.2	-54.1	-56.7	92	-73.4	-65.9	-55.4	-59.6
42	-68.4	-62.7	-53.6	-56.2	93	-70.7	-63.2	-52.8	-57
43	-67.7	-62	-52.9	-55.5	94	-70.1	-62.6	-52.2	-56.4
44	-67.5	-61.8	-52.6	-55.3	95	-58.7	-53	-43.8	-46.5
45	-69.6	-63.8	-54.7	-57.4	96	-52.7	-46.9	-37.8	-40.4
46	-71.7	-64.2	-53.7	-58	97	-31.9	-29.8	-24.4	-24.3
47	-67.7	-61.9	-52.8	-55.5	98	-25.7	-23.6	-18.2	-18.1
48	-68.4	-62.6	-53.5	-56.2	99	-0.2	-0.1	0.9	1.3
49	-69.3	-63.5	-54.4	-57.1	99.5	1.5	1.6	2.6	3
50	-72.8	-65.3	-54.9	-59.1					

Table H20. Section criteria results in the second data set of PLSR models for cumulative boiling point distribution fractions.

% Off (wt.%)	AIC	AICc	AICu	BIC	% Off (wt.%)	AIC	AICc	AICu	BIC
0.5	-15.8	-13.8	-9.4	-10.9	51	-33.5	-30.3	-24.7	-27.4
1	-21.2	-19.2	-14.9	-16.3	52	-33.7	-30.5	-25	-27.6
2	-25.3	-23.3	-19	-20.5	53	-33.4	-30.2	-24.7	-27.3
3	-26.5	-24.5	-20.2	-21.7	54	-34	-30.8	-25.3	-27.9
4	-27	-25	-20.6	-22.1	55	-31.5	-28.4	-22.8	-25.4
5	-27.3	-25.3	-20.9	-22.4	56	-32.2	-29	-23.4	-26.1
6	-27.6	-25.6	-21.2	-22.7	57	-34	-30.8	-25.2	-27.9
7	-27.8	-25.8	-21.4	-22.9	58	-32.6	-29.4	-23.8	-26.5
8	-28.9	-26.9	-22.5	-24	59	-72.7	-57	-44.2	-60.5
9	-29.3	-26.1	-20.5	-23.2	60	-54.8	-45.8	-36.1	-45
10	-29.2	-27.2	-22.8	-24.3	61	-32.6	-30.6	-26.3	-27.7
11	-28.8	-26.8	-22.4	-23.9	62	-31.9	-29.9	-25.6	-27.1
12	-30	-26.8	-21.2	-23.9	63	-31.6	-28.4	-22.9	-25.5
13	-29.8	-27.8	-23.5	-24.9	64	-32.2	-29.1	-23.5	-26.1
14	-30.1	-27	-21.4	-24	65	-32.3	-30.3	-25.9	-27.4
15	-68.5	-52.8	-40	-56.3	66	-31.8	-29.8	-25.5	-27
16	-30	-26.9	-21.3	-23.9	67	-32	-30	-25.6	-27.1
17	-29.9	-26.7	-21.1	-23.8	68	-33.4	-30.3	-24.7	-27.4
18	-29.5	-27.5	-23.1	-24.6	69	-55.3	-46.3	-36.7	-45.6
19	-30	-26.8	-21.2	-23.9	70	-34	-30.8	-25.2	-27.9
20	-29.9	-27.9	-23.5	-25	71	-35.3	-33.3	-29	-30.4
21	-30.1	-26.9	-21.4	-24	72	-35.5	-33.5	-29.2	-30.6
22	-48.4	-39.4	-29.7	-38.6	73	-34.4	-32.4	-28.1	-29.6
23	-28.7	-26.7	-22.3	-23.8	74	-37.1	-35.1	-30.8	-32.3
24	-28.9	-26.9	-22.5	-24	75	-36.1	-34.1	-29.8	-31.3
25	-28.1	-26.1	-21.8	-23.3	76	-33.7	-31.7	-27.3	-28.8
26	-28.7	-26.7	-22.3	-23.8	77	-35.2	-33.2	-28.8	-30.3
27	-29.8	-26.7	-21.1	-23.7	78	-36	-32.8	-27.2	-29.9
28	-30.9	-27.7	-22.1	-24.8	79	-35.9	-33.9	-29.5	-31
29	-30.3	-28.3	-24	-25.4	80	-35.2	-33.2	-28.8	-30.3
30	-51.3	-42.3	-32.6	-41.5	81	-36	-32.8	-27.2	-29.9
31	-31.8	-28.6	-23.1	-25.7	82	-34.5	-32.5	-28.1	-29.6
32	-32.5	-29.4	-23.8	-26.4	83	-35.3	-32.1	-26.5	-29.2
33	-31.7	-28.6	-23	-25.6	84	-34.1	-32.1	-27.7	-29.2
34	-31.7	-28.6	-23	-25.6	85	-52.4	-43.4	-33.8	-42.7
35	-31.8	-29.8	-25.4	-26.9	86	-34.7	-31.5	-26	-28.6
36	-32.1	-30.1	-25.8	-27.2	87	-34.5	-32.5	-28.1	-29.6
37	-72.9	-57.2	-44.4	-60.7	88	-34.7	-32.7	-28.4	-29.8
38	-32.8	-29.7	-24.1	-26.7	89	-35.2	-33.2	-28.8	-30.3
39	-33.1	-29.9	-24.3	-27	90	-35.5	-33.5	-29.2	-30.7
40	-32.7	-30.7	-26.3	-27.8	91	-35.2	-33.2	-28.9	-30.4
41	-32.7	-29.6	-24	-26.6	92	-35.4	-32.2	-26.6	-29.3
42	-32.1	-28.9	-23.4	-26	93	-34.7	-32.7	-28.4	-29.8
43	-31.3	-29.3	-25	-26.5	94	-36.6	-33.5	-27.9	-30.5
44	-31.6	-29.6	-25.2	-26.7	95	-33.4	-30.2	-24.6	-27.3
45	-32.5	-30.5	-26.2	-27.7	96	-30	-26.9	-21.3	-23.9
46	-31.9	-29.9	-25.5	-27	97	-13.7	-13.5	-12.5	-12.5
47	-32	-30	-25.6	-27.1	98	-22.2	-20.2	-15.9	-17.3
48	-32.7	-29.6	-24	-26.7	99	-1.9	-1.4	0.7	0.5
49	-32.3	-30.3	-25.9	-27.4	99.5	-0.1	0.5	2.6	2.4
50	-33.4	-30.2	-24.6	-27.3					

Table H21. Section criteria results in the third data set of PLSR models for cumulative boiling point distribution fractions.

% Off (wt.%)	AIC	AICc	AICu	BIC	% Off (wt.%)	AIC	AICc	AICu	BIC
0.5	-17.7	-17.3	-16.3	-17	51	-39.3	-36	-30.2	-36.8
1	-33.4	-30	-24.2	-30.8	52	-39.8	-36.5	-30.7	-37.3
2	-44.8	-39.8	-31.1	-41.6	53	-38.9	-35.6	-29.7	-36.3
3	-37.8	-34.5	-28.7	-35.3	54	-50	-45	-36.3	-46.8
4	-44.9	-39.9	-31.2	-41.7	55	-40	-36.7	-30.9	-37.5
5	-27	-25	-21.3	-25.1	56	-47.1	-42.1	-33.4	-43.9
6	-45.5	-40.5	-31.8	-42.3	57	-38.9	-35.6	-29.7	-36.3
7	-44	-39	-30.3	-40.8	58	-46.7	-41.7	-33	-43.5
8	-43.7	-38.7	-30.1	-40.6	59	-37.6	-34.3	-28.4	-35
9	-37.1	-33.8	-28	-34.6	60	-43.9	-38.9	-30.2	-40.7
10	-37.3	-34	-28.1	-34.7	61	-37.4	-34	-28.2	-34.8
11	-38.2	-34.9	-29.1	-35.7	62	-43.6	-38.6	-30	-40.4
12	-49.1	-44.1	-35.4	-45.9	63	-45.5	-40.5	-31.9	-42.4
13	-39.9	-36.6	-30.8	-37.4	64	-36.6	-33.3	-27.5	-34.1
14	-49.1	-44.1	-35.4	-45.9	65	-43.2	-38.2	-29.5	-40
15	-38.9	-35.6	-29.7	-36.3	66	-44.2	-39.2	-30.6	-41
16	-38	-34.6	-28.8	-35.4	67	-34.4	-31.1	-25.2	-31.8
17	-37.7	-34.3	-28.5	-35.1	68	-35.2	-31.9	-26.1	-32.7
18	-46.3	-41.3	-32.7	-43.1	69	-38.9	-35.5	-29.7	-36.3
19	-46.1	-41.1	-32.4	-42.9	70	-36.8	-33.4	-27.6	-34.2
20	-37.2	-33.8	-28	-34.6	71	-37.6	-34.2	-28.4	-35
21	-46.2	-41.2	-32.5	-43	72	-47.3	-42.3	-33.6	-44.1
22	-45.8	-40.8	-32.1	-42.6	73	-32.5	-30.5	-26.7	-30.6
23	-46.1	-41.1	-32.4	-42.9	74	-48.6	-43.6	-34.9	-45.4
24	-47.4	-42.4	-33.7	-44.2	75	-39.4	-36.1	-30.2	-36.8
25	-44.5	-39.5	-30.9	-41.3	76	-39.6	-36.3	-30.5	-37.1
26	-35.9	-32.6	-26.8	-33.4	77	-38.6	-35.3	-29.5	-36.1
27	-26	-24	-20.2	-24.1	78	-41.7	-38.4	-32.6	-39.2
28	-26.3	-24.3	-20.5	-24.4	79	-43.1	-39.7	-33.9	-40.5
29	-44.7	-39.7	-31	-41.5	80	-41.8	-38.5	-32.7	-39.3
30	-37.3	-33.9	-28.1	-34.7	81	-42.9	-39.6	-33.7	-40.3
31	-36.5	-33.2	-27.3	-33.9	82	-38.4	-35.1	-29.3	-35.9
32	-37.9	-34.5	-28.7	-35.3	83	-37.3	-34	-28.1	-34.7
33	-46.2	-41.2	-32.5	-43	84	-37.1	-33.7	-27.9	-34.5
34	-38.3	-35	-29.2	-35.8	85	-44.3	-39.3	-30.6	-41.1
35	-47.6	-42.6	-33.9	-44.4	86	-35.2	-31.9	-26	-32.6
36	-41	-37.7	-31.9	-38.5	87	-34.1	-30.8	-24.9	-31.5
37	-47.5	-42.5	-33.8	-44.3	88	-35.7	-32.3	-26.5	-33.1
38	-40.9	-37.5	-31.7	-38.3	89	-36.6	-33.3	-27.5	-34.1
39	-47.3	-42.3	-33.7	-44.1	90	-41.3	-36.3	-27.7	-38.2
40	-48.6	-43.6	-35	-45.4	91	-36.6	-33.3	-27.4	-34
41	-40	-36.7	-30.9	-37.5	92	-42.3	-37.3	-28.6	-39.1
42	-48.3	-43.3	-34.7	-45.1	93	-37.3	-34	-28.1	-34.7
43	-47.3	-42.3	-33.6	-44.1	94	-40.2	-36.8	-31	-37.6
44	-39.7	-36.4	-30.5	-37.1	95	-50.5	-45.5	-36.8	-47.3
45	-40.2	-36.8	-31	-37.6	96	-46.2	-41.2	-32.5	-43
46	-39.1	-35.8	-30	-36.6	97	-47.6	-42.6	-33.9	-44.4
47	-47.6	-42.6	-33.9	-44.4	98	-44.5	-39.5	-30.8	-41.3
48	-48	-43	-34.3	-44.8	99	-45.7	-38.7	-25.8	-41.8
49	-38.3	-35	-29.2	-35.8	99.5	-11	-10.7	-9.7	-10.4
50	-38.8	-35.4	-29.6	-36.2					

485

Table H22. Section criteria results in the fourth data set of PLSR models for cumulative boiling point distribution fractions.

% Off (wt.%)	AIC	AICc	AICu	BIC	% Off (wt.%)	AIC	AICc	AICu	BIC
0.5	-8.1	-7.7	-6.6	-7.7	51	-90	-18	-3.7	-86.8
1	-9.8	-9.4	-8.4	-9.4	52	-63.3	-25.9	-14.8	-60.5
2	-12.3	-11.8	-10.8	-11.9	53	-18.4	-15	-11.5	-17.2
3	-14	-13.5	-12.5	-13.6	54	-63	-25.7	-14.6	-60.2
4	-15	-14.5	-13.5	-14.6	55	-86.5	-14.5	-0.2	-83.3
5	-16.1	-15.7	-14.6	-15.7	56	-68.2	-30.9	-19.7	-65.4
6	-16.3	-15.9	-14.8	-15.9	57	-72.4	-35.1	-23.9	-69.6
7	-15.3	-13.8	-11.6	-14.5	58	-15.3	-14.8	-13.8	-14.9
8	-16.8	-16.4	-15.3	-16.4	59	-62.5	-25.2	-14.1	-59.7
9	-15.7	-14.2	-12	-14.9	60	-74.4	-37.1	-25.9	-71.6
10	-16.7	-16.2	-15.2	-16.3	61	-88.9	-16.9	-2.6	-85.7
11	-16.1	-15.7	-14.6	-15.7	62	-15.1	-14.6	-13.6	-14.7
12	-15.8	-15.4	-14.3	-15.4	63	-18.9	-15.5	-12	-17.7
13	-15.9	-15.5	-14.5	-15.5	64	-15.8	-15.3	-14.3	-15.4
14	-16.3	-15.8	-14.8	-15.9	65	-16.1	-15.7	-14.6	-15.7
15	-16.1	-15.7	-14.6	-15.7	66	-20.6	-17.2	-13.7	-19.4
16	-16.4	-16	-15	-16.1	67	-15.8	-15.3	-14.3	-15.4
17	-20.5	-17.1	-13.6	-19.3	68	-21.5	-14.8	-9.9	-19.9
18	-16.2	-15.8	-14.8	-15.8	69	-15.8	-15.4	-14.3	-15.4
19	-16.9	-16.4	-15.4	-16.5	70	-36.5	-24.5	-17.9	-34.6
20	-16.5	-16	-15	-16.1	71	-16.4	-12.9	-9.4	-15.2
21	-18.3	-14.9	-11.4	-17.1	72	-65.4	-28.1	-17	-62.6
22	-16.9	-16.4	-15.4	-16.5	73	-59.4	-22.1	-10.9	-56.6
23	-16.8	-16.4	-15.3	-16.4	74	-95.7	-23.7	-9.4	-92.6
24	-17.2	-16.8	-15.8	-16.8	75	-58.3	-21	-9.8	-55.5
25	-17.4	-16.9	-15.9	-17	76	-56	-18.7	-7.6	-53.2
26	-19.9	-16.5	-13	-18.7	77	-79.1	-7.1	7.2	-75.9
27	-18.3	-17.9	-16.8	-17.9	78	-57.3	-20	-8.9	-54.6
28	-17.8	-17.3	-16.3	-17.4	79	-78.4	-6.4	7.9	-75.2
29	-18	-17.5	-16.5	-17.6	80	-82.3	-10.3	4	-79.2
30	-18.3	-17.9	-16.8	-17.9	81	-60.1	-22.7	-11.6	-57.3
31	-17.5	-17.1	-16	-17.1	82	-11.5	-11	-10	-11.1
32	-16.6	-16.2	-15.1	-16.2	83	-41.9	-20.9	-12.2	-39.5
33	-16.9	-16.4	-15.4	-16.5	84	-15.8	-9.1	-4.2	-14.2
34	-39.1	-27.1	-20.4	-37.1	85	-12.8	-9.4	-5.8	-11.6
35	-41.6	-29.6	-22.9	-39.6	86	-14.7	-11.3	-7.8	-13.5
36	-90.4	-18.4	-4.1	-87.2	87	-34.6	-22.6	-15.9	-32.6
37	-89.5	-17.5	-3.2	-86.3	88	-16.6	-10	-5	-15
38	-66.3	-29	-17.9	-63.6	89	-16.6	-10	-5	-15
39	-83.1	-45.8	-34.7	-80.3	90	-15	-8.4	-3.4	-13.4
40	-89.6	-17.6	-3.3	-86.4	91	-14.8	-8.1	-3.2	-13.2
41	-14.9	-14.5	-13.4	-14.5	92	-13.2	-6.6	-1.6	-11.7
42	-60.7	-39.7	-31	-58.3	93	-10.8	-4.1	0.9	-9.2
43	-63.3	-26	-14.8	-60.5	94	-8	-7.5	-6.5	-7.6
44	-68.9	-31.6	-20.5	-66.1	95	-6	-5.6	-4.5	-5.6
45	-14.9	-14.4	-13.4	-14.5	96	-4.8	-4.3	-3.3	-4.4
46	-14.6	-14.2	-13.1	-14.2	97	-2.3	-1.8	-0.8	-1.9
47	-87.9	-15.9	-1.6	-84.7	98	-0.1	0.4	1.4	0.3
48	-16.1	-15.7	-14.6	-15.7	99	1.8	2.3	3.3	2.2
49	-21	-14.4	-9.4	-19.4	99.5	1.8	2.2	3.3	2.2
50	-52.1	-31.1	-22.4	-49.7					